Advanced High Resolution Electrospray Ionization Mass Spectrometric Protocols for Imaging Complex Polymer Chain Structures

Zur Erlangung des akademischen Grades eines

DOKTORS DER NATURWISSENSCHAFTEN

(Dr. rer. nat.)

der KIT-Fakultät für Chemie und Biowissenschaften

des Karlsruher Instituts für Technologie (KIT)

genehmigte

DISSERTATION

von

M. Sc. Jan Steinkönig

aus

Karlsruhe, Deutschland

1. Referent: Prof. Dr. Christopher Barner-Kowollik

2. Referent: Prof. Dr. Hans-Achim Wagenknecht

Tag der mündlichen Prüfung: 17.04.2018

Erklärung

Ich erkläre hiermit, dass ich die vorliegende Arbeit im Rahmen der Betreuung durch Prof. Dr. Christopher Barner-Kowollik selbstständig verfasst und keine anderen als die angegebenen Quellen und Hilfsmittel verwendet habe. Wörtlich oder inhaltlich übernommenen Stellen sind als solche kenntlich gemacht und die Satzung des Karlsruher Instituts für Technologie (KIT) zur Sicherung guter wissenschaftlicher Praxis wurde beachtet.

Des Weiteren erkläre ich, dass ich mich derzeit in keinem weitern laufenden Promotionsverfahren befinde und auch keine vorausgegangenen Promotionsversuche unternommen habe.

Karlsruhe, den 14.05.2018

_____

Jan Steinkönig

"The comfort zone is a psychological state in which one feels familiar, safe, at ease, and secure. You never change your life until you step out of your comfort zone; change begins at the end of your comfort zone."

— Roy T. Bennett

ABSTRACT

The systematic assessment of polymeric chain structures is essential for an in-depth mechanistic understanding of macromolecular processes. The access to precise structural information of organic, oligomeric and macromolecular compounds is provided by high resolution electrospray ionization mass spectrometry (ESI MS). The mild conditions associated with the ionization process are essential to retain the chains' covalent bond integrity. In the present thesis, high resolution ESI-Orbitrap MS is used as a platform technology to access chain structure information from complex demanding macromolecular systems. Importantly, the high resolution provided by the Orbitrap's design and data evaluation allow for the precision mass determination associated with a detailed insight into the species' isotopic pattern. The structural assignment of the polymer depends on the comparison of the experimental isotopic pattern with a simulation based on the assigned chemical formula. Critically, a reliable access route to non-polar polyhydrocarbons (such as poly(styrene) and poly(1,4-butadiene)) is established via chloride attachment in negative ion mode. The remarkably strong coordination of halides (here chloride) with aromatic or olefinic motifs promotes ionization beyond singly charged species and showcases that high-molecular weight polyhydrocarbons can be ionized efficiently. Furthermore, the observed polyhydrocarbon's charge state distribution can be adjusted by adding auxiliary supercharging agents such as sulfolane or propylene carbonate to the ESI solution. The established chloride attachment in the negative ion mode is the basis of multiple macromolecular elucidations including poly(ionic liquid)s (PILs), nitroxide-containing polymers and the efficient ionization of degradable step-growth polymers. In addition, ESI MS benefits significantly from the coupling to size exclusion chromatography (SEC-ESI MS). The present thesis describes a powerful characterization techniques for intrachain crosslinked linear precursor polymers to single chain nanoparticles (SCNPs) by SEC-ESI MS hyphenation. The high resolution MS characterization of this important class of nanoparticles provides direct insight into the chemistry of the folding process for every single polymer chain in solution, thus enabling direct insight into the folding mechanism. Finally, the established platform is capable of imaging even complex ter-

and quaterpolymers prepared by a sequence-regulated step-growth Passerini polymerization as demonstrated in the present thesis.

Kurzzusammenfassung

Die systematische Strukturaufklärung von Makromolekülen ist ein wesentlicher Bestandteil zum tiefgehenden Verständnis von makromolekularen Prozessen. Der Zugang zur exakten Strukturaufklärung ist durch die Verwendung von hoch-auflösender Elektrospray-Ionisation (ESI MS) gewährleistet. Die milden Ionisierungsbedingungen sind unentbehrlich um intakte kovalente Bindungen in der Polymerkette sicherzustellen. Die vorliegende Doktorarbeit behandelt die Strukturaufklärung verschiedener komplexer makromolekularer Systeme mittels ESI-Orbitrap MS. Für die exakte Massenbestimmung ist die Hochauflösung entscheidend, die durch das Design der Orbitrap und die Datenverarbeitung bereitgestellt wird. Hierdurch ermöglicht sich die präzise Untersuchung einzelner Spezies und deren Isotopenmuster. Diese bildet die Grundlage nachfolgender Strukturaufklärungen, da das experimentelle mit dem simulierten (aus der zuvor bestimmten chemischen Strukturformel) Isotopenmuster verglichen wird. Zuvor ist die zuverlässige Ionisierung unpolarer Polykohlenwasserstoffe (z.B. Polystyrol und Polybutadien) unerlässlich, die durch die Anlagerung von Chlorid-Ionen gewährleistet wird. Hierfür wird das Massenspektrometer in einer für negative Ionen sensitive Betriebsweise gesetzt. Die Anlagerung von Halogeniden an aromatische oder olefinische Strukturelemente ist bemerkenswert stark, sodass eine Mehrfachionisierung hervorgerufen wird. Darüber hinaus kann die Verteilung des Ladungszustands der Polykohlenwasserstoffe durch einfache Zugabe von sog. 'Supercharging' Agenzien (z.B. Sulfolan oder Propylencarbonat) beeinflusst werden. Die hier neuentwickelte Methode zur Anlagerung von Chlorid-Ionen bildet die Grundlage zur Aufklärung verschiedenster funktionaler Makromoleküle, unter anderem von polyionischen Flüssigkeiten und Polymeren mit Nitroxid-Sturkturelementen. Des Weiteren können degradierbare Stufenwachstumspolymere effizient in die Gasphase versetzt und somit vermessen werden. ESI MS profitiert auch durch eine vorangeschaltete Größenausschlusschromatographie (SEC-ESI MS). Hierdurch können intramolekular vernetzte Polymere – sogenannte Einzelkettennanopartikel – charakterisiert werden, wodurch ein direkter Einblick in die Chemie des Faltungsprozesses ermöglicht wird. Mittels der entwickelten Methode können sogar komplexe Ter- oder Quaterpolymere strukturell aufklären werden.

PUBLICATIONS ARISING FROM THIS DISSERTATION

[8] Radical-Induced Single-Chain Folding of Passerini Sequence-Regulated Polymers Visualized by High-Resolution Mass Spectrometry, Steinkoenig, J.; Nitsche, T.; Tuten, B. T.; Barner-Kowollik, C. *Macromolecules* **2018**, *submitted.*

[7] Unraveling the Spontaneous Zwitterionic Copolymerisation Mechanism of Cyclic Imino Ethers and Acrylic Acid, Steinkoenig, J.; de Jongh, P. J. M.; Haddleton, D.; Goldmann, A. S.; Barner-Kowollik, C.; Kempe, K. *Macromolecules* **2018**, 51, 318-327.

[6] Dual Gated Chain-Shattering Based on Light Responsive Benzophenones and Thermally Responsive Diels-Alder Linkages, Steinkoenig, J.; Zieger, M. M.; Mutlu, H.; Barner-Kowollik, C. *Macromolecules* **2017**, *50*, 5385-5391.

[5] Imaging Single-Chain Nanoparticle Folding via High-Resolution Mass Spectrometry, Steinkoenig, J.; Rothfuss, H.; Lauer, A.; Tuten, B. T.; Barner-Kowollik, C. *J. Am. Chem. Soc.* **2017**, *139*, 51-54.

 [4] Supercharging Synthetic Polymers: Access to Mass Spectrometric Imaging of Non-Polar Synthetic Polymers, Steinkoenig, J.*; Cecchini, M. M.*; Reale, S.; Goldmann, A. S.; Barner-Kowollik, C. *Macromolecules* **2017**, *50*, 8033-8041

[3] Just Add Salt: A Mass Spectrometric Analysis Method for Imaging Anion-Exchanged Poly(Ionic Liquid)s, Steinkoenig, J.*; Cecchini, M. M.*; Goldmann, A. S.; Reale, S.; De Angelis, F.; Barner-Kowollik, C. *Macromol. Rapid Commun.* **2016**, *37*, 1662-1666.

[2] Universal Mass Spectrometric Analysis of Poly(Ionic Liquid)s, Cecchini, M. M.*; Steinkoenig, J.*; Reale, S.; Barner, L.; Yuan, J.; Goldmann, A. S.; De Angelis, F.; Barner-Kowollik, C. *Chem. Sci.* **2016**, *7*, 4912-4921.

[1] Controlled Radical Polymerization and In-Depth Mass-Spectrometric Characterization of Poly(Ionic Liquid)s and their Photopatterning on Surfaces, Steinkoenig, J.; Bloesser, F. R.; Huber, B.; Welle, A.; Trouillet, V.; Weidner, S.; Barner, L.; Roesky, P. W.; Yuan, J.; Goldmann, A. S.; Barner-Kowollik, C. *Polym. Chem.* **2016,** *7*, 451-461.

* These authors contributed equally

CONTENTS

1

INTRODUCTION

"We learned to make elephants fly," said John Fenn, Nobel Prize laureate in 2002 after having developed a soft ionizing method for large (bio)macromolecules via electrospray.[1] By the time his revolutionary research was about to be published in 1988, he was at his age of 70 years and an emeritus at Yale University. The university had downsized his financial situation to a small office without being allowed to supervise graduate students to further develop the technique. Finally, the Virginia Commonwealth University funded his research and provided him with a fully furnished laboratory for his research, where Fenn was able to further develop the electrospray ionization. Despite a legal dispute with Yale University – Fenn held a personal patent on the electrospray techniques, which was against Yale's policies –, he established a fundamental technology to 'make elephants fly'.[2] His endurance to withstand financial pressures and the passion for his research paid off and Fenn became a Novel Prize Laureate. His groundbreaking work is the fundament of the current thesis evaluating

novel access routes for macromolecular ionizations. In Fenn's words: Make the non-polar elephants fly.

Nowadays, soft ionization equips researchers to study the exact structure of natural biomacromolecules, i.e. proteins, DNA and RNA. Interactions between proteins are critical in order to understand the signal transition. Such non-covalent biomolecule complexes can be examined with ESI. The method is superior to other methods regarding its rapidity, sensitivity and identification of the actual interaction. Applications include:[1]

Pharmaceuticals development: The early phase of pharmaceuticals development has undergone a paradigm shift. Combined with liquid separation, ESI MS has enabled the assessment of several hundred compounds per day.[1]

Malaria: Scientists have recently discovered new ways of studying the spread of malaria. Early diagnosis is possible thanks to the soft ionization.[1]

Food control: ESI technology has also progressed to small molecule analysis. An increasing number of substances are hazardous to health, e.g. acrylamide which can cause cancer. Mass spectrometry allows for the rapid analysis of food at various stages of production. By modifying the temperature and the ingredients, potential harmful substances can be avoided or minimized.[1]

By its applications in life sciences i.e. determining the fundamental mechanism how soft matter interact, soft ionization techniques gained great interest in polymer science. The present thesis will draw a detailed picture of Fenn's electrospray ionization technique and equip the reader with the fundamental knowledge of the accepted charge-to-analyte transfer mechanisms. Furthermore, a detailed review of different mass analyzers is presented. Here, Orbitrap is the most prominent candidate as the results presented in the current thesis are based on this specific high resolution mass analyzer.

One overarching aim of the present thesis is to develop ionization platforms to efficiently image non-polar macromolecules (i.e. polyhydrocarbons) and very polar macromolecules (i.e. poly(ionic liquid)s). Both macromolecules are considered to constitute major challenges in mass spectrometry. For instance, polyhydrocarbons are not equipped with dipoles and electron-donating motifs such as esters, ethers or amines. Such motifs are known to efficiently coordinate Na^+. Consequently, the lack of polar groups reduces the ion abundances significantly. An efficient ionization platform for polyhydrocarbons is presented in Chapter 3 implementing for the first time

a negative ionization route via chloride attachment. Poly(ionic liquid)s, on the other hand, are very polar macromolecules ('salt polymers') entailing dipoles and electron-donating motifs. However, the counter ions of the polymers are conductive and the additional ions suppress the polymer signals entirely (ion suppression). Thus, mass spectrometry is a major challenge for this entire class of polyelectrolytes. The current thesis provides an efficient ionization route for the characterization of poly(ionic liquid)s in Chapter 4.

The second overarching aim of the present thesis is to establish mass spectrometry as an approach for mechanistic elucidations. Here, mass spectrometry provides a direct view into the polymer chain structure by specific mass changes that the macromolecule undergoes during reaction. The most important mechanistic assessment covered in the current thesis include intrachain crosslinking reactions (also known as single-chain folding) and light-induced degradation of polymers (self-immolative motifs). In particular, the main characterization route for the hydrodynamic radii changes during a single-chain folding have been assessed via morphological techniques. A direct (mechanistic) view into the formation of nanoparticles during collapse was not available. Here, mass spectrometry can give direct access to the determination and clarification of such folding processes by the specific mass-to-charge ratio, which the chain undergoes during the collapse. The novel characterization technique is presented in Chapter 6. The motivation to study the degradation mechanism of polymers via mass spectrometry is that the soft ionization provides an efficient access to all by-products that accumulate during the disassembly process. Thus, the main characterization routes include size-exclusion chromatography for macromolecular weight determination and nuclear magnetic resonance for structural elucidations. Often, however, the proton resonances of the compound and the small molecules formed after degradation are isochronous, which makes a simple and fast evaluation by their resonances challenging. Mass spectrometry provides a platform to obtain full mechanistic information by chain termini elucidations, and it thus allows to draw a detailed mechanism of the degradation process. Such data evaluation of a degradable polymer is presented in Chapter 7. The following Figure 1 collates the overarching aims of the present thesis and an illustrative representation of the corresponding projects.

Figure 1 Overview of the overarching aims of the present PhD thesis including efficient ionization (with the corresponding projects in Chapter 3 and 4) and mechanistic investigations (with the corresponding projects in Chapters 5-7).

2

THEORETICAL BACKGROUND AND LITERATURE OVERVIEW

The following chapter collates an overview on the theoretical background and literature, to which the projects of the present dissertation are related. The present work is situated at the interface between polymer science and in-depth molecular characterization, in particular represented by high resolution mass spectrometry. Hence, a comprehensive literature overview including the historical evolution, recent developments in the field of soft ionization techniques, and advanced topics on the manipulation of charge states (known as supercharging) in mass spectrometry is provided. Furthermore, an outline of a plethora of polymerization techniques is given constituting the basis of polymer science as well as materials science. The research projects described in the present dissertation were realized by either step-growth or chain-growth polymerization, whose mechanistic differences will be highlighted. For instance, specific functional macromolecules such as poly(ionic liquid)s, single-chain

polymeric nanoparticles and self-immolative polymers will be defined, described and their characteristics explained. Finally, an overview on modular (light-induced) ligation techniques is provided.

2.1. MASS SPECTROMETRY

The thesis addresses advanced mass spectrometric (MS) platforms for the deduction of macromolecular chain structures, including (quantitative) end group determination and the elucidation of complex mechanistic scenarios. Therefore, a critical overview of the relevant literature is given, along with the theoretical background required to understand mass spectrometric concepts.

2.1.1. A brief history

The father of mass spectrometry is J. J. Thomson (Nobel Prize laureate in Physics 1906 for conductivity of electricity by gases)[3,4] who pioneered the field by measuring charge-to-mass ratios (i.e. ionized atoms). Subsequently, Francis Aston (supervised by Thomson) built the first mass spectrometer with the ability to detect charged atoms by using discharge tubes generating the ions.[5] Later, the Manhattan Project and World War II pushed MS as a technique to prove the existence of elemental isotopes.[4] Revolutionary contributions by Alfred Nier, including 60° sector field mass spectrometry (known as Nier-Johnson geometry), enabled the isolation of uranium-235 and provided evidence that ^{235}U undergoes a slow neutron fission.[6-9] Fred McLafferty,[10] Klaus Biemann[11] and Carl Djerassi[11] elucidated the fragmentation mechanism of organic molecules during the ionization process, ultimately allowing chemists to precisely determine the structure of unknown organic molecules. Biemann pioneered in the determination of complex molecules and laid the groundwork for modern proteomics.[12] Nowadays, the contributions of MS to the proteomics sector is remarkable, advancing to the dominant platform for protein and cell compartment determination.[13,14]

However, spectra obtained with mass spectrometers available hitherto had a low signal resolution with large errors making precision chemical formula determination challenging. The resolution (*R*) is a certain value indicating two adjacent signals to be baseline separated (given as $R = m \cdot \Delta m^{-1}$).[15,16] Alan Marshall and Melvin Comisarow

further improved the prevalent measurement techniques of low-resolution mass spectrometry by implementing the well-known phenomenon of ion cyclotron resonance (ICR) (discovered by J. A. Hipple in 1949)[17] coupled with Fourier transformation (FT) to read out the mass-to-charge ratio.[18] Thus, high resolution FT-ICR MS was first reported in 1974 progressing the field of MS significantly by having small errors making chemical formula determination more precise.

In the 1980s, MS was a well-established characterization technique for organic molecules. However, large macromolecules such as nucleic acids, carbohydrates and proteins provided a major challenge as the harsh conditions for ionization induced fragmentation and decomposition. Although fast atom bombardment (FAB), plasma desorption, and thermospray ionization provided access to small proteins, the state or the art technology back in these days were not suitable in ionizing larger proteins.[4] In 1988, electrospray ionization (ESI) and matrix assisted laser desorption ionization (MALDI) were reported – almost simultaneously – revolutionizing biological MS by producing intact peptide ions. Due to their exceptional mild ionization protocols, they are still the dominant pathways to ionize macromolecules. A substantial contribution is attributed to John Fenn[19] (Nobel Prize laureate in Chemistry 2002 for ESI)[20] for discovering the electrospray phenomenon and the idea to introduce a soft ionization method for large (bio)macromolecules. Simultaneously, Franz Hillenkamp and Michael Karas investigated the laser-induced desorption of small molecules from surfaces.[21] Although Koichi Tanaka was awarded the Nobel Prize jointly with John Fenn 2002, Tanaka is not the inventor of MALDI but developed a MALDI-based (soft laser desorption (SLD)) access to high-molecular (bio)macromolecules such as proteins. Both techniques have their advantages, which make them indispensable for a wide variety of applications nowadays. ESI can be readily coupled to separation techniques (i.e. high-pressure liquid chromatography (HPLC), size-exclusion chromatography (SEC)), whereas MALDI tolerates contaminations (i.e. salt, detergent).[4]

The background information provided in the following section showcases the importance of soft ionization techniques to retain the full structural integrity of a macromolecule. Next, the ESI process, especially highlighting the proposed gas-ion formation mechanism, is discussed.

2.1.2. Mass Analyzers

From a historical perspective, the development of precise mass analyzers advanced as standard platform for small molecule analysis and macromolecular characterization alike. Coupled to ionization techniques (ESI/MALDI), the success of mass spectrometry is the unique synergy between ionization and mass separation afforded by a mass analyzers. The present section will focus on mass analyzers that are widely available in combination with soft ionization techniques such as the quadrupole mass filter, time-of-flight (ToF) as well as ion traps such as Orbitrap. The Orbitrap will be discussed in detail as it is the mass analyzer of choice used in all projects described in the following chapters. Ion traps and ToF mass analyzers are economic alternatives and thus widely employed that will be discussed briefly as well in the following section.

Quadrupole Mass Filter

Quadrupole (Q) mass filters (Wolfgang Paul, Nobel Prize laureate 1989) are powerful mass filters whose first utilization dates back to the 1970s.[22] The fabrication of the four parallel metal rods is economic and they are operated by connecting each opposite rod pair electrically, where a radiofrequency (RF) voltage with a direct current offset is applied. As ions travel through the rods, only certain mass-to-charge ratios are stable (their trajectory can be described with the Mathieu differential equation),[23] whereas the unstable trajectories will collide with the rods. The fast scanning of narrow mass windows gave the quadrupole the function as a 'mass filter'. Due to their versatility, quadrupoles are the most widely used devices in mass spectrometry. For instance, employed as hybrid mass spectrometers, quadrupole mass filters find broad application in, e.g. ESI Quadrupole-Time-of-Flight (ESI-QToF) combining a low resolution quadrupole mass filter (Q) and a high-resolution mass analyzation (ToF) or as triple-quadrupole (ESI-QQQ). Developed to avoid each other's disadvantage, quadrupole and Orbitrap have been commercialized as ESI-QOrbitrap settings.

Time-of-Flight (ToF)

ToF analyzers became very important as Hillenkamp and Karas developed MALDI soft ionization. Within this analyzer method, the ions are separated by their time of flight in ultrahigh vacuum. Importantly, ToF analyzers require precise start times, which can be realized, e.g., by pulsed laser desorption methods. Thus, continuous ionization techniques as represented by e.g. ESI, are not well suited. Due to the

ion's kinetic energy deviations caused by the desorption process, modern ToF analyzers are equipped with an ion mirror (reflectron). Hence, the ions a decelerated in an electrostatic field and accelerated in reverse direction resulting in enhanced spectral resolution and ion sensitivity. The mass range of ToF analyzers is unlimited. However, polymer samples have to be well-defined (dispersity below 1.1 give best results, broader samples require work-arounds and can suffer ion sensitivity), and interactions with the incident light beam can photochemically interfere with the sample.
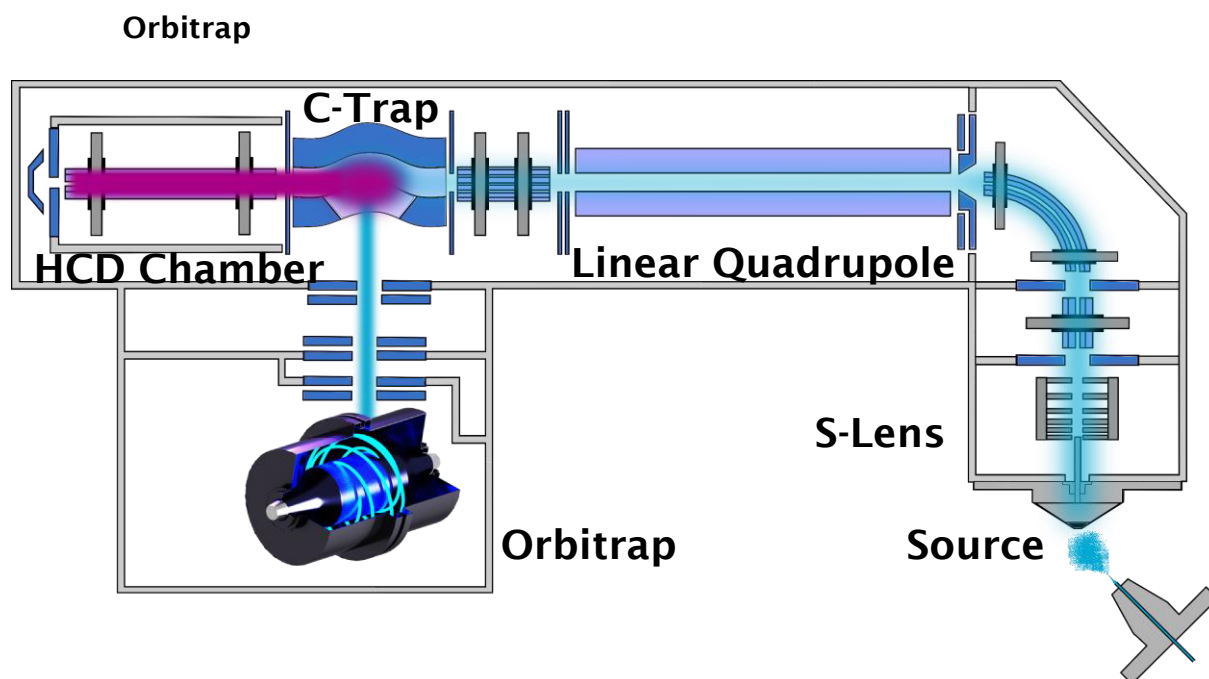
Orbitrap

Figure 2 Scheme of a QExactive Orbitrap mass spectrometer commercialized by Thermo Fisher. Copyright Thermo Fisher 2005.

Orbitraps are ion traps and represent the most modern mass analyzers commercialized in 2005. **Figure 2** collates the setup of modern Orbitraps. After ion generation (detailed process is showcased in the following section) in the atmospheric pressure ionization (API) source, the ions enter a chamber held under vacuum (1.5 Torr) where they enter the S lens setup. The S lens comprises several metal electrodes to focus the ion beam. The mass spectrometer applies a RF voltage to the electrodes, and adjacent electrodes have voltages of opposite phase. As the RF amplitude increases, ions of progressively higher mass-to-charge ratios pass through to the exit lens where the ion beam passes a so-called active beam guide (90° bend flatapole) reducing the noise of neutral species not being guided to the linear quadrupole. Here, in-source collision induced dissociation (CID) can be applied. A source offset ranging from 0 to 100 eV (200 eV in QExacative Plus) can be applied, whereas the DC offset combines the capillary DC, S lens DC and exit lens DC. Thus, the analyte is accelerated into the flatapole, where the species can collide with residual source gas molecules

for an induced fragmentation. Often, in-source CID enhances the ion sensitivity as the analyte is accelerated and does not necessarily undergo a fragmentation.[24,25] The major task of a quadrupole has been outlined previously. The ion beam enters the C-trap, a very crucial component in the mass spectrometer setup: the C-trap is a gas-filled curved linear trap accumulating and decelerating the entering ions. After reaching a certain preset time (e.g. 50 µs) the ions are injected into the Orbitrap for subsequent mass analysis or transferred to the higher-energy collision dissociation (HCD) chamber (sometimes HCD is referred to as higher-energy C-Trap dissociation). The electrical offset (given in eV) between C-Trap and HCD chamber accelerates the ions into a gas-filled chamber where the precursor ions undergo induced fragmentation. Fragment ions are stored in the C-trap and transferred to the Orbitrap. In the Orbitrap, the ion are injected tangentially into an electrostatic field (generated by an inner axial spindle and an outer barrel-like electrode), the carefully manufactured and optimized shape of the electrode balances the centrifugal forces in a way that keeps the ions on stable trajectories orbiting around the spindle. Their high resolving power (up to 280 000) ranks Orbitraps under the most precise bench-top mass analyzers.

2.1.3. Electrospray Ionization Mechanism

The ESI mechanism remains a highly debated subject in mass spectrometry even decades after Fenn's revolutionary discovery. After early ESI MS reports in 1968,[19] a plethora of experiments were performed to identify how charged droplets transfer the charge and subsequently release the charged analyte from the solvent shell to form gas-phase molecular ions. Charged droplets are produced in the electrospray process when an electrically conductive liquid is exposed to an electric field. Due to the solution's surface tension, a deformation occurs countering the electric force. Reaching a specific limit force, the shape of a cone appears emitting a jet (fine mist) of liquid at its tip (called cone-jet) marking the beginning of the electrospraying process. The initial droplets have radii in the micrometer range, yet the analyte is fully surrounded by solvent molecules. Upon Coulomb emission, the droplet size is reduced dramatically on a short time scale by solvent evaporation. The charge density in the droplet increases until the surface tension balances the Coulomb repulsion (Rayleigh limit). Droplets close to the Rayleigh limit undergo jet fission producing

smaller, highly charged offspring droplets. Repeated evaporation/fission events ultimately yield in nanometer sized droplets.

The charge-to-analyte transfer is not fully understood and subject of ongoing research. Recently, the development of advanced molecular dynamics simulations revealed possible scenarios, whose most prominent mechanisms are explained below. Konermann et al. present detailed molecular dynamics simulations based on investigation of the ESI mechanism comprising the ion ejection model (IEM), the charge residual model (CRM) and – for the first time proposed – the chain ejection model (CEM).[26] Historically, the IEM and CRM were controversially discussed with evidence provided for both models. Theoretical considerations regarding the CRM was published by Rayleigh (1882)[27] and Dole contextualized Rayleigh's work with ESI in 1968[28] and 1970.[29] IEM was suggested by Iribane and Thomson in 1975.[30] The CRM is the accepted model for the formation of nanometer sized droplets from micrometer scaled ones. Depending on the analyte size it is proposed that CRM also transfers the charge to the analyte. Representative analytes are native proteins, having a globular shape. In contrast, the IEM is discussed for small analytes. Iribane and Thomson discuss that a charge residual leading to jet emission of small molecules is unlikely since the droplet never become sufficiently small to contain only one analyte. Prior to the jet fission close to the Raleigh limit, the charge density on the surface is so high that the resulting electrostatic field is sufficiently intense to catapult one or more gas-phase ions out of the solvent shell.

To achieve a deeper understanding of the ESI mechanism it is critical to comprehend how charges behave in a droplet close to the Rayleigh limit. Gauss' Law dictates electric charges to migrate to the outer surface (in an isolated conductor). In molecular dynamics simulations, Konermann et al. showed that the ions prefer a position in the droplet interior – well solvated by the solvent.[26] Due to the induced dipole of the polar solvent, the net charge is located at the outer surface and thus obey Gauss' Law.

Ion Ejection Model (IEM)[26]

The IEM is based on a sufficiently high electric field causing the ejection of small solvated ions from the droplet surface. Transition state theory in combination with molecular dynamics simulations suggest that ions need to cross an activation barrier (escaping the attractive energy of solvation) of ~32 kJ·mol^{-1}.[26] After rapturing the parent solvent shell, the very small offspring ion collides with ambient gas and
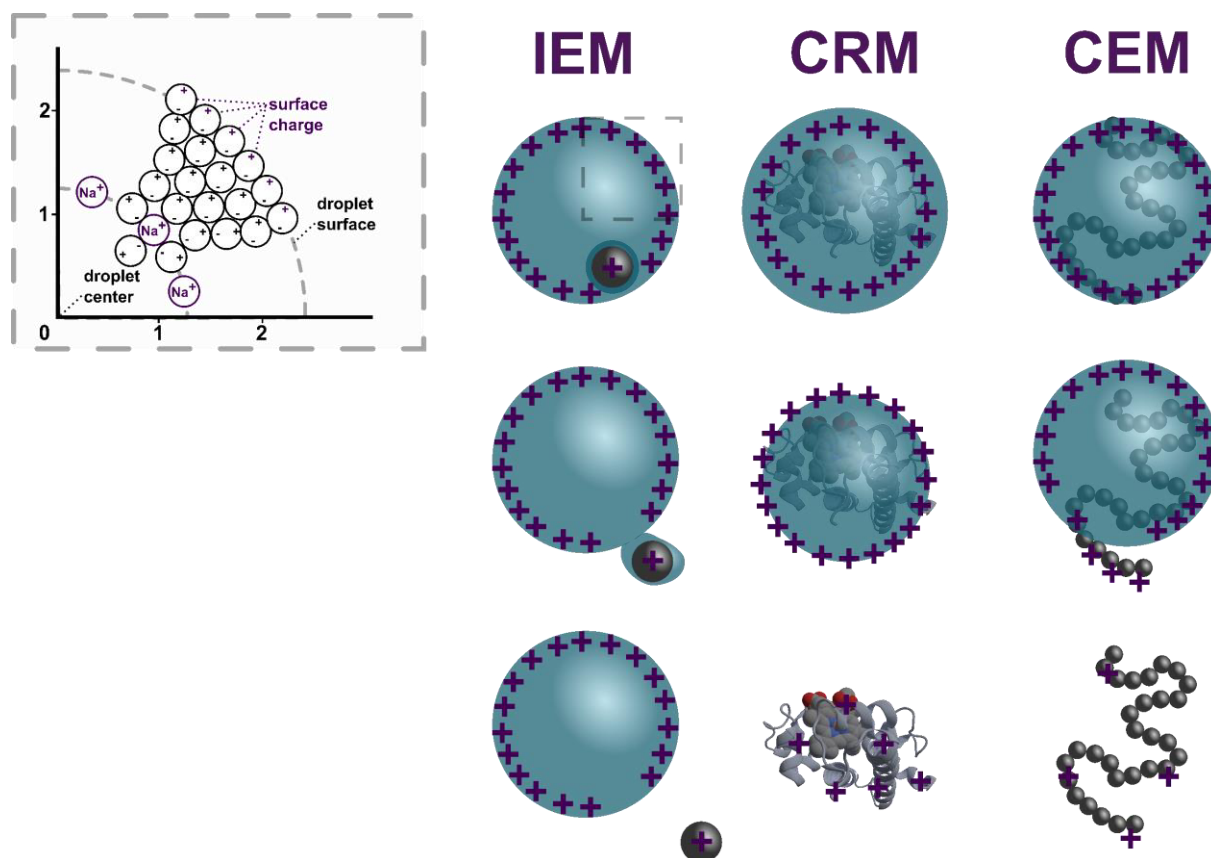
Figure 3 Schematic representation of the ion ejectionmodel (IEM), the charge residual model (CRM) and the chain ejection model (CEM). Cartoon illustration of an ion that interacts with two oriented dipoles (as zoom into the first IEM droplet).

loses the residual solvent molecules. It is believed that small analytes, protonated drugs and metabolites ionize via IEM. Particularly, the high ion abundance caused by non-polar moieties support the IEM since they tend to orient close to the droplet surface (high surface affinity).[26]

Charge Residual Model (CRM)[26]

The CRM is the widely accepted – though controversially debated[31] – model how large, globular species such as natively folded proteins are released into the gas phase. Here, Rayleigh-charged nanodroplets evaporate to dryness, transferring the charge directly to the analyte. Throughout the solvent evaporation, ions (e.g. sodium ions) are ejected into the gas phase via IEM thus keeping the droplet at the Rayleigh limit while its size is decreasing. In contrast to the IEM, the CRM is challenging to simulate via molecular dynamics simulations due to its microseconds time scale.

Nonetheless, computational studies imply that an ejection via the IEM of the folded protein is kinetically not preferred.[26]

Chain ejection model (CEM)[26]

Fenn realized that the charge state of poly(ethylene glycol) (PEG) was higher than the Rayleigh prediction suggested and therefore proposed a different ESI mechanism including a chain elongation caused by Coulomb repulsion of the charges resulting in elongated droplets with conical ends that accumulate the charge density.[31] Molecular dynamics simulations independently performed by Konermann[26,32] and Consta[33,34] revealed alternative scenarios how droplets respond beyond the Rayleigh limit. For instance, Konermann addresses important ESI efficiencies, i.e. a high ESI efficiency entails rapid desolvation (or ejection) from the droplet rather than being imprisoned in the solvent shell being defined as inefficient ESI process.[32] Since the ESI efficiency is dependent on the polarity of the polymer, which is governed by the respective types of monomers,[32] the chain ejection mechanism must be subdivided into polymer type-dependent scenarios (**Figure 4**). A macromolecule with nonpolar side chains is expelled stepwise from the droplets' surface (**Figure 4a**).[32] Interestingly, Consta revealed that the CEM as represented in **Figure 4a**, was confirmed for aqueous solutions only, since PEG behaved differently in organic medium.[33] In methanol, the droplet escape the Rayleigh limit by forming small offspring droplets in a necklace-like orientation (**Figure 4b**). Protonated poly(histidine) as polyelectrolyte in aqueous solution leads to high droplet deformations (spine-like ordered structures).[34]

Although a plethora of (computational) work has afforded an in-depth view into the ESI mechanism, the CEM is still subject of ongoing research. Hitherto, exclusively the positive ion mode (via protonation or sodiation) has been covered in very polar solvents (i.e. water, methanol) and very polar polymers. Nonpolar polymers such as poly(styrene) (PS) and poly(butadiene) (PBD) have very low efficiencies. According to Konermann, such polymers are caught in the solvent shell and might be expelled by a different mechanism.[26]

The present section showcased the ESI mechanism. The next section covers the supercharging effect which manipulates the observed charge states of the macromolecule.
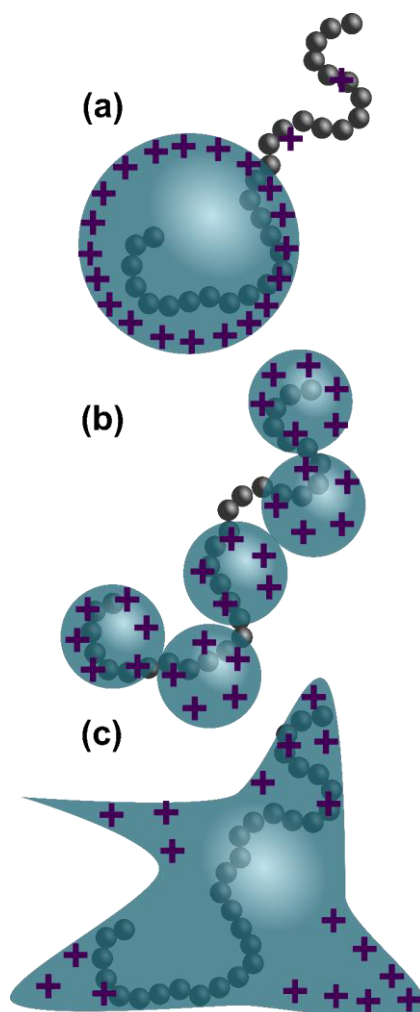
Figure 4 Models of stable droplet-chain conformations beyond Rayleigh limit. (a) A part of the chain is ejected leaving the droplet below Rayleigh limit. (b) The droplet is split into several offspring droplets, each below Rayleigh limit. (c) Observed conformations of charged poly(histidine) in water at high charges. The assumptions of the Rayleigh model are not valid.

2.1.4. Supercharging

During the charge-to-analyte transfer, the droplet's response close to the Rayleigh limit and its impact on the gas phase ion generation is a critical and important aspect to consider. A further crucial parameter is the analyte-charge interaction that influences the ESI mechanism and the ESI efficiency alike. Recently, the analyte-charge interplay became more of a focus in the investigation of the ESI mechanism as Williams[35] proposed the so-called supercharging effect showing that the addition of certain small molecules – with high polarities and surface tension[35,36] – can manipulate the observed charge state of proteins.[37] The shift of a protein's charge state allows for accessing high-molecular weight macromolecules. Even more importantly, many physical properties of the gas phase ion change with its charge state, e.g. proton

transfer,[38] ion-ion reactivity,[39] fragmentation pathway[40] and efficiency of electron-capture cross sections (ECD).[41] Thus, supercharged proteins open avenues for modern proteomics including their precision sequence determination (top down method).[42]

Currently, the supercharging mechanism is highly debated and as the ESI mechanism not fully unraveled. Taking the different ionization models into consideration, four distinct scenarios attempt to explain the charge shift of proteins.

Berkeley mechanism

Discovered by Williams and co-workers at the University of Berkeley,[35] the Berkeley mechanism is the first and most prominent – though controversially debated[43,44] – mechanism. Here, Williams proposes a retarded formation of the gas-phase ions caused by the low volatility of the added molecules.[45] A wide range of such supercharging agents have been discussed in the literature ranging from *m*-nitrobenzyl alcohol (*m*NBA), sulfolane, propylene carbonate (PC), ethylene carbonate (EC), dimethyl sulfoxide (DMSO) and *o*-nitroanisole amongst others.[37,46] All mentioned compounds share the high surface tension as a physical property. Williams and co-workers concluded that the increased surface tension allows droplets to decrease their radii further before the Rayleigh limit is reached.[45] Offspring droplets after Rayleigh fission contain more ions as they would without supercharging agent. Recently, Loo and co-workers introduced further supercharging agents that were added as solids and thus reduce the overall surface tension.[43] Their results and Konermann's molecular dynamics simulations[44] questioned the role of the surface tension and the Berkeley mechanism.

Lewis acid/base mechanism

An essential parameter for high ion abundances is the ESI efficiency, which is governed by the droplet shell escape and the Lewis basicity (ability to coordinate to H^+ or Na^+) as well as Lewis acidity (ability to transfer a proton to the solvent). Under non-supercharging conditions, the solvent and the analyte compete for the available charges in the droplet. Supercharging agents have a lower Lewis basicity than water. Since high amounts of supercharging agents are employed (up to 50% *v*/*v*), the charge competition between water and protein is highly reduced. Thus, the charge-analyte equilibrium is shifted to higher amounts of charged analyte.[47]

Dipole-based mechanism

First proposed by Douglass and co-workers,[36] the dipole-based mechanism is the first approach considering interactions between supercharging agent and analyte.

During the CRM, the maximum amount of the protein's Lewis basic regions limits the theoretical charge state. Experimentally, however, the charge state is limited by the Coulomb repulsion of Lewis basic moieties in close proximity. As proposed, super-charging agents coordinate to the ions after their attachment to the Lewis basic moiety via dipole interactions. Thus, the repulsive interactions are shielded facilitating the attachment of further charges to Lewis basic moieties in close proximity.[48]

Charge-trapping mechanism

Based on molecular dynamics simulations, Konermann et al. studied the interactions of supercharging agent with the solvent and the analyte.[44] Their simulations suggest a solvent segregation leading to an aqueous core containing the analyte and a shell consisting of the supercharging agent. The supercharging mechanism appears to be a two stage process commencing with the ejection of ion/water clusters (e.g. H^+ or Na^+) via IEM thus reducing the droplet's radius containing the analyte, the super-charging agent, water and the ions. As soon as the water is evaporated, the super-charging agents trap the residual ions from escaping the droplet via IEM enabling the transfer of the charge to the analyte via CRM.[44]

In summary, the present section introduced the supercharging effect as useful access tool for multiply charged macromolecules. It aids in understanding the underlying background information for the present thesis. Interested readers are referred to recent articles.[26,45] The following section provides details on a specialized mass spectrometric tool for surface applications.

2.1.5. Surface-Sensitive Ionization: ToF-SIMS

In 1910, J. J. Thomas observed that ion bombardment on solid surfaces induce the release of positive ions and neutral fragments.[49] It took another 30 years, before the pump technology was sufficient to build a first prototype of a secondary ion mass spectrometer (SIMS) by Herzog and Viehböck.[50]

ToF-SIMS as commercialized in its current setup[50] is represented in **Figure 5**.[51] It is a routine MS technique to identify the composition of a solid surface. Hence, a focused primary ion beam sputters the surface and collects all ejecting secondary ions.[52] At the heart of each ToF-SIMS is the primary ion beam source (see **Figure 5** (1) or (2)), where noble gas ions (i.e. Ar^+ and Xe^+), SF_5^+ or C_{60}^+ are generated by electron ionization. An alternative ion beam source – which has also been used for the current thesis in Section 4.4 – provides Cs^+ that evaporate and ionized from a porous tungsten

plug.[53,54] The choice of available ion sources is critical for the surface analysis and is dependent upon the requirement of a continuous or pulsed current. Cs^+ is used in case the specimen contains dominantly electronegative elements i.e. polymer surfaces. C_{60}^+ is used during molecular depth profiling. The ion beam is focused on the target sample, which sputters ionized and neutral atoms off the surface (see **Figure 5** (4)). The ions are focused into the ToF analyzer (refer to Section 2.1.2), where ions are separated and detected with common mass detectors for ToF analyzers being an
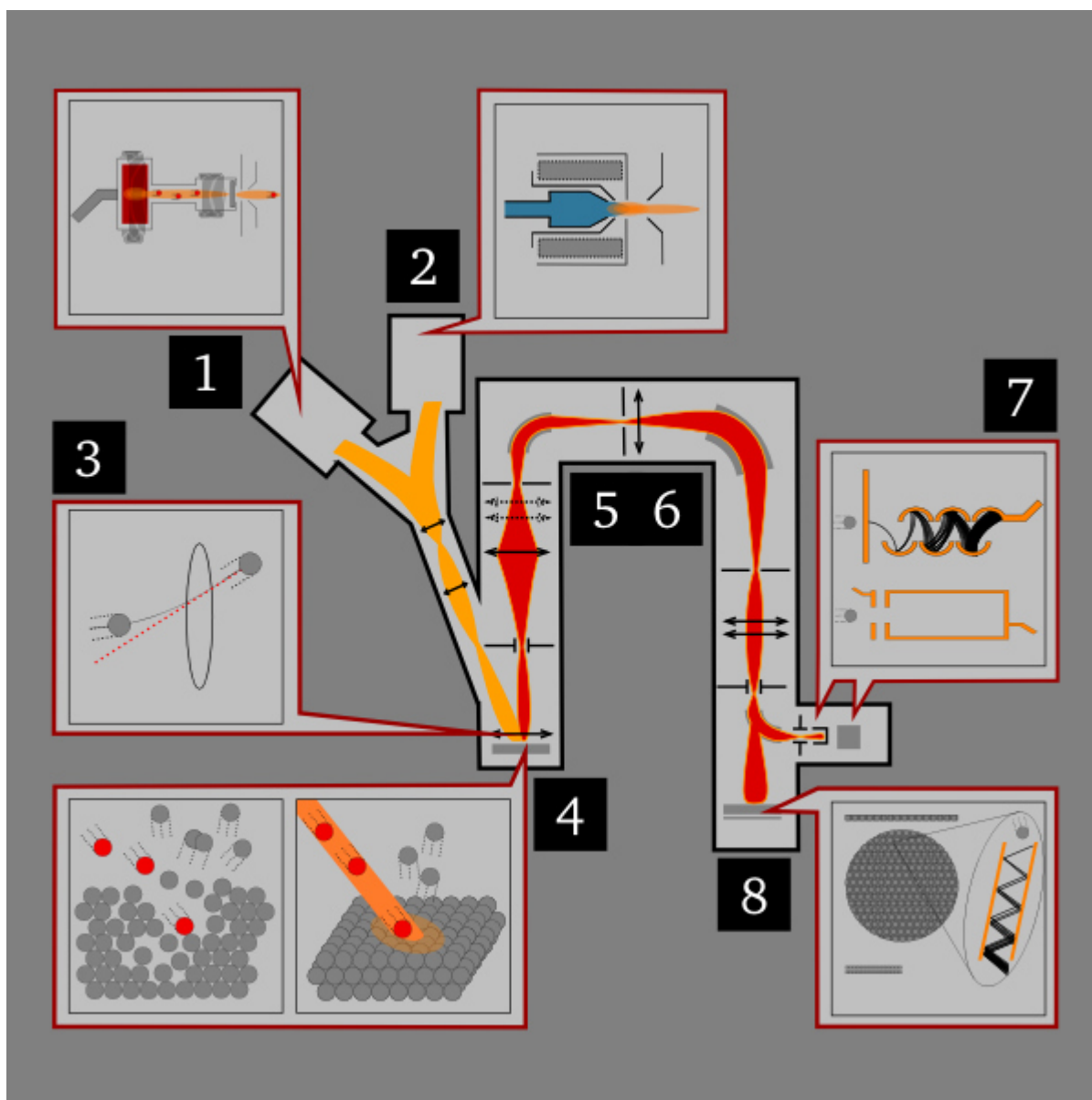
Figure 5 Schematic representation of a typical dynamic SIMS instrument. High energy (usually several keV) ions are supplied by an ion gun (1 or 2) and focused on to the target sample (3), which ionizes and sputters some atoms off the surface (4). These secondary ions are then collected by ion lenses (5) and filtered according to atomic mass (6), then projected onto an electron multiplier (7, top), Faraday cup (7, bottom), or CCD screen (8). Reprinted with permission from Ref. [51].

electron multiplier,[55] a Faraday cup[56] or an electron-multiplying charge-coupled device (CCD).[57–59]

In polymer science, ToF-SIMS is a valuable tool for identifying thin polymer films and to determine their composition. Furthermore, access to spatially resolved surface patterning via photochemistry (see Section 2.5) is an important field of materials science.[60–63] Furthermore, lithography techniques, i.e. 3D laser printing benefit from the spatially resolution of ToF-SIMS, allowing for the identification of specific secondary ions on certain areas of the specimen or the lithographically fabricated macrostructre.[64–67]

In summary, ToF-SIMS is a powerful tool for imaging spatially resolved polymer pattern on surfaces and to determine characteristic secondary ions by their mass-to-charge ratio. The following section will introduce hyphenated techniques (i.e. coupling chromatography techniques to mass spectrometry) for further polymer characterization.

2.1.6. Hyphenated Techniques

Standard measurements give a certain response (e.g. intensity) for a physical parameter resulting in a one dimensional plot. The entropic separation of polymer chains by their individual hydrodynamic radii is utilized in SEC techniques. The separation is driven by geometry-dependent diffusion into pores of the column material or size-dependent exclusion caused by the unfavorable entropy of mixing associated with the partition.[68] These separation techniques are very commonly utilized for hydrodynamic volume determinations of polymers in solution. Coupled with suitable calibration polymer standards, the molecular weight is accessible. However, one dimensional plots can lack in-depth information, in particular for complex structures. A two dimensional (or hyphenated) approach has proven to be successful for the characterization of multi blockcopolymers as well as further advanced architectures.[69,70] In liquid chromatography, hyphenation is realized by coupling two different chromatography techniques. For instance liquid adsorption chromatography at critical conditions (LACCC),[71-73] HPLC[74] or SEC[70] belong to the most often employed hyphenations resulting in LACCC-HPLC, LACCC-SEC or HPLC-SEC. In mass spectrometry, a separation afforded by prior (liquid) chromatography is very beneficial. The information depth is suitable to solve many analytical issues.[69-74] In the following section, the focus will be set primarily on SEC coupled to ESI MS (SEC-ESI MS).

As discussed above, SEC is a liquid chromatography technique separating macromolecules by their hydrodynamic radii. The radius is governed by contour length of the polymer in a specific solvent. Under theta conditions (enthalpy of mixing equals zero), the radius depends on $a\sqrt{N}$, where a is the stiffness of the chain and N represent the repeat unit of the chain.[75,76] The separation of different polymer coils is realized by non-interactive, i.e. enthalpy equals zero, diffusion into pores of a certain size. Resulting in a plot in which large polymers elute first and the smaller later, typical SEC traces have Gaussian shape caused by the chain growth statistic of the polymerization process, and the statistical motion of the particle resulting in diffusion broadening.[77] The detectors employed are most commonly refractive index (RI) or ultraviolet (UV) light of a specific wavelength and depending on the concentration of the sample yet are very accurate. Transformed from the retention time on the column with well-known polymer standards with specific molar masses (calibration of the SEC), the mass axis is beset with large errors (special evaluation methods lower the error to about 5%).[78] In addition to the coil structure of polymer chains, it is important

to understand how nanospheric macromolecules behave in fluids. Such a definition was afforded by Einstein's viscosity model of nanofluids in 1906:

$$\eta = \eta_0(1 + 2.5\phi) \qquad (1)$$

Where η is the viscosity of the nanofluid, η_0 the viscosity of the base fluid and ϕ is the volume fraction of the solute in the solution. Einstein was able to demonstrate that when the solute particles are rigid spheres at infinite dilution, the intrinsic viscosity equals 2.5 and defined the infinite dilution as intrinsic viscosity $[\eta]$. Einstein's equation at intrinsic viscosity can be described as:

$$[\eta] = \lim_{c \to 0} \frac{\eta - \eta_0}{\eta} = \frac{2.5\phi}{c} = \frac{2.5 \cdot N_A \cdot V_h}{M} \qquad (2)$$

Where N_A is the Avogadro constant, $V_h = \frac{4\pi \cdot R_h^3}{3}$ is the hydrodynamic volume, with the hydrodynamic radius R_h and M is the molar mass of the dissolved substance. Benoit and co-workers deduced thus, that Einstein's law can be described as:[79]

$$[\eta] = K \cdot \left(\frac{V_h}{M}\right) \qquad (3)$$

Where K is a constant. Consequently, Equation (3) can be rearranged as:

$$M \cdot [\eta] = K \cdot R_h^3 \cdot g^{x - \frac{3}{2}} \qquad (4)$$

Where g is a parameter introduced by Zimm, with its exponent x ranging from 0.5 to 1.5. Benoit and co-workers concluded that the product $M \cdot [\eta]$ should be universal (i.e. independent of the type of polymer) but only depend on the solvent of choice allowing to determine the molecular weight by SEC of various polymers even if no standard for calibration is accessible. The only limitation is to know the exact intrinsic viscosity of the polymer under identical conditions (temperature, solvent). As the experimental determination of the intrinsic viscosity is time-consuming, modern SEC setups are equipped with viscosimetry detectors determining the intrinsic viscosimetry online and allowing to deduce more accurate universal calibrations. Additionally, a multi-angle laser light scattering (MALLS) detector can be utilized. MALLS detectors allow for the accurate molecular weight determination as described by Zimm.[80] The reader is encouraged to consult the literature for exact molecular weight determination by light scattering.

MS results are entailed with high mass accuracy but their detector response is uncertain (ionization bias).[81] However, hyphenating those two techniques results in

very accurate masses with very accurate concentration determination by the RI detector.[70] Thus, SEC-ESI MS has been used to quantify polymer mixtures, determine Mark-Houwink parameters[82] and to quantify end group conversions.[83–87]
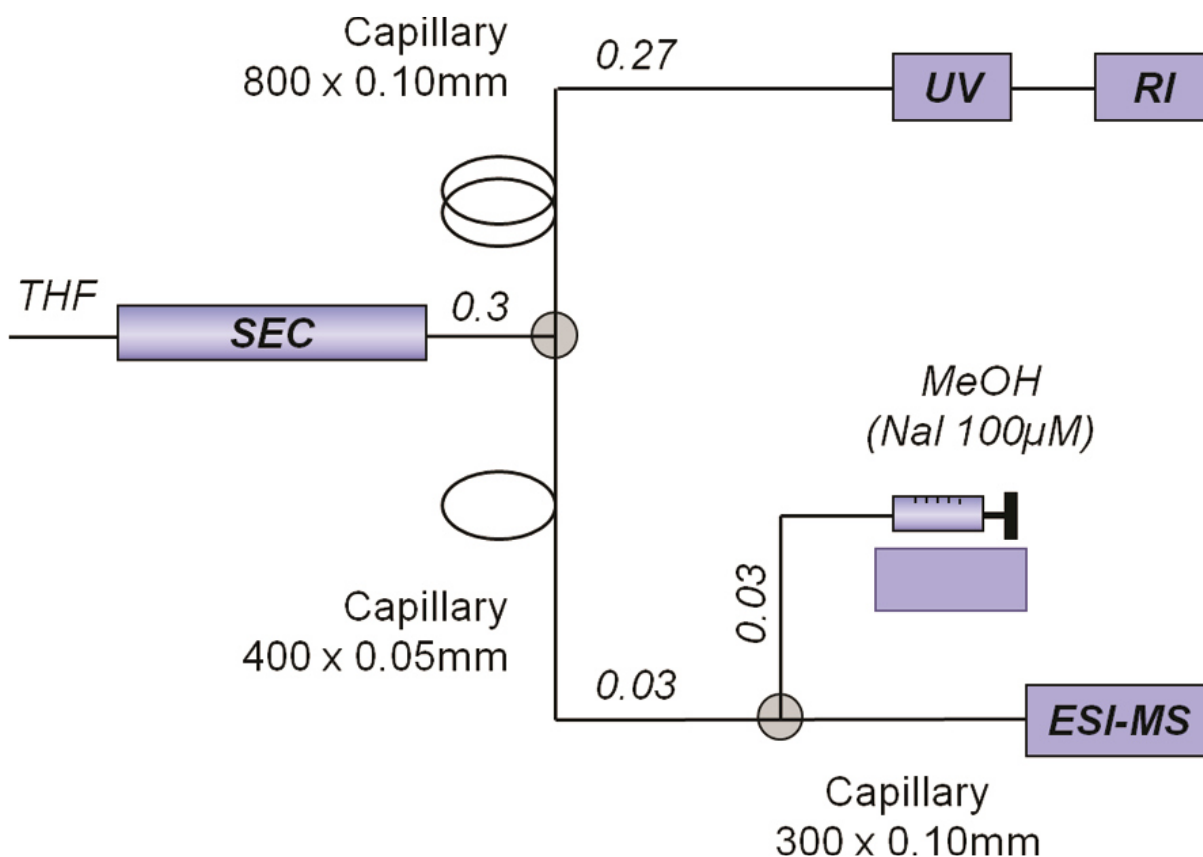

Figure 6 Chromatographic setup employed for coupling the concentration sensitive RI and UV detectors and the electrospray ionization mass spectrometer to the column effluent in parallel. Numbers indicate flow rates in mL min^{-1}. Reprinted with permission from Ref. [70]. Copyright American Chemical Society (2009).

Figure 6 depicts the schematic setup of a SEC-ESI MS measurement: the polymer passes the chromatography (in THF) with a flow rate of 0.3 mL·min^{-1}. Thereafter, the flow splits to both detection: the concentration-dependent RI and UV cells as well as the mass-dependent Orbitrap detector. In order to achieve sufficient ionization, NaI in methanol (100 μM) is added. As high molecular weight polymer chains tend to become multiply charged, SEC-ESI MS is a useful tool to map the sample's individual charge states depending on the elution time (and thus the molecular weight). The reason why larger polymer chains tend to become multiply charged is not fully understood but might be correlated with the unique ionization mechanism.

In summary, mass spectrometry provides access to molecular (polymer) structures based on sophisticated soft ionization protocols (ESI, MALDI), advanced (high-resolution) mass analyzers (ToF, Orbitrap) and structural elucidation via CID experiments. The section provides the reader with the fundamental background information required to navigate through the thesis introducing analytical protocols for various

polymers that provided major challenges in the past. The thesis addresses these challenges by taking advantage of the Orbitrap mass analyzer with enhanced ion sensitivity and high resolution. Further background information is provided on important characterization tools such as SEC coupling (hyphenation technique) and ToF-SIMS, which is a surface sensitive mass spectrometry. The following section will showcase the theoretical background from a synthetic perspective introducing polymerization as access to macromolecules.

2.2. FUNDAMENTALS OF POLYMERIZATION

A precise characterization requires sophisticated polymerization techniques as access route to well-defined materials either defined by high end group fidelity (realized by reversible-deactivation radical polymerization (RDRP)) or by sequence (step-growth polymerization). The present thesis combines modern polymerization techniques with advanced and novel mass spectrometric approaches to elucidate their individual chain structure. The polymerization fundamentals are outlined in the following section.

2.2.1. Chain-Growth and Step-Growth Polymerization

A polymerization transforms monomeric organic molecules into polymers thereby changing the physical properties of the material fundamentally. 1953, Paul Flory categorized polymerizations into two subsets: (*i*) chain-growth polymerizations, which are realized by a reactive, transient chain terminus and (*ii*) step-growth polymerizations, which are characterized by stable intermediates during propagation.[88] Step-growth polymerizations and chain-growth polymerizations follow different kinetics. For instance, during chain-growth, the chain reacts exclusively with monomers whereas during step-growth dimers, trimers and tetramers, etc. can react with each other. While chain-growth polymerizations yield high molecular weight polymers especially during the early stages of the reaction, step-growth polymerizations require very high conversions (>99%) to obtain high molecular weight material (**Figure 7**).[88,89] Their unique polymerization behavior manifests itself in the materials characteristics. Thus, polymers prepared via step-growth polymerization yield polymers with adjustable property profiles. For instance, polycarbonates are robust with high impact strength, stiffness and transparency,[90] whereas polyamides can be processed to flexible fibers with high robustness and toughness.[91]

The material properties of chain-growth polymers are governed by their side groups.[89] In contrast to chemically individual backbones of step-growth polymers, the backbone of chain-growth polymers are represented by CH_2-CH_2 moieties. By varying the chemical motifs of the side group, variable polymers can be obtained. For instance, a phenyl group attachment results in PS, which is hard but sensitive to im-
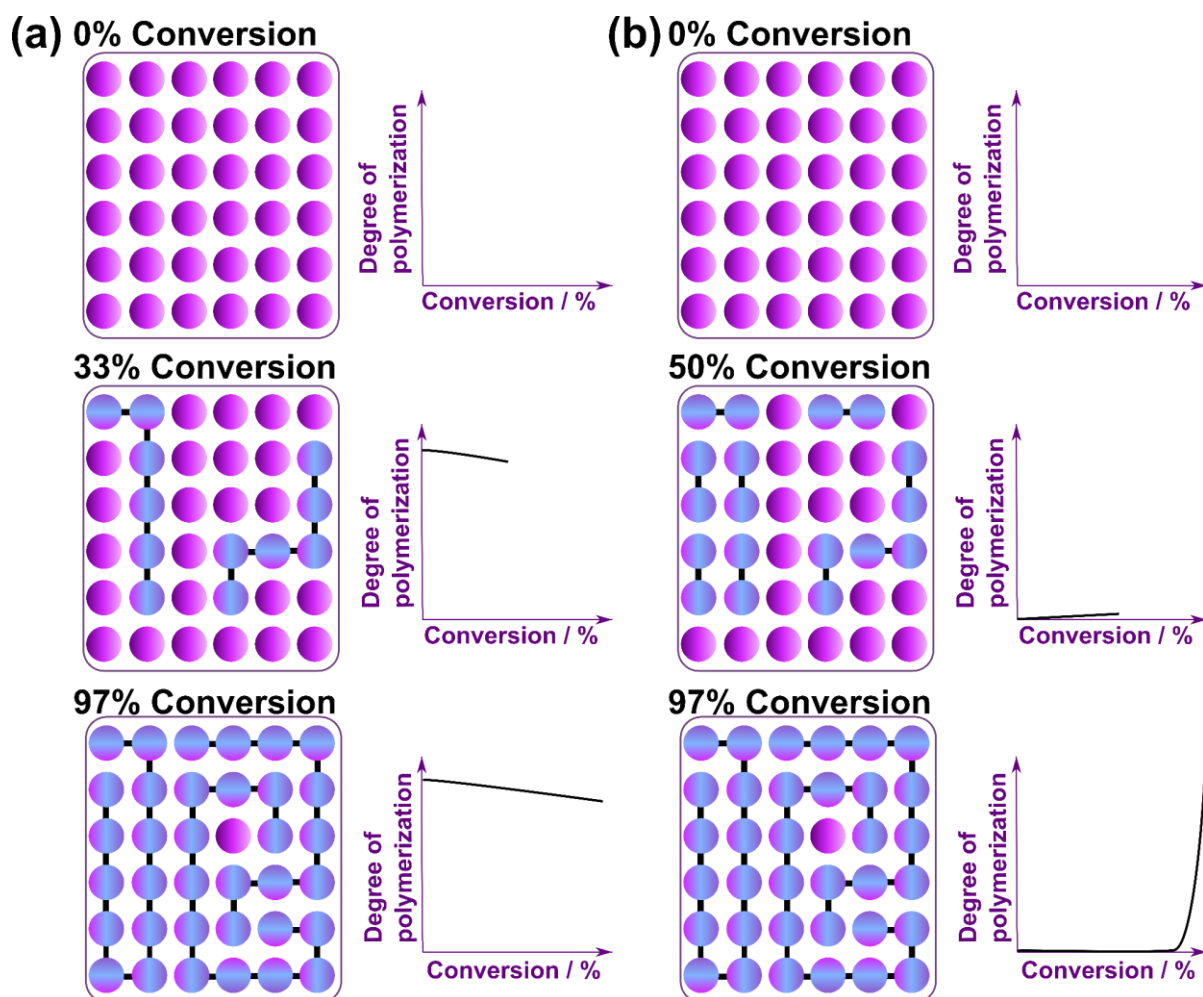
Figure 7 Schematic representation of the chain-growth polymerization (a) and step-growth polymerization (b).

pact,[92] whereas a methyl ester group yields poly(methyacrylate) (PMA) affords transparent materials, which can be processed in a thermally reversible procedure.[93] In recent years, substantial progress has been reported in chain-growth polymerization. A concise literature review on anionic, free radical and ring-opening polymerization is presented in the next section.

2.2.2. Chain-Growth Polymerization

As already discussed, reactive monomers are involved in chain-growth polymerization, featuring an active chain terminus for further monomer addition. The polymerization is started with initiators. Hitherto, a plethora of initiators are available, releasing either radicals (thermally or photochemically) or electrophiles/nucleophiles. Initiators transform monomers from an unreactive (dormant) state and activate them to start further monomer additions (propagation).[89] Active chains propagate until a

termination event quenches the active chain terminus and thus, convert the active state to an unreactive ("dead") end group. Importantly, dead chains cannot be reactivated.[89] The nature of the active propagating species depends on the polymerization techniques being a carbanion for anionic polymerization, carbocation for cationic polymerizations, radicals in a free radical polymerization or an organometallic center for coordinative polymerizations. Consequently, dead chains are generated if the carbanion reacts with an electrophile (e.g. H^+), carbocations are prone to undergo rearrangements or react with nucleophiles (e.g. OH^-) and radicals can recombine or disproportionate. Thus, all chain-growth polymerizations feature a minimum of processes including initiation, propagation, termination and transfer.[89] **Figure 8** collates
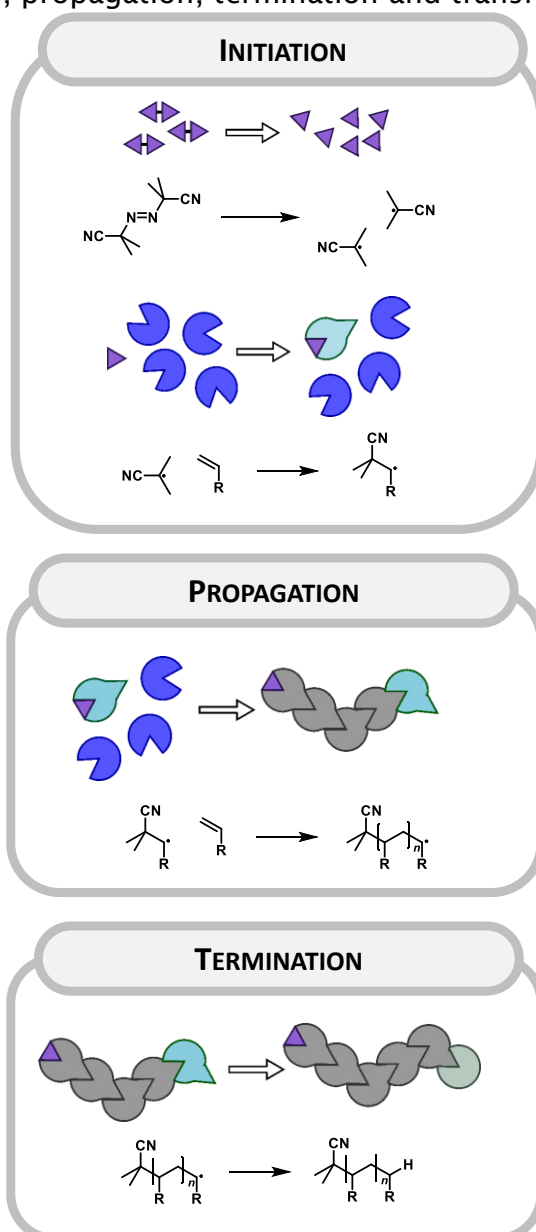
Figure 8 Accepted mechanism of a chain-growth polymerization with initiation, propagation and termination. Exemplarily, a free radical polymerization is depicted. The transfer reaction is not illustrated.

the accepted chain-growth polymerization mechanism. Transfer reactions are not depicted.

In the following, aspects of different chain-growth polymerizations will be highlighted and modern concepts introduced.

Anionic polymerization[89,94]

Anionic polymerization is a subtype of ionic polymerization, i.e. the active chain terminus is a carbanion. The initiation requires strong bases such as alkyllithium, potassium amide or Grignard reagents. Their high reactivity towards double bonds and carbonyls alike makes anionic polymerization rather intolerant for ester-containing monomers. Using catalysts activating the double bond, milder bases and nucleophiles can be used giving direct access to carbonyl-containing monomers such as acrylates, which are susceptible of reacting with strong bases. After initiation, the carbanion of the active chain adds further monomers during propagation. However, two anionic centers do not react with each other. Hence, polymers prepared by anionic have no termination pathway (if operated under strict exclusion of oxygen and water) and active chain termini without termination channel are considered to be "living".[95] After initiation the polymer chains grow without reinitiation and termination, the active chains grow linear with conversion resulting in defined materials with predictable molecular weights, narrow dispersities (below 1.1) and high end group fidelity. After full monomer conversion, a second monomer type can be added to allow for the preparation of block copolymers. The disadvantages of anionic polymerization are a relatively strong restriction in monomer functionality (protic functionalities quench the initiator) and the strict exclusion of water and oxygen limiting the process to advanced Schlenk technique. Thus, more versatile processes are accessible via controlled radical polymerization.

Free radical polymerization

In a free radical polymerization, the active chain end carries a radical capable of adding further monomer units. The initiation proceeds (as depicted in **Figure 8**) via a radical initiator, often azo or peroxy compounds (thermal initiators) or benzoin derivatives (photochemical initiators). The preferred reactivity towards double and triple bonds, while tolerating a plethora of functionalities and the robustness towards water (but not oxygen) makes the free radical polymerization a universal access route to polymeric materials. However, the high reactivity of radicals opens numerous termination pathways, i.e. intra- and inter chain radical transfer reactions, termination via

disproportionation and recombination as well as transfer to solvent molecules.[96] Without additional transfer agent, free radical polymerization techniques are featured by having various end groups and broad dispersities (1.7 – 2.5).[89] Adding transfer agents such as thiols or CCl_4 allow to control the molecular weight while introducing specific end groups, yet provide broad dispersities. In the late 20th century, Australian researchers were leading in developing technologies to control radical polymerization leading to RDRP.[97] Their main approach relied on the reduction of termination pathways, mimicking anionic polymerization. *Nitroxide-mediated polymerization (NMP)* (1970's) was developed by Solomon, Rizzardo and coworkers at the Commonwealth Scientific and Industrial Research Organisation (CSIRO), based on the persistent radical effect of nitroxides to control the polymerization, as it converts the radical reversibly into a dormant (thus unreactive) state.[98–100] In 1995, simultaneously described by Krzysztof Matyjaszewski and Mitsuo Sawamoto, *atom transfer radical polymerization (ATRP)* was pioneered involving redox-active transition metal catalyst (often copper(I)) and alkyl halides as initiators. The fundamental reaction mechanism resembles NMP: the radical reacts reversibly with the transition metal catalyst under reformation of a dormant alkyl halide species.[101,102] In 1998, Rizzardo, Thang and Moad and co-workers developed the *reversible addition-fragmentation chain transfer (RAFT) polymerization* where thioester mediate the polymerization kinetics. Simultaneously, Zard and coworkers reported the macromolecular design by interchange of xanthates (MADIX) process utilizing xanthates as RDRP. In contrast to NMP and ATRP, RAFT does not rely on converting the radical species into a dormant, non-reactive intermediate. The interplay with the (macro)RAFT reagent liberates a radical species, thus the radical concentration remains (nearly) as high as in a non-controlled free radical polymerization. Thus, the life time of a single radical is increased from several seconds to several minutes (even up to hours). Consequently, single polymer chains have an increased overall life time and grow to similar lengths. The result is a low dispersity, high end group fidelity as well as linear molecular growth as observed for anionic polymerization.[103–105]

As a consequence of their versatility, RDRP have enabled a plethora of research areas including biomedicine (development of well-defined micelles based on block copolymers), materials science (e.g. fabrication of membranes with precisely defined pore sizes, responsive as well as self-healing materials) and physics (e.g. precision lithography via 3D printing or stimulated emission depletion (STED) lithogra-

phy). However, monodisperse macromolecules cannot yet be realized with such techniques. Nature has perfected the precision macromolecular preparation of sequence-defined proteins and deoxyribonucleic acid (DNA) including their three dimensional structuring. Synthetic polymer science is at the early stage of preparing sequence-controlled (narrowly disperse multiple block copolymers) and sequence defined materials (precisely monodisperse macromolecules). Synthetic macromolecules with a dispersity of 1.0 and the perfect placement of the monomer units (as nature's proteins and enzymes) are regarded as the next large scientific milestone in the field of polymer chemistry.[106]

Ring-opening polymerization[107]

Conventionally, anionic and radical polymerization involves double bonds of styrene-type and acrylate-type monomers (amongst others). As soon as cyclic monomers participate, it is convenient to refer to such polymerization as ring-opening polymerization (ROP). The initiation process involves the nucleophile, electrophile or radical ring-opening of the cyclic monomer.[89] The active chain, which can be a carbanion,[108] a radical species[109,110] or a carbocation,[111,112] propagates by ring-opening further cyclic monomers. As the transformation from double bond to single bond is associated with the release of enthalpy favoring the formation of polymer chains, the ring-opening process has to be thermodynamically feasible. The Gibb's Free Energy decreases from three-membered rings (e.g. oxirane) to seven-membered rings.[113] Here, the energy from releasing the ring strain is critical. Although the design of cyclic monomers can be sophisticated and less versatile as for conventional polymerizations, synthetic ring-opening macromolecules have a pivotal advantage: The backbone motif contains all functionalities of the cyclic ring instead of simple CH_2-CH_2 motifs. For instance, the most common oxirane is epoxide (ethylene oxide),[112] which ring-opens to poly(ethylene oxide) (PEO) or PEG. In contrast to many other synthetic polymers, PEG is biocompatible, since it is not recognized by the human immune system ('stealth effect').[114] Another example of a biocompatible polymer is poly(lactide), which is prepared by ring-opening the six-membered lactide monomer.[114] In addition to the biocompatibility, poly(lactide) can be degraded through hydrolysis of the ester bonds. Radical-induced ROP of vinyl cyclopropane feature an interesting characteristic: the prepared polymers have the same or a lower density as the monomer. Some applications require that the resulting polymer has the same (or even a larger) volume than
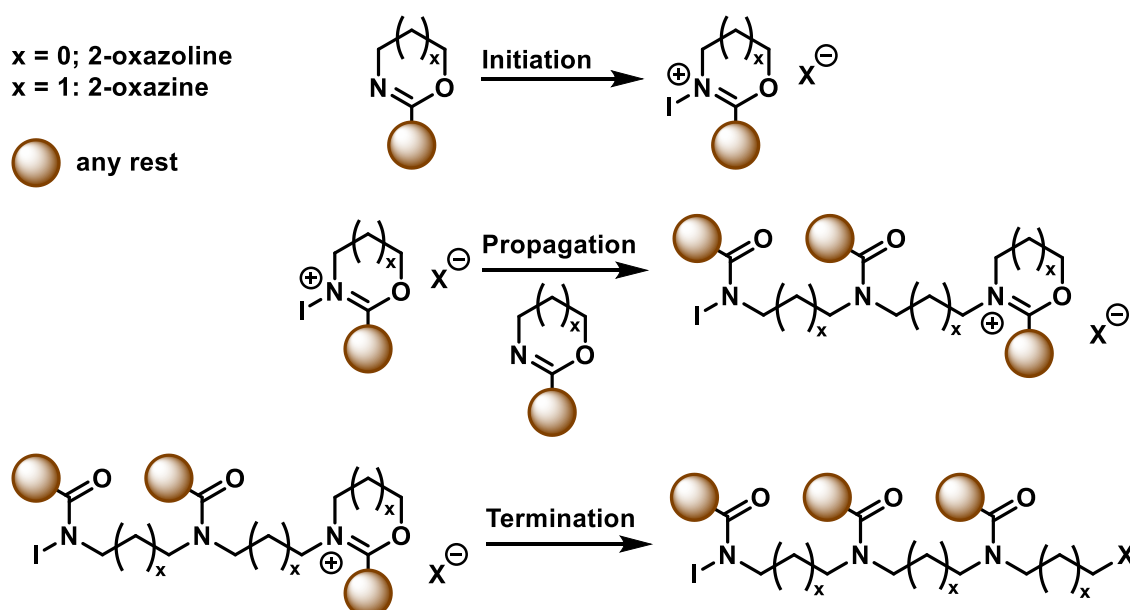
Scheme 1 Ring-opening polymerization of cyclic imino ethers.

the monomer e.g. tooth fillings.[107] Thus, synthetic ROP polymers are versatile in their backbone structure, serving as ideal candidates for biomedical applications.

In the following, cyclic imino ethers as monomer for ring-opening polymerization is discussed as one project within is based on the preparation of poly(ester amide)s (PEA)s.[115,116]

As illustrated in **Scheme 1**, the general polymerization mechanism of cyclic imino ethers involve the initiation by a Lewis acid, followed by a propagation until a Lewis base terminates the polymerization. PEAs have drawn much attention as they serve as a versatile platform for stealth bio-applicable polymers with tailor-made side group functionalities.[117–125]

2.2.3. Step-Growth Polymerization

In addition to ROP and in order to incorporate versatile functionalities into the backbone of a polymer chain, step-growth polymerization is historically the most important access route for macromolecules with a functionalized backbone. Wallace Hume Carothers (†1937) was a pioneer in developing and understanding the mechanism of step-growth polymerization.[89] He obtained fibers from poly(amide)s which can be used to fabricate NYLON™ (1935). NYLON has similar elastic properties as the well-known silk.[126] Carothers shaped the nomenclature for step-growth polymers introducing polyaddition and polycondensation as access routes. In contrast to chain-growth polymerization, no initiators are required to initiate the reaction. Conventionally, re-

action conditions that proved to be successful on organic molecules (e.g. esterifications, alcohol addition to isocyanates) can be applied for the production of macromolecular structures.[89] Most remarkably, the functionalities (e.g. acid and alcohol moieties in the case of polycondensation via esterification) retain their reactivity throughout the monomer addition. Even after the polymerization has been quenched, step-growth polymers have characteristic monomer-derived end groups, which can readily be used for further step-growth polymerization. A critical difference to chain-growth polymerization is the high monomer conversion required to afford sufficiently high molecular weights. Furthermore, step-growth polymerization does not tolerate a dilution of the reaction mixture, leading to ring formation. Macrocyclic species are 'dead' chains as they are not available for any further monomer addition.[89] In the following, more specialized step-growth polymerizations that have been used for projects summarized in Chapter 5, Chapter 6 and Chapter 7 of the present thesis will be discussed.

(Hetero) Diels-Alder polyaddition

Chapter 7 introduces photochemically and thermally degradable polymers prepared by a hetero Diels-Alder polyaddition. Diels-Alder reactions are defined to be thermally-induced concerted reactions between a diene and an ene ([4+2] cycloaddition).[127–131] In rare cases, the diene is generated by a photochemical reaction. The ring-closure to a six-membered cyclic molecule, however, is thermally induced. For their work on this ground-breaking reaction, Otto Diels and Kurt Alder received the Nobel Prize in 1950.[132] Important for the stereochemistry and regioselectivity is the energy of the lowest unoccupied molecular orbital (LUMO) of the diene and the highest occupied molecular orbital (HOMO) of the ene: the smaller the difference of these two orbitals, the more likely is the reaction. The relative orbital geometries resulting from unsymmetrically attached functionalities to either the diene or the ene can be calculated and the strongest HOMO-LUMO overlap will lead to the stereochemically most favored product.[133] The short reaction times, mild reaction conditions and high conversions of the Diels-Alder reaction makes dienes and enes a perfect couple for polyadditions. Recently, Barner-Kowollik and co-workers developed a hetero Diels-Alder reaction involving the thiocarbonyl moiety of RAFT agents as ene with conventional dienes (e.g. cyclopentadiene).

The most remarkable feature of macromolecules prepared via hetero Diels-Alder reaction is the thermal reversibility leading to bonding/debonding on demand accessing self-healing materials.[134–138]
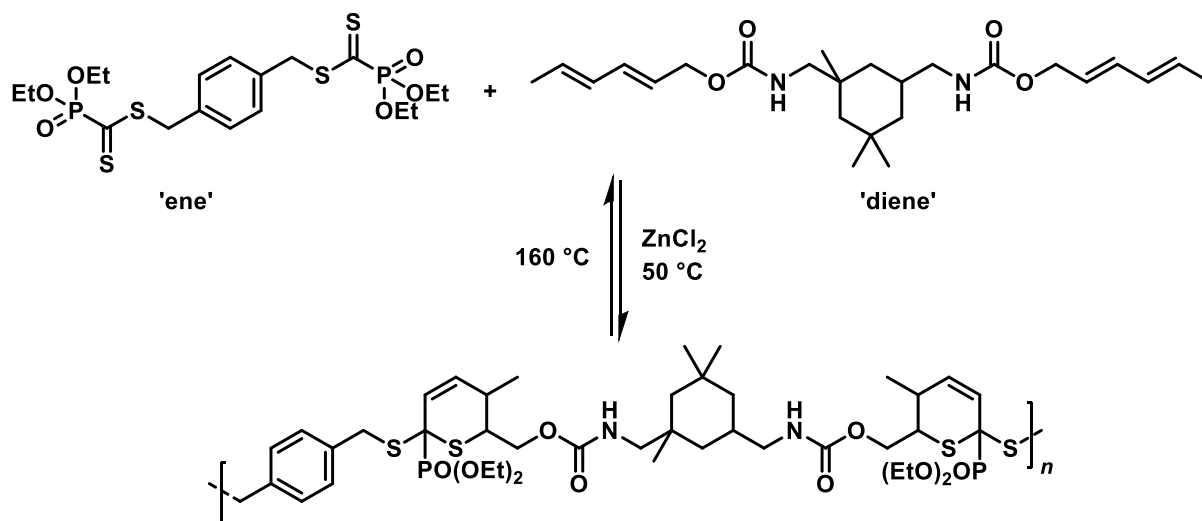
Scheme 2 Hetero Diels-Alder polyaddition as reported by Barner-Kowollik and co-workers.

Spontaneous zwitterionic (alternating) copolymerization (SZWIP)

A step-growth process between two homo bifunctional monomers (e.g. acid and alcohol) leads ultimately to alternating copolymers as the acid reacts with the alcohol but not with other acid functionalities. This high sequence regulation is unique for the step-growth process and is realized in chain-growth polymerizations only under certain circumstances i.e. if high control, quantitative conversions in short polymerization times is granted.[89] Currently, the research focuses on new pathways to obtain sequence control of chain-growth-based monomers. One alternative is the spontaneous zwitterionic copolymerization (SZWIP). Here, an electrophilic monomer (M_E) and a nucleophilic monomer (M_N) react forming zwitterionic intermediates.[115,116] Despite its early discovery in 1977 by Saegusa and numerous reports in the 1970s and 1980s, this polymerization technique has not received much attention mainly as no high molecular weights can be realized.[116,121,139,140] It is assumed that the polymerization mechanism includes side reaction but a full mechanistic study has not yet been accomplished. Further, SZWIP seems to follow a chain/step-growth hybrid mechanism as both characteristics are observed: alternating copolymers with approximately 50% end group of both monomers present in the resulting polymer; initiation and termination steps as they are present in chain-growth polymerization. A detailed mechanistic review is provided in Chapter 5.

Multicomponent polymerization

Multicomponent reactions belong to a versatile type of a synthesis procedure involving three or more organic molecules to form one specific product. Beginning with the Strecker synthesis for amino acids (1850),[141] multicomponent reactions have

Ionic mechanism
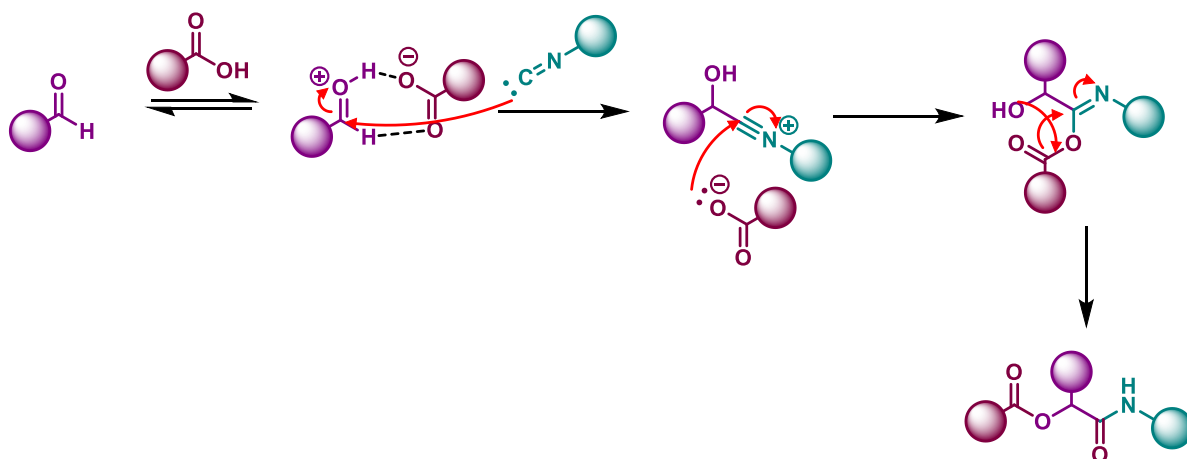
Concerted mechanism
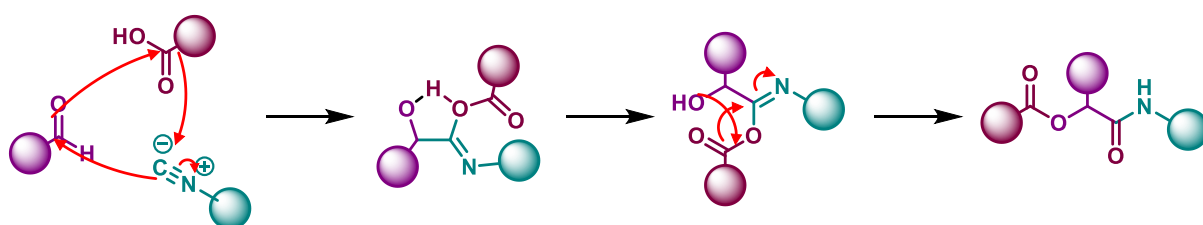
Scheme 3 Proposed Passerini mechanism (a) ionic in polar solvents (ionic) and (b) concerted in non-polar solvents (concerted).

evolved to be a versatile platform for a plethora of functional moieties. A popular multicomponent reaction is Passerini's procedure using isocyanides, aldehydes and carboxylic acids to form α-acyloxy amides.[141] **Scheme 3** illustrates the accepted Passerini mechanism in polar solvents leading to the protonation of the aldehyde and – in a multi-step pathway – the isocyanide and the carboxylic acid attack subsequently followed by a rearrangement. In contrast, non-polar solvents favor a concerted reaction pathway.[142,143]

In 2011, Meier and co-workers implemented the Passerini reaction for a multicomponent step-growth polymerization yielding renewable polymers. The high atom economy and access to versatile functionalities introduced into the backbone makes the Passerini polymerization a competitive alternative to existing procedures.[144–147]

In summary, a plethora of polymerization protocols are available to produce macromolecules with various functionalities. All introduced polymerization techniques are performed in solution (either in bulk or diluted with an appropriate solvent). The next section describes approaches to attach polymer strands to surfaces.

2.2.4. Surface Modification

Computer technology (e.g. microchips),[148] medicinal technology (e.g. anti-fouling surfaces)[149,150] and biological applications (e.g. cellulose modification)[151] benefit significantly from progresses in surface modification. In more detail, the current section will describe the most prominent approaches for generating polymer-coated surfaces.
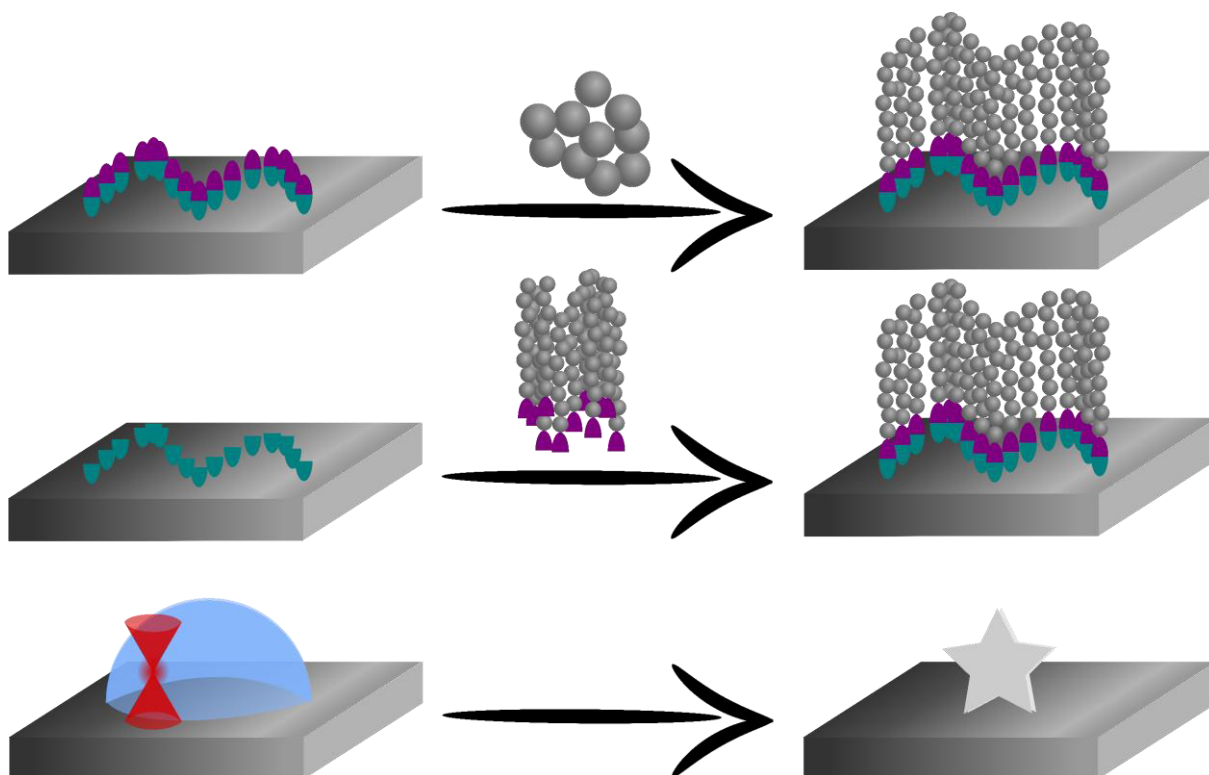
Figure 9 Schematic representation of surface modifications: grafting-from approach based on surface-imitated polymerizations (top); grafting-to approach based on forming covalent bonds between polymer strands and anchors attached to the surface (middle); 3D lithography based two photon absorption initiation processes.

Polymer films can be generated via the grafting-from (**Figure 9 top**) or grafting-to (**Figure 9 middle**) protocol. The grafting-from approach is based on an initiator-coated surface that are placed into the monomer solution. The polymerization is started thermally or photochemically. The grafting-to approach is based on polymer chains entailing reactive motifs for subsequent surface immobilization. Often, Dials-Alder chemistry is employed for grafting-to approaches.[152–158] If sub-micrometer precision is required, grafting approaches are not well suited. Here, 3D lithography (**Figure 9 bottom**) using two photon absorption processes provides small voxels of the incident photon's cross-section. Thus, 300-400 nm line width can be achieved.[159]

In summary, fundamental polymerization protocols have been developed to control chain growth and end group fidelity. For instance, ROP allows for the monomer

functionality to be inserted into the backbone. The present section showcased the most important candidates, which are relevant for the thesis. The following sections will highlight polymeric materials stemming from one of the above discussed polymerization protocols such as polyelectrolytes prepared by FRP, or self-immolative polymers prepared step-growth polymerizations.

2.3. POLY(IONIC LIQUID)S (PILS)

Three projects of the current thesis (summarized in Chapter 4) address a unique class of polyelectrolytes: poly(ionic liquid)s (PILs). Although the free radical polymerization of monomeric ionic liquids (ILs) is straight-forward, the characterization of the resulting PILs is challenging. The current section focuses on the unique properties of PILs required to understand why these polymers are challenging to analyze using standard polymer analytics.

2.3.1. Ionic liquids

In 1979, John S. Wilkes defined ILs as ionic substances (mostly organic cation with an inorganic anion) that melt below 100 ℃. If the salts are liquid at room temperature, he classified them as Room Temperature Ionic Liquids (RTILs). Although Wilkes described and defined ILs to what they are, their early discovery dates back to 1877, when Charles Friedel and James Mason Crafts begun to work on acylation of aromatic systems observing a red oil on the bottom of the reaction flask. Unable to

Figure 10 Common cation and anion structures forming ILs if combined.

identify the exact molecular structure (NMR as a standard technique was not available), Paul Warden contributed characterizing physical properties allowing him to identify the structure of ethylammonium nitrate $[(C_2H_5)NH_3]^+[NO_3]^-$ in 1914.[160,161]

As collated in **Figure 10**, common cations are quaternary ammonium species either incorporated into heterocycles (imidazolium, pyridinium) or tethered with any
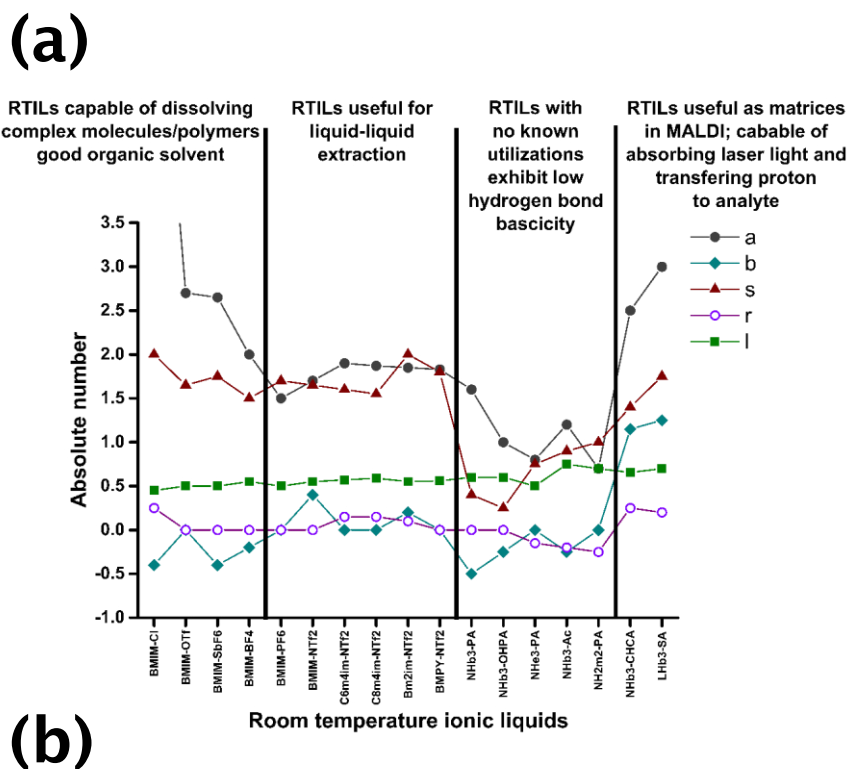
Figure 11 (a) Plot illustrating the magnitude of each interaction parameters for ILs at room temperature: a – hydrogen bond basicity; b – hydrogen bond activity; r – interactions via non-bonding electrons and π-electrons; s – polarizability; l – dispersion forces; **(b)** Possible association site of anion X illustrated on the example of an imidazolium cation: (i) primary C2 H-bond with a bond distance of ~2 Å; (ii) ring C4 and C5 H-bond with a bond distance of ~2.2 Å; (iii) first methylene and first methyl H-bond with bond distances between 2.3 and 2.7 Å; (iv) secondary alkyl H-bond; (v) terminal methyl H-bond. Reprinted with permission from Ref. [166]. Copyright American Chemical Society 2016).

alkyl or aromatic rest. Common anions are halides forming polar ILs with higher melting points around 80 °C and perfluorinated species such as PF_6^- and BF_4^- forming nonpolar RTILs). The physical properties of ILs change drastically depending on the counter anion attached to the cationic core structure such as solubility and viscosity.[162–165] Presumably, the IL structural properties are associated with the interaction of the anion with specific moieties of the core, either in an intramolecular or intermolecular fashion. **Figure 11b** illustrates possible interactions.[166] The stronger the H-bonding properties of the counter ion, the more polar solvents are required to break the associated strong forces. Hence, well H-bonding counter ions (such as chloride) increase the melting point, the viscosity and the ability to function as a solvent itself capable to dissolve very polar macromolecules – even starch and cellulose to a certain extent.[167,168] Exchanging chloride against a more hydrophobic counter ion diminishes the H-bonding interactions fundamentally. PF_6^-, for instance, weakly interconnects ionic liquids making them even liquid at room temperature.[166]

The structure-property relationship of monomeric ILs is unique, which can be translated into the macromolecule after polymerization.[169,170] Although PILs are always solids at room temperature, their viscosity is akin to those of polyelectrolytes and the counter ion exchange imparts them with responsive characteristics. The following section focuses solely on the proposed coiling behavior of polyelectrolytes and the characterization of these materials.

2.3.2. Poly(Ionic Liquid)s: Characterization Aspects

As noted in Section 2.2, polymers prepared via various polymerization techniques are governed by a statistical process. Thus, a complete characterization including structural information (obtained by NMR, ESI MS), molecular weight distribution (obtained for example by SEC, field flow fractionation[171] or analytical ultracentrifugation[172] equipped with concentration-sensitive detectors) and hydrodynamic radii (obtained by diffusion ordered spectroscopy (DOSY) or dynamic light scattering (DLS)) is required. Polyelectrolytes feature specific characteristics as outlined in Section 2.3.1. The counter ion has a strong impact on the global chain properties, including solubility, viscosity and polarity.[160,161,164,166,169,170,173] Furthermore, polyelectrolytes respond strongly to the solute's salt concentration. Polymers in solution coil to maximize favorable interactions (e.g. van-der-Waals interactions, dipole-dipole interactions) and minimize non-favored interactions (e.g. caused by solvation).[169,174] In addition, polyelectrolytes have to maximize the Coulomb interactions in such a fashion that the

repulsive interactions are minimized while maximizing the attractive interactions forcing the polymer chain to form necklace-like conformations. Interestingly, such conformations resemble those illustrated in **Figure 4b**,[173] where the charged macromolecule in an ESI droplet is regarded as a polyelectrolyte. Thus, the charge of a polymer forces the macromolecular chain to change the conformation to a necklace-like state.

Increasing the salt conformation reduces the Debye screening length causing the expansion of the polyelectrolyte. SEC – as hydrodynamic radius sensitive standard characterization – is challenging: the column material and the polymer chain might interact. Commercially available SEC columns are based on PS microspheres. Polyelectrolytes can strongly interact with these column materials, preventing a pure SEC separation mechanism, which needs to be purely entropic ($\Delta S \gg \Delta H$).[169,174] Nowadays, state-of-the-art column materials for polyelectrolyte analysis are polyelectrolyte microspheres being either polycation or polyanion based. Since the Coulomb interaction are purely repulsive, the polymer will elute earlier. Indeed, the penetration depth into the porous material is governed by the maximum repulsive force. Most PILs are polycations, thus, polycationic column material can be utilized for SEC characterization of polar PILs (mostly with a halide as counter ion).[174] As SEC is a relative technique based on calibrating the elution time with molecular weights of fully characterized standards, a polyelectrolyte requires calibration based on a polyelectrolyte (as the hydrodynamic radius depends on the salt concentration). Unfortunately, the controlled preparation of polyelectrolytes is difficult. In general, only a few non-ionic polymers have been commercialized as standards for calibration purposes (such as PEG, PS, PMMA amongst others). Recently, Matyjaszewski and co-workers pioneered a full characterization of hydrophobic PILs by THF-SEC,[175] whereas Taton and co-workers reported a comprehensive study on hydrophilic PILs (H_2O-SEC) adding the PIL's counter ion into the eluent.[174] Mass spectrometry, on the other hand, was employed by several research groups. Moreover, Tenhu and co-workers successfully recorded the molecular weight distribution of different PILs by means of MALDI-ToF spectrometry. However, they could not identify single polymer chains within the obtained data sets.[176] Matyjaszewski and co-workers did not obtain convincing results by employing the ESI MS technique either. [175]

In summary, a careful literature scan on the characterization of PILs evidences major challenges that have been addressed recently. A reason for the fast analytical progress of these polyelectrolytes is based on the fact that more advanced characterization protocols become available. Nowadays, SEC with a plethora of column sets are

commercially available with a broad range of suitable calibration sets. MS as standard analytical tool has also advanced after Orbitrap as benchtop mass analyzer has been commercialized. The analysis of PILs should be feasible based on high-resolution MS with a suitable ionization protocol.

2.4. SINGLE CHAIN POLYMER NANOPARTICLES

Nature has evolved unique techniques to generate precision sequence-defined macromolecules and to assemble them in the three-dimensional space for instance in proteins and DNA.[177] Polymer researchers attempt to obtain similar results synthetically by mimicking nature, however two critical challenges remain: (*i*) the sequence-definition of artificial macromolecules has advanced,[178,179] yet there is no universal technique to produce a sequence-defined polymer on a multi gram scale. The production involves sequential organic synthesis and high efforts.[179] Furthermore, (*ii*), researchers have studied the precision assembly of polymers in three dimensions, yet not achieved access to complex architectures as represented by enzymes. A prominent candidate for the triggered formation of 3D structures are single-chain polymeric nanoparticles (SCNPs).[180-186] As implied in the name, single chains undergo an intra-chain collapse forming nanoparticles. They have found interesting applications in drug delivery,[187] imaging,[188] nano-containers and catalysis.[189] As the present thesis addresses a novel characterization technique for SCNPs, chain collapse technologies and characterization techniques are briefly discussed.

2.4.1. SCNP Collapse

Typically, SCNP collapses are executed in dilute solution (< 1 mg·mL^{-1}) to favor intra-chain crosslinking. To date, a plethora of crosslinking chemistries has been established ranging from covalent crosslinking reactions (e.g. Friedel-Crafts alkylation,[190] thermal[191-193] and photochemical[194-197] cycloadditions, free radical polymerization,[198,199] carbamate/urethane reactions,[200] ring-opening reactions,[201] "click" reactions,[202,203] transition metal-induced coupling reactions,[200] Menschutkin reaction,[204] Bergman cyclization[205,206] and photodimerization[195,207]) to non-covalent processes including supramolecular chemistry (Hamilton wedge/cyanuric acid hydrogen bonding, 2-Ureido-4[1*H*]-pyrimidinone (UPy) hydrogen bonding),[182,208,209] and metal coordination.[210-212] Most commonly, sophisticated synthetic processes have to be designed to equip monomers with a corresponding crosslinking motif. A subsequent (controlled) free radical copolymerization with a non-functional monomer yields macromolecules with statistically distributed crosslinking functionalities.[201] In a selective point folding approach, often orthogonal folding motifs have to be precisely introduced at prese-

lected and defined positions of the polymer chain,[213] whereas in a statistically distributed copolymer, the folding motifs are randomly tethered leading to a repeat unit folding approach (**Figure 12**).[194] Although selective point folding allows for precision collapse and a more defined tertiary structure, the synthetic efforts can be significant. After intra-molecular crosslinking, SCNPs require thorough characterization, which is facilitated by the (partial) disappearance of specific crosslinking moieties and a drastic morphological change. The following section is focused on the standard analytic platforms to probe SCNPs folding.

(a) Selective Point Folding
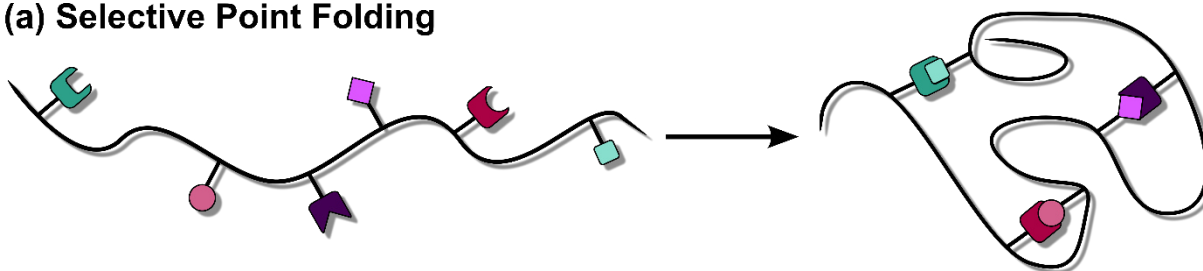
(b) Repeat Unit Folding
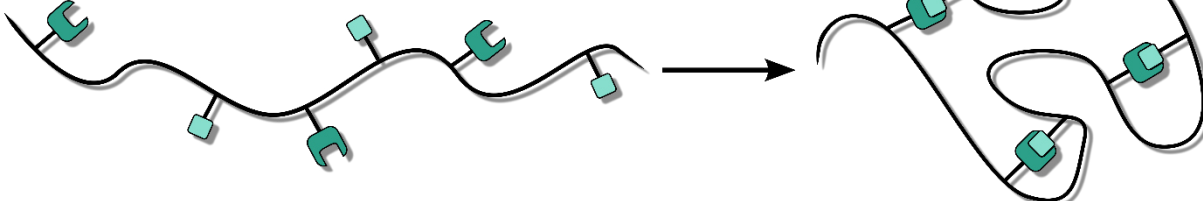
Figure 12 SCNP collapse via (a) selective point folding of orthogonal folding motifs or (b) repeat unit folding of identical folding motifs.

2.4.2. SCNP Characterization Methods

The most powerful characterization tool to follow SCNP folding is SEC.[214] The plethora of eluent/column combinations allow the analysis of a broad range of polymers and intra-chain crosslinked SCNPs. However, the molecular weight of the SCNP is affected by its globular morphology and the absence of suitable calibration standards. A characteristic shift in the SEC trace confirms a reduction of the SCNPs' hydrodynamic radius (high retention volume, low hydrodynamic radius) compared to the linear polymer (low retention volume, large hydrodynamic radius) – as long as the macromolecule elutes without remarkable enthalpy contributions. First theoretical considerations of Pomposo and co-workers[215] can be utilized to calculate the hydrodynamic radius based on the apparent molecular weight. Hence, Equation (2) – introduced in Section 2.1.6 – can be easily rearranged as:

$$V_h = \frac{2 \cdot [\eta] \cdot M}{5 \cdot N_A} \qquad (5)$$

And further to:

$$R_h = 2 \cdot \sqrt[3]{\frac{3 \cdot K^{\alpha+1}}{10\pi}} \qquad (6)$$

Thus, if the Mark-Houwink parameters (K and α) of the polymer system were precisely determined, the hydrodynamic radius can be determined from Equation (6). However, care must be taken that Mark-Houwink parameters of statistical copolymers do not exist for every feed ratio. Hence, the evaluation of the radius is highly uncertain. Furthermore, after crosslinking, the architecture is changed from a linear chain (analogue to the calibration) to an intra-chain crosslinked structure, which will have a different hydrodynamic diameter. Hence, it is highly unlikely that Mark-Houwink parameters exist for single-chain nanoparticle making such calculations arguable.[216]

Dynamic light scattering (DLS)[217] is an alternative valuable technique where light of a specific wavelength (generated by a laser) travels through a solution containing particles. Depending on the particle's size, different scattering scenarios are considered:[218]

- Rayleigh scattering (small particles compared to the light wavelength)
- Mie scattering (particle size in the range of the light wavelength)
- Geometric scattering (large particles compared to the light wavelength)

Rayleigh scattering was first modeled by Lord Rayleigh, where the particle diameter must be smaller than the wavelength of the scattered wave; typically the upper limit is 1/10 of the wavelength. Both Mie and Rayleigh scattering are considered elastic scattering processes,[218] in which the energy (and thus the wavelength and the frequency) of the light is not substantially changed. However, electromagnetic radiation scattered by moving scattering centers undergoes a Doppler shift, which can be detected and used to measure the diffusion coefficient.[219] DLS uses the Doppler Effect of particles in motion relative to the light beam. Due to the Doppler Effect, a frequency shifted spectrum is recorded as an envelope of multiple Lorentzian functions. As the shift in frequency caused by the Doppler shift is small compared to the incoming light beam, an interferometer cannot be used. Instead, it is convenient to Fourier transform the Doppler shift spectrum into a time-resolved autocorrelation function.[220,221] As the intensity of the beam is correlated after a time τ, the correlation is high for very small times τ (few ms) but very small for long times τ (up to μs). The decay of τ with the intensity is exponential. Different algorithms taking the dispersity of the particle into account are available processing the decay producing the diffusion coefficient of the

particle.[221] Best results are generated by monodisperse macromolecules with many scattering points resulting in high detector counts. Specifically, the hydrodynamic radii of SCNPs are ranging in the range of a few nanometers (see detailed and relevant discussion about absolute SCNP sizes below). On a molecular level, every single SCNP has a different hydrodynamic radius based on various assumptions: (i) the sample's dispersity is strongly related to polymer science in general and is – to date – never monodisperse, (ii) the globular polymeric chain in solution is never identical and thus the folding scenarios never occur identically producing various different microarchitectures, and (iii) different loop sizes between crosslinks is generated strictly related to the statistic process underlying in a repeat unit folding approach. Hence, each SCNP will have its distinct diffusion coefficient, and its corresponding Doppler shift during its motion. An autocorrelation function will be the envelope of many Doppler shift spectra, and thus, the evaluation will require sophisticated numerical analytic techniques. Modern DLS setups are equipped with an appropriate software for disperse sample evaluation, yet the diffusion coefficient obtained will only represent the statistical value of all described scenarios.

NMR spectroscopy is a powerful technology in organic synthesis. The high precision afforded by the chemical shift in the magnetic fields allows for fast and quantitative evaluation of the crosslinking process. Gradient pulsed experiments enabled new methodologies to measure molecules spatially resolved. Such diffusion ordered spectroscopy (DOSY) characterizations are powerful in determining the hydrodynamic radius of polymers – especially of SCNPs. At the heart of each DOSY experiment are the gradient pulses encoding and decoding the diffusion information (**Figure
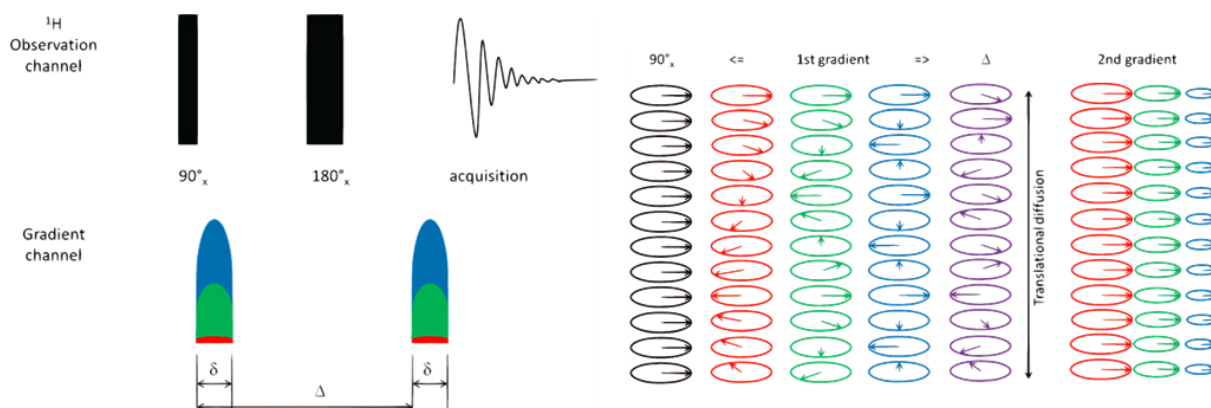
Figure 13 A pictorial description of the simplest DOSY pulse sequence (pulsed field gradient spin-echo). The first ^{1}H pulse aligns the magnetization in the x-direction. The first gradient pulse creates the corkscrew effect. The second ^{1}H pulse inverts the magnetization vector in the x–y plane. The second gradient pulse undoes the corkscrew effect of the first gradient pulse. The data is then acquired. The gradient pulses are color labeled (red = 2%, green = 50%, blue = 95% of the maximum power of the gradient generator). Reprinted with permission from Ref. [222]. Copyright Royal Society of Chemistry (2017).

13).[222] After aligning the molecule's magnetization with a 90° pulse, the gradient (applied in different strengths ranging from 2% to 95%) delocalize the spin along the z-axis in a corkscrew pattern.[222] As molecules are diffusing along the z-axis, the effective magnetization vector will be altered depending on how much time (Δ) they have to diffuse. After time Δ, a second gradient pulse reverses the destructive misalignment effect of the first gradient and the effective magnetization can be measured. As the gradient strength is varied from 2% to 95%, the diffusion coefficient of a molecule can be determined be the decay of the relative intensity measured.[222]

As both techniques measure the diffusion coefficient, the Einstein-Smoluchowski relationship relates the diffusion coefficient D to the particle's mobility μ:[223]

$$D = \mu \cdot k_B \cdot T \qquad (7)$$

If the Reynolds number is very small (as it is for molecules), the equation can be replaced by Stoke's equation for spherical objects leading to Einstein-Stoke's equation (r indicates the hydrodynamic radius of the polymeric particle in the NMR solution):

$$D = \frac{k_B \cdot T}{6\pi \cdot \eta \cdot r} \qquad (8)$$

Further morphological characterization of SCNPs is achieved via small angle X-ray scattering (SAXS),[224] atomic force microscopy (AFM)[188] or transmission electron spectroscopy (TEM).[214] As these techniques have no relevance for the current thesis, the reader is referred to current literature. Most publications are concerned with the relative changes in hydrodynamic radii only. The recent work of Blasco et al. suggests a careful evaluation of these absolute data.[225] For their work, an array of SCNPs reported in the literature by means of their size (either determined by SEC, DLS, DOSY, viscosimetry or microscopic methods) were assessed and correlated to their M_n. Most remarkably, they calculated the density of the SCNPs, which should be between 0.1 and 1.0 g·mL^{-1} and identified that the most reliable data were produced by viscosimetric evaluation. Thus, they "submit that the careful analysis provided […] is critical for moving the field towards not only relative size change observations and their rationalization, but also absolute radii discussions, which are critical for the design of functional biomimetic entities".[225]

In summary, SCNPs are a demanding class of macromolecules from an analytical perspective. Currently, SCNPs are evidenced by a characteristic SEC shift towards higher retention time, or via morphological techniques such as DOSY, DLS, SAXS or

AFM. However, a direct view into the chemistry of the folded particles is not revealed. The present thesis closes this important analytical gap for SCNPs in Chapter 6.

2.5. LIGHT-INDUCED CHEMISTRY

Sun light is a powerful source of energy comprising a broad range of wavelengths from UV light, visible light (400 nm – 650 nm) and infrared light.[226] Nature processes the sun's light energy in photosynthesis to convert CO_2 into high-energy carbohydrates.[227] Soon after the discovery of plant's photosynthesis, scientists realized the versatility of photochemistry and studied first fundamental photoconversions of organic molecules. As the current thesis addresses photodegradable polymers, the following section is focused on photochemical fundamentals with a short summary for photoligations.

2.5.1. Concepts of Photochemistry

The wavelength regime in which molecules absorb light is governed by electronic transition processes from their HOMO to the LUMO.[228] A plethora of organic molecules consist of carbon, hydrogen, oxygen and nitrogen atoms. Such atoms entail 2s and 2p molecular orbitals.[228,229] During bond formation, the s and p orbitals form bonding and antibonding (σ/σ^* as well as π/π^*-orbitals) as well as non-binding orbitals (n).[230] Non-binding orbitals are not involved in a chemical bond (i.e. lone electrons). To enable $\sigma \rightarrow \sigma^*$ electron transitions in saturated hydrocarbons, high amounts of energy (~100-200 nm) are required as the electron experiences high attractive Coloumb forces by the close proximity to the nuclei. $\pi \rightarrow \pi^*$ electron transitions, e.g. in aromatic systems, require less energy than $\sigma \rightarrow \sigma^*$ electron transitions (~200-300 nm) as p-electrons are slightly further apart from their respective nucleus. If the aromatic system is conjugated by adjacent π-systems, the required energy can be decreased, leading to a bathochromic effect (400-700 nm).[231] If non-bonding orbitals are involved in electron transitions, they most likely represent the HOMO and thus, $n \rightarrow \pi^*$ electron transition are possible. Generally, an electron transition is strong for identical orbital symmetry.[232] However, electron transitions between n-orbitals and the π^*-orbital are symmetrically forbidden and exhibit only weak intensities.

After excitation from the ground electron state (HOMO) to a higher electron state (e.g. LUMO), the electron has a certain lifetime in the excited state, upon which the molecule undergoes radiative or non-radiative deactivation.[233]
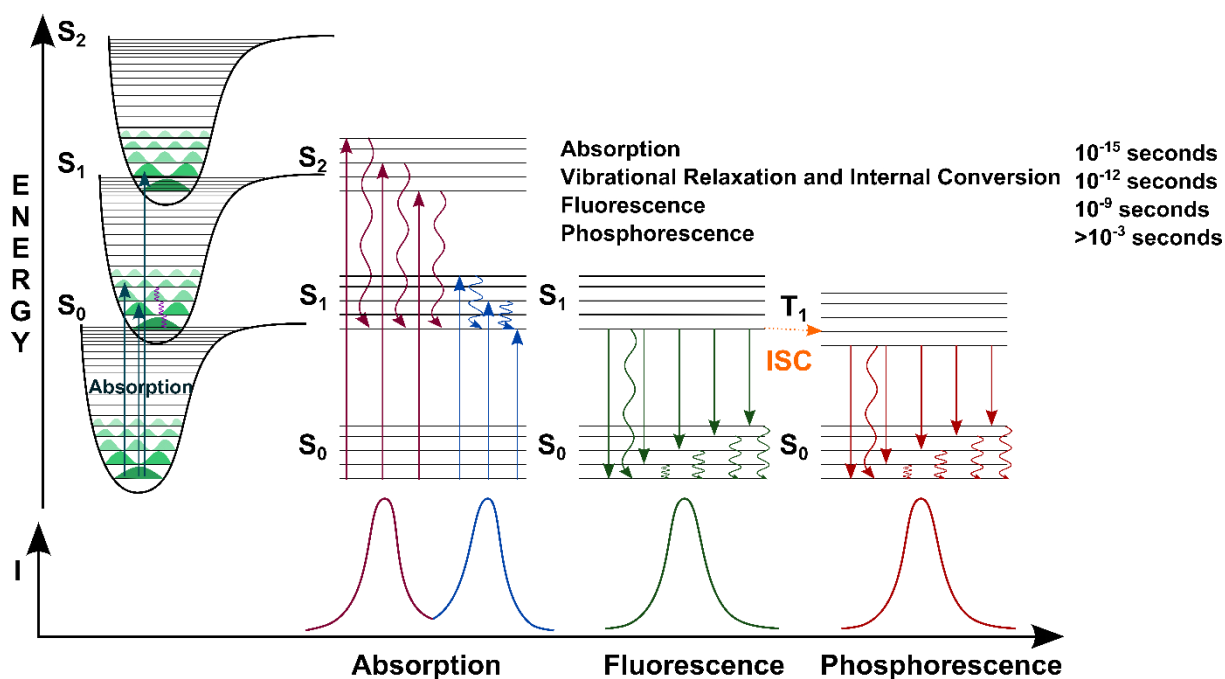
Figure 14 Jablonski diagram representing energy levels and spectra. Solid arrows indicate radiative transitions as occurring by absorption (violet, blue) or emission (green for fluorescence; red for phosphorescence) of a photon. Curvy arrows represent non-radiative transitions (violet, blue, green, red). Internal conversion is a non-radiative transition, which occurs when a vibrational state of a higher electronic state is coupled to a vibrational state of a lower electronic state. In the notation of, for example, $S_{1,0}$, the first subscript refers to the electronic state (first excited) and the second one to the vibrational sublevel (v = 0). In the diagram the following internal conversions are indicated: $S_{2,4} \rightarrow S_{1,0}$, $S_{2,2} \rightarrow S_{1,0}$, $S_{2,0} \rightarrow S_{1,0}$ and $S_{1,0} \rightarrow S_{0,0}$. The dotted arrow from $S_{1,0} \rightarrow T_{1,0}$ is a non-radiative transition called intersystem crossing, because it is a transition between states of different spin multiplicity. Below the diagram sketches of absorption-, fluorescence- and phosphorescence spectra are shown.

Absorption

Absorption transfers the electron into an excited state with the same spin multiplicity (S→S transition). According to Franck and Condon, the electron excitation is sufficiently fast, so that the nuclei motion can be neglected (timescale of 10^{-15} seconds).[234-236] The highest intensities are realized if the electron is excited vertically above to the excited state. **Figure 14** illustrates the Franck-Condon principle, where an absorption from the most populated $S_{0,0} \rightarrow S_{1,1}$ is most favored.[237]

Internal conversion and vibrational relaxation

The excited molecule internally converts the absorbed energy within the same spin system via environmental collision or vibrational relaxation. The so-called internal conversion is a fast pathway of non-radiative deactivation on timescales of 10^{-12} seconds.[238]

Fluorescence

Energy can be released in a radiative pathway within the same spin multiplicity. After non-radiative relaxation (e.g. $S_{1,4} \rightarrow S_{1,0}$ Kasha's rule),[239] the remaining energy

to convert the electron into the ground state is achieved by a spontaneous emission of a photon. The fluorescence lifetime is approx. 10^{-9} seconds.[240]

Intersystem Crossing (ISC)

The molecule can be transferred from an excited singlet spin multiplicity to an energetically lower excited triplet spin multiplicity (electron spin flip). Such transitions are quantum mechanically forbidden and thus only a fraction of excited molecules will undergo the ISC. The underlying mechanism of ISC is a spin-orbit interaction, which correlates with the atomic number. Thus, heavy atoms (high atomic number) accelerate the ISC significantly.[241]

Phosphorescence

In the triplet state, the molecule releases the energy in internal conversions until the triplet's excited ground state is reached (e.g. $T_{1,0}$). An emission via a photon (as in the case of fluorescence) is possible, yet the spin flip is not favored. The molecule is spin trapped and has a lifetime of $>10^{-3}$ seconds to undergo chemical reactions prior to a radiative deactivation by photon emission.[240]

Photoinitiated Processes

Norrish and coworkers studied the electron transition of carbonyl derivatives (n→π* electron transition) extensively.[242] They observed that the photoinduced homolytically carbonyl-carbon bond cleavage in α- or β-position (refer to **Scheme 4**) is more favored from the triplet state after ISC ($S_{1,0}{\rightarrow}T_{1,x}$). As many commercial photoinitiators are based on such Norrish-type reactions, their fundamentals are described in the following. As collated in **Scheme 4**, carbonyl molecules undergo a homolytic α-cleavage (Norrish Type I), resulting in two radical species.[242] They can further react in recombination, disproportionation, H shift or decarboxylation reactions. Yet, in the presence of a monomer, Norrish-Type I photoinitiators start the polymerization, equipping the chain terminus with either one of the two radical species or radical byproducts thereof. If the δ-carbon is subject to a radical-stabilizing environment (e.g. secondary substituted carbon), a Norrish-Type II reaction takes place.[243] After excitation, the oxygen-located radical can abstract the proton from the δ-carbon. Hence, the biradical molecule can undergo a cyclization reaction, a β-cleavage or a recombination to the starting material. If the δ-carbon does not sufficiently stabilize the radical but the carbonyl carbon does (e.g. in case of benzophenone), a proton can be abstracted from donor molecules. The thus generated donor radical can initiate a polymerization.

If no donor molecule is available, excited benzophenone undergoes a fast pinacol coupling.[242]

Norrish Type I

Norrish Type II

Scheme 4 Overview scheme of Norrish type I and type II reaction pathways.[242]
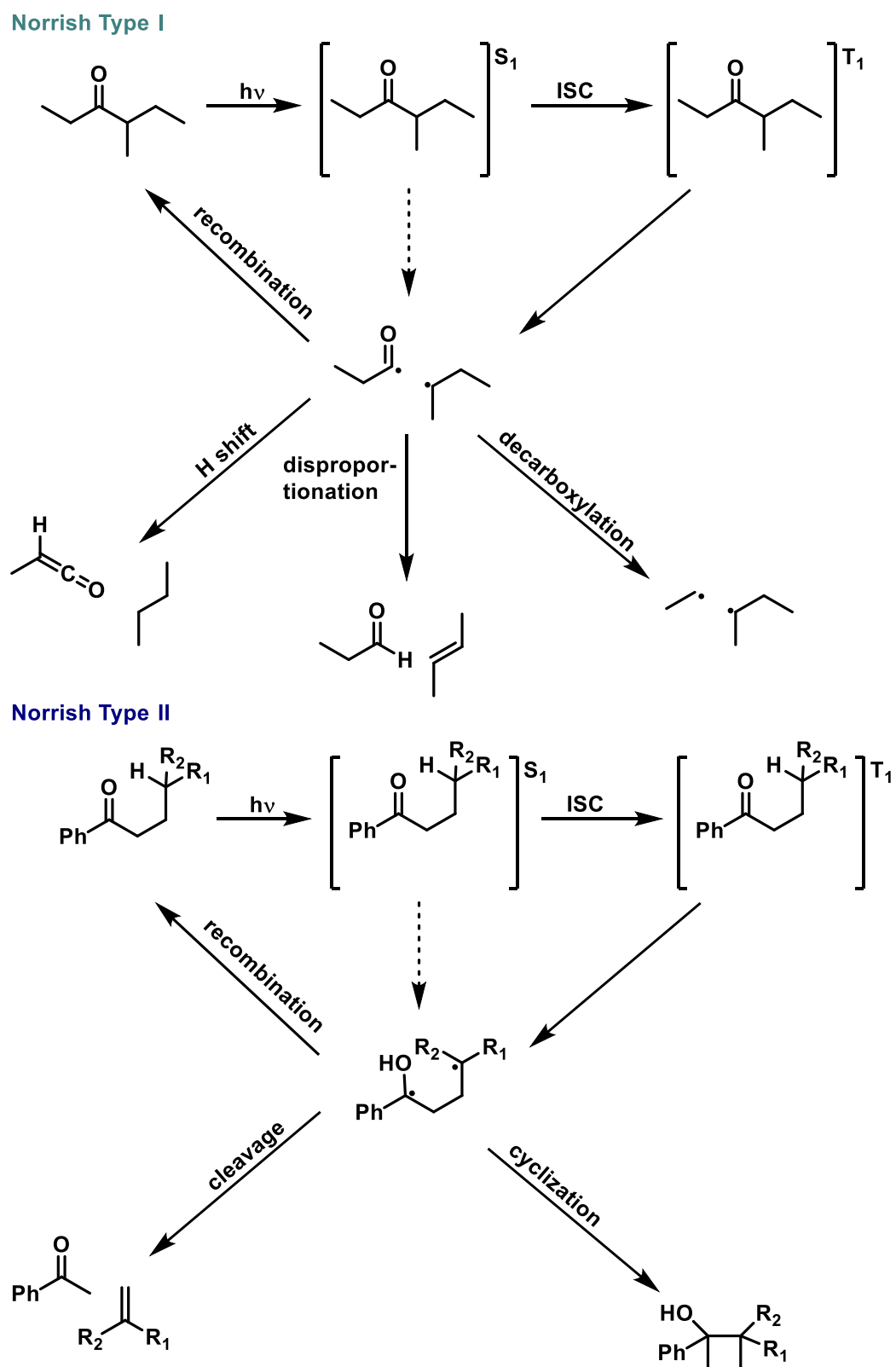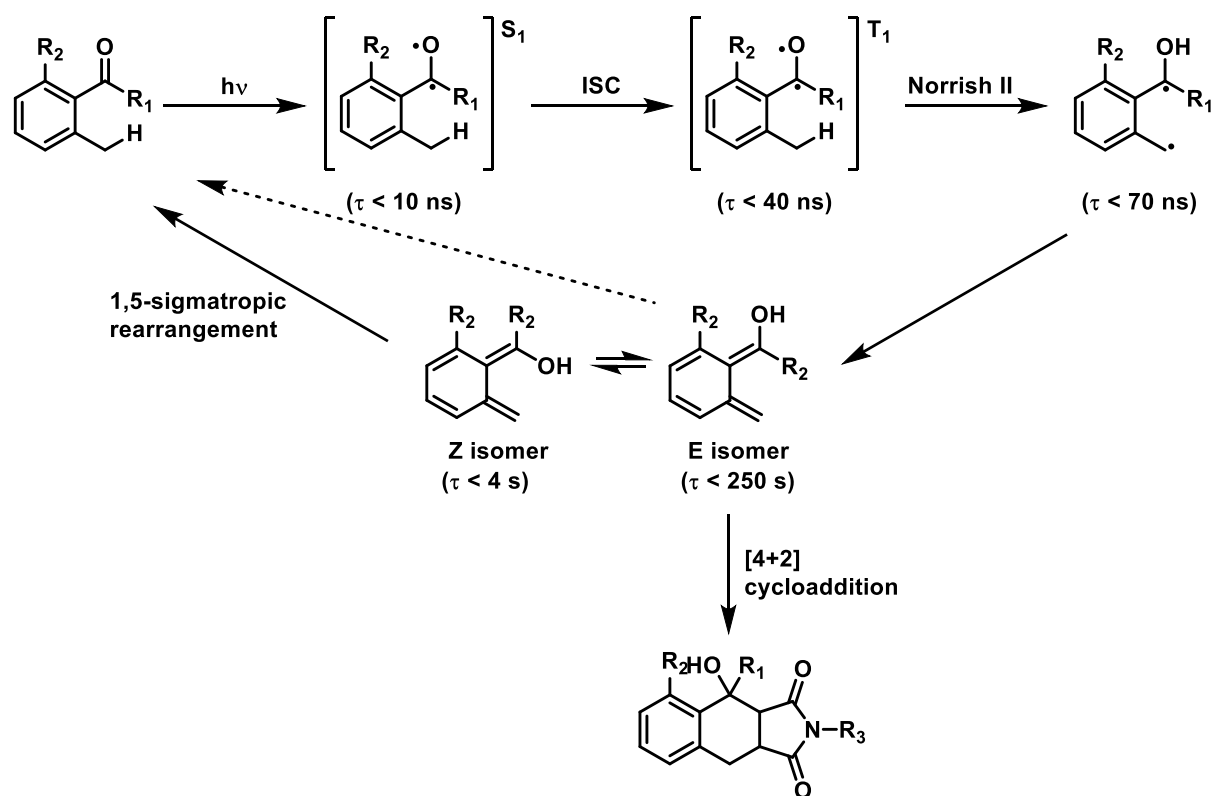
Scheme 5 Mechanism of the *o*-quinodimethane formation as adapted from Porter and Tchir.[246,247]

2.5.2. Photoinduced Diels-Alder Reactions

In the course of the present thesis, selected photoinduced reactions have been utilized to obtain characteristic material properties, including benzophenone initiators (refer to Chapter 7). In addition, *o*-quinodimethane structural motifs have been used as outlined in Section 4.4. The current section will focus on *o*-quinodimethanes for photoinduced Diels-Alder reactions. As introduced by Robert Burns Woodward and Roald Hoffmann in their set of organic rules for pericyclic reactions, Diels-Alder ([4+2]) cycloadditions are thermally induced i.e. the σ bonds are formed at ambient temperature or cleaved upon elevated temperatures.[244] However, the reactive intermediates (i.e. diene or ene) for the thermally driven Diels-Alder reaction can be generated via UV exposure of stable compounds.

The first report of an *o*-quinodimethane was reported in 1961 by Yang and Rivas.[245] However, Porter and Tchir[246,247] finally unraveled their UV-activation mechanism based on the precursor 2-methoxy-6-methylbenzaldehyde. The mechanism is depicted in **Scheme 5**.

Upon UV irradiation, the carbonyl moiety of 2-methoxy-6-methylbenzalde-hyde is excited ($S_{0,0} \rightarrow S_{1,x}$) into a n→π* electron transition followed by a fast ISC into the triplet state ($S_{1,0} \rightarrow T_{1,x}$). Via a Norrish Type II reaction, the proton located at the

methyl group is abstracted and thereby the carbonyl motif of 2-methoxy-6-methylben-zaldehyde forms a biradical. Internal conversion results in two energetically close iso-mers (*E/Z*) as the triplet state conically intersects with the *E/Z* singlet ground state.[248] The *E* isomer displays a reasonable lifetime whereas the *Z* isomer undergoes a rapid 1,5-sigmatropic rearrangement to the starting material. The *E* isomer reacts in a ther-mal Diels-Alder reaction with an 'ene'. As the activation is driven by UV light, spatially resolved structures can be realized (e.g. spatially tethered surfaces). Recently, Barner-Kowollik, Wegener and co-workers took advantage of this powerful photoisomeriza-tion in order to manufacture 3D printed structures below the diffraction limit.[159] The orthogonality to other reaction pathways allows for producing versatile macromolec-ular architectures.[159,249–255]

In summary, photoinduced reactions are a powerful tool to fabricate poly-meric materials. Many light-induced mechanisms have been elucidated by Norrish or Porter and co-workers. The electron excitation to a higher singlet state have all pho-tochemical reactions in common. The excited state constitutes the basis for a plethora of possible pathways for the molecule to process the absorbed energy. Jablonski in-troduced a clear schematic representation on ISC, internal conversion, fluorescence and phosphorescence. Therefore, the present section showcased the fundamentals of photoinduced reactions. The next section will introduce light-responsive trigger units for the design of light degradable polymers.

2.6. Self-Immolative Polymers: Novel Degradable Materials

Progresses in medicine and biology introduce novel methods to fight cancer, (lethal) diseases and dementia. However, the human immune system is exceptional strong in fighting exogenous substances such as an administered drug. Polymer chemistry is a suitable platform for future drug delivery as certain polymers (e.g. PEG,[114] PAEs[115,116] and poly(phosphoester)s (PPE)[256]) are invisible for the human immune system ('stealth' technique). However, the polymeric material will remain in the body after the drug has been delivered, and thus its removal has to be addressed. Here, the interplay of highly functional polymer scaffolds for drug assembly and cleavable backbone structures is important. As result of increased public and private funding, an entire research area focuses on novel degradable polymers for applications in medicine.[257–261]

A widely utilized degradable polymer is the poly(lactide) (PLA), which is obtained by the ROP of lactide. Lactides entail ester moieties enabling a suitable pathway (i.e. hydrolysis) for subsequent degradation. Thus, PLA is utilized e.g. in medicinal threads.[262] Although PLA and its degradation products are biocompatible, the degradation is slow (up to days) and the polymer is not amenable to backbone functionalization and property adjustment. Furthermore, the hydrolysis as degradation trigger is not controlled.

As the present thesis addresses the synthesis and characterization of novel degradable polymers entailing precision (i.e. in each repeat unit) trigger systems, the following section focuses on light-responsive trigger units and their respective SIPs.

2.6.1. Stimuli-Responsive Triggers

Scheeren, Shabat and McGrath reported the first SIPs almost simultaneously,[263–265] implementing self-immolative dendrimers for drug delivery. Boydston and co-workers defined SIPs as "having a linearly depolymerizing main chain of greater than 10 repeat units".[266] Although the synthesis of SIPs is of remarkable interest for the corresponding community, the present section is focused on the disassembly
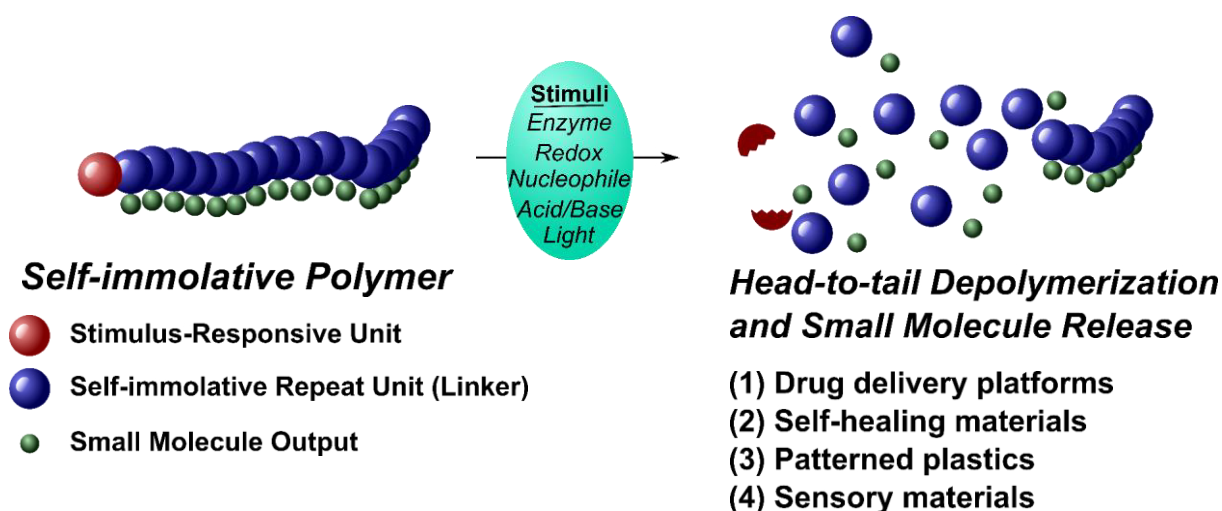
Figure 15 Cartoon of a SIP with a stimulus-responsive unit (red) and self-immolative repeat units (blue) endowed with small molecule output (green). Stimuli applied to SIPs can be enzyme, redox, nucleophile, acid/base or light. Reprinted with permission from Ref. [266]. Copyright American Chemical Society (2012).

mechanism and later on the design of light-responsive trigger units. For further details, the reader is referred to the most recent reviews in the field.[266-269]

Of even more significance than the self-immolative linker are the trigger units, as the choice of stimuli restrains the spatial and temporal control of the triggered destruction of the polymer. As many SIPs have strong association with biological systems due to their envisaged drug delivery, the enzyme-mediated cleavage is a frequently employed trigger.[270-276] For linear SIPs, the enzymatic trigger event was identified as the rate limiting step for the polymer disassembly.[273] Of similar important are redox-mediated cleavages as their installation is accessible via, e.g., transition metal-mediated reductions,[263,277-281] reduction of disulfide linkages[282] or oxidation of boronates with peroxides.[271,283-289] In particular, disulfide triggers are attractive for biological systems as the reducing intracellular environment can initiate the disassembly.[282] Less biologically relevant are nucleophile-mediated motifs. Here, no additional water is required for the trigger event and hydrolytically susceptible SIPs can be fabricated.[290-292]

Photomediated cleavage is arguably the most important trigger and regarded critical for future on-demand debonding systems. As the current thesis presents light-adaptive SIPs, the following part will be entirely focused on the photomediated cleavage. Currently, the demand for spatially and temporally controlled precision payload release under non-invasive, mild conditions drives research interest into light-adaptive SIPs. These degradable materials will disassemble upon irradiation with visible or near infrared (NIR) sources. However, the toolbox of existing photocleavable com-

(A) _o_-nitrobenzyl alcohol

(E)-aci-nitro

(Z)-aci-nitro
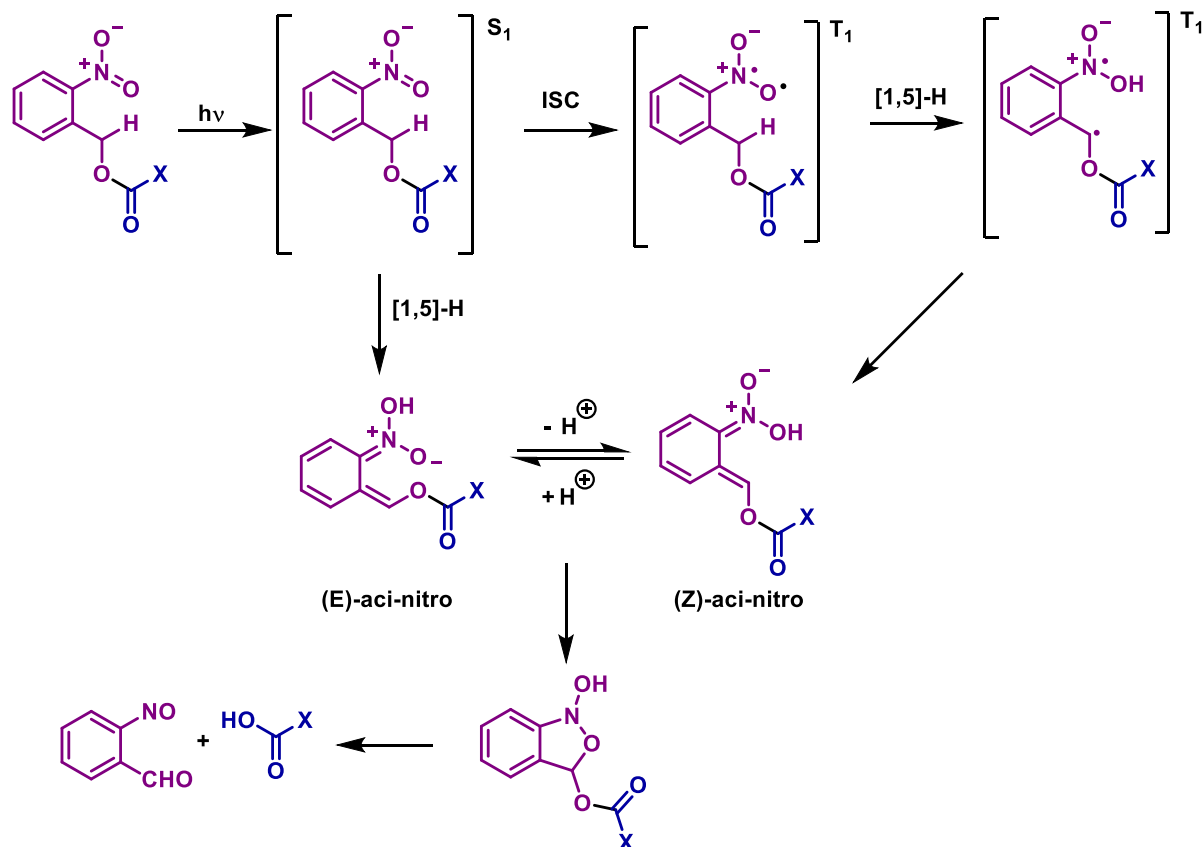
(B) coumarin-4-ylmethyl alcohol
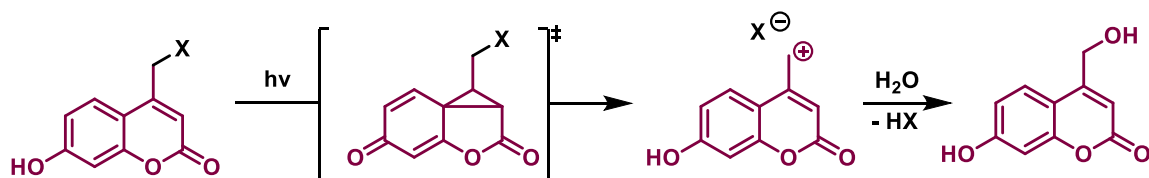
Figure 16 Proposed cleavage mechanisms for _o_-nitrobenzyl alcohol (A) and coumarin-4-ylmethyl alcohol (B).

pounds is small, comprising coumarins,[293-295] _o_-nitrobenzyl alcohol,[296-298] and benzo-quinones.[299] Most current approaches introduce the light responsive unit either as end group[295] or at the end of a branch within each repeating unit.[293,298]

Figure 16 depicts two prominent candidates and their cleavage mechanisms for the photomediated cleavage being _o_-nitrobenzylalcohol (**Figure 16A**) and coumarin-4-ylmethyl alcohol (**Figure 16B**). Both photo-removable protecting groups are able to undergo single photon (1P) and two photons (2P) absorption with reliably high Goeppert-Mayer units ($1\,GM = 10^{-50}\,cm^4 \cdot s \cdot Photon^{-1} \cdot Molecule^{-1}$).[281] The Goeppert–Mayer unit describes the absorption of two incident photons as a cross-section, where both photons have to encounter the material simultaneously. The higher the unit the likelier is an absorption process.[300,301] _o_-Nitrobenzylalcohol was reported in 1970 as an
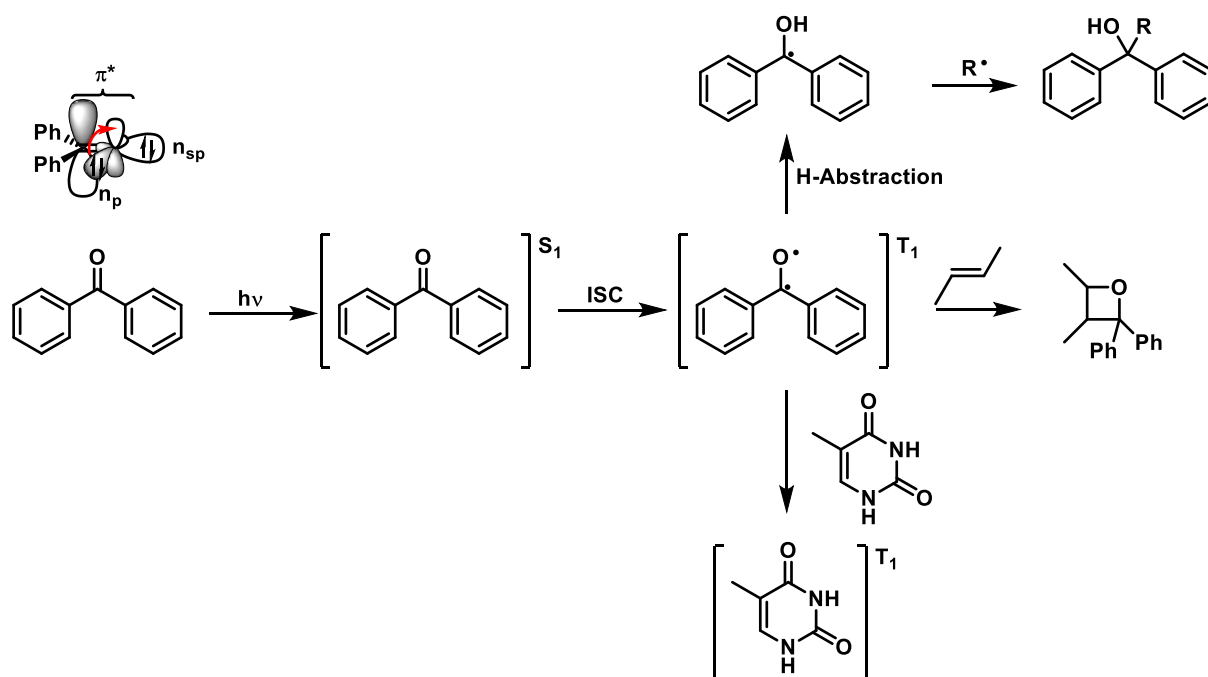
Figure 17 Reaction mechanism of BP via a H-abstraction (photoreduction) and subsequent radical-radical coupling (Oinakol coupling), Paterno-Büchi reaction with a double bond or photosensitizing organic molecules.

effective protecting group.[302] The proposed cleavage mechanism suggests an n→π* electron transition involving the nitroso motif attached to the aryl rest to a singlet state. A 1,5-sigmatropic rearrangement leads to (*E*)-aci-nitro, whereas an ISC to the triplet state followed by a 1,5-sigmatropic rearrangement produces (*Z*)-aci-nitro.[303] Both isomers can undergo a cyclization, whose subsequent ring-opening ultimately liberates the X group as carbonate or carbamate (see **Figure 16A**).

Coumarin-4-ylmethyl motifs are promising candidates for biologically relevant applications.[294,295,304] The attractive feature of the coumarin cage is the (pro)fluorescent property of the material, which can be used as self-reporting materials.[303] Installation of electron-donating groups on the 7-position of the coumarin can red-shift the absorption into the visible light region.[303] The excepted mechanism is illustrated in **Figure 16B**. It is proposed that the coumarin-4-ylmethyl motif is exited in an n→π* electron transition to a singlet state. The leaving group is expelled via a nucleophilic substitution (first order) reaction mechanism, where a carbocation is formed. The carbocation can react with a nucleophile (e.g. water), and thus, liberate the leaving group X.

The present thesis presents light-degradable polymers based on benzophenone (BP) for the photomediated cleavage. A full mechanistic scenario of the degradable BP polymer system is outlined in Chapter 7, whereas the current section focuses on the mechanistic details revealed by various scientists (see **Figure 17**). In 1996,

Porter and coworkers reported 2-benzoylbenzoic acid as highly effective photo protective group for alcohols and thiols.[305] The chemistry of BP is – in general – well explored with a plethora of possible applications in materials science, biological systems and polymer science.[306] After excitation via an n→π* electron transition, BP can be used as photosensitizer, for [2+2] cycloadditions, and most importantly it undergoes H-abstraction and radical recombination.

2.6.2.   Depolymerization Mechanism of SIPs

Upon removal of the triggering group from the SIP chain end, three distinct depolymerization mechanisms have been demonstrated: (*i*) 1,6- and 1,4-eliminations to form quinone methides, (*ii*) cyclization to form imidazolidinones, oxazolidinones, or 1,3-oxathiolan-2-ones, and (*iii*) cleavage of hemiacetals to dialdehyde monomers.[266] Qualitatively, the depolymerization kinetics is as follows: hemiacetal eliminations < 1,6-eliminations < 1,4-eliminations < cyclization–eliminations.[266] Rather than explaining every single depolymerization mechanism, special attention will be paid to a recent fascinating work of Shabat and co-workers.[307] The work of Shabat and co-workers
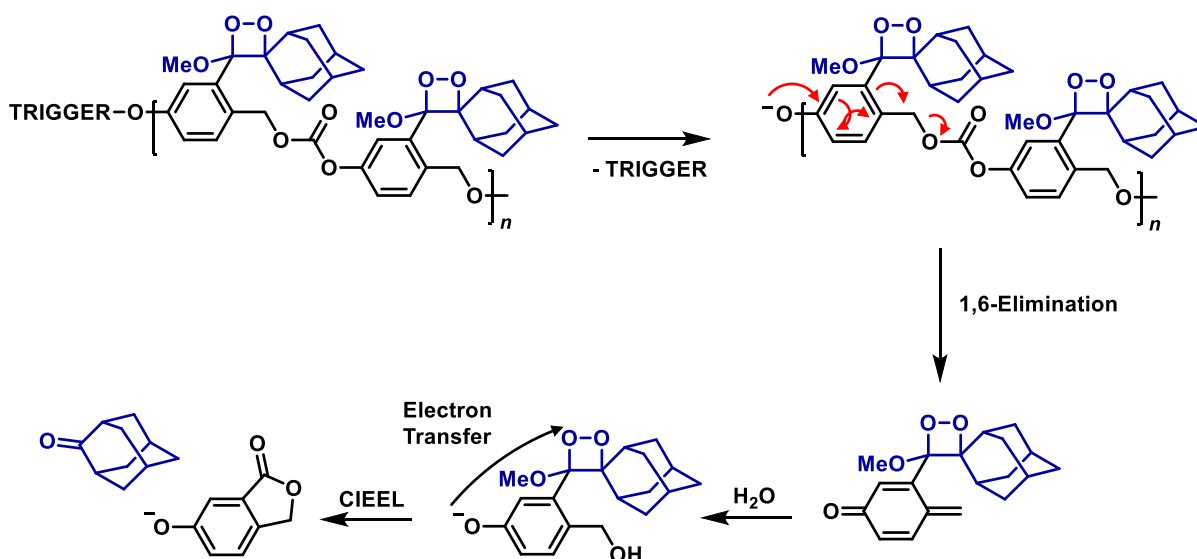
Figure 18 Chemiluminescent SIPs as published by Shabat and co-workers implementing a dioxetan ring as luminescent unit. Various triggers have been utilized (i.e. nucleophilic and redox active). Reproduced with permission from Ref. [307]. Copyright American Chemical Society 2017.

introduce – for the first time reported – a self-reporting SIP based on chemiluminescence, including a degradation of the main chain and the prochemiluminescent motif alike.

As outlined in **Figure 18** a novel self-immolative monomer has been designed and polymerized to yield a polycarbonate. The disassembly is a self-reporting system by virtue of the dioxetan ring, which is prochemiluminescent emitting blue light upon

the degradation. Most remarkably, Shabat and co-workers take advantage of the chemically initiated electron-exchange luminescence (CIEEL) mechanism transferring the energy to the oxetane. Thus, the chemiluminescence reaction is triggered.

In summary, light-triggered chemistry is a valuable strategy to introduce degradable polymers. The present section highlighted SIPs entailing stimulus responsive trigger units as representative candidates for such degradable systems. Furthermore, the disassembly mechanism is illustrated. The section equips the reader with the fundamental knowledge about phototriggered SIPs that are further studied in Chapter 7.

3

SUPERCHARGING SYNTHETIC POLYMERS: MASS SPECTROMETRIC ACCESS TO NON-POLAR SYNTHETIC POLYMERS[1]
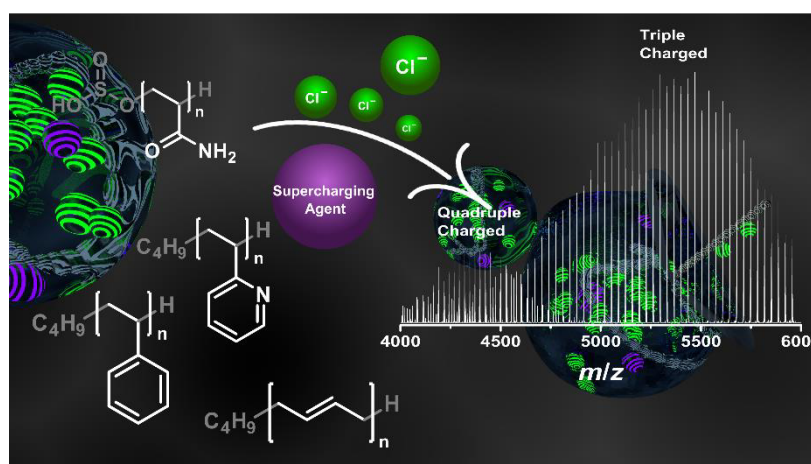
3.1. MOTIVATION

Non-polar polymers represent a vast amount of the industrially produced polymers. Commencing with poly(ethylene), to poly(propylene), poly(vinyl chloride), poly(tetrafluoroethylene), PBD and PS, these polymers have specific properties for unique applications. Furthermore, they are robust and stable, may retaining their structural integrity even at elevated temperatures, under high twisting forces or under high pressure. An in-depth analysis including their structural assessment is thus essential for both academic and industrial research. SEC, NMR, IR and UV have fundamentally contributed to characterizing these materials, however, these techniques fail in imaging the chain structure. MS has advanced as a powerful characterization technique for non-polar polymer structures, mainly due the strong ionization provided by MALDI. Here, poly(hydrocarbons) such as PE, PBD and PS can be ionized sufficiently. However, in order to ionize PE – as the chain structures entails only CH_2 motifs – requires end group modification with a charged chain terminus (e.g. ammonium, phosphonium). As discussed in Section 2.1.3, the ionization mechanism in ESI is complex including solvent/analyte interactions as well as charge/solvent and charge/analyte interactions. In positive ion mode, synthetic polymers can be charged by complexation with protons, alkali metal ions (Li^+, Na^+, K^+), ammonium, silver(I), Cu(II) and Co(I).[308] Before starting the in-depth investigation on sufficiently ionize poly(hydrocarbon)s with low coordination tendency, PS mainly formed singly charged species, whereas ESI failed in ionizing PBD.

Motivated by the current status of insufficient ESI ion abundances for non-polar polymers and the demand to generate multiply charged species (supercharging) allowing to elucidate high-molecular weight polymers even beyond the mass range dictated by the employed mass analyzer (i.e. Orbitrap < 8000 *m/z*), a mass spectrometric access route to analyze non-polar poorly ionizing synthetic polymers is reported, exploiting supercharging technology by chloride attachment. The mass spectrometric procedure allows for the characterization of polyhydrocarbons, including

hardly ionizable polymers such as PS (ranging from 1700 g·mol^{-1} to 18000 g·mol^{-1}), and – for the first time reported using ESI as ionization method – PBD (ranging from 1000 g·mol^{-1} to 10000 g·mol^{-1}). As described in Section 2.1.4, water as ESI solvent is a critical ingredient for a successful supercharging effect. Thus, the method is also applied to water-soluble synthetic polymers including poly(2-vinylpyridine) (P2VP) and poly(acrylamide) (PAAm). The powerful chloride attachment enables the detection of multiply charged polyhydrocarbons (up to quadruply charged). For the current project, a systematic assessment of the manipulation of these charge states using supercharging agents (sulfolane, propylene carbonate and *m*-nitrobenzyl alcohol) is carried out, and described in detailed in the following section.

3.2. RESULTS AND DISCUSSION

The following section is divided into two parts: (*i*) establishing a sufficient ionization pathway generating multiply charged ions during ESI to enable the MS analysis of non-polar polymers, and (*ii*) the manipulation of the charge state of PS, P2VP
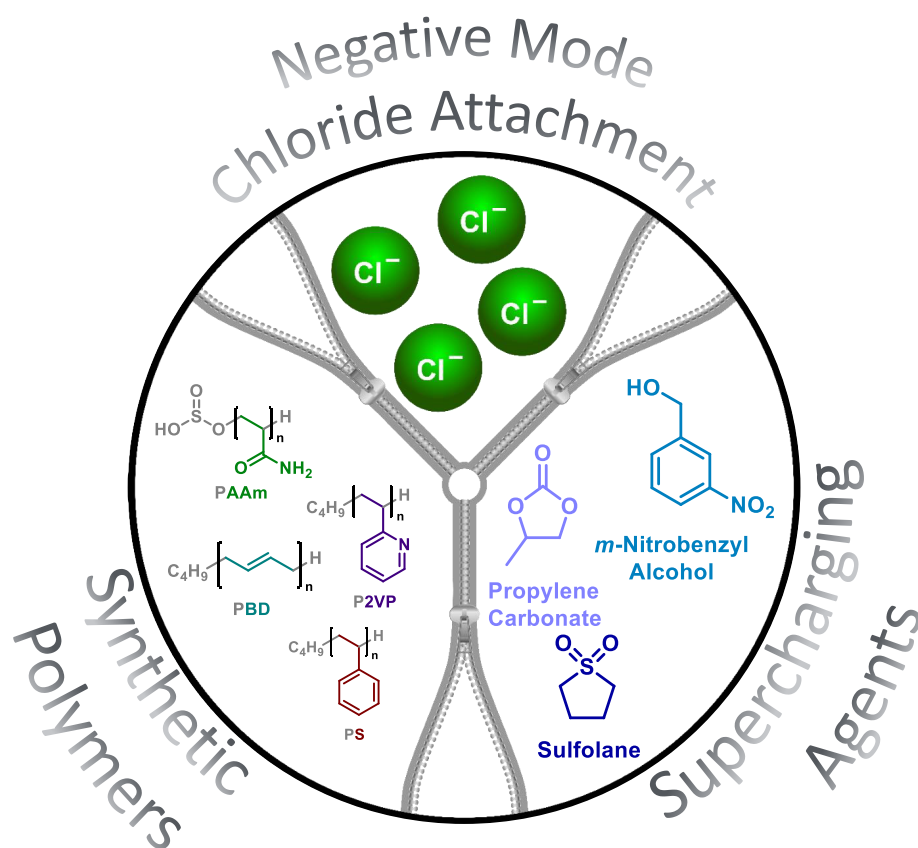
Figure 19 Illustration of the employed supercharging agents (sulfolane, propylene carbonate and *m*-nitrobenzyl alcohol) for the investigation of the polymers (PS, poly(2-vinylpyridine) (P2VP) and poly(acrylamide) (PAAm) via chloride attachment in negative ion mode. Reprinted with permission from Ref. [310]. Copyright American Chemical Society (2017).

and PAAm using supercharging agents.

Figure 19 illustrates the interplay of ionization method, supercharging agents and synthetic polymers explored in the current chapter. Hence, a detailed presentation of the results is carried out.[309]

Negative ion mode ionization via chloride attachment

PS is a versatile polymer enabling the preparation of sophisticated molecular architectures, (amphiphilic) block copolymers,[310] and styrene-type polymers such as poly(vinylbenzyl chloride) serves as a building block for postmodifcation.[311] The main mass spectrometric characterization of PS relies mainly on MALDI-ToF, whereas ESI studies are limited to short PS chains (up to 2000 g·mol^{-1})[312] via various cationizations.[308] The major disadvantage of cationization is that it does not readily promote multiple charging. Although multiply charged ions can cause isotopic overlaps and might hamper a detailed evaluation, highly charged species are the only access route to high-molecular weight polymers having their mass beyond the mass range of the analyzer. Herein, a powerful mass spectrometric technology is presented to analyze PS – even beyond the mass range of the mass analyzer enabled by the generation of multiply charged species via chloride attachment. High signal intensities were achieved by doping the ESI solvent (dichloromethane/methanol = 3:1 (*v*/*v*)) with 0.1% (*w*/*w*) NaCl. No significant [NaCl]$_x$Cl clusters were observed in negative ion mode using the QExactive Orbitrap. However, on a QExacative Plus (BioPharma option) a higher ion sensitivity enabled the detection of salt cluster formation. Thus, it is recommended not to exceed 50 mM NaCl concentration to avoid salt cluster formation. The
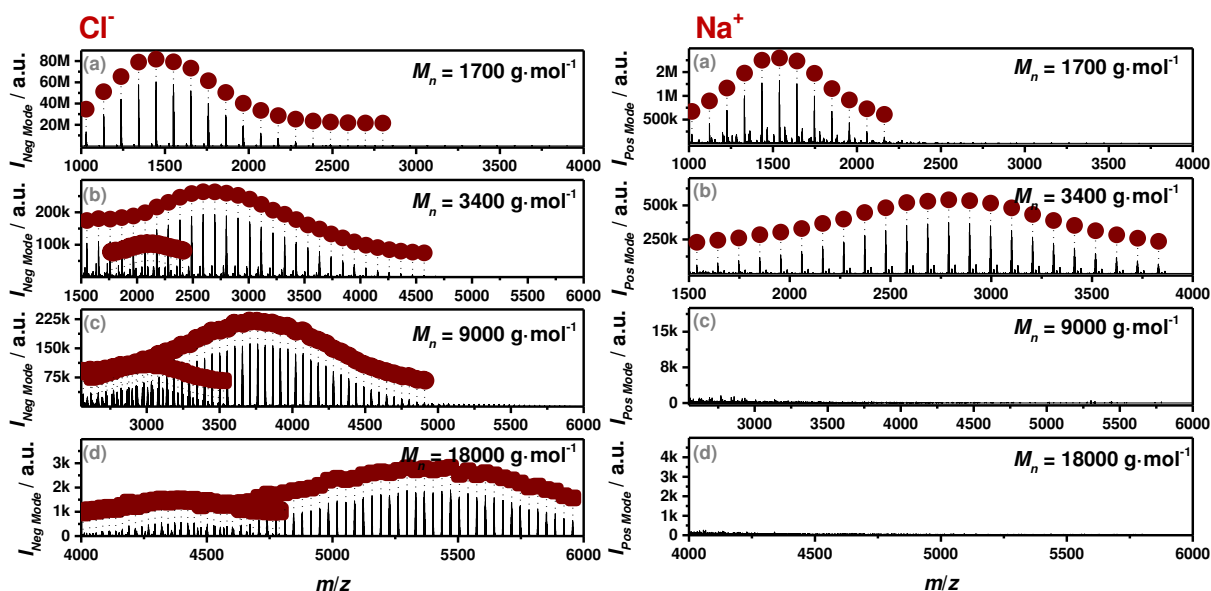
Figure 20 ESI-Orbitrap mass spectra of PS in negative ion mode (via Cl⁻ attachment) (left) and positive ion mode (via Na⁺ attachment) (right). For the molecular weight of M_n = 1700 g·mol⁻¹ PS is entirely singly charged (●) ionized by chloride or sodium ion. At M_n = 3400 g·mol⁻¹ PS is singly charged ionized by sodium, and singly (●) and double charged (○) ionized by chloride. For the molecular weight of M_n = 9000 g·mol⁻¹ PS cannot be detected in positive mode, whereas chloride attachment in negative mode promotes doubly (○) and triply (■) charged species. For the molecular weight of M_n = 18000 g·mol⁻¹ PS cannot be analyzed in positive ion mode, whereas chloride attachment promotes triply (■) and quadruply charged (□) species. All PS samples were obtained from Polymer Standard Service (PSS). Reprinted with permission from Ref. [310]. Copyright American Chemical Society (2017).
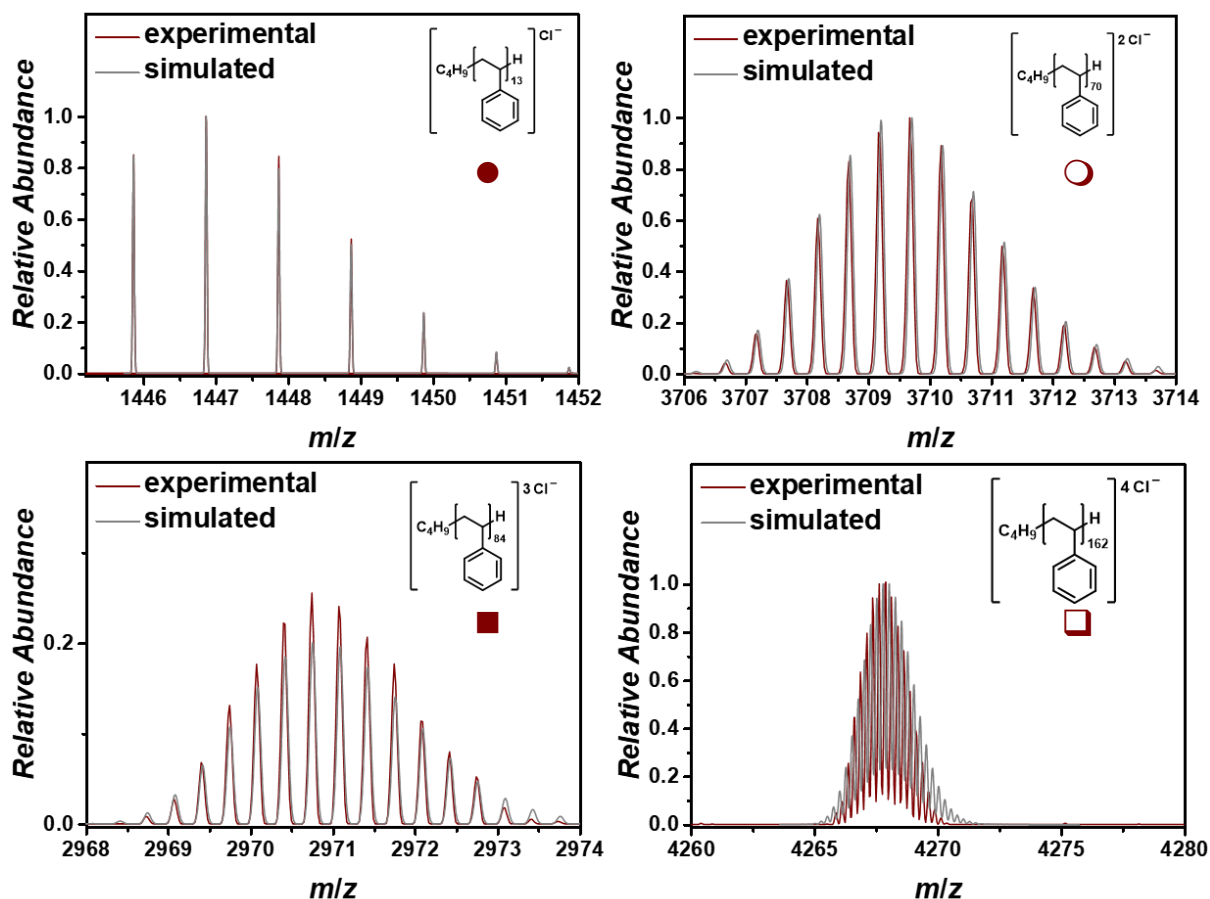
Figure 21 Singly (●), doubly (○), triply (■), and even quadruply (□) charged PS with their individual polymer structure determined by comparing the experiment with the simulation. An expanded spectrum and the assignments can be found in the Appendix (Fig. A 1 and Tab. A 1). Reprinted with permission from Ref. [310]. Copyright American Chemical Society (2017).

comparative study of sodium ionized PS and chloride ionized PS (**Figure 20**) highlights two important aspects of our mass spectrometric technique: (*i*) higher molecular weight PS (M_n = 9000 g·mol^{-1} and M_n = 18000 g·mol^{-1}) cannot be investigated in positive ion mode (via complexation to sodium). As main reason the low metal affinity either to the phenyl structure (ion-π interaction) or to the alkyl chain (H-binding affinity) is cited.[166] Thus, exclusively singly sodiated (●) PS ions were identified in positive ion mode. In contrast, chloride possesses high H-binding affinities resulting in stronger coordination tendency with either the phenyl part or the alkyl part of the polymer.[313] The most evident observations were therefore (*ii*) the doubly (○), triply (■), and even quadruply (□) charged PS species, where PS species with a degree of polymerization (DP_n) up to 180 were detected (refer to **Figure 21**). As revealed by the measurements (refer to **Figure 20**), the charge state increased with increasing molecular weight. These observations were in good agreement with the CEM, where the
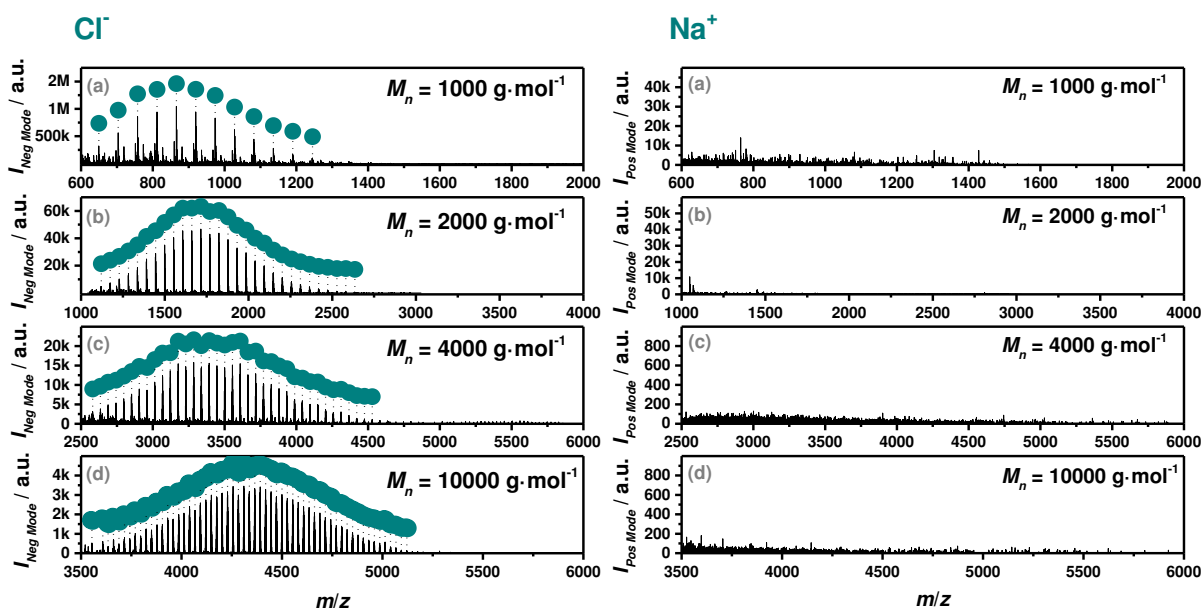
Figure 22 Mass spectra of PBD in negative mode (via Cl⁻ attachment) and positive mode (via Na⁺ attachment). At M_n = 1000 g·mol⁻¹, M_n = 2000 g·mol⁻¹, and M_n = 4000 g·mol⁻¹ PBD is entirely singly charged (●) ionized by chloride. At M_n = 10000 g·mol⁻¹ chloride attachment promotes doubly (○) charged species. PBD cannot be analyzed in positive mode. Reprinted with permission from Ref. [310]. Copyright American Chemical Society (2017).

polymer chain is released incrementally into the gas phase. In line with the CEM ionization (see Section 2.1.3), long polymer chains were capable of carrying more charges due to the reduced Coulomb repulsion afforded by enlarged chain conformations.

The negative ion mode ionization via chloride attachment was further applied on ionization of PBD, where ESI failed in positive ion mode. PBD is a key industrial polymer with multiple applications.[314] Especially, the (block)copolymerizations[315] and advanced post-functionalization of the alkene double bond[316] drive the demand to enhance the existing characterization techniques for this important class of polymer. Similar to PS, chloride possesses a high H-bonding affinity resulting in a strong interaction between the ion and either an alkyl part (H-Cl interaction) or a double bond (π-Cl interaction) of PDB. Herein, the first ESI mass spectrometric analysis of PBD is presented as a new analytical technology platform, which is not restricted to low molecular weight PDB (**Figure 22**) but enables the assessment of molecular weights up to 10000 g·mol⁻¹. As observed for PS, the strong H-bonding of chloride promoted multiple charges, allowing for the detection of masses beyond the analyzer mass range restricted to 6000 *m/z*. As collated in **Figure 22**, four PDB samples ranging from M_n = 1000 g·mol⁻¹ to M_n = 10000 g·mol⁻¹ have been analyzed. Chain-length dependent, the charge state increased from singly charged (labeled with ●) to doubly charged
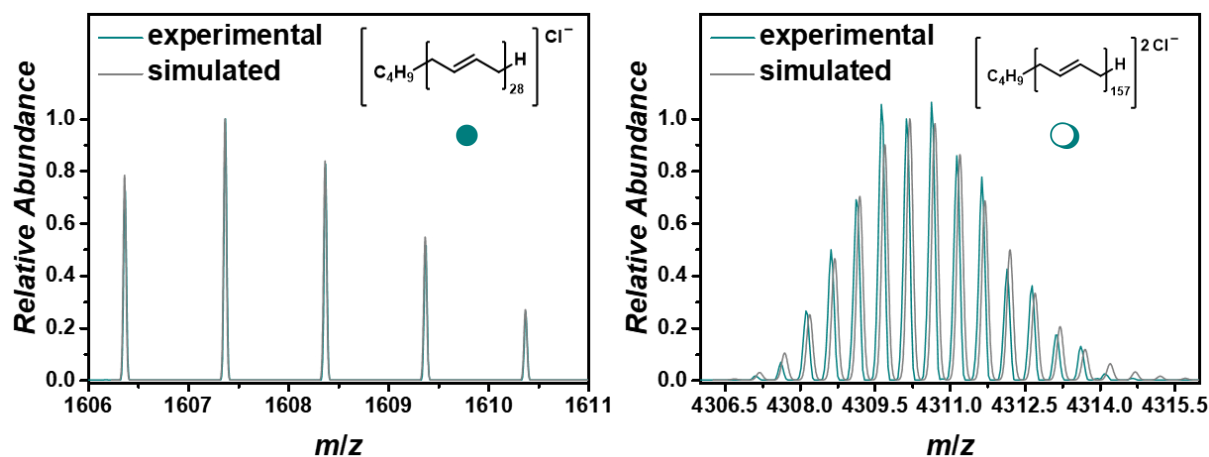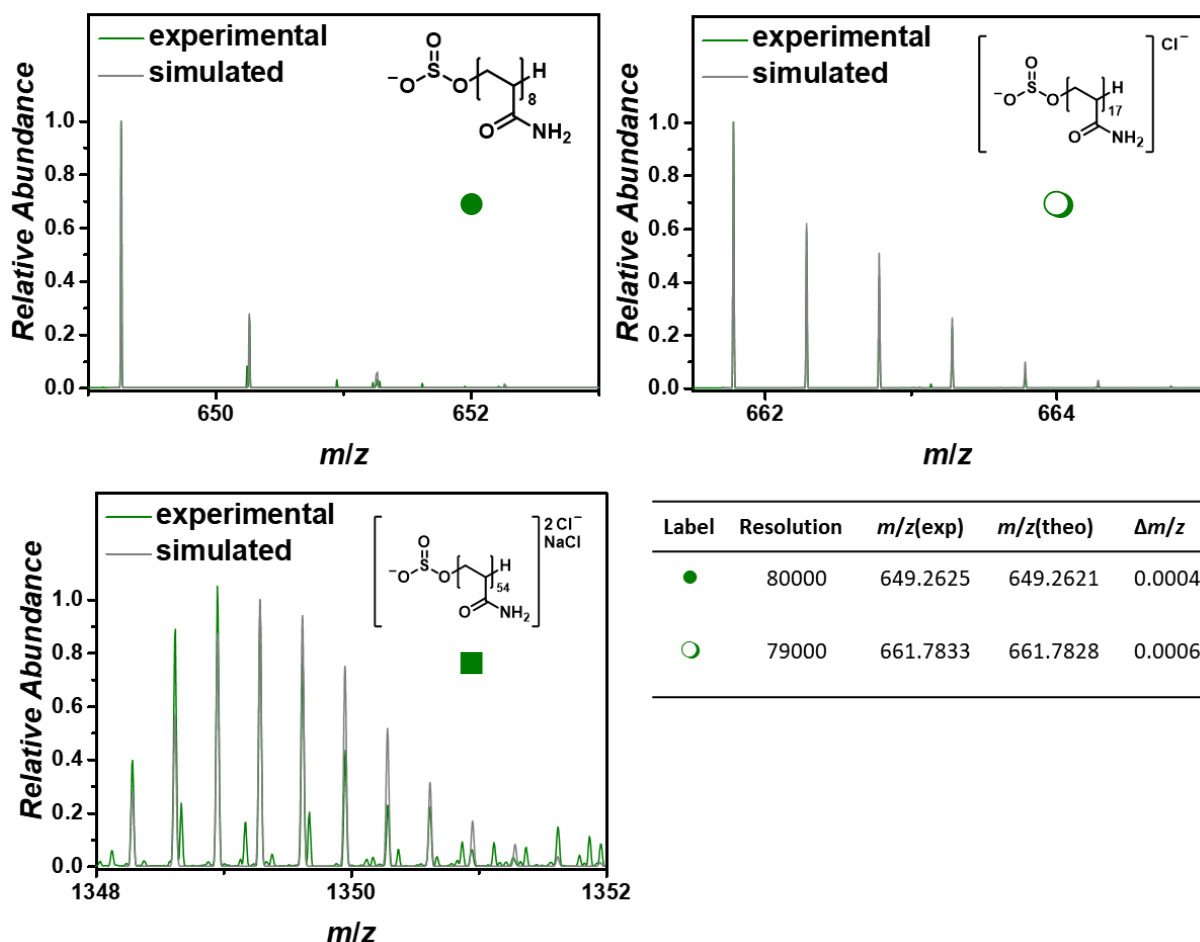
Figure 23 Singly (●), and doubly (○) charged PBD with their individual polymer structure determined by comparing the experiment with the simulation. An expanded spectrum and the assignments can be found in the Appendix (Fig. A 3 and Tab. A 3). Reprinted with permission from Ref. [310]. Copyright American Chemical Society (2017).

(labeled with ○) (refer to **Figure 23**). In contrast, the analysis of PDB in positive ion mode via Na$^+$ attachment was not successful.

High Resolution Mass Spectrometric Access to Nitroxide Containing Polymers[2]

Before a detailed discussion of the charge state manipulate using supercharging agents closes the present section, an important application of the novel negative ion mode attachment technology is presented. A full discussion including potential applications of such polymers will be presented in T. Fischer's doctoral thesis, with whom the candidate shares aspects of the presented results. Here, key findings of the study of nitroxide-containing polymers are reported,[317] which are – due to the presence of unpaired spins – highly challenging to analyze via NMR techniques. Thus, the nitroxide content within the polymer chain structure was varied between 11.3 and 29.1 mol% in a statistical copolymer consisting of poly(styrene-*stat*-vinylbenzyl chloride) (p(S-*stat*-VBC), 4800 ≥ M_n / g·mol^{-1} ≥ 11100), where 4-carboxy-2,2,6,6-tetramethylpiperidine 1-oxyl (4-carboxy-TEMPO) units were attached by post-polymerization modification. By carefully evaluating the isotopic pattern of the nitroxide containing polymers, it was demonstrated that the persistent nitroxyl radical retained its structural integrity during the soft ionization process employing spray currents up to
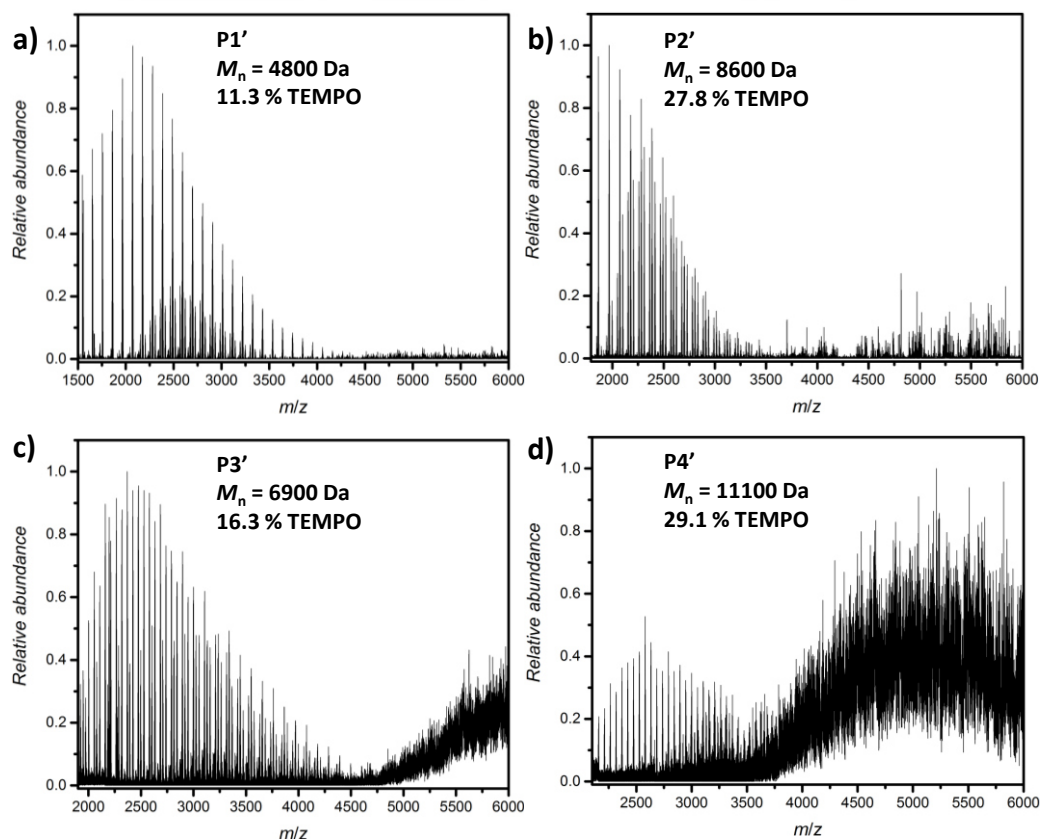
Figure 24 a) Overview ESI mass spectra of the nitroxide containing polymer **P1'** from m/z 1500 to 6000 recorded in negative ion mode, showing some minor high molecular weight species between *m/z* 4000 to *m/z* 6000. b) Overview ESI Orbitrap mass spectrum of **P2'** from *m/z* 1800 to 6000 measured in negative ion mode with increasing ion abundance of higher molecular weight species compared to a). c) Overview ESI Orbitrap mass spectrum of **P3'** from *m/z* 1900 to 6000 measured in negative ion mode, showing a significant increase of ion abundance of higher molecular weight species compare to a) and b). d) Overview ESI Orbitrap mass spectrum of **P4'** from *m/z* 1800 to 6000 recorded in negative ion mode. Clusters detected in the mass range between *m/z* 3500 and *m/z* 6000 cannot be identified due to insufficient resolution. Such high-molecular weight species are out of range for higher-energy collision dissociation tandem MS experiments (<2500 *m/z*). Reprinted with permission from Ref. [318]. Copyright Royal Chemical Society (2017).

4.3 kV and in-source collision induced dissociation energies up to 30 eV using the chloride attachment technology in the negative ion mode. The nitroxide-containing polymers ionized sufficiently, most likely enabled by the styrene motif of the polymer. However, increasing amounts of nitroxide mol% incorporated into the polymer structure led to high-molecular weight gas-phase aggregates (see **Figure 24**). Cimino et al. reported a high tendency to form hydrogen bridges between TEMPO and an H-donor.[318] Additionally, Mendenhall and Ingold reported the reversible dimerization of nitroxide radicals at low temperatures, suggesting the formation of aggregates.[319] With increasing molar ratios of TEMPO, more aggregated species were generated. However, HCD tandem MS experiments potentially allowing for the structural assessment of such aggregated species are limited to a mass range below 2500 *m/z*, and thus, have not been conducted in the present study. The generation of aggregated species was more pronounced in situations when the polymer contained 30 mol% of
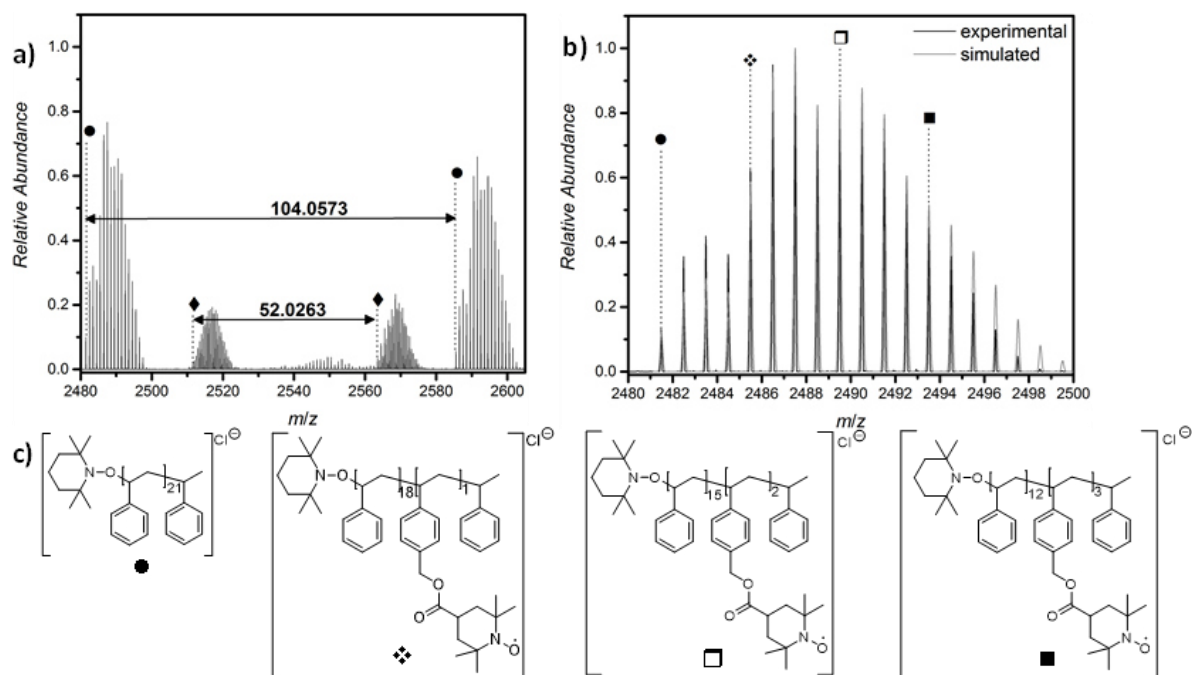
Figure 25 Expanded Region of the ESI-MS spectrum of polymer P1' between 2480 and 2605 *m/z*. The most abundant species are labelled as well as the repeating unit of PS. Reprinted with permission from Ref. [318]. Copyright Royal Chemical Society (2017).

free radicals indicated by a strong baseline drift. Furthermore, when the molecular weight was increased keeping the free radical molar ratio constant at close to 30 mol%, the mass spectrum of **P4'** (**Figure 24d**) had a strong baseline drift, being much more pronounced than for the smaller polymer **P3'**. Nonetheless, the non-aggregated species between 2000 *m/z* and 4000 *m/z* were unambiguously assigned to radical containing species (see **Figure 25**) as identified by their isotopic pattern.

Charge state manipulation by supercharging agents

As discussed in Section 2.1.4, supercharging agents have a fundamental influence on the ionization process. Importantly, in order to study supercharging a crucial requirement is that the species of interest is capable of forming multiple charges. With the negative ion mode chloride attachment developed, the subsequent research interest is to identify parameters effecting the observed charge states. In the literature, an extensive study has been performed on various proteins (as they promote multiply charged species readily in ESI), however, a full synthetic macromolecular assessment has still been missing. The present chapter closes this important analytical gap. In order to provide a well-organized discussion of the supercharging effect, the results of the water-soluble polymers PAAm and P2VP are presented, which are in good agreement to Konermann's molecular dynamics simulations (described in Section 2.1.4). Subsequently, the supercharging results of the non-polar PS are discussed.

Label	Resolution	m/z(exp)	m/z(theo)	Δm/z
●	80000	649.2625	649.2621	0.0004
○	79000	661.7833	661.7828	0.0006

Figure 26 Singly (●), doubly (○) and triply (■) charged PAAm with their individual polymer structure determined by comparing the experiment with the simulation. Peak assignments of the ESI Orbitrap mass spectrum of PAAm showing the labels, the resolution (obtained by the Xcalibur software), the experimental m/z and theoretical m/z values, Δm/z and the proposed chemical structures are provided in the table. Reprinted with permission from Ref. [310]. Copyright American Chemical Society (2017).

As revealed by the supercharging experiments, the charge state of PAAm strongly reacted to the addition of auxiliary agents. It is important to note that PAAm was prepared with a water-soluble initiator and thus carried a sulfite as functional end group (refer to **Figure 26**). Consequently, the end group had a fundamental influence on the charging behavior of the entire polymer and should be considered for the evaluation (and comparison) of the data. PAAm 13700 g·mol⁻¹ **Figure 27** was explored as polymer as the molecular weight is beyond the mass range (here, Orbitrap QExacative was used with a mass limitation of < 6000 m/z). **Figure 27A** compares the influence of sulfolane ranging from 5% (v/v) to 10% (v/v). As the results with propylene carbonate were less successful, the spectra are reported in the Appendix Fig. A 4. Here, only the addition of sulfolane as supercharging agent is discussed. The most important observation is that the ion abundance increases significantly. Furthermore, zooming into the spectra (**Figure 27B**) reveals species of higher charge states appearing in agreement with the increased amount of supercharging agent. Without any

auxiliary agent, the spectrum contained doubly charged species (labeled with ○). After the addition of 5% (*v/v*) and 10% (*v/v*) sulfolane, triply charged (labeled with ■) and quadruply charged species (labeled with ❑) indicated a strong charge shift from entirely doubly charged species to a higher charge state. Thus, the supercharging agent promoted the ionization of large PAAm chains via multiple chloride attachment.
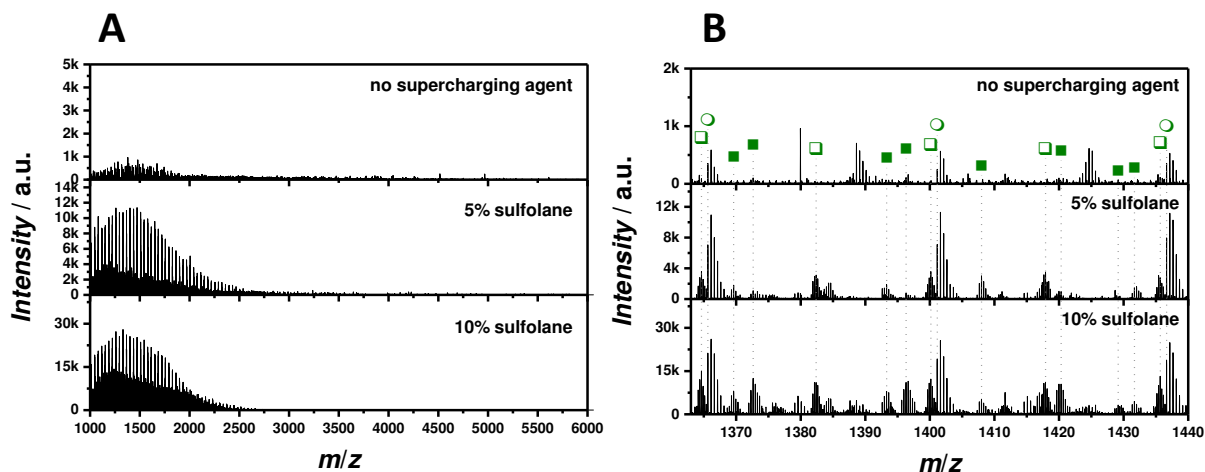
Figure 27 Mass spectra of PAAm 13700 g· mol^{-1} in negative mode (via Cl$^-$ attachment) comparing the influence of sulfolane as supercharging agent (ranging from 1% (*v/v*) to 10% (*v/v*)) in the ESI solvent water/acetonitrile=1:1 (*v/v*). Depicted are the full spectra (left) and a zoom (right) between 1362 *m/z* and 1440 *m/z*. Doubly (○); triply (■), quadruply (❑) charged ions. Reprinted with permission from Ref. [310]. Copyright American Chemical Society (2017).

Next, the supercharging experiments of P2VP are discussed. The results from the negative ion mode elucidation have been placed in the Appendix (Fig. A 4,5 and Tab. A 4,5) in order to avoid a repetitive discussion. P2VP has a high solubility in a broad range of solvents making it a valuable candidate for a supercharging investigation. **Figure 28** illustrates the results obtained for the supercharging investigations in (*i*) methanol/dichloromethane=1:3 (*v/v*) (**Figure 28A**) and in (*ii*) water/acetonitrile=1:1 (*v/v*) **Figure 28B**). Interestingly, the ESI solvent mixture dichloromethane/methanol (no supercharging agent) promoted doubly charged species (labeled with ○), whereas water/acetonitrile (no supercharging) exclusively formed singly charged species (labeled with ●). Supercharging agents, i.e. sulfolane, added to organic solvents (here, dichloromethane/methanol) caused a significant decrease in ion intensity associated with a slight subcharging (increase of the relative intensity of singly charged species). The water/acetonitrile solvent mixture doped with sulfolane as supercharging agent, however, promoted the formation of doubly charged species. Why does dichloromethane/methanol favor the ready formation of multiply charged species? As evidenced by the structural investigation, which is collated in the Appendix (Fig. A 4,5 and Tab. A 4,5), P2VP was ionized by virtue of complexation to the chloride anion in
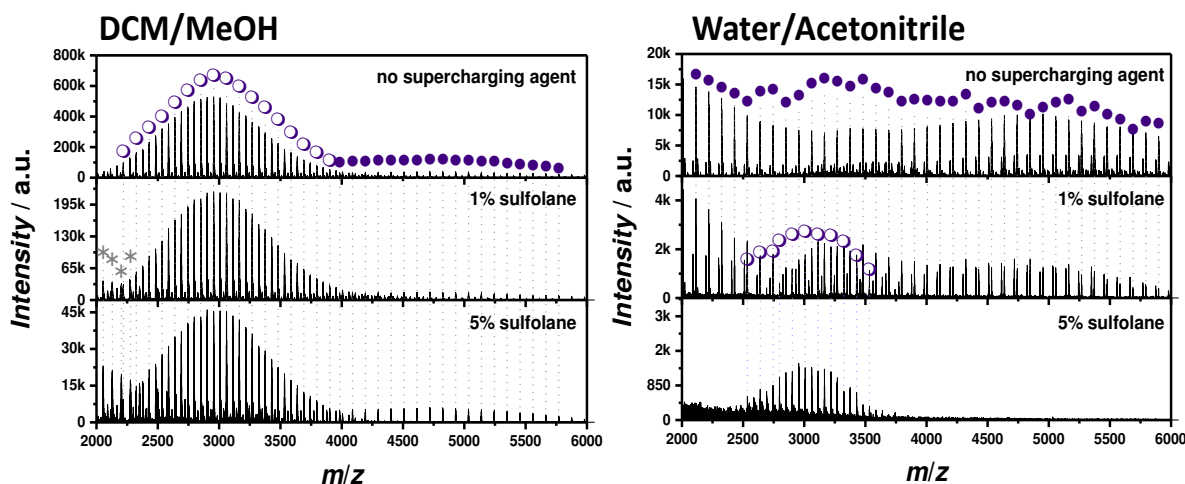
Figure 28 Mass spectra of P2VP 5000 g·mol^{-1} in negative mode (via Cl$^-$ attachment) comparing the influence of 1% (*v/v*) sulfolane and 5% (*v/v*) sulfolane as supercharging additive in the ESI solvents dichloromethane/methanol=3:1 (*v/v*) (right) and water/acetonitrile=1:1 (*v/v*) (left). Singly (●) and doubly (○) charged ions. Signals labelled with an asterisk (✳) stem from PDMS (see SI for details). Reprinted with permission from Ref. [310]. Copyright American Chemical Society (2017).

the case of dichloromethane/methanol, yet by the acetate anion for water/acetonitrile solvent mixture. It was essential to dope the ESI solvent with 1% (*v/v*) acetic acid due to enhance the solubility of the polymer in a slightly acidic medium. In Section 4.3 a detailed investigation of the anion in negative mode ionization is carried out, which results are essential for the discussion here: It has been evidenced that high H-binding anions such as chloride coordinate strongly to the polymer (see also the detailed discussion in "**Negative ion mode ionization via chloride attachment**" of the current section). Weakly coordinating anions, here acetate, do not possess equal H-binding capabilities and thus do not promote multiply charged species. Only the addition of supercharging agents into the water/acetonitrile mixtures increases the formation of doubly charged species. Again, this observation can be explained by the proposed charge-trapping mechanism described by Konermann and co-workers (outlined in Section 2.1.4). Their molecular dynamics simulations led to the conclusion that water plays an essential role in preventing the charge from escaping the nano-droplet.

Finally, the effect of supercharging agent in organic medium was assessed. Here, PS was opted for as the chloride attachment in negative ion mode promoted high ion abundances of multiply charged species (refer to **Figure 20**). **Figure 29** highlights the results obtained for all reported molecular weights of PS with 5% (*v/v*) sulfolane and 5% (*v/v*) propylene carbonate. No further charge state distribution was observed for PS with the molecular weight $M_n = 1700$ g·mol^{-1}. As discussed earlier in the current section, the main reason for singly charged polymers with very low mo-
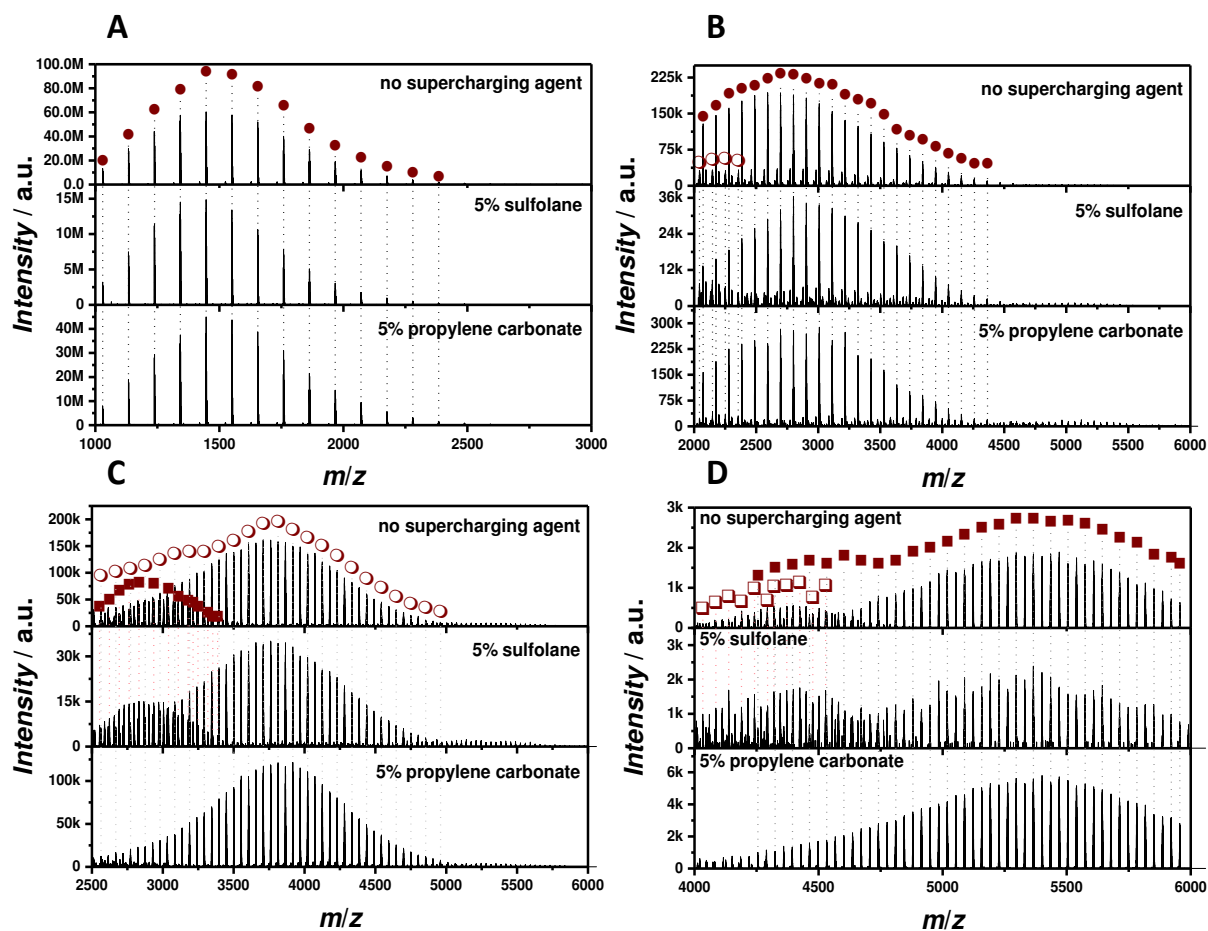
Figure 29 ESI-Orbitrap mass spectra of PS in negative mode (via Cl⁻ attachment) comparing the influence of 5% (*v/v*) sulfolane and 5% (*v/v*) propylene carbonate as supercharging additive in the ESI solvent methanol/dichloromethane=1:3 (*v/v*): (**A**) PS 1700 g·mol⁻¹; (**B**) PS 3400 g·mol⁻¹; (**C**) 9000 g·mol⁻¹; (**D**) 18000 g·mol⁻¹. Singly (●); doubly (○); triply (■), quadruply (□) charged ions. Reprinted with permission from Ref. [310]. Copyright American Chemical Society (2017).

lecular weight was the Coulomb repulsion preventing an additional charge to coordinate to the polymer chain. Furthermore, the ion intensity decreased significantly from approx. $60 \cdot 10^6$ to $15 \cdot 10^6$ with sulfolane and slightly to $50 \cdot 10^6$ with propylene carbonate. A similar trend emerged for PS with $M_n = 3400$ g·mol⁻¹ and PS with $M_n = 9000$ g·mol⁻¹ where the supercharging agent did not shift the charge state forming species of higher charge state (than without supercharging agent). Although the ion intensities decreased significantly for sulfolane-doped mixtures, the relative abundances of singly(●):doubly(○) charged species (PS 3400 g·mol⁻¹) as well as doubly(○):triply(■) charged species (PS 9000 g·mol⁻¹) showed an increased abundance of higher charge species (see **Figure 30**). The relative charge abundance was determined as follows: Integration of the full isotopic pattern of the highest peak in the distribution of the lower charge state was compared with the integrated value of the full isotopic pattern of the highest peak in the distribution of the higher charge state. Always

the same pair of species were used throughout the complete calculation within the supercharging study.
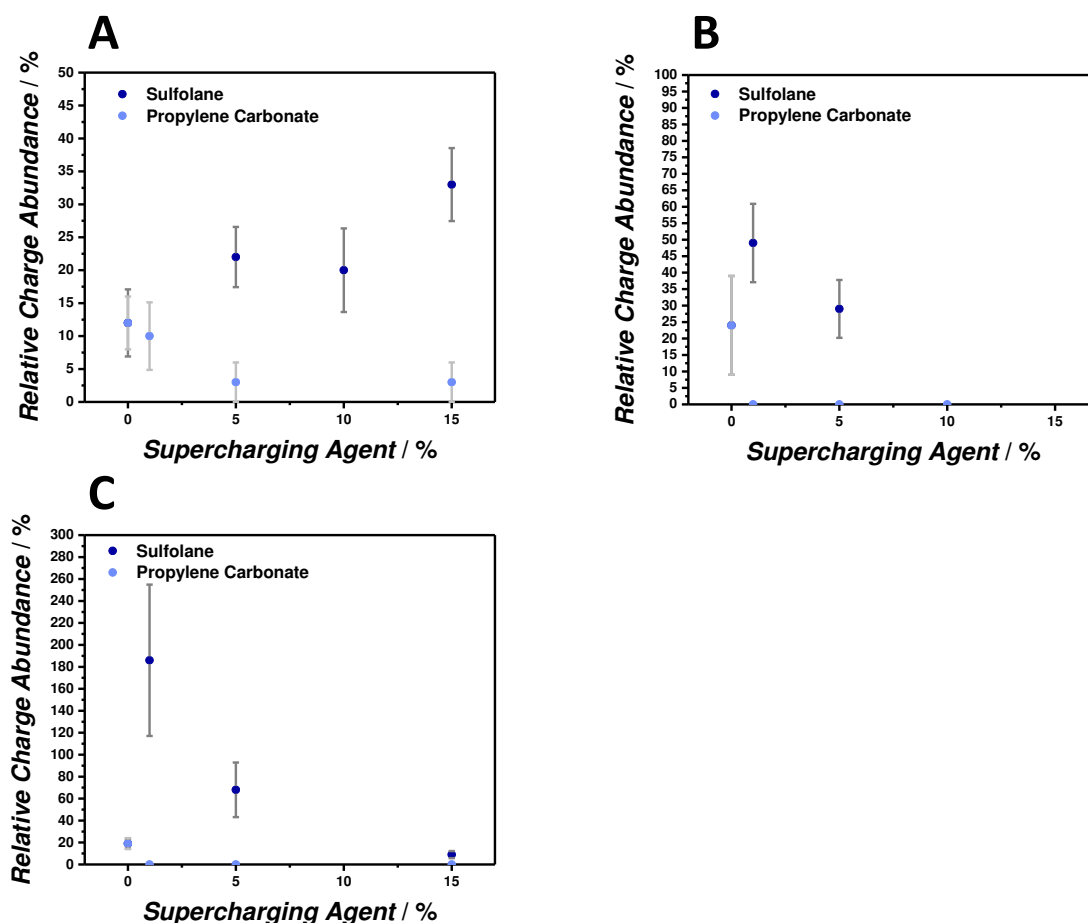
Figure 30 Relative charge abundance of PS with increasing amount of supercharging agents (PC and sulfolane): (A) PS 3400 g·mol⁻¹; (B) PS 9000 g·mol⁻¹ and (C) PS 18000 g·mol⁻¹. Reprinted with permission from Ref. [310]. Copyright American Chemical Society (2017).

For PS with M_n = 3400 g·mol⁻¹ and M_n = 9000 g·mol⁻¹, a relative increase of the higher charge state up to 10-15% was observed. In contrast, when propylene-doped solvents were used, the ion intensity remained constant, but the higher charge state decreased completely (see **Figure 30A and B**). The supercharging experiments of PS with M_n = 18000 g·mol⁻¹ revealed the same trend as discussed previously. Doping the solution with 5% (*v/v*) sulfolane increased the relative abundance of quadruply (❑) charged species drastically (see **Figure 30C**). Interestingly, and in contrast to all other PS samples, the ion intensity did not decrease (refer to **Figure 29D**). Adding 5% (*v/v*) propylene carbonate diminished the abundance of quadruply (❑) charged species to 0% (see **Figure 30C**). Such subcharging phenomena have been discussed in the literature.[320,321] A suitable explanation submits a charge competition mechanism,[35] where the analyte and the supercharging agent bind equally strong to the ion. By applying
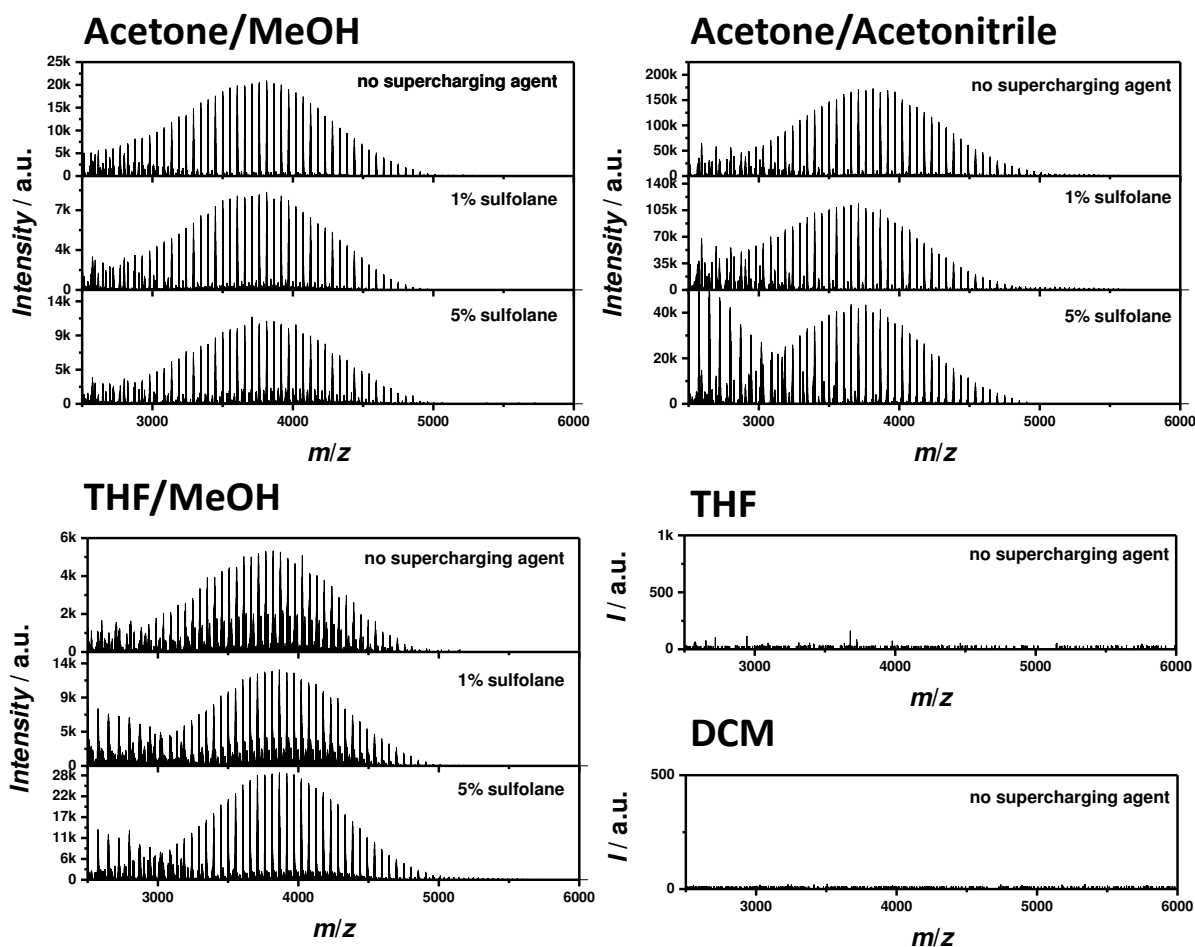
Figure 31 ESI-Orbitrap mass spectra of PS 9000 g· mol^{-1} recorded Acetone/MeOH, Acetone/Acetonitrile, THF/MeOH, THF and DCM as ESI solvent dopes with 0%, 1% and 5% sulfolane as supercharging agent. Reprinted with permission from Ref. [310]. Copyright American Chemical Society (2017).

additional literature-known supercharging agents such as *m*NBA for the analysis of PS with M_n = 9000 g·mol^{-1} gave similar results with a drastic decrease of the ion intensity. As the experiments are of minor significance for the further discussions, the spectra can be found in the Appendix Fig. A 7.

Summarizing the results for the supercharging of PS leads to the conclusion that the type of supercharging agent has a significant influence due to a proposed charge competition mechanism. Further, the amount of supercharging agent is of high importance for ionizing synthetic polymers. Still, no additional charge state was observed for PS. Further, the influence of various solvents and solvent mixtures (acetone/methanol, acetone/acetonitrile, THF/methanol, THF, DCM) in combination with sulfolane as supercharging agent was studied (see **Figure 31** and **Table 1**). An important criterion for the choice of the ESI solvent was the full dissolution of the analyte and sufficient conductivity for the formation of a stable current.[322] Thus, the solvent mixtures acetone/MeOH, acetone/acetonitrile, and THF/MeOH successfully allowed

the detection of negatively ionized PS species, whereas pure dichloromethane and THF did not promote the formation of stable spray currents. Thus, no polymer species were detected. Those solvents with stable spray conditions promote the formation of triply charged (■) PS species, however, adding supercharging agent to the ESI solvent did not shift the charge state.

Table 1 Comparison of maximum ion intensities for PS (9000 g · mol⁻¹) obtained with different ESI solvents and sulfolane as supercharging agent. Reprinted with permission from Ref. [310]. Copyright American Chemical Society (2017).

Solvent Mixture	Max. Ion Intensity no SC	Max. Ion Intensity 1% sulfolane	Max. Ion Intensity 5% sulfolane
DCM/MeOH	160 000	56 000	35 000
DCM/MeOH + 1% water	59 000	13 000	17 000
DCM/MeOH + 5% water	37 000	13 000	24 000
THF/MeOH	5 000	13 000	28 000
THF/water (20vol%)	No species detected	7 000	18 000
Acetone/MeOH	21 000	8 600	12 000
Acetone/Acetonitrile	170 000	113 000	43 000
THF	No species detected	Not determined	Not determined
DCM	No species detected	Not determined	Not determined

3.3. CONCLUSIONS

A novel mass spectrometric procedure for the in-depth characterization of polyhydrocarbons such as PS and PBD via chloride attachment in negative ion mode has been pioneered. It is demonstrated that the coordination of chloride is a powerful method to access high molecular weight polyhydrocarbons by promoting multiply charged species (up to four charges). The charge state distribution can be adjusted via supercharging agents such as sulfolane, propylene carbonate and *m*-nitrobenzyl alcohol. Specifically, supercharging experiments were carried out with the polymers poly(styrene), poly(2-vinylpyridine) and poly(acrylamide). The current section's conclusions are: (*i*) the choice of supercharging agent is crucial for synthetic polymers in negative ion mode via chloride attachment. Explained by the charge competition mechanism, some supercharging agents (e.g. *m*-nitrobenzyl alcohol) may function as subcharging agent. (*ii*) The amount of supercharging agent can have a negative influence on the ion abundance caused by the charge competition mechanism. (*iii*) The choice of ESI solvent can completely impede a potential supercharging effect. Thus,

the charge state modification is most evident for water-soluble polymers (e.g. PAAm) and only slightly in methanol and other organic solvents. (*iv*) The chain length is crucial for observing multiple charges because the conformation has a significant influence on the charge state (e.g PS 18 000 g·mol^{-1} promotes quadruply charged species, PS 1700 g·mol^{-1} remains singly charged). (*v*) The existence of polar groups is important for a strong supercharging effect as previously demonstrated in the mass spectrometric analysis of PAAm. The polymer has functional moieties, which contribute to the supercharging effect, which have to be taken into consideration in order to understand Konermann's supercharging mechanism (see Section 2.1.4). As reported in Section 2.1.4, the supercharging was successfully employed for biomacromolecules and for poly(ethylene glycol), which are very polar substances.[35,45,323-325] The supercharging mechanisms that are in good agreement to the measurements in the present section are Konermann's charge-trapping mechanism (since water had a crucial impact on the efficiency of the supercharging agents) and Donald's dipole-based mechanism (since the presence of functional moieties in PAAm is fundamental for successful supercharging). Thus, the charge state of completely hydrophobic polymers (as PS and PBD) are almost unaffected by auxiliary additives, irrespective of the solvent choice. Under non-stable ESI spraying conditions, the addition of supercharging agent supports the stabilization and the occurrence of a charged species (as evidenced by the THF/water experiments).

3.4. EXPERIMENTAL SECTION

3.4.1. Materials

All polymer standards were purchased or donated by Polymer Standard Service (PSS) in the molecular weight as referenced in the manuscript. The ESI solvents were used without further purification: acetone (Sigma-Aldrich; HPLC grade), acetic acid (Scharlau, analytical grade), acetonitrile (Roth, LC-MS grade), dichloromethane (Roth, HPLC grade), methanol (Roth, HPLC grade), water (Milli-Q), tetrahydrofuran (Scharlau, HPLC grade). All chemicals were used as received: NaCl (Roth, >99%), propylene carbonate (TCI, >98%), sulfolane (Sigma-Aldrich, analytical standard), *m*-nitrobenzyl alcohol (TCI, >99%).

3.4.2. Instrumentation

Electrospray ionization-Orbitrap mass spectrometry (HR ESI MS). Mass spectra were recorded on a Q Exactive (Orbitrap) mass spectrometer (Thermo Fisher Scientific, San Jose, CA, USA) equipped with a HESI II probe. The instrument was calibrated in the m/z range 1000-6000 m/z using ammonium hexafluorophosphate (Thermo Scientific). All spectra were recorded in the negative mode, using the ESI solvents as described in the main text doped with 0.1% (w/w) NaCl. PS; PBD and P2VP were recorded in a concentration of 0.5 mg·mL^{-1}; PAAm was recorded in a concentration of 0.05 mg·mL^{-1}. The FT resolution was set to 140 000 employing 3 microscans during an acquisition time between 2 and 5 min measuring with a capillary temperature of 320 ℃. The aux gas flow was (dimensionless) 0.00, the sheath gas 10.00, and the spare gas 1.00. The flow rate was set to 5 µL·min^{-1}. The spray voltage was set to a specific value (PS: 4.5 kV; P2VP: 3.9 kV; PAAm: 4.0 kV; PBD: 3.6 kV) and kept constant while performing the supercharging experiments. An in-source CID energy of 10 eV was employed for recording PAAm.

4

Mass Spectrometric Analysis of Poly(ionic Liquid)s[3]
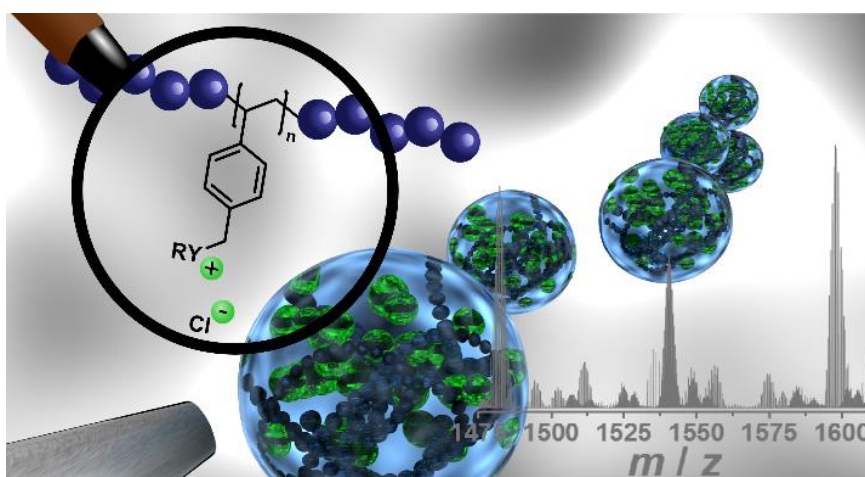
4.1. MOTIVATION

PILs are fascinating polymers with unique properties. They can be readily adapted to many desired functions by exchanging the associated counter ion. To realize their full structural capability, a quantitative salt exchange is critical and often enabled by adding silver salts. Standard characterizations are limited to IR spectroscopy and NMR (in case the exchanged counter ion has a nucleus that can be traced). More advanced characterization techniques providing access to structural information on the molecular level have not been explored so far. Although the salt exchange via silver is convenient, it cannot be applied to porous materials as the precipitating silver halide could potentially block the pores and would require thorough and time-consuming rinsing processes. Apart from the salt exchange, the polymerization of IL monomers can be challenging. Often, PILs are dialyzed after polymerization due to difficult precipitation as both the monomer and the polymer feature the same solubility. Especially ester-containing IL monomers are susceptible for hydrolysis during dialysis. However, SEC characterization cannot reveal potential side-chain cleavage. Further, NMR might be hampered for revealing hydrolytical processes as NMR lacks sensitivity. A valuable alternative would be mass spectrometry as it allows for direct chain visualization. The exact mass determination combined with tandem MS processes and isotopic simulations give access to their structural information. However, Matyjaszewski and co-workers reported that it is very challenging to image PILs via ESI.[175] Although Tenhu and co-workers reported successful MALDI determination, they did not display the corresponding mass spectra in their publication and thus did not allow to determine the chain structure.[176]

Motivated by the current status of lacking mass spectrometric analysis for PILs, a universal high resolution mass spectrometric method for the analysis of PILs is introduced in the following section, which belong to the most challenging polyelectrolytes from an analytical perspective by fusing HR CID-Orbitrap MS with supercharging agents. The current study includes a wide array of hydrophilic halide-containing PILs, which were analyzed in negative ion mode. The influence of the core structures (based on imidazolium, triazolium, ammonium, phosphonium and pyridinium moieties), and variable styrene-, acrylate- and vinyl-type IL polymers on the ionization behavior is mapped in detail. Variable end group functionalities were introduced via functional chain transfer agents (CTA) in RAFT polymerization to assess their influence on the MS analysis.

4.2. RESULTS AND DISCUSSION

4.2.1. Preparation of PILs

Among the many versatile features of the RAFT process,[326] the high tolerance towards functional monomers is an important characteristic for a controlled polymerization process. Hence, RAFT is expected to be a suitable candidate for the precision preparation of monomeric ILs with well-defined chain termini and thus applied in the presented work outlined in the following section. The synthesis and properties of 1-alkyl-3-(p-vinylbenzyl)-imidazolium based PILs were widely investigated,[175,327] yet the RAFT process of the corresponding monomers remains challenging. The current thesis presents the controlled polymerization for the generation of poly(1-butyl-3-(p-vinylbenzyl)-1H-imidazolium chloride) (p([BVBIM]Cl), **3**) and poly(1-butyl-3-(p-vinylben-
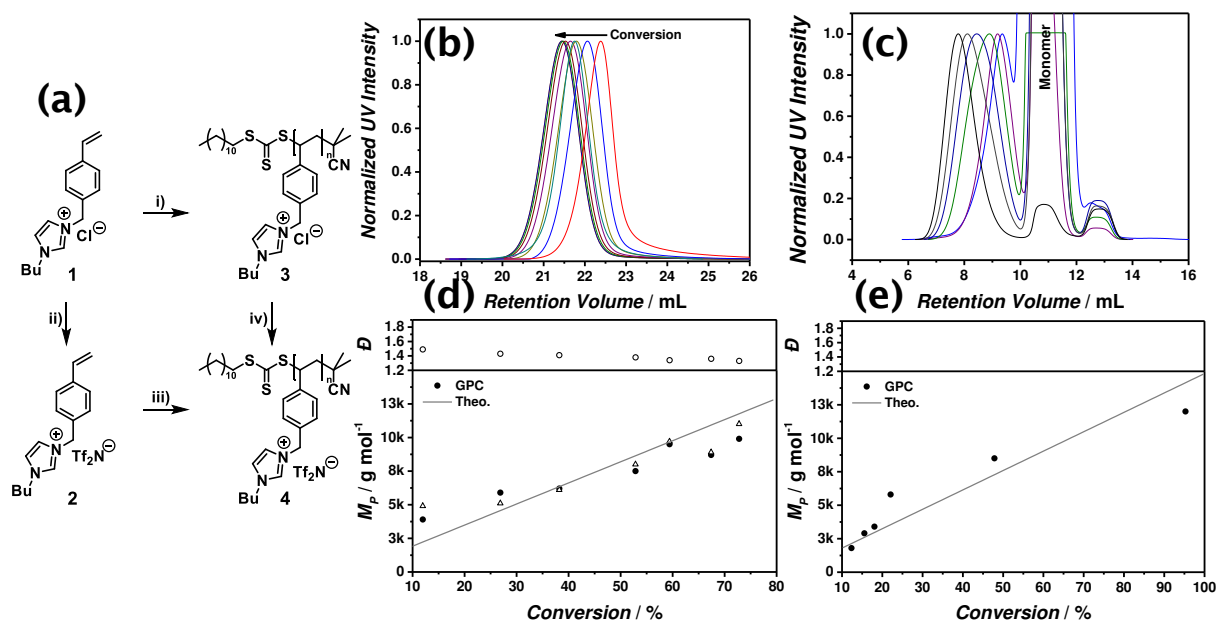
Figure 32 (a) Synthetic approach for the preparation of p([BVBIM]Cl) (**3**) and p([BVBIM]Tf$_2$N) (**4**) from the monomers [BVBIM]Cl (**1**) and [BVBIM]Tf$_2$N (**2**), respectively. Molar ratio [M]:[CTA]:[I] for i) 200:1:0.2 and for iii) 200:1:0.2 (i: RAFT polymerization; ii: anion exchange; iii: RAFT polymerization; iv: anion exchange). **(b)** GPC traces of p[BVBIM]Cl (**3**) via the RAFT mediated polymerization of [BVBIM]Cl (**1**) at 85 ˚C in DMSO. **(c)** Molecular weight evolution of the RAFT polymerization of p([BVBIM]Tf$_2$N) (**4**) at 85 ˚C (left) in butyronitrile. **(d)** Plot of molecular weight (M_n) and dispersity ($Đ$) vs. monomer conversion. Molar ratio of monomer:CTA:initiator 200:1:0.2 (CTA = 2-cyano-2-propyl dodecyl trithiocarbonate; initiator = 1,1'-azobis(cyclohexanecarbonitrile)). H$_2$O-SEC system conditions: water/0.3 M formic acid/0.5 g·L^{-1} NaCl, 30 ˚C, flow rate 1.0 mL·min^{-1}. **(e)** Molecular weight evolution (M_P) with conversion for the RAFT mediated polymerization of (**2**). Molar ratio [M]:[CTA]:[I] 200:1:0.2, 85 ˚C, butyronitrile (CTA: 2-cyano-2-propyl dodecyl trithiocarbonate; I = 1,1'-azobiscyclohexane carbonitrile). THF-SEC system conditions: 10 mmol LiTf$_2$N, 10 mmol n-butylimidazole, 35 ˚C, flow rate 1.0 mL·min^{-1}. Reprinted with permission from Ref. [312]. Copyright Royal Society of Chemistry (2016)

zyl)-1H-imidazol-3-ium bis(trifluoromethanesulfonyl)imide) (p([BVBIM]Tf$_2$N), **3**) as representative candidates for PILs in detail. All other PIL core structures including their characterization is compiled in Appendix Fig. B 1-35.

The polymerization of [BVBIM]Cl (**1**) and BVBIM]Tf$_2$N (**2**) can either be realized by direct polymerization or by the post-polymerization modification of poly(vinylbenzyl chloride) (P(VBC)) followed by counter ion exchange with Tf$_2$N$^-$ (refer to **Figure 32a**). Both monomers [BVBIM]Cl (**1**) and [BVBIM]Tf$_2$N (**2**) were prepared by a quaternization reaction (Menschutkin reaction) between 4-vinylbenzyl chloride and n-butylimidazole with a slightly modified synthesis protocol given in the literature.[328] A rapid counter ion exchange performed in water as solvent resulted in [BVBIM]Tf$_2$N (**2**).

Subsequently, [BVBIM]Cl (**1**) was polymerized in DMSO as solvent of choice ensuring a good dissolution of both the IL monomer (**1**) and 2-cyano-2-propyl dodecyl trithiocarbonate (CPDT) employed as CTA. A molar ratio of the reagents [M]:[CTA]:[I] = 200:1:0.2 (Initiator: 1,1'-azobis(cyclohexanecarbonitrile)) was used. Interestingly, the RAFT polymerization of [BVBIM]Cl (**1**) was highly affected by the choice of the solvent. For instance, protic solvents, such as ethanol, methanol and water, led to a less controlled polymerization (refer to Appendix Tab. B 1). [BVBIM]Tf$_2$N (**2**) was polymerized in butyronitrile as solvent due to its favorable solubility in non-polar/aprotic solvents. The molecular weight evolution of the SEC traces in **Figure 32b,c** verifies the living character of the process. Both 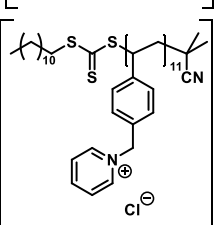the ^{1}H NMR (Appendix Fig. B 20) as well as the SEC results are in good agreement with the theoretically obtained molecular weights (**Figure 32d,e**). P([BVBIM]Cl) (**3**) is a charged polymer and as such it interacts strongly with the column material and other polymer chains through hydrogen bonding of the chloride counter ion. As a consequence, halide-containing PILs often displays a rather broad dispersity in a H$_2$O-SEC system.[329]

The Tf$_2$N$^-$ containing monomeric IL (**2**) can be prepared via a similar synthetic approach: CPDT was used as CTA in butyronitrile at 85 °C and 1,1'-azobiscyclohexanecarbonitrile as initiator. **Figure 32c** shows the molecular weight evolution of the RAFT polymerization of [BVBIM]Tf$_2$N (**4**), where the controlled molecular weight evolution can be verified via the SEC traces (10 mmol LiTf$_2$N, 10 mmol n-butylimidazole, 35 °C, flow rate 1.0 mL·min^{-1}). The molecular weight determination of the polymers (M_n < 10 000 g·mol^{-1}) was hampered by the presence of residual monomer, which cannot be removed by precipitation in methanol/water, or dialysis in water (3 d at ambient temperature as well as for 14 d at elevated temperatures at 40 °C). Dialysis in THF or

acetone – as described by Matyjaszewski and coworkers[175] – may work for high-molecular PILs, however, failed for the low-molecular weight polymers (diffusion out of the membrane). Dialysis in DMSO was successful for certain polymer samples, however, failed as a standard dialysis for Tf_2N^- containing PILs. Thus, the polymer signals
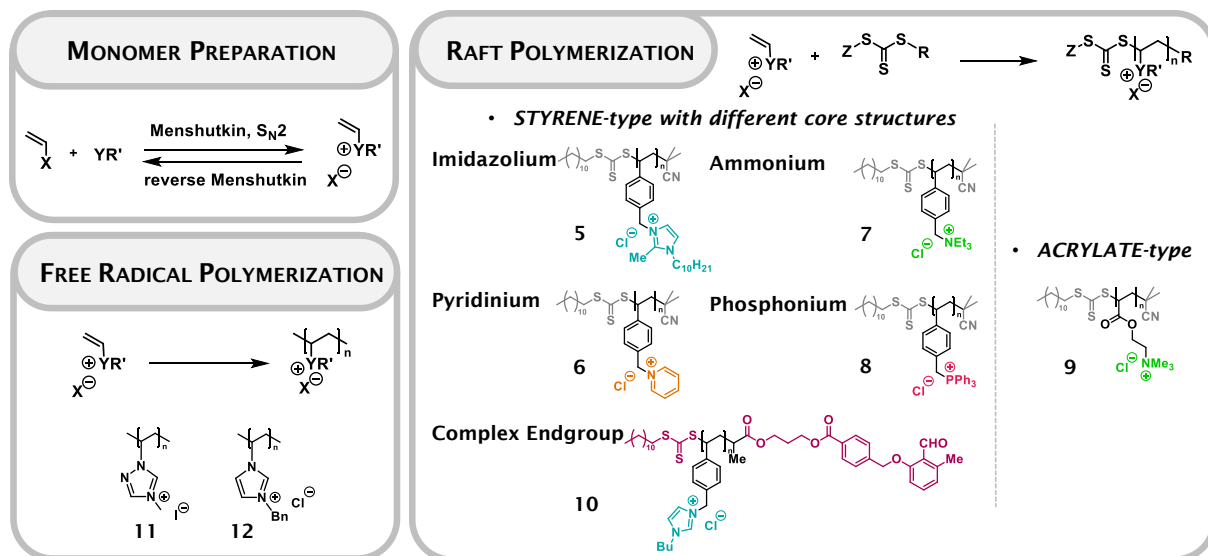
Figure 33 Overview over the IL monomer preparation (X: halide; Y: N or P or S; R': alkyl or aryl), the free radical and RAFT polymerization collating all investigated PILs in the present study (Z: stabilizing group, R: leaving group). Reproduced with permission from Ref. [339]. Copyright Royal Society of Chemistry 2016.

and the monomer signal overlapped significantly in the SEC trace. The overlap was most likely due to the SEC column system that differs slightly from the SEC column system employed by Matyjaszewski and coworkers.[175]

4.2.2. Mass Spectrometric Characterization

As noted above, the current thesis introduces a platform to characterize PIL chain structures by fusing proteomics based supercharging technology with HR ESI-Orbitrap MS. RAFT-prepared PILs bearing different types of core structures (pyridinium, ammonium, phosphonium, imidazolium) and non-controlled prepared PILs (based on imidazolium and triazolium core structures) form the analytical base library (**Figure 33**). Furthermore, the technology was applied to acrylate-type PILs with variable side groups. The present thesis focuses on the description of the analytical method in general and on the results obtained with pyridinium as core structure. As the mass spectrometric elucidation of the remaining PILs is repetitive, the candidate decided to present the data in the Appendix. The reader can access all NMR (monomer and polymer) as well as all expanded spectra with their corresponding isotopic pattern simulations and tables of assignments in the Appendix B.

ESI MS spectra have been recorded in negative ion mode, employing the in-source CID fragmentation technique. CID fragmentation is a technique of tandem mass spectrometry to induce collisions between ions and neutral gas molecules. The collision energy employed for tandem MS in the QExactive Orbitrap MS ranges from 5 up to 100 eV and can collisional activate all ions emitted by the electrospray source. The resulting spectrum is thus a collection of the precursor ions and the product
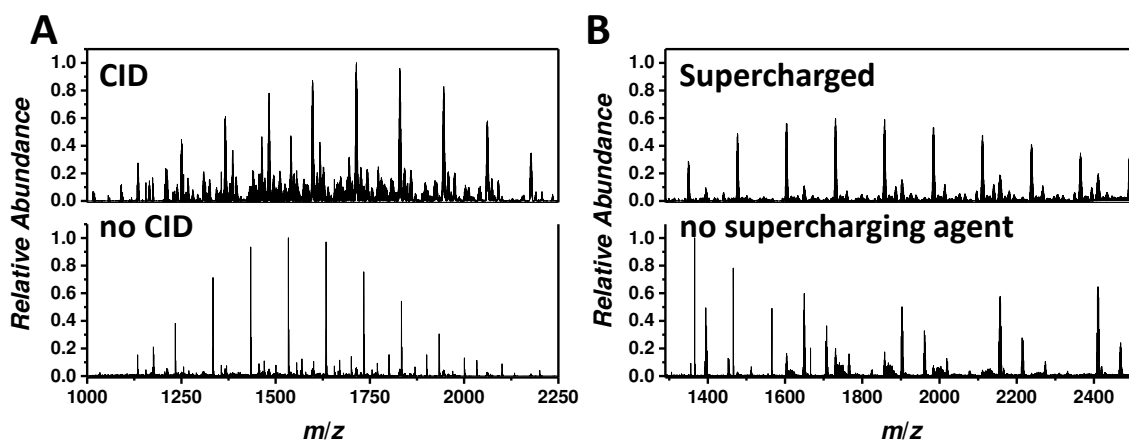
Figure 34 (A) (Top) ESI-CID-Orbitrap spectrum of p([VBPy]Cl) (**6**) employing 10 eV as collision energy. (Bottom) ESI-Orbitrap spectrum of p([VBPy]Cl) (**6**) without employing additional collision energy. Based on information of Thermo Scientific, the background signals stem from residual and hard to remove Ultramark® calibration markers with a characteristic repeating unit of 99.99 Th. These are always visible in negative ion mode. **(B)** (Top) ESI-CID-Orbitrap spectrum of p([TEVBA]Cl) (**7**) utilizing 1% (*v/v*) PC as supercharging agent. (Bottom) ESI-CID-Orbitrap spectrum of p([TEVBA]Cl) (**7**) without any auxiliary additive to the ESI solvent (water/acetonitrile 50:50). Reproduced with permission from Ref. [339]. Copyright Royal Society of Chemistry 2016.

ions.[330] Applying the CID activation strategy to PILs resulted in a sensitive polyelectro-lyte detection, without significant dissociative events (refer to **Figure 34A**).[331]

Since PILs feature strong intra- and intermolecular ionic interactions (see Section 2.3),[332] the in-source CID fragmentation can induce a declustering of polymeric chains. As a result, single PIL chains ionized by chloride attachment in the negative ion mode can be detected rather than polymer clusters, which are nearly undetectable. Importantly – and in addition to CID –, the previously discussed supercharging effect (refer to Section 2.1.4 and Chapter 3) has improved the PIL spectra significantly. Since the repeat unit of PILs can separate corresponding peaks by several hundred Da, a division by two (for doubly charged) or three (for triply charged) has a significant impact on the mass spectra. Although propylene carbonate has shown to be a sub-charging agent for the polyhydrocarbons studied in Chapter 3, it plays a key-role in the extent of charging PILs in the negative ion mode, allowing for the detection of doubly and triply charged species (refer to **Figure 34B**). The proposed PIL supercharg-ing may be attributed to a high halide concentration at the moment of ion formation
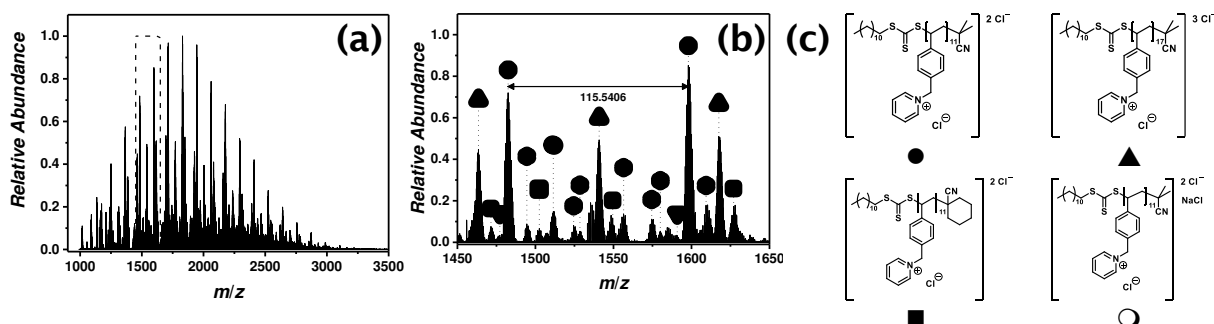
Figure 35 ESI-CID-Orbitrap MS spectra of p([VBPy]Cl) (**6**) (M_n = 1800 g· mol⁻¹, Đ = 1.8) depicting (**A**) the overview spectrum from 1000 *m/z* to 3500 *m/z*; (**B**) zoom into one repeat unit (*m/z*(exp) 115.5406, *m/z*(theo) 115.5412); (**C**) proposed structure of the most abundant species. Species labeled with ∗ derive from (multiple) loss(es) of gaseous HCl. Reproduced with permission from Ref. [339]. Copyright Royal Society of Chemistry 2016.
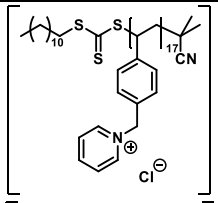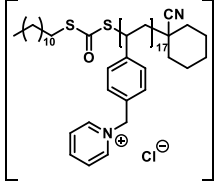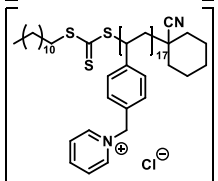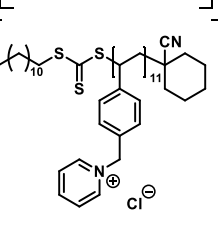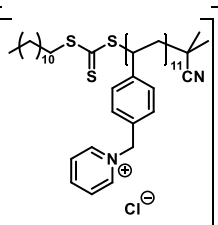
(in accordance to Konermann's trapping mechanism described in Section 2.1.4). The combination of the CID fragmentation technique with a supercharging additive led to the development of a novel mass spectrometric method for the in-depth structural elucidation of PILs.

Pyridinium as core structure

Until now, pyridinium-based PILs have not attracted significant attention in the literature. The chemical difference of pyridinium in comparison with other well-known core structures are significant, making poly(1-(4-vinylbenzyl)pyridin-1-ium chloride) (p([VBPy]Cl), **6**) an interesting candidate for a mass spectrometric investigation. The ESI-CID-Orbitrap measurements of p([VBPy]Cl) (**6**) were performed in negative ion mode using water/acetonitrile (1:1, *v/v*) as ESI solvent. During the analysis of p([VBPy]Cl) (**6**), a CID fragmentation of 10 eV was critical for the detection of the polymer (refer to **Figure 34A**). Promoted without the addition of an auxiliary supercharging agent, the ionization provided doubly and triply charged species (**Figure 35c**) ionized by chloride attachment. The ESI MS profile displayed the typical Gaussian shape of a polymer (**Figure 35a**) in the mass range between 1000 *m/z* to 3500 *m/z*. The expanded spectrum (**Figure 35b**) highlights the repeating peaks of the doubly (labeled with ●) and triply (labeled with ▲) charged species. Interestingly, without the addition of a supercharging agent, p([VBPy]Cl) (**6**) was multiply charged. The repeat unit of the doubly charged species is 115.5406 *m/z* (*m/z*(theo) 115.5412), while the triply charged species are separated by 77.0283 *m/z* (*m/z*(theo) 77.0277). The expanded spectrum (**Figure 35b**) indicates a cyclohexanecarbonitrile moiety stemming from the initiator (1,1'-azobis-(cyclohexanecarbonitrile)) rather than the expected 2-cyano-2-propyl moiety. The corresponding species at 1476.8310 *m/z* (labeled with ▽ for the triply charged ion) and 1502.5176 *m/z* (labeled with □ for the doubly charged

ion) unambiguously identified these end groups. Furthermore, the trithiocarbonate group underwent a partial oxidation, producing the triply charged ions at 1471.4959 *m/z* (labeled with ■). Further species of minor abundance could be assigned to multiple neutral losses of HCl (labeled with ✳) (refer to **Table 2** for the complete list of assignments). A significant contribution to the detected end group variety of p([VBPy]Cl) (**6**) was attributed to the employed CID fragmentation during the acquisition of the mass spectrum.

Table 2 Peak assignment of the ESI-CID-Orbitrap spectrum of p([VBPy])Cl (**6**) from 1460 *m/z* to 1500 *m/z* showing the label (in correspondence to the species in **Figure 35b**), the experimental *m/z* and theoretical *m/z* values (determined by the most abundant isotope of the isotopic pattern), Δ*m/z*, the resolution (obtained by the Xcalibur software), the number of repeating units n, and the structure determination. Due to the deprotonation process, no structure was determined for species labelled with ✳. Reproduced with permission from Ref. [339]. Copyright Royal Society of Chemistry 2016.

Label	*m/z* (exp)	*m/z* (theo)	Δ*m/z*	Resolution	*n*	Structure
▲	1463.4843	1463.4834	0.0009	53500	17	
■	1471.4959	1471.5015	0.0056	49500	17	
▽	1476.8310	1476.8272	0.0039	54600	17	
●	1482.4991	1482.4967	0.0024	53800	11	
□	1502.5176	1502.5124	0.0052	52600	11	
◖	1511.4758	1511.4758	0.0000	53300	11	

Crosthwaite *et al.* investigated the thermal stability of pyridinium and showed a significant difference between a pyridinium and an imidazolium halide,[333] supporting the findings that – during MS/MS analysis of p([VBPy]Cl) (**6**) performed on the ion at 1482±10 *m/z* – a fragmentation according to the reverse Menshutkin mechanism (refer to **Figure 36**) is operational.
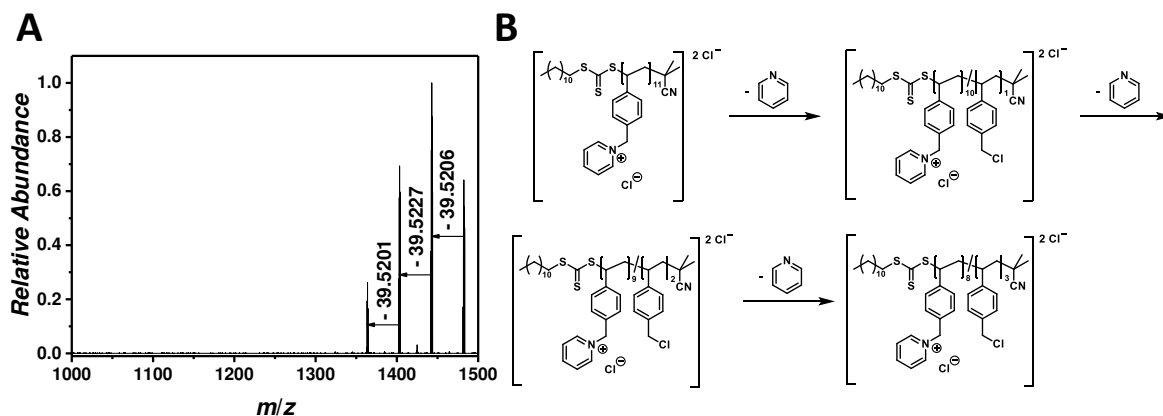
Figure 36 (A) Tandem MS experiment (negative mode) of a double charged species at 1482 *m/z* with a HCD energy of 10 eV. The identification of three double charged species depicting the loss of a pyridine unit (*m/z*(theo) = 39.5216). **(B)** Proposed fragmentation of p([VBPy]Cl) (**6**) via a reverse Menshutkin mechanism including the stepwise nucleophilic attack of the chloride anion at the electrophilic benzylic moiety. Reproduced with permission from Ref. [339]. Copyright Royal Society of Chemistry 2016.

In summary, a unique access route to polymer ionization is presented by the attachment of chloride. In Chapter 3, the chloride attachment has been introduced according to the analyte/charge interactions that have been submitted for non-polar polymers. PILs, however, are highly polar polyelectrolytes, whose corresponding anion has been responsible for charging the entire macromolecule. The sensitive dependence on the charge of the observed species motivated a further study on salt-exchanged PILs measured by MS that is discussed in the next section.

4.3. JUST ADD SALT: A MASS SPECTROMETRIC ANALYSIS METHOD FOR IMAGING ANION-EXCHANGED POLY(IONIC LIQUID)S

4.3.1. Motivation

Section 2.3 highlighted the characteristic properties of PILs associated with their respective counter ion. For instance, exchanging the hydrophilic halide against hydrophobic perfluoroborates or –phosphates alters the materials properties fundamentally, making a quantitative reaction even more important. However, quantitative

information cannot be guaranteed by IR or NMR as characterization techniques: IR requires sophisticated calibration and NMR relies on NMR active nuclei. An often reported work-around is the utilization of silver salts, both introducing the desired ion and guarantee quantitative conversions by precipitating silver halide. The following section is thus motivated by two essential questions: (*i*) is MS as characterization technique sufficiently powerful to proof a quantitative salt exchange on a molecular level? And (*ii*), how does the counter ion influence the ionization of the PILs?

Thus, the first mass spectrometric analysis of PILs containing weakly-coordinating anions is introduced via a fast, simple and quantitative post-modification method on the example of the hydrophilic, well-defined p([VBPy]Cl) (**6**) species, analyzed with an in-source CID-Orbitrap MS protocol. The MS approach allowed for a precise structural elucidation of ion-exchanged p([VBPy]Cl) (**6**) utilizing AgX (X = NO_3^-, $CF_3CO_2^-$, BF_4^-) salts. The anion exchange was quantitative – without observing residual chlorinated PIL – using only filtration as a standard procedure during sample preparation. In addition, the influence of weakly coordinating anions (WCA) on the ionization behavior of PILs was studied in detail.

4.3.2. Results and Discussion
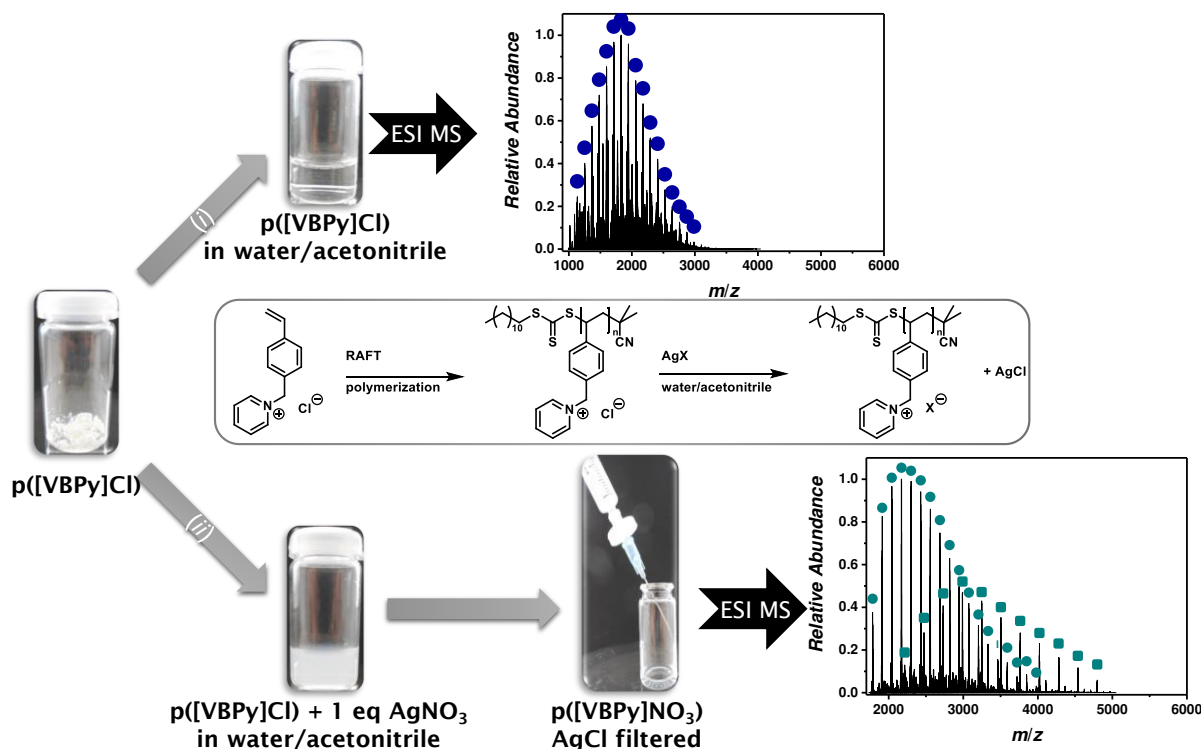
Figure 37. Rapid and facile salt exchange during the sample preparation: p([VBPy]Cl) (**6**) is either dissolved in water/acetonitrile (1:1, v/v), which results in a chloride ionized Orbitrap-CID spectrum in the negative mode (i), or is dissolved in water/acetonitrile (1:1, v/v) in the presence of 1.00 eq of AgX salt (X = NO_3^-, $CF_3CO_2^-$, BF_4^-). The precipitated AgCl forms an opaque solution, which is filtered through default PTFE filters (0.2 μm pore size) in order to remove the silver salt from the solution (ii). Reproduced with permission from Ref. [338]. Copyright Wiley 2016.

Silver salts are commonly used in organic chemistry as precursors for other organometallic compounds,[334] for halide abstraction,[335] for the precipitation of AgX salts (X = Cl^-, Br^-, I^-) and for the Ag(I) binding ability of vinyl- and arene-containing organic compounds.[336] The advantage of the irreversible, and fast precipitation of AgCl to introduce WCAs, such as nitrate (NO_3^-), trifluoroacetate ($CF_3CO_2^-$ or TFA) and tetrafluoroborate (BF_4^-) has been exploited. **Figure 37** collates the ESI MS spectra of (*i*) the chloride-containing precursor PIL ionized by chloride in negative ion mode employing a CID energy of 10 eV and (*ii*) the WCA-containing PILs obtained by rapid counter ion exchange with the respective silver salt and elimination of AgCl by filtration.[337] Process (*i*) is described in detail in Section 4.2.2, whereas the present section focuses on the salt exchange employing equimolar silver salts. Despite the plethora of possible core structures available for PILs (e.g. imidazolium, ammonium, sulfonium, phosphonium), a pyridinium-based PIL was an ideal candidate for the anion exchange studies, as the PIL distribution peaks at approx. 2000 *m/z* allowing for the detection of the anion exchanged PILs. In contrast to chloride as lowest molecular

weight anion, the WCA analogues are heavy, hence, shifting the distribution to higher m/z. (Cl^-: 34.97 m/z; NO_3^-: 61.99 m/z; BF_4^-: 87.00 m/z; $CF_3CO_2^-$: 112.99 m/z) (**Figure 38a**). Furthermore, the pyridinium-based PIL charge state entirely consisted of doubly (and triply) charged species. As discussed in Section 4.2.2, the charge of the PILs always stemmed from the corresponding counter ion (e.g. Cl^- for p([VBPy]Cl) (**6**); NO_3^- for p([VBPy]NO$_3$) (**6b**)), and thus, a modified charge distribution (e.g. from doubly charged to singly charged) allowed for the qualitative assessment of the anion coordination to PILs.

The anion exchanged polymer p([VBPy]NO$_3$) (**6b**) was recorded with an in-source CID energy of 40 eV. During acquisition, the PIL structure was intact without significant fragmentation.[338] The ESI MS profile measured in the mass range from 1750 m/z to 5000 m/z clearly indicated a distribution of singly (labeled with ■) and doubly (labeled with ●) charged species (**Figure 38b**). The good agreement of simulated and experimental isotopic pattern of a doubly charged species of p([VBPy]NO$_3$) (**6b**) at 2815.5589 m/z (m/z(theo) 2815.5726) confirmed the PIL species in which each repeat unit (258.0977 m/z; m/z(theo) 258.1004) along the polymer chain was associated with the exchanged anion (for expanded spectrum refer to Appendix Fig B 67). The shift of the polymer mass distributions towards higher m/z as outlined in **Figure 38a** and **Figure 38b** is best explained by comparing the repeat units of p([VBPy]Cl) (**6**) (m/z(theo) 231.0815) with p([VBPy]NO$_3$) (**6b**) (m/z(theo) 258.1004). After successful salt exchange from chloride to nitrate, the molecular weight of every polymer chain increased by 27.0189 m/z per repeat unit. In addition, in negative ion mode p([VBPy]NO$_3$) (**6b**) was charged by complexation with a NO_3^- anion. Thus, Cl^- stemming from p([VBPy]Cl) (**6**) was removed quantitatively using $AgNO_3$. Interestingly, the charge state subcharged from entirely doubly and triply charged p([VBPy]Cl) (**6**) species to singly and doubly charged p([VBPy]NO$_3$) (**6b**) species. The subcharging effect is attributed to slightly reduced H-bonding of NO_3^- compared to Cl^-.[339] Furthermore, the increased steric hindrance of the nitrate anion might reduce the chance for the attachment of additional nitrate anions to the PIL.
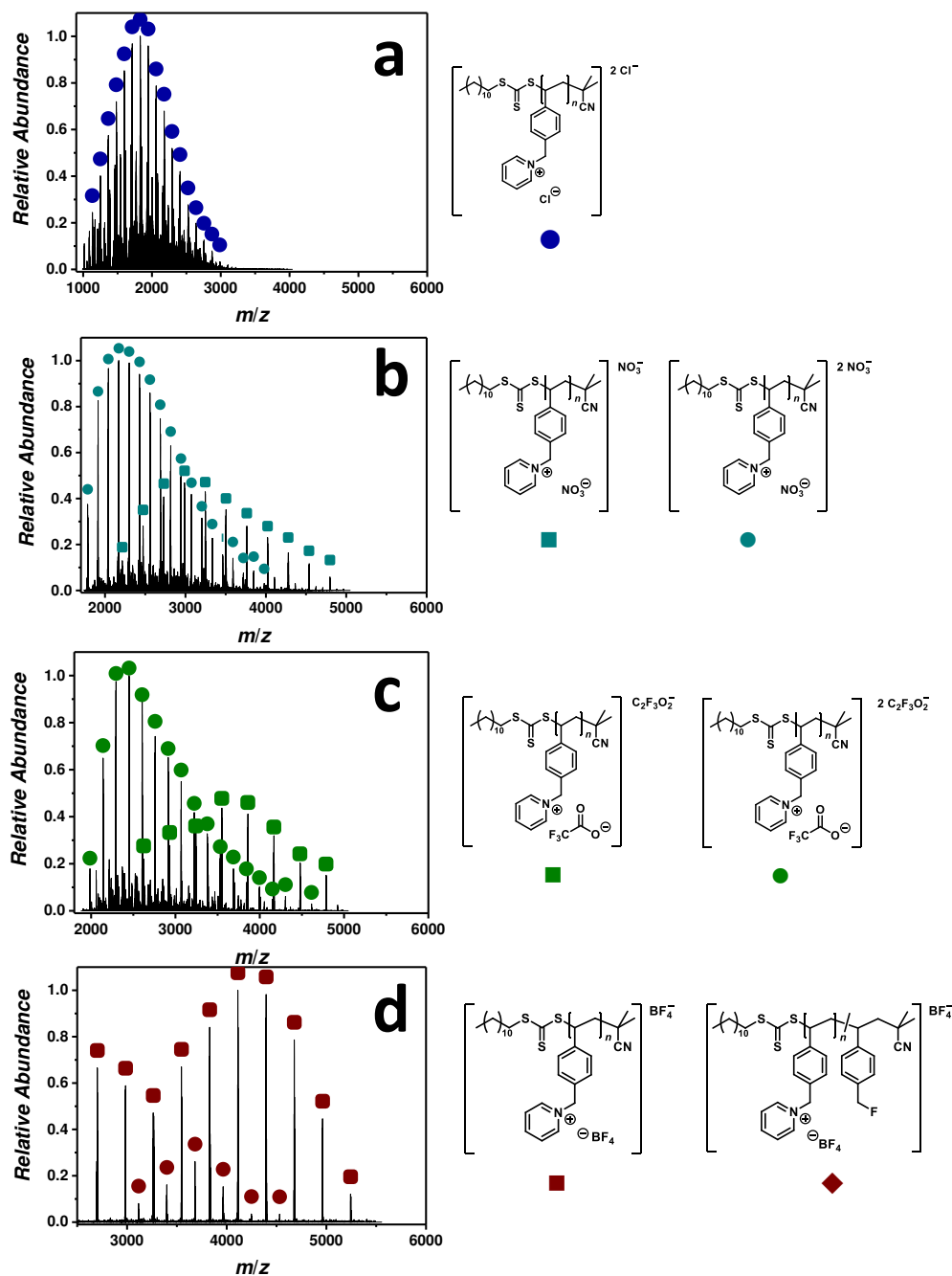
Figure 38 Orbitrap-CID overview spectra and proposed structures of the most abundant species of p([VBPy]Cl) (**6**), p([VBPy]NO₃) (**6b**), p([VBPy]CF₃CO₂) (**6c**), and p([VBPy]BF₄) (**6d**). Reproduced with permission from Ref. [338]. Copyright Wiley 2016.

Motivated by the first successful measurements, TFA was chosen as its H-bonding activity is similar to NO_3^-.[339] Thus, an analogue trend was expected and indeed confirmed after the salt metathesis employing $AgCF_3CO_2$ (**Figure 38c**). The salt-exchanged PIL p([VBPy]CF₃CO₂) (**6c**), ionized with an auxiliary in-source CID energy of 50 eV, was recorded in the mass range from 1900 *m/z* to 5000 *m/z*, revealing two distributions of singly (labeled with ■) and doubly charged (labeled with ●) species. As previously reported for $AgNO_3$ as salt exchange reagent, every single Cl^- anion

along the polymer chain was replaced by $CF_3CO_2^-$. Thus, the repeat unit of p([VBPy]CF_3CO_2) (**6c**) was 309.0887 *m/z* (*m/z*(theo) 309.0977) (for the fully expanded spectrum refer to Appendix Fig. B 70). In negative ion mode, p([VBPy]CF_3CO_2) (**6c**) was charged by complexation with the $CF_3CO_2^-$ anion. As expected, the charge state of entirely doubly and triply charged species (p([VBPy]Cl) (**6**)) was subcharged to doubly and singly charged species for WCA-containing p([VBPy]$CF_3CO_2^-$) (**6c**), however, similar to the nitrate-exchanged p([VBPy]NO_3) (**6b**) (**Figure 38**). As in the order of $Cl^- >> NO_3^- \approx CF_3CO_2^- >> BF_4^-$ tetrafluoroborate (BF_4^-) features the least H-binding activity and is thus the weakest coordinating anion employed in the present section, it was expected that mainly a singly charged state distribution for p([VBPy]BF_4) (**6d**) was observed and – since BF_4^- charged the PIL negatively –, a low ion abundance was anticipated. Indeed, the ESI-CID-Orbitrap spectrum of p([VBPy]BF_4) (**6d**) (**Figure 38d**), recorded with an in-source CID energy of 90 eV, illustrates a polymer distribution with entirely singly charged species (labeled with ■ and ●) in the mass range from 2500 *m/z* to 5500 *m/z*. The repeat unit of p([VBPy]BF_4) (**6d**) was 283.0960 *m/z* (*m/z*(theo) 283.1155) (for expanded spectrum refer to Appendix Fig B 73). The WCA BF_4^- required the harshest conditions (CID 90 eV) for the detection, explaining a further singly charged distribution (labeled with ●) derived from the degradation of one repeat unit following the reverse Menshutkin reaction. Due to the low coordination tendency of BF_4^-, p([VBPy]BF_4) (**6d**) was observed with an ion abundance of 10^2, while the abundances for p([VBPy]NO_3) (**6b**) and p([VBPy]CF_3CO_2) (**6c**) were approx. 10^4. In the present study – due to the low ion abundance –, no degradation of the BF_4^- as counter ion during the structural elucidation of p([VBPy]BF_4) (**6d**) has been observed.

4.4. SURFACE MODIFICATION

Surface design is an important and steadily growing field in contemporary chemistry. PIL-decorated surfaces can serve as imaging, wetting/dewetting, and anti-biofouling interfaces.[340-343] Initiated by the work of Ye *et al.* who investigated grafted PILs via ROMP on TiO_2 substrates and the successful anti-fouling studies,[342] Matyjaszewski and colleagues attached well-characterized, ATRP-prepared PILs on Si substrates via a thermally driven ligation protocol.[340] Furthermore, Drockenmueller and coworkers patterned azide-functionalized copolymerized PILs on a silicon sub-
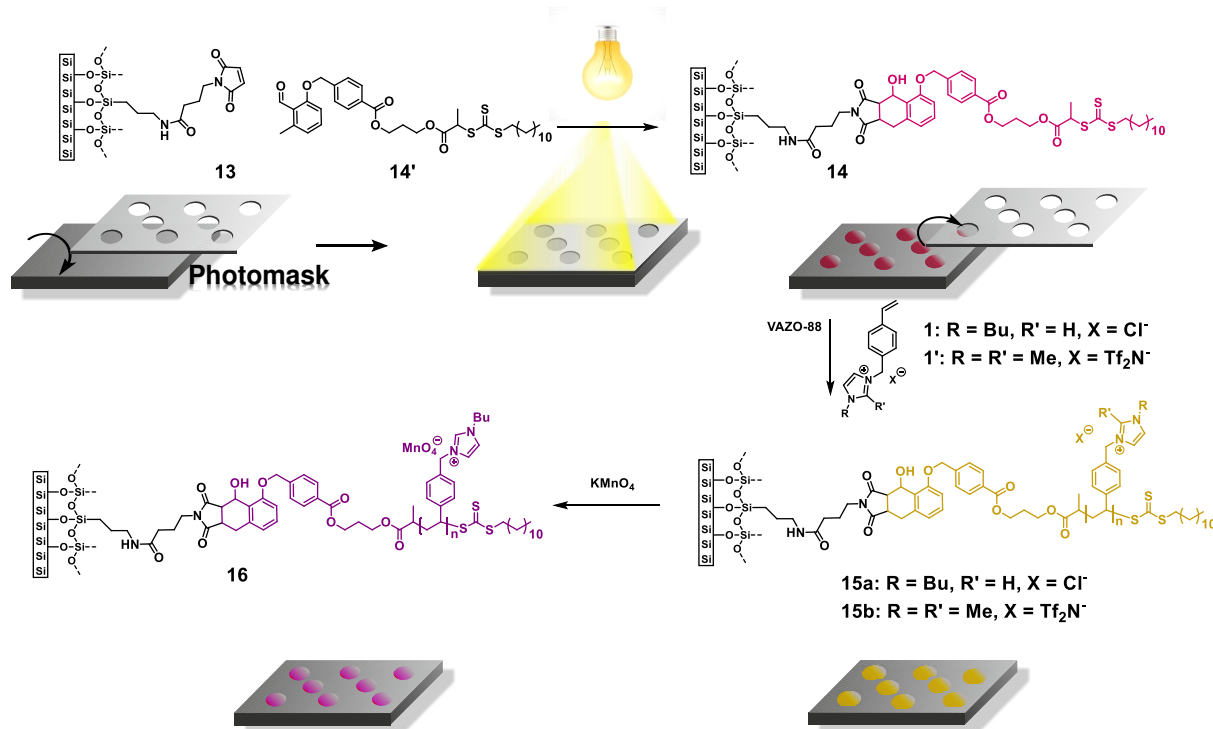
Figure 39 Schematic illustration of the surface functionalization for the spatially resolved surface functionalization of silicon wafers with (**1**) and (**1'**). (3-Aminopropyl)triethoxysilane (APTES)-coated silicon wafers were coated with 4-maleimidobutyroyl chloride to achieve maleimide-functionalized surfaces (**7**). After irradiation, the surfaces covered with a photomask with an ARIMED B6 lamp (λ_{max} = 320 nm) in a solution of the photoenol functional CTA to result in (**8**) followed by RAFT polymerization of (**1**) from the surface. Subsequent salt metathesis of (**9a**) with $KMnO_4$ resulted in a highly violet colored meander pattern of p([BVBIM]MnO_4) (**10**). Reprinted with permission from Ref. [312]. Copyright Royal Society of Chemistry (2016).

strate. The azide motif release highly reactive nitrenes upon UV irradiation, which has been used as surface anchor.[343] The present section covers the characterization of photochemically patterned p([BVBIM]Cl) (**6**) and p[1,2-dimethyl-3-(*p*-vinylbenzyl)-1*H*-imidazol-3-ium bis(trifluoro methanesulfonyl)imide] (p([DMVIM]Tf$_2$N)) via a surface sensitive mass spectrometric analytical method, i.e. ToF-SIMS as well as X-ray photoelectron spectroscopy (XPS).

Figure 39 summarizes the grafting-from approach of the PILs exploiting the RAFT polymerization of (**1**) and (**1'**). Initially, the RAFT agent (**14'**)[344] was photopatterned via *o*-quinodimethane chemistry onto maleimide-functionalized silicon wafers[345] (**7**). Therefore, a blank silicon wafer was activated with Piranha solution (H_2O_2:H_2SO_4 = 1:4 (*v/v*)) and immersed into APTES solution at 70 °C overnight. APTES-coated surfaces,[345] thoroughly cleaned by rinsing with toluene, acetone, methanol and Milli Q water, were placed in a solution of freshly prepared 4-maleimidobutyroyl chloride in dichloromethane. After successful maleimide-functionalization, the wafer was covered with a dotted (or meander-shaped) photo mask in a self-fabricated sample holder and placed in a solution containing the RAFT agent. Irradiation (2.5 h) with ARIMED B6™ lamp (λ_{max} = 320 nm) afforded surface **14**. The grafting-from polymerization with [BVBIM]Cl (**1**) as monomer was subsequently performed in a DMSO/DMF mixture (1:1, *v/v*) at a concentration of approx. 0.6 mol·L^{-1}. 2-(dodecylthiocarbonothioyl-thio)propionic acid (DoPAT) as sacrificial RAFT agent and VAZO-88 as radical starter was added and the mixture degassed by three consecutive freeze-pump-thaw cycles. As demonstrated by Zamfir et al.,[346] a good grafting-from performance is obtained in a 1:1 ratio of CTA:initiator. As due to the hopping mechanism,[347] a steady termination of adjacent radicals on the surface occur, a high initiator concentration is necessary. The polymerization was conducted for 7 h, after which the residual monomer as well as potential polymer attached via physisorption was removed by thorough rinsing of the functionalized surfaces (**15a**) with Milli Q water, methanol, acetone, and Milli Q water followed by immersing the surface in methanol for 12 h. Subsequently, the surface was ultrasonicated in a solution containing 0.5 g·L^{-1} ammonium chloride and rinsed thoroughly with acetone. In contrast, the hydrophobic p([DMVBIM]Tf$_2$N-functionalized surface (**15b**) was cleaned by removal of residual monomer as well as potential polymer attached via physisorption by thorough rinsing with acetone, dichloromethane, methanol and Milli Q water followed by treating the surface in a solution containing 1.0 g·L^{-1} LiTf$_2$N. Residual salt was removed via ultrasonification in acetone. Both surfaces were characterized by surface-sensitive techniques, i.e. XPS and ToF-SIMS.

Figure 40a shows the corresponding XP spectra. The C 1s spectrum shows the (C-C, C-H) component at 285.0 eV, (C-O, C-N) at 286.4 eV and (COO, NCO) at 288.5 eV, which were associated with in the maleimide (surface (**7**)) and the photoenol (surface (**14**)). The photo-ligation of (**7**) was evidenced by the sulfur signal at 163.6 eV indicating the presence of the trithiocarbonate group. After the surface-initiated

(a)

(b)   **(c)**
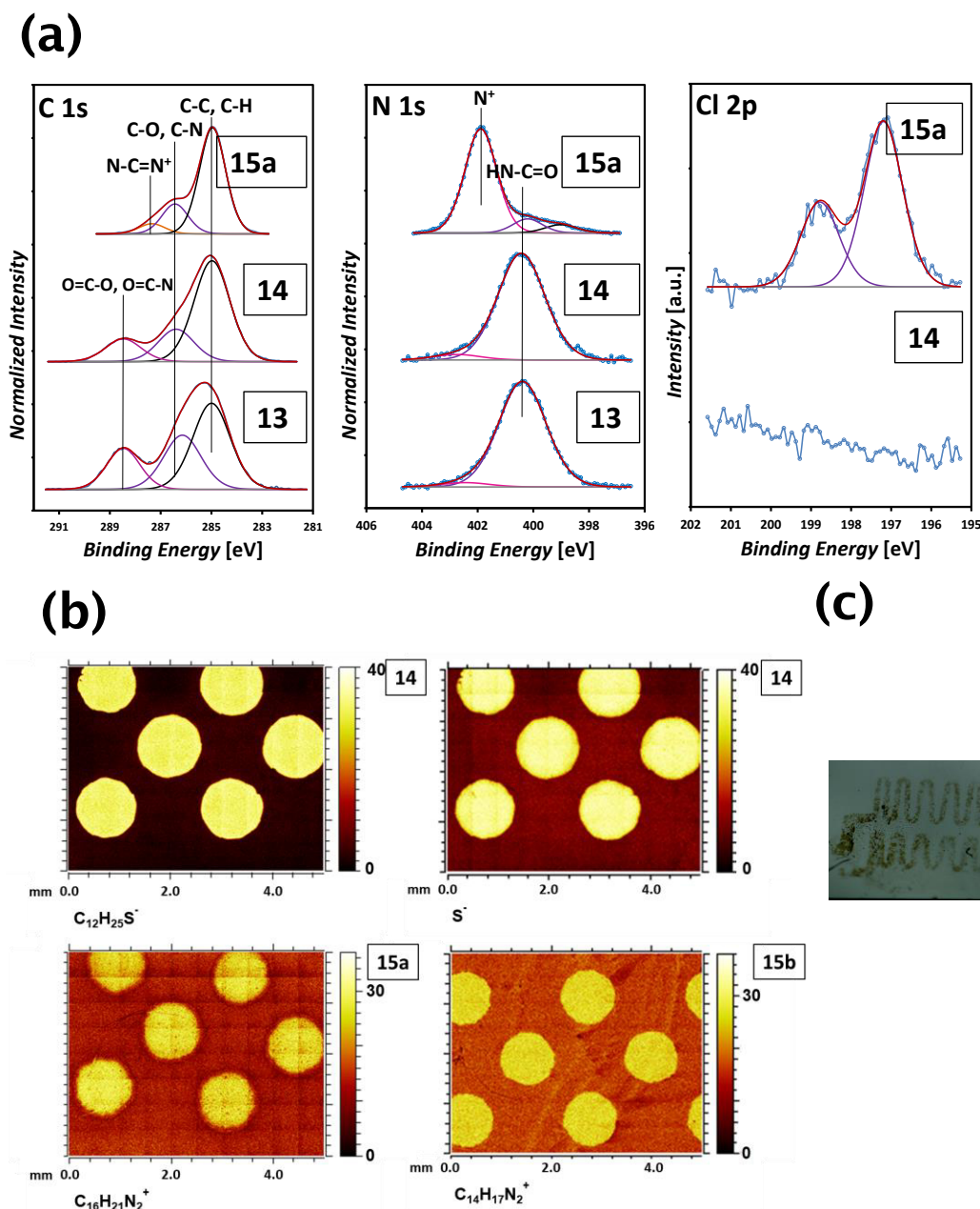
Figure 40 (a) XP spectra of the maleimide functionalization (**13**), photoenol functionalization (**14**) and the grafting-from polymerization (**15a**) with [BVBIM]Cl (**1**). (b) ToF-SIMS images of *o*-quinodimethane functionalization (**14**), grafting-from polymerization (**15a**) with [BVBIM]Cl (**1**), grafting-from polymerization (**9b**) with [DMVBIM]Tf$_2$N (**1'**) and (c) photograph of the violet colored meander pattern of p([BVBIM]MnO$_4$) (**10**) resulting from the salt metathesis of (**15a**) with KMnO$_4$. Reprinted with permission from Ref. [312]. Copyright Royal Society of Chemistry (2016).

polymerization affording (**15a**), the signal at 401.8 eV – characteristic for the imidazole group (N$^+$) – was detected in the N 1s spectrum. The (protonated) amine signal at 401.8 eV increased from 0.3 at% (surface **14**) to 8.9 at% (surface (**15a**)), which could be assigned to the imidazolium group. Most characteristically, a signal originating from Cl 2p indicated the counter ion, which was absent on the APTES/maleimide-coated surface (**7**) as well as on the RAFT agent-functionalized surface (**14**). **Figure 40b** depicts the ToF-SIMS images of C$_{12}$H$_{25}$S$^-$, S$^-$, C$_{16}$H$_{21}$N$_2$$^+$ (surface (**15a**)) and

$C_{14}H_{17}N_2^+$ (surface (**15b**)) fragments. The surface-sensitive mass images confirmed the covalent attachment of (**14**) precisely following the dotted shape of the photomask. As expected, in the areas covered by the photomask, no *o*-quinodimethane reaction occurred and consequently no species stemming from (**14**) were detected. After successful grafting-from of [BVBIM]Cl (**1**), ToF-SIMS measurements in positive ion mode identified repeating unit species ($C_{16}H_{21}N_2^+$; 241.20 *m/z*) on the surface (**15a**). Furthermore, successful grafting of [DMVBIM]Tf$_2$N (**1'**) was confirmed by its characteristic repeating unit species ($C_{14}H_{17}N_2^+$; 213.13 *m/z*) on the surface (**15b**). The presence of the ionic nature of the PIL attached to the surface was supported by a rapid salt metathesis with colorful MnO_4^- (**Figure 40c**).

4.5. CONCLUSIONS

PILs are a fascinating and versatile family of polyelectrolytes. Their properties can be readily adjusted without much synthetic effort by exchanging the counter ion. The present section introduces facile synthetic access to styrenic IL monomer units with various core structures (imidazolium, pyridinium, ammonium and phosphonium) via the RAFT polymerization technique. Furthermore, a detailed and universal mass spectrometric platform for the complete structural elucidation of PILs is provided. ESI-CID-Orbitrap MS in combination with supercharging agents are demonstrated to be powerful characterization access modes to structural information of complex polyelectrolytes. Additionally, it has been demonstrate that sterically more demanding counter ions replace the chloride anion of p([VBPy]Cl) (**6**) by a rapid anion exchange using various silver salts AgX (X = NO_3^-, $CF_3CO_2^-$, BF_4^-). Removing AgCl by simple filtration allows for the direct injection of the filtered solution into the electrospray source. The mass spectrometric method outlined in this section is based on an in-source CID fragmentation technique and constitutes a facile strategy for accessing the structure of weakly-coordinated PILs. The in-depth mass spectrometric characterization of all investigated PIL systems evidences important structure/property relationships: (*i*) the counter ion promotes the ionization, (*ii*) PILs prepared by RAFT keep their full structural integrity although an in-source CID technique was used, (iii) all PIL halides dissolve readily in water/acetonitrile and allow supercharging as described in Section 3 having an exceptional synergy in reducing the PILs' molecular mass of the

repeat unit by increasing the charge state, (iv) PILs can be photopatterned on pre-treated surfaces allowing to adjust the surface's properties, and (v) ToF-SIMS confirms PIL structure as fully intact monomer fragment species.

4.6. EXPERIMENTAL SECTION

4.6.1. Materials

All solvents were obtained from Sigma-Aldrich, Acros Organics or Fischer and used without further purification. Absolute solvents were purchased from Acros Organics and stored under nitrogen and over molecular sieves. Triethylamine was refluxed over CaH_2, freshly distilled under inert atmosphere and stored over molecular sieves (3 Å) at 4 °C. All other reactants were used without further purification. The dialysis tubes were purchased from Spectra/Por (Spectra/Por 7 Dialysis RC Tubing).

1-(chloromethyl)-4-vinylbenzene (90%, Sigma-Aldrich), 2-cyano-2-propyl dodecyl trithiocarbonate (97%, Sigma-Aldrich), 1,2-dimethylimidazole (98%, Acros), 1,1'-azobiscyclohexanecarbonitrile (VAZO-88) (98%, Sigma-Aldrich), 1-butylimidazole (98%, Sigma-Aldrich), $LiTf_2N$ (99%, Acros), $CuSO_4 \cdot 5\ H_2O$ (99%, Acros), $K_2S_2O_8$ (97%, abcr), 2,3-dimethylanisole (97%, abcr), $AlCl_3$ (99%, Acros), methyl-4-bromomethyl benzoate (97%, Fischer), potassium carbonate (99%, Roth), NaOH (99%, Roth), 18-crown-6 (98%, TCI), 4-(dimethylamino)pyridine (99% Sigma-Aldrich), N-(3-dimethylaminopropyl)-N'-ethylcarbodiimide hydrochloride (99%, Sigma-Aldrich), thionyl chloride (>99%, Sigma-Aldrich), (3-aminopropyl)triethoxysilane (99%, Sigma-Aldrich), 4-maleimidobutyric acid (98%, TCI), H_2O_2 (35%, Roth), sulphuric acid (96%, Roth), hydrochloric acid (37%, Roth), sodium hydrogencarbonate (99%, Roth).

2,2′ -Azobis(2-methylpropionitril) (AIBN) was recrystallized twice from methanol. 2-(acryloyloxy)-N,N,N-trimethylethan-1-aminium chloride was purchased from Sigma-Aldrich (80% water solution) and purified by two times precipitation in acetone, dried under high-vacuum and stored at -5 °C. All other reactants were used without further purification.

All solvents for mass spectrometric analysis (Milli-Q water; UHPCL-grade acetonitrile (Thermo Fisher)) were used without further treatment.

1-decyl-2-methylimidazole (98%, Sigma-Aldrich), pyridine (>99%, Acros), trimethylamine (>99%, Merck), triphenylphosphine (>99%, Merck), propylene carbonate (98%, TCI) were used as received.

4.6.2.   Instrumentation

Mass spectra were recorded on a Q Exactive (Orbitrap) mass spectrometer (Thermo Fisher Scientific, San Jose, CA, USA) equipped with a HESI II probe. The instrument was calibrated in the m/z range 1000-6000 m/z using ammonium hexafluorophosphate (Thermo Scientific). All spectra were recorded in the negative mode, using water/acetonitrile (1:1, v/v) in a concentration of 0.5 mg· mL^{-1} as solvent. The FT resolution was set to 140 000 employing 3 microscans during an acquisition time between 2 and 3 min measuring with a capillary temperature of 320 ℃. The aux gas flow was (dimensionless) 0.00, the sheath gas 10.00, and the spare gas 1.00. The flow rate was set to 10 μL· min^{-1}. The spray voltage was set between 2.0 eV and 4.5 eV depending on the S/N ratio. A CID fragmentation was employed depending on the analyzed PIL. The ion optics settings are as follows: the S-lens RF level was set to 68.0, the S-lens voltage to -25.0 V, the skimmer voltage to -15.0 V, the gate lens voltage to -6.00 V and the C-trap RF to 2400.0 V.

4.6.3.   Synthesis

Synthesis   of   1-butyl-3-(4'-vinylbenzyl)-1H-imidazol-3-ium   chloride ([BVBIM]Cl, 1): 9.00 g n-butylimidazole (72.5 mmol, 1.00 eq) was dissolved in 100 mL chloroform and cooled to 0 ℃. Subsequently, 15.4 mL vinylbenzyl chloride (16.6 g, 108.7 mmol, 1.50 eq) was added. The mixture was stirred at 50 ℃ for 24 h. The mixture was extracted with water (3×25 mL), evaporated at reduced pressure to get rid of the residue organic solvents, and freeze-dried. 17.5 g of product 1 (63.1 mmol, 87%) was received as a colorless, highly viscous liquid.

^{1}H NMR (400 MHz, DMSO-d_6, 298 K): δ = 9.72 (s, 1 H, N=C**H**-N), 7.91 (d, ^3J = 13.8 Hz, 2 H, <u>Im</u>-**H**), 7.50 (d, ^3J = 8.2 Hz, 2 H, <u>Ph</u>-**H**), 7.46 (d, ^3J = 8.2 Hz, 2 H, <u>Ph</u>-**H**), 6.72 (dd, ^3J(Z) = 11.0 Hz, ^3J(E) = 17.7 Hz, 1 H, H$_2$C=C**H**), 5.85 (d, ^3J(E) = 17.7 Hz, 1 H, **H**C(H)=CH), 5.49 (s, 2 H, <u>Bn</u>-**H**), 5.27 (d, ^3J(Z) = 11.0 Hz, 1 H, **H**C(H)=CH), 4.20 (t, ^3J = 7.2 Hz, 2 H, N-C**H$_2$**-CH$_2$), 1.92 – 1.60 (m, 2 H, CH$_2$-C**H$_2$**-CH$_2$), 1.43 – 1.02 (m, 2 H, CH$_2$-C**H$_2$**-CH$_3$), 0.87 (t, ^3J(Z) = 7.5 Hz, 3 H, CH$_2$-C**H$_3$**) ppm.

^{13}C-NMR (100 MHz, DMSO-d_6, 298 K): δ = 137.56 (C), 136.17 (C), 135.93 (CH), 134.30 (CH), 128.67 (2 CH), 126.67 (2 CH), 122.79 (CH), 122.54 (CH), 115.29 CH$_2$), 51.65 (CH$_2$), 48.67 (CH$_2$), 31.24 (CH$_2$), 18.79 (CH$_2$), 13.26 (CH$_3$) ppm.

Synthesis of 1-butyl-3-(4'-vinylbenzyl)-1*H*-imidazol-3-ium bis(trifluoro-methanesulfonyl)imide ([BVBIM]Tf$_2$N, 2): 4.50 g *n*-butylimidazole (36.2 mmol, 1.00 eq) was dissolved in 100 mL chloroform and cooled to 0 ˚C. Subsequently, 8.3 g vinylbenzyl chloride (54.4 mmol, 1.50 eq) was added. The mixture was stirred at 50 ˚C for 24 h. The mixture was extracted with water (2×100 mL), and evaporated at reduced pressure to get rid of the residual organic solvents. Afterwards, 10.4 g LiTf$_2$N (36.2 mmol, 1.00 eq) was added. The reaction was allowed to proceed overnight at ambient temperature. The mixture was extracted with ethyl acetate (3×75 mL). The combined organic solvents were washed with water (1×100 mL), and dried over sodium sulfate. 15.97 g of product 2 (30.7 mmol, 84%) was received as a colorless liquid.

^{1}H NMR (400 MHz, DMSO-*d$_6$*, 298 K): δ = 9.29 (s, 1 H, N=C**H**-N), 7.77 (s, 2 H, Im-**H**), 7.52(d, ^3J = 8.1 Hz, 2 H, Ph-**H**), 7.43 (d, ^3J = 8.2 Hz, 2 H, Ph-**H**), 6.74 (dd, ^3J(Z) = 11.0 Hz, ^3J(E) = 17.7 Hz, 1 H, H$_2$C=C**H**), 5.86 (d, ^3J(E) = 17.7 Hz, 1 H, **H**C(H)=CH), 5.42 (s, 2 H, Bn-**H**), 5.29 (d, ^3J(Z) = 11.0 Hz, 1 H, **H**C(H)=CH), 4.19 (t, ^3J = 7.2 Hz, 2 H, N-C**H$_2$**-CH$_2$), 1.79 (quin, ^3J = 7.5 Hz, 2 H, CH$_2$-C**H$_2$**-CH$_2$), 1.28 (m, 2 H, CH$_2$-C**H$_2$**-CH$_3$), 0.90 (t, ^3J = 7.5 Hz, 3 H, CH$_2$-C**H$_3$**) ppm.

^{13}C{^{1}H} NMR (100 MHz, DMSO-*d$_6$*, 298 K): δ = 139.32 (C), 135.90 (C), 135.83 (CH), 131.52 (CH), 129.36 (2 CH), 127.49 (2 CH), 122.30 (CH), 122.08 (CH), 119.95 (q, ^1J = 318.0 Hz, CF$_3$), 115.88 (CH$_2$), 53.59 (CH$_2$), 50.31 (CH$_2$), 32.07 (CH$_2$), 19.49 (CH$_2$), 13.39 (CH$_3$) ppm.

Synthesis of 1,2-dimethyl-3-(4'-vinylbenzyl)-1*H*-imidazol-3-ium bis(trifluo-romethanesulfonyl)imide ([DMVBIM]Tf$_2$N, 1'): A Schlenk tube was charged with 2.00 g 1,2-dimethylimidazole (20.8 mmol, 1.00 eq), dissolved in 10 mL CHCl$_3$ and cooled to 0 ˚C. Subsequently, 3.81 g vinylbenzyl chloride (25.0 mmol, 1.20 eq) was added and the tube was heated from 0 ˚C to 50 ˚C. The mixture was stirred at 50 ˚C for 24 h. The mixture was extracted with water (slow phase separation). Afterwards, 7.17 g LiTf$_2$N (25.0 mmol, 1.2 eq) was added and the mixture stirred for 3 d at ambient temperature. The mixture was extracted with ethyl acetate (3×40 mL) und the organic

solvent washed with water (1×50 mL). The organic layers were dried over sodium sulfate and the solvent was evaporated at reduced pressure. 8.67 g of product **5** (17.6 mmol, 85%) was received as a slightly orange colored liquid.

^{1}H NMR (400 MHz, DMSO-d_6, 298 K): δ = 7.67 (d, ^3J = 20.2 Hz, 2 H, Im-**H**), 7.51 (d, ^3J = 8.2 Hz, 2 H, Ph-**H**), 7.32 (d, ^3J = 8.2 Hz, 2 H, Ph-**H**), 6.74 (dd, ^3J(Z) = 11.0 Hz, ^3J(E) = 17.7 Hz, 1 H, H$_2$C=C**H**), 5.86 (d, ^3J(E) = 17.7 Hz, 1 H, **H**C(H)=CH), 5.41 (s, 2 H, Bn-**H**), 5.29 (d, ^3J(Z) = 11.0 Hz, 1 H, **H**C(H)=CH), 3.77 (s, 3 H, N-C**H$_3$**), 2.60 (s, 3 H, N-C(C**H$_3$**)-N) ppm.

^{13}C{^{1}H} NMR (100 MHz, DMSO-d_6, 298 K): δ = 144.66 (C), 137.42 (C), 135.94 (C), 134.04 (CH), 128.12 (2 CH), 124.36 (2 CH), 122.69 (CH), 121.24 (CH), 119.57 (q, ^1J = 321.8 Hz, CF$_3$), 115.07 (CH$_2$), 50.46 (CH$_2$), 34.78 (CH$_3$), 9.40 (CH$_3$) ppm.

ESI-MS for C$_{14}$H$_{17}$N$_2$$^+$: m/z = 213.14.

Synthesis of poly[1-butyl-3-(4'-vinylbenzyl)-1H-imidazol-3-ium chloride] (3): A Schlenk flask was charged with 2.03 g 1-butyl-3-(4'-vinylbenzyl)-1H-imidazol-3-ium chloride (1) (7.41 mmol, 200.00 eq), 1.8 mg 1,1'-azobis(cyclohexanecarbonitrile) (0.00741 mmol, 0.20 eq) and 12.8 mg 2-cyano-2-propyl dodecyl trithiocarbonate (0.037 mmol, 1.00 eq). The mixture was dissolved in DMSO, degassed by three consecutive freeze-pump-thaw cycles, filled with nitrogen, and subsequently immersed in a preheated oil bath at 85 °C. The polymerization was stopped by sudden freezing in liquid nitrogen, diluting in water and purging with air. Next, the polymer was purified by dialysis in pure water (3 d, a.t., 1 kDa MWCO).

Synthesis of poly[1-butyl-3-(4'-vinylbenzyl)-1H-imidazol-3-ium bis(trifluoromethanesulfonyl)imide] (4): A Schlenk flask was charged with 8.00 g 1-butyl-3-(4'-vinylbenzyl)-1H-imidazol-3-ium bis(trifluoromethane) sulfonimide (2) (15.34 mmol, 200.00 eq), 3.8 mg 1,1'-azobis(cyclohexanecarbonitrile) (0.0153 mmol, 0.20 eq) and 26.5 mg 2-cyano-2-propyl dodecyl trithiocarbonate (0.0767 mmol, 1.00 eq). The mixture was dissolved in BuCN, degassed by three consecutive freeze-pump-thaw cycles, filled with nitrogen and subsequently immersed in a preheated oil bath at 85 °C. The polymerization was stopped by sudden freezing in liquid nitrogen, diluted in acetone and purging with air. After dialysis (pure water or DMSO for 3 d, a.t., 1 kDa MWCO),

the product (4) was obtained as yellow substance depending on the residual monomer as a highly viscous liquid or as a solid.

Synthesis of poly[1-butyl-3-(4'-vinylbenzyl)-1*H*-imidazol-3-ium bis(triluoromethanesulfonyl)imide] (4) by salt metathesis: 21.0 mg poly(1-butyl-3-(4'-vinylbenzyl)-1H-imidazol-3-ium chloride) (8900 g·mol^{-1}, 0.0755 mmol, 1.00 eq) was dissolved in 1 mL water. Subsequently, 26.0 mg LiTf$_2$N (0.0906 mmol, 1.20 eq) was added, and the reaction was allowed to proceed for 24 h at ambient temperature. Next, the product was extracted with ethyl acetate (2×5 mL), dried over sodium acetate, and evaporated at reduced pressure. The product 4 was received as a yellowish solid.

Synthesis of 1-decyl-2-methyl-3-(4-vinylbenzyl)-1*H*-imidazol-3-ium chloride ([DeMVBIM]Cl). A Schlenk tube was charged with 4.50 g 1-decyl-2-methylimidazole (20.2 mmol, 1.00 eq), dissolved in 100 mL CHCl$_3$ and cooled to 0 °C. Subsequently, 4.29 mL vinylbenzyl chloride (30.4 mmol, 1.50 eq) was added and the tube was heated from 0 °C to 50 °C. The mixture was stirred at 50 °C for 24 h. The mixture was extracted with water (1×80 mL) (phase separation overnight), evaporated at reduced pressure to get rid of the residual organic solvents, and freeze-dried. 3.27 g of the product (58%) was received as a colorless liquid.

^{1}H NMR (400 MHz, DMSO-d$_6$, 298 K): δ = 7.82 (d, ^3J = 2.1 Hz, 1H), 7.79 (d, ^3J = 2.1 Hz, 1H), 7.51 (d, ^3J = 8.1 Hz, 2H), 7.31 (d, ^3J = 8.1 Hz, 2H), 6.73 (dd, ^3J(E) = 17.7 Hz, ^3J(E) = 11.0 Hz, 1H), 5.86 (d, ^3J = 17.7 Hz, 1H), 5.43 (s, 2H), 5.29 (d, ^3J = 11.0 Hz, 1H), 4.12 (t, ^3J = 7.4 Hz, 3H), 2.63 (s, 3H), 1.78 – 1.62 (m, 2H), 1.32 – 1.15 (m, 14H), 0.85 (t, ^3J = 6.8 Hz, 4H) ppm.

^{13}C{^{1}H} NMR (100 MHz, DMSO-d$_6$, 298 K): δ = 144.02 (C), 137.28 (CH), 135.92 (C), 134.07 (C), 128.12 (CH), 126.64 (CH), 121.72 (CH), 121.57 (CH), 115.13 (CH$_2$), 50.32 (CH$_2$), 47.63 (CH$_2$), 31.24 (CH$_2$), 28.94 (CH$_2$), 28.84 (CH$_2$), 28.64 (CH$_2$), 28.43 (CH$_2$), 25.58 (CH$_2$), 22.07 (CH$_2$), 13.93 (CH$_3$), 9.50 (CH$_3$) ppm.

Synthesis of 1-(4-vinylbenzyl)pyridin-1-ium chloride ([VBPy]Cl). A Schlenk tube was charged with 2.48 mL pyridine (8.00 g, 52.4 mmol, 1.00 eq), dissolved in 100 mL CHCl$_3$ and cooled to 0 °C. Subsequently, 7.41 mL vinylbenzyl chloride (2.44 g, 30.8 mmol, 1.50 eq) was added and the tube was heated from 0 °C to 50 °C. The mixture was stirred at 50 °C for 24 h. The mixture was extracted with water (3×50 mL),

evaporated at reduced pressure to get rid of the residual organic solvents, and freeze-dried. 4.81 g of the product (40%) were obtained as a colorless, highly viscous liquid.

^{1}H NMR (400 MHz, DMSO-d$_6$, 298 K): δ = 9.37 (d, ^3J = 5.5 Hz, 2H), 8.68 – 8.59 (m, 1H), 8.23 – 8.15 (m, 2H), 7.59 (d, ^3J = 8.3 Hz, 2H), 7.53 (d, ^3J = 8.3 Hz, 2H), 6.73 (dd, ^3J(E) = 17.7, ^3J(Z) = 11.0 Hz, 1H), 5.96 (s, 1H), 5.88 (d, ^3J = 17.7, 1H), 5.30 (d, ^3J = 11.0, 1H) ppm.

^{13}C{^{1}H} NMR (100 MHz, DMSO-d$_6$, 298 K): δ = 145.94 (CH), 144.87 (CH), 138.09 (C), 135.82 (C), 133.83 (CH), 129.30 (CH), 128.43 (CH), 126.82 (CH), 115.68 (CH$_2$), 62.69 (CH$_2$) ppm.

Synthesis of *N,N,N*-triethyl-*N*-(4-vinylbenzyl)ammonium chloride ([TEVBA]Cl). A Schlenk tube was charged with 3.50 g triethylamine (34.6 mmol, 1.00 eq), dissolved in 50 mL CHCl$_3$ and cooled to 0 ˚C. Subsequently, 7.33 mL vinylbenzyl chloride (7.92 g, 51.9 mmol, 1.50 eq) was added and the tube was heated from 0 ˚C to 50 ˚C. The mixture was stirred at 50 ˚C for 24 h. The mixture was extracted with water (3×40 mL), evaporated at reduced pressure to get rid of the residual organic solvents, and freeze-dried. 8.22 g of the product (94%) were obtained as colorless needles.

^{1}H NMR (400 MHz, DMSO-d$_6$, 298 K): δ = 7.59 (d, ^3J = 8.2 Hz, 2H), 7.52 (d, ^3J = 8.2 Hz, 2H), 6.79 (dd, ^3J(E) = 17.7 Hz, ^3J(Z) = 11.0 Hz, 1H), 5.95 (d, ^3J = 17.7 Hz, 1H), 5.37 (d, ^3J = 11.0 Hz, 1H), 4.54 (s, 2H), 3.19 (q, ^3J = 7.1 Hz, 6H), 1.30 (t, ^3J = 7.1 Hz, 9H) ppm.

^{13}C{^{1}H} NMR (100 MHz, DMSO-d$_6$, 298 K): δ = 138.71 (CH), 135.76 (C), 132.88 (CH), 127.38 (C), 126.54 (CH), 116.18 (CH$_2$), 59.27 (CH$_2$), 52.01 (CH$_2$), 7.59 (CH$_3$) ppm.

Synthesis of triphenyl(4-vinylbenzyl)phosphonium chloride ([TPVBP]Cl). 5.00 g vinylbenzyl chloride (29.5 mmol, 1.50 eq) was added dropwise to a stirred solution of 7.73 g triphenylphosphine (29.5 mmol, 1.00 eq) in 20 mL acetonitrile. Subsequently, the homogeneous solution was stirred at 50 ˚C for 24 hours. The reaction mixture was cooled to ambient temperature and the solvent removed under reduced pressure to afford a white solid. The product was thoroughly washed by stirring with three 30 mL portions of acetone. The solid was finally washed with 30 mL of diethyl ether and dried under vacuum overnight.

^{1}H NMR (400 MHz, DMSO-d$_6$, 298 K): δ = 7.95 – 7.86 (m, 3H), 7.80 – 7.67 (m, 12H), 7.33 (d, ^3J = 8.1 Hz, 2H), 6.98 (d, ^3J = 8. Hz, 2H), 6.65 (dd, ^3J(E) = 17.6 Hz,

^3J(Z) = 11.0 Hz, 1H), 5.81 (d, ^3J = 17.6 Hz, 1H), 5.30 (d, ^2J = 15.9 Hz, 2H), 5.25 (d, ^3J = 11.0 Hz, 1H) ppm.

^{13}C{^{1}H} NMR (100 MHz, DMSO-d$_6$, 298 K): δ = 303.70 (d, ^2J = 4.2 Hz, C), 302.50 (C), 301.78 (d, ^4J = 2.7 Hz, CH), 300.79 (d, ^3J = 9.8 Hz, CH), 297.85 (d, ^3J = 5.7 Hz, CH), 296.80 (d, ^2J = 12.4 Hz, CH), 294.19 (CH), 293.11 (d, ^4J = 3.3 Hz, CH), 284.61 (d, ^1J = 85.5 Hz, C), 281.97 (CH$_2$), 194.70 (d, ^1J = 46.4 Hz, CH$_2$) ppm.

^{31}P{^{1}H} NMR (162 MHz, DMSO-d$_6$, 298 K): δ = 22.83 ppm.

Synthesis of 4-methyl-1-vinyl-4*H*-1,2,4-triazol-1-ium iodide ([MVTr]I). A 100 mL flask was filled with a mixture of 5.40 mL 1-vinyl-1,2,4-triazole 1 (5.50 g, 57.8 mmol, 1.00 eq), 5.40 mL iodomethane (12.3 g, 86.7 mmol, 1.50 eq) and 50 mg 2,6-di-tert-butyl-4-methylphenol (0.227 mol). After stirring and heating for 24 h at 50 °C, the crude product was filtered off and washed with THF for three times. A pale yellow solid (13.21 g, 96.4%) was obtained.

^{1}H NMR (400 MHz, DMSO-d$_6$, 298 K): δ = 10.35 (s, 1H), 9.28 (s, 1H), 7.54 (dd, ^3J(E) = 15.3 Hz, ^3J(Z) = 8.6 Hz, 1H), 6.03 (d, ^3J(E) =15.3 Hz, 1H), 5.56 (d, ^3J(Z) =8.6 Hz, 1H), 3.93 (s, 3H) ppm.

^{13}C{^{1}H} NMR (100 MHz, DMSO-d$_6$, 298 K): δ = 145.38 (CH), 142.03 (CH), 128.98 (CH), 110.21 (CH$_2$), 34.70 (CH$_3$) ppm.

Synthesis of 1-benzyl-3-vinyl-1*H*-imidazol-3-ium chloride ([BnVIM]Cl). A mixture of 9.41 g 1-vinyl-imidazole (0.100 mol, 1.00 eq), 12.7 g benzyl chloride (0.100 mol, 1.00 eq) and 20 mL of ethanol with 100 mg 2,6-di-tert-butyl-4-methylphenol as the stabilizer were charged into a 100 mL Schlenk flask. The mixture was stirred at ambient temperature for 1 h and at 35 °C for another hour before it was kept at 60 °C for 24 h. After cooling down to ambient temperature, the mixture was poured into 1 L THF. The liquid oily phase was washed with THF 3 times and dried at ambient

temperature under high vacuum for 4 h. A pale yellow product (17.7 g, 80%) was then stored in a freezer.

^{1}H NMR (400 MHz, D$_2$O, 298 K): δ = 9.06 (s, 1H), 7.70 (s, 1H), 7.46 (s, 1H), 7.44 – 7.26 (m, 5H), 7.05 (dd, ^3J(E) = 15.6 Hz, ^3J(Z) = 8.7 Hz, 1H), 5.73 (d, ^3J(E) = 15.6 Hz, 1H), 5.37 (d, ^3J(Z) = 8.7 Hz, 1H), 5.31 (s, 2H) ppm.

^{13}C{^{1}H} NMR (100 MHz, D$_2$O, 298 K): δ = 134.13 (CH), 133.01 (CH), 129.30 (CH), 129.28 (CH), 128.74 (CH), 127.93 (CH), 122.66 (CH), 119.52 (CH), 109.48 (CH$_2$), 53.02 (CH$_2$) ppm.

Synthesis of poly(1-decyl-2-methyl-3-(4-vinylbenzyl)-1*H*-imidazol-3-ium chloride) (p([DeMVBIM]Cl), 5). A Schlenk flask was charged with 3.85 g 1-decyl-2-methyl-3-(4-vinylbenzyl)-1H-imidazol-3-ium chloride (**1**) (10.26 mmol, 200.00 eq), 2.51 mg 1,1' -azobis(cyclohexanecarbonitrile) (0.0103 mmol, 0.20 eq) and 17.7 mg 2-cyano-2-propyldodecyl trithiocarbonate (0.0513 mmol, 1.00 eq). The mixture was dissolved in 20 mL DMF/EtOH (1:1, *v/v*), degassed by three consecutive freeze-pump-thaw cycles, filled with nitrogen and subsequently immersed in a preheated oil bath at 85 ˚C. The polymerization was stopped by sudden freezing in liquid nitrogen, diluted with water and purged with air. The polymer was purified by dialysis in pure water (3 d, a.t., 1 kDa MWCO).

Synthesis of poly(1-(4-vinylbenzyl)pyridin-1-ium chloride) (p([VBPy]Cl), 6). A Schlenk flask was charged with 4.81 g 1-(4-vinylbenzyl)pyridin-1-ium chloride (**2**) (20.8 mmol, 200.00 eq.), 5.1 mg 1,1' -azobis(cyclohexanecarbonitrile) (0.0208 mmol, 0.20 eq.) and 36.3 mg 2-cyano-2-propyldodecyl trithiocarbonate (0.105 mmol, 1.00 eq.). The mixture was dissolved in 48 mL DMSO and 24 mL DMF, degassed by three consecutive freeze–pump–thaw cycles, filled with nitrogen, and subsequently immersed in a preheated oil bath at 85 ˚C. The polymerization was stopped by sudden freezing in liquid nitrogen, diluted with water and purged with air. The polymer was purified by dialysis in pure water (3 d, a.t., 1 kDa MWCO).

Synthesis of poly(*N,N,N*-triethyl-*N*-(4-vinylbenzyl)ammonium chloride) (p([TEVBA]Cl), 7). A Schlenk flask was charged with 2.70 g *N,N,N*-triethyl-*N*-(4-vinylbenzyl)ammonium chloride (**3**) (63.1 mmol, 200.00 eq), 1.86 mg 1,1' -azobis(cyclohexanecarbonitrile) (0.0076 mmol, 0.20 eq) and 13.1 mg 2-cyano-2-propyldodecyl trithiocarbonate (0.0380 mmol, 1.00 eq). The mixture was dissolved in DMSO (15 mL) and DMF (10 mL), degassed by three consecutive freeze-pump-thaw cycles, filled with nitrogen and subsequently immersed in a preheated oil bath at 85 ˚C. The polymerization was stopped by sudden freezing in liquid nitrogen, diluted with water and

purged with air. The polymer was purified by dialysis in pure water (3 d, a.t., 1 kDa MWCO).

Synthesis of poly(triphenyl(4-vinylbenzyl)phosphonium chloride) (p([TPVBP]Cl), 8). A Schlenk flask was charged with 7.10 g triphenyl(4-vinylbenzyl)phosphonium chloride (**4**) (17.1 mmol, 200.00 eq), 4.2 mg 1,1' -azobis(cyclohexanecarbonitrile) (0.017 mmol, 0.20 eq) and 29.6 mg 2-cyano-2-propyldodecyl trithiocarbonate (0.086 mmol, 1.00 eq). The mixture was dissolved in DMSO (15 mL) and DMF (10 mL), degassed by three consecutive freeze-pump-thaw cycles, filled with nitrogen and subsequently immersed in a preheated oil bath at 85 °C. The polymerization was stopped by sudden freezing in liquid nitrogen, diluted with water and purged with air. The polymer was purified by dialysis in pure water (3 d, a.t., 1 kDa MWCO).

Synthesis of poly(2-(acryloyloxy)-*N,N,N*-trimethylethan-1-aminium chloride) (p([ATMEA]Cl), 9). A Schlenk flask was charged with 4.00 g 2-(acryloyloxy)-*N,N,N*-trimethylethan-1-aminium chloride (**9**) (20.7 mmol, 200.00 eq), 3.4 mg 2,2' -azobis(2-methylpropionitril) (0.0207 mmol, 0.20 eq) and 35.8 mg 2-cyano-2-propyldodecyl trithiocarbonate (0.104 mmol, 1.00 eq). The mixture was dissolved in 20 mL DMSO/H_2O (1:1, *v/v*), degassed by three consecutive freeze-pump-thaw cycles, filled with nitrogen and subsequently immersed in a preheated oil bath at 60 °C. The polymerization was stopped by sudden freezing in liquid nitrogen, diluted with water and purged with air. The polymer was purified by dialysis in pure water (3 d, a.t., 1 kDa MWCO).

Synthesis of poly(1-butyl-3-(4-vinylbenzyl)-1*H*-imidazol-3-ium chloride) (p([BVBIM]Cl), 10). A Schlenk flask was charged with 13.9 g 1-butyl-3-(4-vinylbenzyl)-1*H*-imidazol-3-ium chloride (50.3 mmol, 200 eq), 12.3 mg 1,1'-azobis(cyclohexanecarbonitrile) (0.0503 mmol, 0.20 eq) and 166 mg DoPAT-PE (251 mmol, 1.00 eq). The mixture was dissolved in 75 mL DMSO/DMF (1:1, *v/v*), degassed by three consecutive freeze-pump-thaw cycles, filled with nitrogen and subsequently immersed in a preheated oil bath at 85 °C. The polymerization was stopped by sudden freezing in liquid nitrogen, diluted with water and purged with air. The polymer was purified by dialysis in pure water (3 d, a.t., 1 kDa MWCO).

Synthesis of poly(4-methyl-1-vinyl-4*H*-1,2,4-triazol-1-ium iodide) (p([MVTr]I), 11). A mixture of 5.00 g 4-methyl-1-vinyl-4*H*-1,2,4-triazol-1-ium iodide (21.10 mmol), 50 mg AIBN (0.300 mmol), and 20 mL of anhydrous DMF was put inside a 50 mL Schlenk flask under argon protection. Three freeze-pump-thaw cycles

were applied for oxygen removal. The reaction was stirred at 75 ℃ for 24 h and the crude product was dialyzed in water (2 d, a.t.). A yellow powder was received after removal of solvents, the yield was 3.6 g (72%).

Synthesis of poly(1-benzyl-3-vinyl-1*H*-imidazol-3-ium chloride) (p([BnVIM]Cl), 12). A 100 mL Schlenk flask was filled with a mixture of 5.00 g 1-benzyl-3-vinyl-1*H*-imidazol-3-ium chloride**.** (22.6 mol), 50 mg AIBN (0.300 mmol), and 50 mL DMSO. Then, three freeze-pump-thaw cycles were applied for oxygen removal and argon protection. The reaction was stirred at 90 ℃ for 12 h. After cooling down to ambient temperature, the crude product was precipitated in THF. The precipitate was re-dissolved in methanol and precipitated in THF again. 4.00 g of a white powder (80%) was received after removal of solvents.

Synthesis of the photoenol- functionalized RAFTagent (14')

The synthesis was followed the protocol of Kaupp *et al.*[344]

Synthesis of 4-maleimidobutyroyl chloride

The synthesis was followed the protocol of Hermann *et al.*[348]

APTES-functionalization of Si wafer: The Si surfaces (approx. 1×1 cm^2) were treated with piranha solution (H_2SO_4:H_2O_2, 4:1 *v/v*) for 3 h. Subsequently, the Si wafers were rinsed thoroughly with Milli Q water and dried under a stream of nitrogen. In a further step, the activated surfaces were placed in a solution of 5.0 mL APTES, 70.0 mL toluene and 0.1vol% triethylamine and allowed to react overnight at 80 ℃. The substrates were rinsed with toluene, acetone and methanol, before being dried under a stream of nitrogen.

Maleimide-functionalization of (APTES) Si wafer: The APTES-functionalized Si substrate was immersed in 55 mM DCM solution of TEA. Equal volume of a 50 mM solution of 4-maleimidobutyroyl chloride in dry dichloromethane was added subsequently under inert atmosphere. The reaction was allowed to proceed for 4 h. The surfaces were rinsed with dichloromethane, methanol and Milli Q water and left in a

petri dish with methanol overnight. Next, the surfaces were rinsed with THF, methanol and Milli Q water.

Photo-patterning of DoPAT-PE (14') on the maleimide-functionalized Si wafer (13): The substrate was immersed in a 11 mM solution of DoPAT-PE (14') in acetonitrile, and subsequently degassed by purging with nitrogen for 20 minutes. Next, the wafer was irradiated for 2.5 h (UV lamp: ARIMED B6, λ_{max} = 320 nm). Subsequently, the wafer was rinsed thoroughly with THF, acetone, methanol and Milli Q water and dried under a stream of nitrogen.

Grafting-from polymerization of butylvinylbenzylimidazolium chloride (1): The DoPAT-PE-functionalized substrate 14 was placed in a vial and flushed with argon for 5 minutes. A solution – degassed via three consecutive freeze-pump-thaw cycles – of 5.55 g butylvinylbenzylimidazolium chloride (1) (20.1 mmol, 1500 eq), 4.7 mg DoPAT (0.0134 mmol, 1.00 eq) and 3.3 mg VAZO-88 (0.0134 mmol, 1.00 eq) was added to the wafer and the vial placed in a preheated custom-built heating block at 85 ˚C. After 7 h, the polymerization was stopped by sudden cooling in liquid nitrogen and bubbled with air. The solution was dialyzed in deionized water for 3 d and freeze-dried afterwards. The wafer was rinsed thoroughly with Milli Q water, methanol, acetone and Milli Q water again and left in a petri dish with methanol overnight. The wafer was again rinsed with Milli Q water, methanol and Milli Q water and left for another 24 h in a petri dish with methanol. After 24 h, the wafer was rinsed with Milli Q water, methanol and Milli Q water and dried under a stream of nitrogen.

Reaction of PIL-grafted surface (16) with KMnO₄: The PIL-grafted surface was dipped into a 50 mM solution of $KMnO_4$ in water for 2 to 3 seconds. Subsequently, the surface was rinsed thoroughly with Milli Q water and dried under a stream of nitrogen.

Unraveling the Spontaneous Zwitterionic Copolymerization Mechanism of Cyclic Imino Ethers and Acrylic Acid[4]
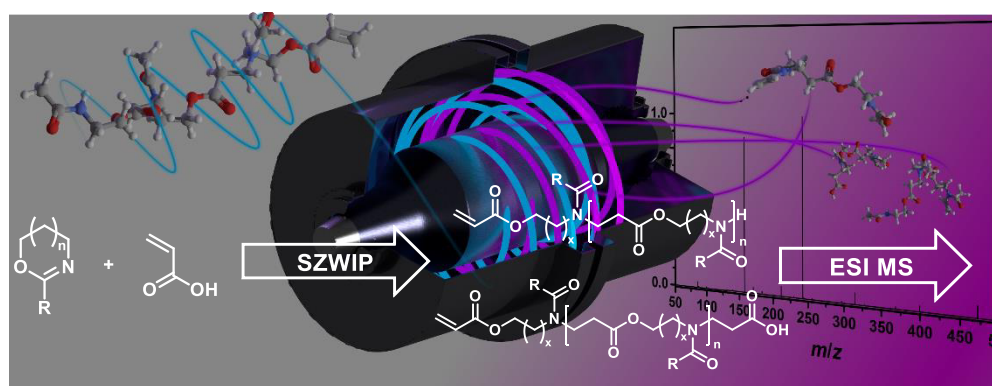
5.1. MOTIVATION

Cyclic imino ethers (CIE) are an important class of monomers for ring-opening polymerization. After polymerization, they form PEAs[115,116] where the ester moiety entails a plethora of motifs e.g. double and triple bonds for subsequent ligation reactions. Their 'stealth' properties – as discussed earlier – makes these polymers ideal platforms for drug delivery. However, their degradability is limited to hydrolysis of the ester side chain. In addition, there is no disassembly pathway to transform the entire polymer chain into small environmentally friendly compartments. An alternative constitutes SZWIP-prepared polymers recently prepared by Kempe and his team (see Section 2.2.3), who rediscovered the reaction between an electrophilic monomer M_E, i.e. CIE, and a nucleophilic monomer M_N, i.e. acrylic acid.[349]

After their first mentioning by Segusa in 1977, the polymerization mechanism was elucidated by techniques available in the 1970s and 80s. A detailed mechanism including a precision determination of by-products has not yet been described. Thus, the present section introduces a HR ESI MS access route leading to in-depths insight into the SZWIP mechanism between CIE (i.e. 2-methyl-2-oxazoline (MeOx), 2-ethyl-2-oxazoline (EtOx) or 2-ethyl-2-oxazine (EtOz)) with acrylic acid (AA), exploiting the characteristic species accumulating during the copolymerization as well as tandem mass spectrometry (MS/MS). Furthermore, preferences in α,ω-end group formation by screening various feed ratios of CIE and AA (e.g. MeOx:AA = 1:1; MeOx:AA = 2:1; MeOx:AA = 1:2) are showcased. Critically, a calibration curve – based on AA-MeOx-AA dimer – was established allowing for the semi-quantitative determination of the end group ratios with different feed ratios of AA. The formation of alternating copolymers was confirmed by MS/MS experiments and deviations from an ideal alternating composition were found to decrease from MeOx to EtOx to EtOz.

5.2. RESULTS AND DISCUSSION
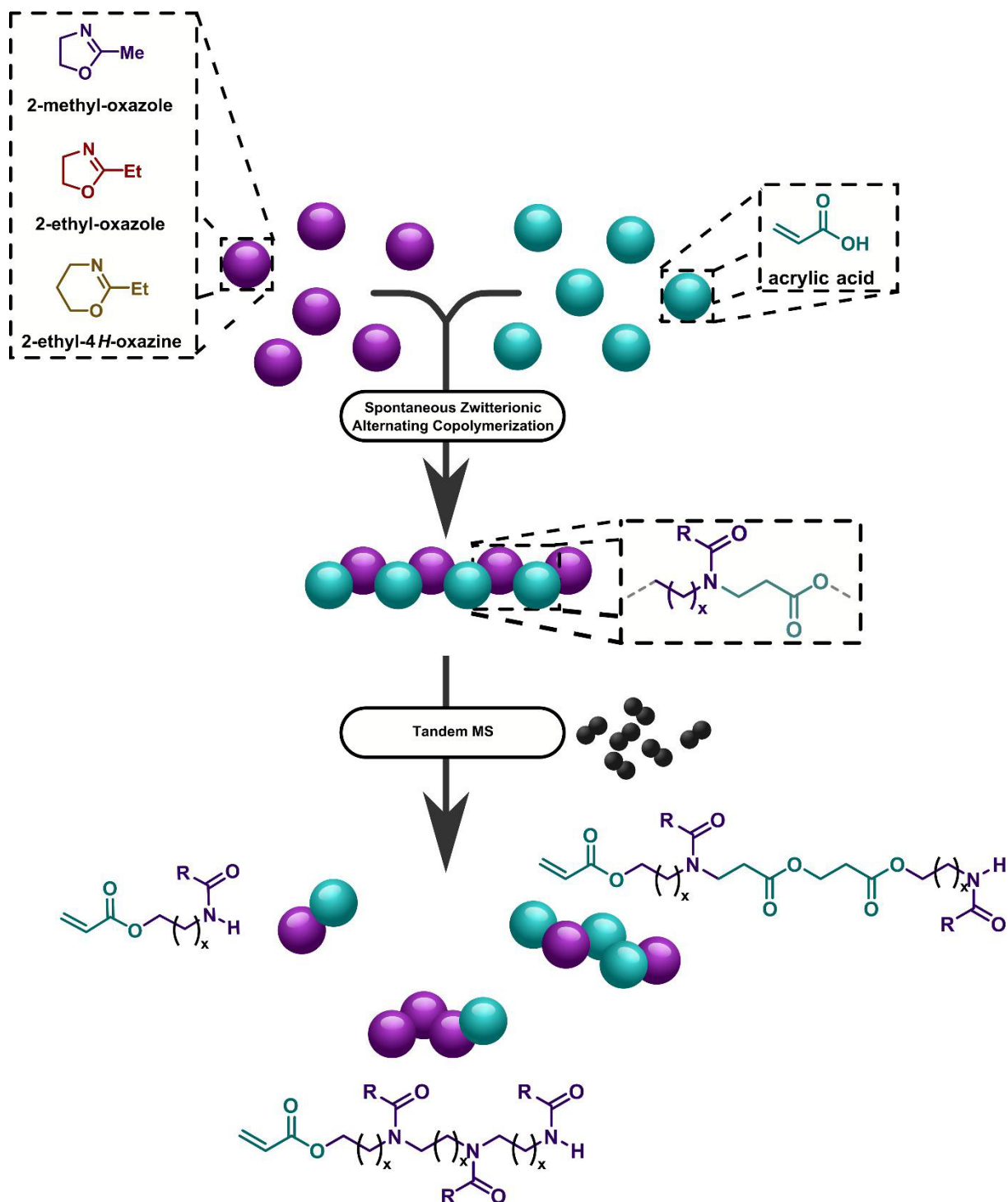
Figure 41 Schematic representation of the SZWIP procedure of 2-methyl-2-oxazoline (MeOx), 2-ethyl-2-oxazoline (EtOx) or 2-ethyl-2-oxazine (EtOz) with acrylic acid (AA) and their analysis via ESI MS and structural identification using tandem MS (x = 1: 2-oxazoline; x = 2: 2-oxazine). Reprinted with permission from Ref. [352]. Copyright American Chemical Society (2018).

A library of oligomeric NPAEs, i.e. oligo(MeOx-*alt*-AA)$_n$A, oligo(EtOx-*alt*-AA)$_n$A and oligo(EtOz-*alt*-AA) was prepared using previously reported procedures.[116,139,140,350] Specifically, CIEs were reacted with AA in different ratios as summarized in **Table 3**.

Structural assessment by ^{1}H NMR was impeded due to the presence of rotamers as well as the existence of different oligomeric species and end groups. Thus, the polymer composition, i.e. ratio of the two monomers, was the only information obtained.[116] A precise structural assignment can only be accessed via high resolution ESI MS. The following mass spectrometric experiments have been performed on an Orbitrap mass analyzer critically surpassing the previously published data on SZWIP-prepared polymers.[116] The oligomers were dissolved in water/acetonitrile/acetic acid (1:1:0.1 (*v/v*)) with a concentration of 0.500 mg·mL^{-1} (the exact mass is crucial for subsequent quantifications). **Figure 41** collates the work that has been performed in the present section comprising oligomer production, detailed full MS as well as MS/MS and mechanistic elucidation based on the post-mortem analysis of specific fragment ions.[351]

Table 3 ^{1}H NMR and SEC characterization data of the oligomeric NPAEs prepared by SZWIP of different cyclic imino ethers (CIEs) and acrylic acid (AA). Reprinted with permission from Ref. [352]. Copyright American Chemical Society (2018).

CIE	CIE : AA	DP[a] (CIE/AA)	$M_{n,NMR}$[a] [g mol^{-1}]	$M_{n,SEC}$[b] [g mol^{-1}]	Đ[b]
MeOx	2 : 1	2.5/2.5	465	1800	1.32
	1 : 1	2.5/2.5	465	1300	1.18
	1 : 2	3.0/3.0	543	1500	1.27
EtOx	1 : 1	2.5/2.5	500	1600	1.30
	1 : 2	2.0/2.0	414	1300	1.17
EtOz	1 : 1	3.0/3.0	627	2000	1.27
	1 : 2	2.5/2.5	535	1600	1.20

[a] Determined from ^{1}H NMR analysis from the peak areas of the vinyl groups and the methylene group of CIE and AA repeating units. [b] Determined by SEC analysis.

For clarity, the current section is divided into four parts: (i) expanded mass spectra highlighting important species (Section 5.2.1), (ii) short MS/MS discussion with one product ion and its fragmentation ions (Section 5.2.2), (iii) quantification of the mass spectra (Section 5.2.3) and (iv) discussion of the suggested polymerization mechanism (Section 5.2.4).

5.2.1. Expanded Spectra of the SZWIP Oligomers
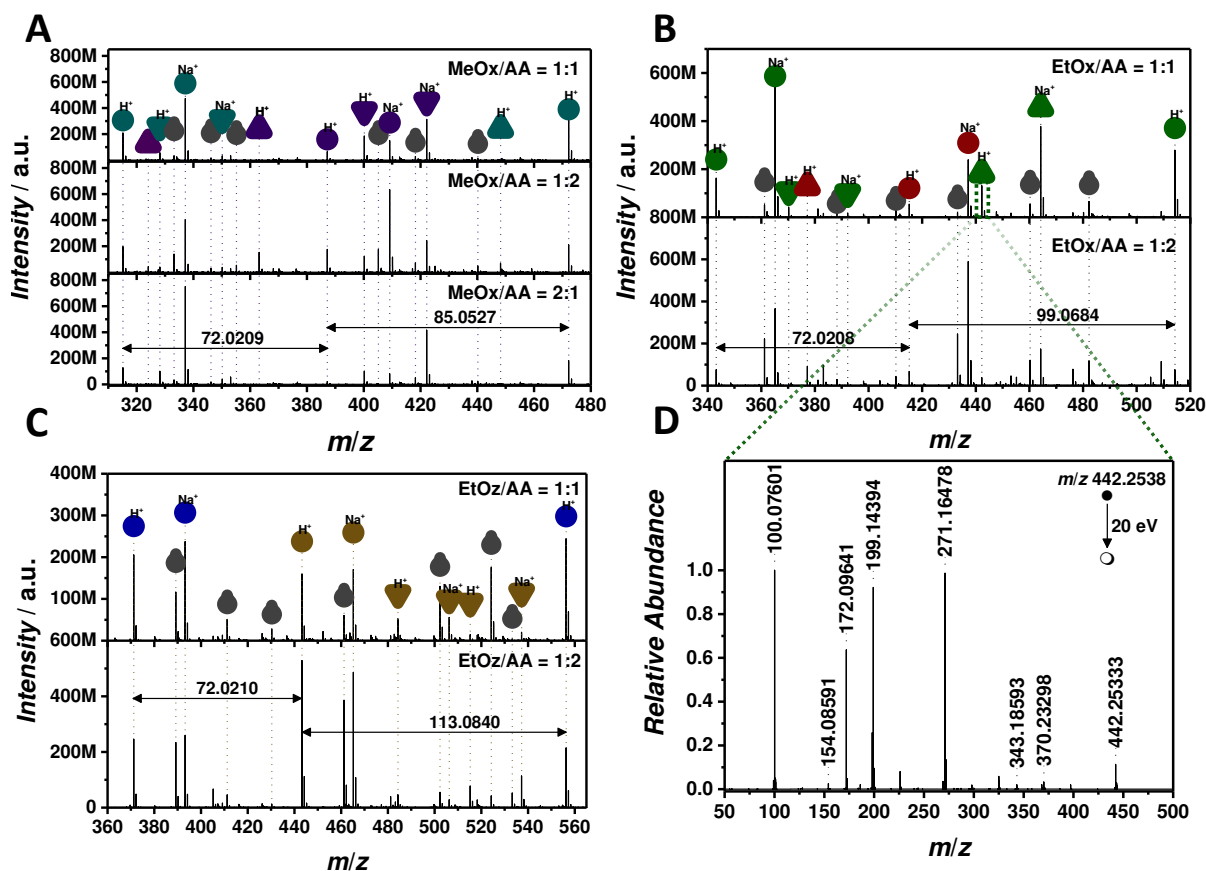
Figure 42 Overview ESI mass spectra of (A) oligo(MeOx-*alt*-AA)$_n$A with feed ratio MeOx/AA =1:1; 1:2 and 2:1; (B) oligo(EtOx-*alt*-AA)$_n$A with feed ratio EtOx/AA = 1:1 and 1:2; (C) oligo(EtOz-*alt*-AA) with feed ratio EtOz/AA = 1:1 and 1:2 recorded in water/acetonitrile/acetic acid (1:1:0.1 *v/v*) in a mass range between *m/z* 200 to 1000. The labels ●, ●, ● correspond to an acid-terminated species (H⁺ ionized), and labels ●, ●, ● indicate the corresponding amide-terminated species (H⁺ ionized). (D) Proposed structural assignment for the ideally alternating copolymers with α-acrylic and ω-amide end groups. Reprinted with permission from Ref. [352]. Copyright American Chemical Society (2018).

The expanded ESI spectra (**Figure 42A-C**) collate all species recorded within one full repeat unit (e.g. *m/z*(MeOx-AA)^{exp} 157.0736; *m/z*(MeOx-AA)^{theo} 157.0739). Most abundant were the H⁺ ionized and Na⁺ ionized alternating copolymer species (ω-acid chain terminus (●, ●, ●) and the ω-amide chain terminus (●, ●, ●)). Further characteristic ions were detected, i.e. a low abundant peak in the MeOx/AA = 1:2 spectrum with 324.1047 *m/z* (labeled with △) representing oligo(MeOx$_1$-*alt*-AA$_3$). The incorporation ratio MeOx/AA=1:3 reveals an AA-AA dimer generated by a Michael addition reaction[352] before it reacts with another MeOx-AA dimer. As such a reaction preferably occurs with a surplus of AA (e.g. MeOx/AA = 1:2), the AA-AA dimer species is of even lower abundance for the other copolymerization ratios (i.e. MeOx/AA = 1:1 and 2:1). A more important side product that has been detected in the course of the mass spectrometric study is based on the homocoupling of CIE (CIE-CIE dimer). For instance, a species at 328.1859 *m/z* (labeled with ▼) was almost equally abundant in

each spectrum, irrespective of the copolymerization ratio and can be assigned as ol-igo(MeOx$_3$-*alt*-AA$_1$). MeOx. If the acrylic acid was incorporated into the main chain, the highly reactive cyclic oxazolinium was susceptible to ring-opening reactions with any nucleophiles (e.g. water). Yet, low abundant species have been detected (labeled with ♦ (**Figure 42**)), where the SZWIP process was terminated by ambient water instead of acrylic acid. **Table 4** collates the species identified in the mass spectra (see **Figure 42**).

Table 4 Peak assignment of the ESI- Orbitrap spectrum showing the label (in correspondence with the species in **Figure 43**), the experimental m/z and theoretical m/z values (determined by the most abundant isotope of the isotopic pattern), $\Delta m/z$, the resolution (obtained by the Xcalibur software), and the structure determination. One of various isobaric structures is depicted. Reprinted with permission from Ref. [352]. Copyright American Chemical Society (2018).

Label	m/z (exp)	m/z (theo)	$\Delta m/z$	Resolution	Structure
●	315.1544	315.1552	0.0012	122800	
△	324.1047	324.1054	0.0007	118500	
▼	328.1859	328.1867	0.0008	118500	
▲	363.1752	363.1762	0.0010	108000	
▼	400.2067	400.2078	0.0011	101400	
●	343.1859	343.1864	0.0005	113800	
△	324.1047	324.1054	0.0007	118500	
▼	370.2329	370.2336	0.0007	111400	

●	415.2063	415.2075	0.0012	104100
▲	442.2535	442.2548	0.0013	97400
●	371.2168	371.2177	0.0009	109000
△	324.1047	324.1054	0.0007	118500
●	443.2378	443.2382	0.0004	99800
▼	484.3006	484.3012	0.0006	97100
△	515.2589	515.2594	0.0005	91700

5.2.2. MS/MS Elucidation

In order to obtain information about the general reaction between AA and CIEs allowing to deduce the polymerization mechanism, a closer look into the micro-structure is important. The oligomer microstructures have been revealed by employ-ing MS/MS (**Figure 42D**), where a precursor ion (442.2538 *m/z*) was fragmented with nitrogen gas by applying a collision energy of 20 eV. The determination of the micro-structure is a complex process as many isobaric structures are possible, comprising (*i*) the development of a feasible fragmentation mechanism;[353,354] (*ii*) their structural assessment; and (*iii*) the identification of key fragment ions unambiguously confirm-ing the microstructure.

Step (*i*): fragmentation mechanism

Exemplary performed on oligo(MeOx$_3$-alt-AA$_1$), such a microstructure determination process is depicted in **Figure 44**. Two dominant fragmentation pathways are discussed: (*i*) a concerted depolymerization via a six-membered transition state occurring at the chain termini and at the main chain fragments alike; and (*ii*) a ring closure depolymerization releasing fragments always in β-position to the acetamide structural unit. Based on the structural assignments of the MS/MS results, it is proposed that the concerted depolymerization is the favored fragmentation pathway. The fragment ion 256.1656 *m/z* represents MeOx$_3$ confirming that the microstructure contains homocoupled MeOx. An important consequence is that AA terminates the SZWIP process by ring opening MeOx. If the AA is incorporated into the main chain, the highly reactive cyclic oxazolinium is susceptible to ring-opening reactions with any nucleophiles (e.g. water). Yet, low abundant species have been detected (labeled with 💧 (**Figure 42**)) where the SZWIP process was terminated by ambient water instead of AA.
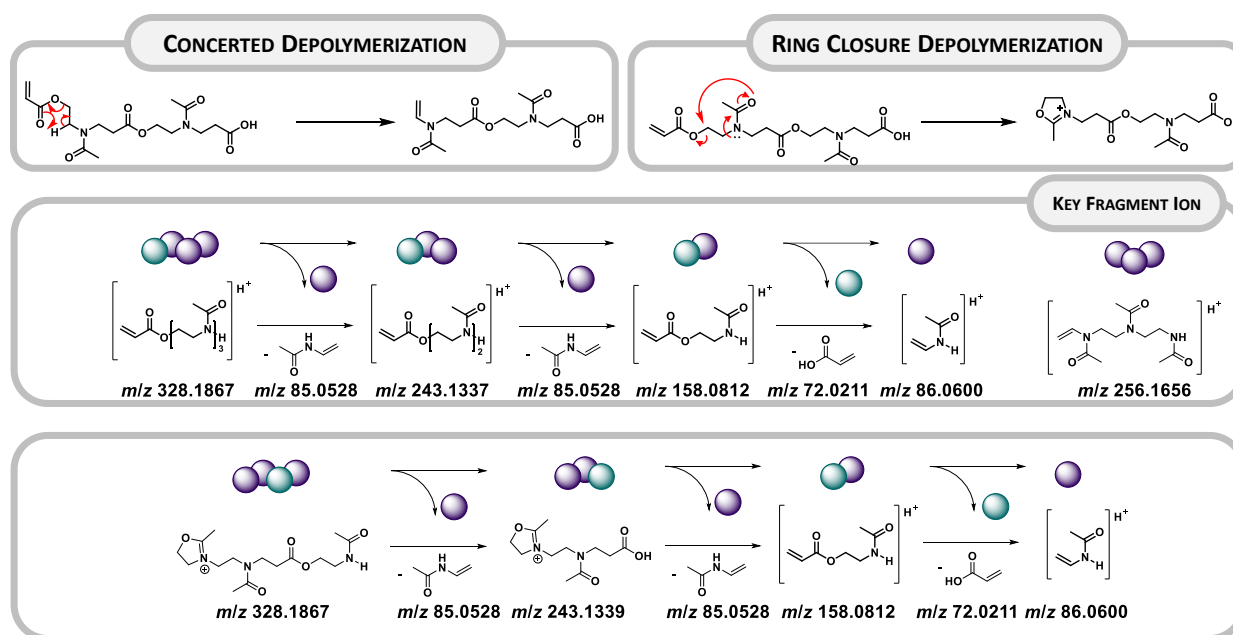
Figure 44 Proposed fragmentation (depolymerization) during MS/MS experiments revealing the microstructure of CIEs. Oligo(MeOx$_3$-*alt*-AA$_1$) having acrylic acid as chain termini (acrylic acid terminates the SZWIP polymerization) yields various fragment ions. A key fragment ion with three MeOx units connected to each other has been detected. An isobaric structure having acrylic acid incorporated into the main chain is unlikely since the cyclic iminium ether is susceptible to ring-opening reactions (e.g. water). Reprinted with permission from Ref. [352]. Copyright American Chemical Society (2018).

Step (*ii*) and (*iii*): structural assessment and key structures

Close interpretation of the peaks observed in the MS spectra is critical for the identification of isobaric structures. Species such as those labeled with ● represent

amide-terminated moieties possessing an ideally alternating microstructure. However, tandem MS is the only technique available to precisely assess microstructural defects. For instance, a species identified as oligo(MeOx$_3$-*alt*-AA$_3$) prepared from a feed ratio MeOx/AA = 1:2 (m/z^{exp} 472.2295; m/z^{theo} 472.2290) is discussed in the following. Strong signals in the MS/MS spectrum (**Figure 45**) indicate the alternating nature of oligo(MeOx$_3$-*alt*-AA$_3$). For instance, a species at 158.0814 m/z represents the AA-MeOx dimer (m/z^{theo} 158.0812; labeled with ●●). Furthermore, an alternating depolymerization sequence starting from 472.2295 to 86.0609 m/z (MeOx monomer) is evident in the MS/MS spectrum. Strikingly, the existence of a MeOx-MeOx sequence is detected at 171.1130 m/z (labeled with ●●) indicating some extent of MeOx homopolymerisation during SZWIP. Applying 18 eV collision energy, 1.49 mol% of this
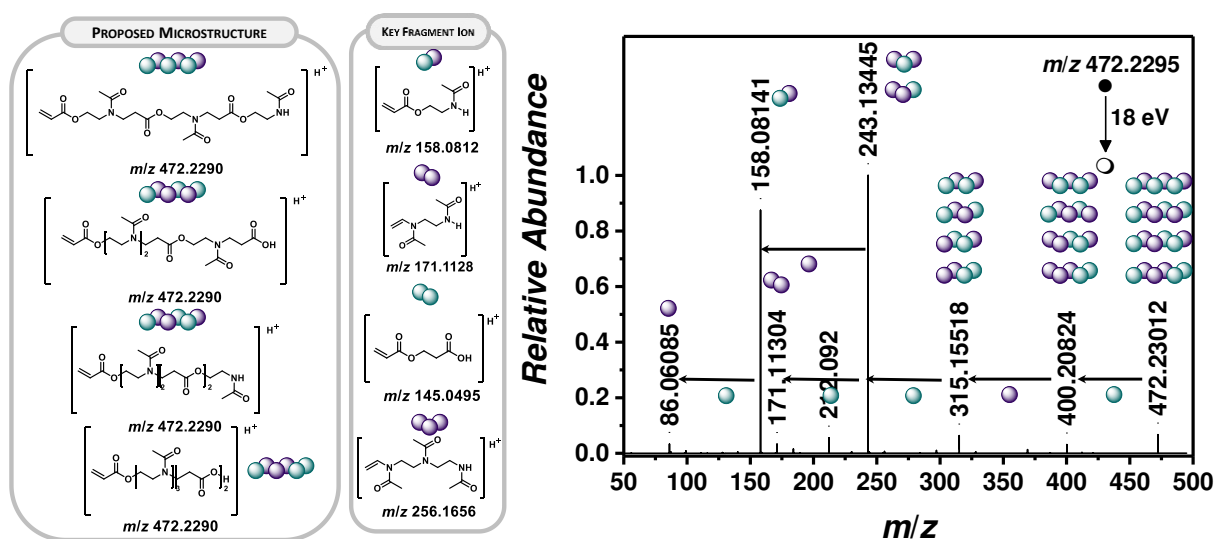
Figure 45 Proposed microstructures of oligo(MeOx$_3$-*alt*-AA$_3$) (m/z^{exp} 472.2295; m/z^{theo} 472.2290) and key fragment ions based on peaks identified. The strong alternating microstructure (●●●●●●) and a microstructure containing a MeOx-MeOx sequence (●●●●●●) can be assigned in the MS/MS spectrum. Reprinted with permission from Ref. [352]. Copyright American Chemical Society (2018).

species is produced as product ion. **Table 5** gives the error of the structural assignments.

Table 5 Peak assignment of ESI MS/MS experiment (**Figure 46**) at 472.2295 m/z with a HCD energy of 18 eV showing the experimental m/z, the theoretical m/z values, and $\Delta m/z$ and the proposed structure. Reprinted with permission from Ref. [352]. Copyright American Chemical Society (2018).

m/z(exp)	m/z(theo)	$\Delta m/z$	Error / ppm
472.2295	472.2290	0.0005	1.06
400.2082	400.2078	0.0004	1.00
315.1552	315.1551	0.0001	0.32
243.1345	243.1339	0.0006	2.47
212.0920	212.0917	0.0003	1.41
171.1130	171.1128	0.0002	1.17
158.0814	158.0812	0.0002	1.27
86.0609	86.0600	0.0009	10.46
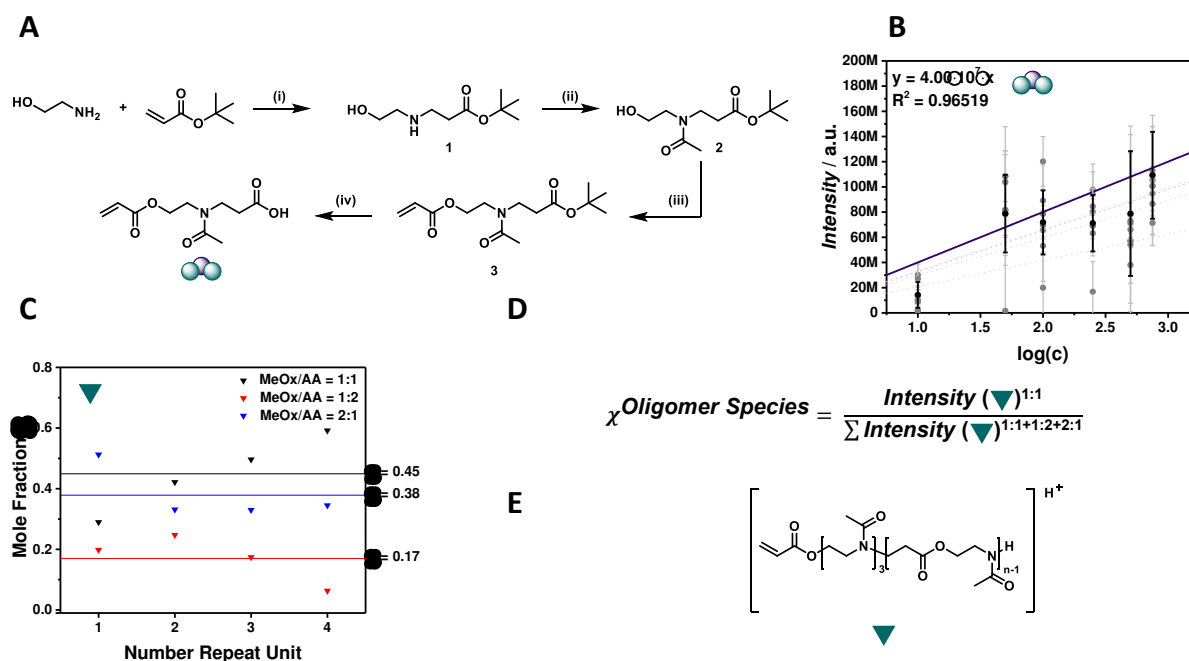
Figure 47. (A) Reaction scheme for the small molecule analogue: (i) a.t., 18 h; (ii) $(CH_3CO)_2O$, Al_2O_3, 10 min; (iii) CH_3COCl, NEt_3, DMF, 0 °C to a.t., 18 h, (iv) trifluoroacetic acid, DMF, 0 °C to a.t., 18 h; (B) calibration curve recorded in single ion monitoring (SIM) mode focusing on the H^+ ionized species (labelled with ●●●); (C) repeat unit dependent evaluation of the mole fraction; (D) equation to obtain the mole fraction (χ) and the results of one species (▼) based on the calibration; (E) general structure of species ▼. Reprinted with permission from Ref. [352]. Copyright American Chemical Society (2018.

5.2.3. Quantitative Assessment

Although MS/MS experiments provide quantitative information based on product ions, spectra acquired in a full range mode (detecting several species) are of limited reliability for quantification. However, it is interesting and important to evaluate the influence of different feed ratios (MeOx/AA = 1:1; 1:2; and 2:1) on their respective end group quantities. To enable (semi-)quantification, a small molecule analogue, the acid-terminated dimer AA-MeOx-AA was prepared (**Figure 47A**) and used to record a calibration curve in single ion monitoring mode ranging from 0.75 mg·mL^{-1} to 0.01 mg·mL^{-1} (m/z^{exp} 230.1019; m/z^{theo} 230.1023) (**Figure 47B**). Here, the protonated species has been evaluated. The calibration curve based on the sodiated species (m/z^{exp} 252.0835) can be found in the Appendix Fig. C 16.

Based on the calibration curve, it was possible to extract semi-quantitative information from all oligo(MeOx-*alt*-AA)$_n$A spectra with the peak used for calibration (230.1019 m/z) being present in all feed ratios (MeOx/AA = 1:1; 1:2; and 2:1). Within the same spectrum (e.g. MeOx/AA = 1:1), semi-quantitative information based on the

mole fraction determination was obtained (**Figure 47D**).[355] The calibration curve provided quantitative values for the acid-terminated oligomers and thus allowed for the semi-quantitatively determination of the mole fractions in all individual spectra (1:1; 1:2 and 2:1), which were compared with each other. Thus, the amide-terminated species has been determined by its mole fraction always referenced to the m/z^{exp} 230.1019 species (**Figure 47A**). Semi-quantitative information from oligo(EtOz-*alt*-AA) and oligo(EtOx-*alt*-AA)$_n$A has been obtained by using the same calibration curve nased on the assumption that the incorporation of additional neutral CH_2 groups (either in the side chain as for EtOx or in both side and main chain as for EtOz) have a limited effect on the ionization of the macromolecule. Key findings of the semi-quantification are illustrated in **Figure 47C** and further discussed in the following.

End group quantification within MeOx: Increasing the acrylic acid content in the feed increases the amount of acid-terminated oligomers (e.g. species at m/z^{exp} 387.1756, labeled with ●) from $\chi^{avg} = 0.27$ (MeOx/AA = 1:1) to $\chi^{avg} = 0.57$ (MeOx/AA = 1:2), whereas a depletion of MeOx (MeOx/AA = 2:1) yields $\chi^{avg} = 0.16$. Increasing the cyclic imino ether in the feed increases the amount of amide-terminated oligomers (e.g. species at m/z^{exp} 315.1455, labeled with ●) from $\chi^{avg} = 0.36$ (MeOx/AA = 1:1) to $\chi^{avg} = 0.49$ (MeOx/AA = 2:1), whereas MeOx/AA = 1:2 yields $\chi^{avg} = 0.20$. The full and detailed quantitative data for each end group and all polymer systems studied can be found in **Figure 48**.

Homocoupling quantification: Species attributed to homocoupling reaction steps (e. g. the species at m/z^{exp} 328.1862, labeled with ▼ refer to **Figure 47**) are most abundant for MeOx/AA = 1:1 ($\chi^{avg} = 0.45$), however strongly reduced for MeOx/AA = 1:2 ($\chi^{avg} = 0.17$). Generally, MeOx homopolymer sequences with up to five repeat units containing H^+ and acrylic acid end groups can be assigned in remarkable abundancies, indicating the ring-opening polymerization of cyclic imino ethers as a competitive pathway. The mole fraction of these species decreases from $\chi^{avg} = 0.36$ (MeOx/AA = 1:1) to $\chi^{avg} = 0.25$ (MeOx/AA = 1:2) and increases slightly under surplus cyclic imino ether in the feed to $\chi^{avg} = 0.39$ (MeOx/AA = 2:1). As the assessment of the homocoupling quantification is exemplarily illustrated in **Figure 47**, it was decided to illustrate the remaining quantitative assessments for several species in the Appendix Tab. C 1-7 and Fig. C 17-21.
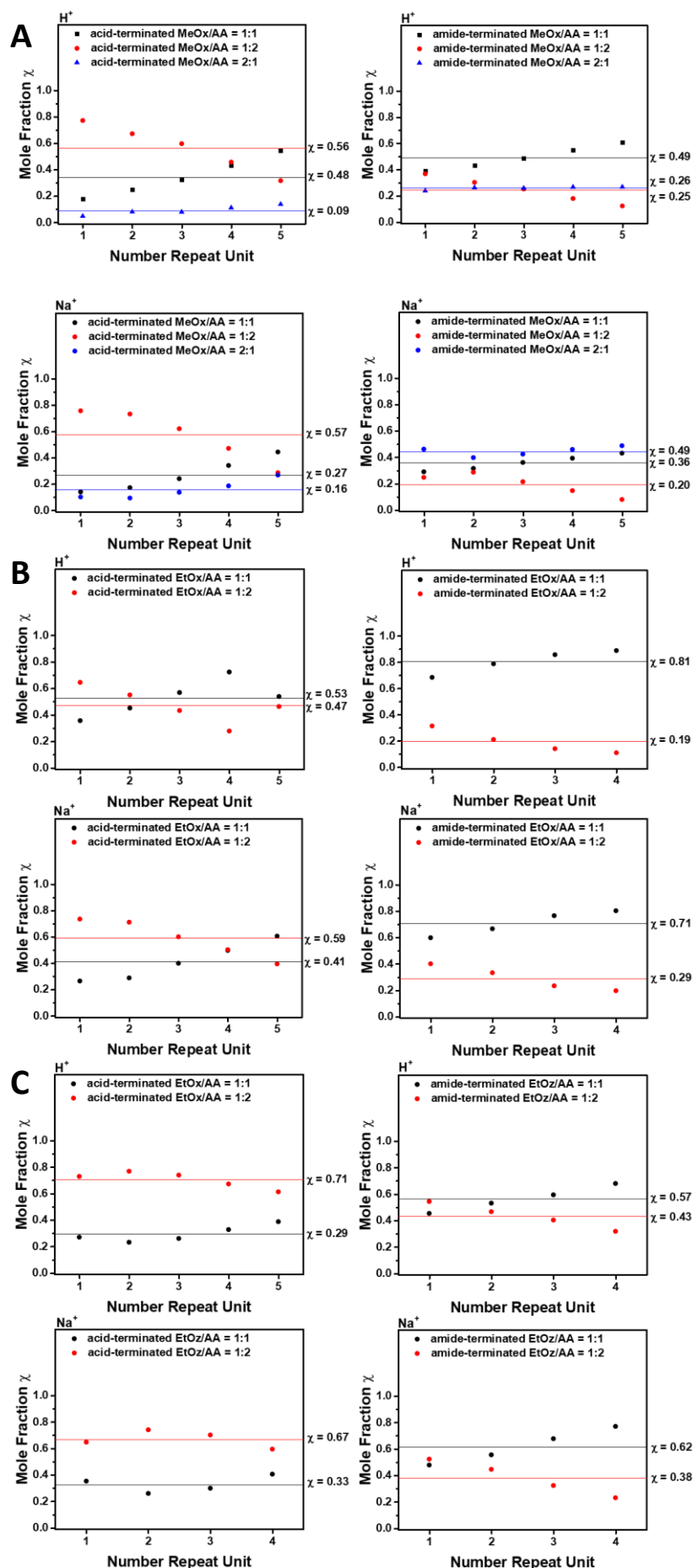
Figure 48 Illustration of the mole fraction along the repeat units of (**A**) MeOx/AA (1:1, 1:s and 2:1), (**B**) EtOx/AA (1:1 and 1:2) and (**C**) EtOz/AA (1:1 and 1:2) determined based on the H+ and Na+ ionized acid- and amide-terminated intensities. Reprinted with permission from Ref. [352]. Copyright American Chemical Society (2018).

Quantification of different CIEs: Changing the 2-oxazoline from MeOx to

EtOx had a strong effect on the end groups. The amide-terminated species increase from $\chi^{avg} = 0.28$ (MeOx/AA = 1:1) to $\chi^{avg} = 0.50$ (EtOx/AA = 1:1). Strikingly, homopolymerization of EtOx decreases from $\chi^{avg} = 0.70$ (MeOx/AA = 1:1) to $\chi^{avg} = 0.27$ (EtOx/AA = 1:1). A likely explanation for the increased abundancies of amide-terminated species is that the zwitterion of AA and EtOx (represented by ●●) forms less rapidly compared to MeOx and AA (represented by ●●) (see the detailed mechanistic approach below). Thus, more ionic adducts such as $[HEtOx]^+[AA]^-$ were present in the mixture, which were responsible for the amide chain termination. Expanding the ring from a five-membered (oxazoline) to a six-membered (oxazine) ring influences the chain terminus ratios even more drastically: amide-terminated species decreased from $\chi^{avg} = 0.28$ (MeOx/AA = 1:1) and $\chi^{avg} = 0.50$ (EtOx/AA = 1:1) to $\chi^{avg} = 0.22$ (EtOz/AA = 1:1). Further, homopolymerization of EtOz decreased from $\chi^{avg} = 0.70$ (MeOx/AA = 1:1) and $\chi^{avg} = 0.27$ (EtOx/AA = 1:1) to only $\chi^{avg} = 0.03$ (EtOz/AA = 1:1). The quantification data within each CIE (i.e. EtOx and EtOz) can be found in **Figure 49**.
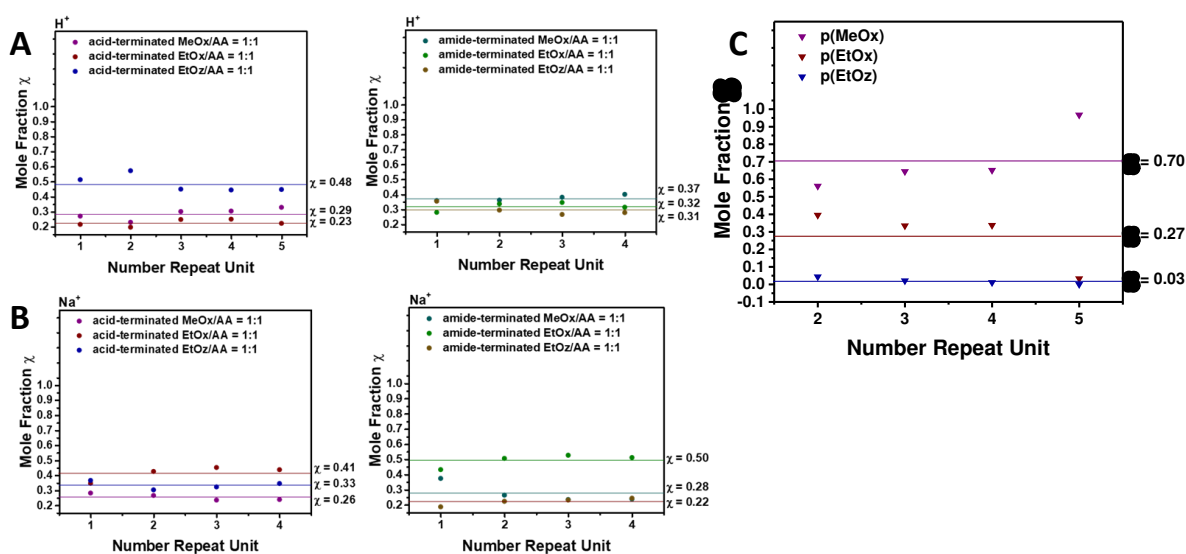
Figure 49 Illustration of the mole fraction along the repeat units of CIE (1:1) determined based on the (**A**) H$^+$ ionized and (**B**) Na$^+$ acid- and amide-terminated intensities. (**C**) Illustration of the mole fraction along the repeat units of p(CIE) determined based on the H$^+$ ionized intensities. Reprinted with permission from Ref. [352]. Copyright American Chemical Society (2018).

5.2.4. Polymerization Mechanism

Supported by previous literature reports and based on the post-mortem analysis of the SZWIP-prepared oligomers by full MS and MS/MS alike, a detailed mechanism for the SZWIP of CIEs and AA is suggested. In general, CIEs and AA can react in two ways either via a Michael addition reaction, which leads to the required reactive zwitterionic species (**Figure 50i** and **ii**) or via an acid-base reaction, which results in

the formation of an ion pair [HCIE]$^+$[AA]$^-$ (**Figure 50iii**). The acid-base reaction depends on the acidity of AA (pK$_a$ = 4.26) and the basicity of the CIEs (MeOx: pK$_b$ = 5.77; EtOx: pK$_b$ = 5.65; EtOz: pK$_b$ = 6.49).[356] As a consequence, the protonation of the CIE is not preferred. However, as revealed by the MS analysis, the formation of an ion pair [HCIE]$^+$[AA]$^-$ seems to be crucial for the generation of the amide chain termini (**Figure 50vii**). Thus, the acid-base equilibrium is an important parameter to consider. As revealed by the end group determination and supported by the pK$_b$ value, EtOx forms the ion pairs most readily, represented as [HEtOx]$^+$[AA]$^-$ yielding ω-amide end groups (see termination discussion below). As noted above, CIEs and AA can undergo an Aza-Michael addition reaction (**Figure 50ii**) followed by an intramolecular proton transfer (**Figure 50i**). The presence of the zwitterion was proven experimentally.[357] Surprisingly, there is not much data available on the Aza-Michael addition kinetics with an acrylate. Reyniers and co-workers[358] have provided calculations that estimate equilibrium constants and kinetics of Aza-Michael additions. An important criterion for the generation of strongly alternating copolymers is the reaction rate of the Aza-Michael addition between a secondary amine and acryl derivative. Such reactions are fast (~10^{-3} L·mol^{-1}·s^{-1}), but thermodynamically not favored (K~10^{-3} L·mol^{-1}). The driving force for the formation of the dimer is the irreversible proton transfer (K~10^{17}).[358]

Three possible propagation reaction pathways are available after the (spontaneous) initiation under zwitterion ion pair formation: (A) dimer-dimer reaction generating ideally alternating copolymer structures; (B) homocoupling of unreacted CIE with the dimer/oligomer producing microstructurally defect alternating copolymers; and (C) initiation of homopolymerization by the ion pair to obtain poly(cyclic imino ether)s. Pathways (B) and (C) depend on the homocoupling kinetics, with MeOx polymerizing faster than EtOx.[359] Due to the six-membered ring of EtOz, the ring-opening reaction is approximately four times slower.[360]

Ultimately, three termination pathways have been revealed by the high resolution MS analysis. The majority of all zwitterionic species will be terminated by AA, which acts as nucleophile in the ring-opening reaction of the activated CIE and also protonates the ω-carboxylate end group (D). Thus, α-acrylic, ω-carboxylic copolymers are generated (**Figure 50vi**). As demonstrated by different feed ratios, the acid end group responds sensitively to any change in feed ratios. In contrast, the amide end group is only little influenced by changes in feed ratio rationalized by the fact that only activated cyclic iminium ethers (e.g. [HCIE]$^+$[AA]$^-$) will yield amide chain termini (**Figure 50vii**) (E). Thus, the formation of α-acrylic, ω-amide copolymers is observed.
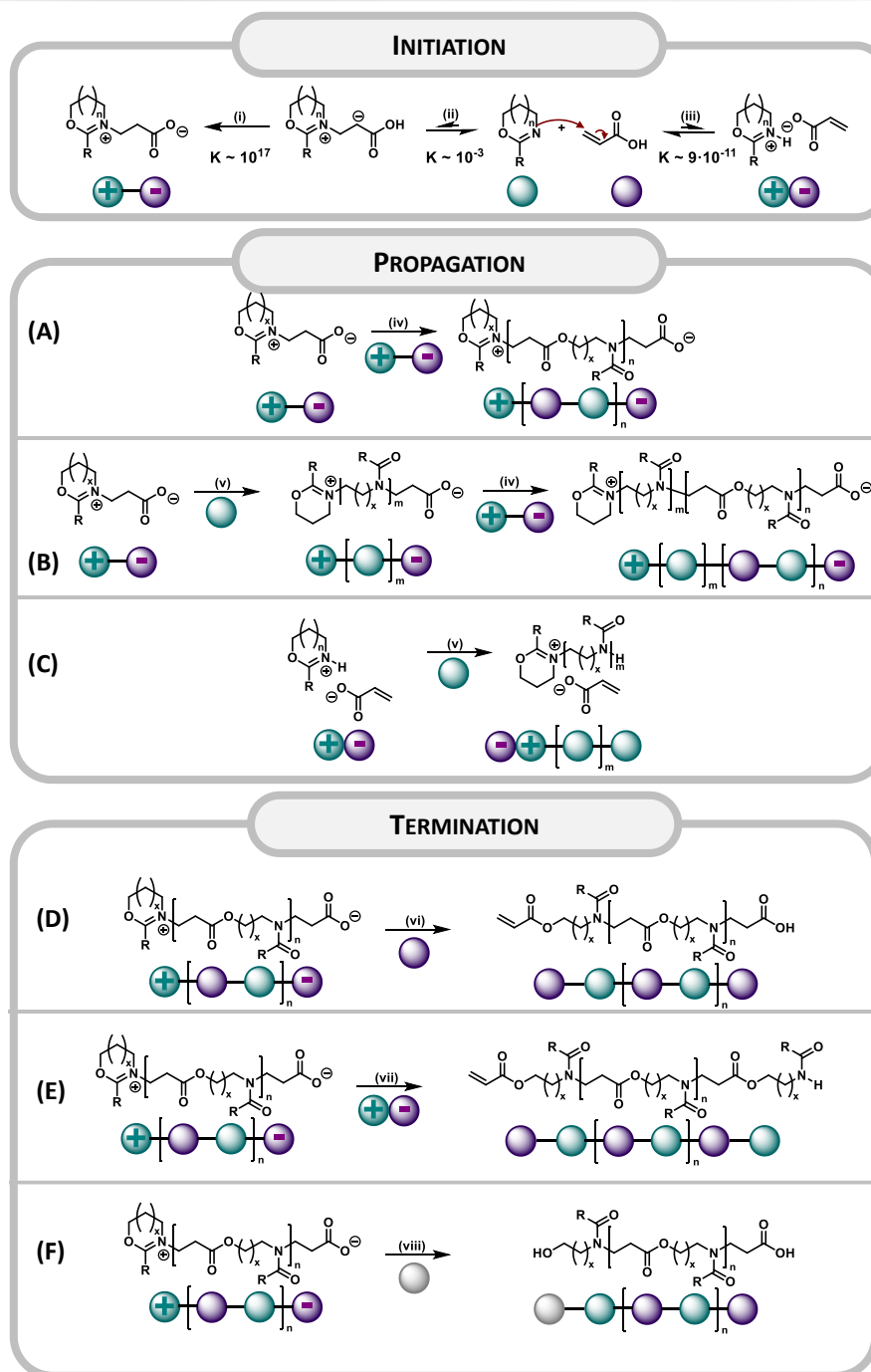
Figure 50 Proposed SZWIP mechanism based on post-mortem species identified during ESI MS and MS/MS experiments. Michael addition (MA) reaction (i, ii) to produce the zwitterionic dimer or acid/base reaction (iii) as competing reactions during initation. Alternating step-growth polymerization of MA dimers (iv), homocoupling to a MA dimer (v) or homopolymerization via consecutive homocouplings as competing reactions during propagation. Acid-induced ring opening reaction (vi) producing α-acrylic, ω-acid chain termini, two ring opening reactions (vii) forming α-acrylic, ω-amide chain termini, and water induced ring opening reaction (viii) as competing reactions during termination. Reprinted with permission from Ref. [352]. Copyright American Chemical Society (2018).

A third possible termination is the quenching of the active end groups by other ambient nucleophiles, such as water, which can ring-open the CIE (F).

5.3. CONCLUSIONS

The present section introduces an in-depth high resolution MS investigation of SZWIP-prepared oligomers of three structurally different CIEs and AA yielding oligo(MeOx-*alt*-AA)$_n$A, oligo(EtOx-*alt*-AA)$_n$A and oligo(EtOz-*alt*-AA)$_n$A. Mass spectra as well as MS/MS profiling of important species unambiguously identify their microstructure with particular focus on the alternating character and end groups of the oligomers. Key findings are: (*i*) An excess of AA influences the amount of ω-carboxylic acid end groups significantly (χ^{avg} = 0.27 (MeOx/AA = 1:1); χ^{avg} = 0.57 (MeOx/AA = 1:2); χ^{avg} = 0.16 (MeOx/AA = 2:1)) due to the fact that AA terminates the polymerization. (*ii*) An excess of CIE does not affect the amide chain terminus abundance similarly to acid excess (χ^{avg} = 0.36 (MeOx/AA = 1:1); χ^{avg} = 0.49 (MeOx/AA = 2:1); χ^{avg} = 0.20 (MeOx/AA = 1:2)) due to the fact that only activated CIEs will react producing ω-amide end groups. (*iii*) The reaction of CIEs and AA either leads to the formation of a zwitterion or an ion pair [HCIE]$^+$[AA]$^-$ containing an activated CIE, which strongly depends on the AA/CIE acid-base equilibrium an thus decreases from EtOx>MeOx>EtOz. Therefore, highest amide end group abundance is realized using EtOx (χ^{avg} = 0.50 (EtOx/AA); χ^{avg} = 0.28 (MeOx/AA); χ^{avg} = 0.22 (EtOz/AA)). (*iv*) Importantly, homocoupling of CIEs as side reaction to the zwitterionic dimer formation introduces defects to the ideal alternating structure. The homocoupling is fast for five-membered rings (MeOx>EtOx) and four times slower for six-membered rings (EtOz) (χ^{avg} = 0.70 (p(MeOx)); χ^{avg} = 0.27 (p(EtOx); χ^{avg} = 0.03 (p(EtOz)). Thus, oligo(EtOz-*alt*-AA)$_n$A is distinguished by only a marginal amount of microstructural defects. A detailed assessment of the polymerization mechanism allows for targeted materials design via end group modification of e.g. the acid functionality. A precise understanding of the SZWIP process helps in preparing ideal alternating copolymeric structures.

5.4. EXPERIMENTAL SECTION

5.4.1. Materials

Acrylic acid (AA, 99%, anhydrous, Sigma Aldrich), acetonitrile (MeCN, 99.8%, Sigma Aldrich), 4-methoxyphenol (MEHQ, 99%, Sigma Aldrich) and diethyl ether (Et$_2$O, >98%, Sigma Aldrich) were used as received. 2-Ethyl-2-oxazine (EtOz) was synthesized

as described elsewhere.[361] 2-Methyl-2-oxazoline (MeOx, 99%, Sigma Aldrich) and 2-ethyl-2-oxazoline (EtOx, >99%, Sigma Aldrich) and EtOz were distilled to dryness over barium oxide (BaO) and stored under nitrogen.

Ethanolamine, *tert*-butyl acrylate, acetyl anhydride, Al_2O_3, acryloyl chloride, trimethylamine, trifluoroacetic acid were purchased from Sigma Aldrich and used as received. *Tert*-butyl 3-((2-hydroxyethyl)amino)propanoate was synthesized according to a literature procedure.[362]

The ESI solvents were used without further purification: acetone (Sigma-Aldrich; HPLC grade), acetic acid (Scharlau, analytical grade), acetonitrile (Roth, LC-MS grade), dichloromethane (Roth, HPLC grade), methanol (Roth, HPLC grade), water (Milli-Q), tetrahydrofuran (Scharlau, HPLC grade).

5.4.2. Instrumentation

^{1}H NMR spectroscopy. ^{1}H NMR spectra were recorded on a Bruker DPX-400 spectrometer using deuterated chloroform ($CDCl_3$) obtained from Sigma Aldrich.

Size exclusion chromatography (SEC). SEC measurements were conducted using an Agilent 390-LC MDS fitted with differential refractive index (DRI), light scattering (LS) and viscometry (VS) detectors Fe7.5 mm) and autosampler. All samples were passed through 0.2 µm nylon filters before analysis. The mobile phase was DMF containing 5 mM NH_4BF_4 with a flow rate of 1 mL min^{-1} at 50 °C. SEC data was analyzed using Agilent Technologies SEC software. Calibration curves were produced using Agilent Easi-Vials linear poly(methyl methacrylate) standards (200 – 4.7 x 10^5 g mol^{-1}).

Electrospray ionization-Orbitrap mass spectrometry. Mass spectra were recorded on a Q Exactive Plus (BioPharma Option) (Orbitrap) mass spectrometer (Thermo Fisher Scientific, San Jose, CA, USA) equipped with a HESI II probe. The instrument was calibrated in the *m/z* range 600-6000 using ammonium hexafluorophosphate (Thermo Scientific). All spectra were recorded in the positive ion mode, water/acetonitrile/acetic acid (1:1:0.1 (*v/v*)). The FT resolution was set to 140000 employing 3 microscans during an acquisition time between 2 min measuring with a capillary temperature of 320 °C. The aux gas flow was (dimensionless) 0.00, the

sheath gas 5.00, and the spare gas 1.00. The flow rate was set to 5 µL· min^{-1}. The spray voltage was set to 3.5 kV and kept constant while performing the experiments.

5.4.3. Semi-Quantification

Calibration: MeOx/AA dimer (*m/z* 230.1019) was dissolved in acetonitrile:water:acetic acid (*v/v* 1:1:0.1) in a concentration of 0.75 mg·mL^{-1}. The stock solution was dilution to 0.5 mg·mL^{-1}, 0.25 mg·mL^{-1}, 0.1 mg·mL^{-1}, 0.05 mg·mL^{-1} and 0.01 mg·mL^{-1} and injected into the ESI system. The calibration was performed three times keeping the instrumental parameters and concentrations constant.

5.4.4. Synthesis

Tert-butyl 3-(*N*-(2-hydroxyethyl)acetamido)propanoate was synthesized based on a literature procedure.[363] Tert-butyl 3-((2-hydroxyethyl)amino)propanoate (1.00 g, 5.30 mmol) was transferred into a 20 mL vial filled with Al$_2$O$_3$ (0.81 g, 7.90 mmol). Acetic anhydride (Ac$_2$O, 0.60 g, 5.80 mmol) was added under ice-cooling without stirring. After 3 minutes the ice-cooling was removed and the reaction was allowed to continue for another 7 minutes. Subsequently, ethyl acetate (20 mL) was added and the mixture was filtered. The organic solvent and residual Ac$_2$O were removed under reduced pressure. Colum chromatography (SiO2, dichloromethane/methanol/hexane 8/1/1) yielded **2** as a colorless liquid (yield: 80%).

HR ESI-MS: *m/z*^{exp} 254.1358 (M+Na); *m/z*^{theo} 254.1363 (M+Na); *m/z*^{exp} 232.1540 (M+H); m/zt^{heo} 232.1543 (M+H).

2-(*N*-(3-(*tert*-butoxy)-3-oxopropyl)acetamido)ethyl acrylate. *Tert*-butyl 3-(N-(2-hydroxyethyl)acetamido)propanoate (500.0 mg, 2.20 mmol) was dissolved in dichloromethane (3 mL). Under ice cooling, triethylamine (0.260 g, 2.60 mmol) was added and the solution was stirred for 5 min before acryloyl chloride (0.240 g, 2.60 mmol) was added over 5 min. Stirring was continued for 18 h and the solution was allowed to come to room temperature. After filtration of the precipitate the solvent and excess reagents were removed under reduced pressure. The slightly yellowish crude 3 was used without further purification (yield: 60%).

3-(*N*-(2-(acryloyloxy)ethyl)acetamido)propanoic acid. 2-(N-(3-(tert-butoxy)-3-oxopropyl)acetamido)ethyl acrylate (0.33 g, 1.20 mmol) was dissolved in dichloromethane (2 mL). Under ice cooling trifluoroacetic acid (0.66 g, 5.80 mmol) in dichloro-

methane (2 mL) was added dropwise. The solution was allowed to come to room temperature and stirred for 18 h. Subsequently, solvent and excess trifluoroacetic acid were removed under reduced pressure. The crude was purified by column chromatography (SiO$_2$, hexane/acetone 1/1 to methanol) to yield **4** as a colorless liquid (yield: 56%). HR ESI MS: m/z^{exp} 230.1019; m/z^{theo} 230.1023.

Typical procedure for the synthesis of the macromonomers. In a dried Schlenk flask equipped with a magnetic stirrer bar, MEHQ (1 mg, 8.06 x 10^{-6} mol) was dissolved in MeCN. The CIE was subsequently added under nitrogen, followed by AA (see Table S1 for exact amounts per reaction). The mixture was placed in an oil bath (70 °C) for 24 h. Subsequently, the polymer solution was cooled down to room temperature, precipitated in Et$_2$O and isolated by centrifugation. The purification method was repeated two more times. To remove the Et$_2$O, the polymer was placed under vacuum to give the products as yellowish oils. The repeating units and molar masses of the oligomers were calculated by ^{1}H NMR, by comparing the ratio of the integrals of the vinyl end group and the ring-opened CIE and AA repeating unit signals. Summary of the characterization data is provided in **Table 6**.

Table 6 Details for the synthesis of the macromonomers.

CIE	CIE AA	[CIE] [mol L^{-1}]	[AA] [mol L^{-1}]
MeOx	1 : 1	9.92	9.92
	1 : 2	4.94	9.92
	2 : 1	6.32	3.16
EtOx	1 : 1	3.71	3.71
	1 : 2	2.17	4.34
EtOz	1 : 1	3.32	3.32
	1 : 2	2.21	4.42

6

IMAGING SINGLE-CHAIN FOLDING VIA HIGH-RESOLUTION MASS SPECTROMETRY[5]
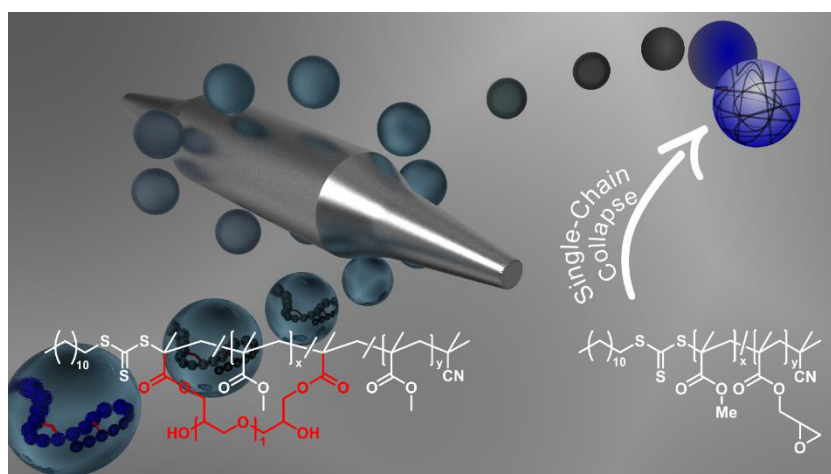
6.1. MOTIVATION

Precisely folded SCNPs have emerged as a major research area in the field of macromolecular architectures,[180-186] with key application as imaging agent, drug delivery vectors or as nano-container.[187,188] Section 2.4 provides a detailed picture of current SCNP research addressing their characterization via SEC, DOSY, DLS and other techniques able to assess hydrodynamic information and sizes. However, a short-coming of these methods lies in the fact that they are not capable of mapping single chains and the individual chemical transformations they undergo. Specifically, SEC, DOSY and DLS provide statistic information of the particle's hydrodynamic radius. As discussed in Section 2.4, one ensemble of SCNPs is constituted of an array of differently folded particles, with different loop sizes and different compaction. Thus, statistical characterization techniques cannot access the uniqueness of the chain structure, their folding motifs and the loop sizes.

The present section is strongly motivated by the overarching aim to develop a new characterization route to access direct information of the chain transformation during SCNP folding. Thus, in the following chapter the first ever approaches to map SCNP folding via HR SEC-ESI MS are introduced. The successful collapse of polymeric chains into SCNPs is imaged by characteristic mass changes, allowing to draw detailed mechanistic information regarding the folding mechanism (Section 6.2.3). The polymeric precursor is methyl methacrylate (MMA) statistically copolymerized with glycidyl methacrylate (GMA) resulting in p(MMA-*stat*-GMA), which is subsequently folded into an SCNP by using $B(C_6F_5)_3$ as ring-opening polymerization catalyst. Both the precursor polymer and the SCNPs can be well-ionized via ESI MS and the covalent crosslinks are stable during ionization. The MS approach can unambiguously differentiate between two mechanistic modes of chain collapse for every chain constituting the SCNP sample. The structural elucidation can be further underpinned by employing HCD as MS/MS technique.

6.2. RESULTS AND DISCUSSION
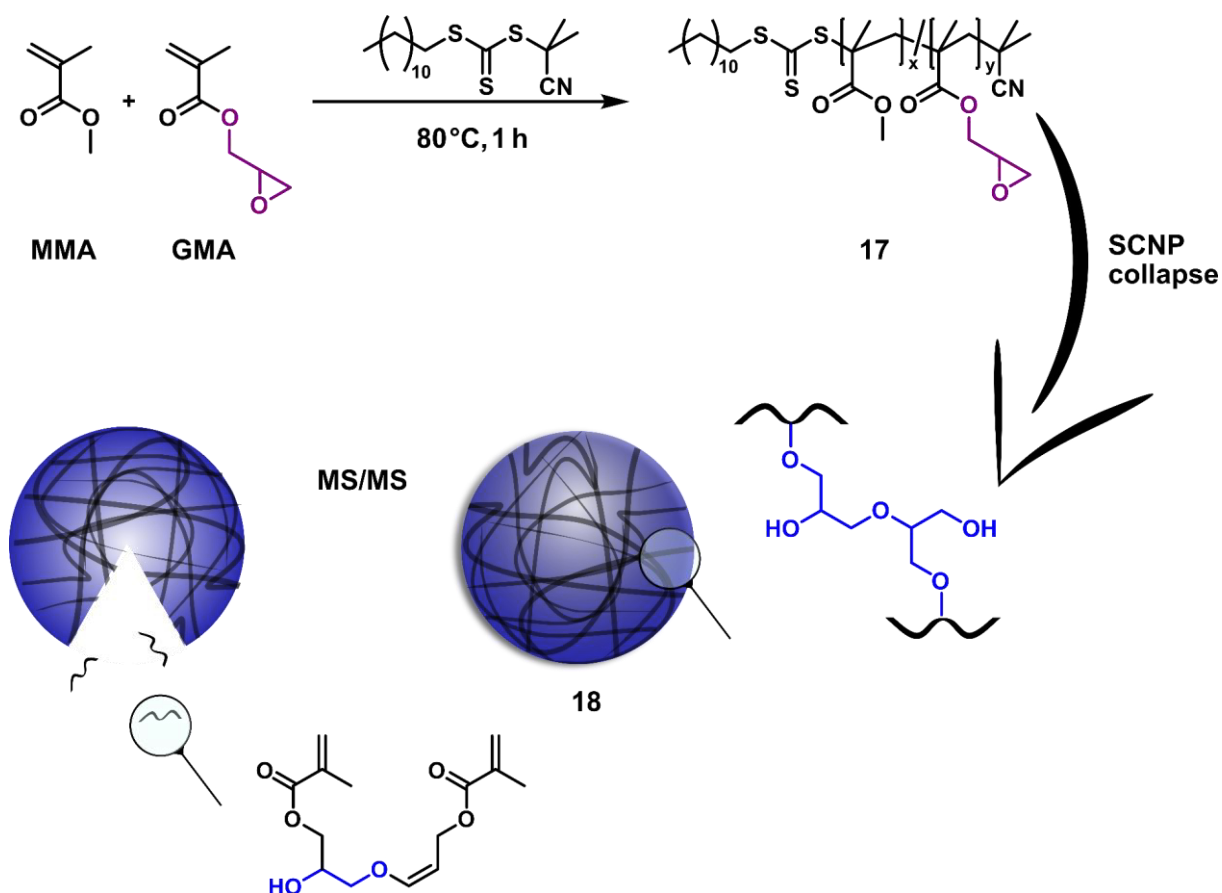
Figure 51 Preparation of p(MMA-*stat*-GMA) (**17**) (M_n = 13100 g·mol^{-1}, $Đ$ = 1.26) under RAFT conditions (bulk, 80 °C, 1 h) and the single-chain collapse using B(C$_6$F$_5$)$_3$ as catalyst for intra-chain ROP (a.t., 72 h). Reprinted with permission from Ref. [377]. Copyright American Chemical Society (2017).

The current section is divided into (*i*) preparation of the polymeric precursor and SCNP collapse, (*ii*) MS elucidation and (*iii*) deduction of a possible folding mechanism. The synthetic strategy is depicted in **Figure 51**.

6.2.1. Synthesis of polymeric precursor and SCNP

The synthetic approach was inspired by the work of Pomposo and co-workers.[201] In contrast to their statistical non-controlled free radical copolymerization of MMA and GMA as precursor polymer p(MMA-*stat*-GMA) (**17**), the current project is based on RAFT polymerization affording excellent end group fidelity. Subsequently, a Lewis acid catalyst B(C$_6$F$_5$)$_3$[364,365] initiates an intra-chain cationic ROP,[366,367] transforming the linear precursor (**17**) into a SCNP (**18**). The present section describes the following experiments: (*i*) direct addition of the catalyst B(C$_6$F$_5$)$_3$; (*ii*) slow addition of the catalyst with a syringe pump at a flow rate of 1 mL·h^{-1}; (*iii*) GMA feed ratios of 10% and

15% where the SCNPs were collapsed by direct addition of the catalyst; (*iv*) SEC-ESI MS/MS experiments to evidence the folding process; and (v) aqueous quenching of all GMA units for a study in negative ion mode.

The SCNP collapse was performed in highly diluted solution (0.2 mg·mL^{-1}) and evidenced by a characteristic SEC shift to higher retention volume (see **Figure 52A**). The resulting SCNP (**18**) features a decreased dispersity ($Đ = 1.19$) as reported for many SCNP systems.[215] The precursor (**17**) and the SCNP (**18**) were utilized for the subsequent MS characterization.

6.2.2. SEC-ESI MS Characterization of SCNPs
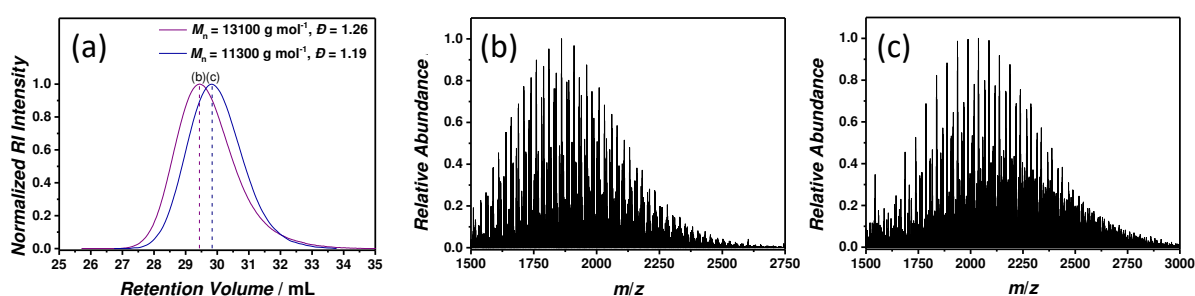
Figure 52 Preparation of p(MMA-*stat*-GMA) (**17**) ($M_n = 13100$ g·mol^{-1}, $Đ = 1.26$) under RAFT conditions (bulk, 80 °C, 1 h) and the single-chain collapse to (**18**) using B(C$_6$F$_5$)$_3$ as catalyst for intra-chain ROP (a.t., 72 h). Reprinted with permission from Ref. [377]. Copyright American Chemical Society (2017).

As noted in Section 6.2.1, a methacrylate-type system is used for imaging SCNPs via mass spectrometry. The decision to rely on Pomposo's[201] system is three-fold: (*i*) PMMA ionizes excellently in positive ion mode; (*ii*) the ethylene glycol motifs from the intra-chain crosslinking event do not negatively affect the ionization,[368] and (*iii*) the intra-chain ROP of glycidyl moieties allows for the elucidation of two possible collapse avenues: via a bimolecular coupling (i.e. a single glycidyl unit finds another glycidyl unit and reacts only once, terminating in a single ether bridge) or via propagation (i.e. one glycidyl unit ring-opens to find another glycidyl unit, which then ring-opens again to find another glycidyl unit, and so on). The excellent solubility of precursor (**17**) and SCNP (**18**) in THF allows for the characterization using SEC-ESI MS (refer to **Figure 52**). The results presented in the current section focus on the doubly charged oligomer profiles (see Section 2.1.6 for a detailed review of SEC-ESI MS) rather than the additionally observed singly, triply and quadrupoly charged oligomer profiles. Thus, the observed doubly charged oligomeric profile covers a broad mass range of p(MMA-*stat*-GMA) (**17**) and the SCNP (**18**). To date, the limitation of the method is dictated by the ionization ability of the polymers (e.g. polar macromolecules), the accessible mass range (e.g. for Orbitrap <6000 *m/z*), and good solubility in THF (for

SEC coupling). A detailed assessment of SEC-ESI MS' general limitations is provided in Section 6.4. The obtained mass spectra of the direct addition of catalyst $B(C_6F_5)_3$ (refer to **Figure 52B** and **C**) clearly illustrates that a chemical modification took place (see Appendix Fig. D 4) for the expanded spectra). Due to statistics of the crosslinking event, it was not expect that well baseline separated peaks were found in the spectrum as illustrated in **Figure 52C** (for the zoomed spectrum refer to Appendix Fig. D 4). Although the ion abundance decreased slightly, SCNP (**18**) ionized representatively and allowed the clear species assignment according to specific mechanisms (see Section 6.2.3). Without further experiments on various SCNP systems, it is unclear what causes a reduction of the ion abundance. An explanation for the SCNP (**18**) in the present section could entail: the strong Lewis acid catalyst $B(C_6F_5)$ forms stable complexes with oxygen,[201] and therefore the catalyst is coordinated to each initially ring-opened epoxide. A Lewis acid exchange with a proton takes place during the aqueous work-up. Hence, each epoxide, which was ring-opened by the catalyst, carries a proton instead of the catalyst and – as proposed – is positively charged before injection into the ESI source. As a consequence, SCNPs containing many crosslinks might become multiply charged (> 4) and cannot be analyzed sufficiently due to the unfavorable mass-to-charge ratio. Moreover, a (cross) ionization between Na^+ (stemming from an external source) and H^+ or entirely by H^+ is observed. To result in 100% sodiated SCNPs, Na^+ stemming from an external source would have to diffuse into the SCNP structure during the spray process and the following ionization mechanism,[26] thereby replacing the protons. It is assumed that this process did not occur as no species has been observed being ionized entirely by Na^+. A similar ionization phenomenon was observed during an additional SCNP MS characterization project, which will be discussed in Section 6.4.

To confirm the SCNP formation, the epoxides of p(MMA-*stat*-GMA) (**17**) were ring-opened with water. Subsequent SEC-ESI MS measurements (see Appendix Fig. D 5) performed in negative ion mode point to hypothetically positively charged SCNPs, since neither complexation to iodide nor by deprotonation events afforded negatively charged SCNPs. Thus, it is believed that the SCNPs form a specific geometry, which hinders external ionization agents (as Na^+ or iodide) to exchange already existing charges such as an H^+ stemming from the Lewis acid exchange). Therefore, direct addition of $B(C_6F_5)_3$ for SCNP collapse results in a mass spectrum (**Figure 53A**) where the species can be assigned to H^+ or H^+/Na^+ ionized structures (**Figure 53B**). Each single isotopic pattern contains up to four individual SCNP species. The presence of
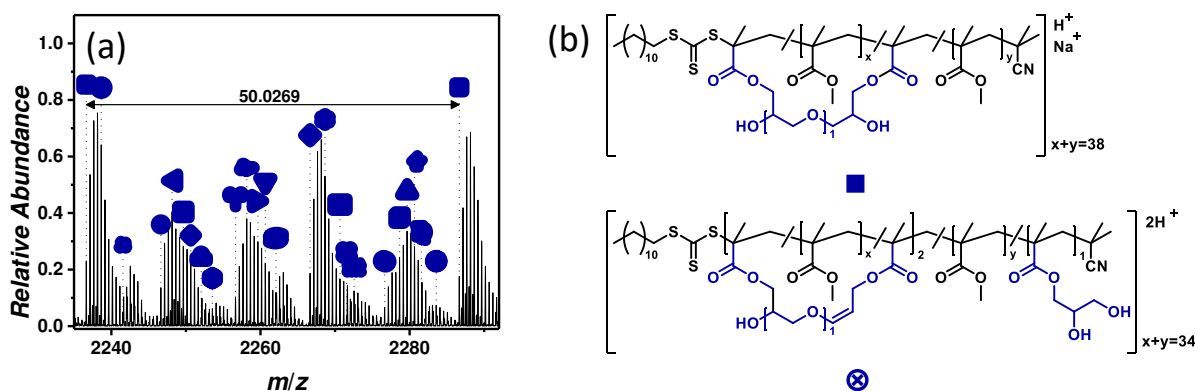
Figure 53 Direct addition of catalyst to produce SCNP (2): (a) zoomed SEC-ESI Orbitrap spectrum (positive mode) between 2235 m/z and 2292 m/z obtained by summing up all species between 14.42 mL and 15.92 mL retention volume. Labeled are the most abundant species and the repeat-ing unit of pMMA (m/z(exp) 50.0269; m/z(theo) 50.0257); (b) structural assignment of the peak at 2238 m/z (see Appendix Fig. D 9-13 for the isotopic simulation). The structures have an estimated ratio of ■:⊗ = 5:1. For all structures and the table of assignment refer to Appendix Tab. D 2. Reprinted with permission from Ref. [377]. Copyright American Chemical Society (2017).

different SCNP species within each peak pattern was evidenced by the fusion of the individual contributing simulated isotopic patterns of each SCNP folding product. The isotopic pattern have been carefully assessed, yet had to be placed in the Appendix D better readability. For instance, a species at 2236 m/z (labeled with ■) was assigned
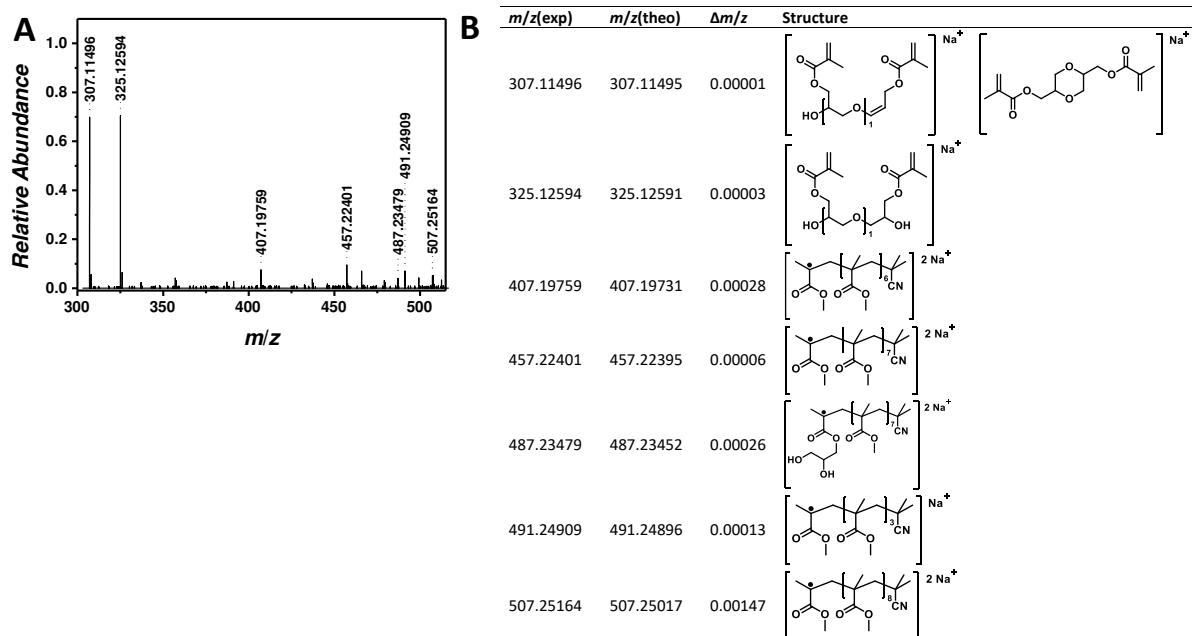
Figure 54 (A) SEC-ESI MS/MS (tandem MS in positive ion mode) of a doubly charged species at 2238 m/z with an HCD energy of 25 eV in the relevant range from 300 m/z and 515 m/z. **(B)** List of assignment for all MS/MS species. Reprinted with permission from Ref. [377]. Copyright American Chemical Society (2017).

to a SCNP where two glycidyl moieties reacted with each other (m/z(exp) 2236.6506; m/z(theo) 2236.6436).

The loop size is defined as numbers of non-crosslinking monomer between two crosslinking monomer and is in this specific system represented by x and y in **Figure 53B**. The question of how many MMA units separate the ethylene glycol bridge formed during the SCNP collapse is another aim of the project. Therefore, SEC-ESI MS/MS experiments on the peak at 2236 m/z has been performed collecting all fragments after the tandem experiment (see **Figure 54**) to find a species which would give the number of MMA units in one loop for determining the loop size. However, even the lowest employed HCD energy resulted in small molecule fragments. The presence of the proposed ethylene glycol moiety (refer to **Figure 54**) could be confirmed identifying characteristic species in the MS/MS spectrum. Although the loop size determination was not successful using tandem MS experiments, the folding mechanism was clearly identified and will be outlined in the subsequent section.

6.2.3. SCNP folding mechanism

Two overarching mechanistic scenarios under which the folding can proceed based on the data shown in **Figure 55** are discussed. The data presentation includes two experiments: first, the SCNPs resulting from direct catalyst addition are summarized and secondly, the SCNPs resulting from a folding experiment where the catalyst is infused via a syringe pump are considered and critically compared to the SCNPs
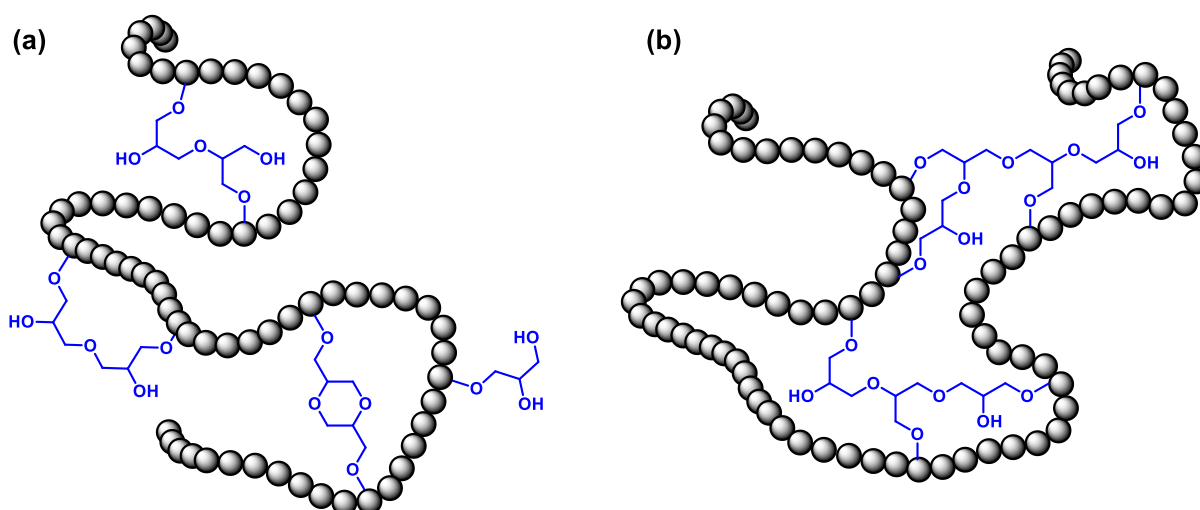
Figure 55 Schematic illustration of (a) bimolecular coupling of two glycidyl moieties in different possible motifs; (b) propagation during cationic ROP with three and four glycidyl units involved. Reprinted with permission from Ref. [377]. Copyright American Chemical Society (2017).

with direct catalyst addition. The mechanistic scenarios are (*i*) bimolecular coupling and (*ii*) propagation.

The bimolecular coupling reaction involves only two GMA units (**Figure 55A**). It is assumed that a bimolecular coupling is entropically favored.[369] In a scenario of a linear chain undergoing a folding process, the global chain flexibility is maximized resulting in maximized entropy. The sterically strained and inflexible loop being formed as a result of the bimolecular coupling reduces the maximized entropy. In a second bimolecular coupling event, the chain loses again an amount of entropy formed by the sterically strained loop at a different position of the chain. Therefore, a bimolecular coupling event always creates a SCNP with maximized entropy by means of the global chain flexibility. SEC-ESI MS experiments confirm higher ion abundance associated with bimolecular coupling species in comparison to the less abundant propagation species.

A propagation mechanism involves three or more GMA units analog to a mechanism described for ROP (see Section 2.2.2 and **Figure 55B**). As proposed, propagation forces the collapsing chain into a certain geometry, resulting from the demand of all epoxides to be in close proximity to each another. The activated epoxide propagates in a short amount of time, leading to a larger loss of entropy than in a bimolecular coupling event. In more detail, it is proposed that the SCNP species labeled with ◀ (*m/z*(exp) 2248.1500; *m/z*(theo) 2248.1492) (see Appendix Tab. D 2) for structure) was produced by first undergoing bimolecular coupling resulting in a collapse with a maximum amount of global chain flexibility. Subsequently, the residual glycidyl moieties intra-chain crosslink via propagation. The corresponding precursor p(MMA-*stat*-GMA) (**18**) with 34 repeat units of MMA and 5 repeat units of GMA was assigned as a peak at *m/z*(exp) 2251.6378 (*m/z*(theo) 2251.6189). Based on the knowledge of the present SEC-ESI MS study and considering the literature,[364–367] the following crosslinking mechanism is proposed taking p(MMA$_{34}$-*stat*-GMA$_5$) (**17**) as model precursor: the strong Lewis acid catalyst B(C$_6$F$_5$)$_3$ activates the epoxide. Due to the high dilution a further epoxide in close proximity ring-opens the activated one. If the highly reactive oxiranium species do not find a further reaction partner, residual water quenches the ROP in a termination event. The three remaining epoxides crosslink via propagation (forming species ◀), or via bimolecular coupling (forming species ♈ after the last epoxide reacts with water). Alternatively, the oxiranium ion can also react via an elimination reaction forming a double bond adjacent to the oxygen (form-

ing species ⊗). Furthermore, the propagating oxiranium can undergo a macrocyclization reaction as described by Barroso-Bujans and co-workers.[370] Elimination and cyclization as termination reactions result in completely isobaric structures.

To investigate if the mode of catalyst addition to the reaction mixture has any fundamental influence on the folding mechanism, an experiment adding $B(C_6F_5)_3$ over
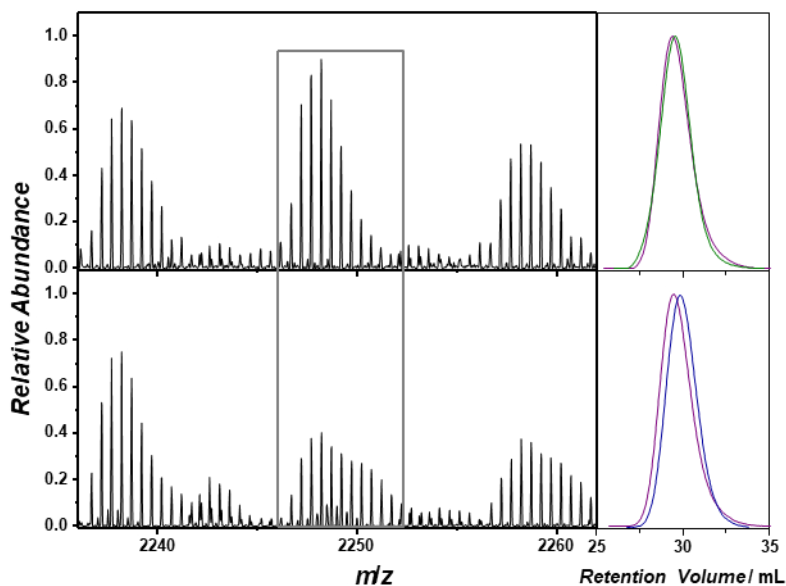
Figure 56 (Top) Syringe pump addition of catalyst: SEC-ESI Obitrap mass spectrum obtained of a SCNP (**18**, green line) sample evidenced by a slight shift in the SEC elugramm; (bottom) direct addition of catalyst: SEC-ESI Orbitrap mass spectrum with a strong shift in the SEC elugramm. The obtained ESI mass spectra are identical except of a broadening of the isotopic pattern in specific mass areas. Reprinted with permission from Ref. [377]. Copyright American Chemical Society (2017).

a period of several hours was performed. Thus, a syringe pump set to a flow rate of $1 \ mL \cdot h^{-1}$ was used. Surprisingly, the SEC trace of the prepared SCNP (**18**) (see **Figure 56**) only indicated a slight shift towards higher retention volume.

Comparing the mass spectrum obtained by direct addition (**Figure 52C**) with the spectrum obtained after adding the catalyst over a period of several hours (see **Figure 56**) gave similar mass signals. Thus, a SCNP collapse took place. However – as evidenced by the SEC trace –, to a lesser degree as observed by direct addition of the Lewis acid. A comparison of both doubly charged single oligomer profiles revealed significantly broadened isotopic pattern for some of the peaks in **Figure 53A** (refer to **Figure 56**). Adding the catalyst over a period of several hours seems to produce preferably SCNPs with bimolecular coupled crosslinks (labeled with ●). Utilizing the isotopic simulation as a sensor, a ratio of the species labeled with ●:◀:□:❖ = 10:3:4:3 was found in the case of direct addition of the catalyst. Using the syringe pump, the isotopic pattern suggests a ratio of ●:◀:□:❖ = 10:1:0:0 (see **Figure 56**). The ion

abundance of important propagating species (labeled with ◀ and ▣) is decreased significantly. Moreover, the species labeled with ❖ (m/z(exp) 2250.6579; m/z(theo) 2250.6423) as a product of three consecutive bimolecular coupling events is absent. Consequently, the slight shift to higher retention time might be explained by strong reduction of propagation and multiple bimolecular coupling events. Similar results were obtained from further experiments utilizing a step-growth Passerini polymer and a radical-induced intra-chain crosslinking that will be discussed in detail in the next section. As mechanistically suggested, propagation forces the collapsing chain into a certain geometry, which might be more compact and thus smaller in its hydrodynamic radius. In contrast, bimolecular coupling allows the chain to almost keep its initial conformation. As proposed, the forming loop results in only slight conformational changes and thus in a slight reduction of the hydrodynamic radius.

6.3. CONCLUSIONS

In summary, SEC-ESI MS as a technique to assess the folding of a collapsed linear polymer into a SCNP is introduced. P(MMA-*stat*-GMA) (**17**) and the resulting SCNPs (**18**) meet essential requirements for the successful ionization. Clearly, two distinct pathways of SCNP collapse have been identified by the high-resolution afforded by the Orbitrap ESI MS technique. Specifically, in addition to the bimolecular coupling as dominant, entropically favored crosslinking process, species arising from a propagation pathway have been assigned in the mass spectra. The work outlined in the current section constitutes a novel characterization platform for SCNPs that can be employed to all SCNP systems that ionize well and provide critical molecular information regarding the folding process.

6.4. RADICAL-INDUCED SINGLE-CHAIN FOLDING OF PASSERINI SEQUENCE-REGULATED POLYMERS VISUALIZED BY HIGH-RESOLUTION MASS SPECTROMETRY[6]

6.4.1. Motivation

As noted in Section 6.2, the loop size characterization poses a major challenge in the field of SCNP characterization. Yet, a reliable access tool to accurate loop sizes is a critical aspect for the perspective design of high-precision crosslinked SCNPs. As shown in Section 6.2, MS is a suitable platform for loop size determination. Yet, MS/MS relies significantly on suitable fragmentation mechanisms and advanced subsequent multidimensional tandem MS to elucidate intact loop structures. An alternative approach is the design of a degradable precursor polymer entailing motifs able to cleave the backbone adjacent to the crosslinking moieties (refer to Section 2.6). Li and co-workers introduced a facile synthesis of photo-cleavable polymers via sequence-regulated Passerini polymerization.[146] Here, the proposed mechanism always cleaves the ester bond between the light-adaptive monomer (introduced as aldehyde in the Passerini polymerization) and the diacid.

In the present section, the versatility of Orbitrap-based HR SEC-ESI was assessed by the – to date – most challenging SCNP system, both in terms of precursor complexity and folding mechanism. Here, sequence-regulated ter- and quaterpolymers prepared by the Passerini multicomponent step-growth polymerization serve as ideal complex precursor structures to identify critical parameters for successful MS mapping and thus understanding of the radical intra-chain compaction process. As Passerini monomers for the terpolymerization, 1,6-diisocyanohexane (1 eq.), HO_2C-PEG_{10-11}-CO_2H (1 eq.) and 4-formyl coumarin equipped with an acrylate (2 eq.) were utilized for subsequent radical-induced single-chain collapse. The characteristic mass species evidence the successful folding, confirming the folding mechanism via bimolecular coupling or propagation. A quaterpolymer containing 1,6-diisocyanohexane (1

eq.), HO$_2$C-PEG$_{10-11}$-CO$_2$H (1 eq.), benzaldehyde (1.7 eq.) and 4-formyl coumarin acrylate (0.3 eq.) is also collapsed, yet cannot be mapped via SEC-ESI MS, as the number of chains entailing a reactive unit is too small, while diffusion ordered NMR spectroscopy (DOSY) can readily witness the compaction. Based on these two precursor systems, criteria were identified that the precursors and the folded system have to fulfill for their successful SEC-ESI MS characterization. The folding mechanism can only be elucidated via mass analysis if (*i*) a minimum of four to five intra SCNP linkages are present, and, thus, (*ii*) the precursor formation needs to lead to a sufficient number of chains that feature reactive coumarin acrylate units. Finally, (*iii*), a chemically too diverse system such as the quarterpolymer leads to a high end group diversity after folding that challenges the MS analysis given the contemporary resolution limits.

6.4.2. Results and Discussion
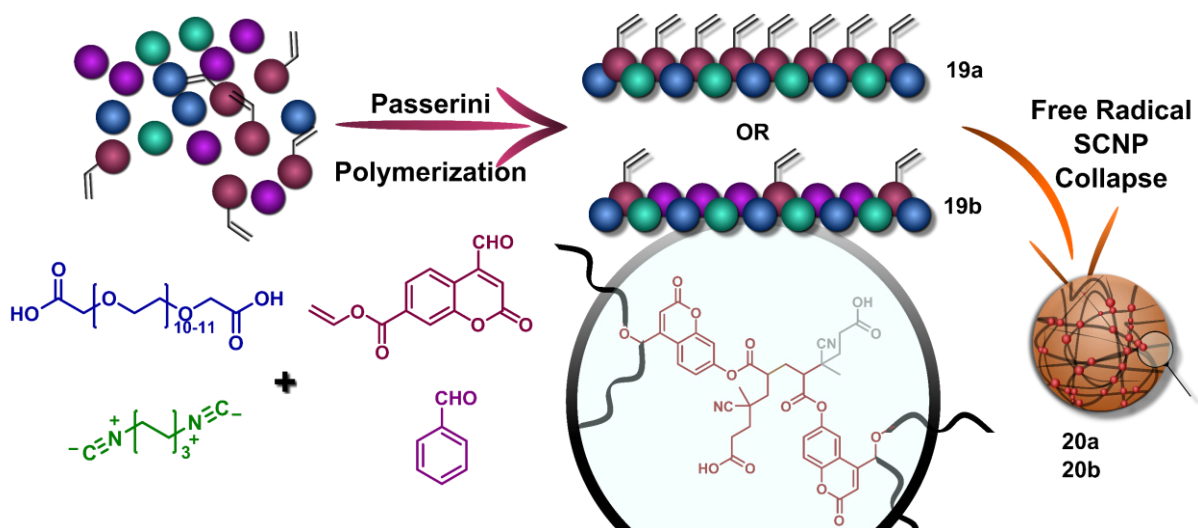
Figure 57 1,6-diisocyanohexane, HO$_2$C-PEG$_{10-11}$-CO$_2$H and 4-formyl coumarin are subjected to a Passerini copolymerization to produce **19a** as terpolymer and statistically with benzaldehyde to afford **19b** as quaterpolymer. The precursors are collapsed via a radical reaction (using 4,4'-azobis(4-cyanovaleric acid) (AVCA) as initiator) of the double bond attached to the coumarin.

As depicted in **Figure 57**, a step-growth polymer based on the sequence-regulated (i.e. precision monomer insertion) Passerini multicomponent polymerization was utilized.[144-146,371] Step-growth polymers are a challenging class of macromolecules for mass analysis – and thus well suited for the purposes of the current study – mainly due to the large repeat units, the resulting high dispersities (*Đ*~2.0) and the high number of disparate monomer units. The high dispersity might hamper high-quality MALDI,[372,373] where the best results are obtained with narrowly dispersed macromolecules. Theoretically, high dispersities cause no disadvantage during ESI-MS analysis. However, due to the high molecular weight of every repeat unit, a few monomer insertions can cover the entire mass range of the analyzer and a bias towards shorter

chains is visible in the resulting spectra.[374,375] Furthermore, conventional step-growth polymers have a low tendency to form stable complexes with Na^+ in positive ion mode.[374] Recently, Meier and co-workers were able to identify the repeat unit of a sequence-regulated Passerini polymer in SEC-ESI MS, which encouraged the current investigation into the Passerini product formation in more detail including end group determination.[145] More importantly, the α-acyloxy amide moiety adds a high degree of functionality to the material, challenging the ESI process even further. Since a plethora of aldehydes can be employed, coumarin as a functional monomer was introduced entailing a double bond for subsequent radical-induced single-chain collapse. Importantly, the Passerini system can be adjusted from 100 mol% of 4-formyl coumarin (affording the terpolymer) or less, replacing it with a non-vinyl moiety containing aldehyde (here benzaldehyde), giving access to a complex quarterpolymer precursor. As the crosslinks resemble a polyacrylate, negative influences on the ionization process after SCNP formation are not expected.[376] Consequently, the SCNP characterization was assessed via SEC-ESI MS considering the following aspects: The effect of the inherently broadly distributed Passerini precursors, a multi-component polymerization leading to end groups that have to date not been mass spectrometrically mapped and a complex composition matrix effected by (*i*) the ratio of 4-formyl coumarin to benzaldehyde (terpolymer vs quarterpolymer), (*ii*) the number of diacid (including variable ethylene glycol repeat units) and (*iii*) isocyanide units within the final chain structure. For each species in the mass spectra, these individual unit numbers have to be carefully varied during the mathematical analysis of the mass spectra, in order to identify the polymer structure.

A radically induced collapse[198,199] was selected, as it introduces even more parameters that have to be considered during the MS data evaluation: Every incorporated coumarin motif entails a double bond that can fold and subsequently terminate either via disproportionation or recombination. Disproportionation results in a vinyl function or a proton as chain terminus. Recombination, on the other hand, can occur with another formed radical or an initiator-derived radical. All possible end groups have to be considered and evaluated. Thus, given the complex nature of our precursor system – arguably the most complex folded SCNP system to date – the current study will demonstrate the power of the newly introduced high resolution mass spectrometric assessment of SCNP folding processes, allowing the identification of the folding mechanism. On this basis, it is ultimately concluded that high resolution ESI MS is essential

during – where possible – all SCNP characterization, as it opens a unique view into the hitherto hidden mechanistic aspects of their fascinating folding chemistry.

The versatile Passerini polymerization yielded **19a** as a terpolymer and **19b** as a quaterpolymer depending if either exclusively 4-formyl coumarin as aldehyde (**19a**, 2.0 eq 4-formyl coumarin) in the multicomponent reaction or additionally benzaldehyde (**19b**, 1.7 eq benzaldehyde and 0.3 eq 4-formyl coumarin) was incorporated. Although the molecular weight distribution of the linear precursors can be determined via SEC and the number-weighted average molecular weight is obtained relative to linear PS samples, substantial uncertainties associated with such measurements are expected. Due to the entirely different chain structure of calibration standard and the employed polymer (**19a**, **19b**), the obtained SEC data is inaccurate and the SEC error will further increase after SCNP collapse.[377-379] Thus, both the precursor's and the SCNP's average molecular weight numbers are not reported, yet for the SCNP assessment the more important characteristic, i.e. the SEC trace's shift to higher retention volume after compaction is employed.
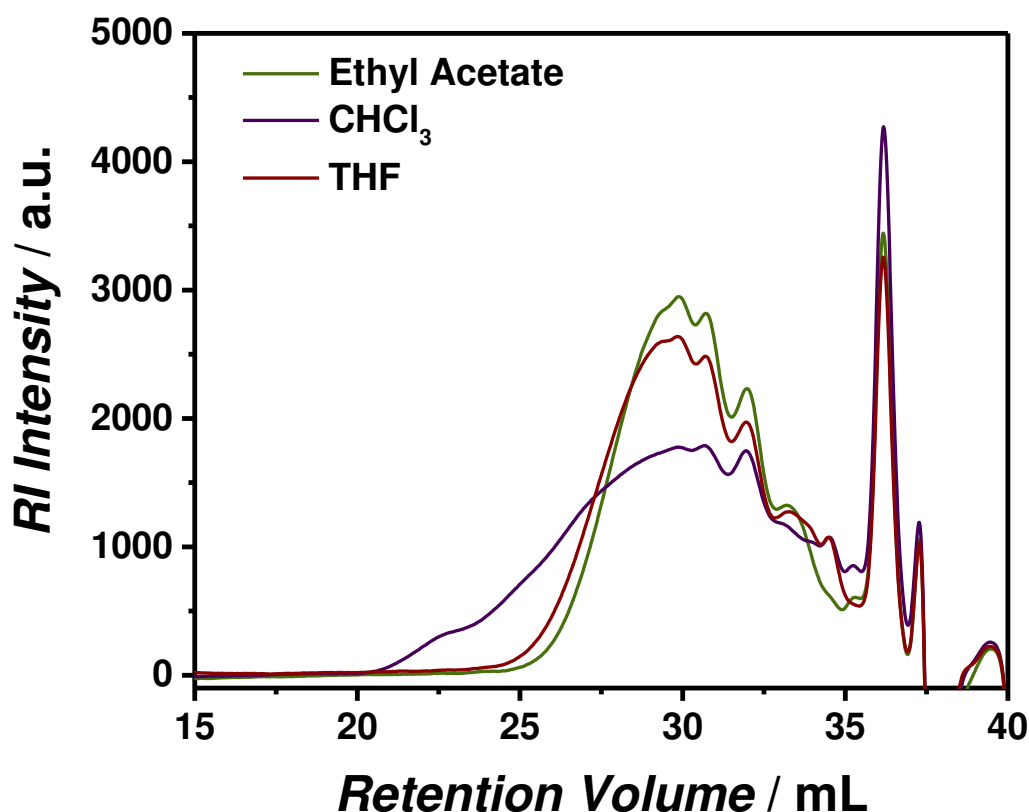
Figure 58 Solvent study of the quaterpolymer formation in ethyl acetate, chloroform and THF after 3 days.

The polymerization was screened carefully with various solvents and reaction times (refer to **Figure 58** for the solvent study). The starting materials were stirred in

1 M chloroform for five days at 45 °C to produce **19b**, whereas the polymerization was terminated after three days in the case of **19a**. Both precursor polymers (**19a** and **19b**) were characterized thoroughly by ^{1}H NMR (1D and 2D; refer to Appendix Fig. D 14-42) as well as SEC-ESI MS (Appendix Fig. D 43, 49). The single-chain collapse of **19a** and **19b** affording SCNP **20a** and SCNP **20b** was conducted under high dilution (0.3 mg·mL^{-1}) in THF using 4,4'-azobis(4-cyanovaleric acid) (AVCA) as initiator. Prior, the polymer and initiator were dissolved in THF for 1 h (at ambient temperature) and subsequently degassed for 45 min by purging with argon. To screen the SCNP collapse, different equivalents of AVCA relative to the amount of 4-formyl-coumarin-7-yl acrylate (0.5 eq, 0.25 eq and 0.1 eq) were employed. The intra-chain crosslinking proceeded for 24 h. SCNPs **20a** and **20b** were thoroughly analyzed by ^{1}H NMR (Appendix Fig. D 1-42) and SEC-ESI MS (Appendix Fig. D 48). All resonances in the NMR spectra were clearly assigned to the polymer protons, and furthermore, the 30 mol% incorporation of 4-formyl coumarin into **19b** was confirmed (refer to Appendix Fig. D 38).

Due to the complexity of the studied polymers (**19a** and **19b**) as well as their corresponding SCNPs (**20a** and **20b**), the below discussion is organized as follows: (*i*) Discussion of SEC-ESI MS results obtained by the terpolymer system (**19a** and **20a**). As three monomers were introduced, the resulting mass spectra can be interpreted as performed in Section 6.2,[376] i.e. the doubly as well as triply charged species (approx. 6 4-formyl-coumarin units available for SCNP formation) assessed. (*ii*) Subsequently,
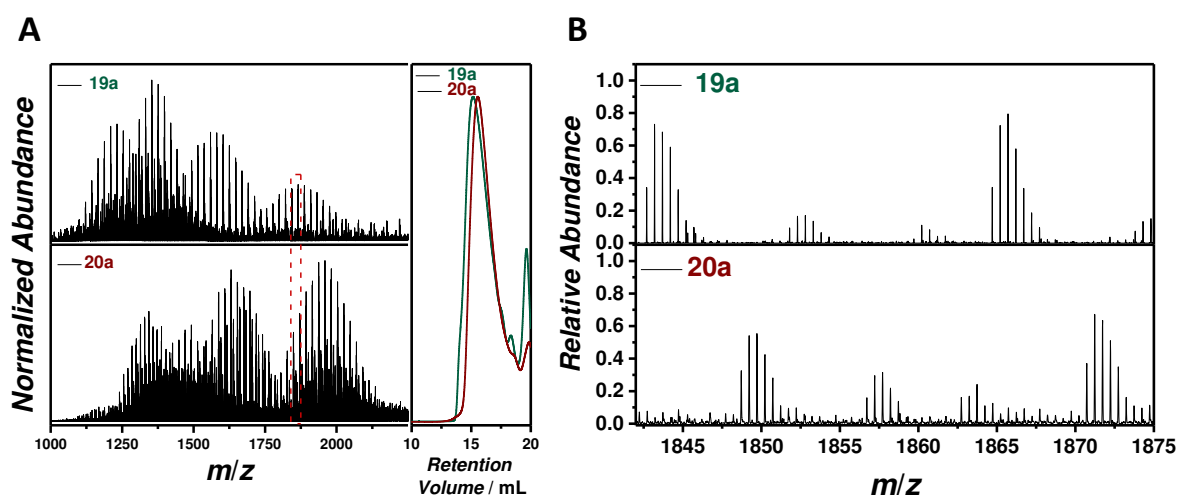
Figure 59 SEC-ESI mass spectra of **19a** (top, cyan) and **19b** (bottom, brown) of the full spectra ranging from 1000 *m/z* to 2250 *m/z* and the corresponding SEC RI traces simultaneously recorded with the ESI MS measurement (**A**). Expanded spectra of **19a** and **19b** ranging from 1842 *m/z* to 1875 *m/z* (**B**). For structural assignments see Appendix Tab. D 3-6.

it will be showcased how diluting can affect the SCNP collapse and therefore the corresponding SEC trace as well as the resulting mass spectra. (*iii*) The quaterpolymer system (**19b** and **20b**) is being discussed.
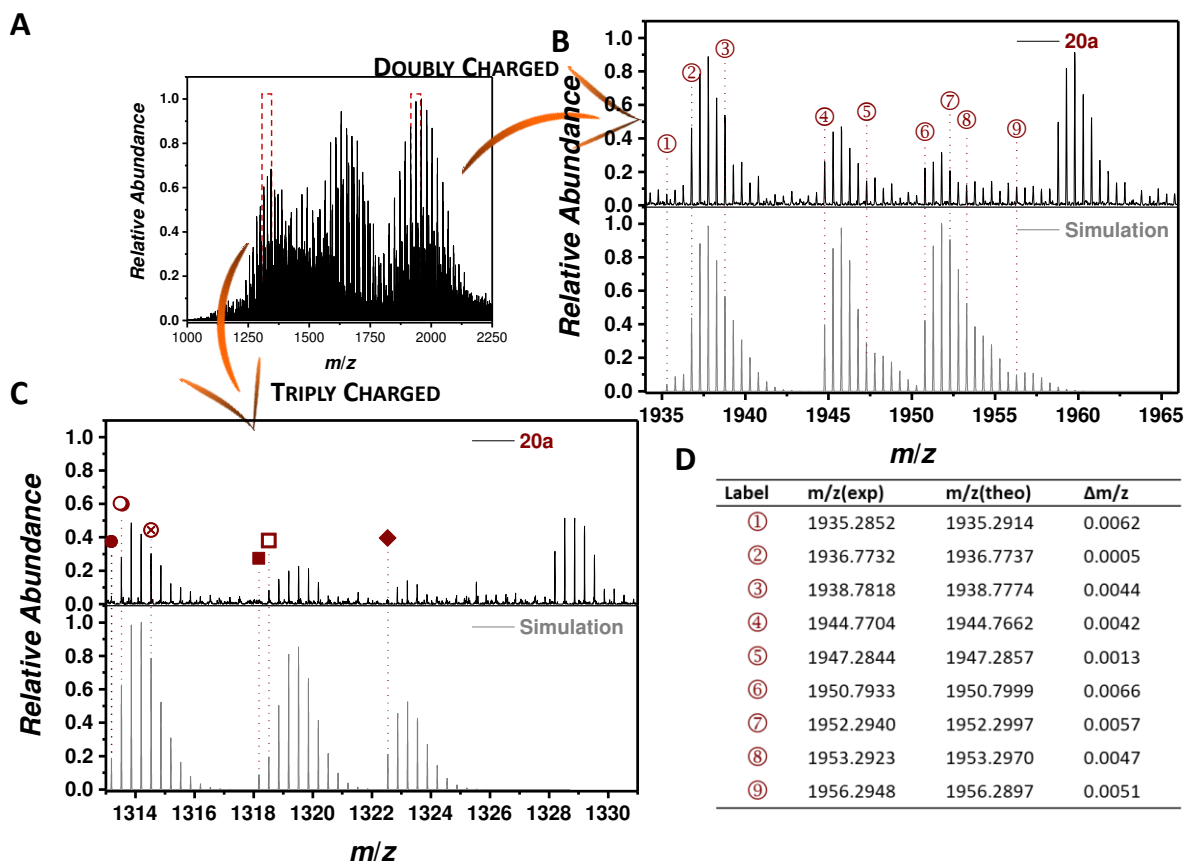
Figure 60 (A) Overview SEC-ESI mass spectrum of SCNP **20a** highlighting the expanded areas; (B) expanded mass spectrum of SCNP **20a** representing doubly charged species (top) and the isotopic pattern simulation (bottom); (C) expanded mass spectrum of SCNP **20a** representing triply charged species (top) and the isotopic pattern simulation (bottom) and (D) table of assignments for the doubly charged species. For full and detailed table of structural assignments see Appendix Tab. D 4,5.

Mass spectra of the terpolymer system (19a and 20a): Figure 59 displays the mass spectra of **19a** and **20a**. The characteristic SEC shift indicateed a successful SCNP collapse. Critically, after SCNP collapse the highest peak abundance of the doubly charged species at 1865 m/z shifted to 1959 m/z, whereas the maximum of the SEC trace shifted from 15.1 mL to 15.6 mL (refer to **Figure 59A**). The expanded mass spectra (refer to **Figure 59B**) demonstrate that each species of **19a** (for the exact assignment refer to Appendix Tab. D 3-6) has been transformed, thereby forming new species after SCNP collapse (**20a**). As the underlying intra-chain crosslinking reaction is a non-controlled free radical polymerization of the acrylate motifs attached to the coumarin, various end group combinations have to be taken into consideration, including recombination, disproportionation (generating an H and a double bond as chain terminus), and initiator-derived radical coupling. Importantly, one initiator fragment can react per one acrylate, generating an entire matrix of possible chain termini. Due to the resulting complexity from a characterization perspective, it is expected

that the employed SCNP system is ideally suited to test the limits of the herein introduced novel high resolution SEC-ESI MS SCNP characterization platform. After a thorough evaluation of the SCNP **20a** mass spectra, the following SCNPs as shown in **Figure 61** were identified (refer to Appendix Tab. D 3-6 for a list of assignments).

In the SEC ESI mas spectrum, an array of SCNP species can be assigned (refer to **Figure 60**), resulting in partly overlapping isotopic patterns. In-line with the evaluation performed in Section 6.2, SCNP species associated with the bimolecular coupling (labeled with □) and with the propagation (labeled with ○) were identified. Species □ (refer to Table S2) was assigned to a mass of 1318.8509 m/z (theo: 1318.8501 m/z), where six coumarin moieties have reacted with six AVCA initiator fragments. Importantly, four AVCA have reacted with a double bond, two of them found another double bond before terminating with another AVCA radical. The two remaining radicals formed by reaction with initiator derived radical fragments terminated in a disproportionation process (with any radical source) forming a double bond in both cases. Species ○ (refer to **Figure 61**) was assigned to a mass of 1313.5250 m/z (theo: 1313.5198 m/z). Here, six coumarin moieties have reacted with only two AVCA radicals initiating two propagations (involving three double bonds) and a termination, generating proton chain termini. Due to the manifold end group combinations and the statistical non-controlled crosslinking process, many resulting SCNP species differ in 1 m/z leading to overlapping isotopic patterns. It is submitted that the intra-chain crosslinking mechanism is similar to a free non-controlled radical polymerization. As such reactions are well-studied, a detailed discussion is not reiterated here. The full and highly detailed lists of all assignments are given in Appendix Tab. D 3-6, evidencing that the approach can elucidate the folding mechanism. Instead, here, an interesting trend is discussed: The more diluted the system (from 0.3 mg·mL^{-1} to 0.2 mg·mL^{-1}), the larger is the SEC trace shift in retention time (15.1 mL to 16.1 mL) although some precursor species are still present (refer to **Figure 62**. At higher concentrations (0.3 mg·mL^{-1}) a smaller SEC trace shift is identified, yet feature quantitative crosslink conversions (i.e. no double bond motif left; refer to **Figure 60**).
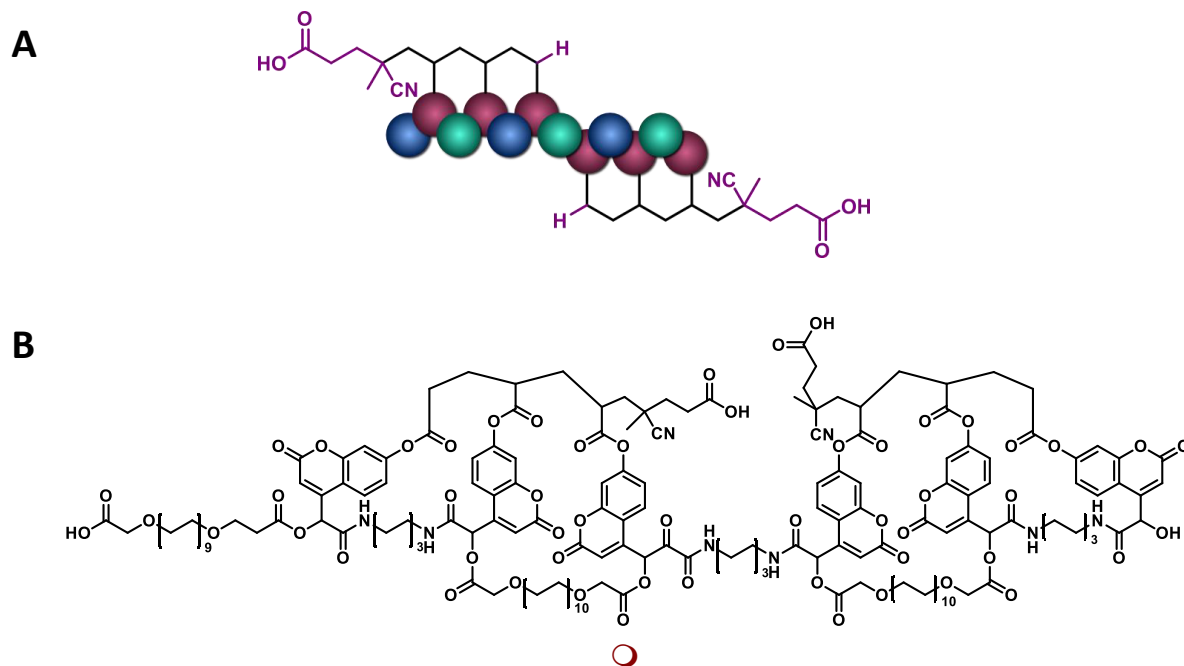
Figure 61 Schematic representation (A) and chemical structure (B) of a SCNP labeled with ◯. Two initiator fragments have initiated and propagated two consecutive double bonds before they have been terminated by disproportionation, forming the –H chain terminus.

Dilution effects on the terpolymer system (20a'): To understand why the more diluted system shows a larger shift towards high retention volumes, close inspection of the isotopic pattern is required (**Figure 63**). As discussed in Section 6.2 the SCNP folding is a dual-gated mechanism,[376] and thus now, (*i*), it is expected that bimolecular coupling reactions lead to loops in the polymer chain resembling a hair-
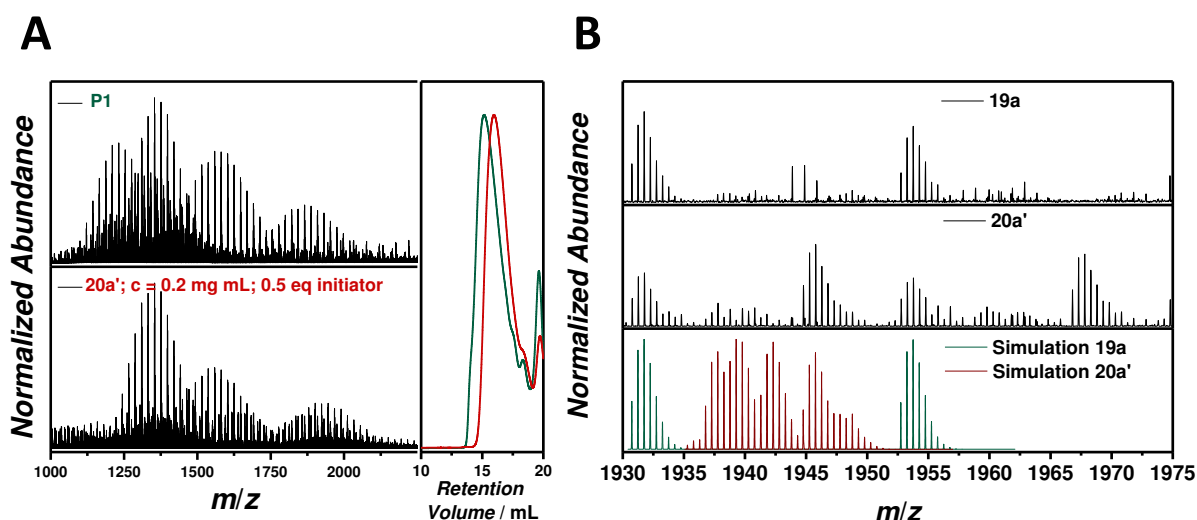
Figure 62 SEC-ESI mass spectra of **19a** (top) and SCNP **20a'** (bottom) (prepared at c = 0.2 mg·mL^{-1}; 0.5 eq initiator) and the simultaneously recorded RI SEC trace (A); expanded mass spectra of **19a** (top), SCNP **20a'** (middle) and simulation (bottom) (B).

pin structure.[377] Based on the hairpin structure, it is hypothesized that the overall size-reduction by the collapse is less significant than in the second scenario, (*ii*), i.e. the
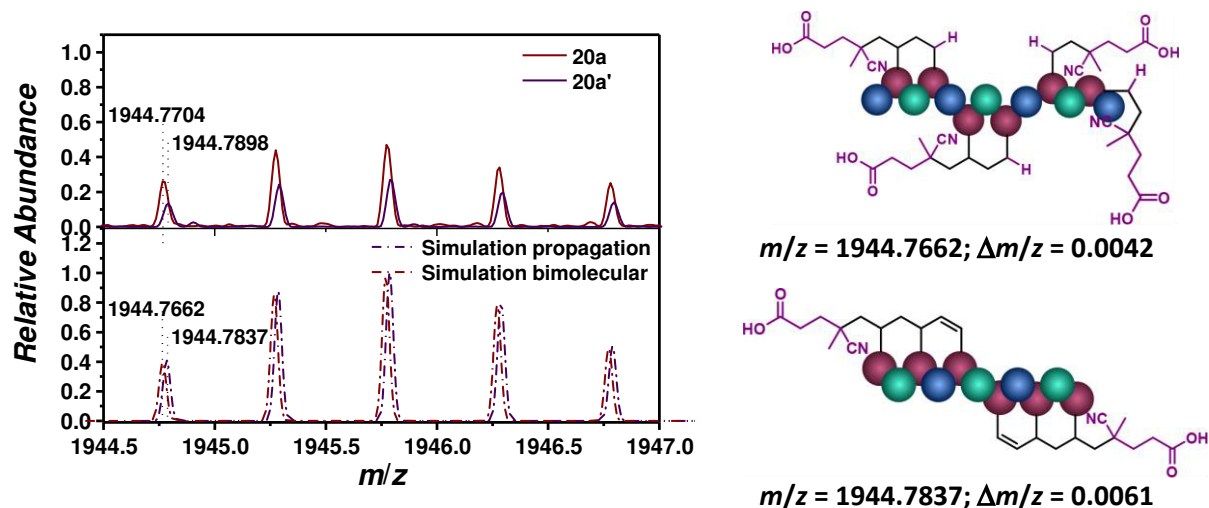
Figure 63 Isotopic comparison of a peak at 1944 m/z of SCNP **20a** and **20a'** (top) with the simulation (bottom) and their corresponding structural assignments.

propagation reaction. Thus, a collapse via propagation leads to a more compact SCNP structure and hence to larger SEC trace shifts in retention time.[376] **Figure 63** illustrates a similar scenario: SCNP **20a** is composed of structures formed by bimolecular reactions (m/z(exp) 1944.7704; m/z(theo) 1944.7662; $\Delta m/z$ 0.0042), whereas species of SCNP **20a'** (higher dilution) can be clearly assigned to propagation (m/z(exp) 1944.7898; m/z(theo) 1944.7837; $\Delta m/z$ 0.0061). However, it remains unresolved why the folding of **19a** does not result in quantitative conversion to SCNP **20a'**.

Finally, the quaterpolymer (**19b**) is subjected to identical conditions (c = 0.3 mg·mL⁻¹) for the SCNP folding and characterization. The SEC trace shifts from 13.7 mL to 14.9 mL (0.5 mol% initiator) indicating the successful SCNP formation (refer to **Figure 64A**). However, the individual chain transformations of SCNP **20b** cannot be visualized by ESI MS as above performed for SCNP **20a** (**Figure 64A** and **B**). Benzaldehyde was identified as the main factor impeding the successful identification of SCNP species. From a statistical perspective, the formation of a precursor polymer, where the chain structure entails only benzaldehyde and no reactive 4-formyl coumarin is likely and was indeed confirmed by the SEC-ESI MS measurement as the main distribution (refer to Appendix Tab. D 3-6 for structural assignment). Using a molar ratio of 1.7 (benzaldehyde) to 0.3 (coumarin), approx. 30 mol% 4-formyl coumarin was introduced into the polymer chain (as evidenced by NMR spectroscopy, refer to Appendix Fig. D 38). Thus, species with, for instance, one 4-formyl coumarin unit and five benzaldehyde units can be detected. However, its ion abundance is low.
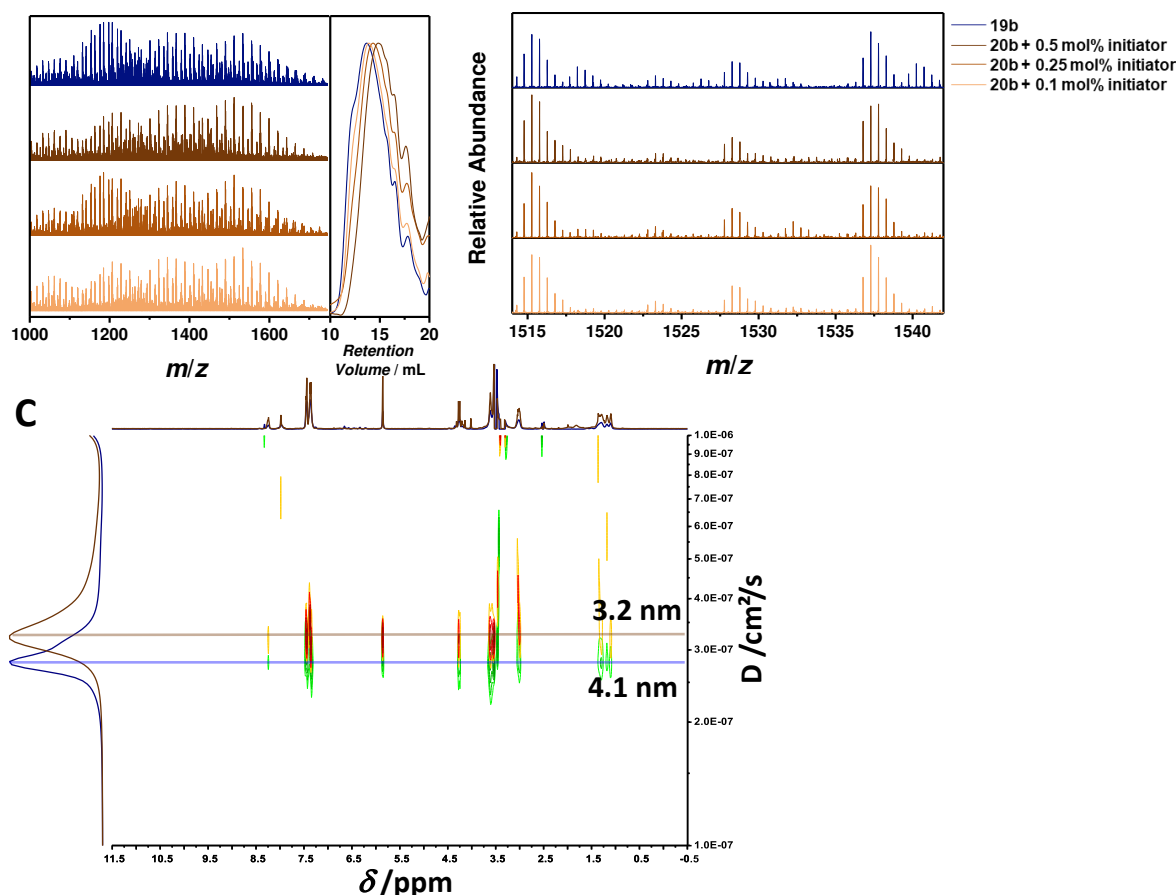
Figure 64 (**A**) SEC-ESI MS spectra of SCNP **20b** collapsed with 0.5 mol% (black-brown), 0.25 mol% (red-brown) and 0.1 mol% (ocher) in comparison to the precursor polymer **19b** (blue) and their corresponding online RI detected SEC traces. (**B**) expanded mass spectra in the mass range between 1512 *m/z* and 1545 *m/z*. (**C**) DOSY (400 MHz, 298 K, DMSO-d₆) spectra of **19b** (diffusion trace in blue) and SCNP **20b** (diffusion trace in brown).

It is expected that quaterpolymers prepared in a step-growth polymerization are unsuitable for our SEC-ESI MS investigation for the following reasons: (*i*) It is necessary to have at least four or five crosslinking motifs to effectively assess the SCNP folding based on the proposed mechanisms, and, (*ii*), the ion abundance of these motifs are reduced significantly in the quaterpolymer due to incorporation statistics. Thus, to prove the successful SCNP formation, the shift of the SEC trace to higher retention volume and changes in the DOSY spectra (refer **Figure 64C**) are provided, both indicating a reduction of the hydrodynamic radius. DLS measurements are not reported as the fluorescence of the polymers (**19a**, **19b**, **20a**, **20b**) may lead to misleading scattering information.[380,381] As indicated by the DOSY experiments, the radius decreases from 4.1 nm to 3.2 nm. A recently published article on SCNP characterization addresses the accuracy of the absolute hydrodynamic radii numbers.[379] Nevertheless, in comparison Zhao and co-workers[382] reported coumarin-based SCNPs and their hydrodynamic radii. Their precursor (5.4 nm; M_n = 13.2 kDa) and SCNP (3 nm) values are in good agreement with the numbers given in the present section.

6.4.3. Conclusions

In summary, the radical-induced single-chain folding of sequence-regulated Passerini step-growth ter- and quarterpolymer precursors is explored in-depth by utilizing a high-resolution SEC-ESI MS approach. The study is designed to assess the strength and limits of the herein introduced novel high resolution MS-based SCNP characterization platform guided by the following factors: (*i*) Step-growth polymers are a challenging class of macromolecules for mass analysis, mainly due to their large repeat units and the high dispersities ($Đ$~2.0), where a few monomer insertions can cover the entire mass range of the analyzer and a bias towards shorter chains may result in the spectra; (*ii*) a highly complex primary polymer structure with varying 4-formyl coumarin, diacid (including variable ethylene glycol repeat units) and diisocyanide contents has to be elucidated by adjusting the number of each unit in the mass spectra in order to identify the corresponding structure; (*iii*) the radical collapse introduces a multitude of reactions into the collapse system, i.e., every incorporated 4-formyl coumarin motif introduces a double bond that can fold and subsequently terminate either via disproportionation or recombination. Disproportionation results in a double bond or a proton as chain terminus. Recombination, on the other hand, can occur with another formed radical or an initiator-derived primary radical and all possible end groups have to be considered and evaluated.

The high resolution ESI MS approach is capable of resolving such a complex structural variety. It can be concluded that the chain transformation during SCNP folding of step-growth prepared precursors can be visualized by SEC-ESI MS, whereby the increased complexity of the quaterpolymer system makes the evaluation highly challenging due to the broad statistical variety within its structure, while the terpolymer SCNP system is fully assessable. Based on the high-resolution MS analysis, it is submitted that at least four to five crosslinking units must be present for deducing a folding mechanism and the precursor formation needs to lead to a sufficient number of chains that feature reactive coumarin acrylate units.

To nevertheless evidence successful quaterpolymer folding, the resulting SCNPs have been assessed by diffusion-ordered NMR spectroscopy (DOSY) and SEC rather than SEC-ESI MS. In summary, the present study has shown that high resolution SEC-ESI MS is indeed a suitable technique to elucidate single-chain folding even when radical processes and structurally highly diverse sequence-regulated precursor are involved. These findings strongly suggest that SEC-ESI MS should be carried out in the

context of SCNP analysis as a matter of course, as it is the only existing approach providing detailed chemical and mechanistic insides into the folding process.

6.5. Experimental Section

6.5.1. Materials

All solvents for synthesis were obtained from Sigma-Aldrich, Acros Organics, Merck or Fischer and used without further purification. Absolute solvents were purchased from Acros Organics and stored under nitrogen and over molecular sieves. 2,2′-Azobis(2-methylpropionitril) (AIBN) was purchased from Acros (98%) and recrystallized twice from methanol. Methyl methacrylate (MMA, Sigma-Aldrich, 99%) and glycidyl methacrylate (GMA, Alfa Aesar, 97%) were deinhibited by passing through a column of basic aluminium oxide. Manganese(IV) oxide, activated, tech., Mn 58% minimum (Alfa Aesar, 58% Mn, product number: 014340) was freshly activated as follows: MnO_2 (50 g) was placed on a large Büchner funnel and 10% nitric acid (80 mL) was added slowly. After the addition was completed, the MnO_2 cake was washed with a large amount of water (2-3 L) or until the filtrate was neutral. The MnO_2 was subsequently dried at 105 °C for two days and could then be stored under normal laboratory conditions for several weeks without loss of activity. Phosphorous(V)oxy chloride (Sigma Aldrich, 99%) was distilled twice at ambient pressure until a colorless liquid remained. Tris(pentafluorophenyl)borane ($B(C_6F_5)_3$) was purchased from TCI (97%) and stored in the glove box. THF (Scharlau, GPC grade) and MeOH (Roth, HPLC ultra gradient grade) for SEC-ESI MS analysis were used without further treatment. 2-cyano-2-propyl dodecyl trithiocarbonate (Sigma-Aldrich, 97%), NaI (Sigma-Aldrich, 99%), 4,4′-azobis(4-cyanovaleric acid) (AVCA) (Sigma-Aldrich, 98%), benzaldehyde (Alfa Aesar, >99%), poly(ethylene glycol) bis(carboxymethyl) ether (Sigma Aldrich, M_w = 600 Da), acryloyl chloride (Sigma Aldrich, 97%), resorcinol (Alfa Aesar, 99%), ethyl 4-chloroacetoacetate (Alfa Aesar, 99%), hexamethylenediamine (Sigma Aldrich, 98%), ethyl formate (>95%), diisopropylamine (Sigma Aldrich, 99%) were used as received.

6.5.2. Instrumentation

Size exclusion chromatography-electrospray ionization mass spectrometry (SEC-ESI MS). Spectra were recorded on a Q Exactive Plus (BioPharma Option) (Orbitrap) mass spectrometer (Thermo Fisher Scientific, San Jose, CA, USA) equipped with an HESI II probe. The instrument was calibrated in the *m/z* range 74-1822 using pre-

mixed calibration solutions and the *m/z* range 600-6000 using ammonium hexafluorophosphate (Thermo Scientific). A constant spray voltage of 4.6 kV, a dimensionless sheath gas of 8, and a dimensionless auxiliary gas flow rate of 2 were applied. The capillary temperature and the S-lens RF level were set to 320 ˚C and 62.0, respectively. The Q Exactive was coupled to an UltiMate 3000 UHPLC System (Dionex, Sunnyvale, CA, USA) consisting of a pump (LPG 3400SD), autosampler (WPS 3000TSL), and a thermostated column department (TCC 3000SD). Separation was performed on two mixed bed size exclusion chromatography columns (Polymer Laboratories, Mesopore 250 × 4.6 mm, particle diameter 3 μm) with precolumn (Mesopore 50 × 4.6 mm) operating at 30 ˚C. THF at a flow rate of 0.30 mL· min^{-1} was used as eluent. The mass spectrometer was coupled to the column in parallel to (an UV detector (VWD 3400 RS), and) a RI detector (RefractoMax520, ERC, Japan) in a setup described earlier.[383] 0.27 mL· min^{-1} of the eluent were directed through the RI-detector and 30 μL· min^{-1} infused into the electrospray source after postcolumn addition of a 50 μM solution of sodium iodide in methanol at 20 μL· min^{-1} by a micro-flow HPLC syringe pump (Teledyne ISCO, Model 100DM). A 100 μL aliquot of a polymer solution with a concentration of 2 mg· mL^{-1} was injected onto the HPLC system.

Nuclear magnetic resonance (NMR) spectroscopy. ^{1}H, ^{13}C as well as COSY and HSQC-spectra were recorded on a Bruker System 600 Ascend LH, equipped with an ONP-Probe (5 mm) with z-gradient (^{1}H: 600 MHz, ^{13}C 151 MHz). The δ-scale was normalized relative to the solvent signal of DMSO-d$_6$ for ^{1}H spectra and for ^{13}C spectra to DMSO-d$_6$.

6.5.3. Synthesis

Poly(methyl methacrylate-*stat*-glycidyl methacrylate) (17). 3.53 mL methyl methacrylate (3.32 g, 33.2 mmol, 233 eq), 500 μL glycidyl methacrylate (0.53 g, 3.70 mmol, 26.0 eq), 2.80 mg AIBN (0.017 mmol, 0.12 eq) and 49.2 mg 2-cyano-2-propyl dodecyl trithiocarbonate (0.142 mmol, 1.00 eq) were placed in a dry glass vial with a septum cap, degassed by purging nitrogen through the reaction mixture for 30 min and then placed in an oil bath thermostated at 80 ˚C. After 60 min, the resulting p(MMA-*stat*-GMA) was recovered by precipitation in MeOH and dried under vacuum at 55 ˚C. The MMA:GMA=7:1 ratio was determined by NMR spectroscopy.

Single-chain folding of poly(methyl methacrylate-*stat*-glycidyl methacrylate) (17) to SCNP (18). A flame-dried Schlenk flask was charged with 40.0 mg poly(methyl methacrylate-*stat*-glycidyl methacrylate) (**17**) (0.053 mmol GMA, 1.00 eq)

and dissolved in 200 mL dry dichloromethane. After 5 min of magnetic stirring, 13.3 mg $B(C_6F_5)_3$ (0.026 mmol, 0.49 eq) was added to the reaction mixture in one portion. The mixture was stirred for 72 h at ambient temperature. Subsequently, the mixture was washed with brine (50 mL), the phases were separated and concentrated under reduced pressure (avoiding evaporation to complete dryness). The polymer was recovered by precipitation in cold cyclohexane resulting in a white powder after filtration and drying under high vacuum.

1,6-Diisocyanohexane. The synthesis was adapted from the literature.[384]

4-(chloromethyl)-7-hydroxy-coumarin. 11.0 g resorcinol (99.9 mmol, 1.00 eq) was carefully dissolved in 90 mL H_2SO_4 (96%) at 0 °C, while stirring vigorously. 18.1 g ethyl 4-chloroacetoacetate (110 mmol, 1.10 eq) was slowly added to the solution and the reaction mixture was stirred at 0 °C to ambient temperature for 5 h. The solution was slowly poured into an ice/water mixture (700 mL) and a large amount of a white solid precipitated. The precipitate was filtered and washed with water several times. The precipitate was recrystallized from ethanol. 14.7 g (60%) of an off-white solid was obtained.

^{1}H NMR (400 MHz, DMSO-d_6) δ/ppm = 7.66 (d, ^3J = 8.8 Hz, 1H), 6.83 (dd, ^3J = 8.8, ^4J = 2.4 Hz, 1H), 6.75 (d, ^4J = 2.4 Hz, 1H), 6.40 (s, 1H), 4.94 (s, 2H).

^{13}C{^{1}H} NMR (101 MHz, DMSO-d_6) δ/ppm = 161.66, 160.50, 155.49, 151.21, 126.72, 113.37, 111.24, 109.57, 102.74, 41.56.

4-(hydroxymethyl)-7-hydroxy-coumarin. 600 mL water was added to 5.00 g 4-(chloromethyl)-7-hydroxy-coumarin (23.7 mmol). The dispersion was stirred vigorously and heated to 110 °C. After 2 days of stirring, the solid was completely dissolved forming a slightly yellow colored, yet clear aqueous solution. Stirring and heating was continued for 1 day. Subsequently, the mixture was hot filtered and cooled to ambient temperature. Further cooling in the fridge overnight yielded in off-white needles. The product was filtered dried under high vacuum at 55 °C (4.5 g, 99%).

^{1}H NMR (400 MHz, DMSO-d_6) δ/ppm = 10.50 (s, 1H), 7.52 (d, ^3J = 8.7 Hz, 1H), 6.77 (dd, ^3J = 8.7, ^4J = 2.4 Hz, 1H), 6.72 (d, ^4J = 2.4 Hz, 1H), 6.26 – 6.19 (m, 1H), 5.57 (t, ^3J = 5.6 Hz, 1H), 4.70 (dd, ^3J = 5.6, ^4J = 1.6 Hz, 2H).

^{13}C{^{1}H} NMR (101 MHz, DMSO-d_6) δ/ppm = 160.99, 160.63, 156.82, 154.86, 125.50, 112.83, 109.55, 106.53, 102.29, 59.07.

4-formyl-3-hydroxy coumarin. To a solution of 100 mg 4-(hydroxymethyl)-7-hydroxy-coumarin (0.520 mmol, 1.00 eq) in anhydrous THF (3 mL) under an Argon atmosphere was added 1.00 g freshly activated manganese oxide. After the suspension was stirred at 50 °C overnight, the black solid was removed by filtration (short silica gel column flushed with ethyl acetate:cyclohexane = 1:1). The yellow fraction was collected, and the solvent removed under reduced pressure. 80 mg yellow product (84%) was obtained.

^{1}H NMR (400 MHz, DMSO-d$_6$) δ /ppm = 10.72 (s, 1H), 10.08 (s, 1H), 8.30 (d, ^3J = 8.8 Hz, 1H), 6.89 (s, 1H), 6.85 (dd, ^3J = 8.8, ^4J = 2.1 Hz, 1H), 6.78 (d, ^4J = 2.1 Hz, 1H).

^{13}C NMR (101 MHz, DMSO-d$_6$) δ /ppm = 194.34, 162.02, 161.03, 156.47, 144.22, 127.66, 120.73, 114.13, 107.56, 103.10.

HR ESI MS m/z^{exp} 189.0185; m/z^{theo} 189.0193

4-formyl-coumarin-7-yl acrylate. A solution of 1.67 g 4-formyl-7-hydroxy coumarin (8.80 mmol, 1.00 eq) in 88 mL dichloromethane (0.1 M) was cooled to 0 °C. Subsequently, 1.65 mL DIPEA (1.25 g, 9.68 mmol, 1.10 eq) was added and stirred for 5 min. 1.07 mL acryloyl chloride (1.19 g, 13.1 mmol, 1.50 eq) as 0.1 M solution in anhydrous DCM (13 mL) was added carefully. The solution was stirred for 16 h. The mixture was diluted with 50 mL dichloromethane and washed with water (3×100 mL) and brine (1×100 mL). The organic layer was dried over sodium sulfate and the solvent was evaporated at reduced pressure (25 °C, ~500 mbar). The yellow solid was suspended in ethyl acetate (15 mL) and shortly heated to 55 °C in a water bath. The organic solvent adapted the yellow color, whereas the solids remained as an off-white powder. The suspension was left in the freezer overnight and 1.18 g of the product (4.84 mmol, 55%) was collected after filtration.

^{1}H NMR (600 MHz, DMSO-d$_6$) δ /ppm = 10.14 (s, 1H), 8.54 (d, ^3J = 8.8 Hz, 1H), 7.46 (d, ^4J = 2.3 Hz, 1H), 7.30 (dd, ^3J = 8.8, ^4J = 2.3 Hz, 1H), 7.20 (s, 1H), 6.59 (dd, ^2J = 17.3, ^3J = 1.1 Hz, 1H), 6.45 (dd, ^2J = 17.3, ^2J = 10.4 Hz, 1H), 6.22 (dd, ^2J = 10.4, ^3J = 1.1 Hz, 1H).

^{13}C NMR (151 MHz, DMSO-d$_6$) δ 193.86, 164.08, 160.38, 155.03, 153.29, 143.50, 134.95, 127.70, 127.46, 125.10, 119.41, 113.49, 111.04.

HR ESI MS m/z^{exp} 267.0265; m/z^{theo} 267.0264

Passerini terpolymer 19a. A mixture of 363.7 mg 4-formyl-coumarin-7-yl acrylate (1.49 mmol, 2.00 eq), 446.8 mg HO_2C-PEG-CO_2H (0.745 mmol, 1.00 eq) and 101.3 mg 1,6-diisocyanohexane (0.744 mmol, 1.00 eq) was dissolved in 730 µL $CHCl_3$ (1.0 M) and stirred at 45 °C for 3 days. The polymer was obtained by precipitation in cold diethyl ether. Diethyl ether was decanted, the yellow substance was washed twice with cold diethyl ether and the polymer was dried under high vacuum overnight.

Terpolymer SCNP collapse to 20a. 47.5 mg **19a** (38.8 µmol, 1.00 eq) and 5.4 mg 4,4'-azobis(4-cyanovaeleric acid) (19.4 µmol, 0.5 eq) were dissolved in 316 mL anhydrous THF (destabilized; $c = 0.3 \text{ mg} \cdot \text{mL}^{-1}$) and purged with Argon for 45 min while stirring. The mixture was heated from ambient temperature to 60 °C and stirred for 24 h at 60 °C. Subsequently, the solvent was removed under reduced pressure.

Passerini quaterpolymer 19b. A mixture of 308.3 mg 4-formyl-coumarin-7-yl acrylate (1.26 mmol, 0.3 eq), 759.2 mg benzaldehyde (7.15 mmol, 1.70 eq), 2.53 g HO_2C-PEG-CO_2H (4.21 mmol, 1.00 eq) and 573.2 mg 1,6-diisocyanohexane (4.21 mmol, 1.00 eq) was dissolved in 4.2 mL $CHCl_3$ (1.0 M) and stirred at 45 °C for 5 days. The polymer was obtained by precipitation in cold diethyl ether. Diethyl ether was decanted, the yellow substance was washed twice with cold diethyl ether and the polymer was dried under high vacuum overnight.

Quaterpolymer SCNP collapse to 20b. 47.5 mg **19b** (38.8 µmol, 1.00 eq) and 5.4 mg 4,4'-azobis(4-cyanovaeleric acid) (19.4 µmol, 0.5 eq) were dissolved in 316 mL anhydrous THF (destabilized; $c = 0.3 \text{ mg} \cdot \text{mL}^{-1}$) and purged with Argon for 45 min while stirring. The mixture was heated to 60 °C and stirred for 24 h. Subsequently, the solvent was removed under reduced pressure.

7

Dual-Gated Chain-Shattering Based on Light Responsive Benzophenones and Thermally Responsive Diels-Alder Linkages[7]
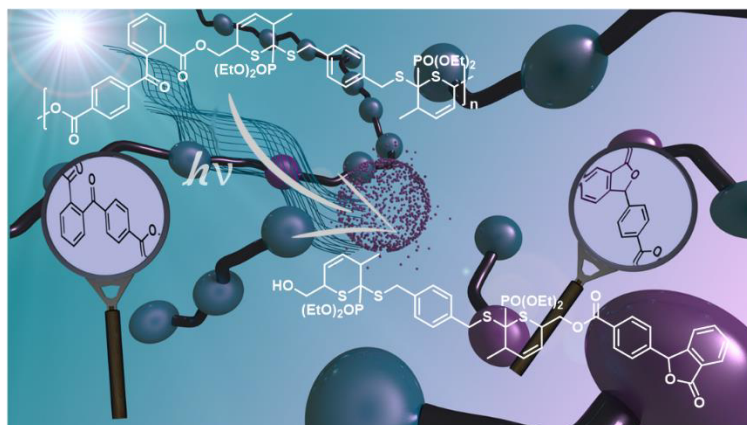
7.1. MOTIVATION

As discussed in Section 2.6, the highly defined degradation of functional polymer systems by applying a controlled and mild external trigger signal, leading to non-toxic, and environmentally compatible small molecules via a chain-shatter mechanism, is a critical prerequisite for specific biomedical applications. The photoreduction of BP, known for more than a half century, is an important example of a reaction featuring a very high quantum yield (Φ = 1.4±0.4).[385,386] Thus, BP has proven to be highly useful in a wide variety of key fundamental and practical applications, as it is chemically more robust than alternative molecules and stable to ambient illumination. However, it can be activated using light of a certain wavelengths, which do not damage the majority of biomolecules.[387,388] For instance, BP finds use as photoinitiator for polymerizations (type II initiators), in ink and coating applications and to protect personal care products from being damaged by UV light. [389-392] BP derivatives are chemically robust and are toxicologically benign. Thus, it comes as a surprise that BPs have not been exploited in degradable polymer systems.

The current section is strongly motivated by the light-adaptive characteristics of BP. BP is exploited to introduce a chain-shattering degradation mechanism triggered by light (λ_{max} = 365 nm, 36 W). Incorporated in every repeat unit via a step-growth polymerization of AA- and BB-type difunctional monomers, the BP functional group enables the disassembly of the on-demand degradable polymers within a few hours into small molecules. Specifically, the BP unit is photoactivated to reversibly generate a biradicaloid triplet state on each monomer moiety, in which the radicals can recombine in an inter-chain crosslinking reaction (Pinacol coupling) or undergo a reduction process, the latter one being key to the disassembly (refer to Section 2.6.1 for more details). The newly formed hydroxyl functionality in *ortho* position to the ester bond induces the chain-shattering process via an intramolecular lactonization reaction. The polymerization and the light-triggered degradation are assessed in detail by SEC, and – for the first time performed for chain-shattering polymer systems –

by HR ESI MS. The degradation mechanism can be unambiguously confirmed by characteristic transformations during the ring-closure reaction forming lactones as stable intermediates in the chain-shattering reaction. Finally, the present section showcases that the system can rapidly undergo gated and orthogonal thermally induced degradation, which can be useful for recycling applications of the polymer.

7.2. RESULTS AND DISCUSSION
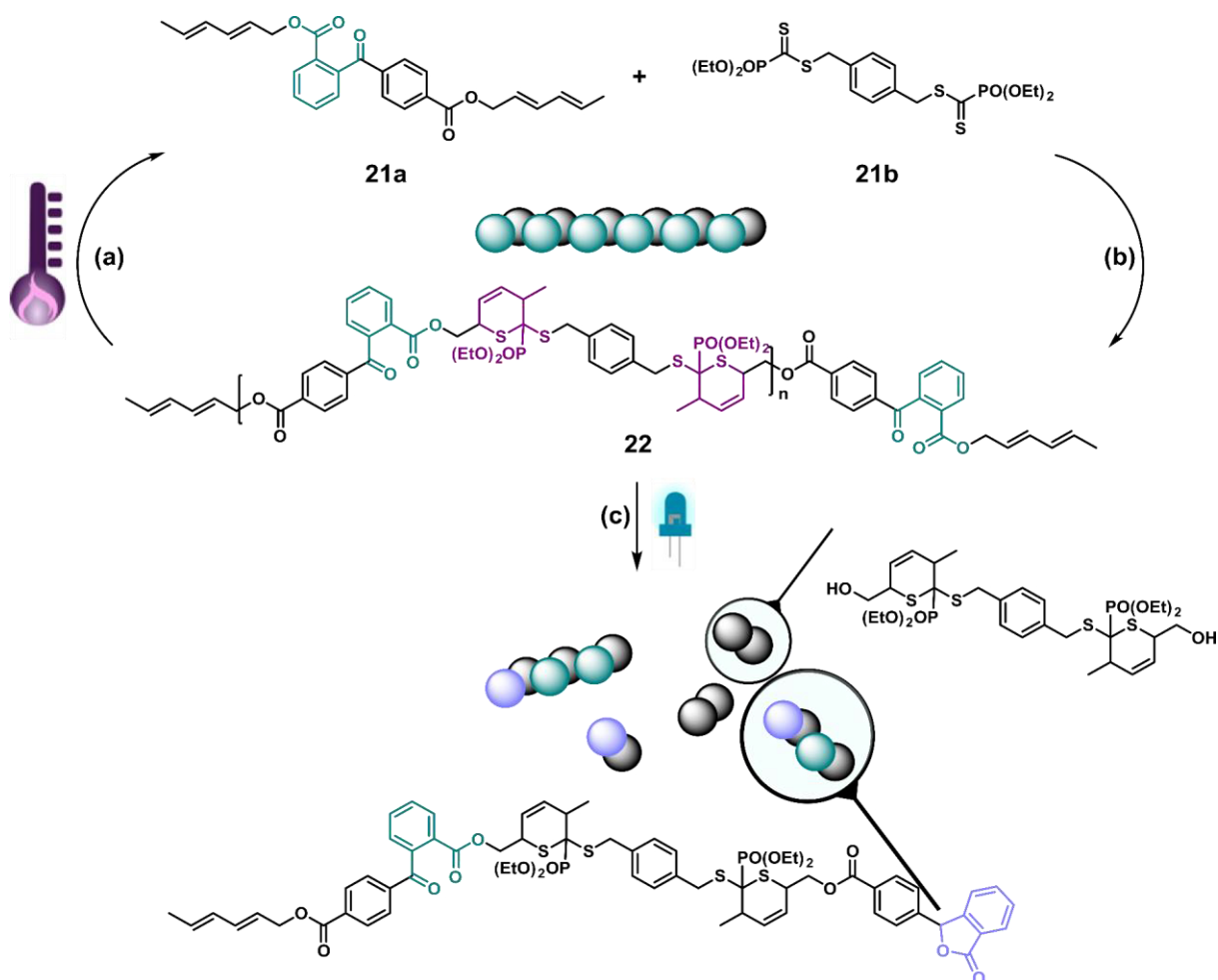
Figure 65 Synthesis and degradation of the dual responsive chain-shattering polymer (**22**): (a) thermally-triggered degradation via heating to 160 °C for 40 min; (b) hetero Diels-Alder step-growth polymerization of **21a** and **21b** under Lewis acidic conditions; (c) light-triggered disassembly under irradiation with λ_{max} = 365 nm using isopropyl alcohol as redox partner. As a simplification, only one selected isomer is depicted. Thermal responsive moieties are shown in purple, while photo-sensitive moieties are represented in cyan. Reprinted with permission from Ref. [375]. Copyright American Chemical Society (2017).

As depicted in **Figure 65**, an HDA polymerization was selected for the synthesis of the benzophenone-based polymers for the following reasons: (*i*) the mild Lewis acid (*i.e.* ZnCl$_2$) catalyzed conditions efficiently yield a sequence-regulated linear macromolecule;[393] (*ii*) the HDA polymerization has a high tolerance towards functional

groups – a broad variety of dienes and dienophiles can be potentially utilized, thus allowing the adjustment of the temperature range in which the bonding/debonding proceeds;[394,395] and (*iii*) the 3,6-dihydro-2*H*-thiopyran ring is chemically robust and tolerates irradiation in the ultraviolet/visible (UV/vis) light regime.[396]

7.2.1. Synthesis and Light-Triggered Degradation

A benzophenone-based light-responsive monomer (2*E*,4*E*)-hexa-2,4-dienyl 2-(4-((((2*E*,4*E*)-hexa-2,4-dienyl)-oxy)carbonyl)benzoyl)benzoate (**21a**) was designed, which was subsequently polymerized with 1,4-phenylenebis(methylene) bis((diethoxyphosphoryl)methanedithioformate) (**21b**) adapting a previously described procedure (**Figure 65**).[393] The reaction conditions were screened carefully by varying the solvent (i.e. acetone, dichloromethane, ethyl acetate and tetrahydrofuran) (refer to **Figure 66**). The highest molecular weight was realized in ethyl acetate, in which polymer **22** precipitates after a few hours of polymerization. More polar solvents (e.g. dichloromethane) disallowed the formation of the target macromolecule resulting in an oligomeric reaction mixture even after 24 h although all components were well dissolved (refer to **Figure 66**). Polymer **22** was characterized via ESI MS (refer to Appendix Fig. E 10), MS/MS (refer to **Figure 69B**), NMR (see Appendix Fig. E 1-5), SEC (**Figure 67A**) and UV-visible (UV-vis) spectroscopy (refer to **Figure 74C**). As discussed in Section 2.6.1, BP is photoreduced upon irradiation (λ_{max} = 365 nm, refer to Appendix Fig. E 18

A

B

Solvent	M_n / g·mol^{-1}	M_w / g·mol^{-1}	$Đ$
EtAc	2500	5600	2.19
THF	2200	4300	1.95
Acetone	2200	4600	2.09
DCM	1500	2800	1.82
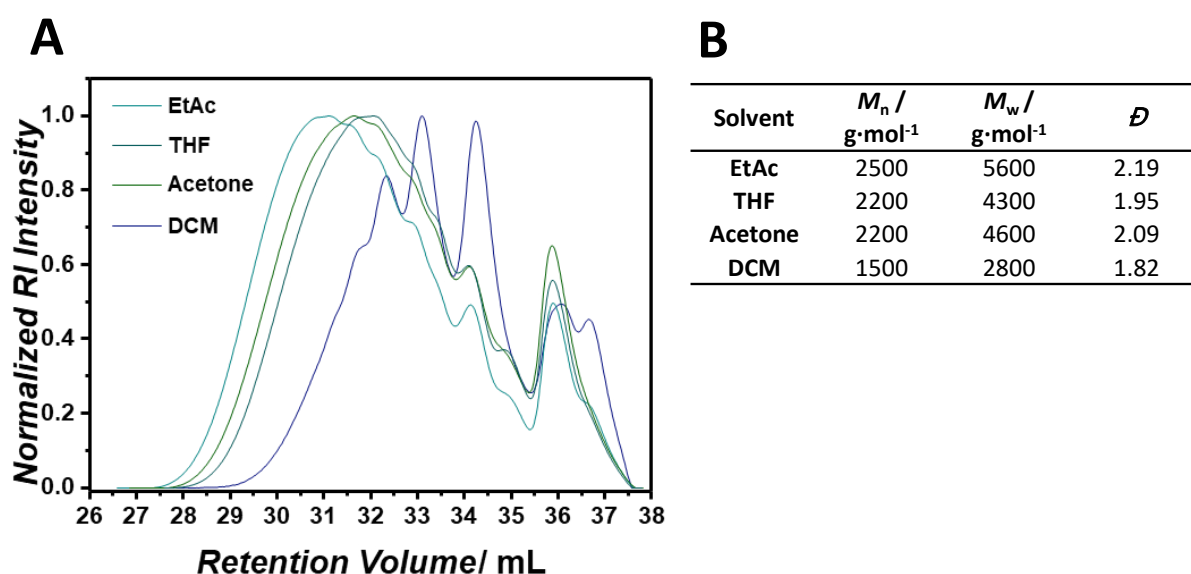
Figure 66 (**A**) SEC traces of polymer **22** after 8 h polymerization using ethyl acetate (EtAc) (bright cyan), THF (dark cyan), acetone (green) and dichloromethane (DCM) (blue) as polymerization solvent. Conditions: THF SEC performing at 30 °C and a flow rate of 1 mL·min^{-1}. (**B**) Polymer characterization (M_n, M_w and $Đ$) obtained from SEC measurements in different solvents. Calibration was relative to poly(styrene) standards. Reprinted with permission from Ref. [375]. Copyright American Chemical Society (2017).

for the light emission spectrum) in the presence of isopropyl alcohol as redox partner.
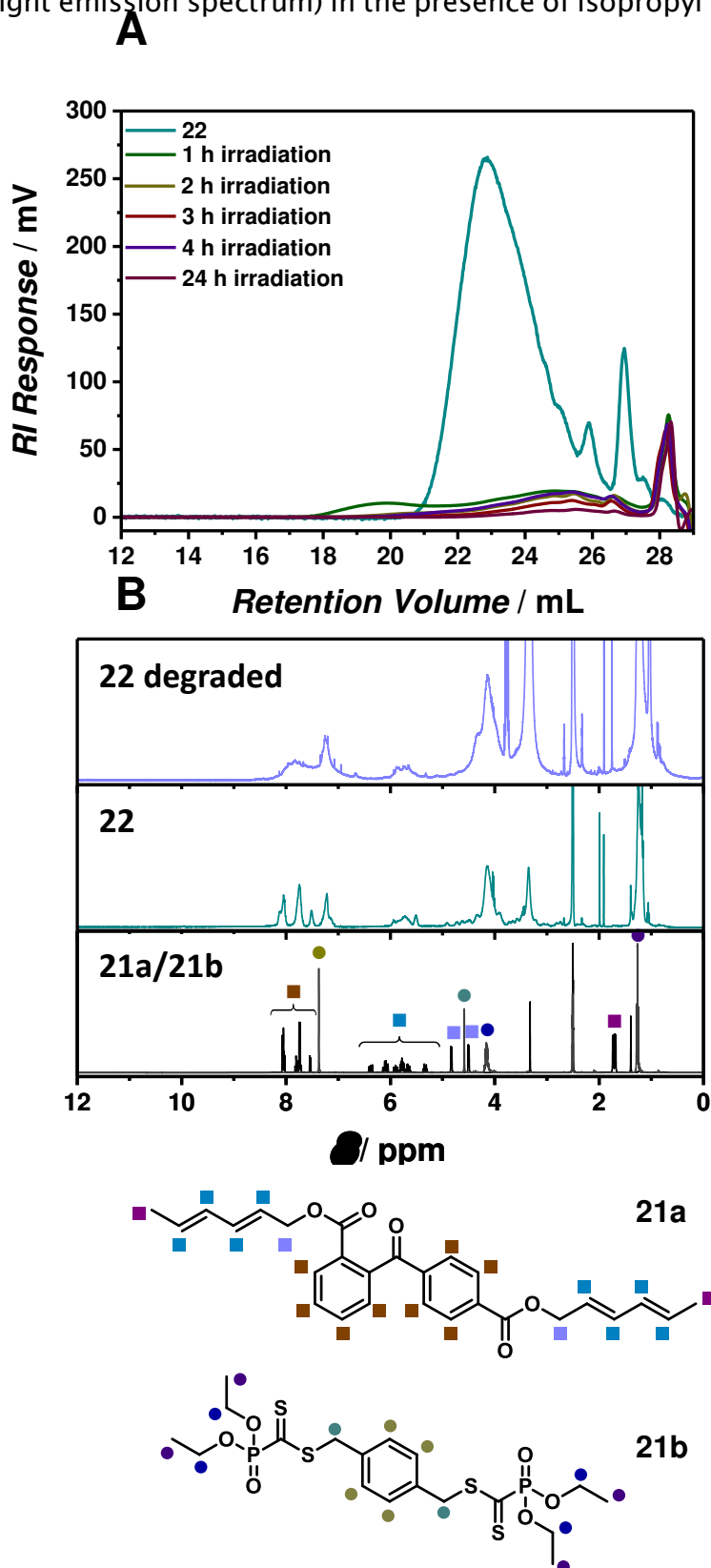
Figure 67 SEC traces of intact polymer (**22**) (M_w = 14 kDa; M_n = 7 kDa; Đ = 2.0), and after irradiation with light (λ_{max} = 365 nm) for 1 h, 2 h, 3 h, 4 h and 24 h leading to small components (M_w = 5.4 kDa; M_n = 3.3 kDa; Đ = 1.6) (A); NMR spectra (DMSO-d$_6$, 298 K, 400 MHz) of a 1:1 mixture of **21a**, **21b**, **22** as well as **22** before and after 2 h irradiation (B). For the proton resonance assignments of polymer **22** refer to Appendix Fig. E 3. Reprinted with permission from Ref. [375]. Copyright American Chemical Society (2017).

The degradation was monitored using NMR, SEC and HR ESI MS. The results will be discussed as follows: (*i*) assessment of the SEC traces; (*ii*) evaluation of the ESI MS data monitoring the light-triggered degradation and (*iii*) establishment of a detailed mechanism based on the ESI MS results. Finally, (*iv*), the thermal degradation is presented.

SEC is a powerful tool to assess the size distribution's retention time changes (correlating with changes in the molecular weight based on a certain calibration) during the chain-shattering of polymer **22**. To study the light-induced degradation, polymer **22** was dissolved in acetonitrile/isopropyl alcohol = 1:1 (*v/v*) at a concentration of 2 mg·mL^{-1}. Prior to irradiation with λ_{max} = 365 nm (36 W), the solution was degassed by purging with nitrogen for 15 min to avoid side reactions due to the biradical character of oxygen.[397] As collated in **Figure 67A**, polymer **22** (M_w = 14 kDa; M_n = 7 kDa; $Đ$ = 2.0) dissembles within 2 h into oligomers (M_w = 10 kDa; M_n = 4 kDa; $Đ$ = 2.6) and after 24 h into small molecules (M_w = 5.4 kDa; M_n = 3.3 kDa; $Đ$ = 1.6). As the molecular weight of a possible fragment after disassembly is 985 Da (refer to Appendix Fig. E 12), the chain shattering does not produce entirely small molecules. Interestingly, a short irradiation time of 1 h results in a clearly bimodal molecular weight distribution, displaying two peaks with one maximum at approx. 19 mL (M_w = 250 kDa; M_n = 170 kDa) and one maximum at approx. 25 mL (M_w = 6.8 kDa; M_n = 4.6 kDa). The formation of high-molecular components is due to the radical-based mechanism (refer to the detailed discussion below). While the changes in retention time evidences the size reduction of polymer **22** due to chain-shattering, molecular changes can only be revealed by 1D and 2D NMR as well as ESI MS. **Figure 67B** shows the NMR spectra of a 1:1 mixture of the monomers **21a** and **21b**, polymer **22** before and after 2 h degradation (for detailed 2D NMR spectra of **21a** and polymer **22** refer to Appendix Fig. E 4,5 and **Figure 68**, respectively). The most significant transformation indicated by ^{1}H NMR analysis is the disappearance of the resonances associated with the methyl groups of monomer **21a** (1.7 ppm), whereas the proton resonances of the 3,6-dihydro-2*H*-thiopyran ring appear at 4.1 and 5.5 ppm. However, many proton resonances of the polymer are isochronous with their resonance position appearing between 4.0 and 6.0 ppm (**Figure 68**). After irradiation with UV-vis light (λ_{max} = 365 nm, 36 W), the magnetic resonance within the aromatic range of the spectrum, i.e. between 7.0 and 8.0 ppm, undergoes the most apparent transformation: Prior to inducing the degradation by the photoredox reaction between BP and isopropyl alcohol, the aromatic range exhibits four broad resonances representing the BP core of monomer **21a** and
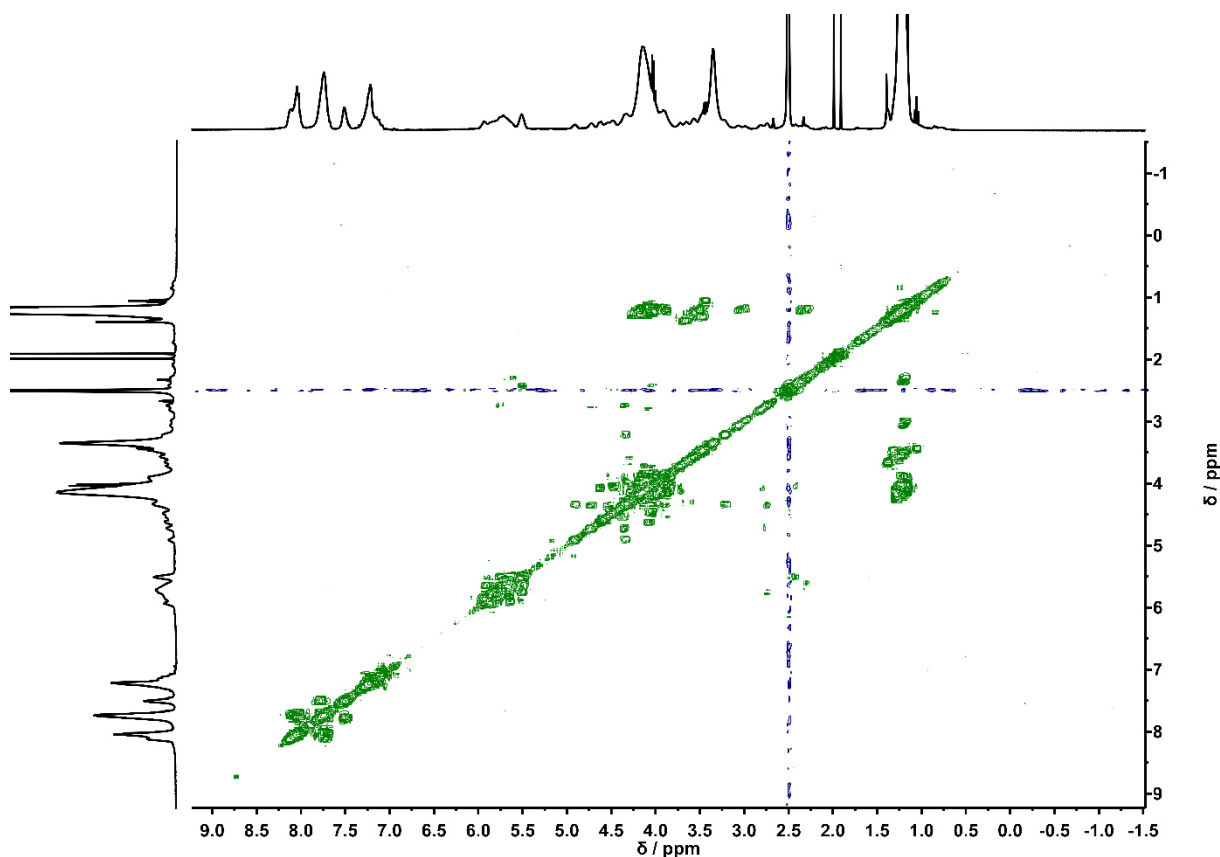
Figure 68 ^{1}H-^{1}H COSY (298 K) spectrum of polymer **22** in DMSO-d$_6$. Reprinted with permission from Ref. [375]. Copyright American Chemical Society (2017).

the phenyl core of **21b** (as shown in **Figure 67B**). After 2 h irradiation, the three resonances associated with the BP core were merged to one very broad resonance representing a plethora of degradation products, associated with all isomers produced by the HDA chemistry. Consequently, although NMR is a compelling and selective characterization technique, it is of limited use for the determination of the specific degradation products in the current system. Thus, the attention turned to HR Orbitrap ESI MS for a detailed molecular analysis.

An ESI MS kinetic monitoring study of the photocleavage of the BP-based polymers (**22**) was performed under highly diluted conditions (0.5 mg·mL^{-1} in isopropyl alcohol/acetonitrile = 1:1 (*v/v*)) after purging the solution with nitrogen for 15 min. The spectra were recorded in negative ion mode taking advantage of the strong chloride attachment ionization as reported in Chapter 3. In addition, SEC-ESI MS as hyphenated technique (refer to Section 2.1.6) was carried out, identifying the small molecule components formed during degradation. The small molecules ionize sufficiently in positive ion mode (refer to Appendix Fig. E 11-17 for the isotopic simulations of the degraded species). As evident from **Figure 70A/C**, ESI MS is indeed the method
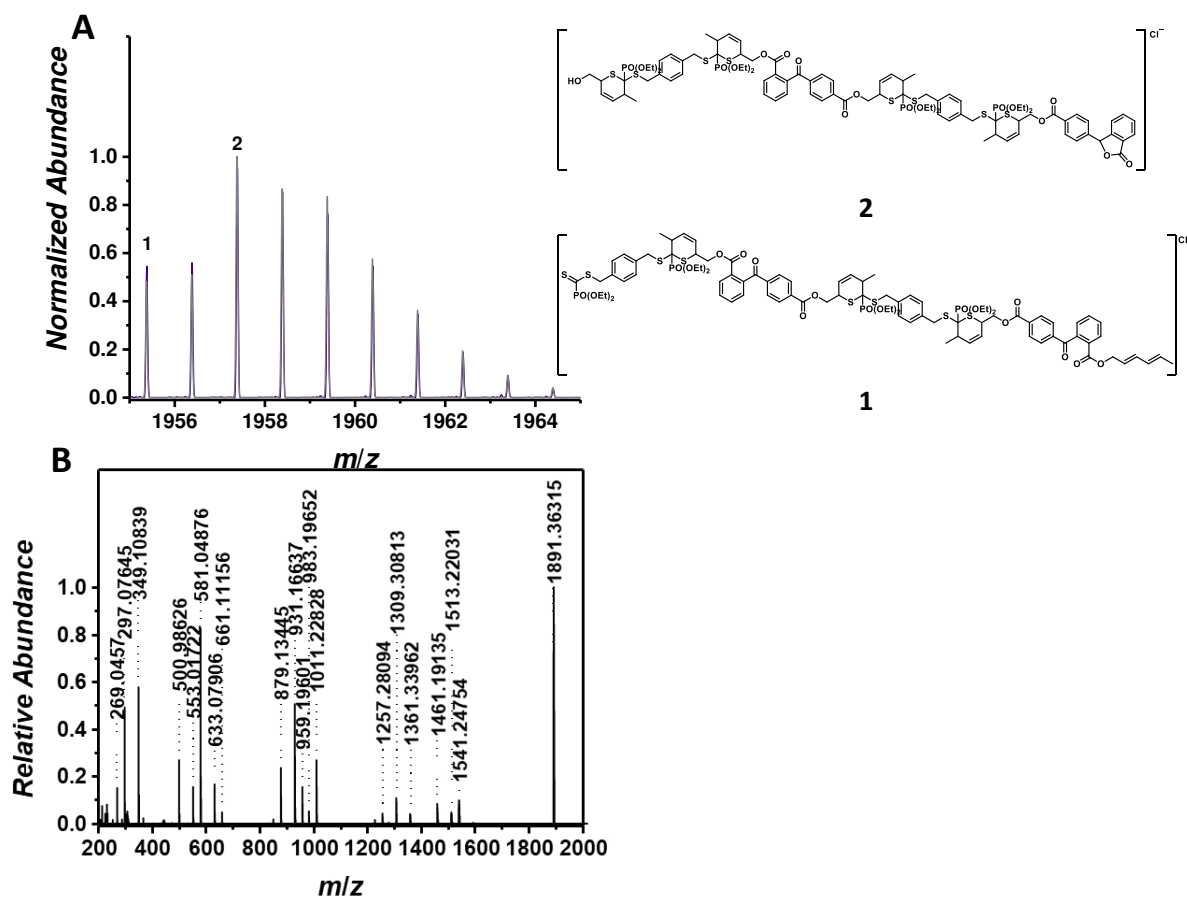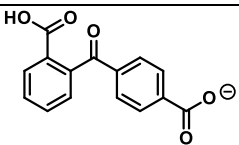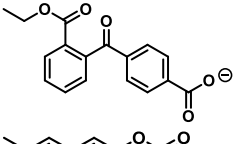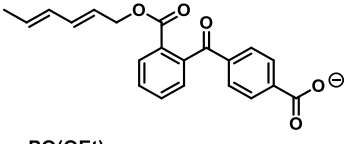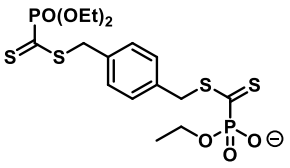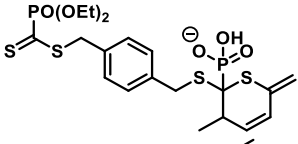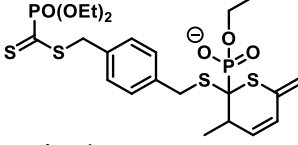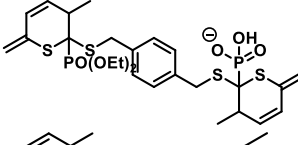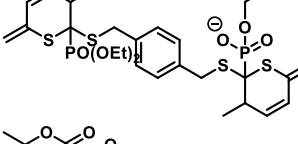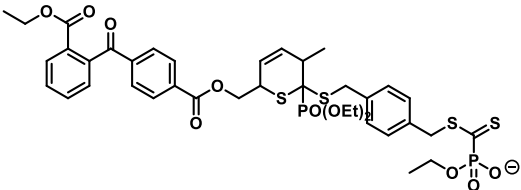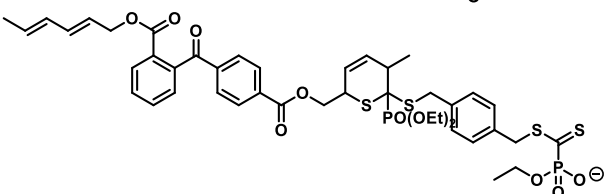
Figure 69 (**A**) Isotopic simulation of a selected degradation species at 1955 *m/z* comparing the experiment (purple line) and the simulation (grey line) of degraded polymer **22**. The ion abundance of the lactone at 1957 *m/z* indicates the successful degradation. (**B**) ESI MS/MS (tandem MS in negative ion mode) of polymer **22** isolating a species at 1955 *m/z* with a HCD energy of 14 eV in the relevant range from 200 *m/z* and 2000 *m/z*. Reprinted with permission from Ref. [375]. Copyright American Chemical Society (2017).

of choice to assess the triggered degradation of polymer **22** and the transformation the macromolecule undergoes during the disassembly, surpassing NMR in this particular case in information depth. After 20 min of irradiation, distinct degradation products started to appear: (*i*) the isotopic pattern of the species at 1955 *m/z* (**Figure 70B**) undergoes a significant transformation indicating a mixture of two species. As illustrated in **Figure 69A**, the species at 1955 *m/z* represented the intact polymer chain structure (refer to **Figure 69B** for the full MS/MS analysis of the intact polymer structure), whereas the increasing ion abundance at 1957 *m/z* indicated the formation of a new species.

The MS/MS experiments clearly confirmed the polymer structure by specific product ions from the precursors ion at 1955 *m/z*. A HCD energy of 14 eV generated sufficient ion abundance to fully assess the polymer fragmentation. The assigned product ions are collated in **Table 7**.

Table 7 Peak assignment of the ESI MS/MS experiment conducted on polymer **22** at 1955 m/z with a HCD energy of 14 eV showing the experimental *m/z*, the theoretical *m/z* values, and Δ*m/z* and the proposed structure. Reprinted with permission from Ref. [375]. Copyright American Chemical Society (2017).

m/z(exp)	*m/z*(theo)	Δ*m/z*	Structure
269.0457	269.0455	0.0002	
297.0765	297.0768	0.0003	
349.1084	349.1081	0.0003	
500.9863	500.9858	0.0005	
553.0172	553.0171	0.0001	
581.0488	581.0484	0.0004	
633.0791	633.0797	0.0006	
661.1116	661.1110	0.0006	
879.1345	879.1325	0.0020	
931.1664	931.1638	0.0026	

959.1960	959.1951	0.0009	
983.1965	983.1951	0.0014	
1011.2283	1011.2264	0.0019	
1257.2809	1257.2793	0.0016	
1309.3081	1309.3106	0.0025	
1361.3396	1361.3419	0.0023	
1461.1914	1461.1882	0.0032	
1513.2203	1513.2195	0.0008	
1541.2475	1541.2508	0.0033	

1891.3632   1891.3663   0.0031
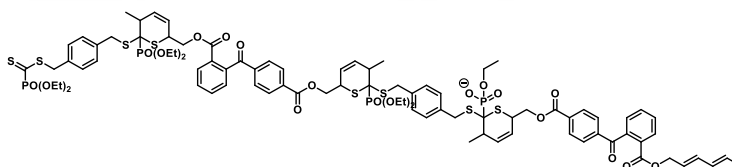
Further, the detailed isotopic pattern simulations (see **Figure 69A)** revealed that the species resulted from the degradation process of polymer **22** (refer to **Figure 71** for the degradation mechanism). Here, the ester bond in *ortho* position to the BP carbonyl has been cleaved and a lactone was formed in a ring-closing reaction. The remaining isotopic pattern simulations have been placed in the Appendix Fig. E 8,9. (*ii*) A further characteristic species appears at 2017 *m/z*, which represents a ring-opening reaction product by nucleophilic attack of an isopropyl alcohol. Additionally, due to the strong coordination of the polymer **22** to the Lewis acid $ZnCl_2$, many species were ionized by chloride attachment along with the formation of a complex resulting in $[ZnCl_3]^-$ (for easier readability, the peak assignments can be found in Appendix Fig. E 7). The presence of such species were in good agreement with the literature.[393] Thus, (*iii*), species ionized by the zinc complexes were highly abundant in the mass spectra. The ion at 2091 *m/z* represented the degradation product, in which the lactone is formed as the first stable intermediate. Furthermore, the abundance of the high-molecular weight species recorded in the range between 3125 *m/z* and 3700 *m/z* were rapidly reduced, and disappeared within 120 min (refer to **Figure 70C**).

Thus, based on the conducted ESI MS analysis (refer to **Figure 70**), the following degradation mechanism for polymer **22** is submitted: Upon irradiation, the carbonyl bond of BP undergoes a *n-π** electron transition to an excited state.[398] After inter-
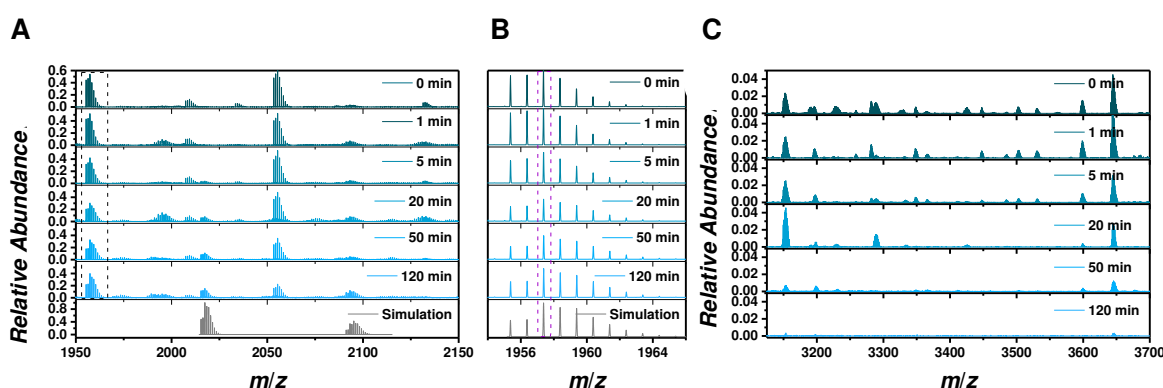
Figure 70 (A) ESI-Orbitrap mass spectra of polymer **22** before and after irradiation with light (λ_{max} = 365 nm, 36 W) for 1, 5, 20, 50 and 120 min. in the mass range between *m/z* 1950 and *m/z* 2150 with the simulated isotopic pattern of important degradation products; (B) expanded *m/z* area of the isotopic pattern of the species at *m/z* 1955 indicating the formation of a degradation product at *m/z* 1957 (the first peak of the isotopic pattern is highlighted); (C) high-molecular weight range between *m/z* 3125 and *m/z* 3700 illustrates the disappearance of high-molecular species upon irradiation. For detailed peak assignments and isotopic pattern simulations refer to Appendix Fig. E 8,9. Reprinted with permission from Ref. [375]. Copyright American Chemical Society (2017).

system crossing (ISC),[397,399] the biradical benzophenone can react via two distinct

mechanistic pathways: (*i*) the radicals find each other in an inter-chain bimolecular coupling reaction or (*ii*) the radical species are reduced to the corresponding alcohol derivative (refer to Section 2.6.1 for a detailed revision). At the beginning of the degradation two types of reactions compete – i.e. the bimolecular (Pinacol) coupling and the reduction –, which was visualized by SEC analysis after one hour of irradiation (**Figure 67A**). The peak with its maximum at 19 mL retention volume (M_w = 250 kDa; M_n = 170 kDa) represented high-molecular compartments produced by the crosslinking reaction. As illustrated in **Figure 71**, a ring-closure reaction can proceed forming a lactone after successful radical coupling leading to a chain scission. Accordingly, degradation product structures were identified in ESI MS. However, such species were isobaric to their linear chain analogues. The subsequent degradation of inter-chain crosslinked macromolecules also resulted in lower molecular weight fragments as indicated by the SEC traces (2 h-24 h, **Figure 67A**). The retention volume's signal climaxing at 19 mL disappeared completely, supporting the proposed degradation of the intermittently formed crosslinked structures. In contrast to inter-chain radical coupling, the photoreduction of the BP unit to benzhydrol as an alternative reaction pathway has often been described in the literature.[306] As unambiguously confirmed by the ESI MS investigation, photoreduced BP formed a lactone if an ester in *ortho* position was available for ring closure. Both fragments of the previously noted cleavage scenario – i.e. the lactone-terminated polymer chain as well as the alcohol-terminated polymer chain – could be identified by HR ESI MS. Furthermore, isopropyl alcohol can act as a nucleophile preceding a ring-opening reaction.[400] Most importantly, as evidenced by ESI MS, the residual polymer backbone represented by the 3,6-dihydro-2*H*-thiopyran ring in benzyl position to the phenyl core kept its full structural integrity as no associated degradation species have been identified.
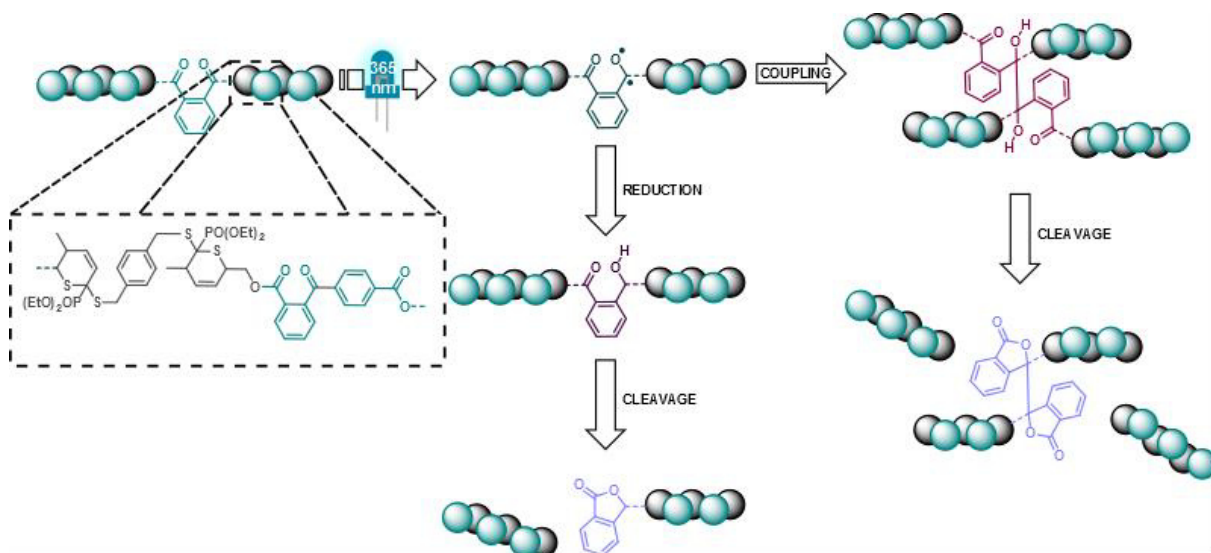
Figure 71 Proposed degradation mechanism: (*i*) irradiation at λ_{max} = 365 nm (36 W) induces the formation of a biradical species; (*ii*) the radicals react in an inter-chain crosslinking reaction or in a reduction reaction; (*iii*) the alcohol in *ortho*-position to the ester bond induces the chain-shattering process forming a lactone as stable degradation product. Reprinted with permission from Ref. [375]. Copyright American Chemical Society (2017).

7.2.2. Thermally-Triggered Degradation

The thermal approach of the chain shattering process of polymer **22** was demonstrated via SEC, online high-temperature ^{1}H NMR (**Figure 74A** and **B**) as well as UV-vis spectroscopy (refer to **Figure 73**). The thermally induced degradation was accomplished by dissolving polymer **22** in acetonitrile (20 mg·mL^{-1}) in a pressure tube. The solution was kept at 160 °C for 40 min and rapidly cooled in liquid nitrogen to prevent the reformation of Diels-Alder linkages. **Figure 74A** represents the SEC trace recorded after polymer **22** was degraded thermally: the parent polymer (M_w = 14 kDa; M_n = 7 kDa; $Đ$ = 2.0) disassembles rapidly to small molecules (M_w = 2.8 kDa; M_n = 1.2 kDa; $Đ$ = 2.2). Online high-temperature NMR spectroscopy (**Figure 74B**) allowed for a chemical assessment of the debonding process: the specific double bond resonances of (*i*) the 3,6-dihydro-2*H*-thiopyran ring (between 5.5 and 6.0 ppm) and (*ii*) the residual diene resonances (between 4.3 and 5.0 ppm) become more pronounced in the course of the thermal treatment between 25 and 125 °C. Importantly, some diene resonances are isochronous with the 3,6-dihydro-2*H*-thiopyran ring proton resonances impeding a strongly visible change in the region between 5.5 and 6.0 ppm. Nevertheless, the percentage of unreacted diene can be deduced as follows: The aromatic region (6.945 – 8.303 ppm) was normalized to 12 H; the olefin region (4.400 – 6.500 ppm) was integrated with constant set boundaries. For 0% debonding: the
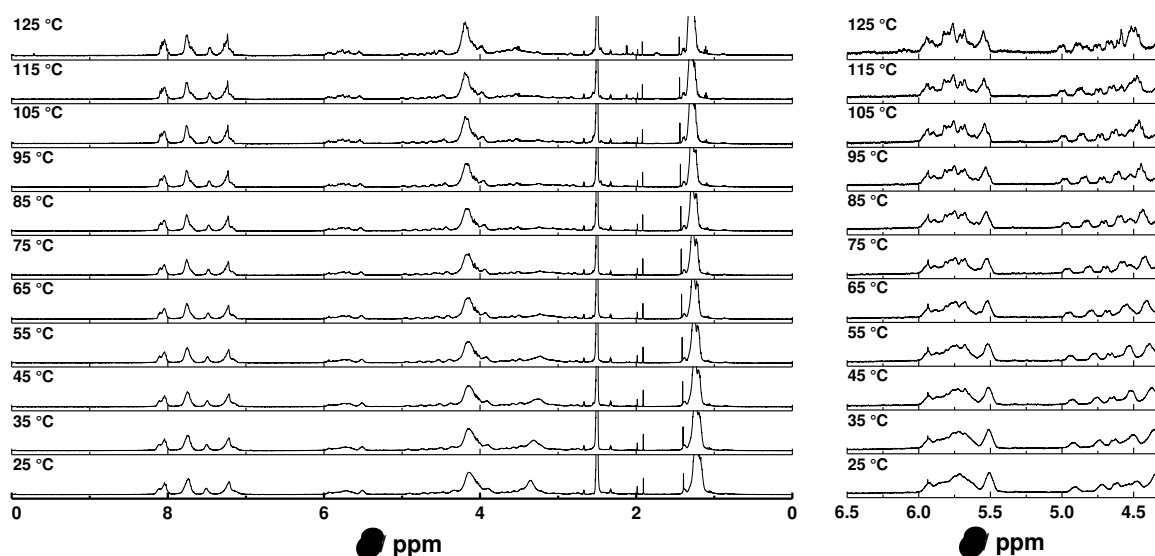
Figure 72 Overview spectra of the online HT NMR (400 MHz, DMSO-d₆) experiment of polymer **22** in the temperature range between 298 and 398 K. Reprinted with permission from Ref. [375]. Copyright American Chemical Society (2017).

thiopyrane ring is represented by 4 H, whereas the free diene resonance integrals is 0 H. Thus:

$$0\%: 4 = (4H - 4 \cdot XH) + 12 \cdot XH$$

$$\rightarrow 4 = 4H + 8 \cdot XH$$

$$\rightarrow \frac{4}{4H} = 1 + 2X$$
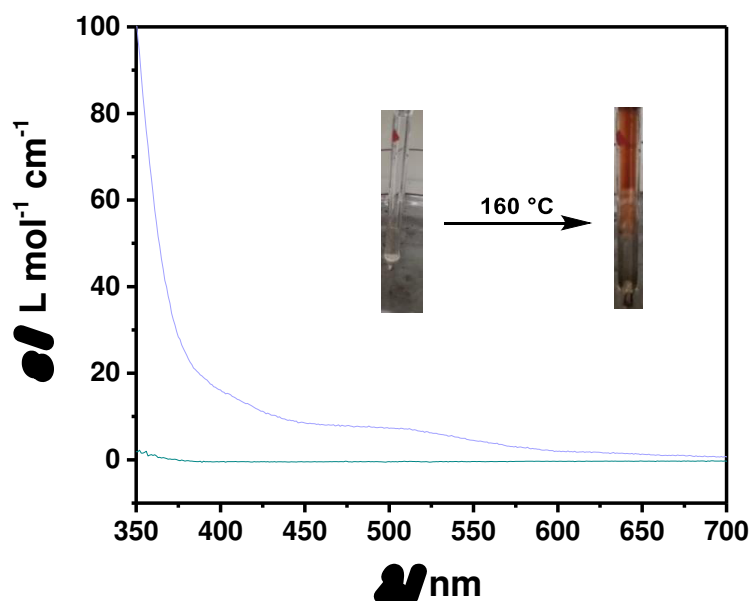
Figure 73 UV/visible measurement of polymer **22** in acetonitrile (298 K) before (cyan line) and after temperature increase to 160 °C for 40 min (light purple line). The photos indicate the color change from colorless to red after heating to 160 °C. Reprinted with permission from Ref. [375]. Copyright American Chemical Society (2017).
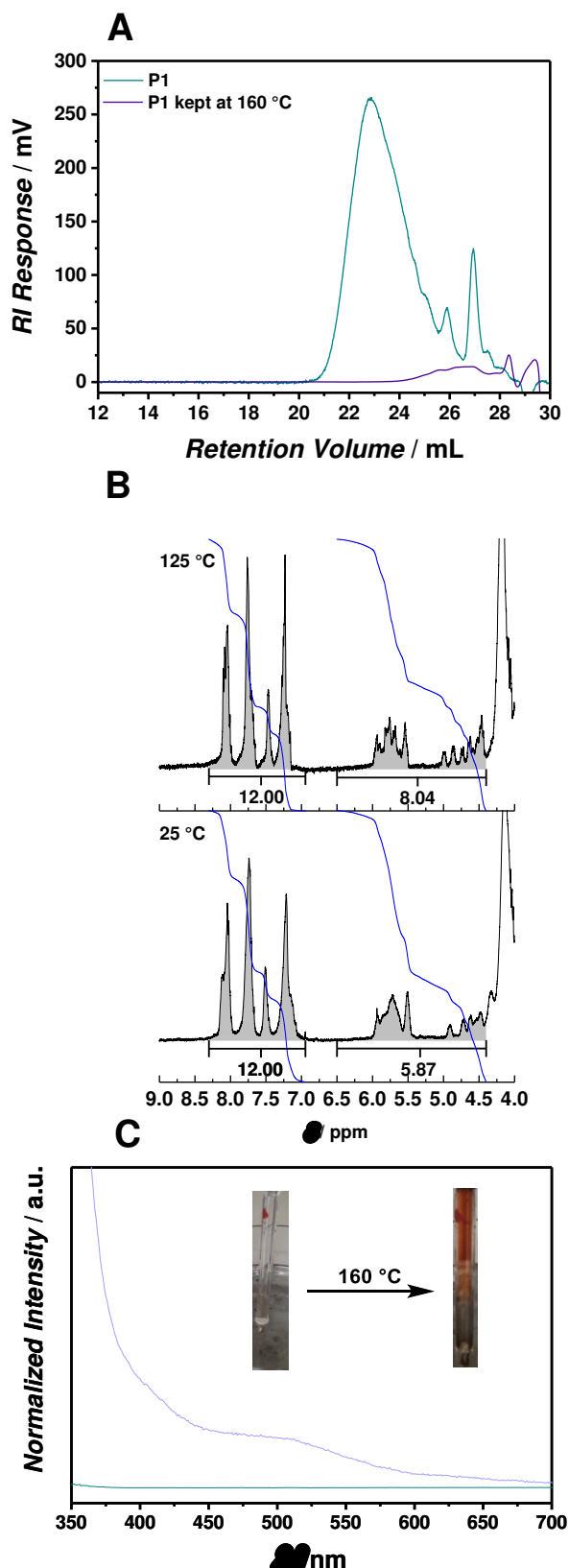
Figure 74 SEC traces of the intact polymer (**22**) (M_w = 14 kDa; M_n = 7 kDa; $Đ$ = 2.0), and after thermally induced degradation at 160 °C (40 min) leading to small components (M_w = 2.8 kDa; M_n = 1.2 kDa; $Đ$ = 2.2) (A); online high-temperature ^{1}H NMR spectra (DMSO-d_6, 400 MHz) of polymer **22** at 25 and 125 °C illustrating the significant double bond resonances (integrated) in the chemical shift regime between 4.3 and 6.5 ppm as well as the aromatic resonances (integrated to 12 H) between 7.0 and 8.5 ppm(B). Reprinted with permission from Ref. [375]. Copyright American Chemical Society (2017).

During the polymerization reaction, less than 100% of the dienes have been

consumed and at 25 ˚C the degree of debonding (*X*) can be calculated as:

$$25\,°C: \frac{5.87}{4H} = 1 + 2X$$

$$\rightarrow X = 0.23$$

At 25 ˚C, the olefin resonance regime integrates to 5.87 representing 23% debonding (**Figure 74B and Figure 72**); at 125 ˚C, the integrated value increases to 8.04 representing 51% debonding. Thus, 28% additional diene species have formed during thermal treatment at 125 ˚C. Furthermore, the integrated value of the diene resonance indicates the recovery of **21a** (for the full online HT NMR spectra refer to **Figure 72**). The thermally-gated degradation of polymer **22** entails recycling, yielding both monomer species **21a** and **21b**. Alternatively, **21b** can be recovered after thermal treatment of the light-induced degradation mixture. Further, UV-vis spectroscopy (refer to **Figure 73**) indicates the reformation of the dithioester group possessing a high absorbance between 500 and 550 nm and between 275 and 400 nm.[401]

7.3. CONCLUSION

In summary, a novel dual-responsive polymer system was introduced, which can be degraded into environmentally compatible small molecules by taking advantage of the light-adaptive properties of the BP trigger motif and the thermo-responsive reversible HDA linkages. The successful formation of the polymer via mild hetero Diels-Alder polymerization was evidenced by a detailed SEC and NMR characterization. Most importantly, the advanced self-immolative polymers retain their full structural integrity until the precision chain-shattering is started upon external light irradiation (λ_{max} = 365 nm). SEC and ESI MS enabled the monitoring of the degradation reaction. The specific degradation species ionize efficiently in negative ion mode via chloride attachment, allowing for the unambiguous identification of the formed products. The chain-shattering character of the BP-based degradable polymer relies on a photoreduction between the carbonyl motif and isopropyl alocohol as key intermediate step, cleaving the chain backbone via intramolecular lactone formation. Alternatively, the polymer can be degraded via a thermal gate, which proceeds orthogonally to the light induced process.

7.4. Experimental Section

7.4.1. Materials

All solvents for synthesis were obtained from Sigma-Aldrich, Acros Organics or Fischer and used without further purification. The benzophenone-2,4'-dicarboxylic acid monohydrate (TCI, >98%), *trans*,*trans*-2,4-hexadien-1-ol (Alfa Aesar, 98%), α,α'-dibromo-*p*-xylene (Sigma Aldrich, 98%), carbon disulfide (VWR, 99.9%), diethyl phosphite (Fluka, >95%), sodium hydride (Sigma Aldrich, 95%) and zinc chloride (Sigma Aldrich, >98%) were used as received. THF (Scharlau, GPC grade), MeOH (Roth, HPLC ultra gradient grade) and NaI (Sigma-Aldrich, 99%) for SEC-ESI MS analysis were used without further treatment.

7.4.2. Instrumentation

Electrospray ionization-Orbitrap mass spectrometry (ESI-Orbitrap MS). Mass spectra were recorded on a Q Exactive (Orbitrap) mass spectrometer (Thermo Fisher Scientific, San Jose, CA, USA) equipped with a HESI II probe. The instrument was calibrated in the m/z range 74-1822 using premixed calibration solutions (Thermo Scientific) and in m/z range 1000-6000 Th using ammonium hexafluorophosphate (Thermo Scientific). All spectra were recorded in the negative mode, using isopropyl alcohol/acetonitrile = 1:1 (*v/v*) as ESI solvent. The spectra were recorded in a concentration of 0.5 mg· mL^{-1}. Prior to the time-dependent irradiation of polymer **22** with light (λ_{max} = 365 nm), the solvent was degassed by purging with nitrogen for 15 min. The FT resolution was set to 140000 employing 3 microscans during an acquisition time between 2 and 5 min measuring with a capillary temperature of 320 °C. The aux gas flow was (dimensionless) 0.00, the sheath gas 10.00, and the spare gas 1.00. The flow rate was set to 5 µL· min^{-1}. The spray voltage was set to 4.6 kV and kept constant throughout the irradiation study.

Size exclusion chromatography coupled with electrospray ionization mass spectrometry (SEC-ESI MS). Spectra were recorded on a LTQ Orbitrap XL Q Exactive mass spectrometer (Thermo Fisher Scientific, San Jose, CA, USA) equipped with an HESI II probe. The instrument was calibrated in the m/z range 74-1822 using premixed calibration solutions (Thermo Scientific) and in m/z range 1000-6000 Th using ammonium hexafluorophosphate (Thermo Scientific). A constant spray voltage

of 4.6 kV, a dimensionless sheath gas of 8, and a dimensionless auxiliary gas flow rate of 2 were applied. The capillary temperature and the S-lens RF level were set to 320 °C and 62.0, respectively. The Q Exactive was coupled to an UltiMate 3000 UHPLC System (Dionex, Sunnyvale, CA, USA) consisting of a pump (LPG 3400SD), autosampler (WPS 3000TSL), and a thermostated column department (TCC 3000SD). Separation was performed on two mixed bed size exclusion chromatography columns (Polymer Laboratories, Mesopore 250 × 4.6 mm, particle diameter 3 µm) with precolumn (Mesopore 50 × 4.6 mm) operating at 30 °C. THF at a flow rate of 0.30 mL· min⁻¹ was used as eluent. The mass spectrometer was coupled to the column in parallel to a RI-detector (RefractoMax520, ERC, Japan). 0.27 mL· min⁻¹ of the eluent were directed through the RI-detector and 30 µL· min⁻¹ infused into the electrospray source after postcolumn addition of a 100 µM solution of sodium iodide in methanol at 20 µL· min⁻¹ by a microflow HPLC syringe pump (Teledyne ISCO, Model 100DM). A 50 µL aliquot of a polymer solution with a concentration of 2 mg· mL⁻¹ was injected onto the HPLC system.

7.4.3. Synthesis

(2*E*,4*E*)-hexa-2,4-dienyl 2-(4-(((((2*E*,4*E*)-hexa-2,4-dienyl)oxy)carbonyl)benzoyl)benzoate (21a). To a stirred solution of 500 mg benzophenone-2,4'-dicarboxylic acid monohydrate (1.74 mmol, 1.00 eq) (protected from ambient light) in 1.2 mL anhydrous DMF (1.5 M), 106.0 mg DMAP (0.867 mmol, 0.50 eq) and 426 mg sorbin alcohol (4.34 mmol, 2.50 eq) were added. 831 mg EDC·HCl (4.33 mmol, 2.50 eq) was added to the reaction mixture at 0 °C, which was then stirred for 5 min at 0 °C and for 48 h at ambient temperature. The mixture was subsequently diluted with 200 mL dichloromethane, washed twice with water and once with brine. The organic phase was dried over Na_2SO_4 and evaporated at reduced pressure. The product was obtained as colorless oil (322 mg, 0.746 mmol, 43%) after flash chromatography using cyclohexane:ethyl acetate = 10:1 as eluent.

R_f = 0.54 (cyclohexane:ethyl acetate = 2:1)

¹H NMR (400 MHz, 298 K, DMSO-d₆): δ = 8.05 (m, 3H), 7.88 – 7.64 (m, 4H), 7.54 (dd, ^3J = 7.5 Hz, ^4J = 0.9 Hz, 1H), 6.38 (m, 1H), 6.17 – 6.01 (m, 2H), 5.96 – 5.59 (m, 4H), 5.41 – 5.26 (m, 1H), 4.83 (d, ^3J = 6.4 Hz, 2H), 4.50 (d, ^3J = 6.4 Hz, 2H), 1.71 (m, 6H).

¹³C NMR (101 MHz, 298 K, DMSO-d₆) δ = 195.55 (C), 165.00 (C), 164.76 (C), 140.54 (C), 140.08 (C), 134.64 (CH), 134.57 (CH), 133.34 (CH), 133.16 (CH), 131.08 (CH), 130.97 (CH), 130.48 (CH), 130.42 (CH), 130.34 (CH), 129.82 (CH), 129.57 (CH),

129.08 (CH), 128.55 (CH), 127.86 (CH), 123.84 (CH), 122.98 (CH), 65.45 (CH_2), 65.39 (CH_2), 17.90 (CH_3), 17.84 (CH_3).

HR ESI MS: [**21a**+Na]: *m/z* 453.1669 (*m/z*(theo) 453.1672)

1,4-phenylenebis(methylene) bis((diethoxyphosphoryl)methanedithiofor-mate) (21b): The synthesis was adapted from the literature.[133]

Hetero Diels-Alder step-growth polymerization to yield polymer 22. 100 mg (2*E*,4*E*)-hexa-2,4-dienyl 2-(4-((((2*E*,4*E*)-hexa-2,4-dienyl)oxy)carbonyl)ben-zoyl)benzoate (**21a**) (0.232 mmol, 1.00 eq), 123.2 mg 1,4-phenylenebis(methylene) bis((diethoxyphosphoryl)methanedithioformate) (**21b**) (0.232 mmol, 1.00 eq) and 34.8 mg $ZnCl_2$ (0.256 mmol, 1.10 eq) were stirred in 780 µL ethyl acetate at 50 ˚C. After 24 h, the solids were filtered, washed with cold ethyl acetate and dried under a high vacuum. Polymer **22** was obtained as pale brown solid (quantitative yield).

Light-triggered degradation of polymer 22: 10 mg polymer 22 (M_w = 14 kDa; M_n = 7 kDa; Đ = 2.0) was dissolved in 5 mL isopropyl alcohol:acetoni-trile = 1:1 (*v/v*) in a concentration of 2 mg·mL^{-1} and portioned equally to 5 sealed vials. The solution was degassed by purging with nitrogen for 15 min and subse-quently irradiated using a Philips Cleo Compact PL-L fluorescent lamp (36 Watt, λ_{max} = 350 nm) in a self-made photo reactor. After 1, 2, 3, 4 and 24 h, respectively, an aliquot was taken, and the solvent was removed under reduced pressure prior to analytical characterization.

Thermally-triggered degradation of polymer 22: 20 mg polymer 22 (M_w = 14 kDa; M_n = 7 kDa; Đ = 2.0) was placed in a pressure tube and dissolved in 0.5 mL acetonitrile. The red color indicated the formation of the thiocarbonyl group (see **Figure 73**). After 40 min, the reaction was rapidly cooled in liquid nitrogen to prevent potential Diels-Alder reactions.

8

CONCLUSIONS AND OUTLOOK

The present thesis addresses two overarching aims: (*i*) establishing efficient routes for macromolecular ionization in electrospray ionization mass spectrometry and (*ii*) elucidating chemical reaction pathways during the degradation of macromolecules into small molecules or the single chain folding polymers. Within the following section, a critical assessment of the thesis' objectives is carried out.

In Chapter 3, an efficient ionization route to access non-polar polymers via chloride attachment in negative ion mode is described. The chloride attachment provides an ion abundance between 10^5 and 10^8 of the non-polar macromolecular analyte. In contrast to the sodium attachment, multiply charged species – and for the first time described – quadruply charged polystyrene were detected. In addition, the ionization platform establishes an efficient ionization route for polybutadiene, representing its

first time successful analysis by electrospray ionization. Although the ionization plat-form is very powerful for a large array of non-polar polymers, some polystyrene-type polymers remain still challenging.
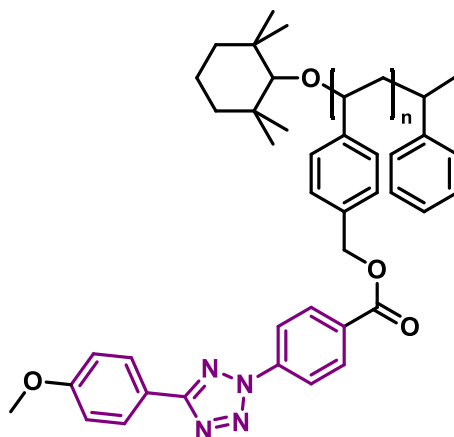
Figure 75 Exemplary representation of non-polar styrene-type polymers that are challenging to ionize via chloride attachment in negative ion mode.

The structure represented in **Figure 75** is a tetrazole functionalized polymer. As recently observed, tetrazole functionalized polymers do not exhibit good ioniza-tion in electrospray ionization. The tetrazole motif is a large conjugated π system (highlighted in purple), which should be capable of coordinating to chloride ions via negative ion attachment. However, preliminary tests indicate a low ion abundance, which might be associated with the nitrogen entailed within the tetrazole. It is pro-posed that the nitrogen can be converted into a protonated species resembling a polyelectrolyte. Yet, it is still unclear why both positive and negative ion mode do not promote the sufficient ionization of tetrazole tethered polymers. In Chapter 3, NaCl was utilized for doping the ESI solvent. A more potent alternative is Ph_4PCl, which dissociates readily.[402] Furthermore, the cation (Ph_4P^+) has a low tendency to coordinate to any structural motifs in the polymer, and thus, does not contribute to an ion abun-dancy reduction by a charge competition mechanism.[26,35,37,45]

Supercharging – also described in Chapter 3 – is a powerful route to promote multiply charged analytes. As assessed in the current thesis, the supercharging effect is most prominent in water. Thus, highly polar macromolecules such as poly(ionic liquid)s benefit strongly from the supercharging effect allowing their mapping in neg-ative ion mode. Without supercharging agent, the ion abundance of poly(ionic liquid)s is very low. The results are described in detail in Chapter 4. Thus, the present thesis reports for the first time an in-depth mass spectrometric elucidation of an entire class of polymers. In Chapter 4, the results described for the mass spectrometric analysis

of poly(ionic liquid)s formulate chloride as counter ion, which also promotes the ionization in negative ion mode. A fast and quantitative salt exchange imparted into the sample preparation has been reported in Chapter 4, Section 4.3. Here, a detailed elucidation of the influence of an exchanged counter ion on the ionization behavior in negative ion mode was studied. Strikingly, the data was correlated with the H-bonding activity of the counter ions being most pronounced for chloride and weak for perfluorinated species such as tetrafluoroborate. The described electrospray ionization platform critically aids in determining PILs' structure including defects resulting from, e.g., hydrolysis events in case of an acrylate-type PIL. The current work paves the way for detailed polymerization mechanism studies via a pulsed laser polymerization method, which is helpful to further understand this unique class of polyelectrolytes.

In Chapter 5, the polymerization mechanism of a spontaneous zwitterionic alternating copolymerization between various cyclic imino ethers and acrylic acid was elucidated by a post-mortem high resolution mass spectrometric analysis of the polymeric material. Importantly, a calibration curve was established to semi-quantify the end group and different species in the mass spectrum. Based on the quantification and detailed MS/MS measurements, the polymerization mechanism was unraveled. The data for chain termini quantification should to process the material in a more efficient fashion, e.g. via a post-polymerization functionalization introducing functionalities such as anchors for surface decoration or peptide modification.

A topic with high future potential was introduced in Chapter 6. Here, for the first time reported, a detailed investigation into single chain collapsed nanoparticles by high resolution mass spectrometry reveals a fascinating and precise view into the folding mechanism of such nanoparticles. As research on single chain nanoparticles is rapidly expanding, it is expected that the herein established high resolution mass spectrometry protocols will critically extend the toolbox of existing morphological techniques including SEC, DOSY, DLS, SAXS and AFM, providing a unique view on chain folding processes. In Chapter 6, first results indicate the great potential of imaging single chain nanoparticles via electrospray ionization.

What is next? One envisaged project could focus on the determination and quantification of specific folding points. Here, the analytics benefit from systems where a small molecule per formed crosslinking point is released. For instance, a suitable ligation with small molecule release is the light-induced nitrilimine formation of tetrazole precursors that reacts rapidly with double bonds in a 1,3-dipolar cycloaddition. Upon light exposure, tetrazole releases molecular nitrogen (24 Da), which can

be used to count the number of ligation points within the single chain nanoparticle (refer to **Figure 76**).
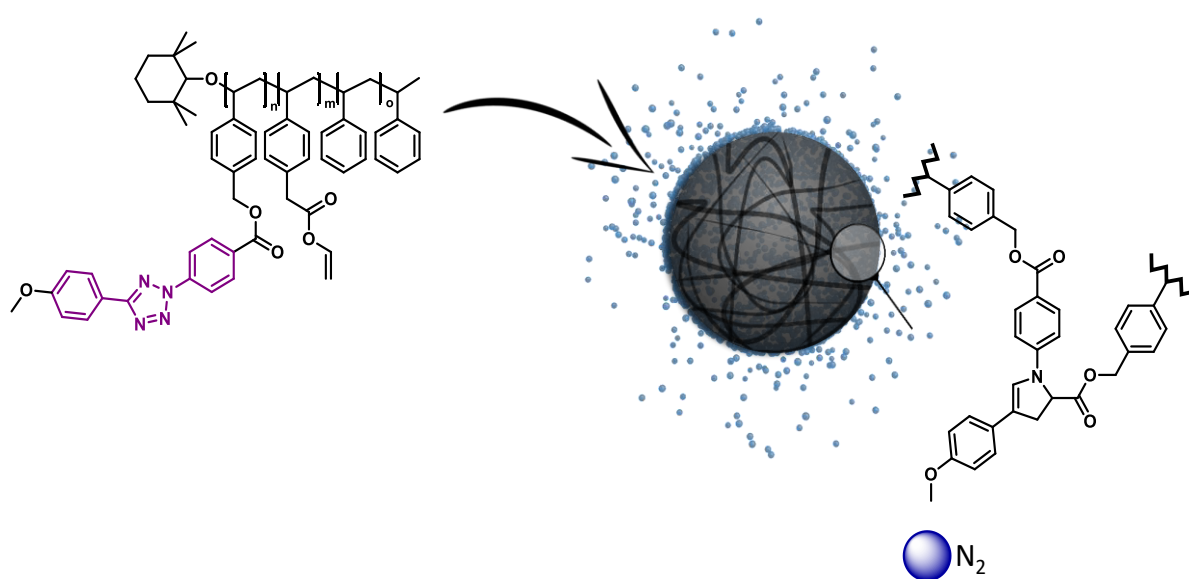
Figure 76 Cartoon of the tetrazole-mediated SCNP formation releasing molecular nitrogen.

Alternatively, a thermal nitrogen releasing system can be introduced via nitrene crosslinking chemistry.[403] The second major challenge is the determination of loop sizes. Here, a clever chemical system has to be introduced, which cleaves the midchain bonds only after successful crosslink formation. In addition, the cleavage must be carried in such a fashion that the loops stay intact.

Finally, the photodegradation of polymers was introduced in Chapter 7. The research on self-immolative polymers with chain shattering characteristic is young and dynamic and it is expected that a rapid growth of the research will lead to the development of novel drug delivery systems as well as provide access medical implant applications. Apart from the investigation of novel trigger systems – including a detailed analysis as performed in Chapter 7 – future objectives are most likely in the fabrication of locally degradable 3D structures.[404] Here, the materials properties can be easily adjusted from hydrophobic motifs to hydrophilic motifs (e.g. carboxyl groups) after deprotection.[405]

In summary, the present thesis introduces new ionization protocols for electrospray ionization. The powerful negative mode ionization allows for the efficient mapping of a broad range of polyhydrocarbons, yet is challenging for large π systems (likely associated with π-π stacking) or if multiple nitrogen atoms are present that

can become positively charged. The positive charge counters the negative chloride attachment resulting in neutral species disallowing the mapping via electrospray ionization. A detailed study on how supercharging agents can influence the charge state of macromolecules is provided. Here, the successful ionization of PILs is described, which significantly benefit from the charge state promotion afforded by the supercharging agents. Moreover, the thesis presents detailed insights into polymerization, folding mechanisms and degradation mechanisms of polymer systems based a powerful high resolution ESI MS platform.

<div align="right">

9

</div>

INSTRUMENTATION

The following section comprises the instrumental information of the characterization methods used for the entire thesis. If not indicated in the corresponding section, the general instrumentation is displayed as follows:

9.1. SIZE EXCLUSION CHROMATOGRAPHY (SEC)

THF SEC was performed on an Agilent Series 1200 HPLC system, comprising an autosampler, one SDV column (particle size 10 μm, dimension 300 × 8 mm, porosity 1000 Å) and a UV/vis detector using THF/10 mM $LiTf_2N$/10 mM n-butylimidazole as the eluent at 35 ℃ with a flow rate of 1 mL·min^{-1}. The SEC system was calibrated using linear polystyrene standards ranging from 470 to 2.5^6 g mol^{-1}. Appropriate SEC

calibrations were carried out relative to a polystyrene calibration (Mark Houwink parameters $K = 14.1 \cdot 10^{-5}$ dL·g^{-1}; α = 0.7).

Water-based SEC was performed on a PSS WinGPC, comprising an autosampler, a PSS Novema Max precolumn, one PSS Novema Max (particle size 10 μm, dimension 8.00 × 300.00 mm, porosity 30 Å), two PSS Novema Max (particle size 10 μm, dimension 8.00 × 300.00 mm, porosity 1000 Å), and a differential refractive index detector (PSS SECcurity RI) as well as an UV detector (PSS SECcurity UV) using water, 0.1 g·L^{-1} NaCl and 0.3 M formic acid as the eluent at 30 °C with a flow rate of 1 mL·min^{-1}. The SEC system was calibrated using linear poly(2-vinyl pyridine) standards ranging from 1100 to $1.06 \cdot 10^{6}$ g·mol^{-1}. SEC calibration was carried out relative to poly(2-vinyl pyridine) calibrations (Mark Houwink parameters $K = 2.5 \cdot 10^{-5}$ dL·g^{-1}; α = 0.93).

DMAc-based SEC was performed on a Polymer Laboratories PLGPC 50 Plus Integrated System, comprising an autosampler, a PLgel 5 μm bead-size guard column (50×7.5 mm) followed by three PLgel 5 μm MixedC columns (300×7.5 mm) and a differential refractive index detector using *N,N*-dimethylacetamide (DMAc) containing 0.03 wt% LiBr as eluent at 50 °C with a flow rate of 1.0 mL min^{-1}. The SEC system was calibrated against linear poly(styrene) standards with molecular weights ranging from 700 to $2 \cdot 10^{6}$ g mol^{-1}.

9.2. NMR SPECTROSCOPY

Proton nuclear magnetic resonance (^{1}H NMR) spectra were recorded on a Bruker AM 400 (400 MHz) spectrometer. Chemical shifts are expressed in parts per million (ppm) and calibrated on characteristic solvent signals as internal standards. All coupling constants are absolute values and *J* values are expressed in Hertz (Hz).The description of signals include: s = singlet, bs = broad singlet, d = doublet, dd = double doublet, t = triplet, q = quartet, m = multiplet.

Carbon nuclear magnetic resonance (^{13}C NMR) spectra were recorded on a Bruker AM 400 (100 MHz) spectrometer.

Phosphorus nuclear magnetic resonance (^{31}P{^{1}H} NMR) spectra were recorded on a Bruker AM 400 (162 MHz) spectrometer.

DOSY spectra were recorded on a Bruker Ultrashield 400, equipped with a BBO-Probe (5 mm) with z-gradient (^{1}H: 400 MHz) utilizing the ledgp2s pulse sequence. The δ-scale was normalized relative to the solvent signal of DMSO-d$_6$ for 1H spectra.

9.3. X-Ray Photoelectron Spectroscopy (XPS)

X-Ray photoelectron spectroscopy (XPS). XPS measurements were performed using a K-Alpha + XPS spectrometer (Thermo Fisher Scientific, East Grinstead, UK). Data acquisition and processing using the Thermo Avantage software is described elsewhere.[8] All thin films were analyzed using a microfocused, monochromated Al Kα X-ray source (400 µm spot size). The K-Alpha charge compensation system was employed during analysis, using electrons of 8 eV energy, and low-energy argon ions to prevent any localized charge build-up. The kinetic energy of the electrons was measured by a 180° hemispherical energy analyzer operated in the constant analyzer energy mode (CAE) at 50 eV pass energy for elemental spectra. The spectra were fitted with one or more Voigt profiles (BE uncertainty: $\pm$0.2 eV) and Scofield sensitivity factors were applied for quantification.[9] All spectra were referenced to the C1s peak (C-C, C-H) at 285.0 eV binding energy controlled by means of the well known photoelectron peaks of metallic Cu, Ag, and Au, respectively.

9.4. Time-of-flight secondary ion mass spectrometry (ToF-SIMS)

ToF-SIMS was performed on a TOF.SIMS5 instrument (ION-TOF GmbH, Münster, Germany), equipped with a Bi cluster primary ion source and a reflectron type time-of-flight analyzer. UHV base pressure was < 5·10^{-9} mbar. For high mass resolution the Bi source was operated in the "high current bunched" mode providing short Bi$_3^+$ primary ion pulses at 25 keV energy and a lateral resolution of approx. 4 µm. The short pulse length of 1.1 ns allowed for high mass resolution. Primary ion doses were

---

[8] K. L. Parry, A. G. Shard, R. D. Short, R. G. White, J. D. Whittle, A. Wright, *Surf. .Interface Anal.,* **2006**, *38*, 1497.

[9] J. H. Scofield, *J. Electron Spectr. Relat. Phen.,* **1976**, 8, 129.

kept below 10^{11} ions/cm^2 (static SIMS limit). Spectra were calibrated on the omnipresent C$^-$, C$_2^-$, C$_3^-$, or on the C$^+$, CH$^+$, CH$_2^+$, and CH$_3^+$ peaks. Based on these datasets the chemical assignments for characteristic fragments were determined. Images larger than the maximum deflection range of the primary ion gun of 500×500 μm^2 were obtained using the manipulator stage scan mode.

9.5. UV-VISIBLE SPECTROSCOPY

UV-visible spectroscopy was performed using a Cary 300 Bio spectrophotometer (Varian) featuring a thermostated (298 K) sample cell holder. Absorption spectra of the samples were recorded with a resolution of 1 nm and a slit width of 2 nm in a quartz glass cuvette (VWR, quartz glass, SUPRASIL®).

10

BIBLIOGRAPHY

(1)   The 2002 Nobel Prize in Chemistry https://www.nobelprize.org/nobel_prizes/chemistry/laureates/2002/popular.html (accessed Feb 15, 2018).

(2)   John Fenn obituary | Science | The Guardian https://www.theguardian.com/science/2011/jan/13/john-fenn-obituary (accessed Feb 15, 2018).

(3)   Thomson, J. J. Nobel Prize in Physics 1906 - Presentation Speech https://www.nobelprize.org/nobel_prizes/physics/laureates/1906/press.html.

(4)   Griffiths, J. A Brief History of Mass Spectrometry. *Anal. Chem.* **2008**, *80*, 5678–5683.

(5)   Dahl, P. F. *Flash of the Cathode Rays : A History of J.J. Thomson's Electron*; Institute of Physics Pub, 1997.

(6)   Nier, A. O. A Mass Spectrometer for Routine Isotope Abundance Measurements. *Rev. Sci. Instrum.* **1940**, *11*, 212–216.

(7)   Nier, A. O. A Mass Spectrometer for Isotope and Gas Analysis. *Rev. Sci. Instrum.* **1947**, *18*, 398–411.

(8)   Nier, A. O.; Booth, E. T.; Dunning, J. R.; Grosse, A. V. Further Experiments on Fission of Separated Uranium Isotopes. *Phys. Rev.* **1940**, *57*, 748–748.

(9)   Nier, A. O.; Booth, E. T.; Dunning, J. R.; Grosse, A. V. Nuclear Fission of Separated Uranium Isotopes. *Phys. Rev.* **1940**, *57*, 546–546.

(10)   McLafferty, F. W. Mass Spectrometric Analysis. Molecular Rearrangements. *Anal. Chem.* **1959**, *31*, 82–87.

(11)   Biemann, K.; Vetter, W. Separation of Peptide Derivatives by Gas Chromatography Combined with the Mass Spectrometric Determination of the Amino Acid Sequence. *Biochem. Biophys. Res. Commun.* **1960**, *3*, 578–584.

(12)   Biemann, K. Laying the Groundwork for Proteomics. *Int. J. Mass Spectrom.* **2007**, *259*, 1–7.

(13)   Aebersold, R.; Goodlett, D. Mass Spectrometry in Proteomics. *Chem. Rev.* **2001**, *101*, 269–296.

(14)   Aebersold, R.; Mann, M. Mass Spectrometry-Based Proteomics. *Nature* **2003**, *422*, 198–207.

(15)   *Mass Spectrometry in Polymer Chemistry*; Barner-Kowollik, C., Ed.; Wiley-VCH: Weinheim.

(16)   IUPAC the "Gold Book." resolution in mass spectroscopy http://goldbook.iupac.org/R05318.html (accessed Jan 4, 2018).

(17)   Hipple, J. A.; Sommer, H.; Thomas, H. A. A Precise Method of Determining the Faraday by Magnetic Resonance. *Phys. Rev.* **1949**, *76*, 1877–1878.

(18)   Comisarow, M. B.; Marshall, A. G. Fourier Transform Ion Cyclotron Resonance Spectroscopy. *Chem. Phys. Lett.* **1974**, *25*, 282–283.

(19)   Fenn, J.; Mann, M.; Chin-kai, M.; Shek-fu, W.; Whitehouse, C. Y. O. Electrospray Ionization for Mass Spectrometry of Large Biomolecules. *Science (80-.).* **1989**, *246*, 64–71.

(20)   Fenn, J. B. Electrospray Ionization Mass Spectrometry: How It All Began. *J. Biomol. Tech.* **2002**, *13*, 101–118.

(21)   Karas, M.; Hillenkamp, F. Laser Desorption Ionization of Proteins with Molecular Masses Exceeding 10 000 Daltons. *Anal. Chem.* **1988**, *60*, 2299–2301.

(22)   Thompson, R. I.; Harmon, T. J.; Ball, M. G. The Rotating-Saddle Trap: A Mechanical Analogy to RF-Electric-Quadrupole Ion Trapping? *Can. J. Phys.* **2002**, *80*, 1433–1448.

(23)   Teschl, G.; Cox, D. *Ordinary Differential Equations and Dynamical Systems*; American Mathematical Society, 2004; Vol. 1.

(24)   Lesiak, A. D.; Cody, R. B.; Dane, A. J.; Musah, R. A. Plant Seed Species Identification from Chemical Fingerprints: A High-Throughput Application of Direct Analysis in Real Time Mass Spectrometry. *Anal. Chem.* **2015**, *87*, 8748–8757.

(25)   Abrankó, L.; García-Reyes, J. F.; Molina-Díaz, A. In-Source Fragmentation and Accurate Mass Analysis of Multiclass Flavonoid Conjugates by Electrospray Ionization Time-of-Flight Mass Spectrometry. *J. Mass Spectrom.* **2011**, *46*, 478–488.

(26)   Konermann, L.; Ahadi, E.; Rodriguez, A. D.; Vahidi, S. Unraveling the Mechanism

of Electrospray Ionization. *Anal. Chem.* **2013**, *85*, 2–9.

(27) Rayleigh, Lord. XX. On the Equilibrium of Liquid Conducting Masses Charged with Electricity. *Philos. Mag. Ser. 5* **1882**, *14*, 184–186.

(28) Dole, M.; Mack, L. L.; Hines, R. L.; Mobley, R. C.; Ferguson, L. D.; Alice, M. B. Molecular Beams of Macroions. *J. Chem. Phys.* **1968**, *49*, 2240–2249.

(29) Mack, L. L.; Kralik, P.; Rheude, A.; Dole, M. Molecular Beams of Macroions. II. *J. Chem. Phys.* **1970**, *52*, 4977–4986.

(30) Iribarne, J. V.; Thomson, B. A. On the Evaporation of Small Ions from Charged Droplets. *J. Chem. Phys.* **1976**, *64*, 2287–2294.

(31) Nguyen, S.; Fenn, J. B. Gas-Phase Ions of Solute Species from Charged Droplets of Solutions. *Proc. Natl. Acad. Sci. U. S. A.* **2007**, *104*, 1111–1117.

(32) Ahadi, E.; Konermann, L. Modeling the Behavior of Coarse-Grained Polymer Chains in Charged Water Droplets: Implications for the Mechanism of Electrospray Ionization. *J. Phys. Chem. B* **2012**, *116*, 104–112.

(33) Consta, S.; Malevanets, A. Classification of the Ejection Mechanisms of Charged Macromolecules from Liquid Droplets. *J. Chem. Phys.* **2013**, *138*, 44314.

(34) Consta, S. Manifestation of Rayleigh Instability in Droplets Containing Multiply Charged Macroions. *J. Phys. Chem. B* **2010**, *114*, 5263–5268.

(35) Iavarone, A. T.; Williams, E. R. Supercharging in Electrospray Ionization: Effects on Signal and Charge. *Int. J. Mass Spectrom.* **2002**, *219*, 63–72.

(36) Douglass, K. A.; Venter, A. R. Investigating the Role of Adducts in Protein Supercharging with Sulfolane. *J. Am. Soc. Mass Spectrom.* **2012**, *23*, 489–497.

(37) Teo, C. A.; Donald, W. A. Solution Additives for Supercharging Proteins beyond the Theoretical Maximum Proton-Transfer Limit in Electrospray Ionization Mass Spectrometry. *Anal. Chem.* **2014**, *86*, 4455–4462.

(38) Wiliams, E. R. Proton Transfer Reactivity of Large Multiply Charged Ions. *J. Mass Spectrom.* **1996**, *31*, 831–842.

(39) McLuckey, S. A.; Glish, G. L.; Van Berkel, G. J. Charge Determination of Product Ions Formed from Collision-Induced Dissociation of Multiply Protonated Molecules via Ion/molecule Reactions. *Anal. Chem.* **1991**, *63*, 1971–1978.

(40) Jockusch, R. A.; Schnier, P. D.; Price, W. D.; Strittmatter, E. F.; Demirev, P. A.; Williams, E. R. Effects of Charge State on Fragmentation Pathways, Dynamics, and Activation Energies of Ubiquitin Ions Measured by Blackbody Infrared Radiative Dissociation. *Anal. Chem.* **1997**, *69*, 1119–1126.

(41) Zubarev, R. A.; Horn, D. M.; Fridriksson, E. K.; Kelleher, N. L.; Kruger, N. A.; Lewis, M. A.; Carpenter, B. K.; McLafferty, F. W. Electron Capture Dissociation for Structural Characterization of Multiply Charged Protein Cations. *Anal. Chem.* **2000**, *72*, 563–573.

(42) Kelleher, N. L. Peer Reviewed: Top-Down Proteomics. *Anal. Chem.* **2004**, *76* (11), 196 A-203 A.

(43) Lomeli, S. H.; Peng, I. X.; Yin, S.; Ogorzalek Loo, R. R.; Loo, J. A. New Reagents for Increasing ESI Multiple Charging of Proteins and Protein Complexes. *J. Am. Soc. Mass Spectrom.* **2010**, *21*, 127–131.

(44) Metwally, H.; McAllister, R. G.; Popa, V.; Konermann, L. Mechanism of Protein

Supercharging by Sulfolane and M-Nitrobenzyl Alcohol: Molecular Dynamics Simulations of the Electrospray Process. *Anal. Chem.* **2016**, *88*, 5345–5354.

(45) Iavarone, A. T.; Williams, E. R. Mechanism of Charging and Supercharging Molecules in Electrospray Ionization. *J. Am. Chem. Soc.* **2003**, *125*, 2319–2327.

(46) Zenaidee, M. A.; Donald, W. A. Extremely Supercharged Proteins in Mass Spectrometry: Profiling the pH of Electrospray Generated Droplets, Narrowing Charge State Distributions, and Increasing Ion Fragmentation. *Analyst* **2015**, *140*, 1894–1905.

(47) Ogorzalek Loo, R. R.; Lakshmanan, R.; Loo, J. A. NIH Public Access. **2014**, *25*, 1675–1693.

(48) Zenaidee, M. A.; Donald, W. A. Extremely Supercharged Proteins in Mass Spectrometry: Profiling the pH of Electrospray Generated Droplets, Narrowing Charge State Distributions, and Increasing Ion Fragmentation. *Analyst* **2015**, *140*, 1894–1905.

(49) Thomson, J. J. Rays of Positive Electricity. *Nature* **1908**, *79*, 52–56.

(50) Herzog, R. F. K.; Viehböck, F. P. Ion Source for Mass Spectrography. *Phys. Rev.* **1949**, *76*, 855–856.

(51) SIMS instrument scheme Wikimedia Commons https://commons.wikimedia.org/wiki/File:SIMS_instrument_scheme_600x600. png (accessed Feb 24, 2018).

(52) Honig, R. E. Sputtering of Surfaces by Positive Ion Beams of Low Energy. *J. Appl. Phys.* **1958**, *29*, 549–555.

(53) Van den Berg, J. Neutral and Ion Beam SIMS of Non-Conducting Materials. *Vacuum* **1986**, *36*, 981–989.

(54) Pachuta, S. J.; Cooks, R. G. Mechanisms in Molecular SIMS. *Chem. Rev.* **1987**, *87*, 647–669.

(55) Allen, J. S. The Detection of Single Positive Ions, Electrons and Photons by a Secondary Electron Multiplier. *Phys. Rev.* **1939**, *55*, 966–971.

(56) Brown, K. L.; Tautfest, G. W. Faraday-Cup Monitors for High-Energy Electron Beams. *Rev. Sci. Instrum.* **1956**, *27*, 696–702.

(57) Denvir, D. J.; Conroy, E. Electron-Multiplying CCD: The New ICCD. *Proc. SPIE* **2003**, *4796*, 164–174.

(58) De Vree, G. A.; Westra, A. H.; Moody, I.; Van Have, F. Der; Ligtvoet, K. M.; Beekman, F. J. Photon-Counting Gamma Camera Based on an Electron-Multiplying CCD. *IEEE Trans. Nucl. Sci.* **2005**, *52*, 580–588.

(59) Burkhardt, M.; Schwille, P. Electron Multiplying CCD Based Detection for Spatially Resolved Fluorescence Correlation Spectroscopy. *Opt. Express* **2006**, *14*, 5013–5020.

(60) Abt, D.; Schmidt, B. V. K. J.; Pop-Georgievski, O.; Quick, A. S.; Danilov, D.; Kostina, N. Y.; Bruns, M.; Wenzel, W.; Wegener, M.; Rodriguez-Emmenegger, C.; et al. Designing Molecular Printboards: A Photolithographic Platform for Recodable Surfaces. *Chem. - A Eur. J.* **2015**, *21*, 13186–13190.

(61) Kaupp, M.; Quick, A. S.; Rodriguez-Emmenegger, C.; Welle, A.; Trouillet, V.; Pop-Georgievski, O.; Wegener, M.; Barner-Kowollik, C. Photo-Induced

Functionalization of Spherical and Planar Surfaces via Caged Thioaldehyde End-Functional Polymers. *Adv. Funct. Mater.* **2014**, *24*, 5649–5661.

(62)   Altintas, O.; Glassner, M.; Rodriguez-Emmenegger, C.; Welle, A.; Trouillet, V.; Barner-Kowollik, C. Macromolecular Surface Design: Photopatterning of Functional Stable Nitrile Oxides. *Angew. Chemie - Int. Ed.* **2015**, *54*, 5777–5783.

(63)   Stolzer, L.; Quick, A. S.; Abt, D.; Welle, A.; Naumenko, D.; Lazzarino, M.; Wegener, M.; Barner-Kowollik, C.; Fruk, L. Photo-Induced Surface Encoding of Gold Nanoparticles. *Chem. Commun.* **2015**, *51*, 3363–3366.

(64)   Quick, A. S.; Rothfuss, H.; Welle, A.; Richter, B.; Fischer, J.; Wegener, M.; Barner-Kowollik, C. Fabrication and Spatially Resolved Functionalization of 3D Microstructures via Multiphoton-Induced Diels-Alder Chemistry. *Adv. Funct. Mater.* **2014**, *24*, 3571–3580.

(65)   Lang, C.; Bestgen, S.; Welle, A.; Müller, R.; Roesky, P. W.; Barner-Kowollik, C. Photolithographic Encoding of Metal Complexes. *Chem. - A Eur. J.* **2015**, *21*, 14728–14731.

(66)   Blasco, E.; Yameen, B.; Quick, A. S.; Krolla-Sidenstein, P.; Welle, A.; Wegener, M.; Barner-Kowollik, C. Designing π-Conjugated Polymeric Nano- and Microstructures via Light Induced Chemistry. *Macromolecules* **2015**, *48*, 8718–8728.

(67)   Claus, T. K.; Richter, B.; Hahn, V.; Welle, A.; Kayser, S.; Wegener, M.; Bastmeyer, M.; Delaittre, G.; Barner-Kowollik, C. Simultaneous Dual Encoding of Three-Dimensional Structures by Light-Induced Modular Ligation. *Angew. Chemie - Int. Ed.* **2016**, *55*, 3817–3822.

(68)   Brooks, D. E.; Haynes, C. A.; Hritcu, D.; Steels, B. M.; Müller, W. Size Exclusion Chromatography Does Not Require Pores. *Proc. Natl. Acad. Sci. U. S. A.* **2000**, *97*, 7064–7067.

(69)   Pasch, H. Hyphenated Techniques in Liquid Chromatography of Polymers; Springer, Berlin, Heidelberg, 2000; pp 1–66.

(70)   Gruendling, T.; Guilhaus, M.; Barner-Kowollik, C. Quantitative LC–MS of Polymers: Determining Accurate Molecular Weight Distributions by Combined Size Exclusion Chromatography and Electrospray Mass Spectrometry with Maximum Entropy Data Processing. *Anal. Chem.* **2008**, *80*, 6915–6927.

(71)   Falkenhagen, J.; Much, H.; Stauf, W.; Müller, A. H. E. Characterization of Block Copolymers by Liquid Adsorption Chromatography at Critical Conditions. 1. Diblock Copolymers. *Macromolecules* **2000**, *33*, 3687–3693.

(72)   Falkenhagen, J.; Friedrich, J. F.; Schulz, G.; Krüger, R.-P.; Much, H.; Weidner, S. Liquid Adsorption Chromatography near Critical Conditions of Adsorption Coupled with Matrix-Assisted Laser Desorption/Ionization Mass Spectrometry. *Int. J. Polym. Anal. Charact.* **2000**, *5*, 549–562.

(73)   Kowalczyk, K.; Spychaj, T.; Krala, G. High-Build Alkyd Urethane Coating Materials with a Partially Solvolyzed Waste Polyurethane Foam. *Polym. Eng. Sci.* **2015**, *55*, 2174–2183.

(74)   Gerber, F.; Krummen, M.; Potgeter, H.; Roth, A.; Siffrin, C.; Spoendlin, C. Practical Aspects of Fast Reversed-Phase High-Performance Liquid Chromatography Using 3 Mm Particle Packed Columns and Monolithic Columns in Pharmaceutical Development and Production Working under Current Good

Manufacturing Practice. *J. Chromatogr. A* **2004**, *1036*, 127–133.

(75) James E. Mark. *Physical Properties of Polymers Handbook*; Springer, 2007.

(76) Flory, P. J. Spatial Configuration of Macromolecular Chains. *Nobel Lect.* **1974**, 156–177.

(77) Paul-Dauphin, S.; Karaca, F.; Morgan, T. J.; Millan-Agorio, M.; Herod, A. A.; Kandiyoti, R. Probing Size Exclusion Mechanisms of Complex Hydrocarbon Mixtures: The Effect of Altering Eluent Compositions. *Energy & Fuels* **2007**, *21*, 3484–3489.

(78) Lustig, S. R. Peak-Referenced Integral Method for Size Exclusion Chromatography and Its Application to Aromatic Polyesters. *J. Chromatogr. A* **1999**, *839*, 1–14.

(79) Grubisic, Z.; Rempp, P.; Benoit, H. A Universal Calibration for Gel Permeation Chromatography. *J. Polym. Sci. Part B Polym. Lett.* **1967**, *5*, 753–759.

(80) Zimm, B. H. Apparatus and Methods for Measurement and Interpretation of the Angular Variation of Light Scattering; Preliminary Results on Polystyrene Solutions. *J. Chem. Phys.* **1948**, *16*, 1099–1116.

(81) Page, J. S.; Marginean, I.; Baker, E. S.; Kelly, R. T.; Tang, K.; Smith, R. D. Biases in Ion Transmission through an Electrospray Ionization-Mass Spectrometry Capillary Inlet. *J. Am. Soc. Mass Spectrom.* **2009**, *20*, 2265–2272.

(82) Gruendling, T.; Voll, D.; Guilhaus, M.; Barner-Kowollik, C. A Perfect Couple: PLP/SEC/ESI-MS for the Accurate Determination of Propagation Rate Coefficients in Free Radical Polymerization. *Macromol. Chem. Phys.* **2010**, *211*, 80–90.

(83) Frick, E.; Anastasaki, A.; Haddleton, D. M.; Barner-Kowollik, C. Enlightening the Mechanism of Copper Mediated PhotoRDRP via High-Resolution Mass Spectrometry. *J. Am. Chem. Soc.* **2015**, *137*, 6889–6896.

(84) Fast, D. E.; Zalibera, M.; Lauer, A.; Eibel, A.; Schweigert, C.; Kelterer, A.-M.; Spichty, M.; Neshchadin, D.; Voll, D.; Ernst, H.; et al. Bis(mesitoyl)phosphinic Acid: Photo-Triggered Release of Metaphosphorous Acid in Solution. *Chem. Commun.* **2016**, *52*, 9917–9920.

(85) Hurrle, S.; Lauer, A.; Gliemann, H.; Mutlu, H.; Wöll, C.; Goldmann, A. S.; Barner-Kowollik, C. Two-in-One: λ-Orthogonal Photochemistry on a Radical Photoinitiating System. *Macromol. Rapid Commun.* **2017**, *38*, 1600598.

(86) Lauer, A.; Fast, D. E.; Steinkoenig, J.; Kelterer, A.-M.; Gescheidt, G.; Barner-Kowollik, C. Wavelength-Dependent Photochemical Stability of Photoinitiator-Derived Macromolecular Chain Termini. *ACS Macro Lett.* **2017**, *6*, 952–958.

(87) Jöckle, P.; Schweigert, C.; Lamparth, I.; Moszner, N.; Unterreiner, A.-N.; Barner-Kowollik, C. An In-Depth Mechanistic Investigation of the Radical Initiation Behavior of Monoacylgermanes. *Macromolecules* **2017**, *50*, 8894–8906.

(88) Flory, P. J. *In Principles of Polymer Chemistry*, First Edit.; Cornell University Press: Ithaca, 1953.

(89) Odian, G. *Principles of Polymerization*, Third Edit.; John Wiley & Sons, Inc.: New York, 1991.

(90) Polymer Properties Database. Polycarbonates http://polymerdatabase.com/polymer classes/Polycarbonate type.html (accessed Dec 14, 2017).

192

(91)   Polymer Properties Database. Polyamides http://polymerdatabase.com/polymer classes/Polyamide type.html (accessed Dec 14, 2017).

(92)   Polymer Properties Database. Polystyrenes http://polymerdatabase.com/polymer classes/polystyrene type.html (accessed Dec 14, 2017).

(93)   Polymer Properties Database. Polymethacrylates http://polymerdatabase.com/polymer classes/Polymethacrylate type.html (accessed Dec 14, 2017).

(94)   Hsieh, H.; Quirk, R. *Anionic Polymerization: Principles and Practical Applications*; Marcel Dekker, Inc: New York, 1996.

(95)   Szwarc, M. "Living" Polymers. *Nature* **1956**, *178*, 1168–1169.

(96)   Barner-Kowollik, C.; Russell, G. T. Chain-Length-Dependent Termination in Radical Polymerization: Subtle Revolution in Tackling a Long-Standing Challenge. *Progress in Polymer Science (Oxford)*. Pergamon November 1, 2009, pp 1211–1259.

(97)   *Handbook of Radical Polymerization*; Matyjaszewski, K., Davis, T. P., Eds.; John Wiley & Sons, Inc.: Hoboken, NJ, USA, 2002.

(98)   Rodlert, M.; Harth, E.; Rees, I.; Hawker, C. J. End- group Fidelity in Nitroxide-mediated Living Free- radical Polymerizations. *J. Polym. Sci. Part A Polym. Chem.* **2000**, *38*, 4749–4763.

(99)   Studer, A.; Schulte, T. Nitroxide-Mediated Radical Processes. *Chem. Rec.* **2005**, *5*, 27–35.

(100) Moad, G.; Rizzardo, E. Alkoxyamine-Initiated Living Radical Polymerization: Factors Affecting Alkoxyamine Homolysis Rates. *Macromolecules* **1995**, *28*, 8722–8728.

(101) Wang, J. S.; Matyjaszewski, K. Controlled/"Living" Radical Polymerization. Atom Transfer Radical Polymerization in the Presence of Transition-Metal Complexes. *J. Am. Chem. Soc.* **1995**, *117*, 5614–5615.

(102) Kato, M.; Kamigaito, M.; Sawamoto, M.; Higashimura, T. Polymerization of Methyl Methacrylate with the Carbon Tetrachloride/Dichlorotris-(triphenylphosphine)ruthenium(II)/Methylaluminum Bis(2,6-Di-Tert-Butylphenoxide) Initiating System: Possibility of Living Radical Polymerization. *Macromolecules* **1995**, *28*, 1721–1723.

(103) Coote, M. L. Ab Initio Study of the Addition-Fragmentation Equilibrium in RAFT Polymerization: When Is Polymerization Retarded? *Macromolecules* **2004**, *37*, 5023–5031.

(104) Moad, G.; Chong, Y. K.; Postma, A.; Rizzardo, E.; Thang, S. H. Advances in RAFT Polymerization: The Synthesis of Polymers with Defined End-Groups. *Polymer* **2005**, *46*, 8458–8468.

(105) McCormick, C. L.; Lowe, A. B. Aqueous RAFT Polymerization: Recent Developments in Synthesis of Functional Water-Soluble (Co)polymers with Controlled Structures. *Acc. Chem. Res.* **2004**, *37*, 312–325.

(106) Lutz, J.-F. Sequence-Controlled Polymerizations: The next Holy Grail in Polymer Science? *Polym. Chem.* **2010**, *1*, 55.

(107) Nuyken, O.; Pask, S. D. Ring-Opening Polymerization-An Introductory Review. *Polymers (Basel)*. **2013**, *5*, 361–403.

(108) Dove, A. P. Controlled Ring-Opening Polymerisation of Cyclic Esters: Polymer Blocks in Self-Assembled Nanostructures. *Chem. Commun.* **2008**, *0*, 6446.

(109) Mori, H.; Masuda, S.; Endo, T. Ring-Opening RAFT Polymerization Based on Aromatization as Driving Force: Synthesis of Well-Defined Polymers Containing Anthracene Units in the Main Chain. *Macromolecules* **2006**, *39*, 5976–5978.

(110) Nuyken, O.; Pask, S. D. Ring-Opening Polymerization-An Introductory Review. *Polymers (Basel)*. **2013**, *5*, 361–403.

(111) Paul, S.; Zhu, Y.; Romain, C.; Brooks, R.; Saini, P. K.; Williams, C. K. Ring-Opening Copolymerization (ROCOP): Synthesis and Properties of Polyesters and Polycarbonates. *Chem. Commun.* **2015**, *51*, 6459–6479.

(112) Spears, B. R.; Marin, M. A.; Montenegro-Burke, J. R.; Evans, B. C.; McLean, J.; Harth, E. Aqueous Epoxide Ring-Opening Polymerization (AEROP): Green Synthesis of Polyglycidol with Ultralow Branching. *Macromolecules* **2016**, *49*, 2022–2027.

(113) Dubois, P.; Coulembier, O.; Raquez, J.-M. *Handbook of Ring-Opening Polymerization*; Wiley-VCH: Weinheim, 2009.

(114) Immordino, M. L.; Dosio, F.; Cattel, L. Stealth Liposomes: Review of the Basic Science, Rationale, and Clinical Applications, Existing and Potential. *International Journal of Nanomedicine*. Dove Press 2006, pp 297–315.

(115) Saegusa, T. Spontaneous Alternating Copolymerization. *Angew. Chemie Int. Ed.* **1977**, *16*, 826–835.

(116) Kempe, K.; de Jongh, P. A. J. M.; Anastasaki, A.; Wilson, P.; Haddleton, D. M. Novel Comb Polymers from Alternating N-Acylated Poly(aminoester)s Obtained by Spontaneous Zwitterionic Copolymerisation. *Chem. Commun.* **2015**, *51*, 16213–16216.

(117) Hoogenboom, R. Poly(2-Oxazoline)s: A Polymer Class with Numerous Potential Applications. *Angew. Chemie Int. Ed.* **2009**, *48*, 7978–7994.

(118) De La Rosa, V. R. Poly(2-Oxazoline)s as Materials for Biomedical Applications. *J. Mater. Sci. Mater. Med.* **2014**, *25*, 1211–1225.

(119) Luxenhofer, R.; Han, Y.; Schulz, A.; Tong, J.; He, Z.; Kabanov, A. V; Jordan, R. Poly(2-Oxazoline)s as Polymer Therapeutics. *Macromol. Rapid Commun.* **2012**, *33*, 1613–1631.

(120) Wilson, P.; Ke, P. C.; Davis, T. P.; Kempe, K. Poly(2-Oxazoline)-Based Micro- and Nanoparticles: A Review. *Eur. Polym. J.* **2017**, *88*, 486–515.

(121) Kempe, K. Chain and Step Growth Polymerizations of Cyclic Imino Ethers: From Poly(2-Oxazoline)s to Poly(ester Amide)s. *Macromol. Chem. Phys.* **2017**, *218*, 1–17.

(122) Winnacker, M.; Rieger, B. Poly(ester Amide)s: Recent Insights into Synthesis, Stability and Biomedical Applications. *Polym. Chem.* **2016**, *7*, 7039–7046.

(123) Fonseca, A. C.; Gil, M. H.; Simões, P. N. Biodegradable Poly(ester Amide)s - A Remarkable Opportunity for the Biomedical Area: Review on the Synthesis, Characterization and Applications. *Prog. Polym. Sci.* **2014**, *39*, 1291–1311.

(124) Rodriguez-Galan, A.; Franco, L.; Puiggali, J. Degradable Poly(ester Amide)s for Biomedical Applications. *Polymer* **2011**, *3*, 65–99.

(125) Díaz, A.; Katsarava, R.; Puiggalí, J. Synthesis, Properties and Applications of Biodegradable Polymers Derived from Diols and Dicarboxylic Acids: From Polyesters to Poly(ester Amide)s. *Int. J. Mol. Sci.* **2014**, *15*, 7064–7123.

(126) Palmer, R. J. *Polyamides, Plastics*; John Wiley & Sons, Inc.: Hoboken, NJ, USA, 2001; Vol. 3.

(127) Diels, O.; Alder, K. Synthesen in Der Hydroaromatischen Reihe, V. Mitteilung: Ueber delts4-Tetrahydro-O-Phthhalsaeure (Stellungnahme Zu Der Mitteilung von E. H. Farmer Und F. L .Warren: Eigenschaften Konjugierter Doppelbindungen, VII.). *Ber. dtsch. Chem. Ges.* **1929**, *62*, 2087–2090.

(128) Diels, O.; Alder, K. Syntesen in Der Hyrdoaromatischen Reihe, IV. Mitteilung: Ueber Die Anlagerung von Maleinsaeure-Anhydrid an Arylierte Diene, Triene Und Fulvene. *Ber. dtsch. Chem. Ges.* **1929**, *62*, 2081–2087.

(129) Diels, O.; Alder, K. Synthesen in Der Hydroaromatischen Reihe. III. Mitteilung: Synthese von Terpenen, Camphern, Hydroaromatischen Und Heterocyclischen Systemen. Mitbearbeitet von Den Herren Wolfgang L??bbert, Erich Naujoks, Franz Querberitz, Karl R??hl, Harro Segeberg. *Justus Liebigs Ann. Chem.* **1929**, *470*, 62–103.

(130) Diels, O.; Alder, K. Synthesen in Der Hydro-Aromatischen Reihe, II. Mitteilung: Über Cantharidin. *Berichte der Dtsch. Chem. Gesellschaft (A B Ser.* **1929**, *62*, 554–562.

(131) Diels, O.; Alder, K. Synthese Der Hydroaromatischen Reihe 13. *Justus Liebigs Ann. Chem.* **1931**, *490*, 257–266.

(132) Nobelprize.org. The Nobel Prize in Chemistry 1950 https://www.nobelprize.org/nobel_prizes/chemistry/laureates/1950/ (accessed Dec 18, 2017).

(133) Dewar, M. J. S.; Stewart, J. J. P.; Olivella, S. Mechanism of the Diels-Alder Reaction: Reactions of Butadiene with Ethylene and Cyanoethylenes. *J. Am. Chem. Soc.* **1986**, *108*, 5771–5779.

(134) Brandt, J.; Oehlenschlaeger, K. K.; Schmidt, F. G.; Barner-Kowollik, C.; Lederer, A. State-of-the-Art Analytical Methods for Assessing Dynamic Bonding Soft Matter Materials. *Advanced Materials*. September 1, 2014, pp 5758–5785.

(135) Pahnke, K.; Brandt, J.; Gryn'ova, G.; Lindner, P.; Schweins, R.; Schmidt, F. G.; Lederer, A.; Coote, M. L.; Barner-Kowollik, C. Entropy Driven Chain Effects on Ligation Chemistry. *Chem. Sci.* **2015**, *6*, 1061–1074.

(136) Guimard, N. K.; Ho, J.; Brandt, J.; Lin, C. Y.; Namazian, M.; Mueller, J. O.; Oehlenschlaeger, K. K.; Hilf, S.; Lederer, A.; Schmidt, F. G.; et al. Harnessing Entropy to Direct the Bonding/debonding of Polymer Systems Based on Reversible Chemistry. *Chem. Sci.* **2013**, *4*, 2752.

(137) Mutlu, H.; Schmitt, C. W.; Jasinski, N.; Woehlk, H.; Fairfull-Smith, K.; Blinco, J. P.; Barner-Kowollik, C. Spin Fluorescence Silencing Enables an Efficient Thermally Driven Self-Reporting Polymer Release System. *Polym. Chem.* **2017**, *8*, 6199–6203.

(138) Oehlenschlaeger, K. K.; Guimard, N. K.; Brandt, J.; Mueller, J. O.; Lin, C. Y.; Hilf, S.; Lederer, A.; Coote, M. L.; Schmidt, F. G.; Barner-Kowollik, C. Fast and

Catalyst-Free Hetero-Diels–Alder Chemistry for on Demand Cyclable Bonding/debonding Materials. *Polym. Chem.* **2013**, *4*, 4348.

(139) de Jongh, P. A. J. M.; Bennett, M. R.; Sulley, G. S.; Wilson, P.; Davis, T. P.; Haddleton, D. M.; Kempe, K. Facile One-Pot/one-Step Synthesis of Heterotelechelic N-Acylated Poly(aminoester) Macromonomers for Carboxylic Acid Decoracted Comb Polymers. *Polym. Chem.* **2016**, *7*, 6703–6707.

(140) De Jongh, P. A. J. M.; Mortiboy, A.; Sulley, G. S.; Bennett, M. R.; Anastasaki, A.; Wilson, P.; Haddleton, D. M.; Kempe, K. Dual Stimuli-Responsive Comb Polymers from Modular N-Acylated Poly(aminoester)-Based Macromonomers. *ACS Macro Lett.* **2016**, *5*, 321–325.

(141) Strecker, A. Ueber Die Künstliche Bildung Der Milchsäure Und Einen Neuen, Dem Glycocoll Homologen Körper; *Justus Liebigs Ann. Chem.* **1850**, *75*, 27–45.

(142) Ramozzi, R.; Morokuma, K. Revisiting the Passerini Reaction Mechanism: Existence of the Nitrilium, Organocatalysis of Its Formation, and Solvent Effect. *J. Org. Chem.* **2015**, *80*, 5652–5657.

(143) Banfi, L.; Riva, R.; Banfi, L.; Riva, R. The Passerini Reaction. In *Organic Reactions*; John Wiley & Sons, Inc.: Hoboken, NJ, USA, 2005; pp 1–140.

(144) Kreye, O.; Tóth, T.; Meier, M. A. R. Introducing Multicomponent Reactions to Polymer Science: Passerini Reactions of Renewable Monomers. *J. Am. Chem. Soc.* **2011**, *133*, 1790–1792.

(145) Oelmann, S.; Solleder, S. C.; Meier, M. A. R. Controlling Molecular Weight and Polymer Architecture during the Passerini Three Component Step-Growth Polymerization. *Polym. Chem.* **2016**, *7*, 1857–1860.

(146) Li, L.; Lv, A.; Deng, X.-X.; Du, F.-S.; Li, Z.-C. Facile Synthesis of Photo-Cleavable Polymers via Passerini Reaction. *Chem. Commun.* **2013**, *49*, 8549.

(147) Sehlinger, A.; Schneider, R.; Meier, M. A. R. Passerini Addition Polymerization of an AB-Type Monomer - A Convenient Route to Versatile Polyesters. *Eur. Polym. J.* **2014**, *50*, 150–157.

(148) Pimpin, A.; Srituravanich, W. Reviews on Micro- and Nanolithography Techniques and Their Applications. *Eng. J.* **2012**, *16*, 37–55.

(149) Flemming, H. C. Biofouling in Water Systems - Cases, Causes and Countermeasures. *Appl. Microbiol. Biotechnol.* **2002**, *59*, 629–640.

(150) Zhang, H.; Chiao, M. Anti-Fouling Coatings of Poly(dimethylsiloxane) Devices for Biological and Biomedical Applications. *J. Med. Biol. Eng.* **2015**, *35*, 143–155.

(151) Roy, D.; Semsarilar, M.; Guthrie, J. T.; Perrier, S. Cellulose Modification by Polymer Grafting: A Review. *Chem. Soc. Rev.* **2009**, *38*, 2046.

(152) Roeder, R. D.; Garcia-Valdez, O.; Whitney, R. A.; Champagne, P.; Cunningham, M. F. Graft Modification of Cellulose Nanocrystals via Nitroxide-Mediated Polymerisation. *Polym. Chem.* **2016**, *7*, 6383–6390.

(153) Minko, S. Grafting on Solid Surfaces: Grafting to and Grafting from Methods. In *Polymer Surfaces and Interfaces: Characterization, Modification and Applications*; Springer Berlin Heidelberg: Berlin, Heidelberg, 2008; pp 215–234.

(154) Grande, C. D.; Tria, M. C.; Felipe, M. J.; Zuluaga, F.; Advincula, R. RAFT "grafting-Through" approach to Surface-Anchored Polymers: Electrodeposition of an Electroactive Methacrylate Monomer. *Eur. Phys. J. E* **2011**, *34*, 15.

(155) Ma, M.; Zheng, S.; Chen, H.; Yao, M.; Zhang, K.; Jia, X.; Mou, J.; Xu, H.; Wu, R.; Shi, J. A Combined "RAFT" and "Graft From" Polymerization Strategy for Surface Modification of Mesoporous Silica Nanoparticles: Towards Enhanced Tumor Accumulation and Cancer Therapy Efficacy. *J. Mater. Chem. B* **2014**, *2*, 5828–5836.

(156) Matyjaszewski, K.; Hongchen, D.; Jakubowski, W.; Pietrasik, J.; Kusumo, A. Grafting from Surfaces For "everyone": ARGET ATRP in the Presence of Air. *Langmuir* **2007**, *23*, 4528–4531.

(157) Carlmark, A.; Malmström, E. E. ATRP Grafting from Cellulose Fibers to Create Block-Copolymer Grafts. *Biomacromolecules* **2003**, *4*, 1740–1745.

(158) Zammarelli, N.; Luksin, M.; Raschke, H.; Hergenröder, R.; Weberskirch, R. "grafting-from" Polymerization of PMMA from Stainless Steel Surfaces by a Raft-Mediated Polymerization Process. *Langmuir* **2013**, *29*, 12834–12843.

(159) Mueller, P.; Zieger, M. M.; Richter, B.; Quick, A. S.; Fischer, J.; Mueller, J. B.; Zhou, L.; Nienhaus, G. U.; Bastmeyer, M.; Barner-Kowollik, C.; et al. Molecular Switch for Sub-Diffraction Laser Lithography by Photoenol Intermediate-State Cis–Trans Isomerization. *ACS Nano* **2017**, *11*, 6396–6403.

(160) Wasserscheid, P.; Welton, T. *Ionic Liquid in Synthesis*; 2008.

(161) Wilkes, J. S. A Short History of Ionic Liquids—from Molten Salts to Neoteric Solvents. *Green Chem.* **2002**, *4*, 73–80.

(162) Mecerreyes, D. Polymeric Ionic Liquids: Broadening the Properties and Applications of Polyelectrolytes. *Prog. Polym. Sci.* **2011**, *36*, 1629–1648.

(163) Lu, J.; Yan, F.; Texter, J. Advanced Applications of Ionic Liquids in Polymer Science. *Prog. Polym. Sci.* **2009**, *34*, 431–448.

(164) Yan, F.; Texter, J. Solvent-Reversible Poration in Ionic Liquid Copolymers. *Angew. Chemie - Int. Ed.* **2007**, *46* (14), 2440–2443.

(165) Greaves, T. L.; Drummond, C. J. Protic Ionic Liquids : Properties and Applications. **2008**, 206–237.

(166) Hunt, P. A.; Ashworth, C. R.; Matthews, R. P. Hydrogen Bonding in Ionic Liquids. *Chem. Soc. Rev.* **2015**, *44*, 1257–1288.

(167) Isik, M.; Sardon, H.; Mecerreyes, D. Ionic Liquids and Cellulose: Dissolution, Chemical Modification and Preparation of New Cellulosic Materials. *Int. J. Mol. Sci.* **2014**, *15*, 11922–11940.

(168) Zhang, J.; Wu, J.; Yu, J.; Zhang, X.; He, J.; Zhang, J. Application of Ionic Liquids for Dissolving Cellulose and Fabricating Cellulose-Based Materials: State of the Art and Future Trends. *Mater. Chem. Front.* **2017**, *1*, 1273–1290.

(169) Yuan, J.; Antonietti, M. Poly(ionic Liquid)s: Polymers Expanding Classical Property Profiles. *Polymer* **2011**, *52*, 1469–1482.

(170) Yuan, J.; Mecerreyes, D.; Antonietti, M. Poly(ionic Liquid)s: An Update. *Prog. Polym. Sci.* **2013**, *38*, 1009–1036.

(171) Johann, C.; Elsenberg, S.; Roesch, U.; Rambaldi, D. C.; Zattoni, A.; Reschiglian, P. A Novel Approach to Improve Operation and Performance in Flow Field-Flow Fractionation. *J. Chromatogr. A* **2011**, *1218*, 4126–4131.

(172) Ghirlando, R. The Analysis of Macromolecular Interactions by Sedimentation

Equilibrium. *Methods* **2011**, *54*, 145–156.

(173) Dobrynin, A. V.; Rubinstein, M. Theory of Polyelectrolytes in Solutions and at Surfaces. *Prog. Polym. Sci.* **2005**, *30*, 1049–1118.

(174) Coupillaud, P.; Pinaud, J.; Guidolin, N.; Vignolle, J.; Fèvre, M.; Veaudecrenne, E.; Mecerreyes, D.; Taton, D. Poly(ionic Liquid)s Based on Imidazolium Hydrogen Carbonate Monomer Units as Recyclable Polymer-Supported N-Heterocyclic Carbenes: Use in Organocatalysis. *J. Polym. Sci. Part A Polym. Chem.* **2013**, *51*, 4530–4540.

(175) He, H.; Zhong, M.; Adzima, B.; Luebke, D.; Nulwala, H.; Matyjaszewski, K. A Simple and Universal Gel Permeation Chromatography Technique for Precise Molecular Weight Characterization of Well-Defined Poly(ionic Liquid)s. *J. Am. Chem. Soc.* **2013**, *135*, 4227–4230.

(176) Karjalainen, E.; Izquierdo, D. F.; Martí-Centelles, V.; Luis, S. V.; Tenhu, H.; García-Verdugo, E. An Enzymatic Biomimetic System: Enhancement of Catalytic Efficiency with New Polymeric Chiral Ionic Liquids Synthesised by Controlled Radical Polymerisation. *Polym. Chem.* **2014**, *5*, 1437–1446.

(177) Karplus, M.; Weaver, D. L. Protein-Folding Dynamics. *Nature* **1976**, *260*, 404–406.

(178) Lehto, T.; Wagner, E. Sequence-Defined Polymers for the Delivery of Oligonucleotides. *Nanomedicine* **2014**, *9*, 2843–2859.

(179) Zydziak, N.; Konrad, W.; Feist, F.; Afonin, S.; Weidner, S.; Barner-Kowollik, C. Coding and Decoding Libraries of Sequence-Defined Functional Copolymers Synthesized via Photoligation. *Nat. Commun.* **2016**, *7*, 13672.

(180) Altintas, O.; Barner-Kowollik, C. Single Chain Folding of Synthetic Polymers by Covalent and Non-Covalent Interactions: Current Status and Future Perspectives. *Macromol. Rapid Commun.* **2012**, *33*, 958–971.

(181) Altintas, O.; Barner-Kowollik, C. Single-Chain Folding of Synthetic Polymers: A Critical Update. *Macromol. Rapid Commun.* **2016**, *37*, 29–46.

(182) Sanchez-Sanchez, A.; Pomposo, J. A. Single-Chain Polymer Nanoparticles via Non-Covalent and Dynamic Covalent Bonds. *Part. Part. Syst. Charact.* **2014**, *31*, 11–23.

(183) Lyon, C. K.; Prasher, A.; Hanlon, A. M.; Tuten, B. T.; Tooley, C. A.; Frank, P. G.; Berda, E. B. A Brief User's Guide to Single-Chain Nanoparticles. *Polym. Chem.* **2014**, *6*, 181–197.

(184) Mavila, S.; Eivgi, O.; Berkovich, I.; Lemcoff, N. G. Intramolecular Cross-Linking Methodologies for the Synthesis of Polymer Nanoparticles. *Chem. Rev.* **2016**, *116*, 878–961.

(185) Hanlon, A. M.; Lyon, C. K.; Berda, E. B. What Is Next in Single-Chain Nanoparticles? *Macromolecules* **2016**, *49*, 2–14.

(186) Ouchi, M.; Badi, N.; Lutz, J.-F.; Sawamoto, M. Single-Chain Technology Using Discrete Synthetic Macromolecules. *Nat. Chem.* **2011**, *3*, 917–924.

(187) Niemeyer, C. M. Biotechnology Meets Materials Science. *Mater. Sci.* **2001**, *40*, 4128–4158.

(188) Willenbacher, J.; Wuest, K. N. R.; Mueller, J. O.; Kaupp, M.; Wagenknecht, H. A.; Barner-Kowollik, C. Photochemical Design of Functional Fluorescent Single-

Chain Nanoparticles. *ACS Macro Lett.* **2014**, *3*, 574–579.

(189) Terashima, T.; Mes, T.; De Greef, T. F. A.; Gillissen, M. A. J.; Besenius, P.; Palmans, A. R. A.; Meijer, E. W. Single-Chain Folding of Polymers for Catalytic Systems in Water. *J. Am. Chem. Soc.* **2011**, *133*, 4742–4745.

(190) Davankov, V. A.; Ilyin, M. M.; Tsyurupa, M. P.; Timofeeva, G. I.; Dubrovina, L. V. From a Dissolved Polystyrene Coil to an Intramolecularly-Hyper-Cross-Linked `Nanosponge'. *Macromolecules* **1996**, *29*, 8398–8403.

(191) Dukette, T. E.; Mackay, M. E.; Van Horn, B.; Wooley, K. L.; Drockenmuller, E.; Malkoch, M.; Hawker, C. J. Conformation of Intramolecularly Cross-Linked Polymer Nanoparticles on Solid Substrates. *Nano Lett.* **2005**, *5*, 1704–1709.

(192) Tuteja, A.; Mackay, M. E.; Hawker, C. J.; Van Horn, B.; Ho, D. L. Molecular Architecture and Rheological Characterization of Novel Intramolecularly Crosslinked Polystyrene Nanoparticles. *J. Polym. Sci. Part B Polym. Phys.* **2006**, *44*, 1930–1947.

(193) Harth, E.; Van Horn, B.; Lee, V. Y.; Germack, D. S.; Gonzales, C. P.; Miller, R. D.; Hawker, C. J. A Facile Approach to Architecturally Defined Nanoparticles via Intramolecular Chain Collapse. *J. Am. Chem. Soc.* **2002**, *124*, 8653–8660.

(194) Heiler, C.; Offenloch, J. T.; Blasco, E.; Barner-Kowollik, C. Photochemically Induced Folding of Single Chain Polymer Nanoparticles in Water. *ACS Macro Lett.* **2017**, *6*, 56–61.

(195) Claus, T. K.; Zhang, J.; Martin, L.; Hartlieb, M.; Mutlu, H.; Perrier, S.; Delaittre, G.; Barner-Kowollik, C. Stepwise Light-Induced Dual Compaction of Single-Chain Nanoparticles. *Macromol. Rapid Commun.* **2017**, *38*, 1700264.

(196) Wuest, K. N. R.; Lu, H.; Thomas, D. S.; Goldmann, A. S.; Stenzel, M. H.; Barner-Kowollik, C. Fluorescent Glyco Single-Chain Nanoparticle-Decorated Nanodiamonds. *ACS Macro Lett.* **2017**, *6*, 1168–1174.

(197) Offenloch, J. T.; Willenbacher, J.; Tzvetkova, P.; Heiler, C.; Mutlu, H.; Barner-Kowollik, C. Degradable Fluorescent Single-Chain Nanoparticles Based on Metathesis Polymers. *Chem. Commun.* **2017**, *53*, 775–778.

(198) Mecerreyes, D.; Lee, V.; Hawker, C. J.; Hedrick, J. L.; Wursch, A.; Volksen, W.; Magbitang, T.; Huang, E.; Miller, R. D. Novel Approach to Functionalized Nanoparticles: Self-Crosslinking of Macromolecules in Ultradilute Solution. *Adv. Mater.* **2001**, *13*, 204–208.

(199) Jiang, J.; Thayumanavan, S. Synthesis and Characterization of Amine-Functionalized Polystyrene Nanoparticles. *Macromolecules* **2005**, *38*, 5886–5891.

(200) Beck, J. B.; Killops, K. L.; Kang, T.; Sivanandan, K.; Bayles, A.; Mackay, M. E.; Wooley, K. L.; Hawker, C. J. Facile Preparation of Nanoparticles by Intramolecular Cross-Linking of Isocyanate Functionalized Copolymers. *Macromolecules* **2009**, *42*, 5629–5635.

(201) Perez-Baena, I.; Barroso-Bujans, F.; Gasser, U.; Arbe, A.; Moreno, A. J.; Colmenero, J.; Pomposo, J. a. Endowing Single-Chain Polymer Nanoparticles with Enzyme-Mimetic Activity. *ACS Macro Lett.* **2013**, *2*, 775–779.

(202) Altintas, O.; Willenbacher, J.; Wuest, K. N. R.; Oehlenschlaeger, K. K.; Krolla-Sidenstein, P.; Gliemann, H.; Barner-Kowollik, C. A Mild and Efficient Approach to Functional Single-Chain Polymeric Nanoparticles via Photoinduced Diels-Alder

Ligation. *Macromolecules* **2013**, *46*, 8092–8101.

(203) De Luzuriaga, A. R.; Ormategui, N.; Grande, H. J.; Odriozola, I.; Pomposo, J. a.; Loinaz, I. Intramolecular Click Cycloaddition: An Efficient Room-Temperature Route towards Bioconjugable Polymeric Nanoparticles. *Macromol. Rapid Commun.* **2008**, *29*, 1156–1160.

(204) Wen, J.; Yuan, L.; Yang, Y.; Liu, L.; Zhao, H. Self-Assembly of Monotethered Single-Chain Nanoparticle Shape Amphiphiles. *ACS Macro Lett.* **2013**, *2*, 100–106.

(205) Zhu, B.; Ma, J.; Li, Z.; Hou, J.; Cheng, X.; Qian, G.; Liu, P.; Hu, A. Formation of Polymeric Nanoparticles via Bergman Cyclization Mediated Intramolecular Chain Collapse. *J. Mater. Chem.* **2011**, *21*, 2679.

(206) Zhu, B.; Ma, J.; Li, Z.; Hou, J.; Cheng, X.; Qian, G.; Liu, P.; Hu, A. A Convergence of Photo-Bergman Cyclization and Intramolecular Chain Collapse towards Polymeric Nanoparticles. *J. Mater. Chem.* **2011**, *21*, 2679.

(207) Fan, W.; Tong, X.; Yan, Q.; Fu, S.; Zhao, Y. Photodegradable and Size-Tunable Single-Chain Nanoparticles Prepared from a Single Main-Chain Coumarin-Containing Polymer Precursor. *Chem. Commun.* **2014**, *50*, 13492–13494.

(208) Foster, E. J.; Berda, E. B.; Meijer, E. W. Metastable Supramolecular Polymer Nanoparticles via Intramolecular Collapse of Single Polymer Chains. *J. Am. Chem. Soc.* **2009**, *131*, 6964–6966.

(209) Romulus, J.; Weck, M. Single-Chain Polymer Self-Assembly Using Complementary Hydrogen Bonding Units. *Macromol. Rapid Commun.* **2013**, *34*, 1518–1523.

(210) Willenbacher, J.; Altintas, O.; Trouillet, V.; Knöfel, N.; Monteiro, M. J.; Roesky, P. W.; Barner-Kowollik, C. Pd-Complex Driven Formation of Single-Chain Nanoparticles. *Polym. Chem.* **2015**, *6*, 4358–4365.

(211) Sanchez-Sanchez, A.; Arbe, A.; Colmenero, J.; Pomposo, J. A. Metallo-Folded Single-Chain Nanoparticles with Catalytic Selectivity. *ACS Macro Lett.* **2014**, *3*, 439–443.

(212) Greb, L.; Mutlu, H.; Barner-Kowollik, C.; Lehn, J. M. Photo- and Metallo-Responsive N-Alkyl α-Bisimines as Orthogonally Addressable Main-Chain Functional Groups in Metathesis Polymers. *J. Am. Chem. Soc.* **2016**, *138*, 1142–1145.

(213) Fischer, T. S.; Schulze-Sünninghausen, D.; Luy, B.; Altintas, O.; Barner-Kowollik, C. Stepwise Unfolding of Single-Chain Nanoparticles by Chemically Triggered Gates. *Angew. Chemie - Int. Ed.* **2016**, *55*, 11276–11280.

(214) Frank, P. G.; Tuten, B. T.; Prasher, A.; Chao, D.; Berda, E. B. Intra-Chain Photodimerization of Pendant Anthracene Units as an Efficient Route to Single-Chain Nanoparticle Fabrication. *Macromol. Rapid Commun.* **2014**, *35*, 249–253.

(215) Pomposo, J. A.; Perez-Baena, I.; Buruaga, L.; Alegría, A.; Moreno, A. J.; Colmenero, J. On the Apparent SEC Molecular Weight and Polydispersity Reduction upon Intramolecular Collapse of Polydisperse Chains to Unimolecular Nanoparticles. *Macromolecules* **2011**, *44*, 8644–8649.

(216) Wuest, K. N. R.; Lu, H.; Thomas, D. S.; Goldmann, A. S.; Stenzel, M. H.; Barner-Kowollik, C. Fluorescent Glyco Single-Chain Nanoparticle-Decorated Nanodiamonds. *ACS Macro Lett.* **2017**, *6*, 1168–1174.

(217) Chu, B. Laser Light Scattering. *Annu. Rev. Phys. Chem.* **1970**, *21*, 145–174.

(218) Cox, A. J.; DeWeerd, A. J.; Linden, J. An Experiment to Measure Mie and Rayleigh Total Scattering Cross Sections. *Am. J. Phys.* **2002**, *70*, 620–625.

(219) Pecora, R. Doppler Shifts in Light Scattering from Pure Liquids and Polymer Solutions. *J. Chem. Phys.* **1964**, *40*, 1604–1614.

(220) Koppel, D. E. Analysis of Macromolecular Polydispersity in Intensity Correlation Spectroscopy: The Method of Cumulants. *J. Chem. Phys.* **1972**, *57*, 4814–4820.

(221) Provencher, S. W. CONTIN: A General Purpose Constrained Regularization Program for Inverting Noisy Linear Algebraic and Integral Equations. *Comput. Phys. Commun.* **1982**, *27*, 229–242.

(222) Groves, P. Diffusion Ordered Spectroscopy (DOSY) as Applied to Polymers. *Polym. Chem.* **2017**, *8*, 6700–6708.

(223) Einstein, A. Ueber Die von Der Molekularkinetischen Theorie Der Waerme Geforderte Bewegung von in Ruhenden Fluessigkeiten Suspendierten Teilchen. *Ann. Phys.* **1905**, *322*, 549–560.

(224) Pomposo, J. A.; Perez-Baena, I.; Lo Verso, F.; Moreno, A. J.; Arbe, A.; Colmenero, J. How Far Are Single-Chain Polymer Nanoparticles in Solution from the Globular State? *ACS Macro Lett.* **2014**, *3*, 767–772.

(225) Blasco, E.; Tuten, B. T.; Frisch, H.; Lederer, A.; Barner-Kowollik, C. Characterizing Single Chain Nanoparticles (SCNPs): A Critical Survey. *Polym. Chem.* **2017**, *8*, 5845–5851.

(226) NASA. Sun - By the Numbers https://solarsystem.nasa.gov/planets/sun/facts (accessed Jan 5, 2018).

(227) Price, G. D.; Howitt, S. M. Towards Turbocharged Photosynthesis. *Nature* **2014**, *513*, 497–498.

(228) Griffith, J. S.; Orgel, L. E. Ligand-Field Theory. *Q. Rev. Chem. Soc.* **1957**, *11*, 381.

(229) Griffiths, D. J.; Harris, E. G. Introduction to Quantum Mechanics. *Am. J. Phys.* **1995**, *63*, 767–768.

(230) Lennard-Jones, J. E. The Electronic Structure of Some Diatomic Molecules. *Trans. Faraday Soc.* **1929**, *25*, 668.

(231) Silverstein, R.; Webster, F.; Kiemle, D.; Bryce, D. *Spectrometric Identification of Organic Compounds*; 2005.

(232) Mango, F. D.; Schachtschneider, J. H. Molecular Orbital Symmetry Conservation in Transition Metal Catalyzed Transformations. *J. Am. Chem. Soc.* **1967**, *89*, 2484–2486.

(233) Jablonski, A. Efficiency of Anti-Stokes Fluorescence in Dyes. *Nature* **1933**, *131*, 839–840.

(234) Franck, J.; Dymond, E. G. Elementary Processes of Photochemical Reactions. *Trans. Faraday Soc.* **1926**, *21*, 536.

(235) Condon, E. A Theory of Intensity Distribution in Band Systems. *Phys. Rev.* **1926**, *28*, 1182–1201.

(236) Condon, E. U. Nuclear Motions Associated with Electron Transitions in Diatomic Molecules. *Phys. Rev.* **1928**, *32*, 858–872.

(237) Coolidge, A. S.; James, H. M.; Present, R. D. A Study of the Franck- Condon Principle. *J. Chem. Phys.* **1936**, *4*, 193–211.

(238) Barbatti, M.; Aquino, A. J. A.; Lischka, H.; Schriever, C.; Lochbrunner, S.; Riedle, E. Ultrafast Internal Conversion Pathway and Mechanism in 2-(2′ - Hydroxyphenyl)benzothiazole: A Case Study for Excited-State Intramolecular Proton Transfer Systems. *Phys. Chem. Chem. Phys.* **2009**, *11*, 1406.

(239) Nič , M.; Jirát, J.; Košata, B.; Jenkins, A.; McNaught, A. Kasha Rule. In *IUPAC Compendium of Chemical Terminology*; IUPAC: Research Triangle Park, NC, 1997.

(240) Atkins, P. J.; De Paula, J.; Keeler, J. *Atkins Physical Chemistry*; Oxford Univ. Press, 2017.

(241) Marian, C. M. Spin-Orbit Coupling and Intersystem Crossing in Molecules. *Wiley Interdiscip. Rev. Comput. Mol. Sci.* **2012**, *2*, 187–203.

(242) Albini, A.; Fagnoni, M. *Handbook of Synthetic Photochemistry*; WILEY-VCH Verlag GmbH: Weinheim, 2009.

(243) Norrish, R. G. W.; Bamford, C. H. Photo-Decomposition of Aldehydes and Ketones. *Nature* **1937**, *140*, 195–196.

(244) Geerlings, P.; Ayers, P. W.; Toro-Labbé, A.; Chattaraj, P. K.; De Proft, F. The Woodward-Hoffmann Rules Reinterpreted by Conceptual Density Functional Theory. *Acc. Chem. Res.* **2012**, *45*, 683–695.

(245) Yang, N. C.; Rivas, C. A New Photochemical Primary Process, the Photochemical Enolization of O-Substituted Benzophenones. *J. Am. Chem. Soc.* **1961**, *9*, 2213.

(246) Porter, G.; Tchir, M. Flash Photolysis of an Ortho-Alkyl-Benzophenone. *J. Chem. Soc. D Chem.* **1970**, *0*, 1372–1373.

(247) Porter, G.; Tchir, M. Photoenolization of Ortho-Substituted Benzophenones by Flash Photolysis. *J. Chem. Soc. A* **1971**, *0*, 3772–3777.

(248) Farag, M. H.; Jansen, T. L. C.; Knoester, J. Probing the Interstate Coupling near a Conical Intersection by Optical Spectroscopy. *J. Phys. Chem. Lett.* **2016**, *7*, 3328–3334.

(249) Vigovskaya, A.; Abt, D.; Ahmed, I.; Niemeyer, C. M.; Barner-Kowollik, C.; Fruk, L. Photo-Induced Chemistry for the Design of Oligonucleotide Conjugates and Surfaces. *J. Mater. Chem. B* **2016**, *4*, 442–449.

(250) Sun, P.; Liu, J.; Zhang, Z.; Zhang, K. Scalable Preparation of Cyclic Polymers by the Ring-Closure Method Assisted by the Continuous-Flow Technique. *Polym. Chem.* **2016**, *7*, 2239–2244.

(251) Zydziak, N.; Konrad, W.; Feist, F.; Afonin, S.; Weidner, S.; Barner-Kowollik, C. Coding and Decoding Libraries of Sequence-Defined Functional Copolymers Synthesized via Photoligation. *Nat. Commun.* **2016**, *7*, 13672.

(252) Wuest, K. N. R.; Trouillet, V.; Köppe, R.; Roesky, P. W.; Goldmann, A. S.; Stenzel, M. H.; Barner-Kowollik, C. Direct Light-Induced (Co-)Grafting of Photoactive Polymers to Graphitic Nanodiamonds. *Polym. Chem.* **2017**, *8*, 838–842.

(253) Hiltebrandt, K.; Kaupp, M.; Molle, E.; Menzel, J. P.; Blinco, J. P.; Barner-Kowollik, C. Star Polymer Synthesis via λ -Orthogonal Photochemistry. *Chem. Commun.* **2016**, *52*, 9426–9429.

(254) Houck, H. A.; Du Prez, F. E.; Barner-Kowollik, C. Controlling Thermal Reactivity

with Different Colors of Light. *Nat. Commun.* **2017**, *8*, 1869.

(255) Oehlenschlaeger, K. K.; Mueller, J. O.; Heine, N. B.; Glassner, M.; Guimard, N. K.; Delaittre, G.; Schmidt, F. G.; Barner-Kowollik, C. Lichtinduzierte Modulare Ligation von Konventionellen RAFT-Polymeren. *Angew. Chemie* **2013**, *125*, 791–796.

(256) Steinbach, T.; Ritz, S.; Wurm, F. R. Water-Soluble Poly(phosphonate)s via Living Ring-Opening Polymerization. *ACS Macro Lett.* **2014**, *3*, 244–248.

(257) Sadeghi-Varkani, A.; Emam-Djomeh, Z.; Askari, G. Physicochemical and Microstructural Properties of a Novel Edible Film Synthesized from Balangu Seed Mucilage. *International Journal of Biological Macromolecules*. Elsevier November 7, 2017.

(258) Kumar, A. A.; K., K. Properties of Biodegradable Polymers and Degradation for Sustainable Development. *Int. J. Chem. Eng. Appl.* **2011**, *2*, 164–167.

(259) Martin, O.; Avérous, L. Poly(lactic Acid): Plasticization and Properties of Biodegradable Multiphase Systems. *Polymer* **2001**, *42*, 6209–6219.

(260) Martina, M.; Hutmacher, D. W. Biodegradable Polymers Applied in Tissue Engineering Research: A Review. *Polymer International*. John Wiley & Sons, Ltd. February 1, 2007, pp 145–157.

(261) Middleton, J. C.; Tipton, A. J. Synthetic Biodegradable Polymers as Orthopedic Devices. *Biomaterials* **2000**, *21*, 2335–2346.

(262) Burger, C.; Kabir, K.; Rangger, C.; Mueller, M.; Minor, T.; Tolba, R. H. Polylactide (LTS) Causes Less Inflammation Response than Polydioxanone (PDS): A Meniscus Repair Model in Sheep. *Arch. Orthop. Trauma Surg.* **2006**, *126*, 695–705.

(263) Li, S.; Szalai, M. L.; Kevwitch, R. M.; McGrath, D. V. Dendrimer Disassembly by Benzyl Ether Depolymerization. *J. Am. Chem. Soc.* **2003**, *125*, 10516–10517.

(264) Amir, R. J.; Pessah, N.; Shamis, M.; Shabat, D. Self-Immolative Dendrimers. *Angew. Chemie - Int. Ed.* **2003**, *42*, 4494–4499.

(265) De Groot, F. M. H.; Albrecht, C.; Koekkoek, R.; Beusker, P. H.; Scheeren, H. W. "Cascade-Release Dendrimers" liberate All End Groups upon a Single Triggering Event in the Dendritic Core. *Angew. Chemie - Int. Ed.* **2003**, *42*, 4490–4494.

(266) Peterson, G. I.; Larsen, M. B.; Boydston, A. J. Controlled Depolymerization: Stimuli-Responsive Self-Immolative Polymers. *Macromolecules* **2012**, *45*, 7317–7328.

(267) Blencowe, C. A.; Russell, A. T.; Greco, F.; Hayes, W.; Thornthwaite, D. W. Self-Immolative Linkers in Polymeric Delivery Systems. *Polym. Chem.* **2011**, *2*, 773–790.

(268) Wong, A. D.; DeWit, M. A.; Gillies, E. R. Amplified Release through the Stimulus Triggered Degradation of Self-Immolative Oligomers, Dendrimers, and Linear Polymers. *Adv. Drug Deliv. Rev.* **2012**, *64*, 1031–1045.

(269) Avital-Shmilovici, M.; Shabat, D. Self-Immolative Dendrimers: A Distinctive Approach to Molecular Amplification. *Soft Matter* **2010**, *6*, 1073.

(270) Shamis, M.; Lode, H. N.; Shabat, D. Bioactivation of Self-Immolative Dendritic Prodrugs by Catalytic Antibody 38C2. *J. Am. Chem. Soc.* **2004**, *126*, 1726–1731.

(271) Weinstain, R.; Baran, P. S.; Shabat, D. Activity-Linked Labeling of Enzymes by Self-Immolative Polymers. *Bioconjug. Chem.* **2009**, *20*, 1783–1791.

(272) Weinstain, R.; Sagi, A.; Karton, N.; Shabat, D. Self-Immolative Comb-Polymers: Multiple-Release of Side-Reporters by a Single Stimulus Event. *Chem. - A Eur. J.* **2008**, *14*, 6857–6861.

(273) Sagi, A.; Weinstain, R.; Karton, N.; Shabat, D. Self-Immolative Polymers. *J. Am. Chem. Soc.* **2008**, *130*, 5434–5435.

(274) Grinda, M.; Clarhaut, J.; Renoux, B.; Tranoy-Opalinski, I.; Papot, S. A Self-Immolative Dendritic Glucuronide Prodrug of Doxorubicin. *Med. Chem. Commun.* **2012**, *3*, 68–70.

(275) Erez, R.; Segal, E.; Miller, K.; Satchi-Fainaro, R.; Shabat, D. Enhanced Cytotoxicity of a Polymer-Drug Conjugate with Triple Payload of Paclitaxel. *Bioorganic Med. Chem.* **2009**, *17*, 4327–4335.

(276) De Groot, F. M. H.; Loos, W. J.; Koekkoek, R.; Van Berkom, L. W. A.; Busscher, G. F.; Seelen, A. E.; Albrecht, C.; De Bruijn, P.; Scheeren, H. W. Elongated Multiple Electronic Cascade and Cyclization Spacer Systems in Activatible Anticancer Prodrugs for Enhanced Drug Release. *J. Org. Chem.* **2001**, *66*, 8815–8830.

(277) Seo, W.; Phillips, S. T. Patterned Plastics That Change Physical Structure in Response to Applied Chemical Signals. *J. Am. Chem. Soc.* **2010**, *132*, 9234–9235.

(278) Kevwitch, R. M.; Shanahan, C. S.; McGrath, D. V. Vanillin and O-Vanillin Oligomers as Models for Dendrimer Disassembly. *New J. Chem.* **2012**, *36*, 492–505.

(279) Warnecke, A.; Kratz, F. 2,4-Bis(hydroxymethyl)aniline as a Building Block for Oligomers with Self-Eliminating and Multiple Release Properties. *J. Org. Chem.* **2008**, *73*, 1546–1552.

(280) Szalai, M. L.; Kevwitch, R. M.; McGrath, D. V. Geometric Disassembly of Dendrimers: Dendritic Amplification. *J. Am. Chem. Soc.* **2003**, *125*, 15688–15689.

(281) De Groot, F. M. H.; Albrecht, C.; Koekkoek, R.; Beusker, P. H.; Scheeren, H. W. "Cascade-Release Dendrimers" liberate All End Groups upon a Single Triggering Event in the Dendritic Core. *Angew. Chemie - Int. Ed.* **2003**, *42*, 4490–4494.

(282) Dewit, M. A.; Beaton, A.; Gillies, E. R. A Reduction Sensitive Cascade Biodegradable Linear Polymer. *J. Polym. Sci. Part A Polym. Chem.* **2010**, *48*, 3977–3985.

(283) Karton-Lifshin, N.; Shabat, D. Exponential Diagnostic Signal Amplification via Dendritic Chain Reaction: The Dendritic Effect of a Self-Immolative Amplifier Component. *New J. Chem.* **2012**, *36*, 386–393.

(284) Jourden, J. L. M.; Daniel, K. B.; Cohen, S. M. Investigation of Self-Immolative Linkers in the Design of Hydrogen Peroxide Activated Metalloprotein Inhibitors. *Chem. Commun.* **2011**, *47*, 7968.

(285) Seila, E.; Lubelski, A.; Klafter, J.; Shabat, D. Two-Component Dendritic Chain Reactions: Experiment and Theory. *J. Am. Chem. Soc.* **2010**, *132*, 3945–3952.

(286) Avital-Shmilovici, M.; Shabat, D. Dendritic Chain Reaction: Responsive Release of Hydrogen Peroxide upon Generation and Enzymatic Oxidation of Methanol.

Bioorganic Med. Chem. **2010**, *18*, 3643–3647.

(287) Sella, E.; Shabat, D. Dendritic Chain Reaction. *J. Am. Chem. Soc.* **2009**, *131*, 9934–9936.

(288) Sella, E.; Shabat, D. Self-Immolative Dendritic Probe for Direct Detection of Triacetone Triperoxide. *Chem. Commun.* **2008**, *0*, 5701.

(289) Redy, O.; Kisin-Finfer, E.; Sella, E.; Shabat, D. A Simple FRET-Based Modular Design for Diagnostic Probes. *Org. Biomol. Chem.* **2012**, *10*, 710–715.

(290) Perry-Feigenbaum, R.; Sella, E.; Shabat, D. Autoinductive Exponential Signal Amplification: A Diagnostic Probe for Direct Detection of Fluoride. *Chem. - A Eur. J.* **2011**, *17*, 12123–12128.

(291) Zhang, H.; Yeung, K.; Robbins, J. S.; Pavlick, R. A.; Wu, M.; Liu, R.; Sen, A.; Phillips, S. T. Self-Powered Microscale Pumps Based on Analyte-Initiated Depolymerization Reactions. *Angew. Chemie - Int. Ed.* **2012**, *51*, 2400–2404.

(292) DeWit, M. A.; Gillies, E. R. A Cascade Biodegradable Polymer Based on Alternating Cyclization and Elimination Reactions. *J. Am. Chem. Soc.* **2009**, *131*, 18327–18334.

(293) Fomina, N.; McFearin, C. L.; Sermsakdi, M.; Morachis, J. M.; Almutairi, A. Low Power, Biologically Benign NIR Light Triggers Polymer Disassembly. *Macromolecules* **2011**, *44*, 8590–8597.

(294) Fomina, N.; McFearin, C. L.; Almutairi, A. Increasing Materials' Response to Two-Photon NIR Light via Self-Immolative Dendritic Scaffolds. *Chem. Commun.* **2012**, *48*, 9138.

(295) De Gracia Lux, C.; McFearin, C. L.; Joshi-Barr, S.; Sankaranarayanan, J.; Fomina, N.; Almutairi, A. Single UV or near IR Triggering Event Leads to Polymer Degradation into Small Molecules. *ACS Macro Lett.* **2012**, *1*, 922–926.

(296) Olejniczak, J.; Nguyen Huu, V. A.; Lux, J.; Grossman, M.; He, S.; Almutairi, A. Light-Triggered Chemical Amplification to Accelerate Degradation and Release from Polymeric Particles. *Chem. Commun.* **2015**, *51*, 16980–16983.

(297) Viger, M. L.; Grossman, M.; Fomina, N.; Almutairi, A. Low Power Upconverted near-IR Light for Efficient Polymeric Nanoparticle Degradation and Cargo Release. *Adv. Mater.* **2013**, *25*, 3733–3738.

(298) Olejniczak, J.; Chan, M.; Almutairi, A. Light-Triggered Intramolecular Cyclization in Poly(lactic- Co -Glycolic Acid)-Based Polymers for Controlled Degradation. *Macromolecules* **2015**, *48*, 3166–3172.

(299) Carling, C.-J.; Olejniczak, J.; Foucault-Collet, A.; Collet, G.; Viger, M. L.; Nguyen Huu, V. A.; Duggan, B. M.; Almutairi, A. Efficient Red Light Photo-Uncaging of Active Molecules in Water upon Assembly into Nanoparticles. *Chem. Sci.* **2016**, *7*, 2392–2398.

(300) Göppert- Mayer, M. Über Elementarakte Mit Zwei Quantensprüngen. *Ann. Phys.* **1931**, *401*, 273–294.

(301) Pawlicki, M.; Collins, H. A.; Denning, R. G.; Anderson, H. L. Zweiphotonenabsorption Und Das Design von Zweiphotonenfarbstoffen. *Angew. Chemie* **2009**, *121*, 3292–3316.

(302) Patchornik, A.; Amit, B.; Woodward, R. B. Photosensitive Protecting Groups. *J. Am. Chem. Soc.* **1970**, *92*, 6333–6335.

(303) Klán, P.; Šolomek, T.; Bochet, C. G.; Blanc, A.; Givens, R.; Rubina, M.; Popik, V.; Kostikov, A.; Wirz, J. Photoremovable Protecting Groups in Chemistry and Biology: Reaction Mechanisms and Efficacy. *Chem. Rev.* **2013**, *113*, 119–191.

(304) Sankaranarayanan, J.; Mahmoud, E. A.; Kim, G.; Morachis, J. M.; Almutairi, A. Multiresponse Strategies to Modulate Burst Degradation and Release from Nanoparticles. *ACS Nano* **2010**, *4*, 5930–5936.

(305) Jones, P. B.; Pollastri, M. P.; Porter, N. A. 2-Benzoylbenzoic Acid: A Photolabile Mask for Alcohols and Thiols. *J. Org. Chem.* **1996**, *61*, 9455–9461.

(306) Dormán, G.; Nakamura, H.; Pulsipher, A.; Prestwich, G. D. The Life of Pi Star: Exploring the Exciting and Forbidden Worlds of the Benzophenone Photophore. *Chem. Rev.* **2016**, *116*, 15284–15398.

(307) Gnaim, S.; Shabat, D. Self-Immolative Chemiluminescence Polymers: Innate Assimilation of Chemiexcitation in a Domino-like Depolymerization. *J. Am. Chem. Soc.* **2017**, *139*, 10002–10008.

(308) Deery, M. J.; Jennings, K. R.; Jasieczek, C. B.; Haddleton, D. M.; Jackson, A. T.; Yates, H. T.; Scrivens, J. H. A Study of Cation Attachment to Polystyrene by Means of Matrix-Assisted Laser Desorption/ionization and Electrospray Ionization-Mass Spectrometry. *Rapid Commun. Mass Spectrom.* **1997**, *11*, 57–62.

(309) Steinkoenig, J.; Cecchini, M. M.; Reale, S.; Goldmann, A. S.; Barner-Kowollik, C. Supercharging Synthetic Polymers: Mass Spectrometric Access to Nonpolar Synthetic Polymers. *Macromolecules* **2017**, *50*, 8033–8041.

(310) Schmidt, B. V. K. J.; Hetzer, M.; Ritter, H.; Barner-Kowollik, C. Complex Macromolecular Architecture Design via Cyclodextrin Host/guest Complexes. *Prog. Polym. Sci.* **2014**, *39*, 235–249.

(311) Steinkoenig, J.; Bloesser, F. R.; Huber, B.; Welle, A.; Trouillet, V.; Weidner, S.; Barner, L.; Roesky, P.; Yuan, J.; Goldmann, A. S.; et al. Controlled Radical Polymerization and In-Depth Mass-Spectrometric Characterization of Poly(Ionic Liquid)s and Their Photopatterning on Surfaces. *Polym. Chem.* **2016**, *7*, 451–461.

(312) Ladavière, C.; Lacroix-Desmazes, P.; Delolme, F. First Systematic MALDI / ESI Mass Spectrometry Comparison to Characterize Polystyrene Synthesized by Different Controlled Radical Polymerizations First Systematic MALDI / ESI Mass Spectrometry Comparison to Characterize Polystyrene Synthesized by Differen. *Macromolecules* **2009**, *42*, 70–84.

(313) Hunt, P. A.; Ashworth, C. R.; Matthews, R. P. Hydrogen Bonding in Ionic Liquids. *Chem. Soc. Rev.* **2015**, *44*, 1257–1288.

(314) Kaita, S.; Yamanaka, M.; Horiuchi, A. C.; Wakatsuki, Y. Butadiene Polymerization Catalyzed by Lanthanide Metallocene - Alkylaluminum Complexes with Cocatalysts: Metal-Dependent Control of 1,4-Cis/trans Stereoselectivity and Molecular Weight. *Macromolecules* **2006**, *39*, 1359–1363.

(315) Obrecht, W.; Lambert, J.; Happ, M.; Oppenheimer-Stix, C.; Dunn, J.; Kruger, R. Rubber, 4. Emulsion Rubbers. *Ullmann's Encycl. Ind. Chem.* **2012**, *31*, 623–648.

(316) Geiselhart, C. M.; Offenloch, J. T.; Mutlu, H.; Barner-Kowollik, C. Polybutadiene Functionalization via an Efficient Avenue. *ACS Macro Lett.* **2016**, *5*, 1146–1151.

(317) Fischer, T. S.; Steinkoenig, J.; Woehlk, H.; Blinco, J. P.; Fairfull-Smith, K.; Barner-

Kowollik, C. High Resolution Mass Spectrometric Access to Nitroxide Containing Polymers. *Polym. Chem.* **2017**, *8*, 5269–5274.

(318) Cimino, P.; Pavone, M.; Barone, V. Structural, Thermodynamic, and Magnetic Properties of Adducts between TEMPO Radical and Alcohols in Solution: New Insights from DFT and Discrete-Continuum Solvent Models. *Chem. Phys. Lett.* **2006**, *419*, 106–110.

(319) Mendenhall, G. D.; Ingold, K. U. Reversible Dimerization and Some Solid-State Properties of Two Bicyclic Nitroxides. *J. Am. Chem. Soc.* **1973**, *95*, 6390–6394.

(320) Chan, D. S.-H.; Matak-Vinković, D.; Coyne, A. G.; Abell, C. Insight into Protein Conformation and Subcharging by DMSO from Native Ion Mobility Mass Spectrometry. *ChemistrySelect* **2016**, *1*, 5686–5690.

(321) Ogorzalek Loo, R. R.; Lakshmanan, R.; Loo, J. A. What Protein Charging (and Supercharging) Reveal about the Mechanism of Electrospray Ionization. *J. Am. Soc. Mass Spectrom.* **2014**, *25*, 1675–1693.

(322) Henderson, M. a.; McIndoe, J. S. Ionic Liquids Enable Electrospray Ionisation Mass Spectrometry in Hexane. *Chem. Commun.* **2006**, 2872.

(323) Flick, T. G.; Williams, E. R. Supercharging with Trivalent Metal Ions in Native Mass Spectrometry. *J. Am. Soc. Mass Spectrom.* **2012**, *23*, 1885–1895.

(324) Wong, S. F.; Meng, C. K.; Fenn, J. B. Multiple Charging in Electrospray Ionization of Poly(ethylene Glycols). *J. Phys. Chem* **1988**, *92*, 546–550.

(325) Konermann, L.; Ahadi, E.; Rodriguez, A. D.; Vahidi, S. Unraveling the Mechanism of Electrospray Ionization. *Anal. Chem.* **2013**, *85*, 2–9.

(326) *Handbook of RAFT Polymerization*; Barner-Kowollik, C., Ed.; WILEY-VCH Verlag GmbH: Weinheim, 2008.

(327) Li, Y.; Li, G.; Wang, X.; Zhu, Z.; Ma, H.; Zhang, T.; Jin, J. Poly(ionic Liquid)-Wrapped Single-Walled Carbon Nanotubes for Sub-Ppb Detection of CO2. *Chem. Commun.* **2012**, *48*, 8222.

(328) Bara, J. E.; Carlisle, T. K.; Gabriel, C. J.; Camper, D.; Finotello, A.; Gin, D. L.; Noble, R. D. Guide to CO 2 Separations in Imidazolium-Based Room-Temperature Ionic Liquids. *Ind. Eng. Chem. Res.* **2009**, *48*, 2739–2751.

(329) Mori, H.; Yahagi, M.; Endo, T. RAFT Polymerization of *N* -Vinylimidazolium Salts and Synthesis of Thermoresponsive Ionic Liquid Block Copolymers. *Macromolecules* **2009**, *42* (21), 8082–8092.

(330) Gabellca, V.; De Pauw, E. Internal Energy and Fragmentation of Ions Produced in Electrospray Sources. *Mass Spectrom. Rev.* **2005**, *24*, 566–587.

(331) Sleno, L.; Volmer, D. A. Ion Activation Methods for Tandem Mass Spectrometry. *J. Mass Spectrom.* **2004**, *39*, 1091–1112.

(332) Dobrynin, A. V; Rubinstein, M. Theory of Polyelectrolytes in Solutions and at Surfaces. *Prog. Polym. Sci.* **2005**, *30*, 1049–1118.

(333) Crosthwaite, J. M.; Muldoon, M. J.; Dixon, J. K.; Anderson, J. L.; Brennecke, J. F. Phase Transition and Decomposition Temperatures, Heat Capacities and Viscosities of Pyridinium Ionic Liquids. *J. Chem. Thermodyn.* **2005**, *37*, 559–568.

(334) Marcilla, R.; Blazquez, J. A.; Fernandez, R.; Grande, H.; Pomposo, J. A.;

Mecerreyes, D. Synthesis of Novel Polycations Using the Chemistry of Ionic Liquids. *Macromol. Chem. Phys.* **2005**, *206*, 299–304.

(335) Brookhart, M.; Grant, B. E. Mechanism of. *Inorg. Chem.* **1981**, *20*, 3186–3189.

(336) Gruendling, T.; Hart-Smith, G.; Davis, T. P.; Stenzel, M. H.; Barner-Kowollik, C. Enhanced Ionization in Electrospray Ionization Mass Spectrometry of Labile End-Group-Containing Polystyrenes Using silver(I) Tetrafluoroborate as Doping Salt. *Macromolecules* **2008**, *41*, 1966–1971.

(337) Steinkoenig, J.; Cecchini, M. M.; Goldmann, A. S.; Reale, S.; Angelis, F. De; Barner-Kowollik, C. Just Add Salt: A Mass Spectrometric Analysis Method for Imaging Anion-Exchanged Poly(Ionic Liquid)s. *Macromol. Rapid Commun.* **2016**, *37*, 1662–1666.

(338) Cecchini, M. M.; Steinkoenig, J.; Reale, S.; Barner, L.; Yuan, J.; Goldmann, A. S.; De Angelis, F.; Barner-Kowollik, C. Universal Mass Spectrometric Analysis of Poly(ionic Liquid)s. *Chem. Sci.* **2016**, *7*, 4912–4921.

(339) Cammarata, L.; Kazarian, S. G.; Salter, P. A.; Welton, T. Molecular States of Water in Room Temperature Ionic Liquids. *Phys. Chem. Chem. Phys.* **2001**, *3*, 5192–5200.

(340) He, H.; Averick, S.; Roth, E.; Luebke, D.; Nulwala, H.; Matyjaszewski, K. Clickable Poly(ionic Liquid)s for Modification of Glass and Silicon Surfaces. *Polymer* **2014**, *55*, 3330–3338.

(341) England, D.; Tambe, N.; Texter, J. Stimuli-Responsive Nanolatexes: Porating Films. *ACS Macro Lett.* **2012**, *1*, 310–314.

(342) Ye, Q.; Gao, T.; Wan, F.; Yu, B.; Pei, X.; Zhou, F.; Xue, Q. Grafting Poly(ionic Liquid) Brushes for Anti-Bacterial and Anti-Biofouling Applications. *J. Mater. Chem.* **2012**, *22*, 13123.

(343) Abdelhedi-Miladi, I.; Montarnal, D.; Obadia, M. M.; Ben Romdhane, H.; Drockenmuller, E. UV-Patterning of Ion Conducting Negative Tone Photoresists Using Azide-Functionalized Poly(Ionic Liquid)s. *ACS Macro Lett.* **2014**, *3*, 1187–1190.

(344) Kaupp, M.; Tischer, T.; Hirschbiel, A. F.; Vogt, A. P.; Geckle, U.; Trouillet, V.; Hofe, T.; Stenzel, M. H.; Barner-Kowollik, C. Photo-Sensitive RAFT-Agents for Advanced Microparticle Design. *Macromolecules* **2013**, *46*, 6858–6872.

(345) Yameen, B.; Rodriguez-Emmenegger, C.; Preuss, C. M.; Pop-Georgievski, O.; Verveniotis, E.; Trouillet, V.; Rezek, B.; Barner-Kowollik, C. A Facile Avenue to Conductive Polymer Brushes via Cyclopentadiene–maleimide Diels–Alder Ligation. *Chem. Commun.* **2013**, *49*, 8623.

(346) Zamfir, M.; Rodriguez-Emmenegger, C.; Bauer, S.; Barner, L.; Rosenhahn, A.; Barner-Kowollik, C. Controlled Growth of Protein Resistant PHEMA Brushes via S-RAFT Polymerization. *J. Mater. Chem. B* **2013**, *1*, 6027.

(347) Zhou, D.; Gao, X.; Wang, W. J.; Zhu, S. Termination of Surface Radicals and Kinetic Modeling of ATRP Grafting from Flat Surfaces by Addition of Deactivator. *Macromolecules* **2012**, *45*, 1198–1208.

(348) Herrmann, A.; Mihov, G.; Vandermeulen, G. W. .; Klok, H.-A.; Müllen, K. Peptide-Functionalized Polyphenylene Dendrimers. *Tetrahedron* **2003**, *59*, 3925–3935.

(349) Saegusa, T.; Kobayashi, S.; Furukawa, J. Polymerization via Zwitterion. 10.

Alternating Cooligomerization of 2-Methyl-2-Oxazoline with Ethylenesulfonamide. *Macromolecules* **1976**, *9*, 728–731.

(350) Odian, G.; Gunatillake, P. Zwitterion Polymerization of 2-Methyl-2-Oxazoline and Acrylic Acid. *Am. Chem. Soc. Polym. Prepr. Div. Polym. Chem.* **1983**, *24*, 135–136.

(351) Steinkoenig, J.; Zieger, M. M.; Mutlu, H.; Barner-Kowollik, C. Dual-Gated Chain Shattering Based on Light Responsive Benzophenones and Thermally Responsive Diels-Alder Linkages. *Macromolecules* **2017**, *50*, 5385–5391.

(352) Fujita, M.; Iizuka, Y.; Miyake, A. Thermal and Kinetic Analyses on Michael Addition Reaction of Acrylic Acid. *J. Therm. Anal. Calorim.* **2017**, *128*, 1227–1233.

(353) Altuntaş , E.; Krieg, A.; Baumgaertel, A.; Crecelius, A. C.; Schubert, U. S. ESI, APCI, and MALDI Tandem Mass Spectrometry of Poly(methyl Acrylate)s: A Comparison Study for the Structural Characterization of Polymers Synthesized via CRP Techniques and the Software Application to Analyze MS/MS Data. *J. Polym. Sci. Part A Polym. Chem.* **2013**, *51*, 1595–1605.

(354) Bridoux, M. C.; Machuron-Mandard, X. Capabilities and Limitations of Direct Analysis in Real Time Orbitrap Mass Spectrometry and Tandem Mass Spectrometry for the Analysis of Synthetic and Natural Polymers. *Rapid Commun. Mass Spectrom.* **2013**, *27*, 2057–2070.

(355) Voll, D.; Junkers, T.; Barner-Kowollik, C. A Qualitative and Quantitative Post-Mortem Analysis: Studying Free-Radical Initiation Processes via Soft Ionization Mass Spectrometry. *J. Polym. Sci. A Polym. Chem.* **2012**, *50*, 2739–2757.

(356) All pKs Values Are Predicted Values.

(357) Saegusa, T.; Kimura, Y.; Kobayashi, S. Polymerization via Zwitterion. 14. Alternating Copolymerizations of Cyclic Imino Ethers with Acrylic Acid and with Beta-Propiolactone. *Macromolecules* **1976**, *10*, 236–239.

(358) Desmet, G. B.; D'Hooge, D. R.; Omurtag, P. S.; Espeel, P.; Marin, G. B.; Du Prez, F. E.; Reyniers, M. F. Quantitative First-Principles Kinetic Modeling of the Aza-Michael Addition to Acrylates in Polar Aprotic Solvents. *J. Org. Chem.* **2016**, *81*, 12291–12302.

(359) Wiesbrock, F.; Hoogenboom, R.; Leenen, M. A. M.; Meier, M. A. R.; Schubert, U. S. Investigation of the Living Cationic Ring-Opening Polymerization of 2-Methyl-, 2-Ethyl-, 2-Nonyl-, and 2-Phenyl-2-Oxazoline in a Single-Mode Microwave Reactor. *Macromolecules* **2005**, *38*, 5025–5034.

(360) Bloksma, M. M.; Paulus, R. M.; Van Kuringen, H. P. C.; Van Der Woerdt, F.; Lambermont-Thijs, H. M. L.; Schubert, U. S.; Hoogenboom, R. Thermoresponsive poly(2-Oxazine)s. *Macromol. Rapid Commun.* **2012**, *33*, 92–96.

(361) Bloksma, M. M.; Paulus, R. M.; Van Kuringen, H. P. C.; Van Der Woerdt, F.; Lambermont-Thijs, H. M. L.; Schubert, U. S.; Hoogenboom, R. Thermoresponsive poly(2-Oxazine)s. *Macromol. Rapid Commun.* **2012**, *33*, 92–96.

(362) US patent application. Novel Heterocyclyl Compounds, 2010.

(363) Zadav, V. K.; Ganesh Babu, K. Reactions on a Solid Surface. A Simple, Economical, and Efficient Acylation of Alcohols and Amines over Al2O3. *J. Org. Chem.* **2004**, *69*, 577/580.

(364) Britovsek, G. J. P.; Ugolotti, J.; White, A. J. P. From B(C6F5)3 to B(OC6F5)3: Synthesis of (C6F5)2BOC6F5 and C6F5B(OC6F5)2 and Their Relative Lewis Acidity. *Organometallics* **2005**, *24*, 1685–1691.

(365) Asenjo-Sanz, I.; Veloso, A.; Miranda, J. I.; Pomposo, J. a.; Barroso-Bujans, F. Zwitterionic Polymerization of Glycidyl Monomers to Cyclic Polyethers with B(C6F5)3. *Polym. Chem.* **2014**, *5*, 6905–6908.

(366) Sunder, A.; Hanselmann, R.; Frey, H.; Mülhaupt, R. Controlled Synthesis of Hyperbranched Polyglycerols by Ring-Opening Multibranching Polymerization. *Macromolecules* **1999**, *32*, 4240–4246.

(367) Tokar, R.; Kubisa, P.; Penczek, S.; Dworak, A. Cationic Polymerization of Glycidol: Coexistence of the Activated Monomer and Active Chain End Mechanism. *Macromolecules* **1994**, *27*, 320–322.

(368) Tracy, J. B.; Kalyuzhny, G.; Crowe, M. C.; Balasubramanian, R.; Choi, J.; Murray, R. W.; Laboratories, K.; Uni, V.; Hill, C.; Carolina, N. Poly (Ethylene Glycol) Ligands for High-Resolution Nanoparticle Mass Spectrometry. *J. Am. Chem. Soc.* **2007**, *129*, 6706–6707.

(369) Pahnke, K.; Brandt, J.; Gryn'ova, G.; Lindner, P.; Schweins, R.; Schmidt, F. G.; Lederer, A.; Coote, M. L.; Barner-Kowollik, C. Entropy Driven Chain Effects on Ligation Chemistry. *Chem. Sci.* **2015**, *6*, 1061–1074.

(370) Asenjo-Sanz, I.; Veloso, A.; Miranda, J. I.; Pomposo, J. a.; Barroso-Bujans, F. Zwitterionic Polymerization of Glycidyl Monomers to Cyclic Polyethers with B(C6F5)3. *Polym. Chem.* **2014**, *5*, 6905–6908.

(371) Deng, X. X.; Li, L.; Li, Z. L.; Lv, A.; Du, F. S.; Li, Z. C. Sequence Regulated Poly(ester-Amide)s Based on Passerini Reaction. *ACS Macro Lett.* **2012**, *1*, 1300–1303.

(372) McEwen, C. N.; Jackson, C.; Larsen, B. S. Instrumental Effects in the Analysis of Polymers of Wide Polydispersity by MALDI Mass Spectrometry. *Int. J. Mass Spectrom. Ion Process.* **1997**, *160*, 387–394.

(373) Michelle Byrd HC; McEwen. The Limitations of MALDI-TOF Mass Spectrometry in the Analysis of Wide Polydisperse Polymers. *Anal. Chem.* **2000**, *72*, 4568–4576.

(374) Steinkoenig, J.; Zieger, M. M.; Mutlu, H.; Barner-Kowollik, C. Dual-Gated Chain Shattering Based on Light Responsive Benzophenones and Thermally Responsive Diels–Alder Linkages. *Macromolecules* **2017**, *50*, 5385–5391.

(375) Gegenhuber, T.; De Keer, L.; Goldmann, A. S.; Van Steenberge, P. H. M.; Mueller, J. O.; Reyniers, M.-F.; Menzel, J. P.; D'hooge, D. R.; Barner-Kowollik, C. Fusing Light-Induced Step-Growth Processes with RAFT Chemistry for Segmented Copolymer Synthesis: A Synergetic Experimental and Kinetic Modeling Study. *Macromolecules* **2017**, *50*, 6451–6467.

(376) Steinkoenig, J.; Rothfuss, H.; Lauer, A.; Tuten, B. T.; Barner-Kowollik, C. Imaging Single-Chain Nanoparticle Folding via High-Resolution Mass Spectrometry. *J. Am. Chem. Soc.* **2017**, *139*, 51–54.

(377) Pomposo, J. A.; Perez-Baena, I.; Lo Verso, F.; Moreno, A. J.; Arbe, A.; Colmenero, J. How Far Are Single-Chain Polymer Nanoparticles in Solution from the Globular State? *ACS Macro Lett.* **2014**, *3*, 767–772.

(378) Latorre-Sánchez, A.; Alegría, A.; Lo Verso, F.; Moreno, A. J.; Arbe, A.; Colmenero, J.; Pomposo, J. A. A Useful Methodology for Determining the Compaction Degree

of Single-Chain Nanoparticles by Conventional SEC. *Part. Part. Syst. Charact.* **2016**, *33*, 373–381.

(379) Blasco, E.; Tuten, B. T.; Frisch, H.; Lederer, A.; Barner-Kowollik, C. Characterizing Single Chain Nanoparticles (SCNPs): A Critical Survey. *Polym. Chem.* **2017**, *8*, 5845–5851.

(380) Seixas de Melo, J.; Fernandes, P. . Spectroscopy and Photophysics of 4- and 7-Hydroxycoumarins and Their Thione Analogs. *J. Mol. Struct.* **2001**, *565–566*, 69–78.

(381) Geißler, D.; Gollwitzer, C.; Sikora, A.; Minelli, C.; Krumrey, M.; Resch-Genger, U. Effect of Fluorescent Staining on Size Measurements of Polymeric Nanoparticles Using DLS and SAXS. *Anal. Methods* **2015**, *7*, 9785–9790.

(382) Fan, W.; Tong, X.; Yan, Q.; Fu, S.; Zhao, Y. Photodegradable and Size-Tunable Single-Chain Nanoparticles Prepared from a Single Main-Chain Coumarin-Containing Polymer Precursor. *Chem. Commun.* **2014**, *50*, 13492–13494.

(383) Gruendling, T.; Guilhaus, M.; Barner-Kowollik, C. Quantitative LC-MS of Polymers: Determining Accurate Molecular Weight Distributions by Combined Size Exclusion Chromatography and Electrospray Mass Spectrometry with Maximum Entropy Data Processing. *Anal. Chem.* **2008**, *80*, 6915–6927.

(384) Sehlinger, A.; Dannecker, P.-K.; Kreye, O.; Meier, M. A. R. Diversely Substituted Polyamides: Macromolecular Design Using the Ugi Four-Component Reaction. *Macromolecules* **2014**, *47*, 2774–2783.

(385) Chi, S. N.; Coz, C.; Chi, F.; Nz, C.; Ar, C. The Limiting Quantum Yield for the Photoreduction of Benzophenone with Isopropyl Alcohol. *J. Phys. Chem.* **1963**, *11*, 214–217.

(386) Dormán, G.; Nakamura, H.; Pulsipher, A.; Prestwich, G. D. The Life of Pi Star: Exploring the Exciting and Forbidden Worlds of the Benzophenone Photophore. *Chem. Rev.* **2016**, *116*, 15284–15398.

(387) Nakagawa, Y.; Suzuki, T.; Tayama, S. Metabolism and Toxicity of Benzophenone in Isolated Rat Hepatocytes and Estrogenic Activity of Its Metabolites in MCF-7 Cells. *Toxicology* **2000**, *156*, 27–36.

(388) Santos, A. L.; Oliveira, V.; Baptista, I.; Henriques, I.; Gomes, N. C. M.; Almeida, A.; Correia, A.; Cunha, Â. Wavelength Dependence of Biological Damage Induced by UV Radiation on Bacteria. *Arch. Microbiol.* **2013**, *195*, 63–74.

(389) Ligon, S. C.; Husár, B.; Wutzel, H.; Holman, R.; Liska, R. Strategies to Reduce Oxygen Inhibition in Photoinduced Polymerization. *Chem. Rev.* **2014**, *114*, 577–589.

(390) Liu, Y.; Zhong, G.; Liu, Z.; Meng, M.; Jiang, Y.; Ni, L.; Guo, W.; Liu, F. Preparation of Core–shell Ion Imprinted Nanoparticles via Photoinitiated Polymerization at Ambient Temperature for Dynamic Removal of Cobalt in Aqueous Solution. *RSC Adv.* **2015**, *5*, 85691–85704.

(391) Schneider, M. H.; Tran, Y.; Tabeling, P. Benzophenone Absorption and Diffusion in Poly(dimethylsiloxane) and Its Role in Graft Photo-Polymerization for Surface Modification. *Langmuir* **2011**, *27*, 1232–1240.

(392) Anderson, W. a C.; Castle, L. Benzophenone in Cartonboard Packaging Materials and the Factors That Influence Its Migration into Food. *Food Addit. Contam.* **2003**, *20* (6), 607–618.

(393) Zhou, J.; Guimard, N. K.; Inglis, A. J.; Namazian, M.; Lin, C. Y.; Coote, M. L.; Spyrou, E.; Hilf, S.; Schmidt, F. G.; Barner-Kowollik, C. Thermally Reversible Diels–Alder-Based Polymerization: An Experimental and Theoretical Assessment. *Polym. Chem.* **2012**, *3*, 628.

(394) Chen, X.; Dam, M. A.; Ono, K.; Mal, A.; Shen, H.; Nutt, S. R.; Sheran, K.; Wudl, F. A Thermally Re-Mendable Cross-Linked Polymeric Material. *Science (80-.).* **2002**, *295*, 1698–1702.

(395) Inglis, A. J.; Sinnwell, S.; Davis, T. P.; Barner-Kowollik, C.; Stenzel, M. H. Reversible Addition Fragmentation Chain Transfer (RAFT) and Hetero-Diels-Alder Chemistry as a Convenient Conjugation Tool for Access to Complex Macromolecular Designs. *Macromolecules* **2008**, *41*, 4120–4126.

(396) Zydziak, N.; Feist, F.; Huber, B.; Mueller, J. O.; Barner-Kowollik, C. Photo-Induced Sequence Defined Macromolecules via Hetero Bifunctional Synthons. *Chem. Commun.* **2015**, *51*, 1799–1802.

(397) Konosonoks, A.; Wright, P. J.; Tsao, M.; Pika, J.; Novak, K.; Sarah, M.; Bauer, J. a K.; Bohne, C.; Gudmundsdóttir, A. D. Supporting Information for : Photoenolization of 2- (2-Methyl Benzoyl) Benzoic Acid , Methyl Ester : The Effect of The Lifetime of the E Photoenol on the Photochemistry. *J. Org. Chem.* **2005**, *70* (c), 2763–2770.

(398) Dormán, G.; Prestwich, G. D. Benzophenone Photophores in Biochemistry. *Biochemistry* **1994**, *33*, 5661–5673.

(399) Cai, X.; Sakamoto, M.; Yamaji, M.; Fujitsuka, M.; Majima, T. C-O Bond Cleavage of Benzophenone Substituted by 4-CH2or (R= C6H5 and CH3) with Stepwise Two-Photon Excitation. *J. Phys. Chem. A* **2005**, *109*, 5989–5994.

(400) Otera, J. Transesterification. *Chem. Rev.* **1993**, *93*, 1449–1470.

(401) Schenzel, A. M.; Klein, C.; Rist, K.; Moszner, N.; Barner-Kowollik, C. Reversing Adhesion: A Triggered Release Self-Reporting Adhesive. *Adv. Sci.* **2016**, *3*, 1500361.

(402) Zhu, J.; Cole, R. B. Formation and Decompositions of Chloride Adduct Ions, [M + Cl]−, in Negative Ion Electrospray Ionization Mass Spectrometry. *J. Am. Soc. Mass Spectrom.* **2000**, *11*, 932–941.

(403) González-Burgos, M.; Alegría, A.; Arbe, A.; Colmenero, J.; Pomposo, J. A. An Unexpected Route to Aldehyde-Decorated Single-Chain Nanoparticles from Azides. *Polym. Chem.* **2016**, *7*, 6570–6574.

(404) Zieger, M. M.; Mueller, P.; Quick, A. S.; Wegener, M.; Barner-Kowollik, C. Cleaving Direct-Laser-Written Microstructures on Demand. *Angew. Chemie Int. Ed.* **2017**, *56*, 5625–5629.

(405) Han, D.; Tong, X.; Zhao, Y. Fast Photodegradable Block Copolymer Micelles for Burst Release. *Macromolecules* **2011**, *44*, 437–439.

A

APPENDIX

CHLORIDE ATTACHMENT IN NEGATIVE ION MODE

Poly(styrene)
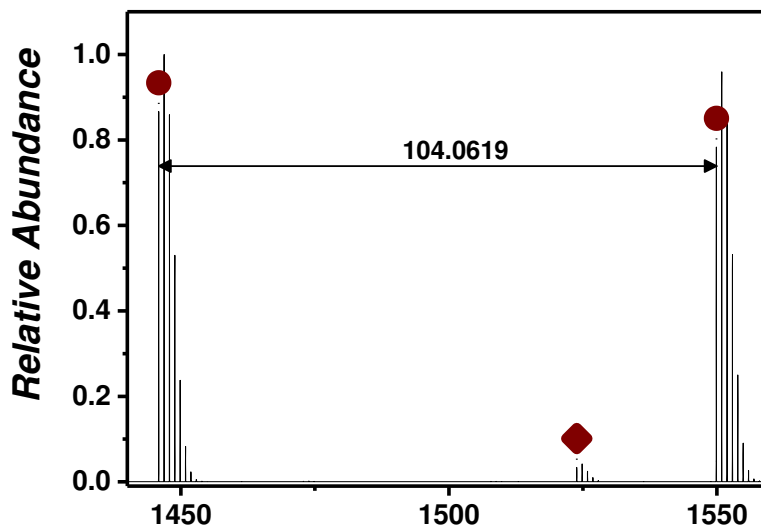
Fig. A 1 Expanded ESI Orbitrap mass spectrum (negative ion mode via Cl⁻ attachment) of PS 1700 g·mol⁻¹ between 1440 *m/z* and 1560 *m/z*. Labeled are the most abundant species and the repeating unit of PS (*m/z*(exp) 104.0619; *m/z*(theo) 104.0626).

Tab. A 1 Peak assignment of the ESI Orbitrap mass spectrum of PS showing the labels (corresponding to the species in Fig. A 1), the resolution (obtained by the Xcalibur software), the experimental m/z and theoretical m/z values, Δm/z and the proposed chemical structures.

Label	Resolution	*m/z*(exp)	*m/z*(theo)	Δ*m/z*	Structure
●	58000	1445.8618	1445.8615	0.0003	
◆	78000	1523.8774	1523.8720	0.0054	$C_{113}H_{116}ClO^-$
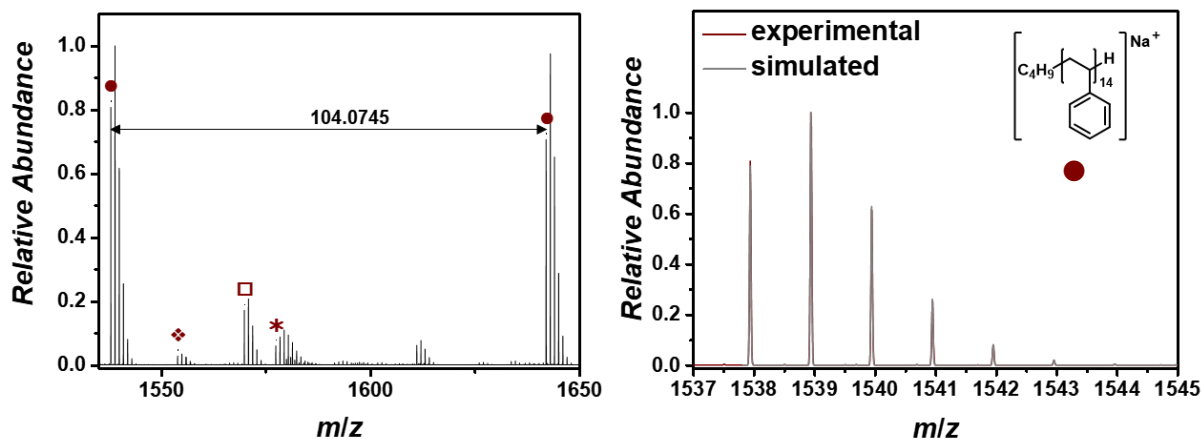
Fig. A 2 Expanded ESI Orbitrap mass spectrum (positive ion mode via Na⁺ attachment) of PS 1700 g·mol⁻¹ between 1535 *m/z* and 1650 *m/z*. Labeled are the most abundant species and the repeating unit of PS (m/z(exp) 104.0745; m/z(theo) 104.0626). Species labeled with ∗ stem from present poly(dimethylsiloxane) (PDMS) (repeating unit: *m/z*(exp) 74.0189; m/z(theo) 74.0188).

Tab. A 2 Peak assignment of the ESI Orbitrap mass spectrum of PS showing the labels (corresponding to the species in Fig. A 2), the resolution (obtained by the Xcalibur software), the experimental *m/z* and theoretical *m/z* values, Δ*m/z* and the proposed chemical structures.

Label	Resolution	*m/z*(exp)	*m/z*(theo)	Δ*m/z*	Structure
●	54000	1537.9455	1537.9439	0.0016	
❖	53000	1553.9223	1553.9388	0.0164	
□	53000	1569.8581	1569.8561	0.0020	

Poly(1,4 butadiene)
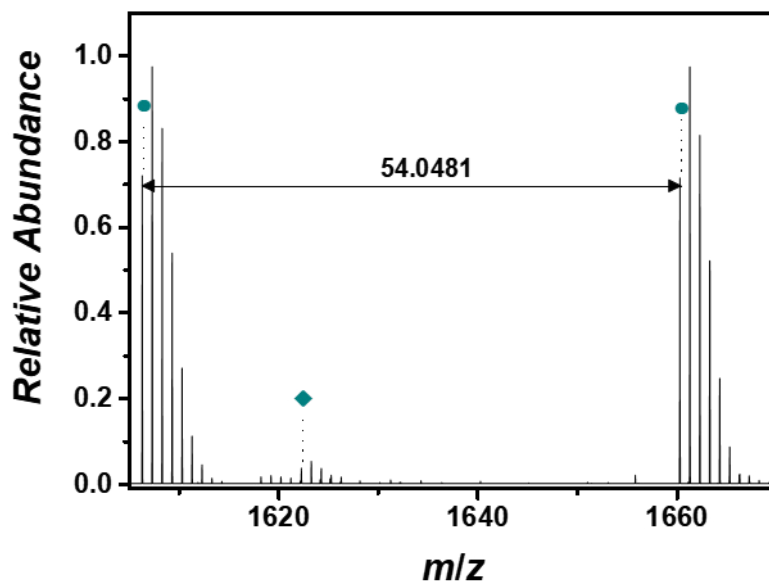
Fig. A 3 Expanded ESI Orbitrap mass spectrum (negative mode via Cl⁻ attachment) of PBD 2000 g·mol⁻¹ between 1605 *m/z* and 1670 *m/z*. Labeled are the most abundant species and the repeating unit of PBD (m/z(exp) 54.0481; m/z(theo) 54.0470).

Tab. A 3 Peak assignment of the ESI Orbitrap mass spectrum of PS showing the labels (corresponding to the species in Fig. A 3), the resolution (obtained by the Xcalibur software), the experimental *m/z* and theoretical *m/z* values, Δ*m/z* and the proposed chemical structures.

Label	Resolution	*m/z*(exp)	*m/z*(theo)	Δ*m/z*	Structure
●	50000	1606.3663	1606.3612	0.0052	$\left[C_4H_9 \diagup\diagdown\diagup H \right]_{28} Cl^-$
◆	53000	1622.3599	1622.3561	0.0039	$\left[C_4H_9 \diagup\diagdown\diagup OH \right]_{28} Cl^-$

Poly(2-vinylpyridine)
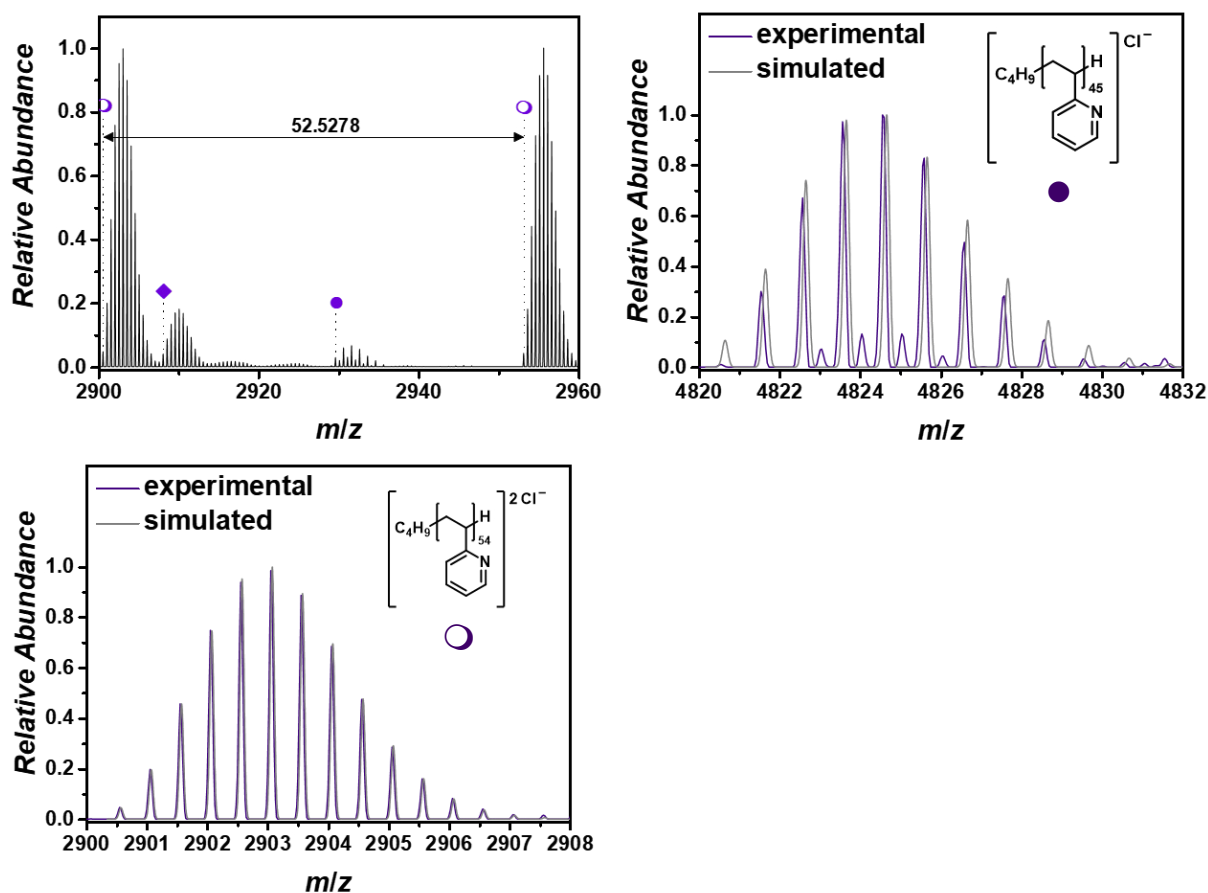
Fig. A 4 Expanded ESI Orbitrap mass spectrum (negative mode via Cl⁻ attachment) of P2VP 5000 g·mol⁻¹ (recorded in DCM/MeOH) between 2900 m/z and 2960 m/z. Labeled are the most abundant species and the repeating unit of P2VP (m/z(exp) 52.5278; m/z(theo) 52.5295). Isotopic simulation of the singly (●) and doubly (○) charged P2VP with their individual polymer structure determined by comparing the experiment with the simulation.

Tab. A 4 Peak assignment of the ESI Orbitrap mass spectrum of PS showing the labels (corresponding to the species in Fig. A 4), the resolution (obtained by the Xcalibur software), the experimental m/z and theoretical m/z values, $\Delta m/z$ and the proposed chemical structures.

Label	Resolution	m/z(exp)	m/z(theo)	$\Delta m/z$	Structure
○	38000	2900.5532	2900.5705	0.0173	
◆	38000	2908.0619	2908.0759	0.0140	
●	39000	2929.5849	2929.6096	0.0247	

V
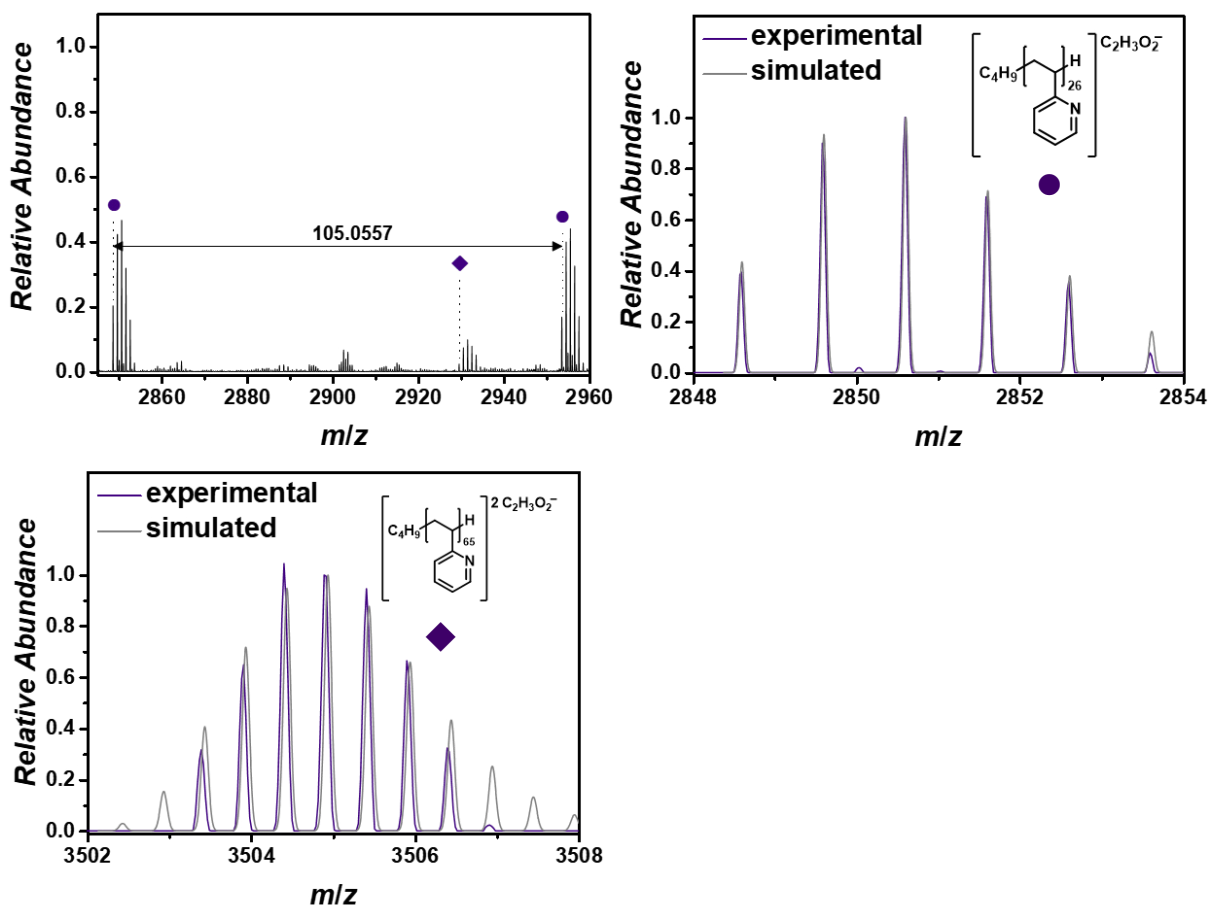
Fig. A 5 Expanded ESI Orbitrap mass spectrum (negative mode via Cl⁻ attachment) of P2VP 5000 g·mol⁻¹ (recorded in water/acetonitrile with 0.1% acetic acid) between 2845 m/z and 2960 m/z. Labeled are the most abundant species and the repeating unit of P2VP (m/z(exp) 105.0557; m/z(theo) 105.0578). Isotopic simulation of the singly (●) and doubly (◆) charged P2VP with their individual polymer structure determined by comparing the experiment with the simulation.

Tab. A 5 Peak assignment of the ESI Orbitrap mass spectrum of PS showing the labels (corresponding to the species in Fig. A 5), the resolution (obtained by the Xcalibur software), the experimental m/z and theoretical m/z values, $\Delta m/z$ and the proposed chemical structures.

Label	Resolution	m/z(exp)	m/z(theo)	$\Delta m/z$	Structure
●	38000	2848.5840	2848.5962	0.0121	
◆	39000	2930.5909	2930.5993	0.0084	

CHARGE STATE MANIPULATION BY SUPERCHARGING AGENTS

Poly(acrylamide)
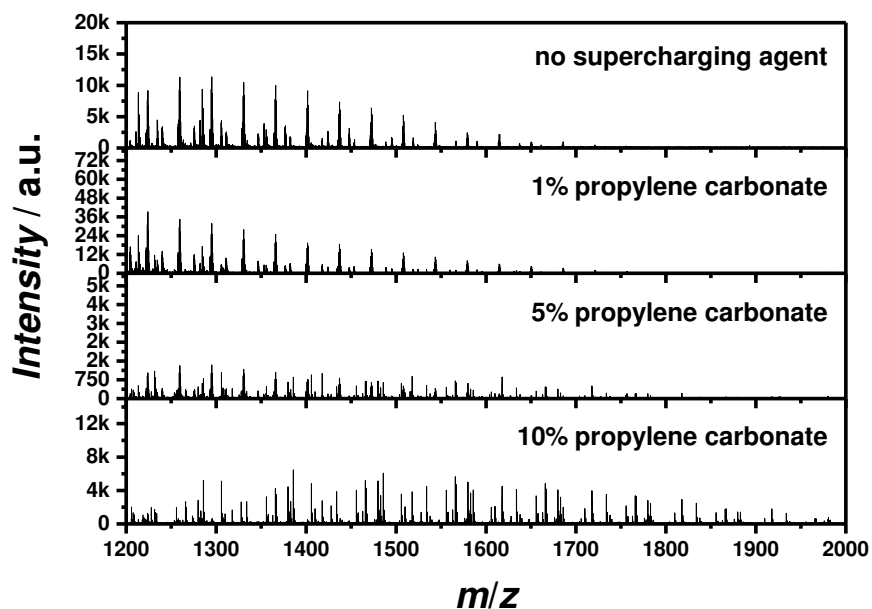
Fig. A 6 ESI-Orbitrap mass spectra of PAAm 13700 g·mol^{-1} in negative mode (partly via Cl^{-} attachment) comparing the influence of different amounts of propylene carbonate as supercharging agent ranging from 0% (v/v) to 10% (v/v). No PAAm species can be detected recording the spectrum with 10% PC.

Poly(styrene)
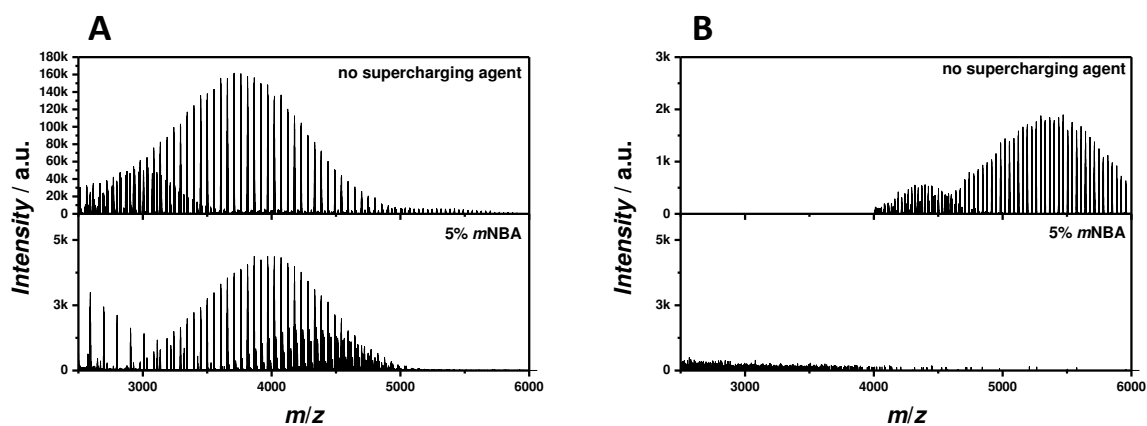
Fig. A 7 ESI-Orbitrap mass spectra of PS 9000 g· mol^{-1} (A) and 18000 g· mol^{-1} (B) recorded with 5% (v/v) mNBA.

B

APPENDIX

Synthesis of Poly(Ionic Liquid)s

Tab. B 1 RAFT polymerization of [BVBIM]Cl employing ethanol and DMSO/water (1:1, *v/v*) as solvents.

| Entry | Ethanol | | | | | | H₂O/DMSO (1:1, v/v) | | | | | |
| | t | $M_n^{theo.}$ | M_n^{NMR} | M_n^{SEC} | $Đ^{SEC}$ | Conv. | t | $M_n^{theo.}$ | M_n^{NMR} | M_n^{SEC} | $Đ^{SEC}$ | Conv. |
	[h]	[g mol⁻¹]	[g mol⁻¹]	[g mol⁻¹]		[%]	[h]	[g mol⁻¹]	[g mol⁻¹]	[g mol⁻¹]		[%]
1	2	5100	6200	1100	6.44	13	2	5000	3700	2300	2.0	20
2	4	8900	8700	11700	1.90	23	4	6300	4000	4000	1.7	25
3	5	13300	12000	17000	1.69	35	6	12000	8000	8200	1.6	48
4	8	17400	15000	20000	1.76	47	8	16000	6400	8900	1.6	67

NMR Data
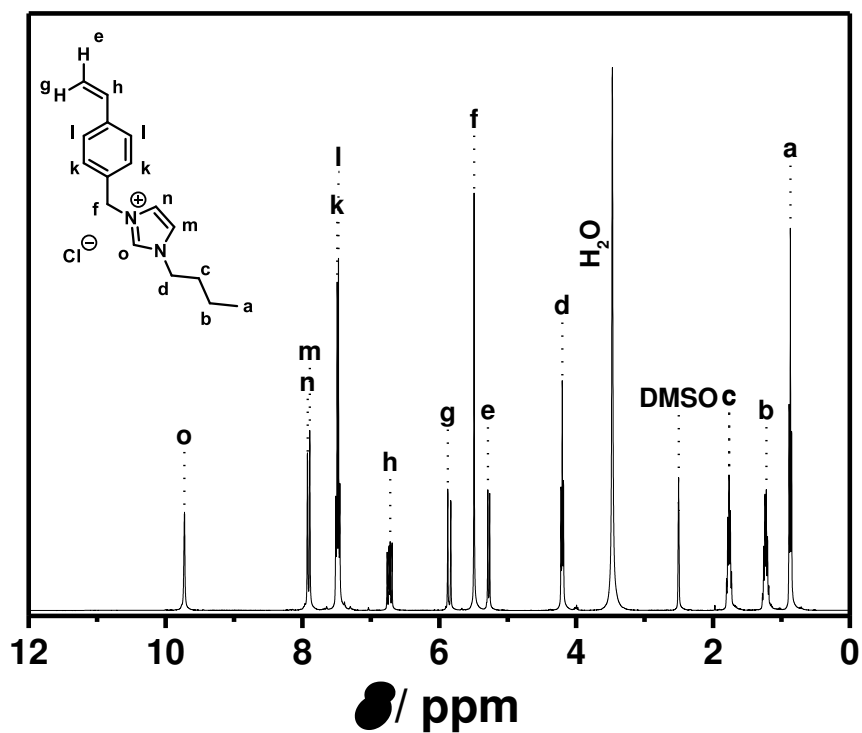
Fig. B 1 ^{1}H NMR (400 MHz, 298 K) of monomer **1** in DMSO-d_6.
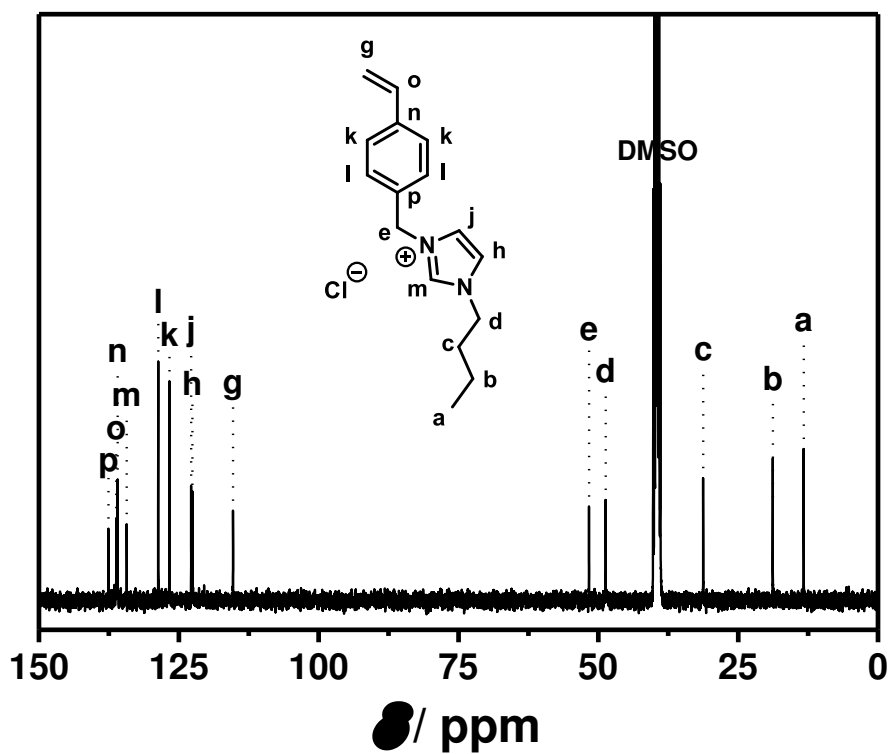
Fig. B 2 ^{13}C{^{1}H} (100 MHz, 298 K) of monomer **1** in DMSO-d_6.

X
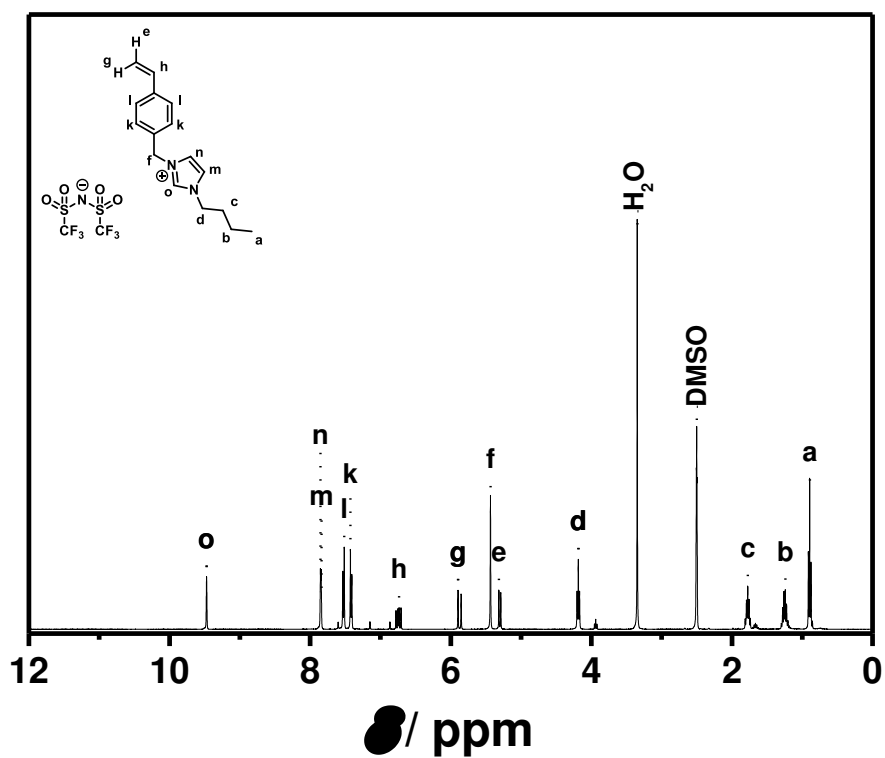
Fig. B 3 ^{1}H NMR (400 MHz, 298 K) of monomer **2** in DMSO-d$_6$.
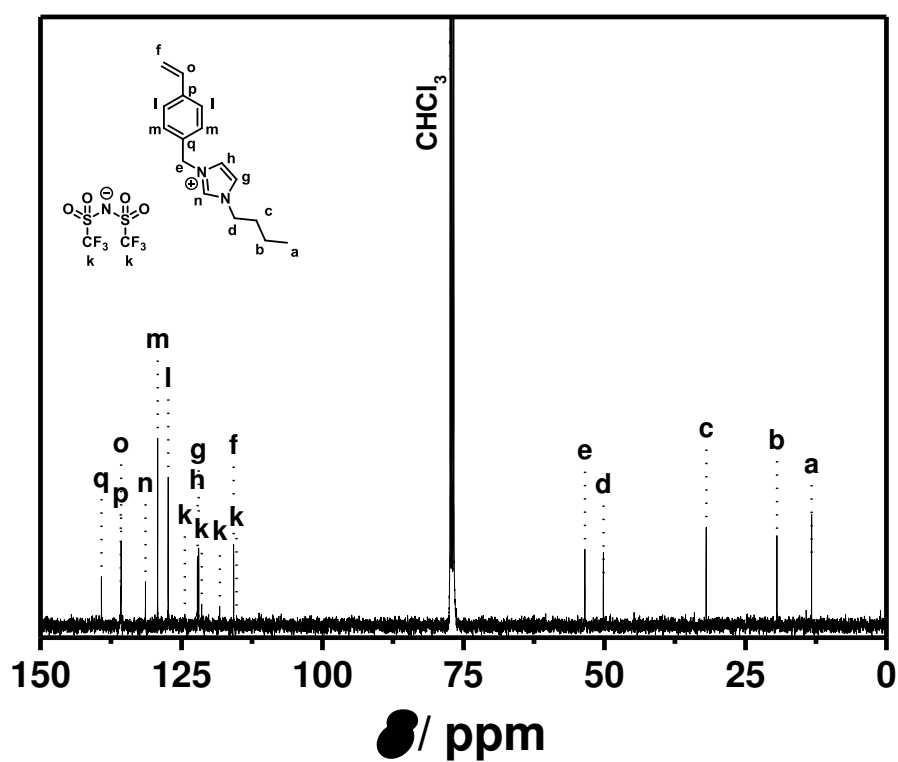
Fig. B 4 ^{13}C{^{1}H} (100 MHz, 298 K) of monomer **2** in CDCl$_3$.
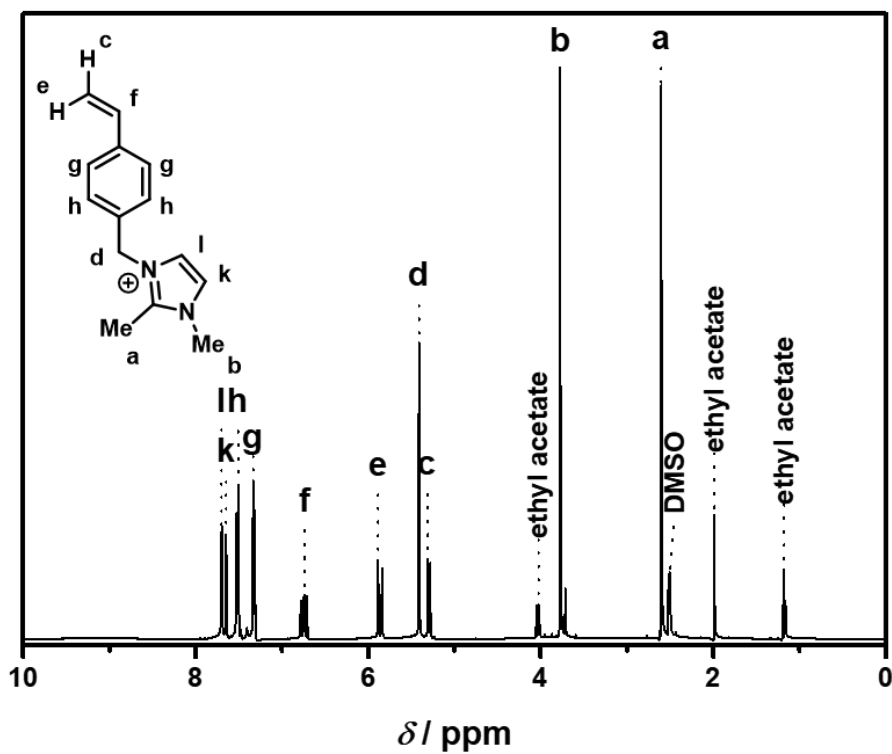
Fig. B 5 ^{1}H NMR (400 MHz, 298 K) of monomer **1'** in DMSO-d$_6$.
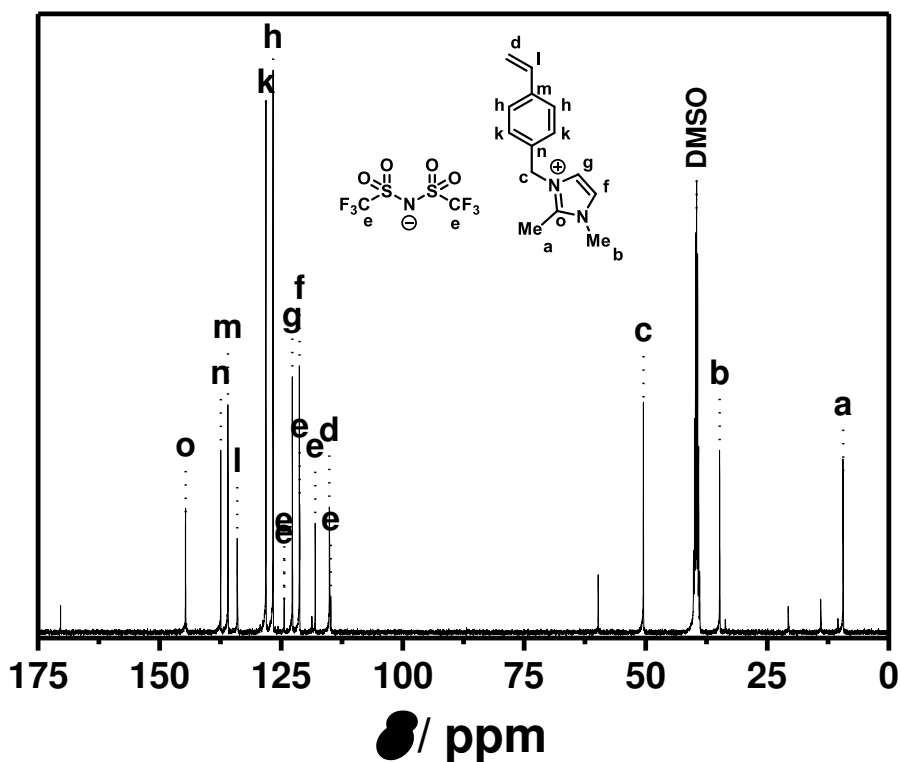
Fig. B 6 ^{13}C{^{1}H} (100 MHz, 298 K) of monomer **1'** in DMSO-d$_6$.

XII
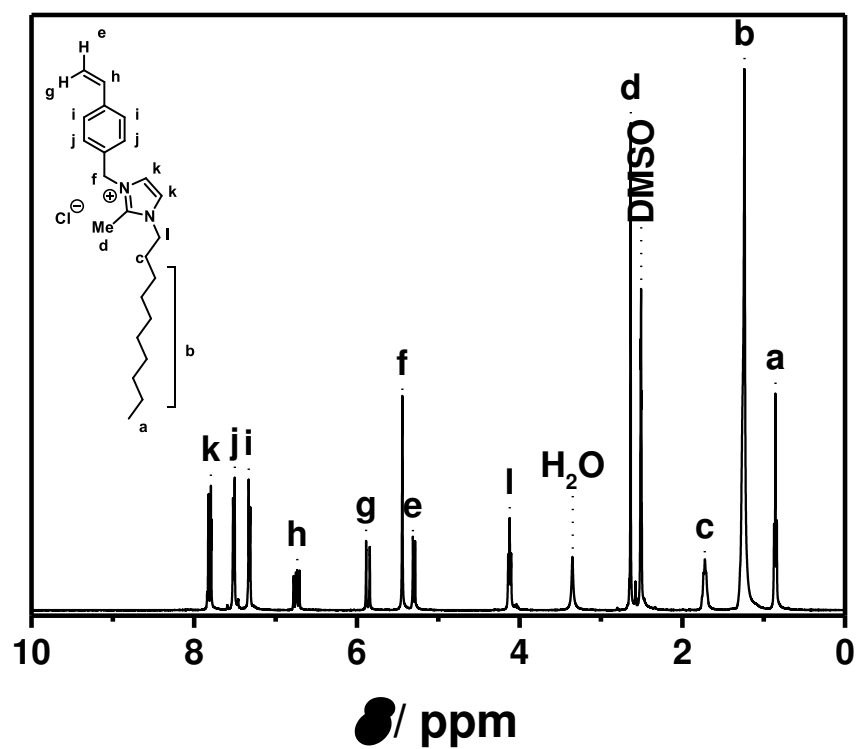
Fig. B 7 ¹H NMR (400 MHz, 298 K) of [DeMVBIM]Cl in DMSO-d_6.
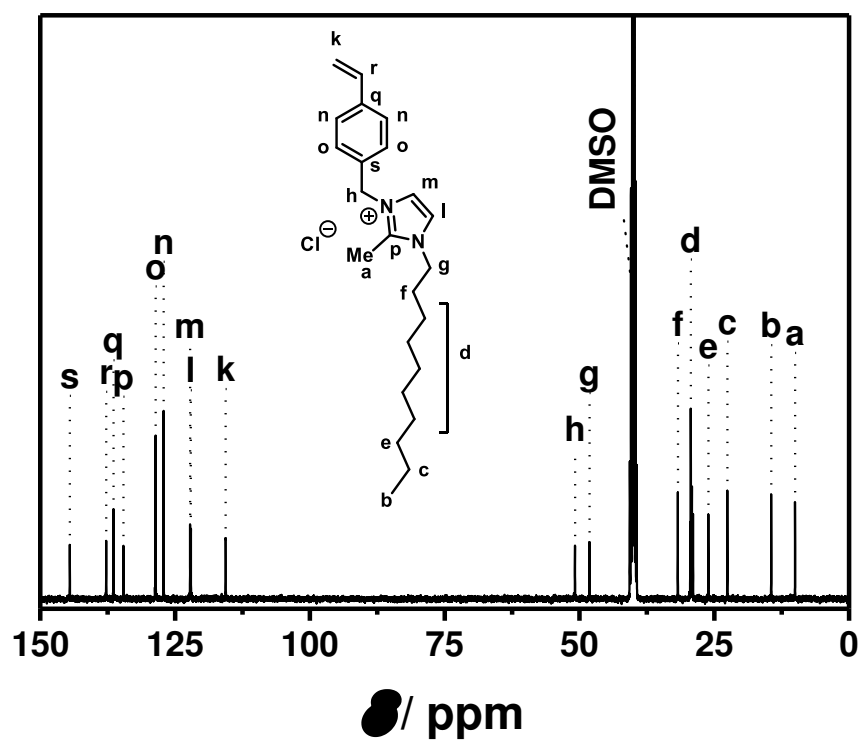
Fig. B 8 ¹³C{¹H} NMR (100 MHz, 298 K) of [DeMVBIM]Cl in DMSO-d_6.
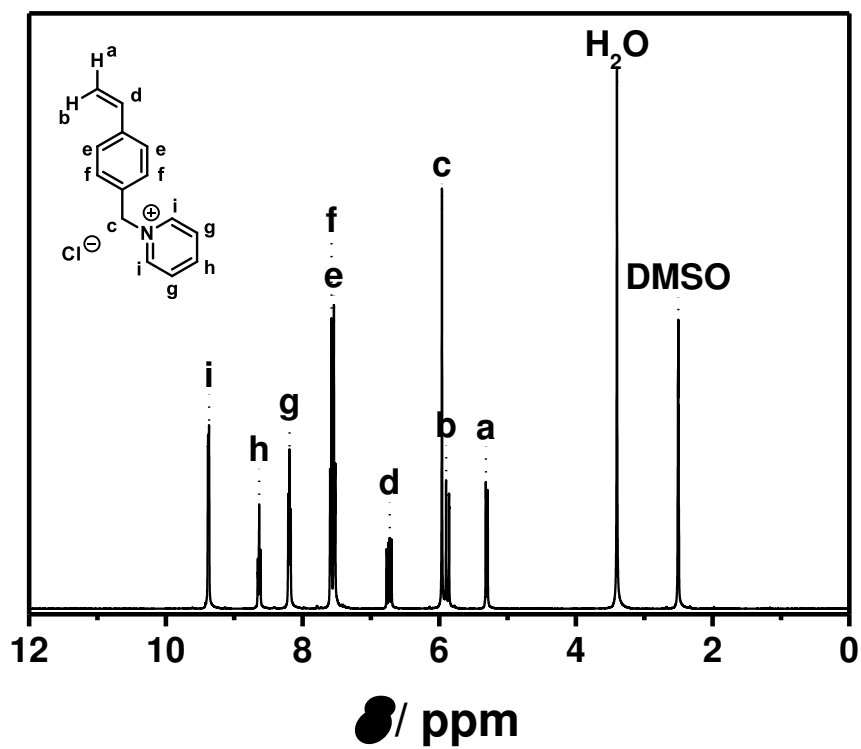
Fig. B 9 ^{1}H NMR (400 MHz, 298 K) of [VBPy]Cl in DMSO-d$_6$.
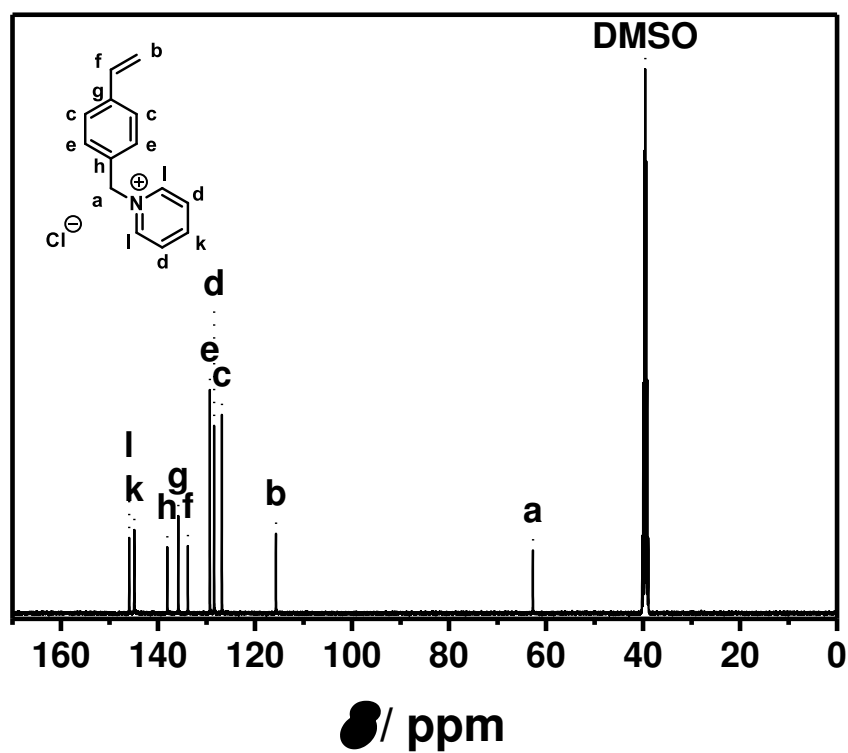
Fig. B 10 ^{13}C{^{1}H} NMR (100 MHz, 298 K) of [VBPy]Cl in DMSO-d$_6$.

XIV
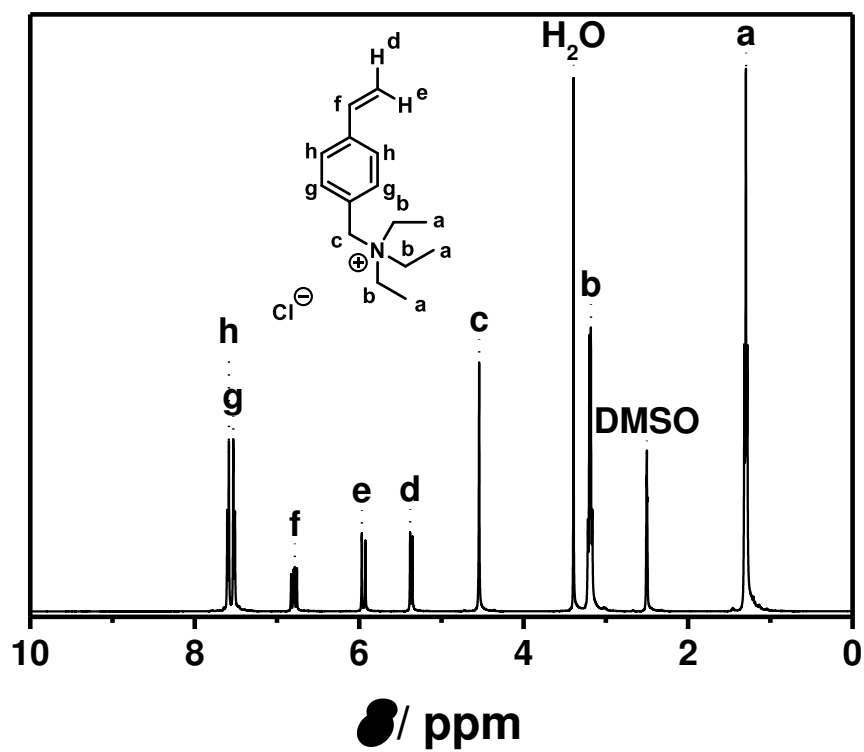
Fig. B 11 ^{1}H NMR (400 MHz, 298 K) of [TEVBA]Cl in DMSO-d$_6$.
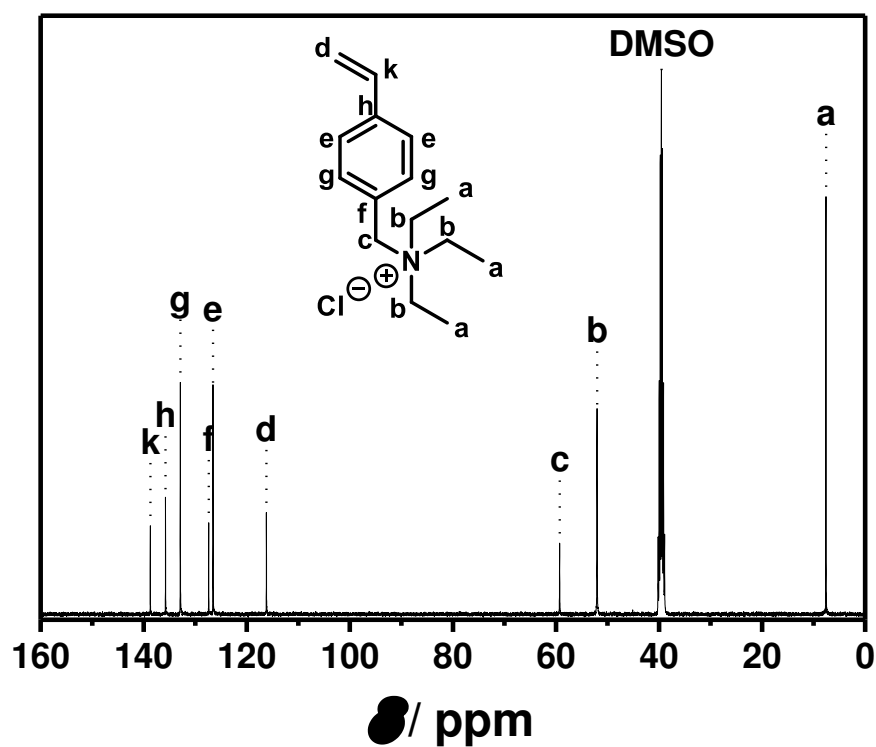
Fig. B 12 ^{13}C{^{1}H} NMR (100 MHz, 298 K) of [TEVBA]Cl in DMSO-d$_6$.
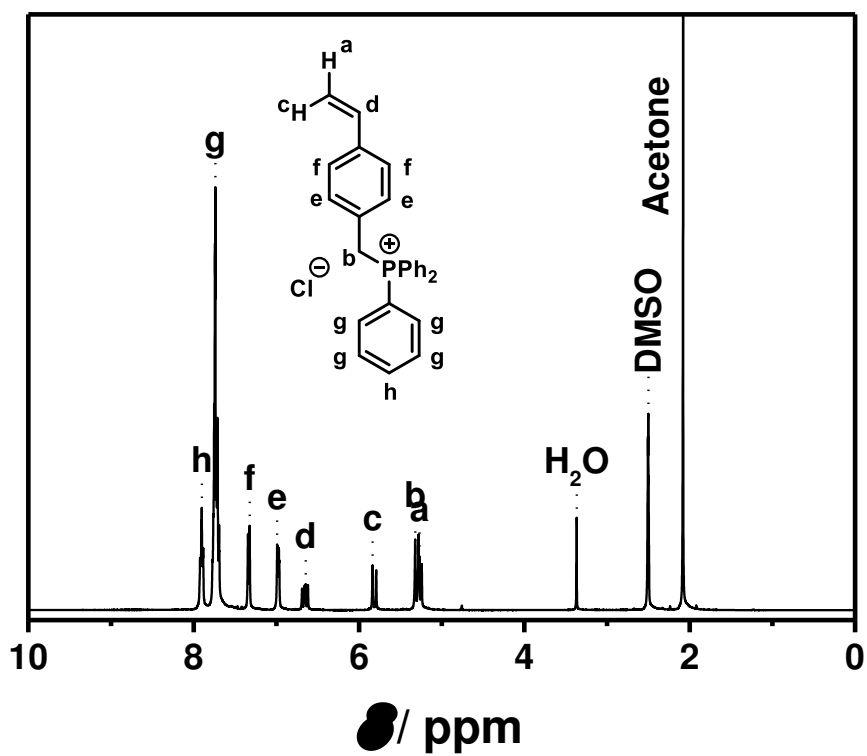
Fig. B 13 ^{1}H NMR (400 MHz, 298 K) of [TPVBP]Cl in DMSO-d_6.
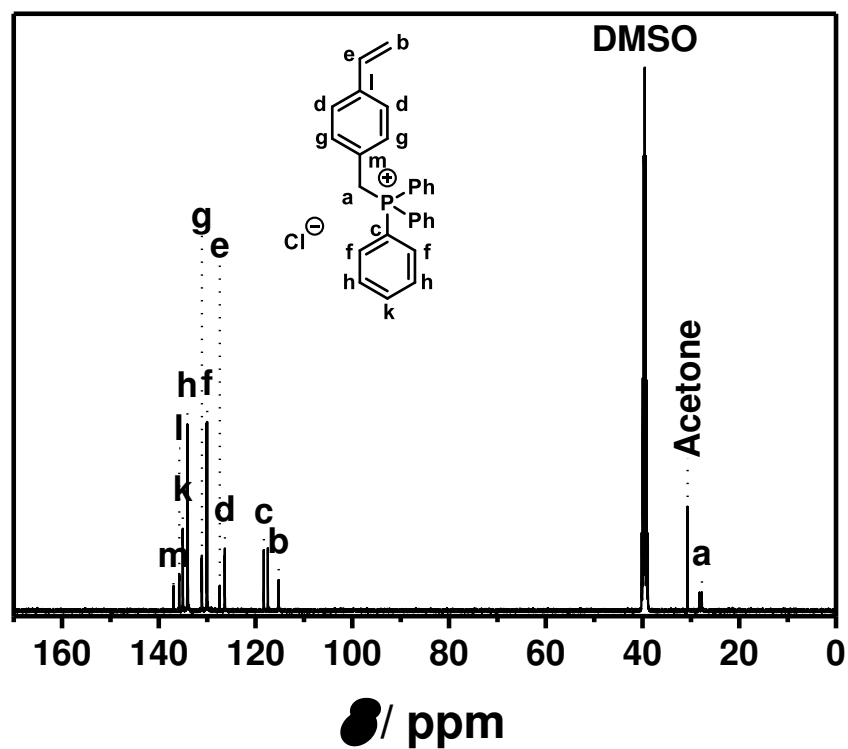
Fig. B 14 ^{13}C{^{1}H} NMR (100 MHz, 298 K) of [TPVBP]Cl in DMSO-d_6.
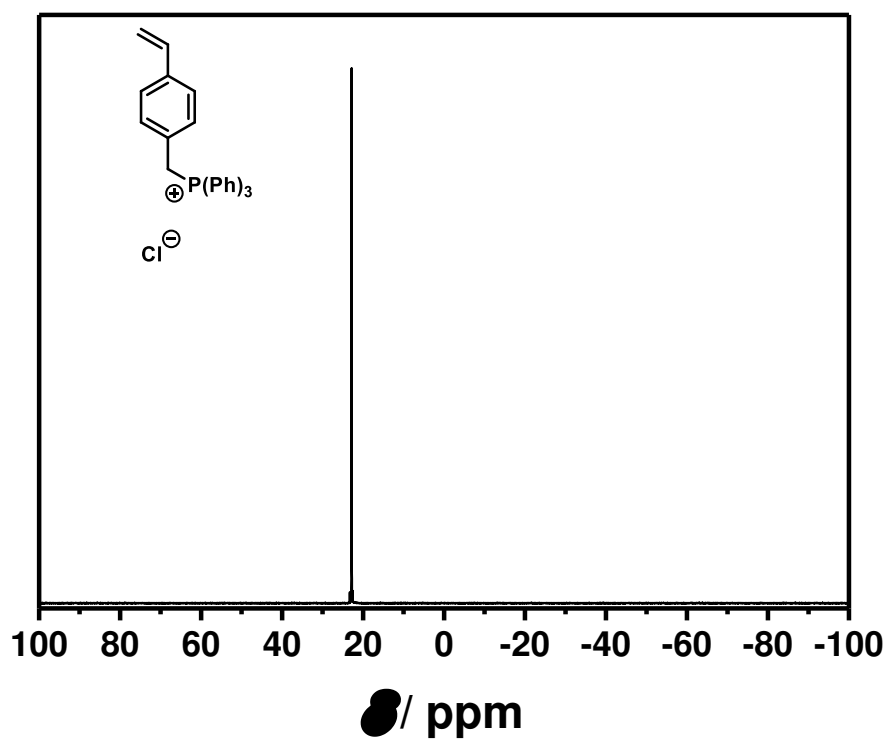
Fig. B 15 ^{31}P{^{1}H} NMR (162 MHz, 298 K) of [TPVBP]Cl in DMSO-d$_6$.
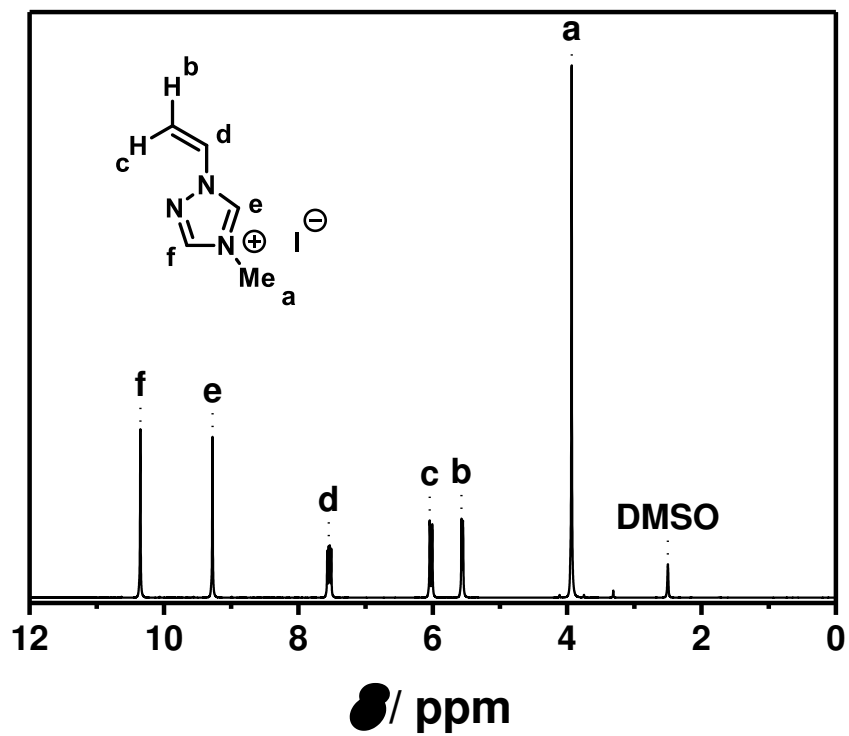
Fig. B 16 ^{1}H NMR (400 MHz, 298 K) of [MVTr]I in DMSO-d$_6$.
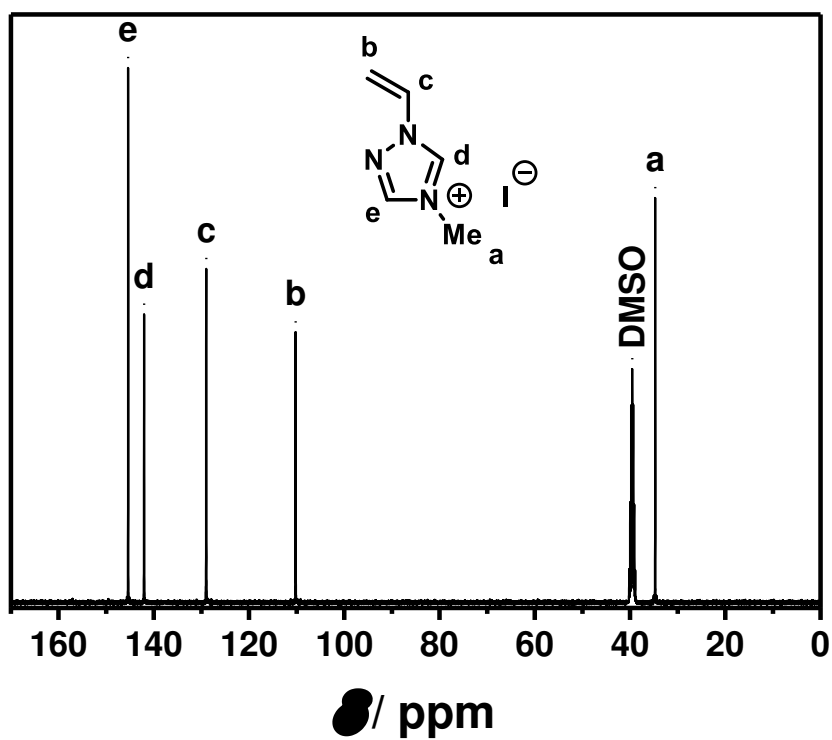
Fig. B 17 ^{13}C{^{1}H} NMR (100 MHz, 298 K) of [MVTr]I in DMSO-d$_6$.

XVIII
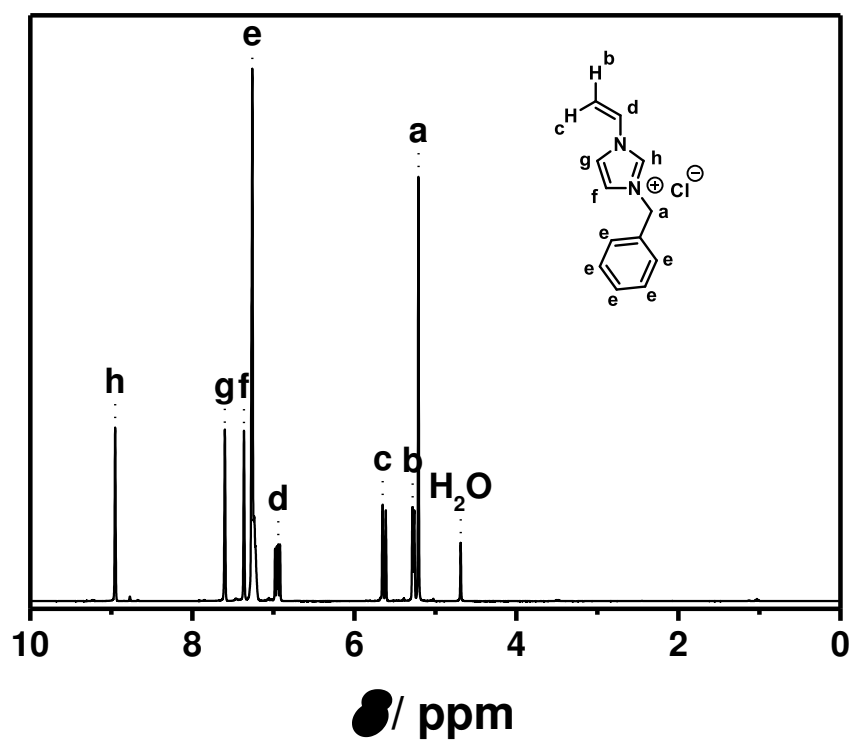
Fig. B 18 ^{1}H NMR (400 MHz, 298 K) of [BnVIM]Cl in D$_2$O.
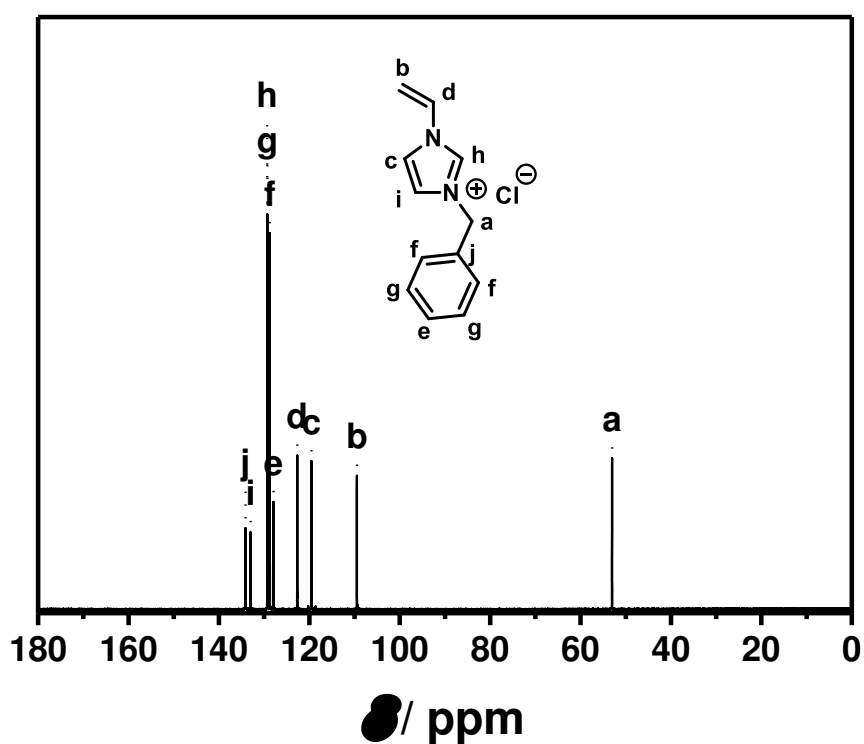
Fig. B 19 ^{13}C{^{1}H} NMR (100 MHz, 298 K) of [BnVIM]Cl in D$_2$O.
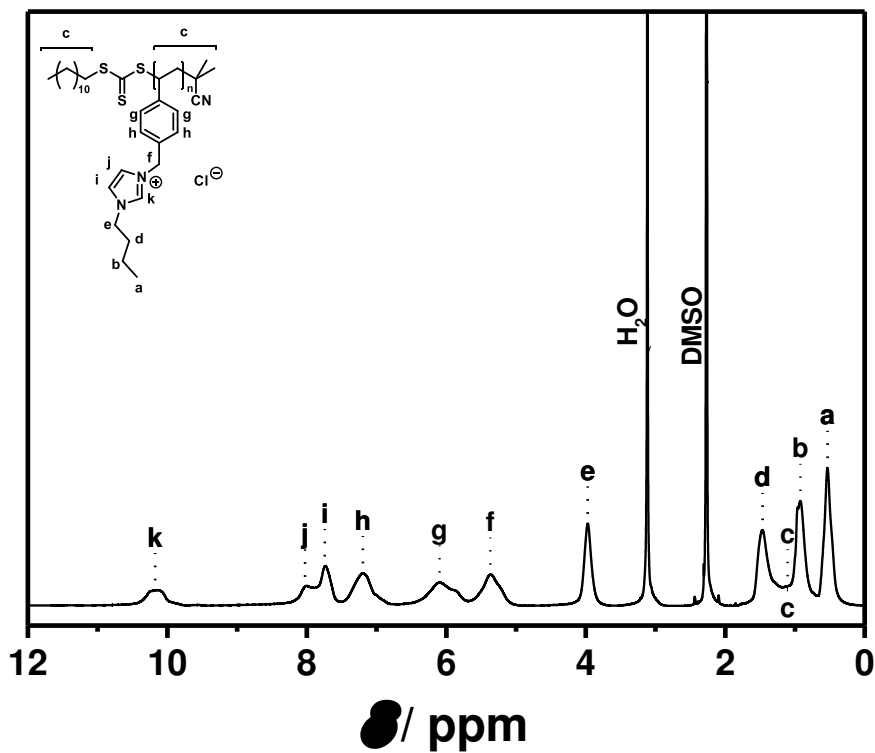
Fig. B 20 ^{1}H NMR (400 MHz, 298 K) of polymer (**3**) in DMSO-d$_6$.
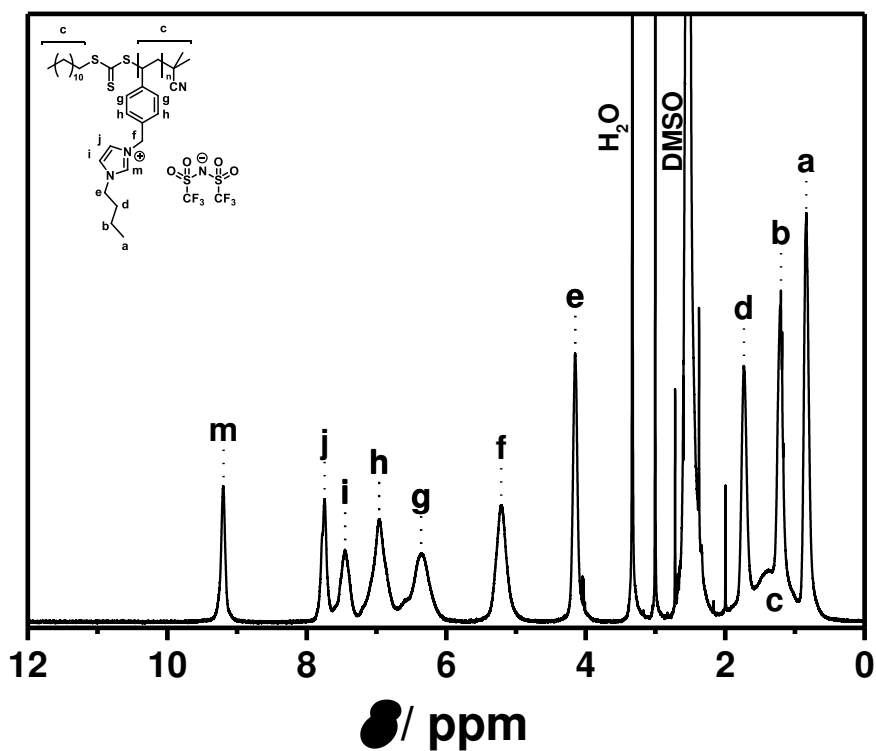
Fig. B 21 ^{1}H NMR (400 MHz, 298 K) of polymer (**4**) in DMSO-d$_6$.

XX
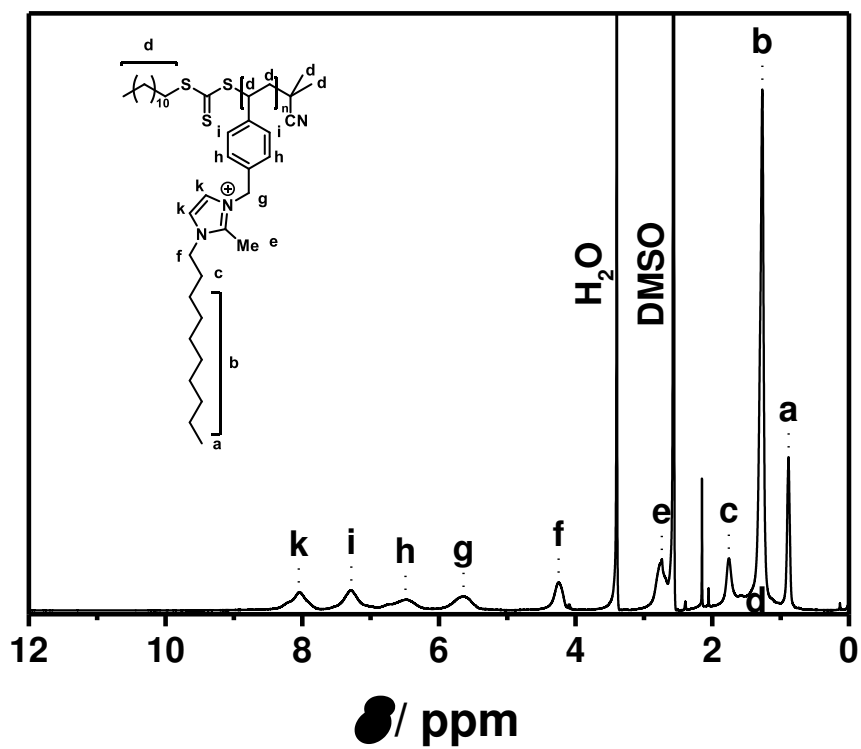
Fig. B 22 ^{1}H NMR (400 MHz, 298 K) of p([DeMVBIM]Cl) (**5**) in DMSO-d$_6$.
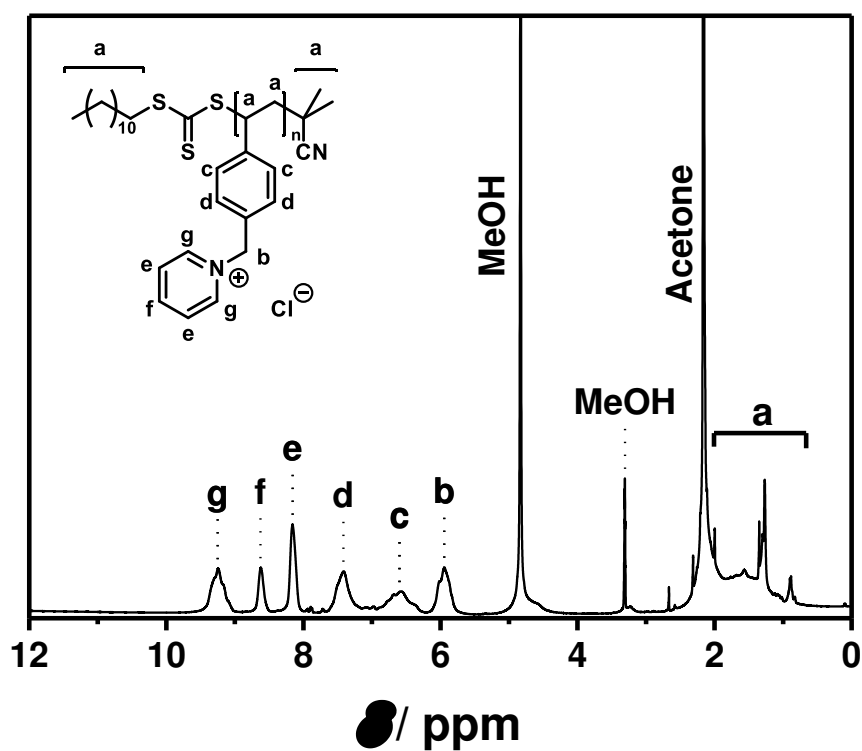
Fig. B 23 ^{1}H NMR (400 MHz, 298 K) of p([VBPy]Cl) (**6**) in MeOD.
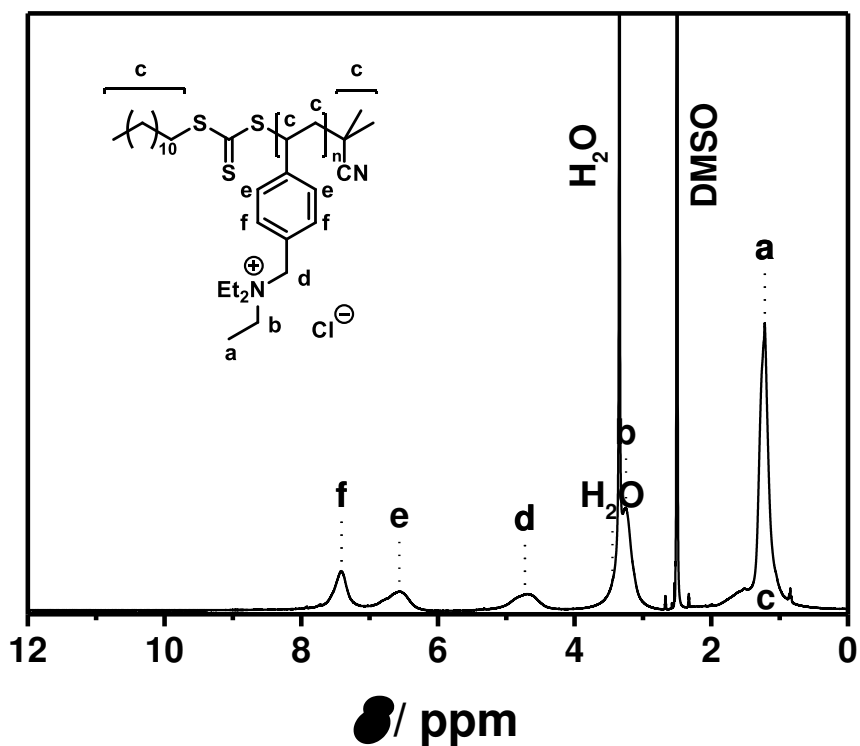
Fig. B 24 ^{1}H NMR (400 MHz, 298 K) of p([TEVBA]Cl) (**7**) in DMSO-d$_6$.
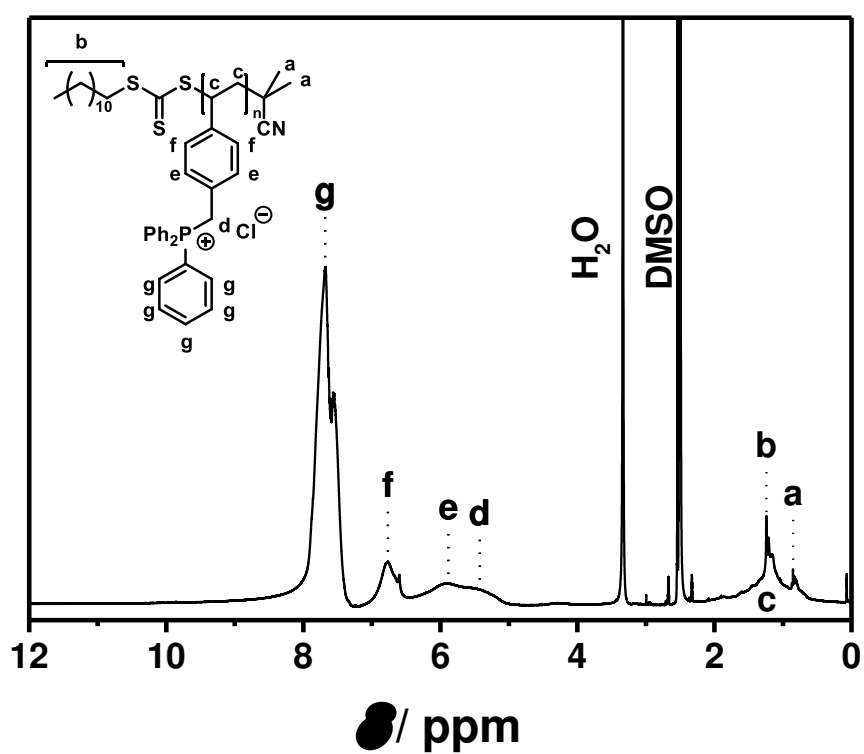
Fig. B 25 ^{1}H NMR (400 MHz, 298 K) of p([TPVBP]Cl) (**8**) in DMSO-d$_6$.
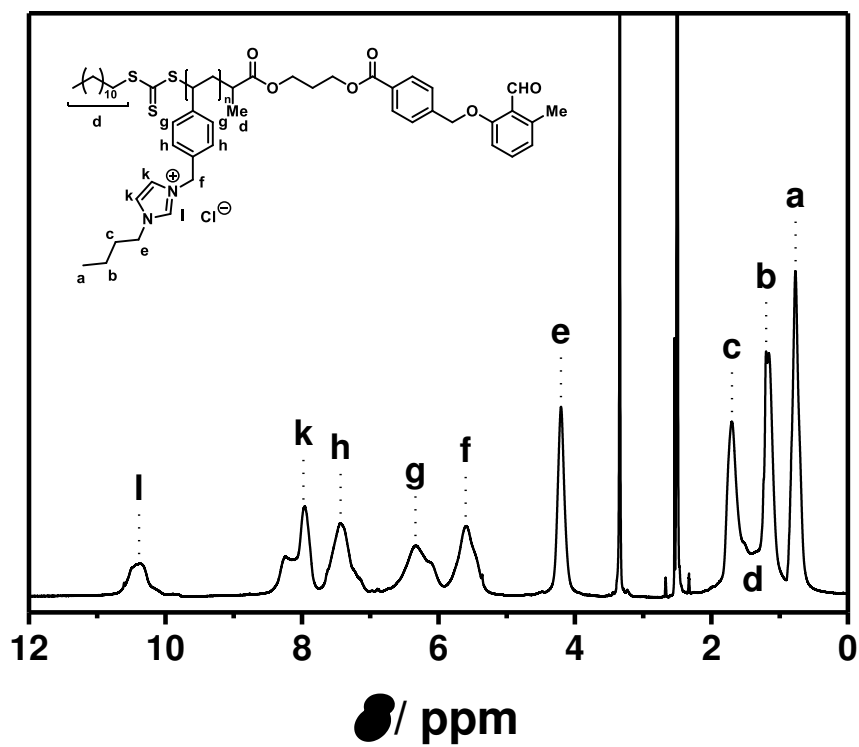
Fig. B 26 ^{1}H NMR (400 MHz, 298 K) of p([BVBIM]Cl) (**10**) in DMSO-d$_6$.
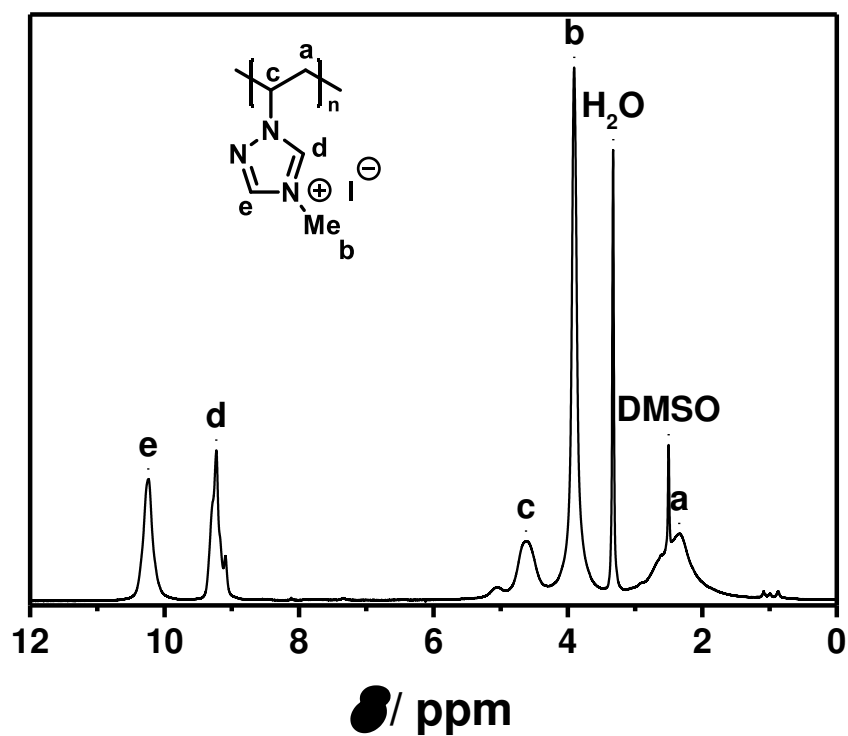
Fig. B 27 ^{1}H NMR (400 MHz, 298 K) of p([MVTr]I) (**11**) in DMSO-d$_6$.
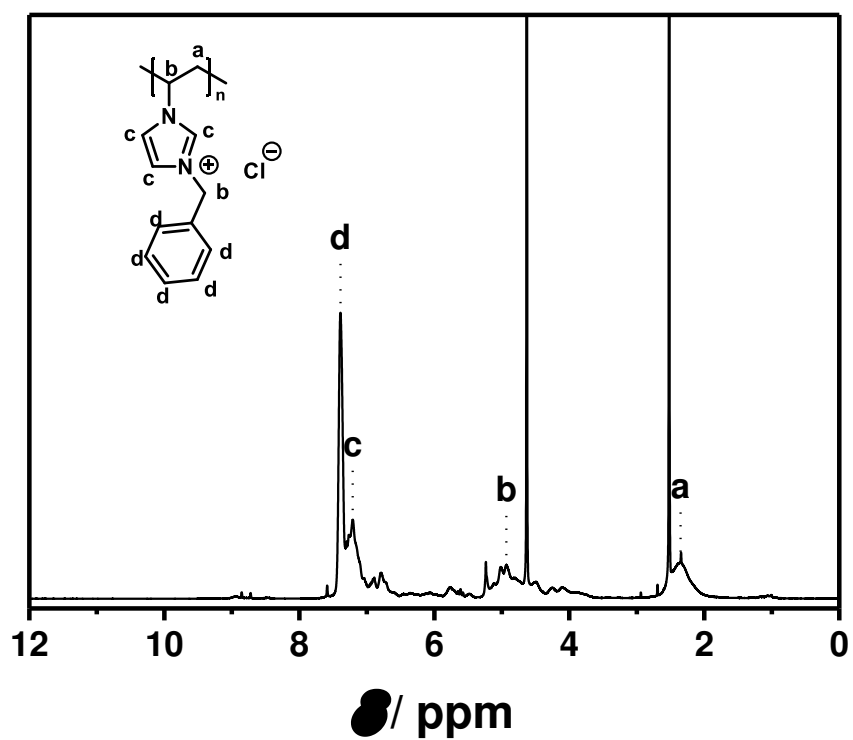
Fig. B 28 ¹H NMR (400 MHz, 298 K) of p([BnVIM]Cl) (**12**) in D₂O.

SEC Traces
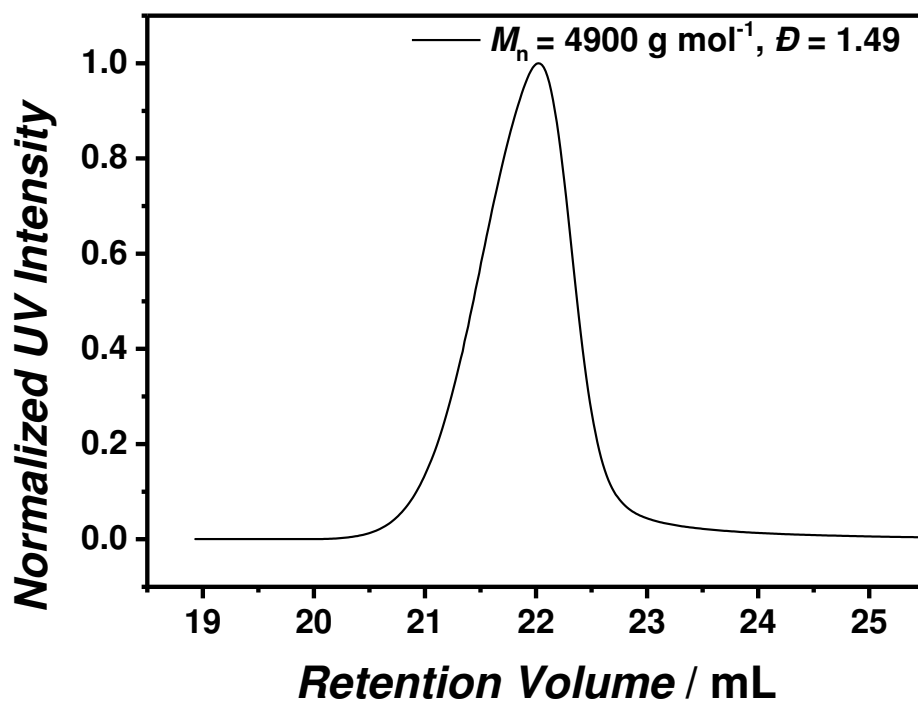
Fig. B 29 SEC trace (eluent: water/0.3 M formic acid/0.5 g·L^{-1} NaCl) of p([DeMVBIM]Cl) (**5**).
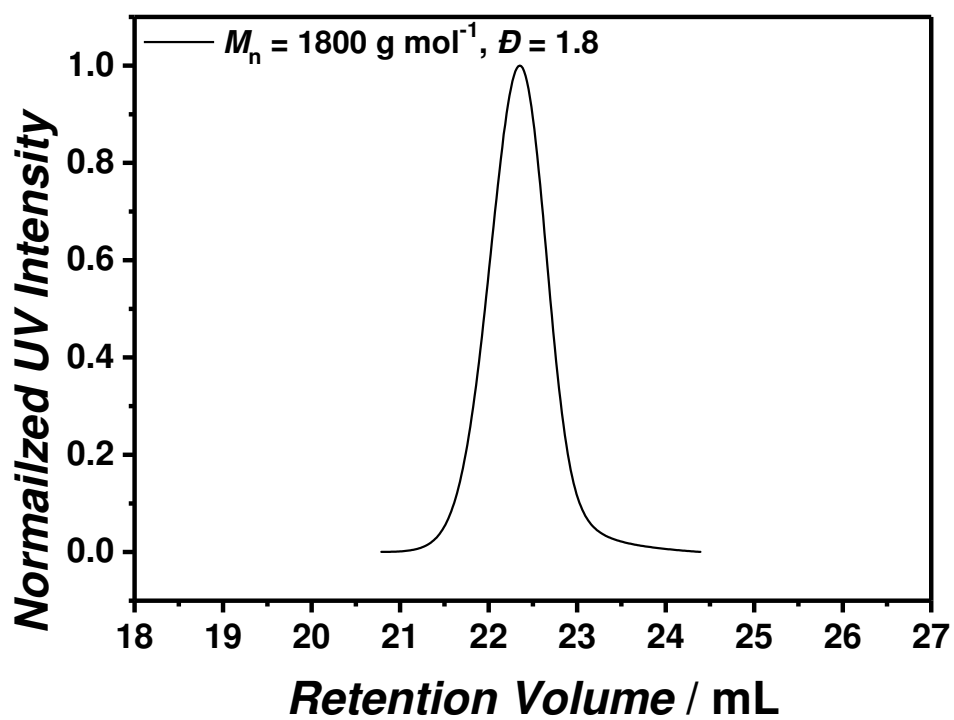
Fig. B 30 SEC trace (eluent: water/0.3 M formic acid/0.5 g·L^{-1} NaCl) of p([VBPy]Cl) (**6**).
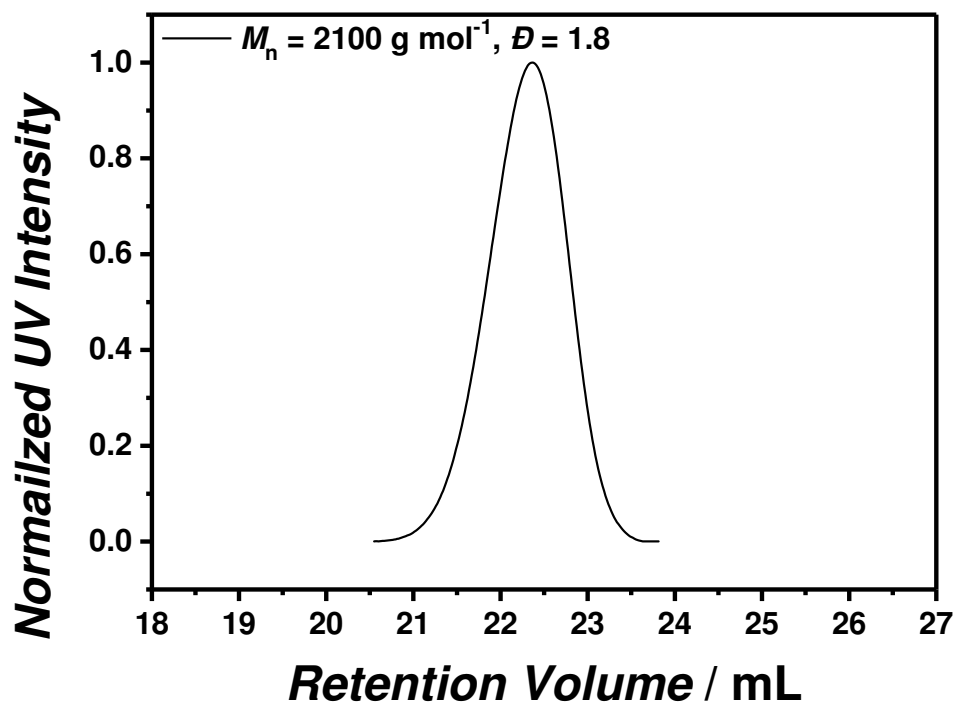
Fig. B 31 SEC trace (eluent: water/0.3 M formic acid/0.5 g·L^{-1} NaCl) of p([TEVBA]Cl) (**7**).
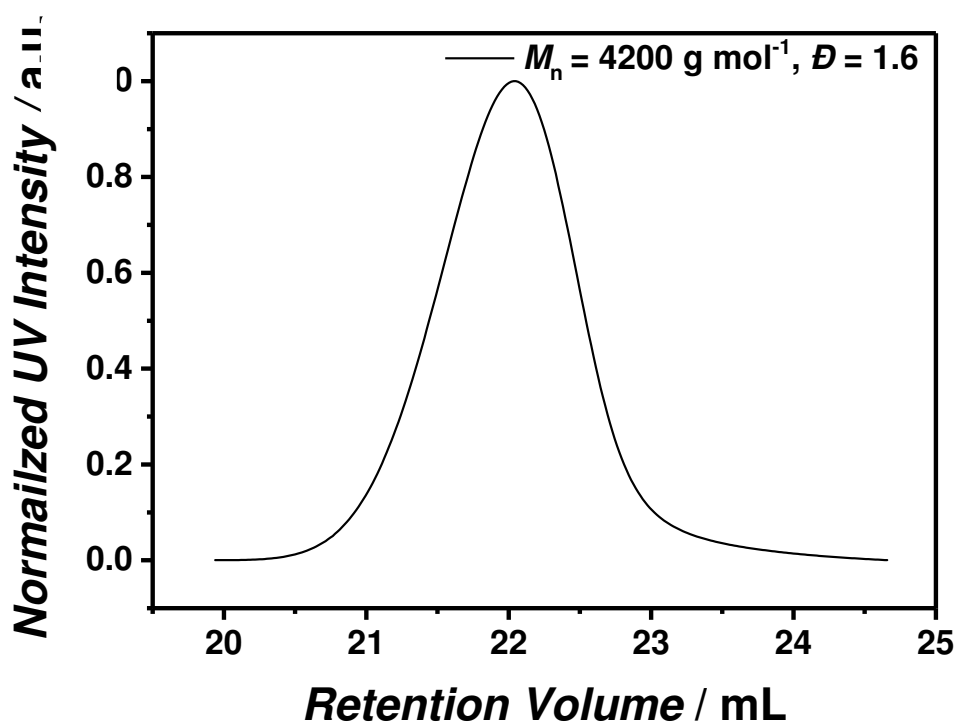
Fig. B 32 SEC trace (eluent: water/0.3 M formic acid/0.5 g·L^{-1} NaCl) of p([TPVBP]Cl) (**8**).
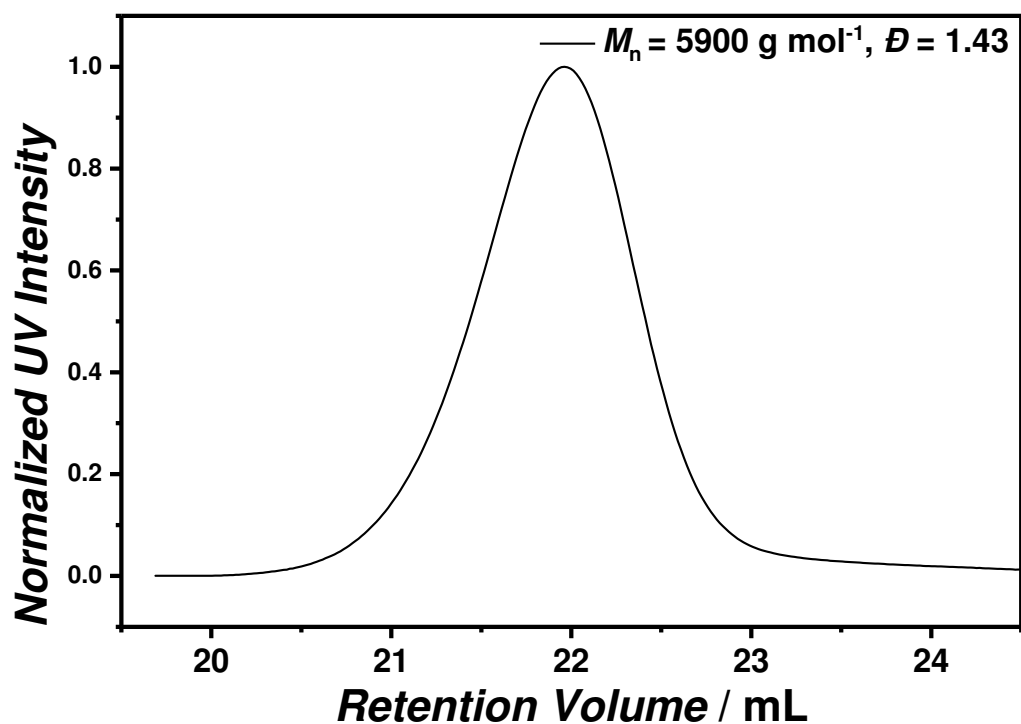
Fig. B 33 SEC trace (eluent: water/0.3 M formic acid/0.5 g · L^{-1} NaCl) of DoPAT-PE polymerized p([BVBIM]Cl) (**10**).
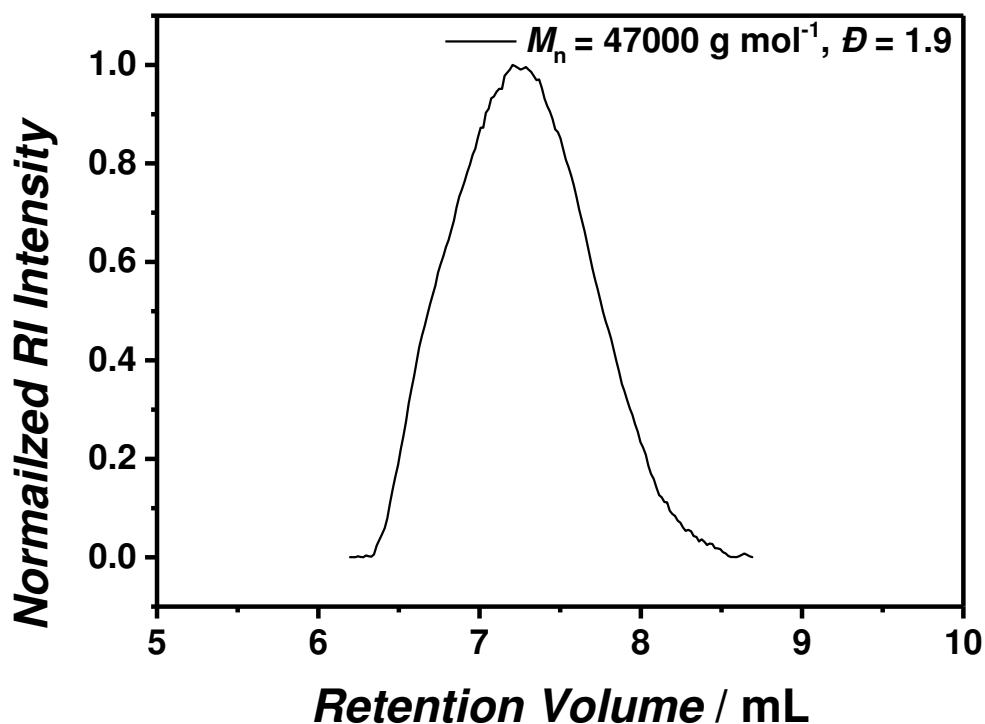
Fig. B 34 SEC trace (eluent: aqueous acetate buffer/methanol (8:2, *v/v*), calibration standard pullulan) of p[([MVTr]I) (**11**).
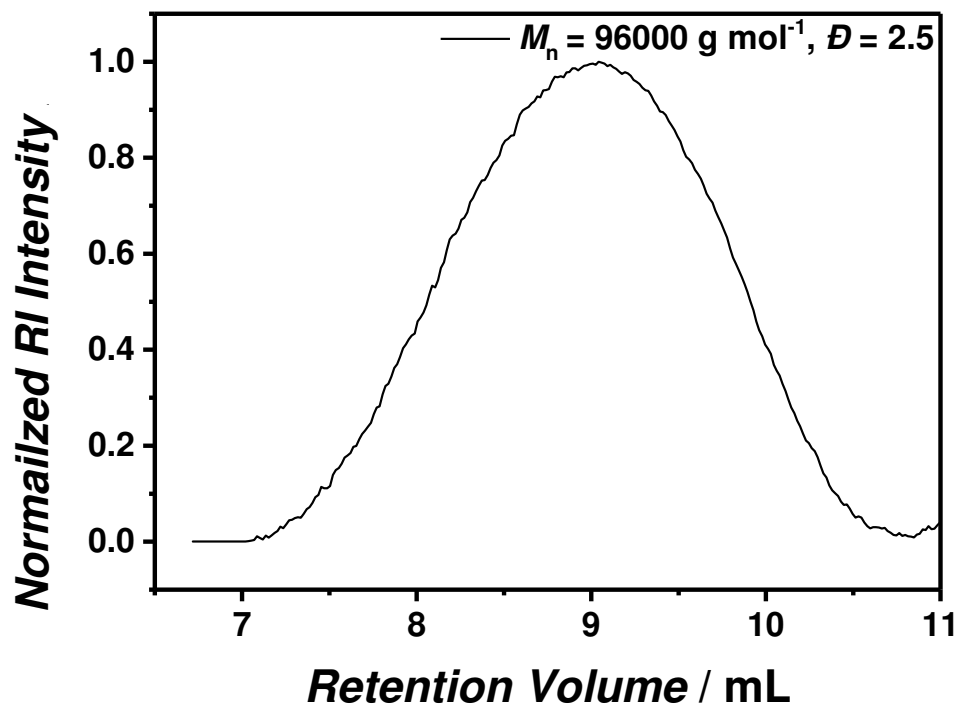
Fig. B 35 SEC trace (eluent: aqueous acetate buffer/methanol (8:2, *v/v*), calibration standard pullulan) of p[([BnVIM]Cl) (**12**).

MASS SPECTROMETRIC ELUCIDATIONS
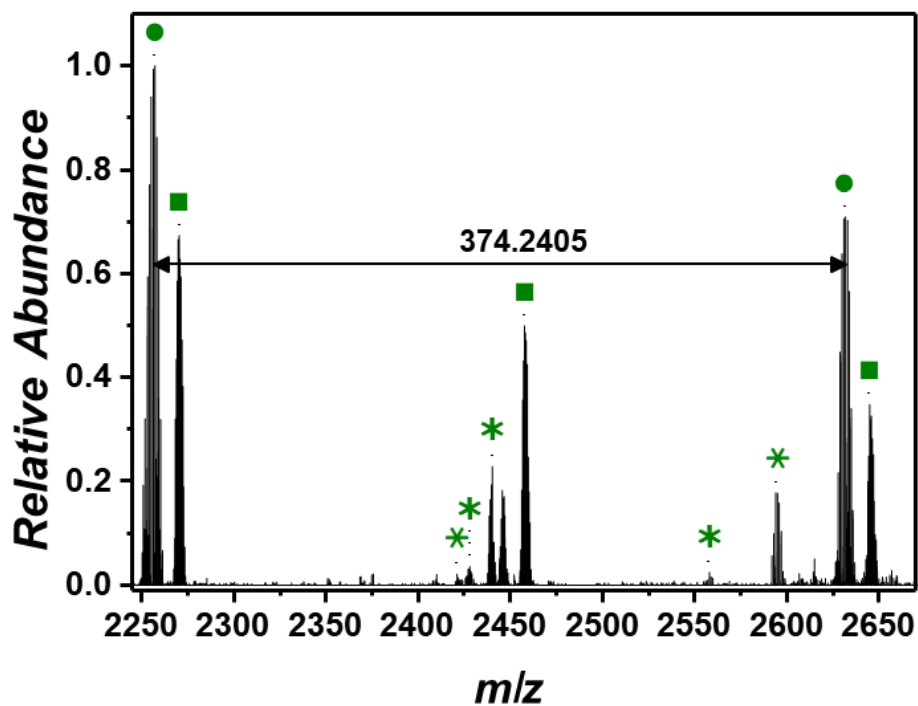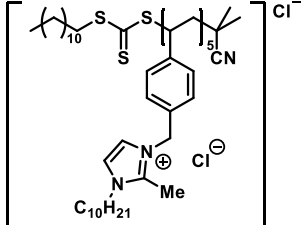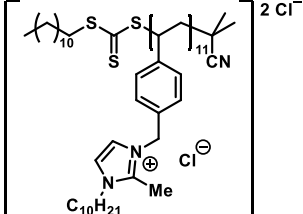
XXIX

p([DeMVBIM]Cl) (5)

Fig. B 36 Expanded spectrum (negative ion mode) of p([DeMVBIM]Cl) (**5**) obtained via ESI-CID-Orbitrap MS doped with 2.0% (*v/v*) propylene carbonate depicting the repeating unit of 374.2405 *m/z* (*m*/z(theo) 347.2489) of the most abundant species (labeled with ●). Species labeled with ✳ derive from (multiple) loss(es) of gaseous HCl.

Tab. B 2 Peak assignment of the ESI-CID-Orbitrap spectrum of p([DeMVBIM])Cl (**5**) from 2690 *m/z* to 2870 *m/z* showing the label (in corr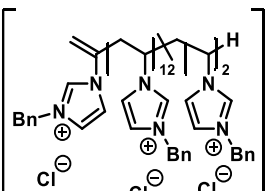espondence to the species in Fig. B 36Fig. B 36 Expanded spectrum (negative ion mode) of p([DeMVBIM]Cl) (**5**) obtained via ESI-CID-Orbitrap MS doped with 2.0% (*v/v*) propylene carbonate depicting the repeating unit of 374.2405 *m/z* (*m/z*(theo) 347.2489) of the most abundant species (labeled with ●). Species labeled with ✳ derive from (multiple) loss(es) of gaseous HCl.), the experimental *m/z* and theoretical *m/z* values (determined by the most abundant isotope of the isotopic pattern), Δ*m/z*, the resolution (obtained by the Xcalibur software), the number of repeating units *n*, and the structure determination. Due to the deprotonation process, no structure was determined for species labeled with ✳.

Label	*m/z* (exp)	*m/z* (theo)	Δ*m/z*	Resolution	*n*	Structure
●	2256.3679	2256.3758	0.0078	43600	5	
■	2270.4142	2270.4196	0.0053	44200	11	
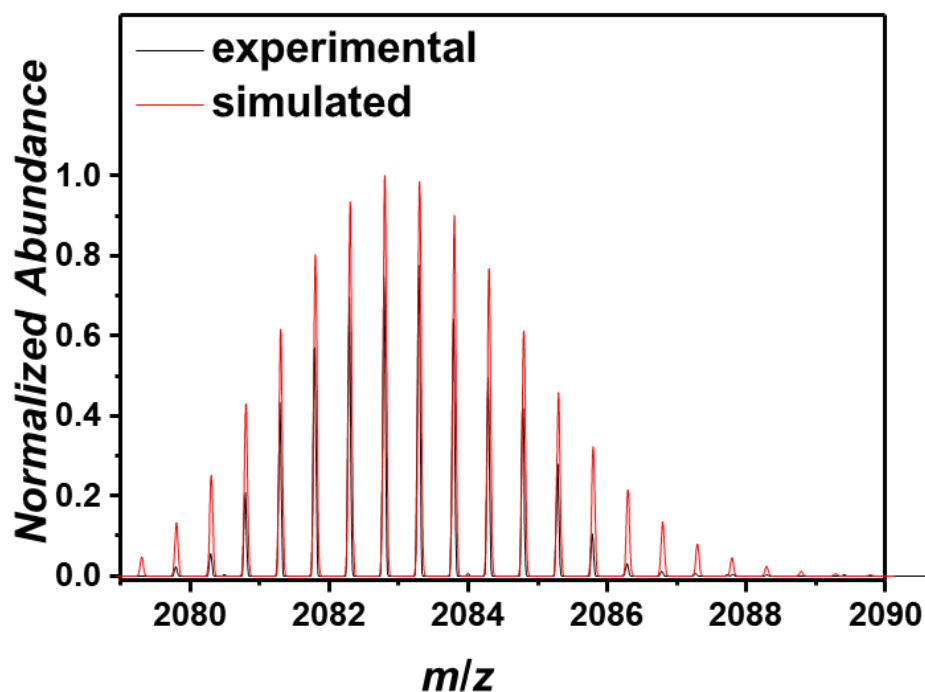
Fig. B 37 Isotopic pattern of one selected peak at 2083 *m/z* comparing the experiment (black line) and the simulation (red line) with a resolution of 45900.

XXX
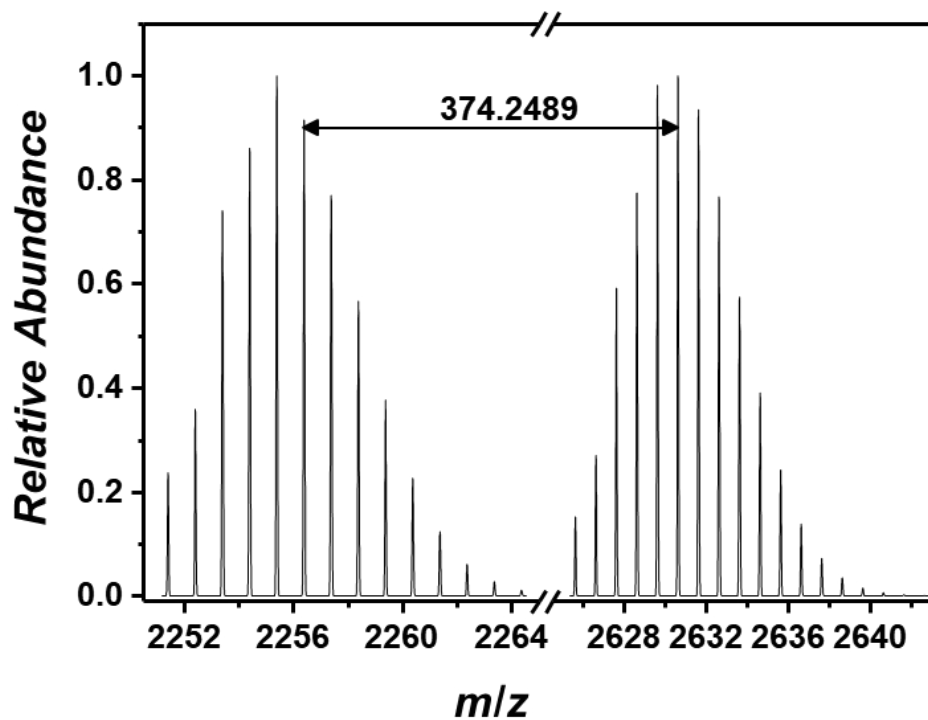
Fig. B 38 Illustration of two simulated isotopic pattern representing the species at 2256 *m/z* and 2631 *m/z*. The difference of the 91% intensity peak and the 100% intensity peak corresponds to the theoretical value of the repeating unit.

Tandem MS experiment of p([DeMVBIM]Cl) (5)
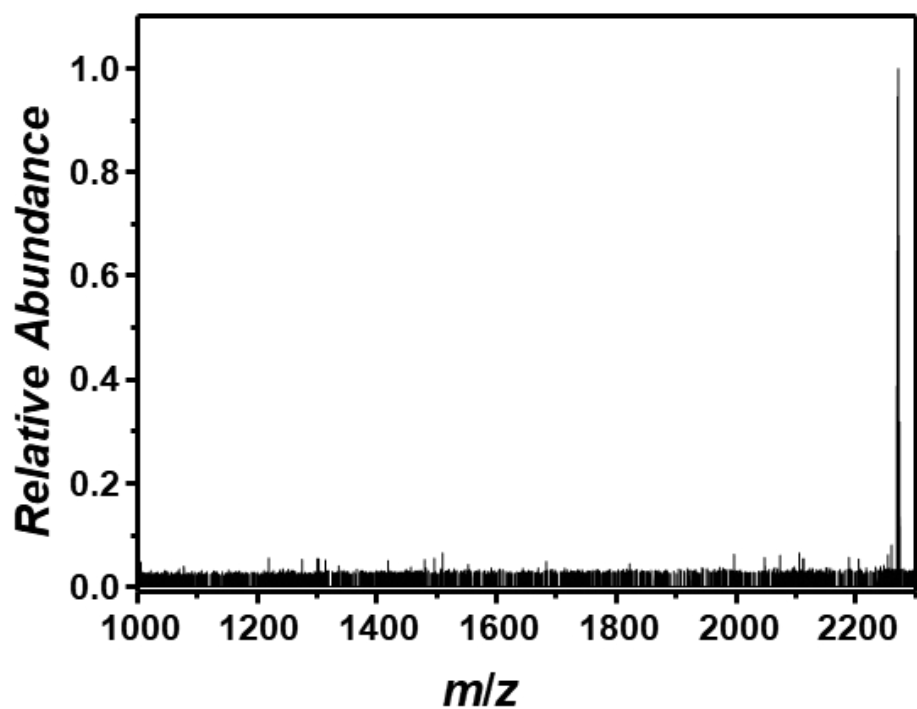
Fig. B 39 Tandem MS experiment (negative mode) of a double charged species at 2270 *m/z* under harsh conditions employing a HCD energy of 40 eV and a CID energy of 25 eV. No apparent reverse Menshutkin fragmentation was observed although a feasible cleavage of the imidazolium moiety was expected due to a – for a nucleophilic attack favored – planar geometry of the imidazolium.

p([VBPy]Cl) (6)
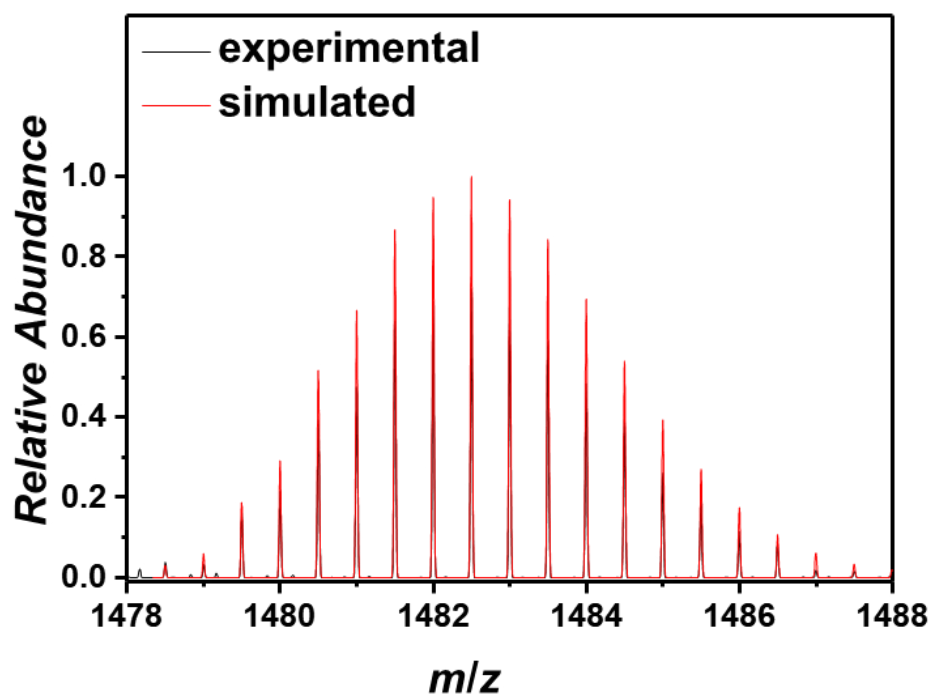
Fig. B 40 Isotopic pattern of one selected peak at 1482 *m/z* comparing the experiment (black line) and the simulation (red line) with a resolution of 53800.
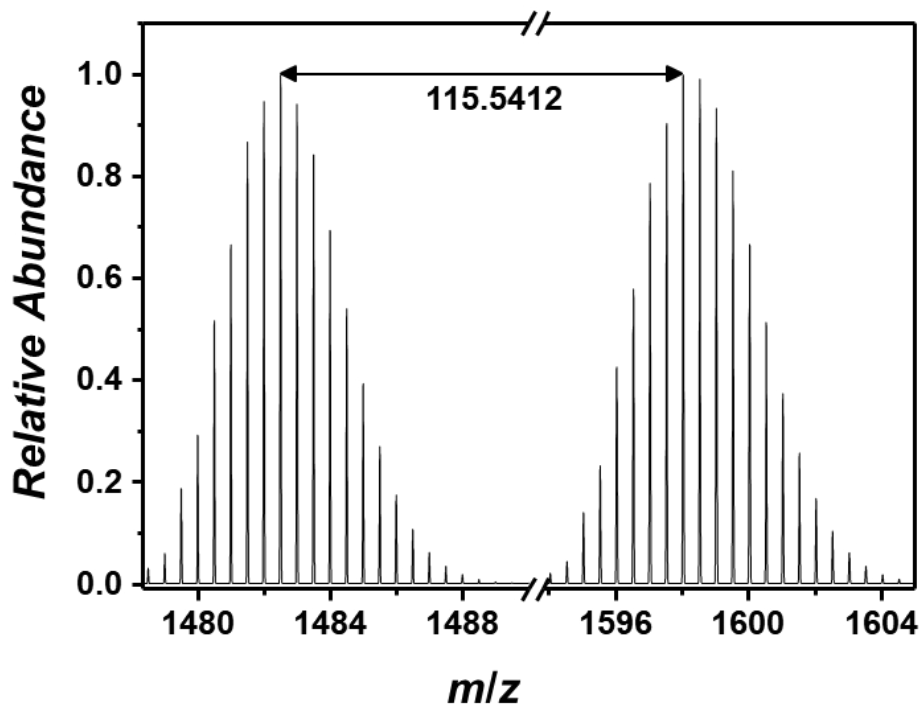
Fig. B 41 Illustration of two simulated isotopic pattern representing the species at 1482 *m/z* and 1598 *m/z*. The difference of each highest peaks corresponds to the theoretical value of the repeating unit.

p([TEVBA]Cl) (7)
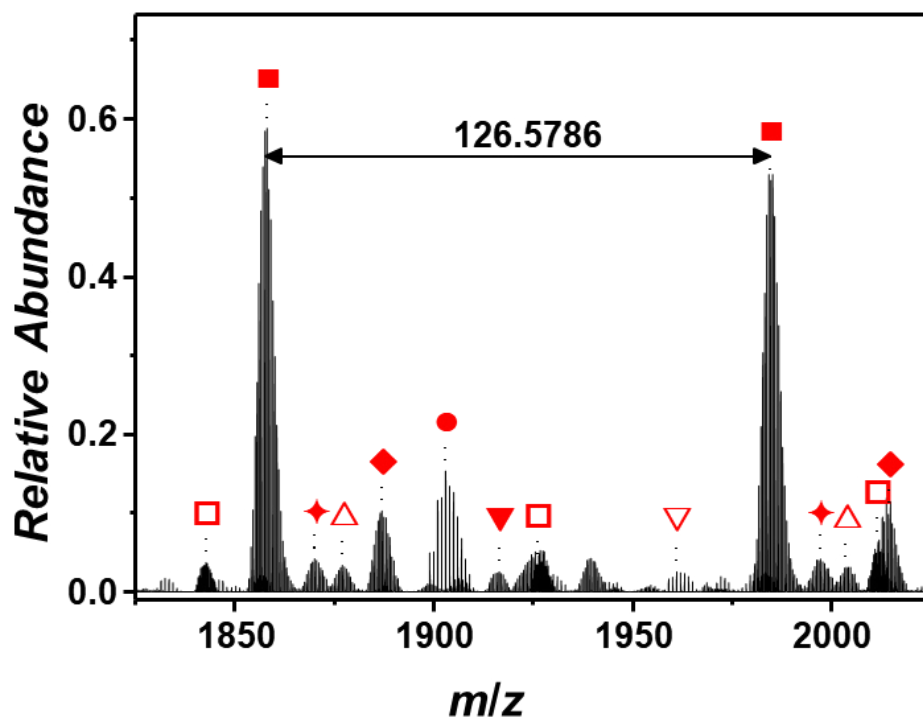
Fig. B 42 Zoomed spectrum (negative mode) of p([TEVBA])Cl (**7**) obtained *via* ESI-CID-Orbitrap MS doped with 0.5% (*v/v*) propylene carbonate depicting the repeating unit of 126.5786 *m/z* (*m/z(theo)* 126.5799) of the most abundant species (labeled with ■).

Tab. B 3 Peak assignment of the ESI-CID-Orbitrap spectrum of p([TEVBA])Cl (**7**) from 1840 *m/z* to 1960 *m/z* showing the label (in correspondence to the species in Fehler! Verweisquelle konnte nicht gefunden werden.), the experimental *m/z* and theoretical *m/z* values (determined by the most abundant isotope of the isotopic pattern), Δ*m/z*, the resolution (obtained by the Xcalibur software), the number of repeating units *n*, and the structure determination.

| Label	*m/z* (exp)	*m/z* (theo)	Δ*m/z*	Resolution	*n*	Structure
□	1842.7522	1842.7530	0.0008	50300	20	
■	1858.0859	1858.0867	0.0008	49900	13	
✦	1870.5965	1870.5950	0.0015	46000	13	
△	1877.1090	1877.1031	0.0059	48500	13	
◆	1887.0626	1887.0659	0.0033	48000	13	
●	1903.0852	1903.0837	0.0014	48127	6	
▼	1916.5422	1916.5447	0.0025	48500	13	
▽	1961.0461	1961.0461	0.0000	45100	6	
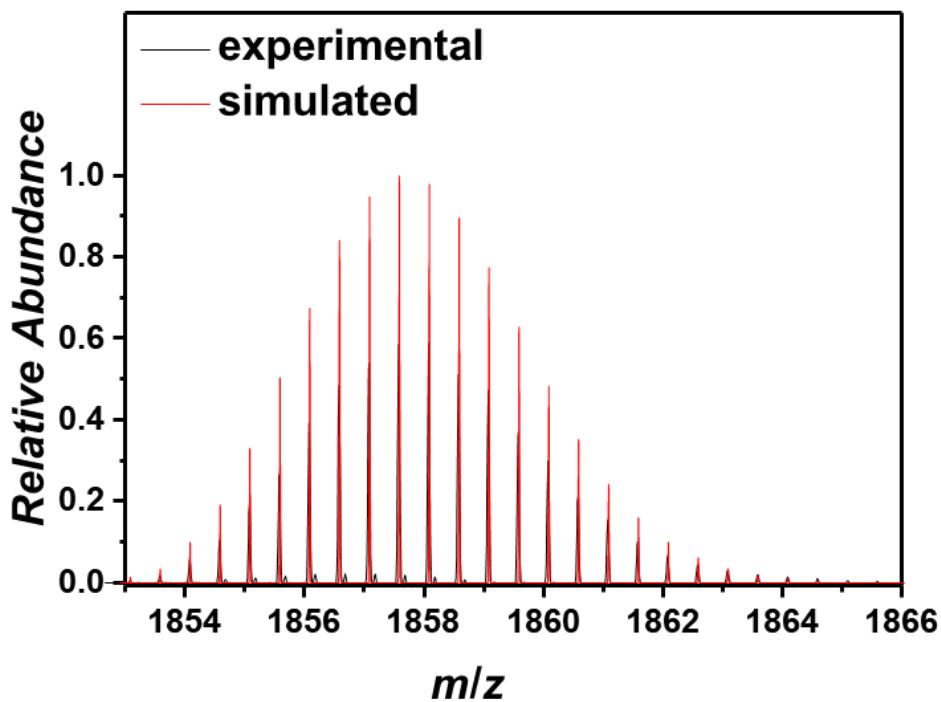
Fig. B 44 Isotopic pattern of one peak at 1858 *m/z* comparing the experiment (black line) and the simulation (red line) with a resolution of 49900.
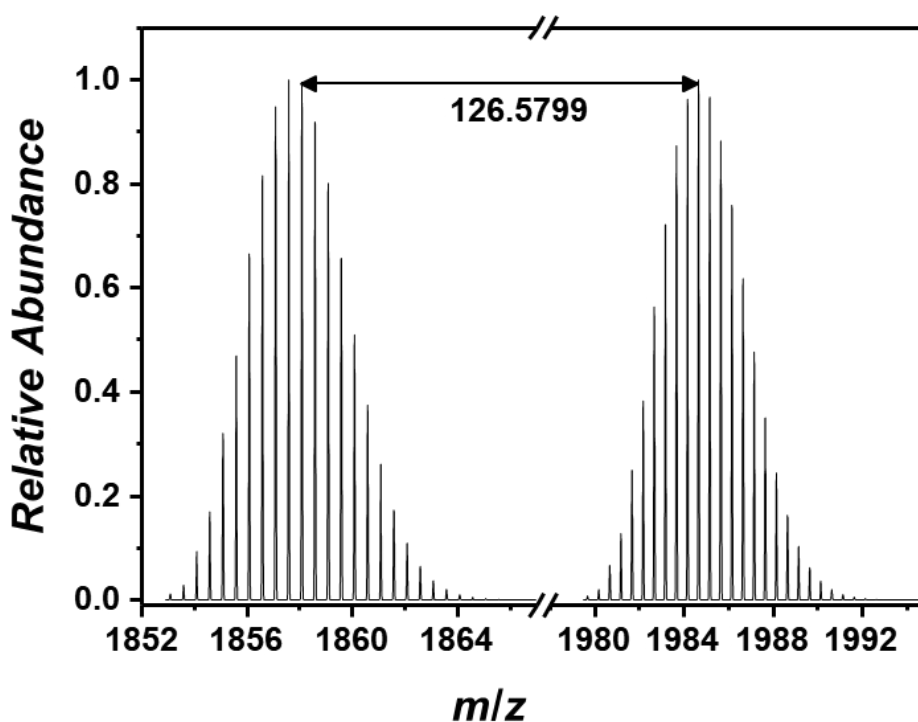
Fig. B 43 Illustration of two simulated isotopic pattern representing the species at 1858 *m/z* and 1984 *m/z*. The difference of the 98% intensity peak and the 100% intensity peak corresponds to the theoretical value of the repeating unit.

Tandem MS experiment of p([TEVBA])Cl (7)
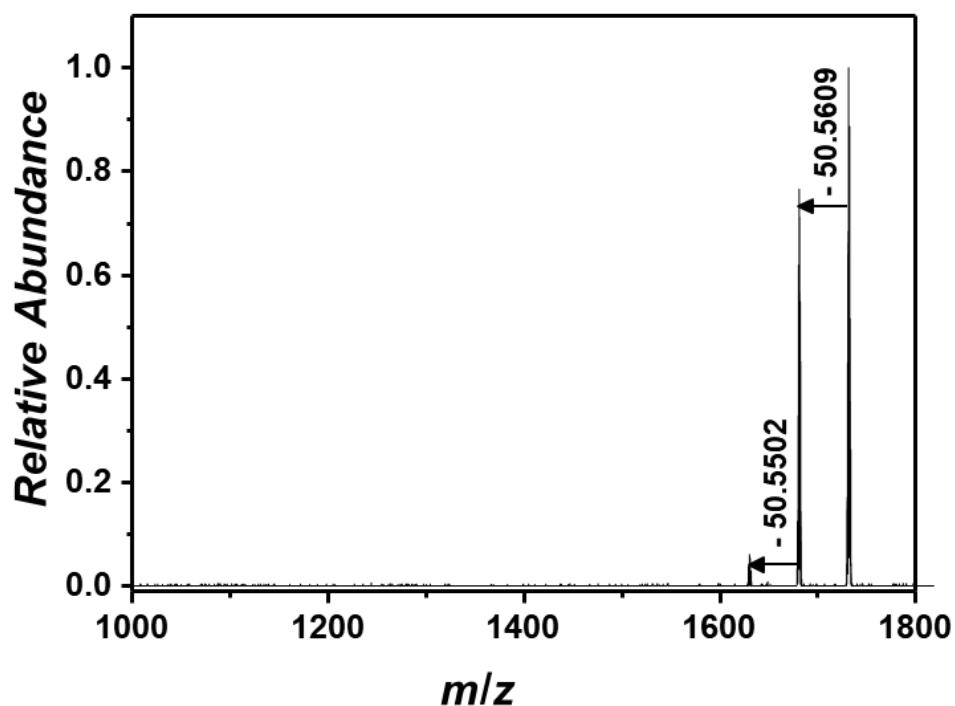
Fig. B 45 Tandem MS experiment (negative ion mode) of a double charged species at 1731 m/z with a HCD energy of 35 eV. The identification of two double charged species depicting the loss of a triethylamine unit (m/z(theo) 50.5608).
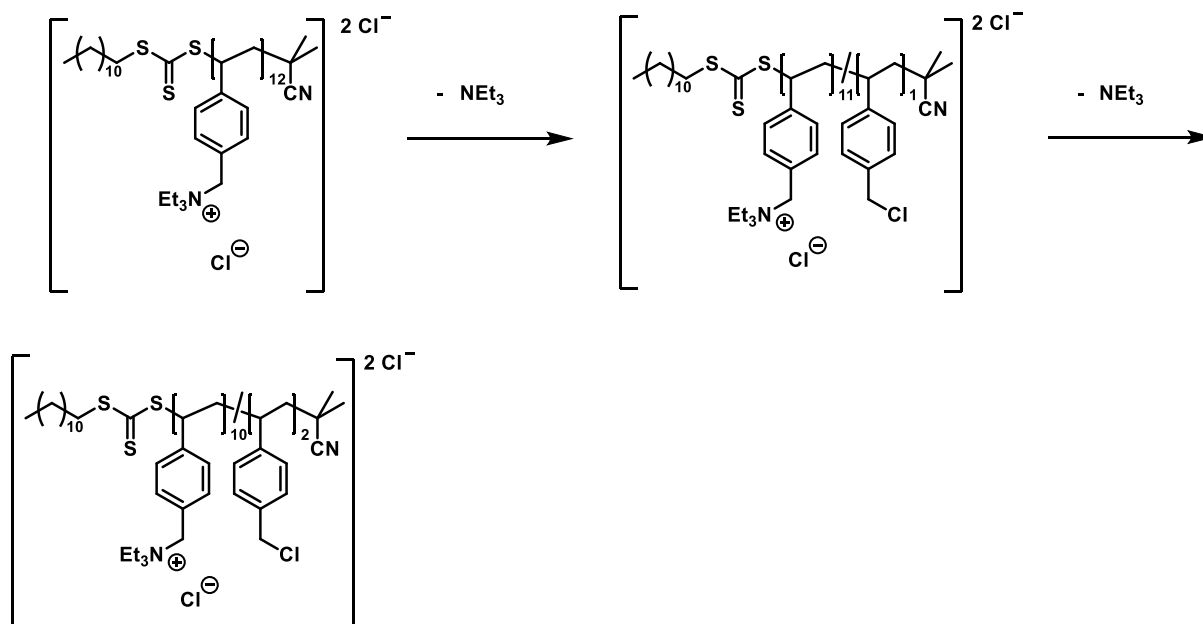
Scheme B 1 Proposed fragmentation process of p([TEVBA])Cl (**7**) *via* a reverse Menshutkin mechanism including the stepwise nucleophilic attack of the chloride anion at the electrophilic benzylic moiety.

p([TPVBP]Cl) (8)
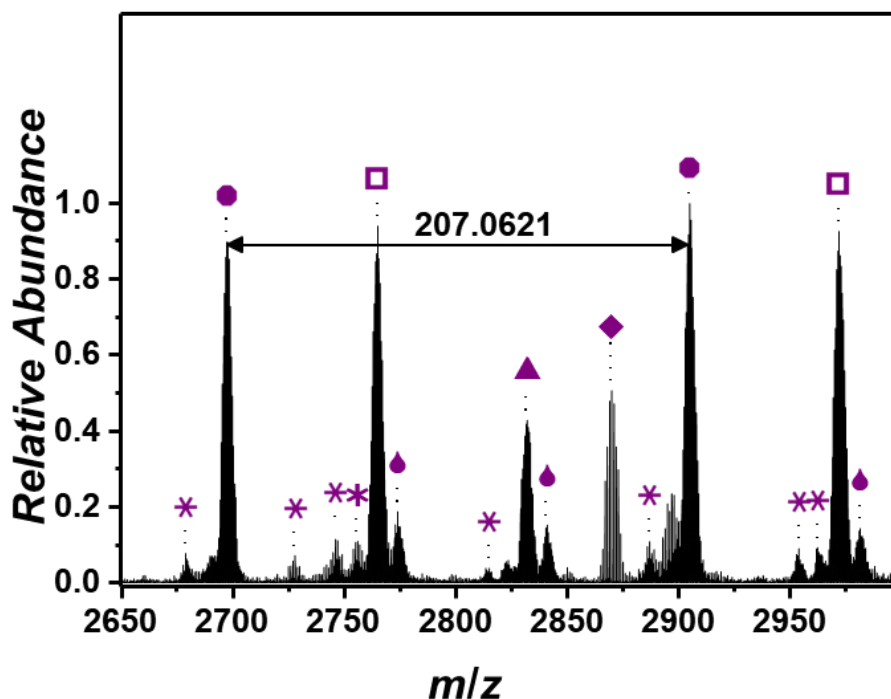
Fig. B 46 Expanded spectrum (negative ion mode) of p([TPVBP]Cl) (**8**) obtained via ESI-CID-Orbitrap MS doped with 1.0% (*v/v*) propylene carbonate depicting the repeating unit of 207.0621 *m/z* (*m/z*(theo) 207.0658) of the most abundant species (labeled with ●). Species labeled with ✲ derive from (multiple) loss(es) of gaseous HCl.

Tab. B 4 Peak assignment of the ESI-CID-Orbitrap spectrum of p([TPVBP])Cl (**8**) from 2690 *m/z* to 2870 *m/z* showing the label (in correspondence to the species in Fig. B 47 Fehler! Verweisquelle konnte nicht gefunden werden.), the experimental *m/z* and theoretical *m/z* values (determined by the most abundant isotope of the isotopic pattern), Δ*m/z*, the resolution (obtained by the Xcalibur software), the number of repeating units *n*, and the structure determination. Due to the deprotonation process, no structure was determined for species labeled with ✲. Species labeled with ♦ are H_2O adducts.

Label	*m/z* (exp)	*m/z* (theo)	Δ*m/z*	Resolution	N	Structure
●	2697.3183	2697.3339	0.0156	40000	12	
□	2764.8487	2764.8705	0.0218	38600	13	
▲	2831.8759	2831.9073	0.0314	35000	14	

XXXVIII

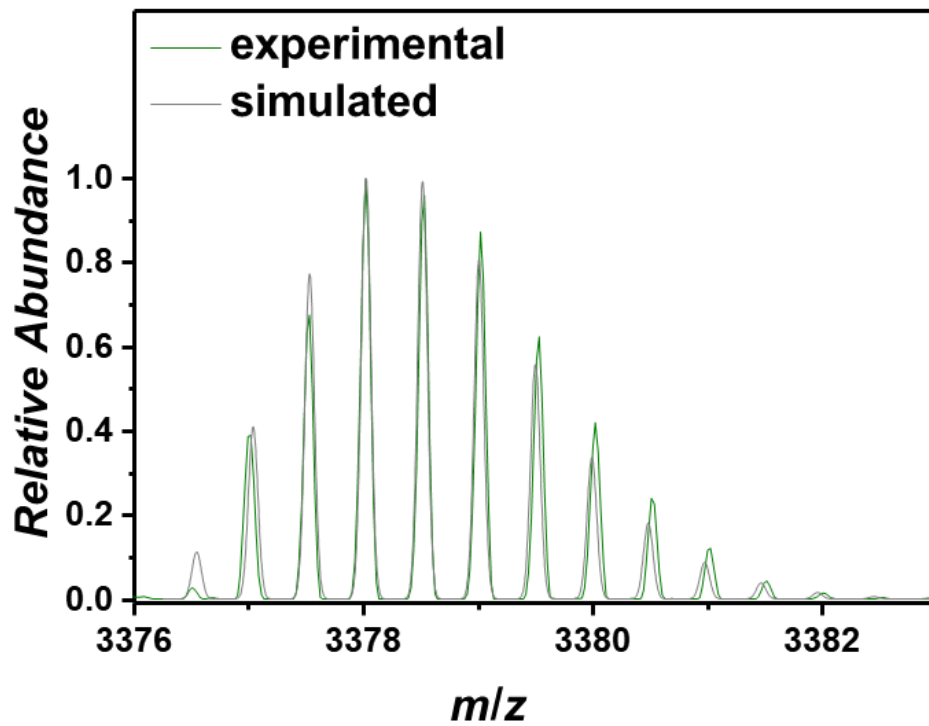| | 2869.8960 | 2869.9152 | 0.0192 | 39000 | 6 |
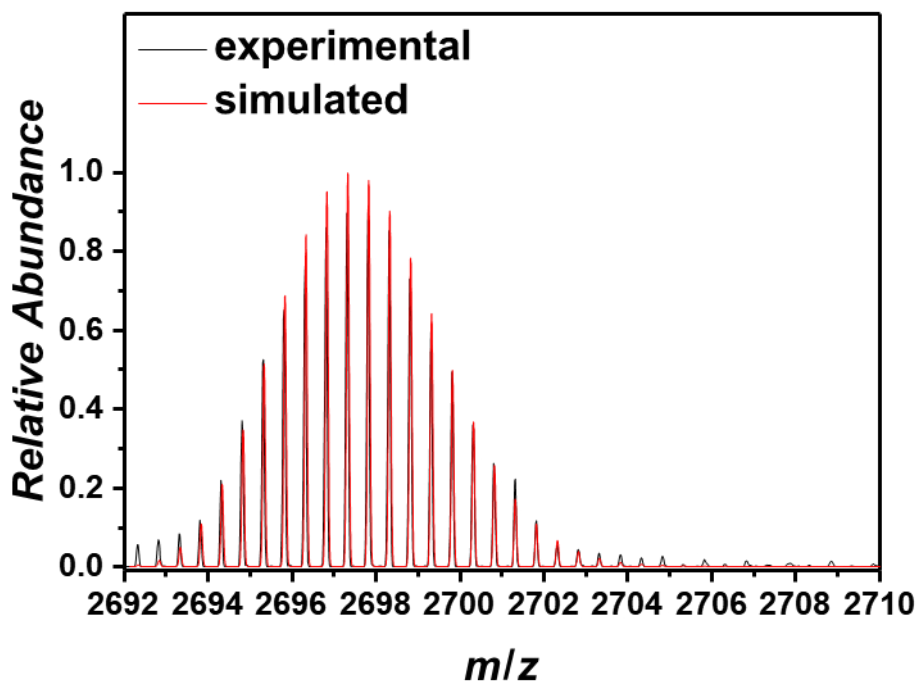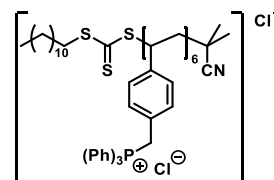
Fig. B 48 Isotopic pattern of one selected peak at 2697 *m/z* comparing the experiment (black line) and the simulation (red line) with a resolution of 40000.
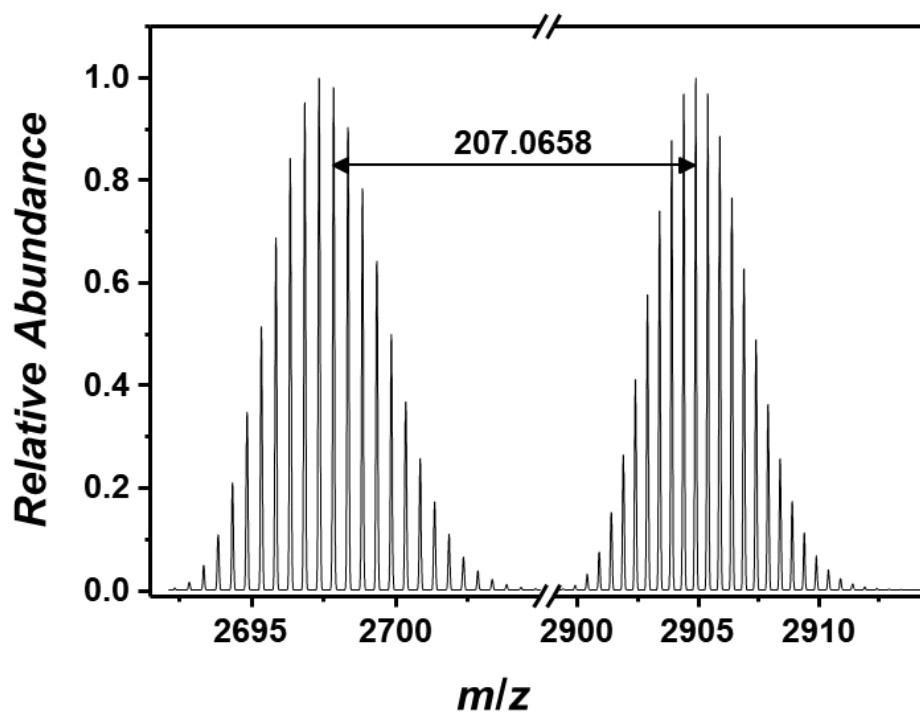
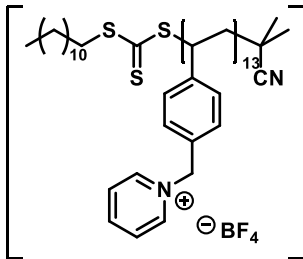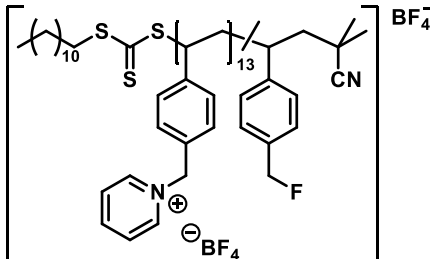Fig. B 50 Illustration of two simulated isotopic pattern representing the species at 2697 Th and 2904 Th. The difference of the 98% intensity peak and the 100% intensity peak corresponds to the theoretical value of the repeating unit.

Tandem MS experiment of p([TPVBP]Cl) (8)
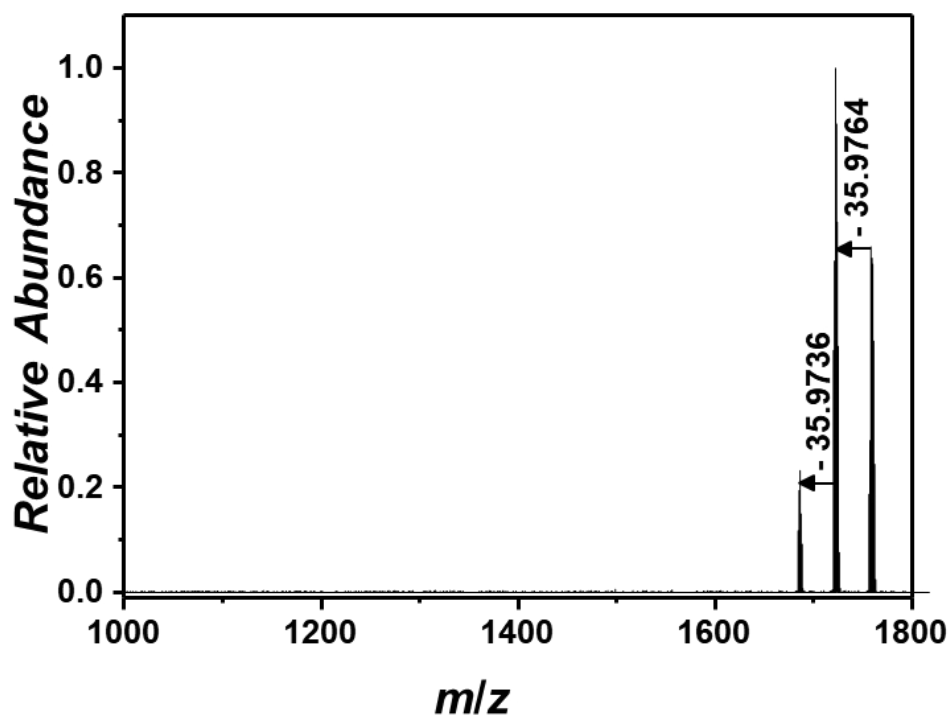
Fig. B 49 Tandem MS experiment (negative ion mode) of a single charged species at 1758 *m/z* with a HCD energy of 24 eV. The identification of two single charged species depicting the loss of a gaseous HCl (*m/z*(theo) 35.9767).

XL
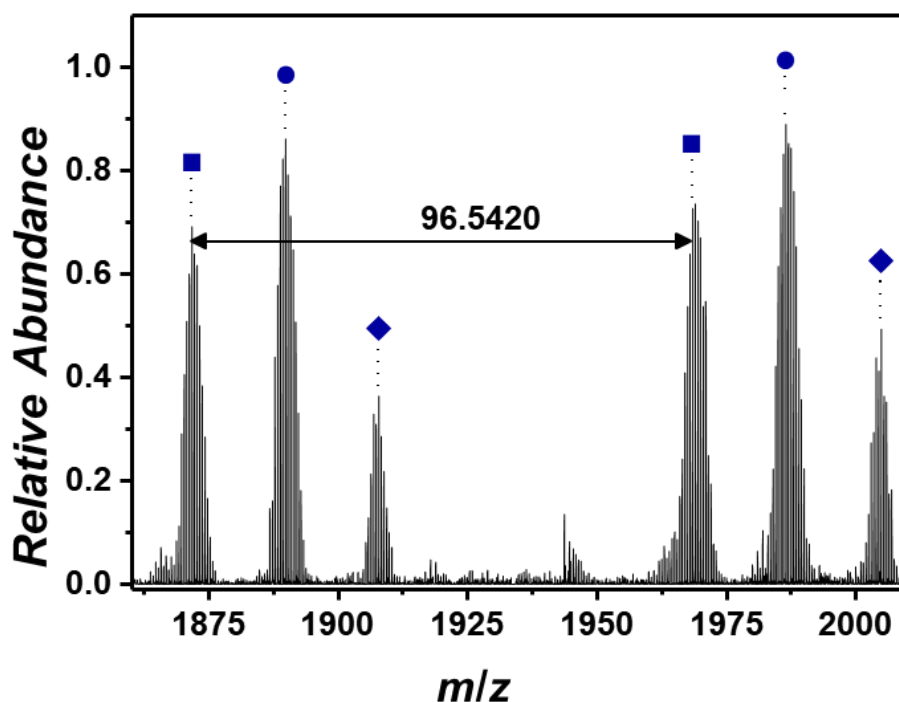
p([ATMEA]Cl) (9)

Fig. B 51 Expanded spectrum (negative ion mode) of p([ATMEA]Cl) (**9**) obtained *via* ESI-CID-Orbitrap MS doped with 1.0% (*v/v*) propylene carbonate depicting the repeating unit of 96.5420 *m/z* (*m/z*(theo) 96.5440) of one species (labeled with ■).

Tab. B 5 Peak assignment of the ESI-CID-Orbitrap spectrum of p([ATMEA]Cl) (**9**) from 1775 *m/z* to 1810 *m/z* showing the label (in correspondence to the species in Fig. B 52), the experimental *m/z* and theoretical *m/z* values (determined by the most abundant isotope of the isotopic pattern), Δ*m/z*, the resolution (obtained by the Xcalibur software), the number of repeating units *n*, and the structure determination.

| Label	*m/z* (exp)	*m/z* (theo)	Δ*m/z*	Resolution	*n*	Structure
■	1871.8086	1871.8082	0.0004	50800	18	
●	1889.8308	1889.8307	0.0001	49900	19	
◆	1908.3517	1908.3530	0.0013	47300	20	
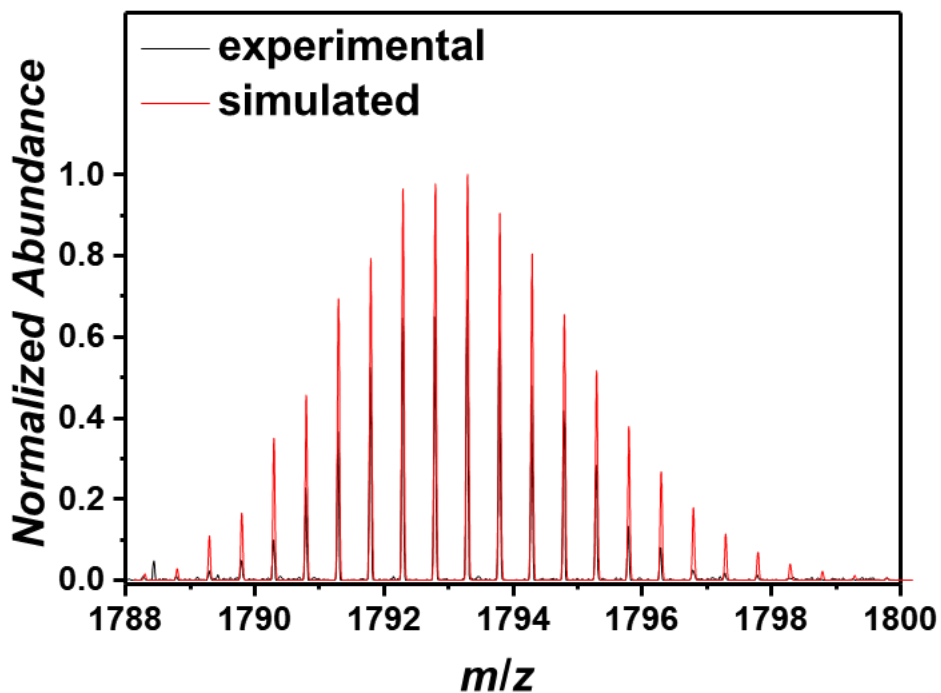
Fig. B 54 Isotopic pattern of one selected peak at 1793 *m/z* comparing the experiment (black line) and the simulation (red line) with a resolution of 50000.
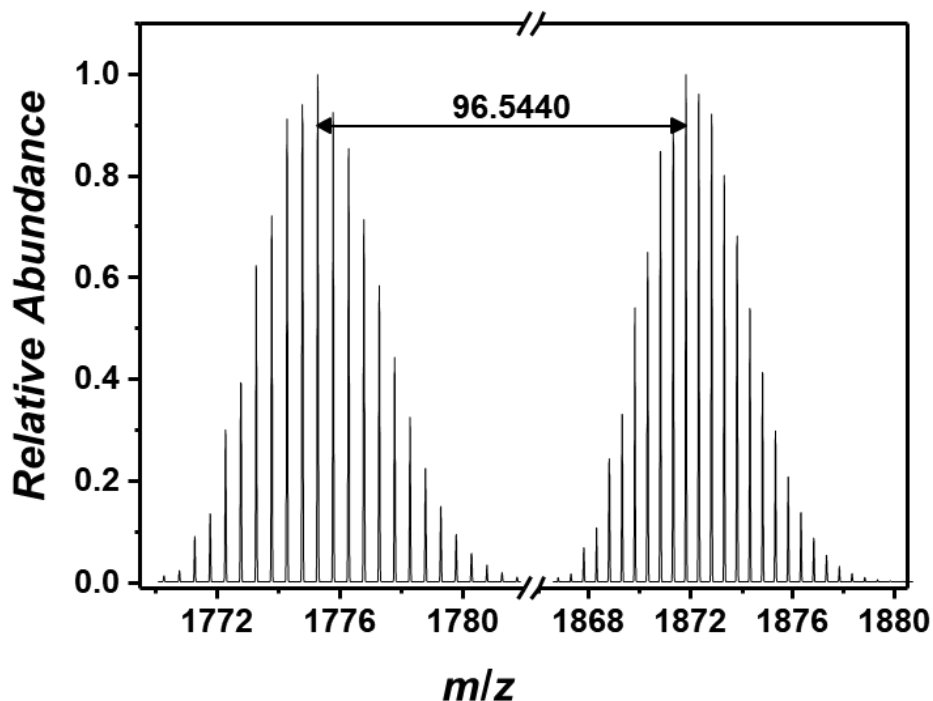

Fig. B 53 Illustration of two simulated isotopic pattern representing the species at 2256 *m/z* and 2631 *m/z*. The difference between each highest peak corresponds to the theoretical value of the repeating unit.

Tandem MS experiment of p([ATMEA]Cl) (9)

A tandem MS experiment of p([ATMEA]Cl) (**9**) was not possible due to the low ion density. The collision-induced dissociation (CID) of 25 eV was sufficient to give both a spectrum of p([ATMEA]Cl) (**9**) and a cleavage of the vulnerable acrylate ester bond. The cleavage of 2-hydroxy-*N*,*N*,*N*-trimethylethan-1-aminium chloride can be considered as an indirect structural proof.

p([BVBIM]Cl) (10)
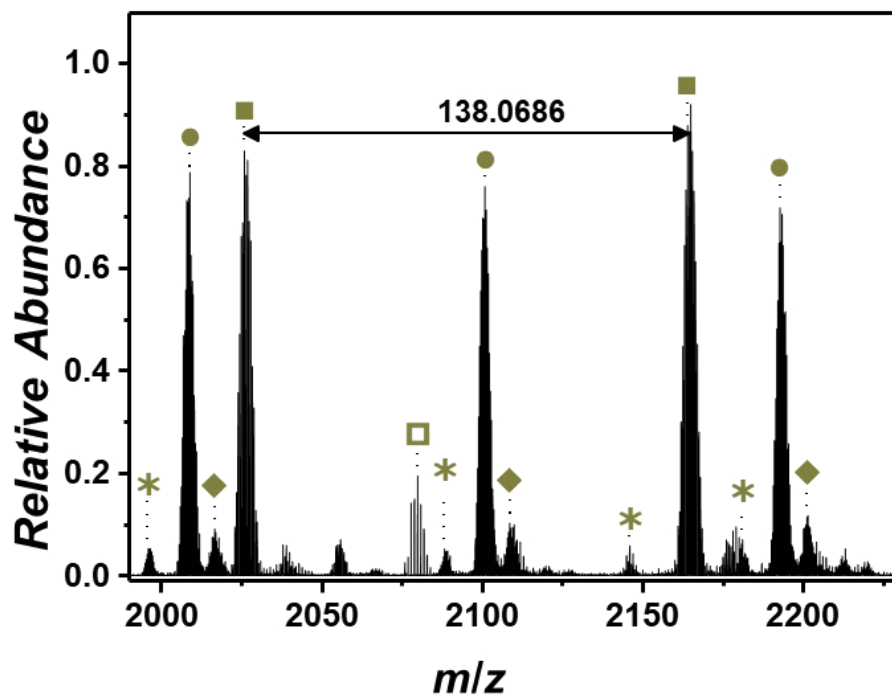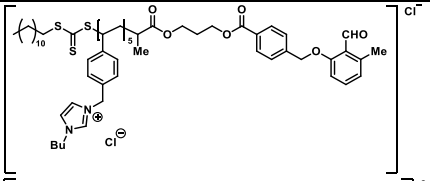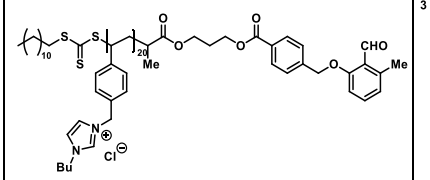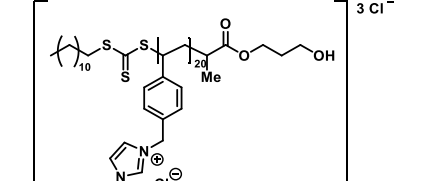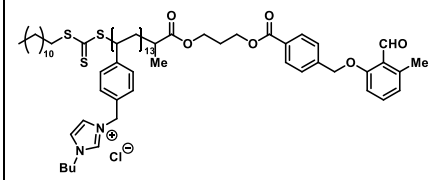
Fig. B 55 Expanded spectrum (negative ion mode) of p([BVBIM]Cl) (**10**) obtained *via* ESI-CID-Orbitrap MS depicting the repeating unit of 138.0686 *m/z* (*m/z*(theo) 138.0702) of the most abundant species (labeled with ■). Species labeled with ✳ derive from (multiple) loss(es) of gaseous HCl.

Tab. B 6 Peak assignment of the ESI-CID-Orbitrap spectrum of p([BVBIM]Cl) (**10**) from 2079 *m/z* to 2165 *m/z* showing the label (in correspondence to the species in Fig. B 56), the experimental *m/z* and theoretical *m/z* values (determined by the most abundant isotope of the isotopic pattern), Δ*m/z*, the resolution (obtained by the Xcalibur software), the number of repeating units *n*, and the structure determination. Due to the deprotonation process, no structure was determined for species labeled with ∗.

Label	*m/z* (exp)	*m/z* (theo)	Δ*m/z*	R	*n*	Structure
☐	2079.9240	2079.9264	0.0024	46400	6	
●	2100.9830	2100.9840	0.0010	45400	20	
◆	2109.6604	2109.6703	0.0099	44700	21	
■	2165.0008	2165.0045	0.0037	43500	13	
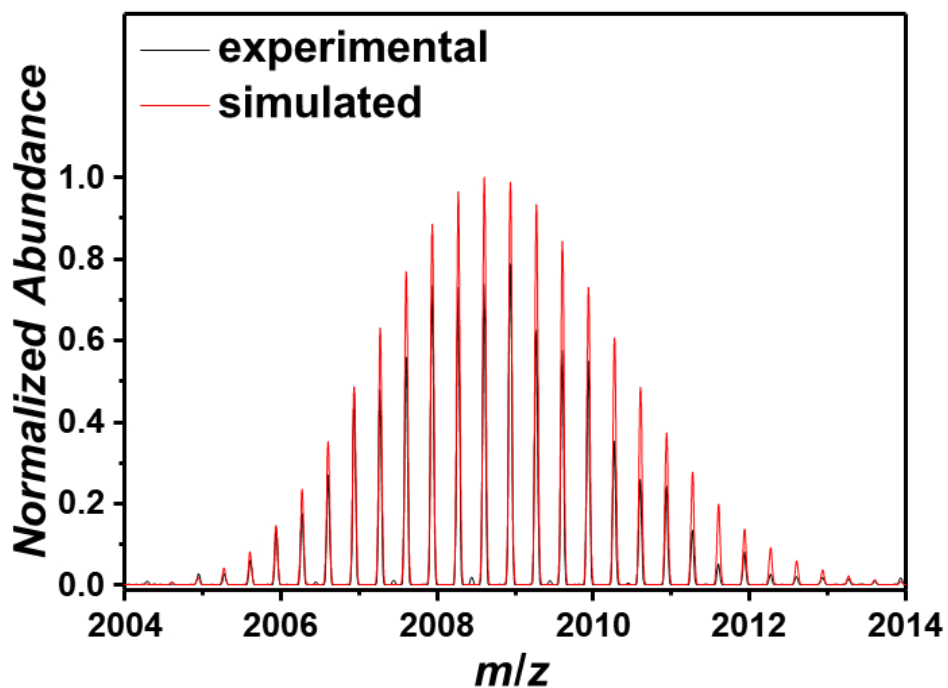
Fig. B 58 Isotopic pattern of one selected peak at 2009 *m/z* comparing the experiment (black line) and the simulation (red line) with a resolution of 48000.
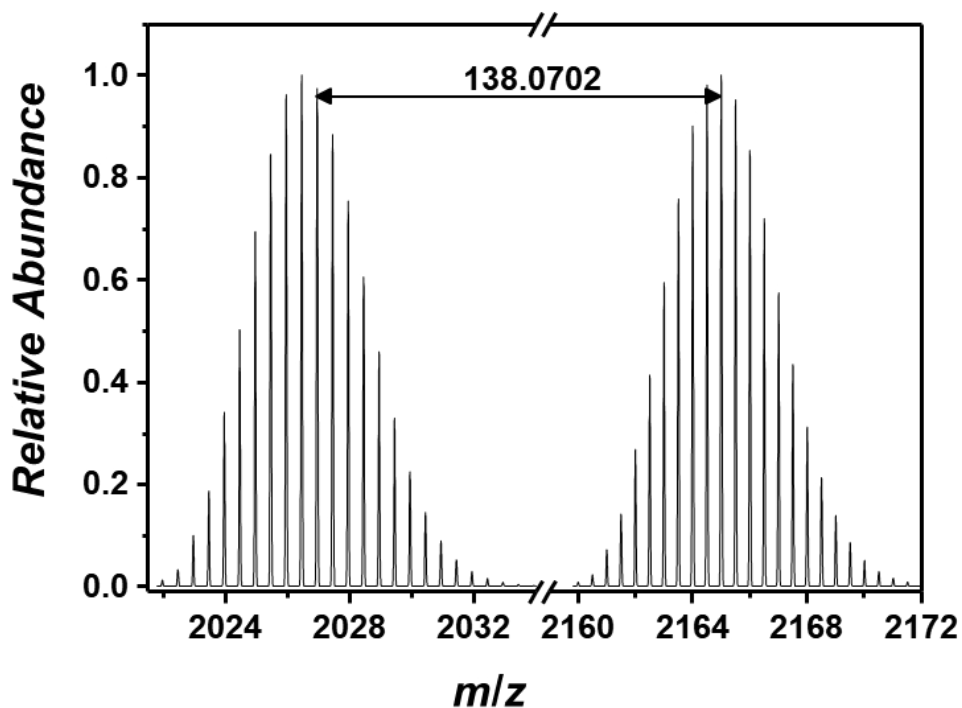
Fig. B 57 Illustration of two simulated isotopic pattern representing the species deriving from disproportionation at 2026 *m/z* and 2165 *m/z*. The difference of the 98% intensity peak and the 100% intensity peak corresponds to the theoretical value of the repeating unit.

p([MVTr]I) (11)
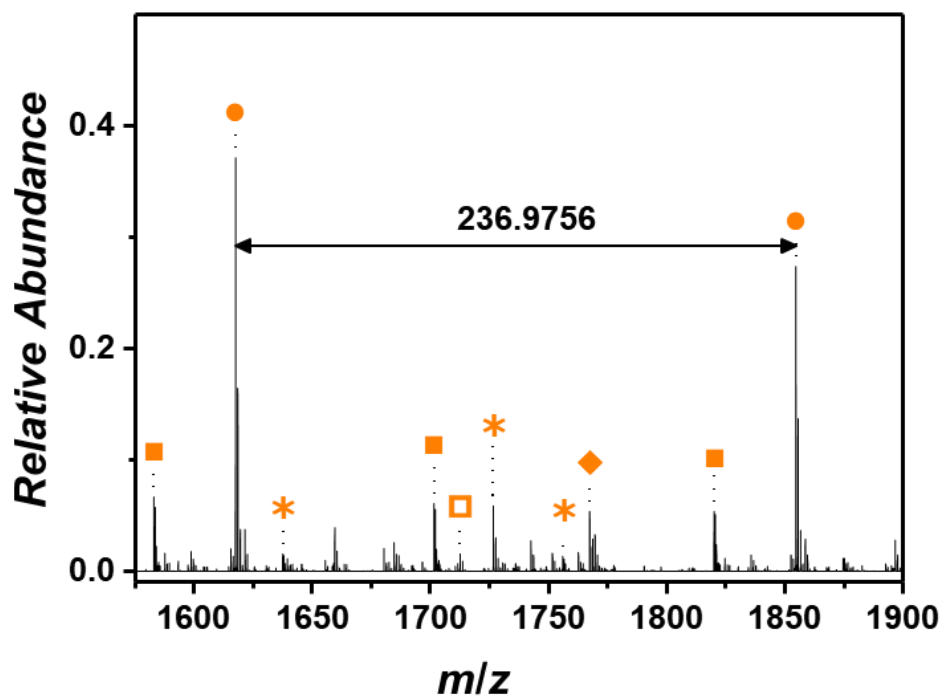
Fig. B 59 Expanded spectrum (negative ion mode) of p([MVTr]I) (**11**) obtained *via* ESI-CID-Orbitrap MS depicting the repeating unit of 236.9756 *m/z* (*m/z*(theo) 236.9763) of the most abundant species (labeled with ●). Species labeled with ✳ derive from (multiple) loss(es) of gaseous HI.

Tab. B 7 Peak assignment of the ESI-CID-Orbitrap spectrum of p([MVTr]I) (**11**) from 1583 m/z to 1767 m/z showing the label (in correspondence to the species in Fig. B 60), the experimental m/z and theoretical m/z values (determined by the most abundant isotope of the isotopic pattern), $\Delta m/z$, the resolution (obtained by the Xcalibur software), the number of repeating units n, and the structure determination (as representative candidate the saturated polymer chain was chosen). Due to the deprotonation process, no structure was determined for species labeled with *.

Label	m/z (exp)	m/z (theo)	$\Delta m/z$	Resolution	n	Structure
■	1583.2922	1583.2917	0.0006	27700	12	
●	1617.8189	1617.8206	0.0008	28200	6	
☐	1712.8668	1712.8690	0.0021	24000	7	
◆	1767.7148	1767.7148	0.0000	26300	6	
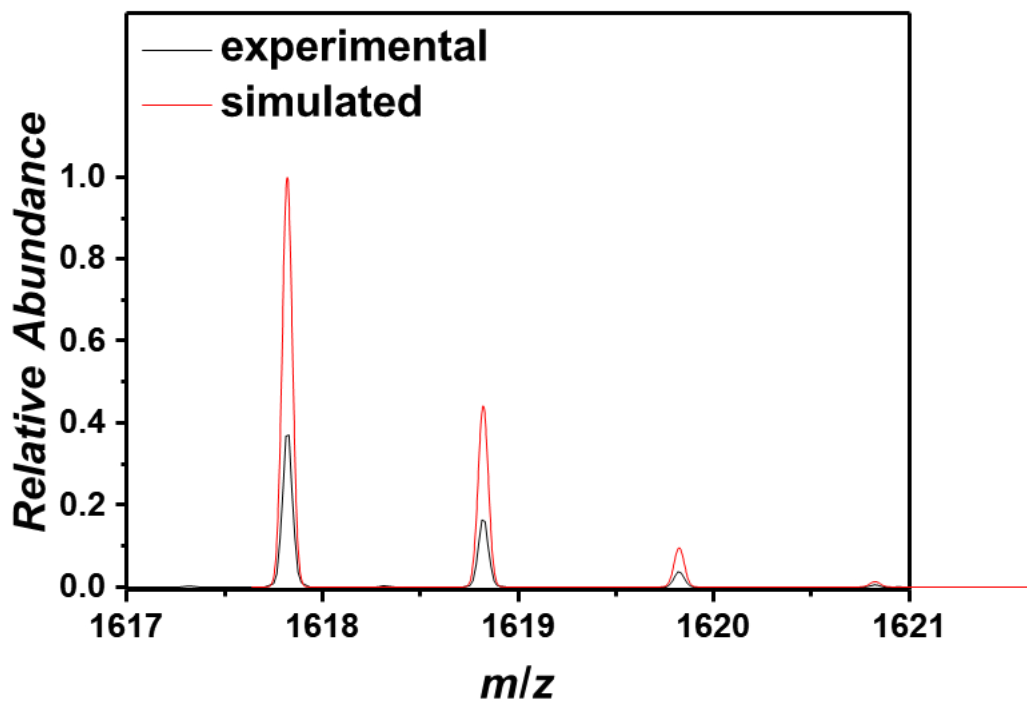
Fig. B 61 Isotopic pattern of one selected peak at 1617 *m/z* comparing the experiment (black line) and the simulation (red line) with a resolution of 28200.

Tandem MS experiment of p([MVTr]I) (11)
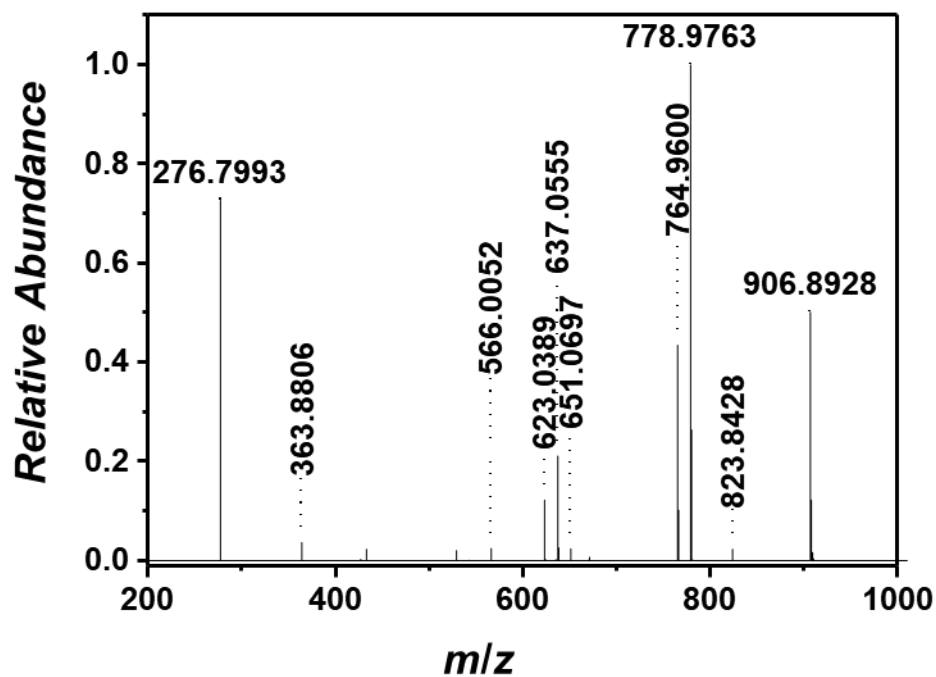
Fig. B 62 Tandem MS experiment (negative ion mode) of a single charged species at 906 *m/z* with a HCD energy of 13 eV.

L

623.0359   764.9638   906.8917   669.9154   432.9392

– MeI   – MeI

– HI   – HI

637.0515   778.9794

823.8434

– HI

651.0672

363.8813

Additional ions: NaI   I⁻
276.7987
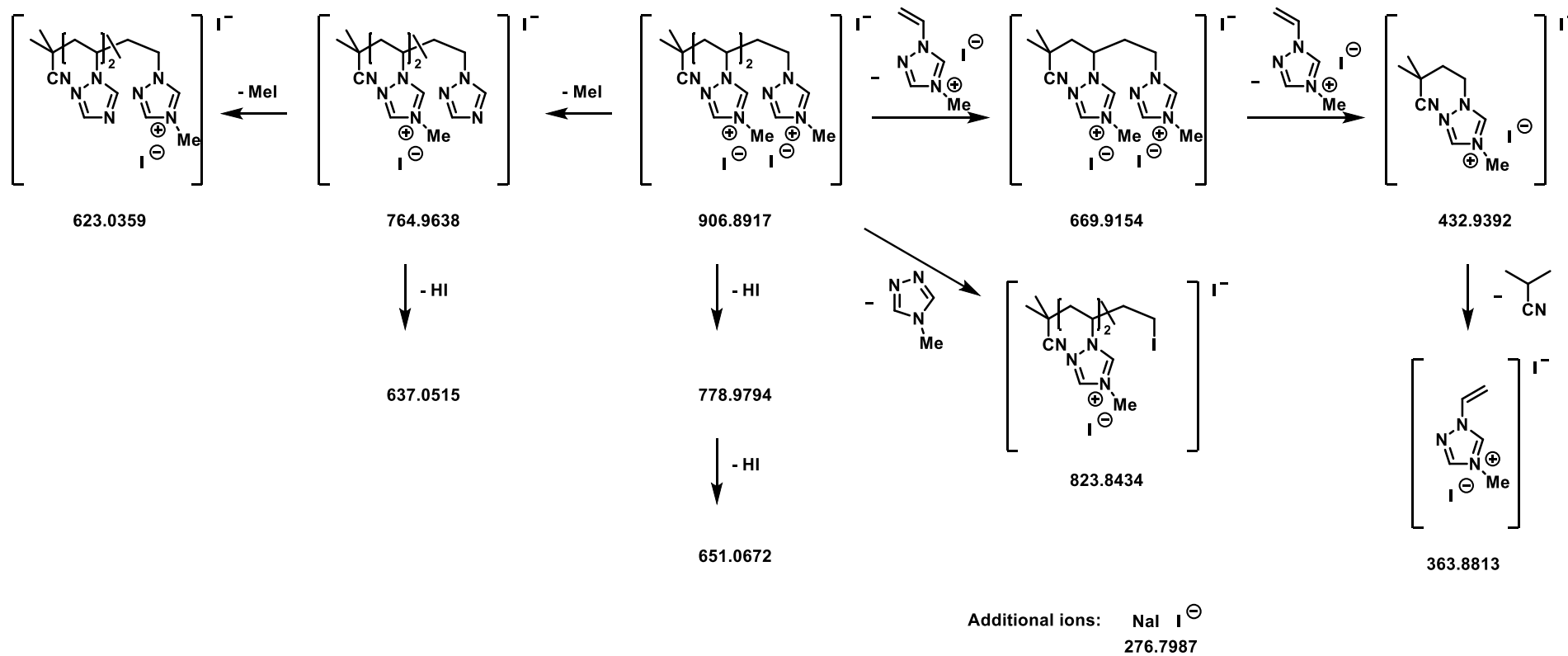
Scheme B 2 Proposed fragmentation of p([MVTr]I) (**11**) via three reaction pathways: a reverse Menshutkin mechanism including the stepwise nucleophilic attack of the iodide anion at the methyl moiety (loss of MeI); stepwise main chain depolymerization leading to the short-chained analogues of **11**; stepwise deprotonation via the release of gaseous HI.

LI
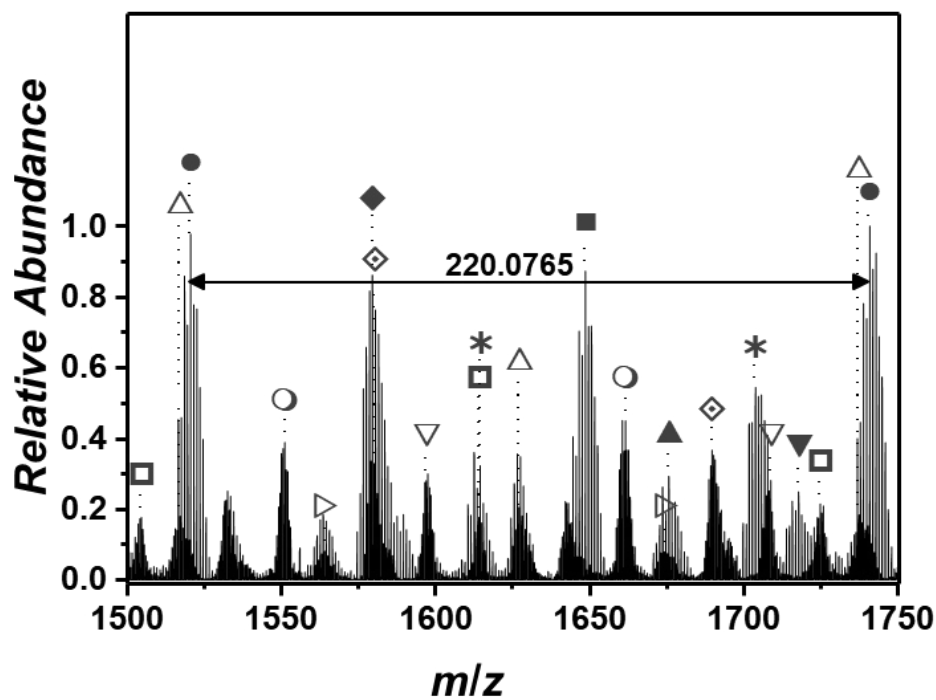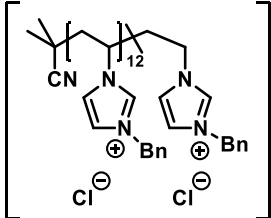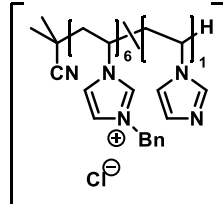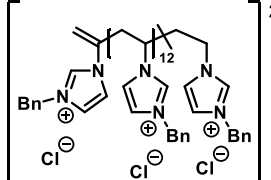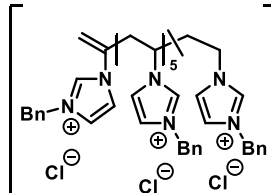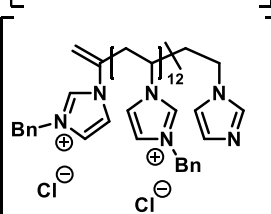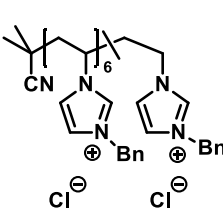
p([BnVIM]Cl) (12)

Fig. B 63 Expanded spectrum (negative ion mode) of p([BnVIM]Cl) (**12**) obtained via ESI-CID-Orbitrap MS depicting the repeating unit of 220.0765 *m/z* (*m/z*(theo) 220.0767) of the most abundant species (labeled with ●). Species labeled with ✻ derive from (multiple) loss(es) of gaseous HCl.

Tab. B 8 Peak assignment of the ESI-CID-Orbitrap spectrum of p([BnVIM]Cl) (**12**) from 1504 *m/z* to 1717 *m/z* showing the label (in correspondence to the species in Fig. B 64), the experimental *m/z* and theoretical *m/z* values (determined by the most abundant isotope of the isotopic pattern), Δ*m/z*, the resolution (obtained by the Xcalibur software), the number of repeating units *n*, and the structure determination (as representative candidate the saturated polymer chain was chosen). Due to the deprotonation process, no structure was determined for species labeled with ∗.

Label	*m/z* (exp)	*m/z* (theo)	Δ*m/z*	Resolution	*n*	Structure
□	1504.5024	1504.4947	0.0078	27800	13	
●	1522.5273	1522.5378	0.0105	26100	7	
◇	1579.0432	1579.0051	0.0382	28500	14	
◆	1579.5655	1579.5034	0.0621	25300	7	
▷	1564.0478	1564.0189	0.0288	25800	15	
△	1517.0268	1516.9923	0.0345	28500	14	
■	1648.5595	1648.5614	0.0019	25300	7	

○	1551.0228	1551.0215	0.0013	26900	14
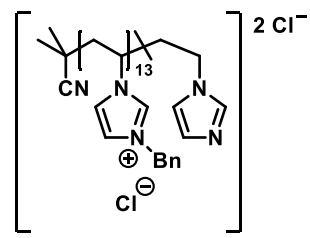
▽	1597.5482	1597.5488	0.0006	28800	15
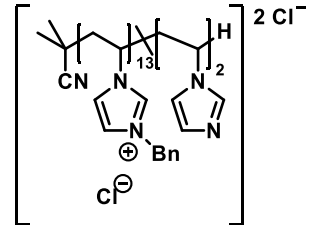
▼	1673.6112	1673.5567	0.0545	26300	7
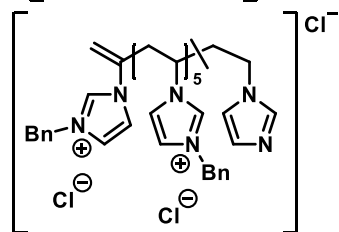
▼	1717.6002	1717.6024	0.0022	27400	7

LIV
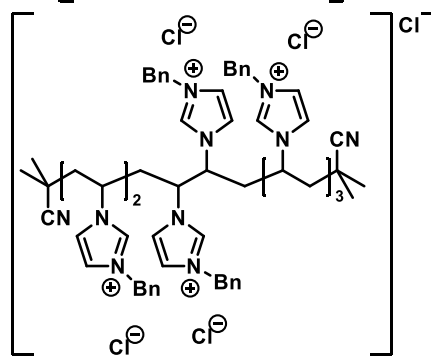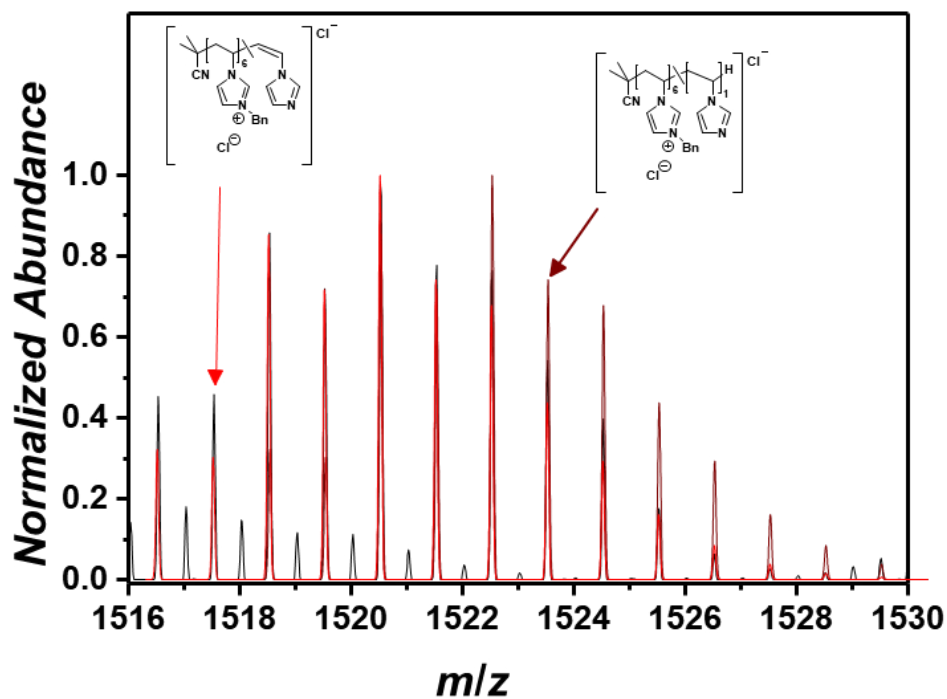
Fig. B 66 Isotopic pattern of one selected peak at 1522 *m/z* comparing the experiment (black line) and the simulation (red line) with a resolution of 26100. The isotopic pattern consists of both expected disproportion products.
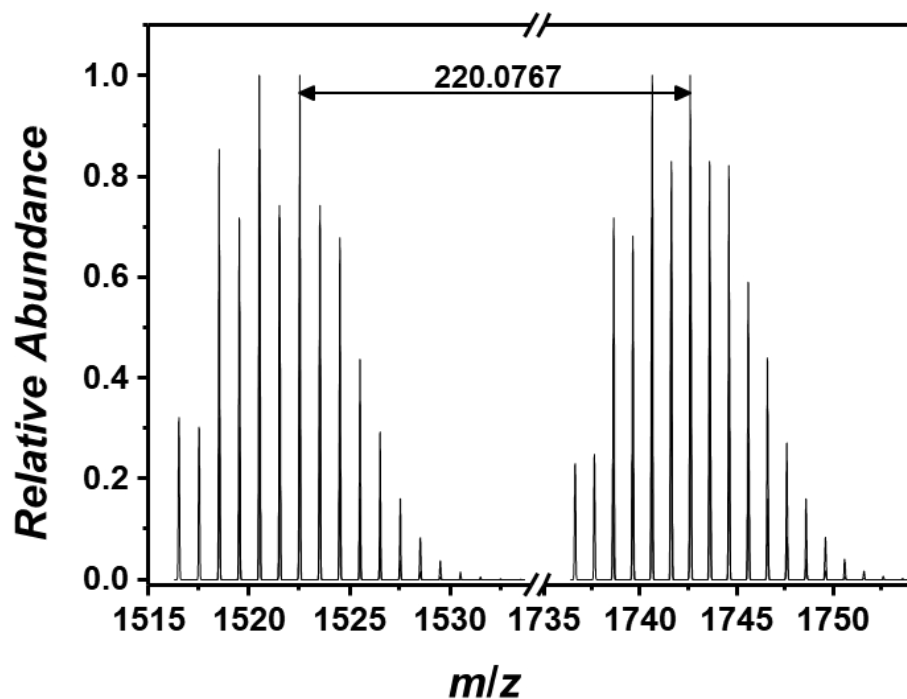
Fig. B 65 Illustration of two simulated isotopic pattern representing the species deriving from disproportionation at 1520 *m/z* and 1740 *m/z*. The difference of each highest peaks corresponds to the theoretical value of the repeating unit.

p([VBPy]NO₃) (6b)
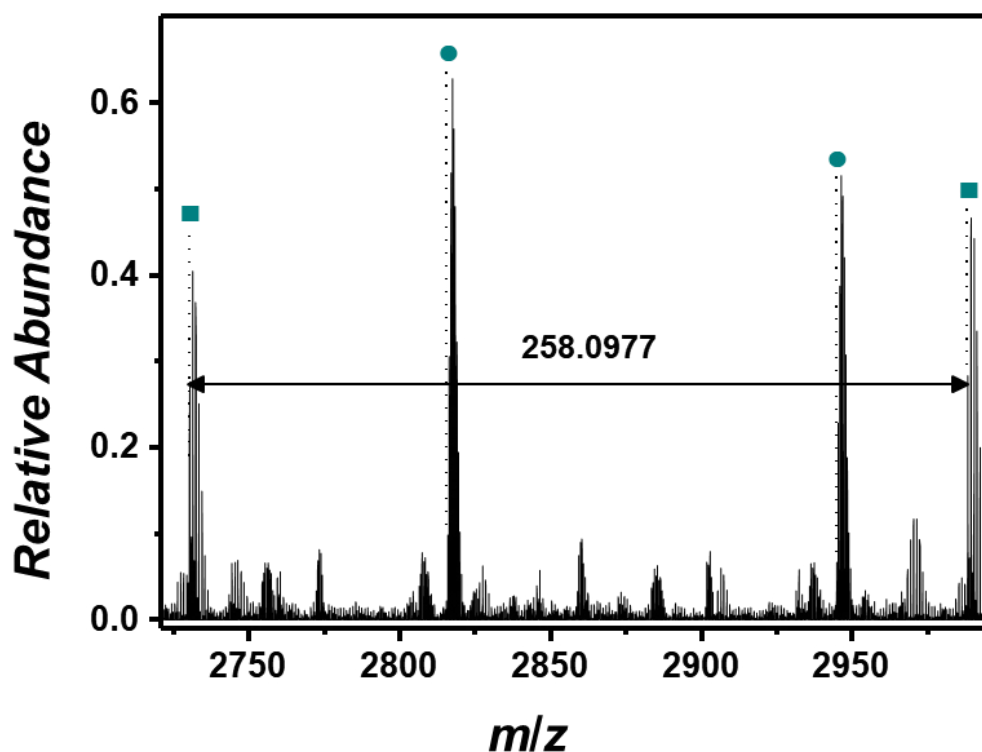
Fig. B 67 Expanded Orbitrap-CID mass spectrum of p([VBPy]NO₃) (**6b**) depicting the repeating unit of 258.0977 *m/z* (*m/z*(theo) 258.1004).

Tab. B 9 Peak assignment of the ESI-CID-Orbitrap spectrum of p([VBPy]NO₃) (**6b**) showing the label (in correspondence to the species in Fig. B 68), the resolution (obtained by the Xcalibur software), the number of repeating units *n*, the experimental *m/z* and theoretical *m/z* values, Δ*m/z* and the corresponding structure.

Label	Resolution	*n*	*m/z*(exp)	*m/z*(theo)	Δ*m/z*	Structure
■	36400	9	2730.0358	2730.0531	0.0173	
●	38400	20	2815.5589	2815.5726	0.0137	

LVI
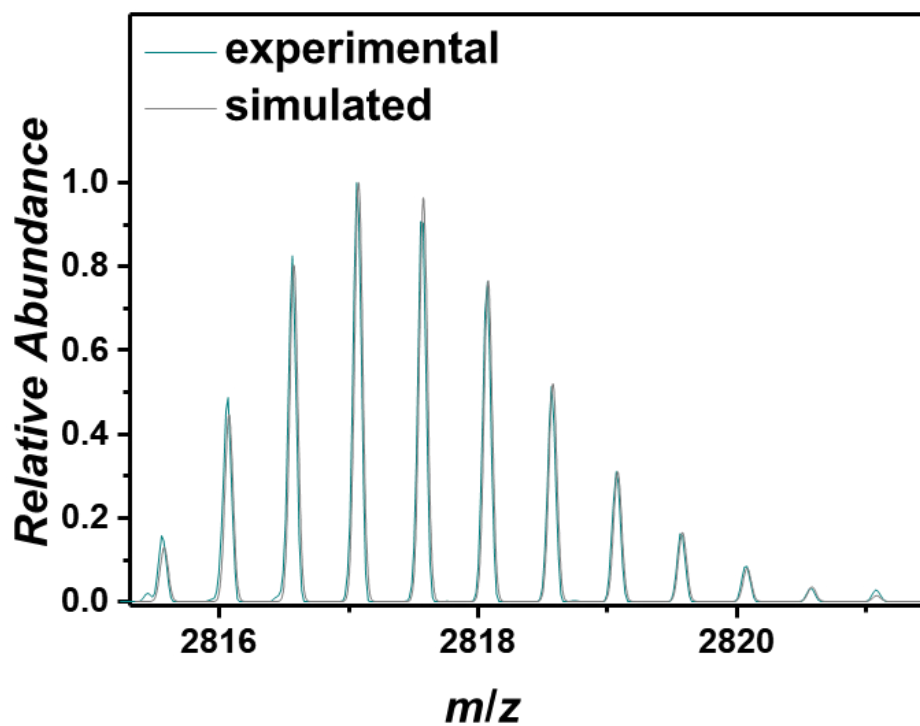
Fig. B 69 Isotopic pattern of one selected double charged peak at 2815 *m/z* comparing the experiment (blue line) and the simulation (grey line) with a resolution of 38400.

p([VBPy]CF₃CO₂) (6c)
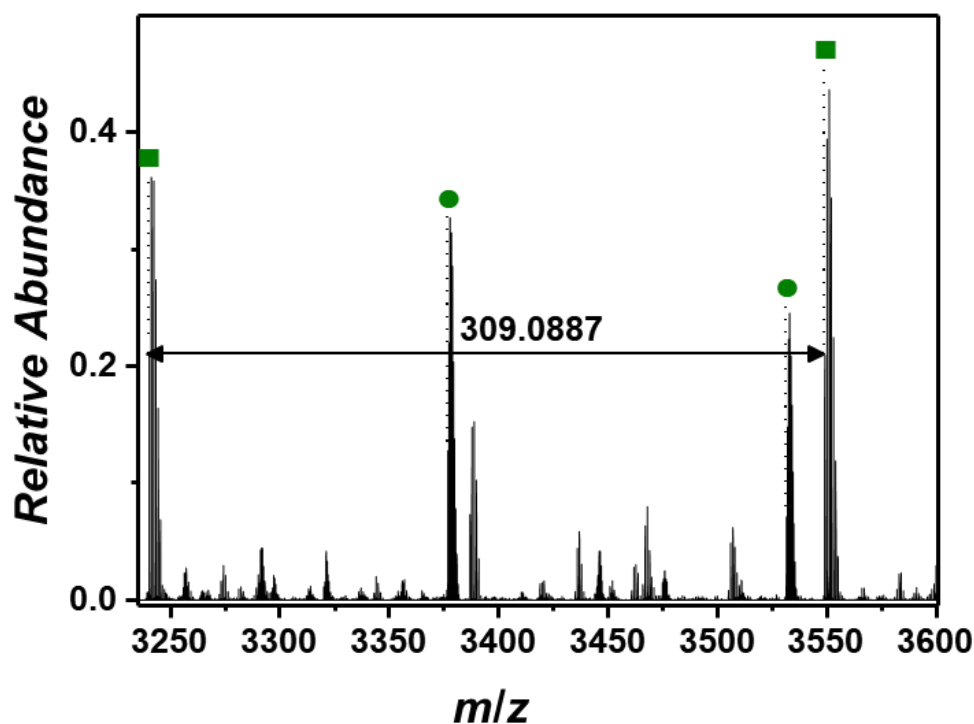
Fig. B 70 Expanded Orbitrap-CID mass spectrum of p([VBPy]CF$_3$CO$_2$) (**6c**) depicting the repeating unit of 309.0887 m/z (m/z(theo) 309.0977).

Tab. B 10 Peak assignment of the ESI-CID-Orbitrap spectrum of p([VBPy]CF$_3$CO$_2$) (**6c**) showing the label (in correspondence to the species in Fig. B 71), the resolution (obtained by the Xcalibur software), the number of repeating units n, the experimental m/z and theoretical m/z values, $\Delta m/z$ and the corresponding structure.

Label	Resolution	n	m/z(exp)	m/z(theo)	$\Delta m/z$	Structure
■	35500	9	3239.9949	3240.0253	0.0305	
●	34700	20	3376.5025	3376.5421	0.0395	

Fig. B 72 Isotopic pattern of one selected peak at 3376 *m/z* comparing the experiment (green line) and the simulation (grey line) with a resolution of 34700.

p([VBPy]BF₄) (6d)
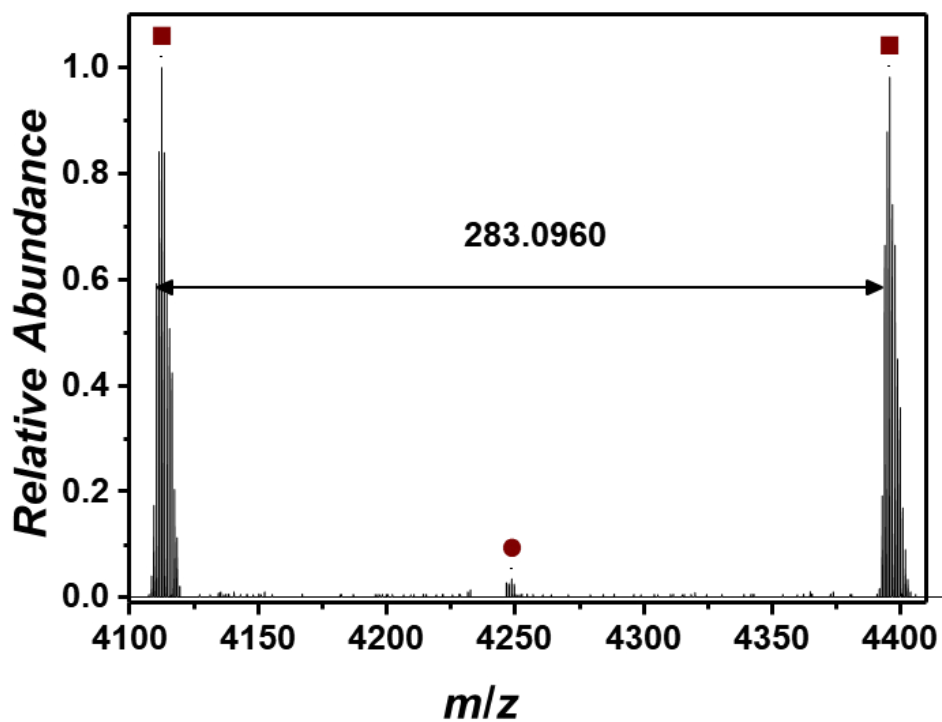
Fig. B 73 Expanded Orbitrap-CID mass spectrum of p([VBPy]BF₄) (**6d**) depicting the repeating unit of 283.0960 *m/z* (*m/z*(theo) 283.1155).

Tab. B 11 Peak assignment of the ESI-CID-Orbitrap spectrum of p([VBPy]BF$_4$) (**6d**) showing the label (in correspondence to the species in Fig. B 74), the resolution (obtained by the Xcalibur software), the number of repeating units *n*, the experimental *m/z* and theoretical *m/z* values, Δ*m/z* and the corresponding structure. Due to the low total ion current (10^2), the most abundant peak was used for labelling.

Label	Resolution	*n*	*m/z*(exp)	*m/z*(theo)	Δ*m/z*	Structure
■	35200	13	4112.6126	4112.6817	0.0691	
●	34500	14	4248.6581	4248.7509	0.0928	
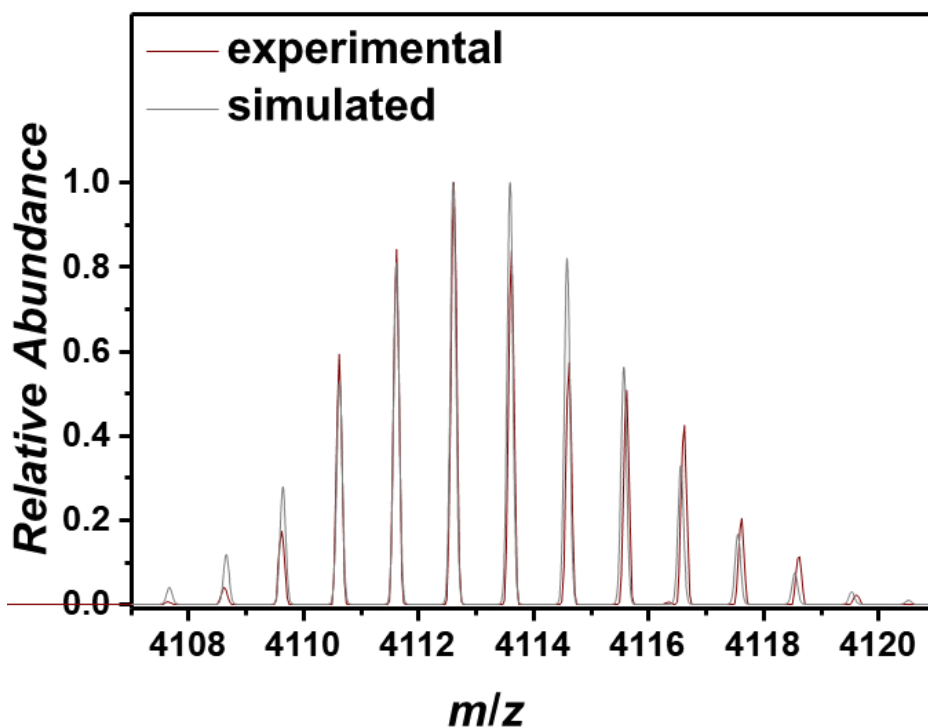
Fig. B 75 Isotopic pattern of one selected peak at 4112 *m/z* comparing the experiment (red line) and the simulation (red line) with a resolution of 35200.

Surface Modification
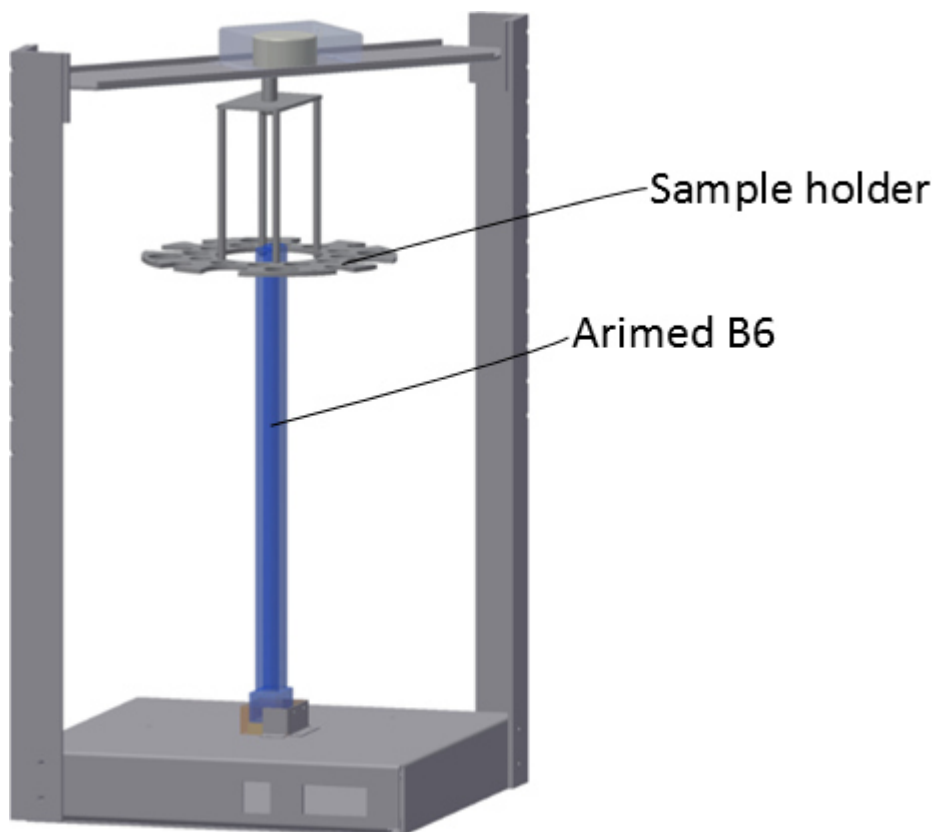
Fig. B 77 Schematic representation of the custom-built photoreactor employed in the current study for the surface-patterning of PILs with the Arimed B6 bulb in the middle with a motor operated carousel as sample holder.
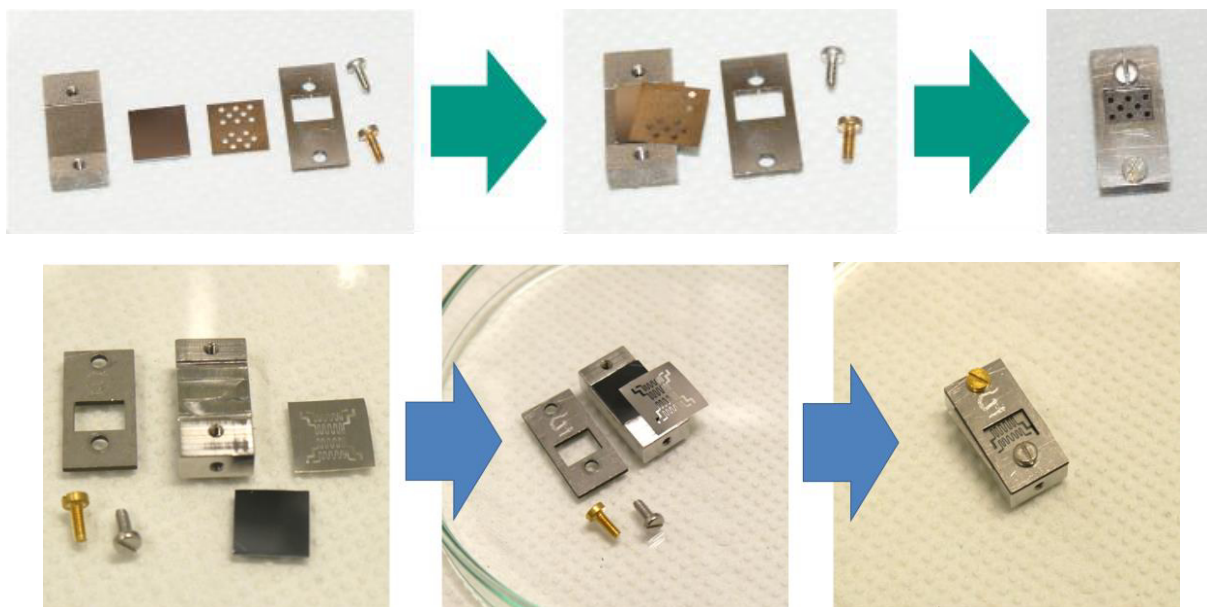
Fig. B 76 Sample holders and the shadow masks utilized for the reaction to obtain the dotted pattern (top) and the meander structure (below) on the surfaces.

C

APPENDIX

Synthesis
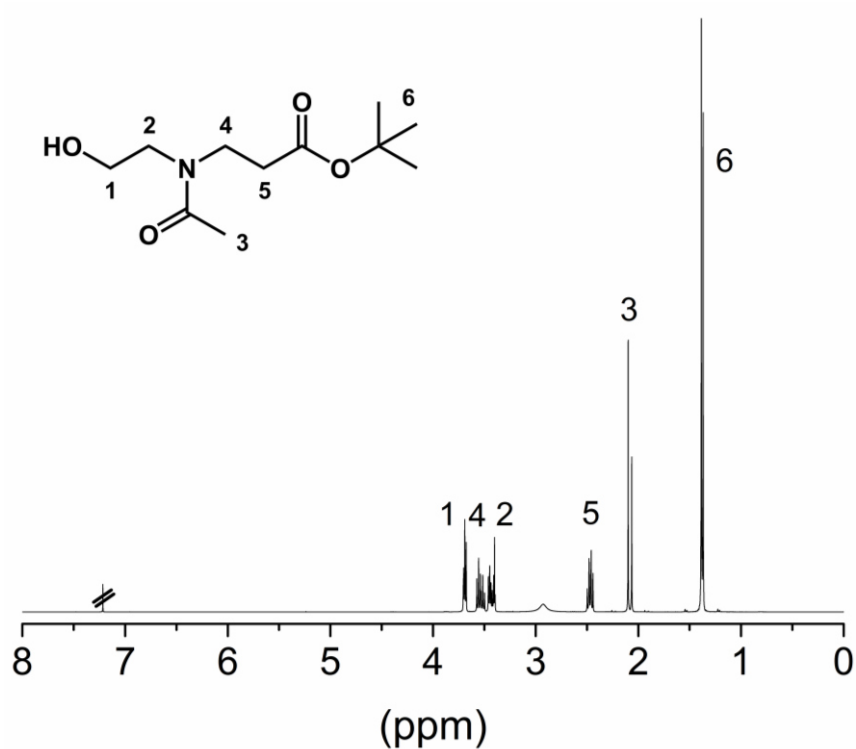
Fig. C 1 ^{1}H NMR (CDCl$_3$, 400 MHz) spectrum of tert-butyl 3-(N-(2-hydroxyethyl)acetamido)propanoate.
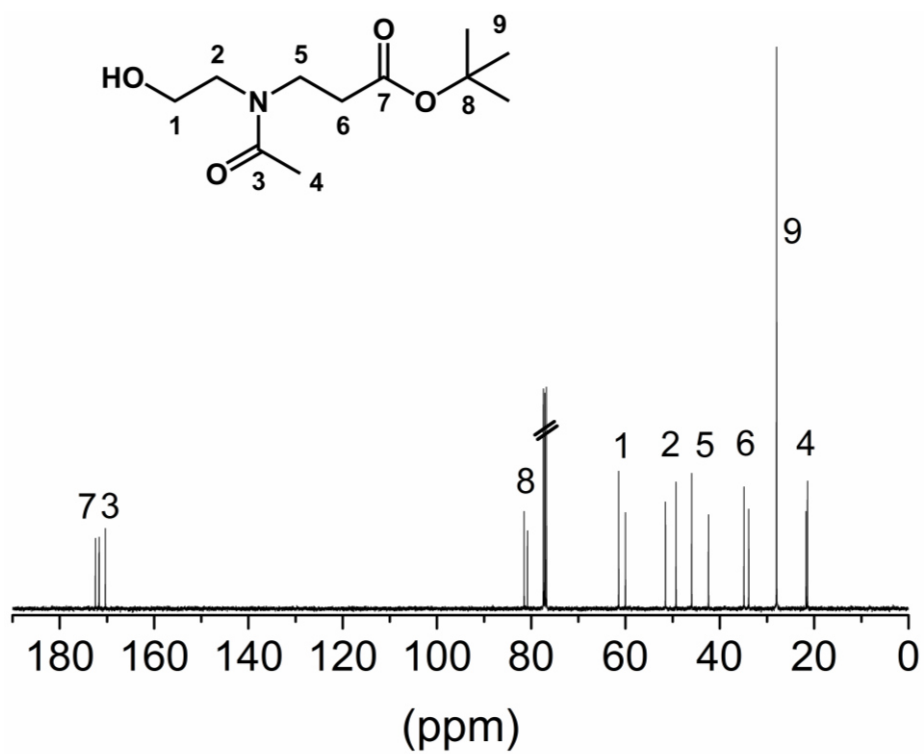
Fig. C 2 ^{13}C{^{1}H} NMR (CDCl$_3$, 400 MHz) spectrum of tert-butyl 3-(N-(2-hydroxyethyl)acetamido)propanoate.
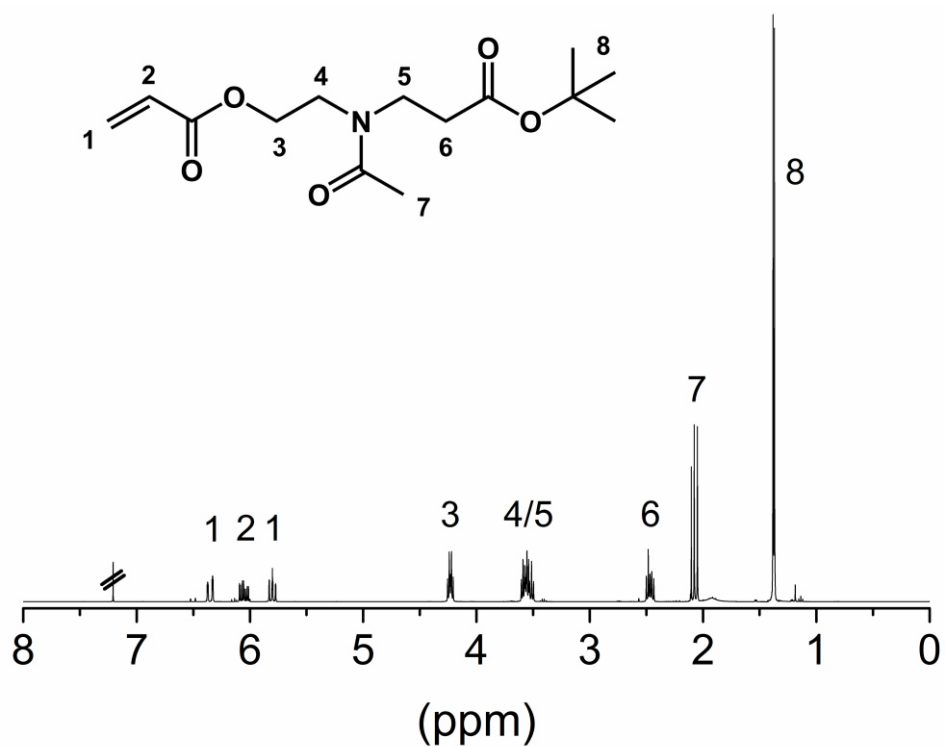
Fig. C 4 ^{1}H NMR (CDCl3, 400 MHz) spectrum of crude 2-(N-(3-(tert-butoxy)-3-oxopropyl)acetamido)ethyl acrylate.
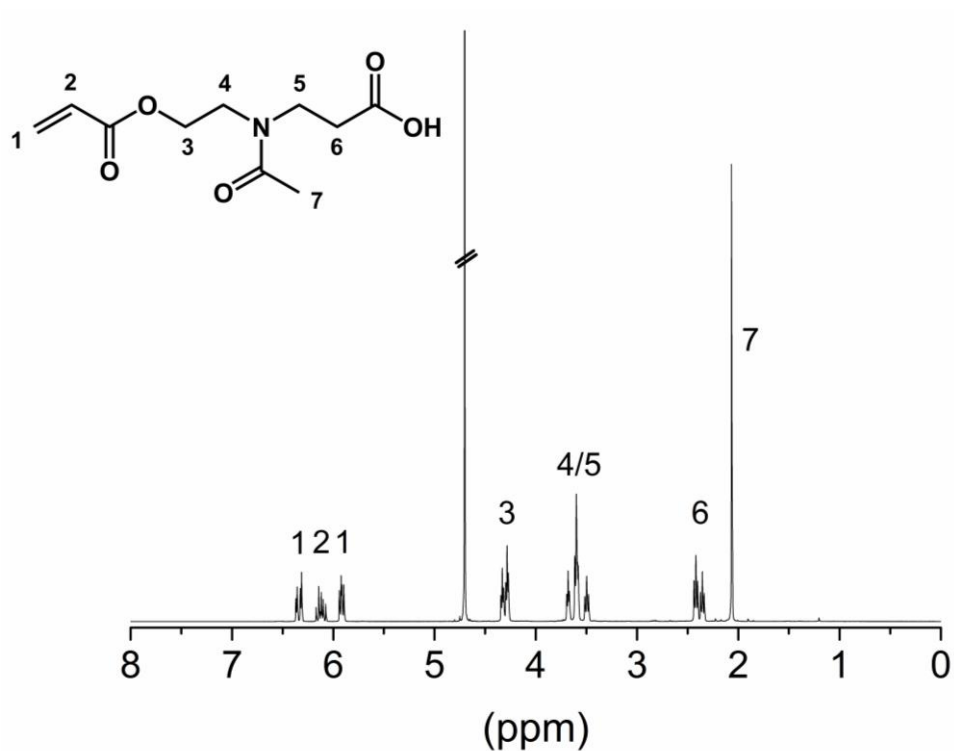
Fig. C 3 ^{1}H NMR (D_2O, 400 MHz) spectrum of 3-(N-(2-(acryloyloxy)ethyl)acetamido)propanoic acid.
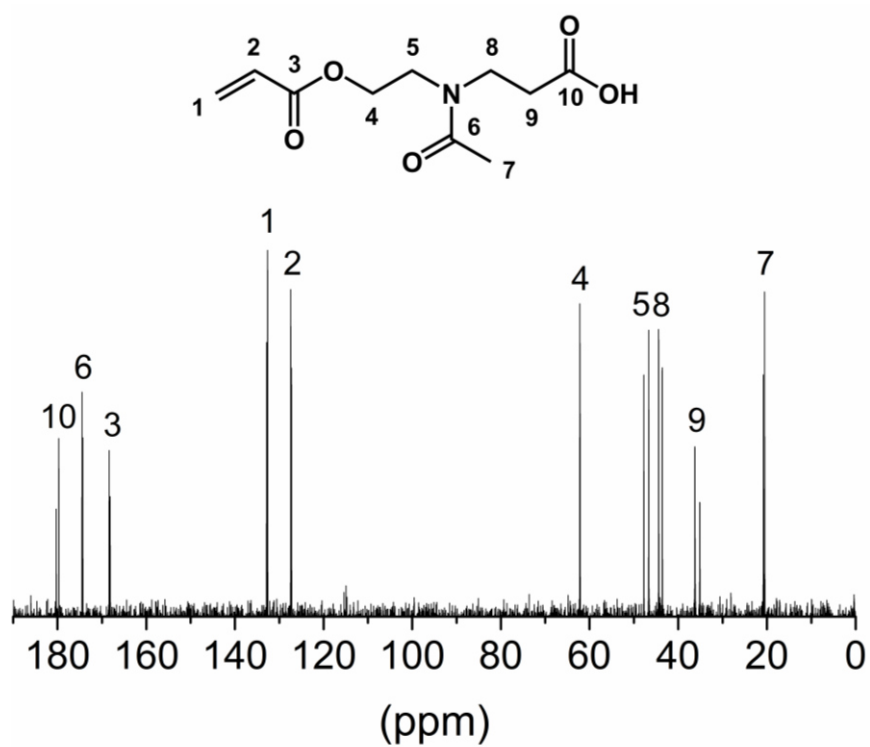
Fig. C 5 $^{13}C\{^1H\}$ NMR (D$_2$O, 400 MHz) spectrum of 3-(N-(2-(acryloyloxy)ethyl)acetamido)propanoic acid.

LXVI

Polymer Synthesis
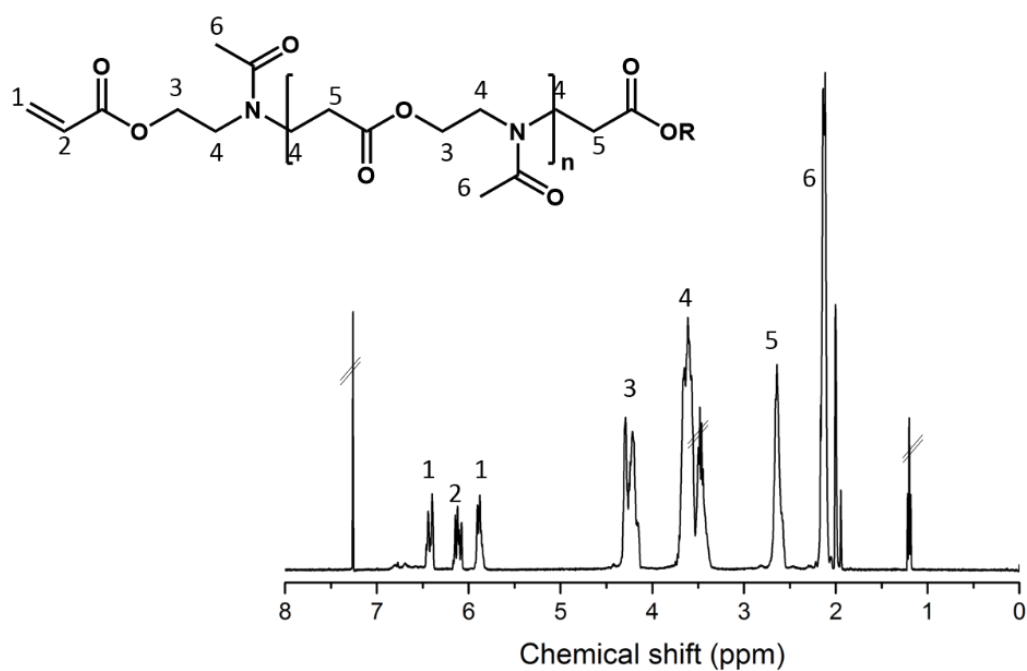
Fig. C 6 ¹H NMR (400 MHz, CDCl₃) of oligo(MeOx-alt-AA)ₙA (1:1).
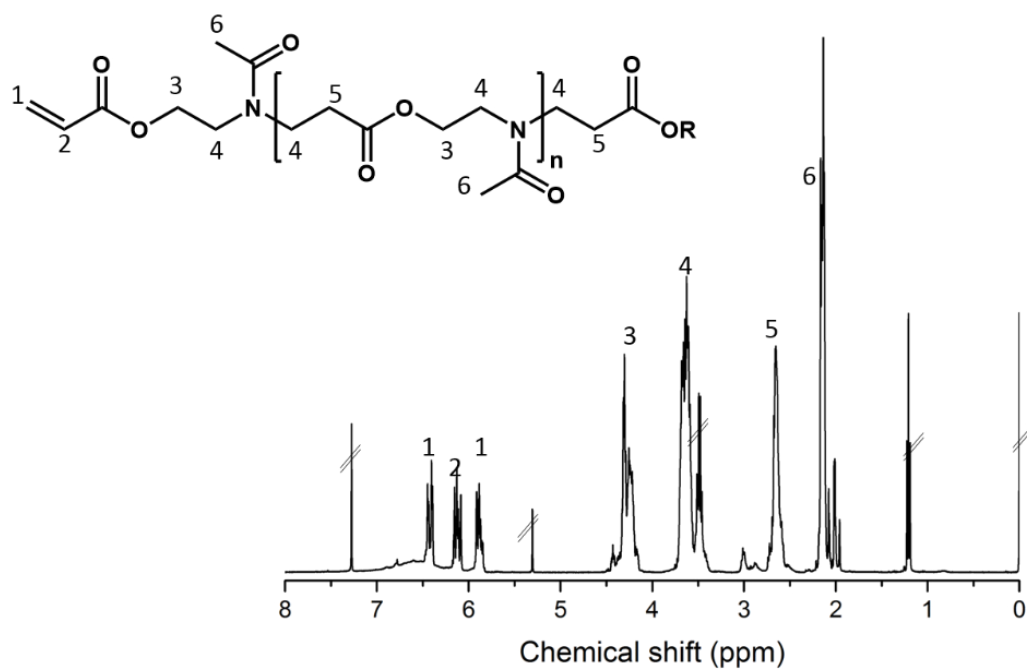
Fig. C 7 ¹H NMR (400 MHz, CDCl₃) of oligo(MeOx-alt-AA)ₙA (1:2).
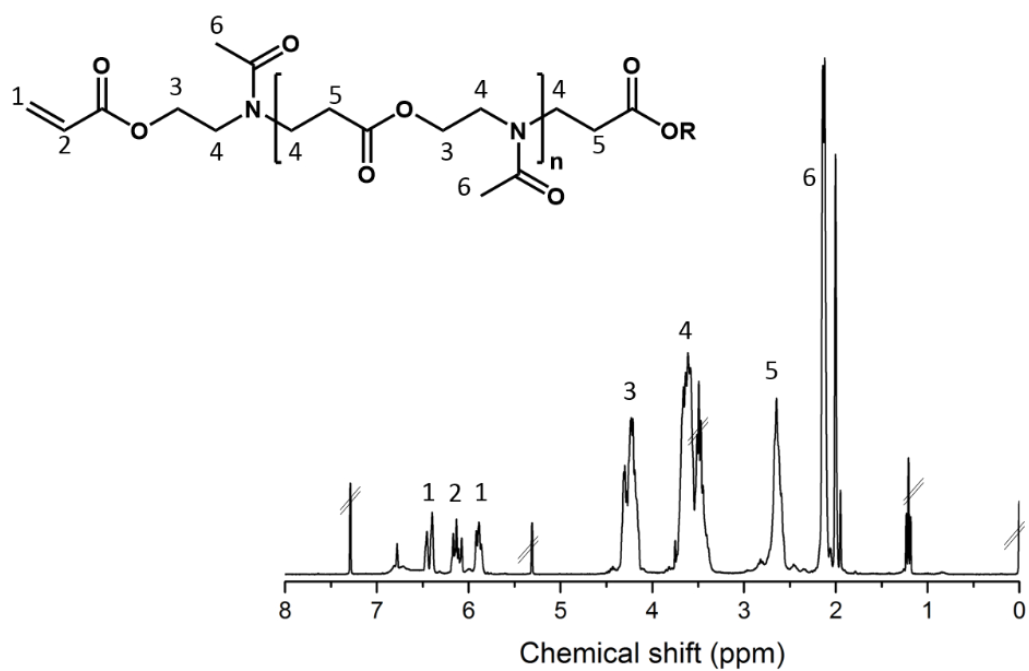
Fig. C 9 ^{1}H NMR (400 MHz, CDCl$_3$) of oligo(MeOx-alt-AA)$_n$A (2:1).
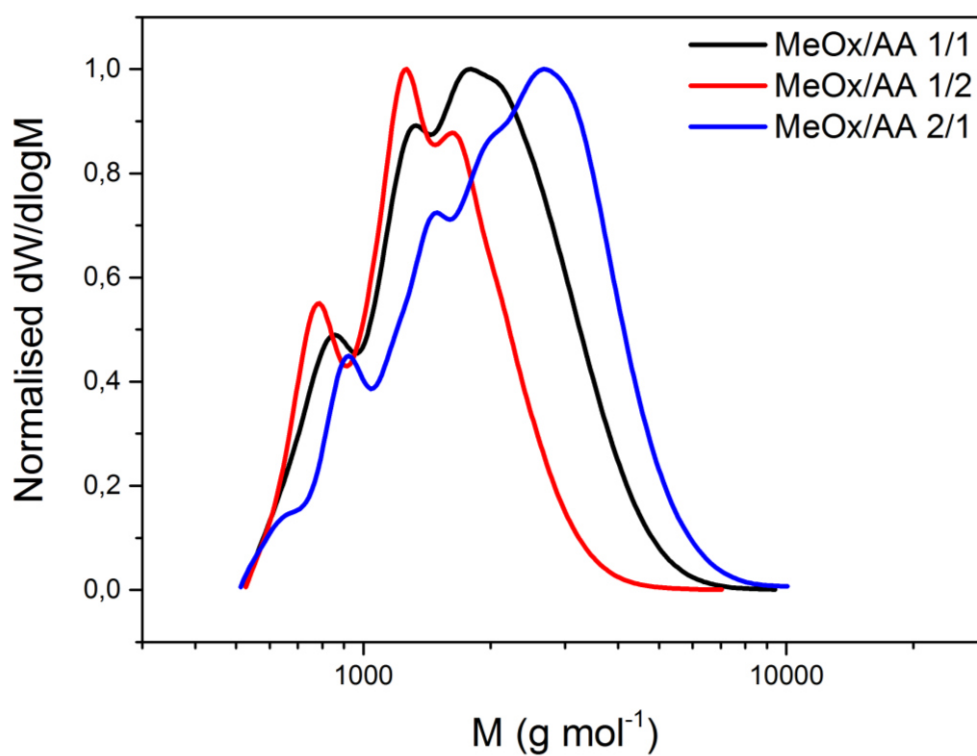
Fig. C 8 SEC analysis of oligo(MeOx-alt-AA)$_n$A (1:1 (black); 1:2 (red); 2:1 (blue)) in DMF containing 5 mM NH$_4$BF$_4$ relative to PMMA calibration.
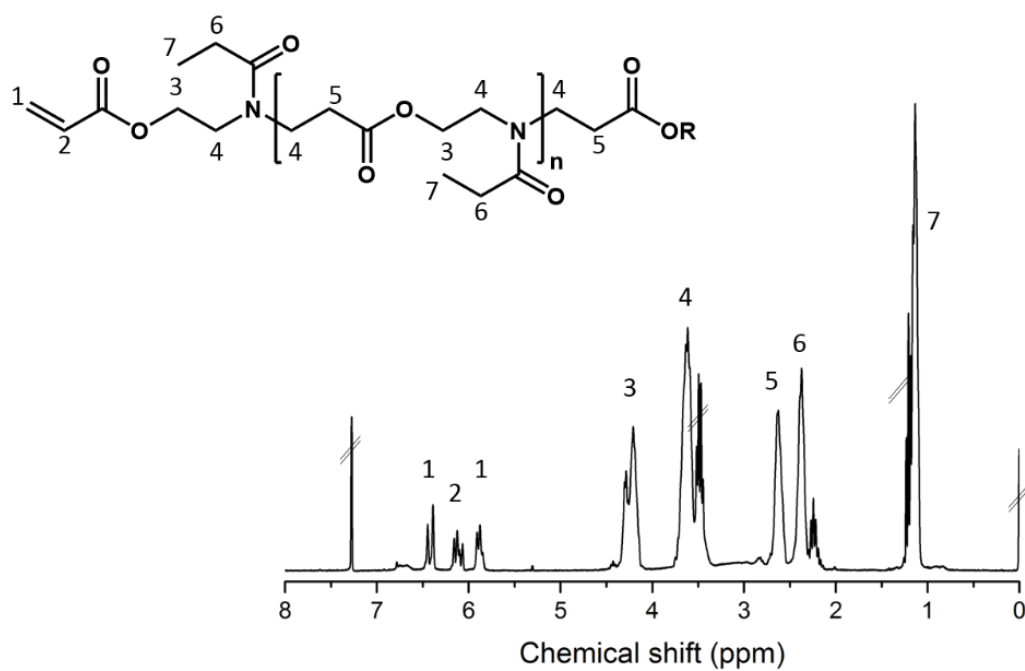
Fig. C 11 ^{1}H NMR (400 MHz, CDCl3) of oligo(EtOx-alt-AA)nA (1:1).
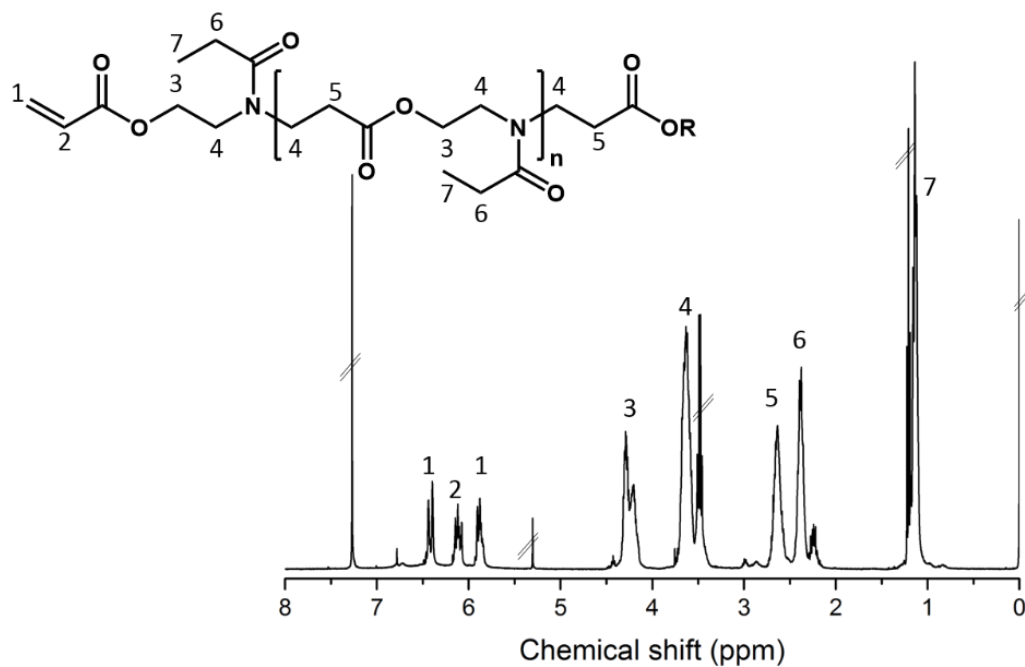
Fig. C 10 ^{1}H NMR (400 MHz, CDCl3) of oligo(EtOx-alt-AA)nA (1:2).
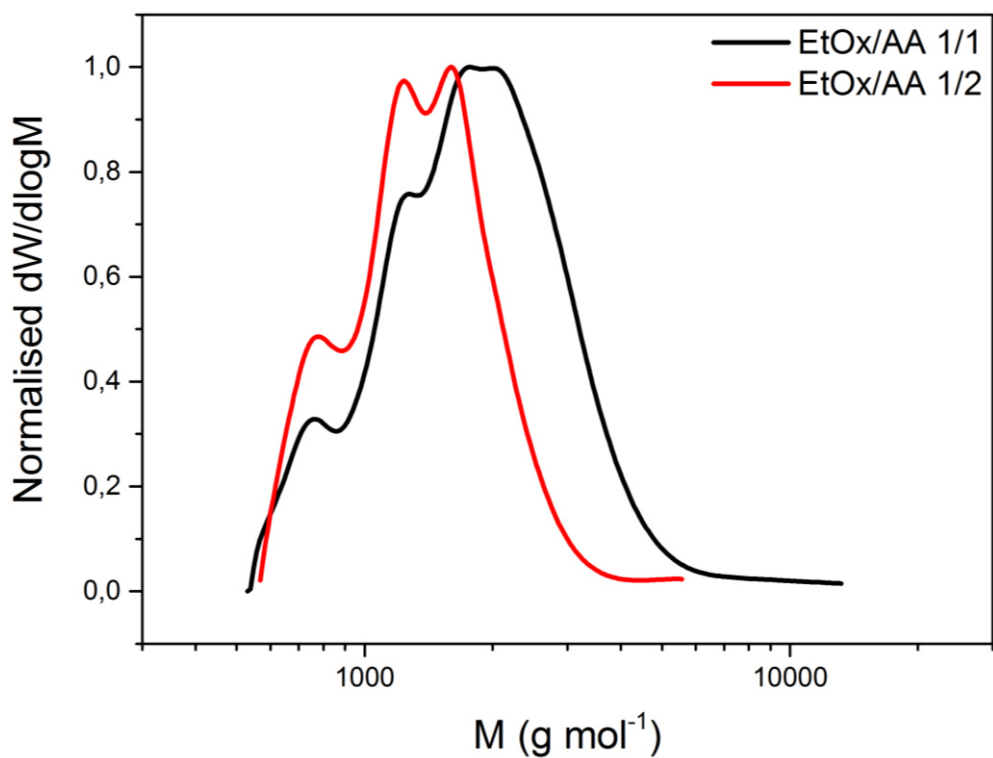
Fig. C 13 SEC analysis of oligo(EtOx-alt-AA)$_n$A (1:1 (black); 1:2 (red) in DMF containing 5 mM NH_4BF_4 relative to PMMA calibration.
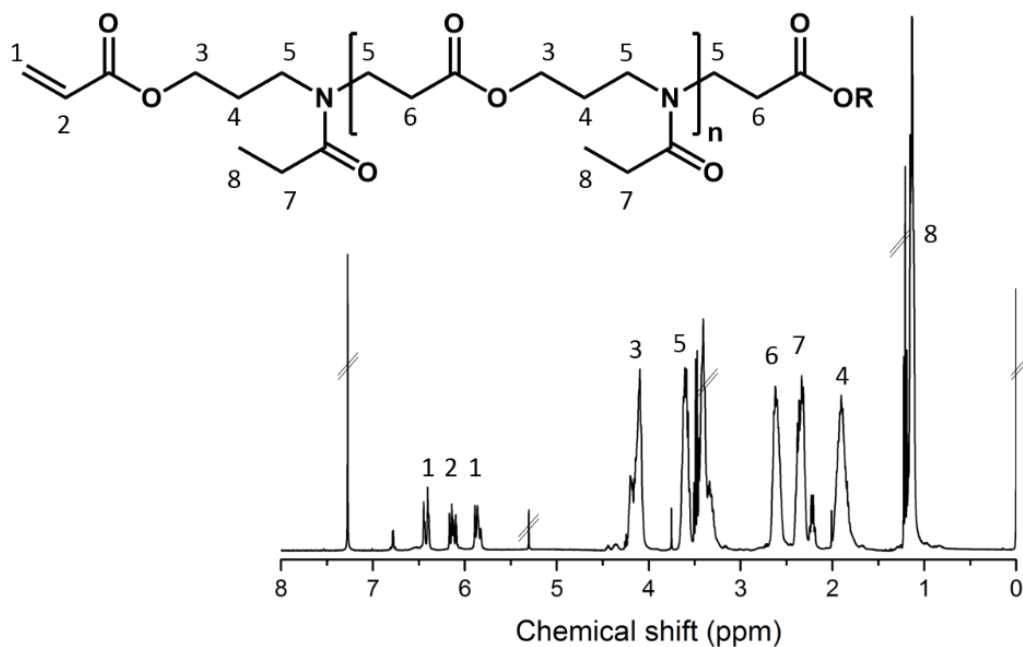
Fig. C 12 ^{1}H NMR (400 MHz, CDCl3) of oligo(EtOz-alt-AA)$_n$A (1:1).
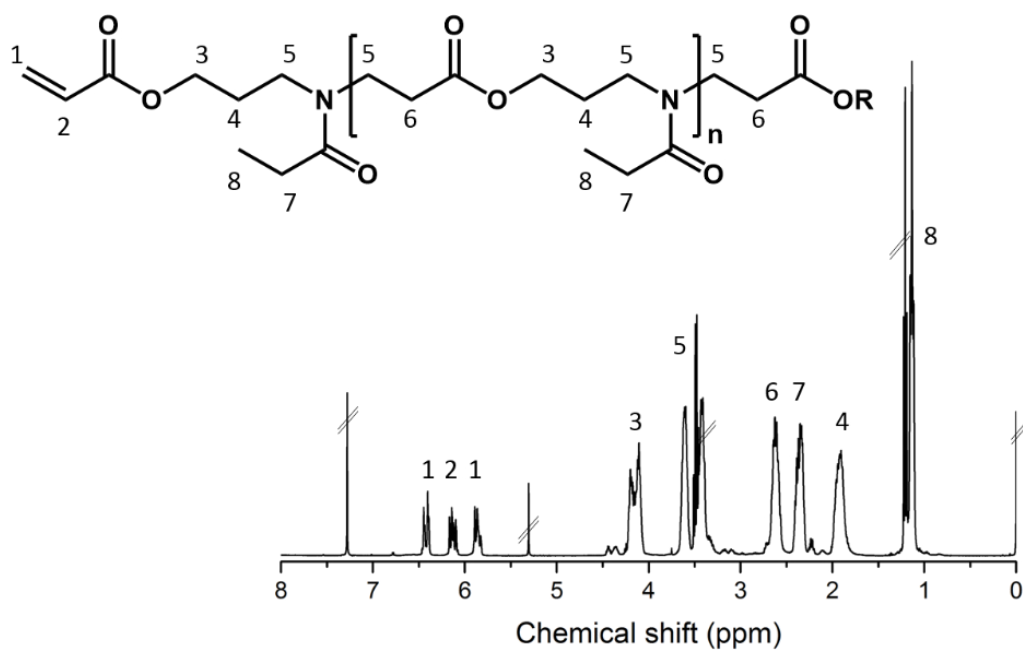
Fig. C 15 ^{1}H NMR (400 MHz, CDCl3) of oligo(EtOz-alt-AA)$_n$A (1:2).
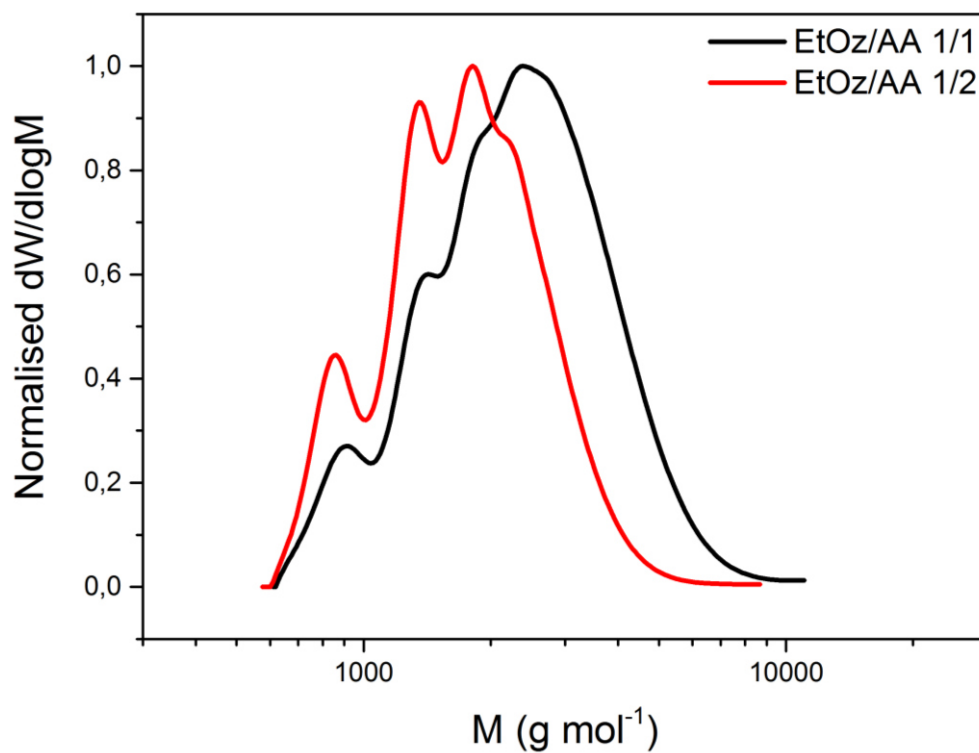
Fig. C 14 SEC analysis of oligo(EtOz-alt-AA)$_n$A (1:1 (black); 1:2 (red) in DMF containing 5 mM NH$_4$BF$_4$ relative to PMMA calibration.

SEMI-QUANTIFICATION
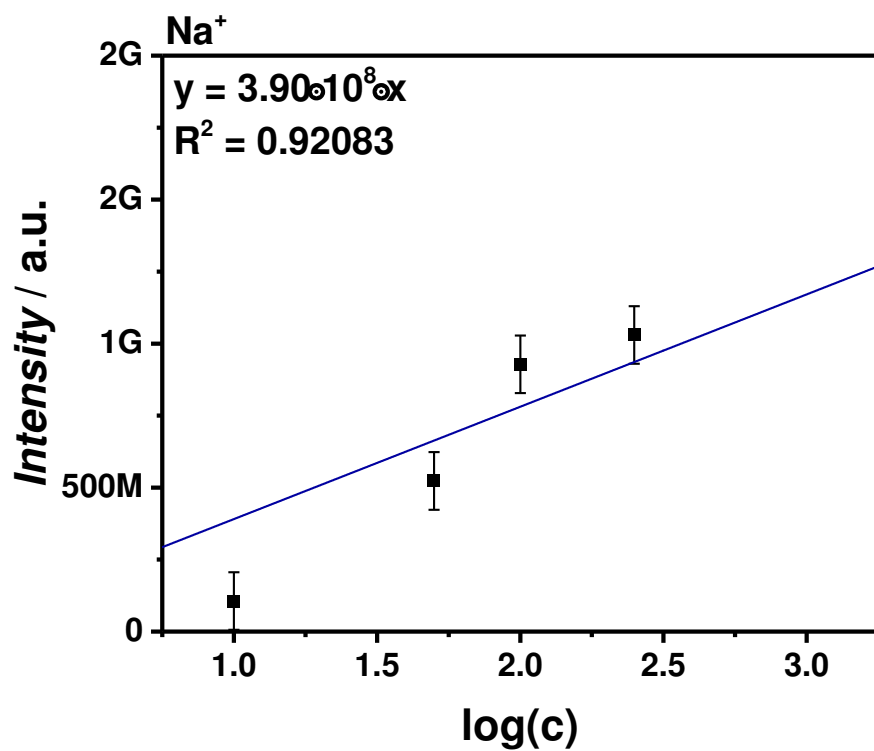
Fig. C 16 Calibration curve determined by measuring the intensity in a dilution series of an acid-terminated MeOx/AA dimer (252.0835 *m/z*).

Tab. C 1 Quantitative calculations based on the calibration curve referred to the overview spectrum showing the m/z, the peak intensities, and the mole fraction χ.

MeOx / AA = 1:1   c / mg mL⁻¹   0.50

REPEAT UNIT H⁺			REPEAT UNIT Na⁺		
m/z	Intensity	Mole Fraction χ	m/z	Intensity	Mole Fraction χ
230.1019	2.20E+07	0.18	252.0836	8.03E+07	0.14
315.1543	2.08E+08	0.39	337.1365	4.72E+08	0.29
387.1756	6.39E+07	0.25	409.1575	1.49E+08	0.17
472.2285	2.99E+08	0.43	494.2094	5.02E+08	0.32
544.2496	9.95E+07	0.32	566.2314	1.31E+08	0.24
629.3008	1.88E+08	0.49	651.2829	3.02E+08	0.36
701.3233	5.02E+07	0.43	723.3045	7.44E+06	0.05
786.3755	7.18E+07	0.55	808.3581	1.01E+08	0.39
858.3955	1.90E+07	0.55	880.3782	2.57E+07	0.44
943.4495	2.43E+07	0.61	965.4294	3.09E+07	0.43

MeOx / AA = 1:2   c / mg mL⁻¹   0.50

REPEAT UNIT H⁺			REPEAT UNIT Na⁺		
m/z	Intensity	Mole Fraction χ	m/z	Intensity	Mole Fraction χ
230.1019	9.50E+07	0.77	252.0835	4.34E+08	0.76
315.1543	1.96E+08	0.37	337.1365	4.02E+08	0.25
387.1747	1.74E+08	0.67	409.1575	6.33E+08	0.73
472.2282	2.10E+08	0.30	494.2095	4.56E+08	0.29
544.2492	1.84E+08	0.60	566.2300	3.36E+08	0.62
629.3022	9.79E+07	0.25	651.2831	1.80E+08	0.21
701.3223	5.33E+07	0.46	723.3049	1.03E+08	0.68
786.3748	2.36E+07	0.18	808.3559	3.80E+07	0.15
858.3947	1.10E+07	0.32	880.3789	1.66E+07	0.29
943.4485	4.99E+06	0.12	965.4338	5.64E+06	0.08

MeOx / AA = 2:1   c / mg mL⁻¹   0.50

REPEAT UNIT H⁺			REPEAT UNIT Na⁺		
m/z	Intensity	Mole Fraction χ	m/z	Intensity	Mole Fraction χ
230.1019	5.81E+06	0.05	252.0835	5.84E+07	0.10
315.1543	1.27E+08	0.24	337.1363	7.50E+08	0.46
387.1753	2.08E+07	0.08	409.1573	8.08E+07	0.09
472.2274	1.82E+08	0.26	494.2104	6.32E+08	0.40
544.2482	2.42E+07	0.08	566.2310	7.44E+07	0.14
629.3011	1.00E+08	0.26	651.2823	3.56E+08	0.42
701.3215	1.29E+07	0.11	723.3039	4.06E+07	0.27
786.3760	3.50E+07	0.27	808.3573	1.18E+08	0.46
858.3961	4.80E+06	0.14	880.3773	1.56E+07	0.27
943.4503	1.08E+07	0.27	965.4319	3.49E+07	0.49

Tab. C 2 Quantitative calculations based on the calibration curve referred to the expanded spectrum showing the m/z, the peak intensities, and the mole fraction χ .

MeOx / AA = 1:1   c / mg mL^{-1} 0.50

	REPEAT UNIT		
Label	**m/z**	**Intensity**	**Mole Fraction χ**
	230.1019	2.20E+07	0.18
●	315.1543	2.08E+08	0.39
△	324.1047	6.22E+06	0.12
▼	328.1862	5.64E+07	0.29
●	387.1756	6.39E+07	0.25
▼	400.2073	1.84E+08	0.45
●	472.2285	2.99E+08	0.43
△	481.1780	1.32E+07	0.10
▼	485.2593	5.55E+07	0.42
●	544.2496	9.95E+07	0.32
▼	557.2800	1.54E+08	0.49
●	629.3008	1.88E+08	0.49
△	638.2519	9.66E+06	0.21
▼	642.3334	4.56E+07	0.50
●	701.3233	5.02E+07	0.43
▼	714.3548	8.28E+07	0.54
●	786.3755	7.18E+07	0.55
△	795.3271	7.11E+06	0.17
▼	799.4059	2.50E+07	0.59
●	858.3955	1.90E+07	0.55
▼	871.4288	3.46E+07	0.59

MeOx / AA = 1:2   c / mg mL^{-1} 0.50

	REPEAT UNIT		
Label	**m/z**	**Intensity**	**Mole Fraction χ**
	230.1019	9.31E+07	0.77
●	315.1543	1.27E+08	0.24
△	324.1047	4.23E+07	0.82
▼	328.1861	3.86E+07	0.20
●	387.1753	1.74E+08	0.67
▼	400.2064	1.21E+08	0.30
●	472.2285	2.10E+08	0.30
△	481.1780	1.13E+08	0.87
▼	485.2593	3.25E+07	0.25
●	544.2496	1.84E+08	0.60
▼	557.2800	7.65E+07	0.24
●	629.3008	9.79E+07	0.25
△	638.2519	3.11E+07	0.69
▼	642.3334	1.60E+07	0.17

Label	m/z	Intensity	Mole Fraction χ
●	701.3233	5.33E+07	0.46
▼	714.3548	2.59E+07	0.17
●	786.3755	2.36E+07	0.18
△	795.3271	3.28E+07	0.77
▼	799.4059	2.67E+06	0.06
●	858.3955	1.10E+07	0.32
▼	871.4288	6.46E+06	0.11

MeOx / AA = 2:1 c / mg mL^{-1} 0.50

Label	REPEAT UNIT		
Label	m/z	Intensity	Mole Fraction χ
	230.1019	5.81E+06	0.05
●	315.1543	1.96E+08	0.37
△	324.1045	2.94E+06	0.06
▼	328.1860	9.99E+07	0.51
●	387.1747	2.08E+07	0.08
▼	400.2071	1.00E+08	0.25
●	472.2285	1.82E+08	0.26
△	481.1780	4.40E+06	0.03
▼	485.2593	4.36E+07	0.33
●	544.2496	2.42E+07	0.08
▼	557.2800	8.59E+07	0.27
●	629.3008	1.00E+08	0.26
△	638.2519	4.39E+06	0.10
▼	642.3334	3.03E+07	0.33
●	701.3233	1.29E+07	0.11
▼	714.3548	4.48E+07	0.29
●	786.3755	3.50E+07	0.27
△	795.3271	2.48E+06	0.06
▼	799.4059	1.46E+07	0.34
●	858.3955	4.80E+06	0.14
▼	871.4288	1.76E+07	0.30

Tab. C 3 Quantitative calculations based on the calibration curve for the homocoupling showing the m/z, the peak intensities, and the mole fraction χ.

MeOx / AA = 1:1

	REPEAT UNIT		
n	**m/z**	**Intensity**	**Mole Fraction χ**
2	265.1154	1.48E+08	0.27
3	350.1681	3.16E+07	0.29
4	435.2206	6.11E+06	0.30
5	520.2737	7.91E+05	0.58

MeOx / AA = 1:2

	REPEAT UNIT		
n	**m/z**	**Intensity**	**Mole Fraction χ**
2	265.1153	1.45E+08	0.26
3	350.1681	3.66E+07	0.34
4	435.2206	7.64E+06	0.38
5	520.2752	3.26E+04	0.02

MeOx / AA = 2:1

	REPEAT UNIT		
n	**m/z**	**Intensity**	**Mole Fraction χ**
2	265.1153	2.63E+08	0.47
3	350.1679	3.95E+07	0.37
4	435.2203	6.42E+06	0.32
5	520.2747	5.49E+05	0.40

Tab. C 4 Quantitative calculations based on the calibration curve referred to the overview spectrum showing the m/z, the peak intensities, and the mole fraction χ.

EtOx/AA = 1:1   c / mg mL^{-1} 0.50

REPEAT UNIT H$^+$			REPEAT UNIT Na$^+$		
m/z	Intensity	Mole Fraction χ	m/z	Intensity	Mole Fraction χ
244.1174	1.75E+07	0.36	266.0990	9.86E+07	0.26
343.1860	1.62E+08	0.68	365.1674	5.45E+08	0.60
415.2069	5.47E+07	0.45	437.1882	2.38E+08	0.29
514.2745	2.78E+08	0.79	536.2565	9.58E+08	0.67
586.2967	8.20E+07	0.57	608.2778	2.68E+08	0.40
685.3636	1.71E+08	0.86	707.3464	6.75E+08	0.77
757.3850	4.14E+07	0.72	779.3661	1.53E+08	0.50
856.4545	5.65E+07	0.89	878.4362	2.16E+08	0.80
928.4753	1.28E+07	0.54	950.4554	4.63E+07	0.61
244.1174	1.75E+07	0.36	266.0990	9.86E+07	0.26

EtOx/AA = 1:2   c / mg mL^{-1} 0.50

REPEAT UNIT H$^+$			REPEAT UNIT Na$^+$		
m/z	Intensity	Mole Fraction χ	m/z	Intensity	Mole Fraction χ
244.1174	3.17E+07	0.64	266.0992	2.74E+08	0.74
343.1855	7.48E+07	0.32	365.1676	3.65E+08	0.40
415.2062	6.67E+07	0.55	437.1885	5.89E+08	0.71
514.2748	7.50E+07	0.21	536.2567	4.79E+08	0.33
586.2952	6.23E+07	0.43	608.2780	4.03E+08	0.60
685.3638	2.83E+07	0.14	707.3443	2.06E+08	0.23
757.3851	1.59E+07	0.28	779.3662	1.55E+08	0.50
856.4515	7.08E+06	0.11	878.4332	5.30E+07	0.20
928.4753	1.10E+07	0.46	950.4553	3.01E+07	0.39
244.1174	3.17E+07	0.64	266.0992	2.74E+08	0.74

Tab. C 5 Quantitative calculations based on the calibration curve for the homocoupling showing the m/z, the peak intensities, and the mole fraction χ .

EtOx / AA = 1:1

	REPEAT UNIT		
n	m/z	Intensity	Mole Fraction χ
2	271.1647	1.44E+08	0.70
3	370.2330	4.15E+07	0.83
4	469.3013	7.09E+06	0.88
5	568.3695	5.30E+05	1.00

EtOx / AA = 1:2

	REPEAT UNIT		
n	m/z	Intensity	Mole Fraction χ
2	271.1647	6.16E+07	0.30
3	370.2330	8.64E+06	0.17
4	469.3013	1.00E+06	0.12
5	568.3695	0.00E+00	0.00

Tab. C 6 Quantitative calculations based on the calibration curve referred to the overview spectrum showing the m/z, the peak intensities, and the mole fraction χ.

EtOz/AA = 1:1

c / mg mL^{-1} 0.50

REPEAT UNIT H$^+$			REPEAT UNIT Na$^+$		
m/z	Intensity	Mole Fraction χ	m/z	Intensity	Mole Fraction χ
258.133	4.17E+07	0.27	280.1148	1.04E+08	0.35
371.2173	2.05E+08	0.46	393.1988	2.37E+08	0.48
443.2381	1.59E+08	0.23	465.2193	1.70E+08	0.26
556.3218	2.44E+08	0.53	578.3040	4.25E+08	0.55
628.3434	1.49E+08	0.26	650.3240	1.91E+08	0.30
741.4259	1.31E+08	0.60	763.4082	2.99E+08	0.68
813.4469	7.34E+07	0.33	835.4305	1.21E+08	0.41
926.5327	5.01E+07	0.68	948.5127	1.03E+08	0.77
998.5529	2.58E+07	0.39			

EtOz/AA = 1:2

c / mg mL^{-1} 0.50

REPEAT UNIT H$^+$			REPEAT UNIT Na$^+$		
m/z	Intensity	Mole Fraction χ	m/z	Intensity	Mole Fraction χ
258.1333	1.12E+08	0.73	280.1151	1.91E+08	0.65
371.2169	2.46E+08	0.54	393.1984	2.60E+08	0.52
443.2376	5.28E+08	0.77	465.2200	4.86E+08	0.74
556.3226	2.14E+08	0.47	578.3031	3.41E+08	0.45
628.3423	4.22E+08	0.74	650.3246	4.49E+08	0.70
741.4265	8.94E+07	0.40	763.4088	1.43E+08	0.32
813.4474	1.50E+08	0.67	835.4284	1.77E+08	0.59
926.5330	2.35E+07	0.32	948.5131	3.10E+07	0.23
998.5530	4.09E+07	0.61			

Tab. C 7 Quantitative calculations based on the calibration curve for the homocoupling showing the m/z, the peak intensities, and the mole fraction χ .

EtOz / AA = 1:1

n	m/z	Intensity	Mole Fraction χ
		REPEAT UNIT	
2	299.1960	3.64E+07	0.48
3	412.2797	2.35E+06	0.89
4	525.3640	1.88E+04	1.00
5	638.4487	0.00E+00	0.00

EtOz / AA = 1:2

n	m/z	Intensity	Mole Fraction χ
		REPEAT UNIT	
2	299.1960	3.93E+07	0.52
3	412.2797	2.97E+05	0.11
4	525.3640	0.00E+00	0.00
5	638.4487	0.00E+00	0.00
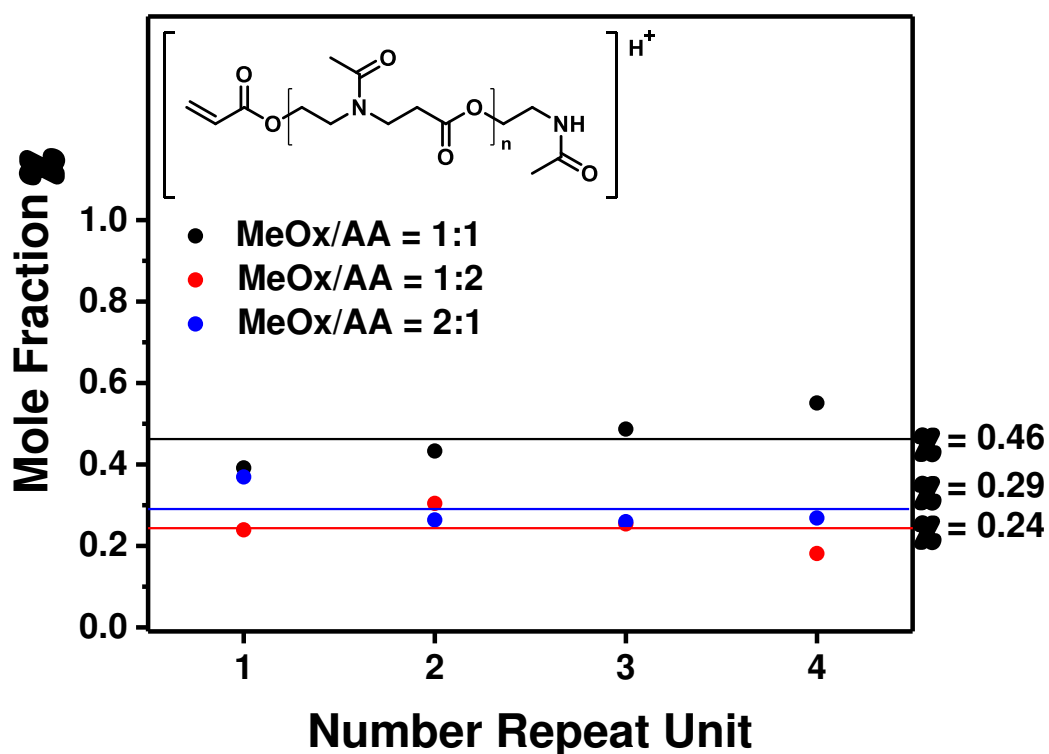
Fig. C 17 Illustration of the mole fraction along the repeat units of MeOx/AA (1:1; 1:2 and 2:1) determined based on the H⁺ ionized ● labeled intensities.

LXXX
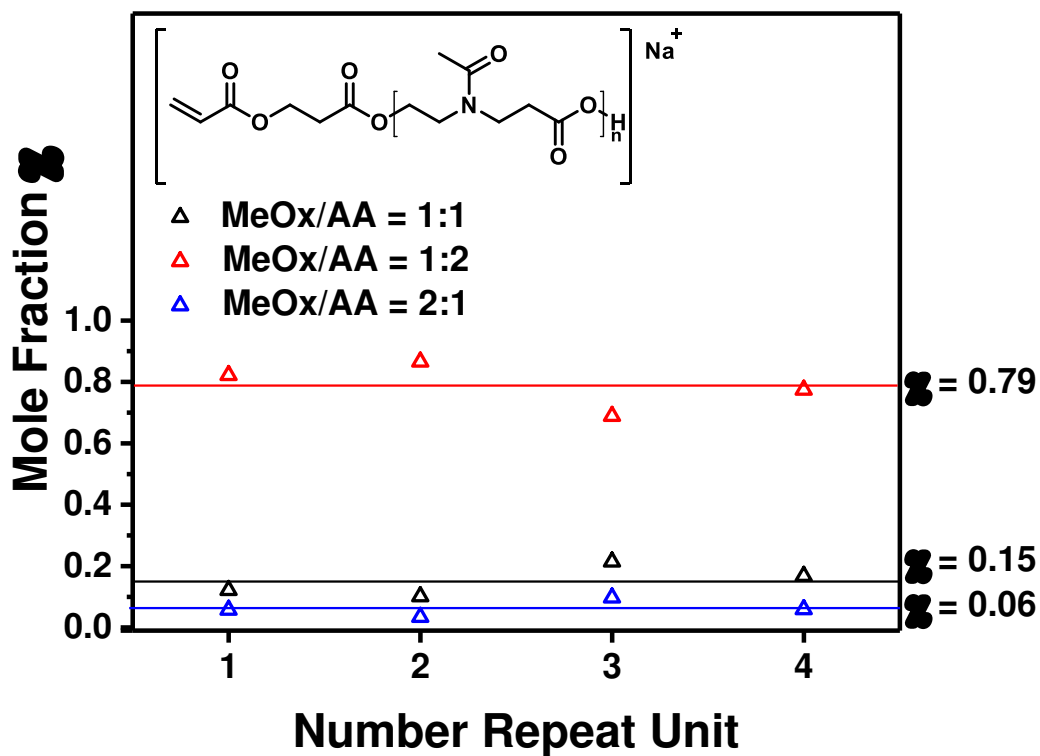
Illustration of the mole fraction along the repeat units of MeOx/AA (1:1; 1:2 and 2:1) determined based on the Na⁺ ionized △ labeled intensities.
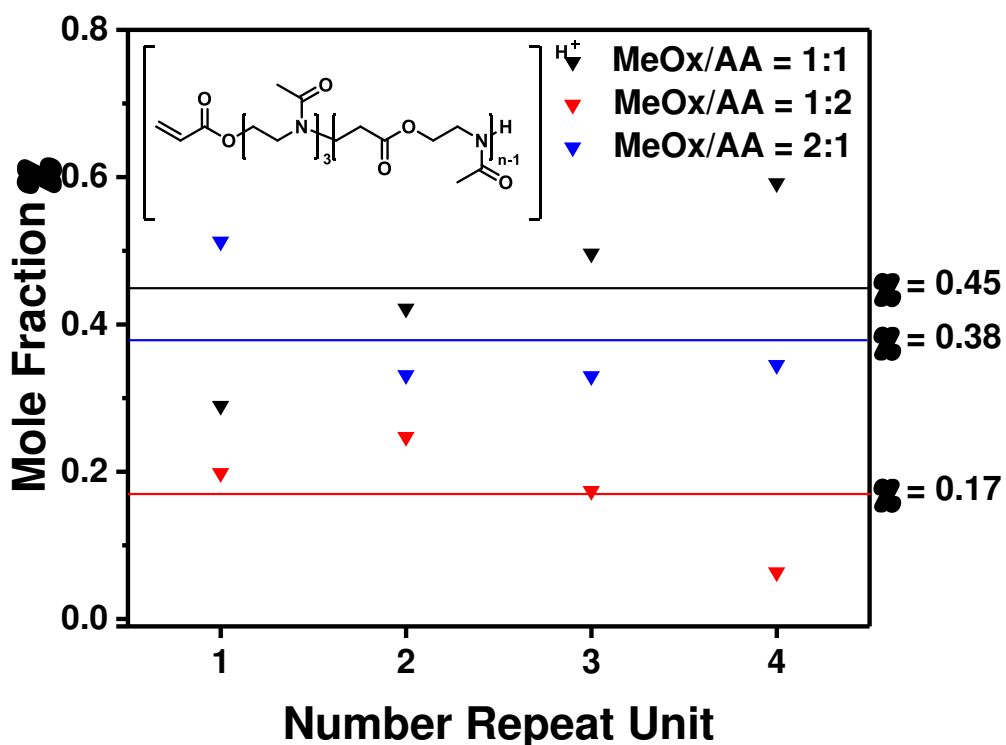
Fig. C 18 Illustration of the mole fraction along the repeat units of MeOx/AA (1:1; 1:2 and 2:1) determined based on the H⁺ ionized ▼ labeled intensities.
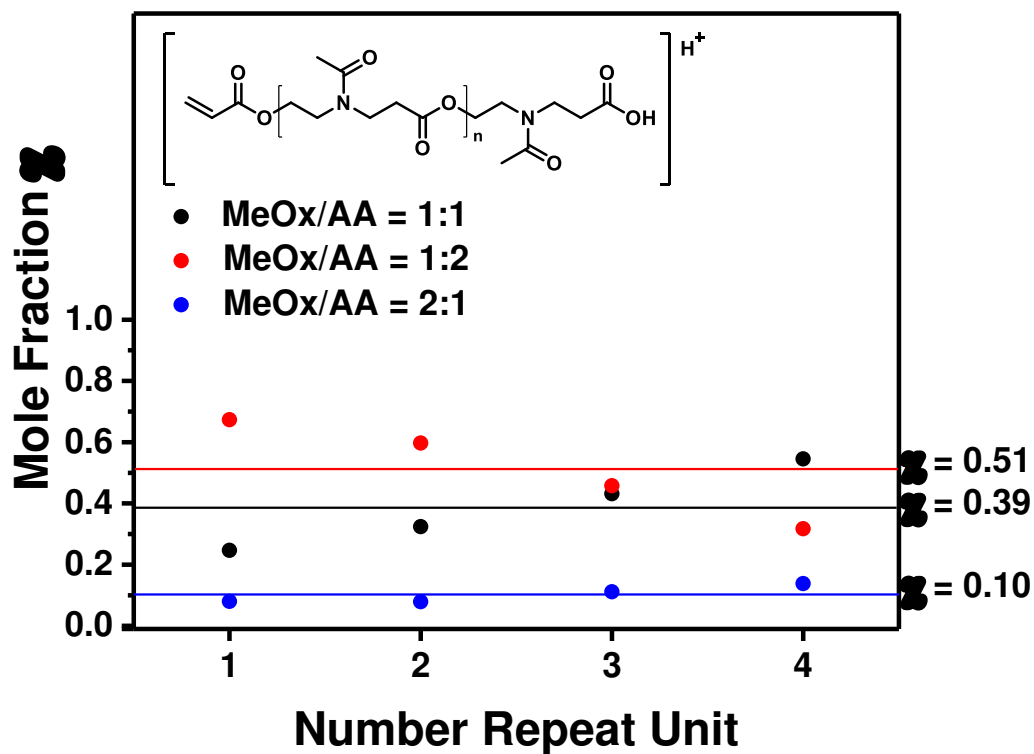
Fig. C 20 Illustration of the mole fraction along the repeat units of MeOx/AA (1:1; 1:2 and 2:1) determined based on the H⁺ ionized ● labeled intensities.
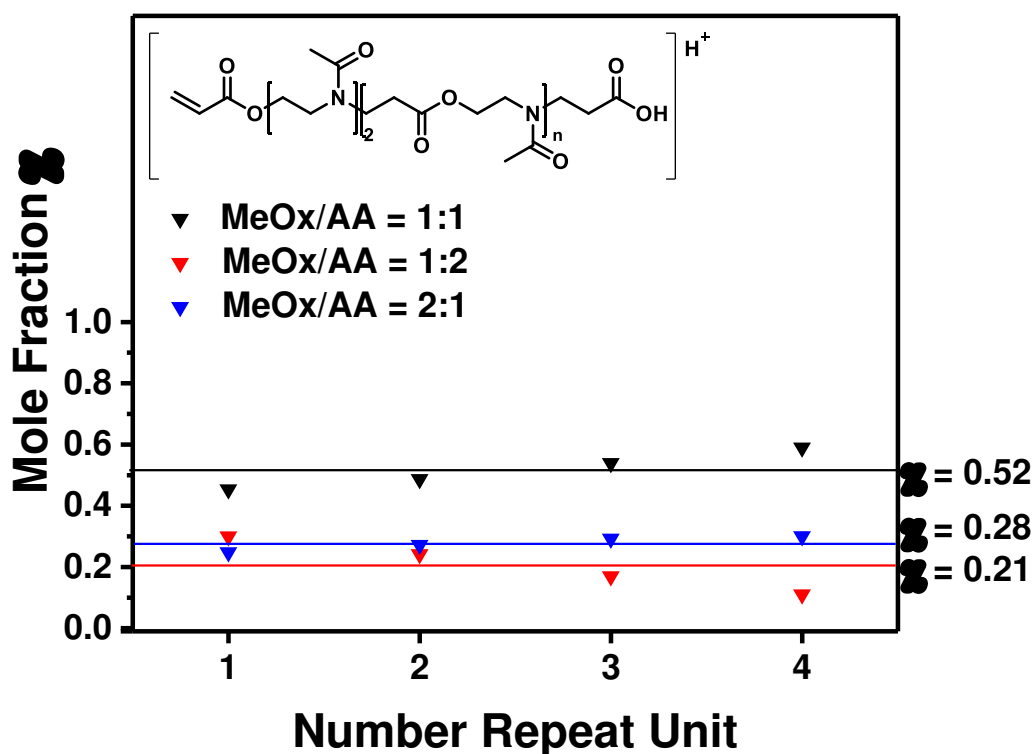
Fig. C 19 Illustration of the mole fraction along the repeat units of MeOx/AA (1:1; 1:2 and 2:1) determined based on the H⁺ ionized ▼ labeled intensities.
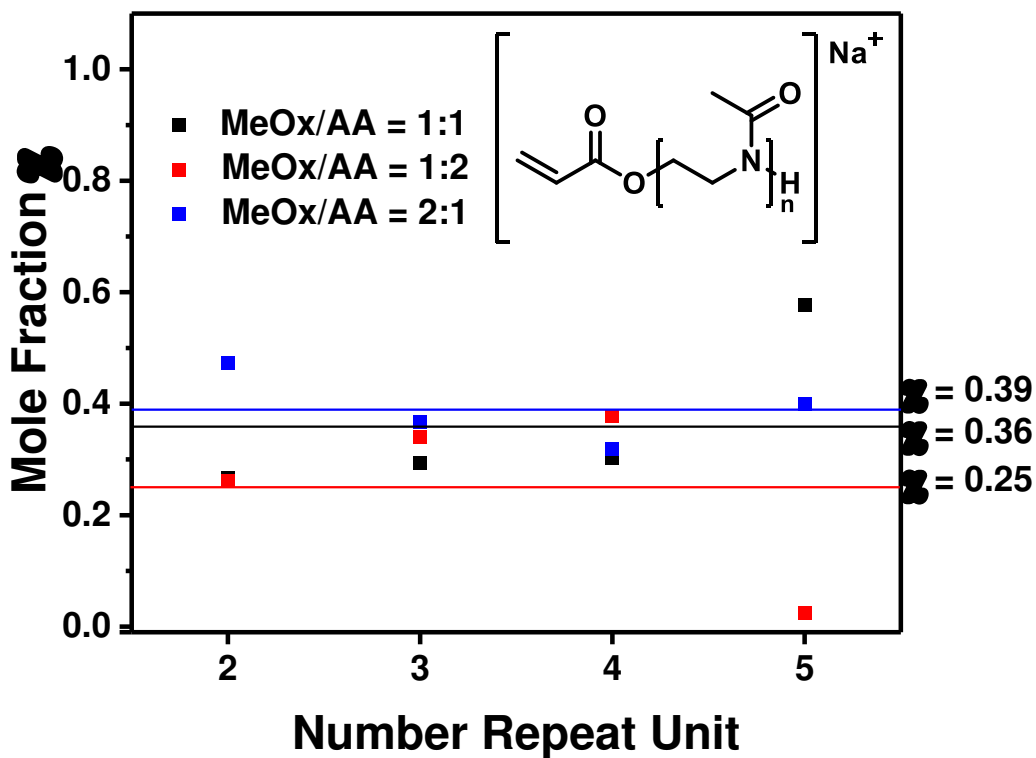
Fig. C 22 Illustration of the mole fraction along the repeat units of MeOx/AA (1:1; 1:2 and 2:1) determined based on the H+ ionized p(MeOx) intensities.
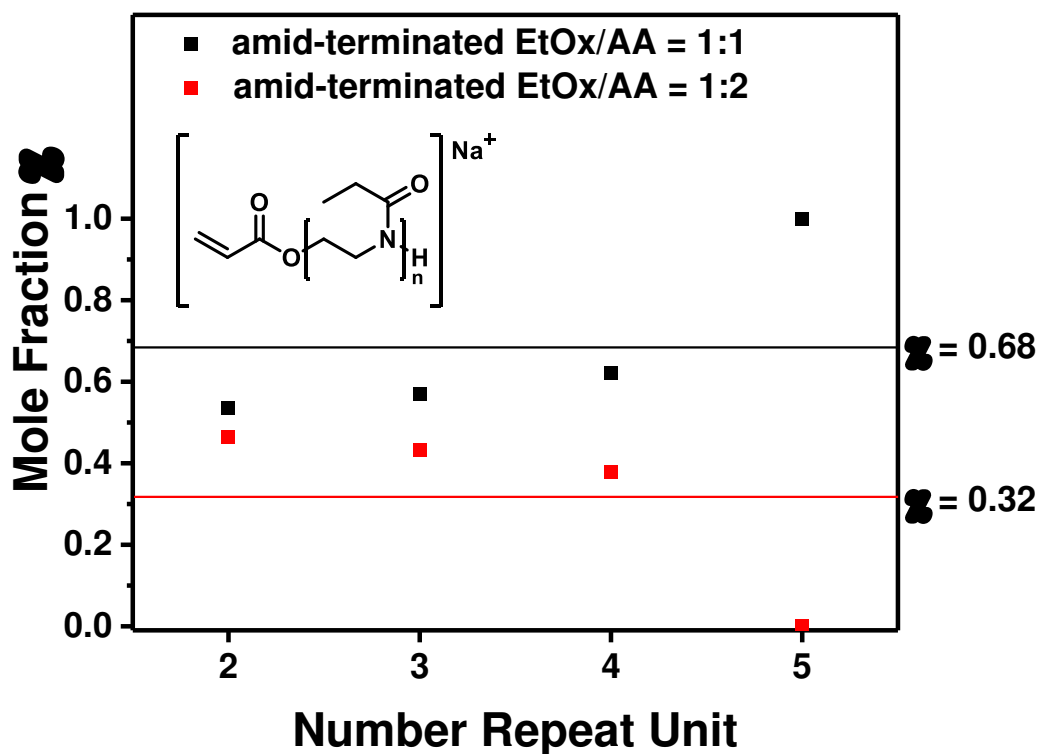
Fig. C 21 Illustration of the mole fraction along the repeat units of EtOx/AA (1:1 and 1:2) determined based on the H+ ionized p(EtOx) intensities.
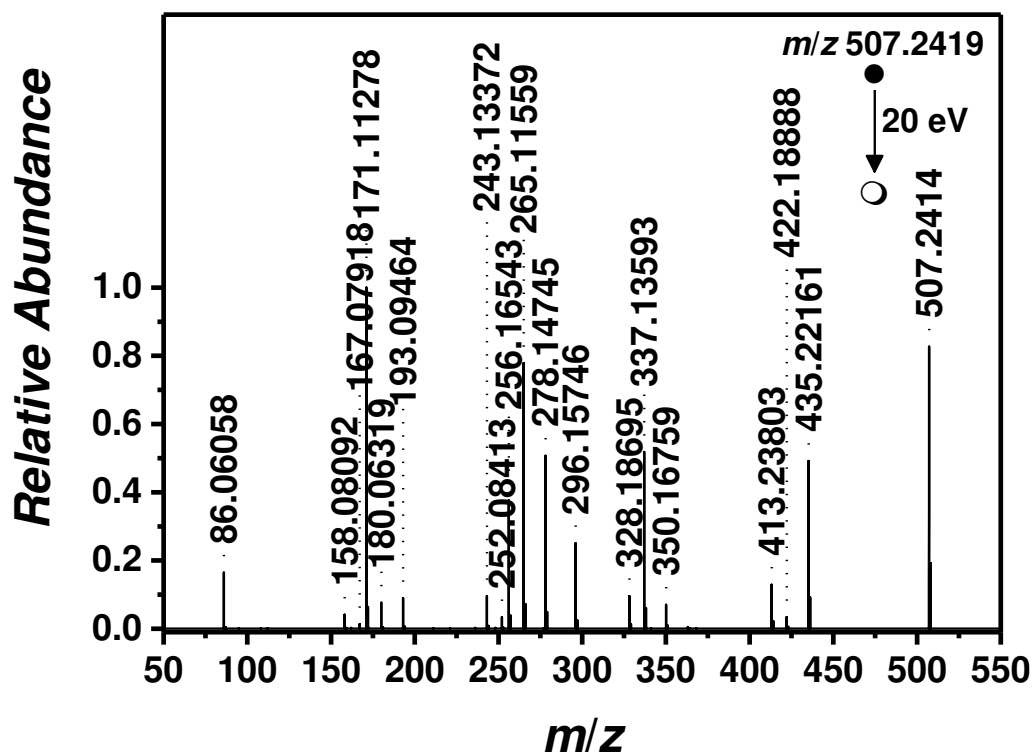
MS/MS Results
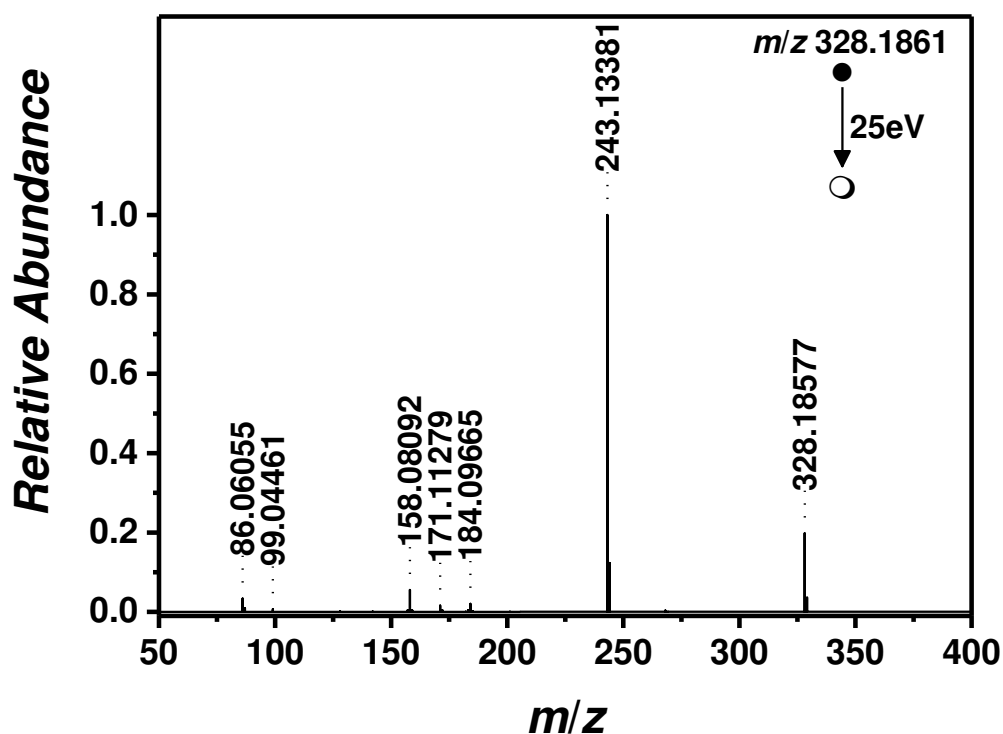
Fig. C 23 ESI MS/MS (tandem MS in positive ion mode) of MeOx/AA (1/1) isolating a species at 328 *m/z* with a HCD energy of 25 eV in the relevant range from 50 *m/z* and 400 *m/z*.

Tab. C 8 Peak assignment of ESI MS/MS experiment (Fig. C 23) at 328.1861 m/z with a HCD energy of 25 eV showing the experimental *m/z*, the theoretical *m/z* values, and Δ*m/z* and the proposed structure. The proposed structures can be found in Scheme C 3.

m/z(exp)	*m/z*(theo)	Δ*m/z*	Error / ppm
328.1858	328.1867	0.0009	2.74
256.1660	256.1656	0.0004	1.56
243.1338	243.1337	0.0001	0.41
184.0967	184.0968	0.0001	0.54
171.1127	171.1128	0.0001	0.58
158.0811	158.0812	0.0001	0.63
99.0446	99.0441	0.0005	5.05
86.0606	86.0600	0.0006	6.97
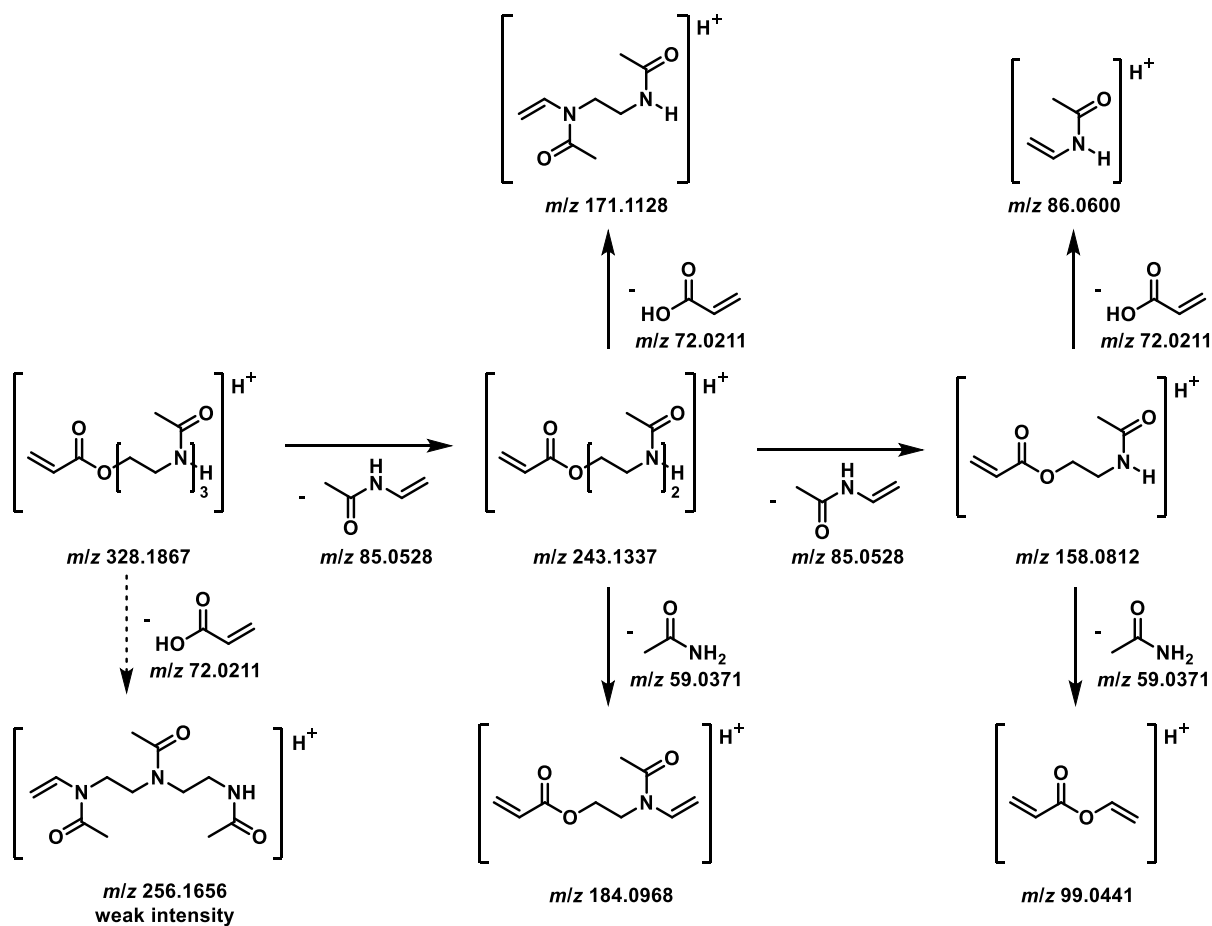
Scheme C 4 Fragmentation scheme for precursor ion at 328.1867 *m/z* with an HCD energy of 25 eV. Product ion at 171.1128 *m/z* represents a key structure for a dimerization of MeOx.
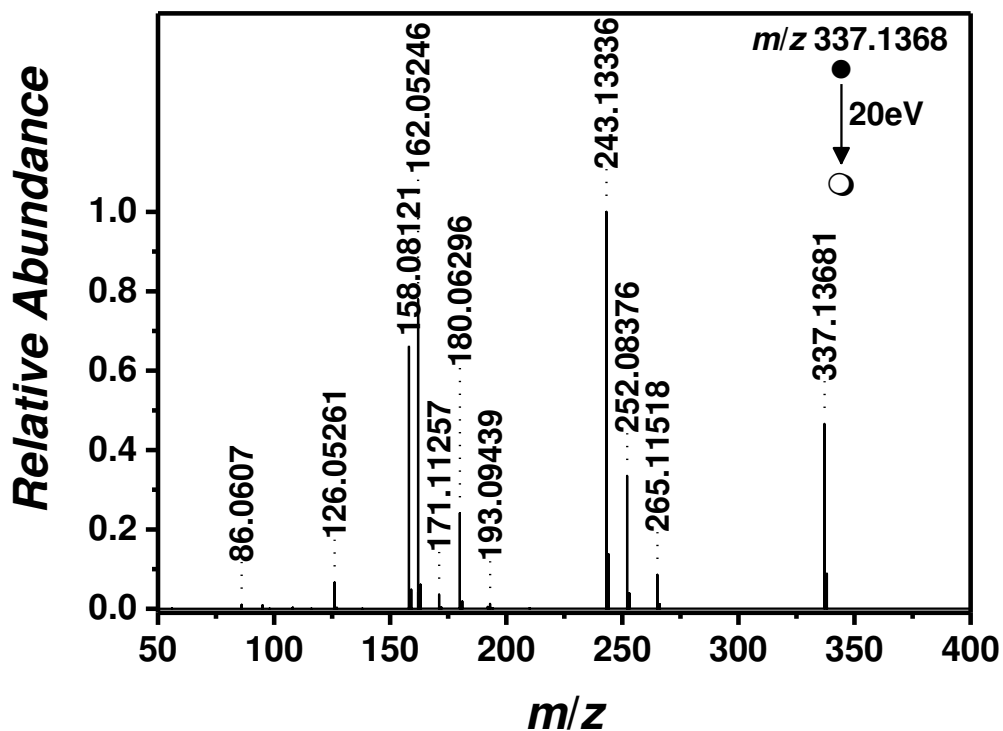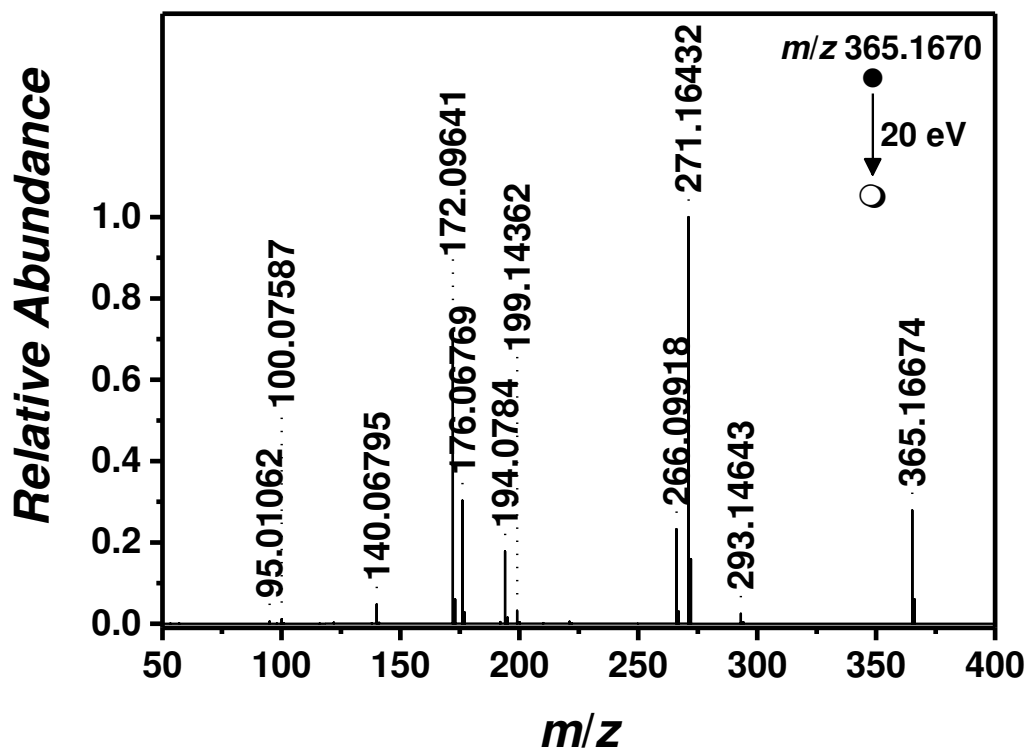
Fig. C 24 ESI MS/MS (tandem MS in positive ion mode) of MeOx/AA (1/1) isolating a species at 337 *m/z* with a HCD energy of 20 eV in the relevant range from 50 *m/z* and 400 *m/z*.

Tab. C 9 Peak assignment of ESI MS/MS experiment (Fig. C 24) at 337.1368 *m/z* with a HCD energy of 20 eV showing the experimental *m/z*, the theoretical *m/z* values, and Δ*m/z*. The proposed structures can be found in Scheme C 5.

m/z(exp)	*m/z*(theo)	Δ*m/z*	Error / ppm
337.1368	337.1370	0.0002	0.59
265.1152	265.1159	0.0007	2.64
252.0837	252.0842	0.0005	1.98
243.1333	243.1337	0.0006	1.65
193.0944	193.0947	0.0003	1.55
180.0630	180.0631	0.0001	0.56
171.1126	171.1128	0.0002	1.17
162.0525	162.0525	0.0000	0.00
158.0812	158.0812	0.0000	0.00
126.0526	126.0525	0.0001	0.79
86.0607	86.0600	0.0007	8.13
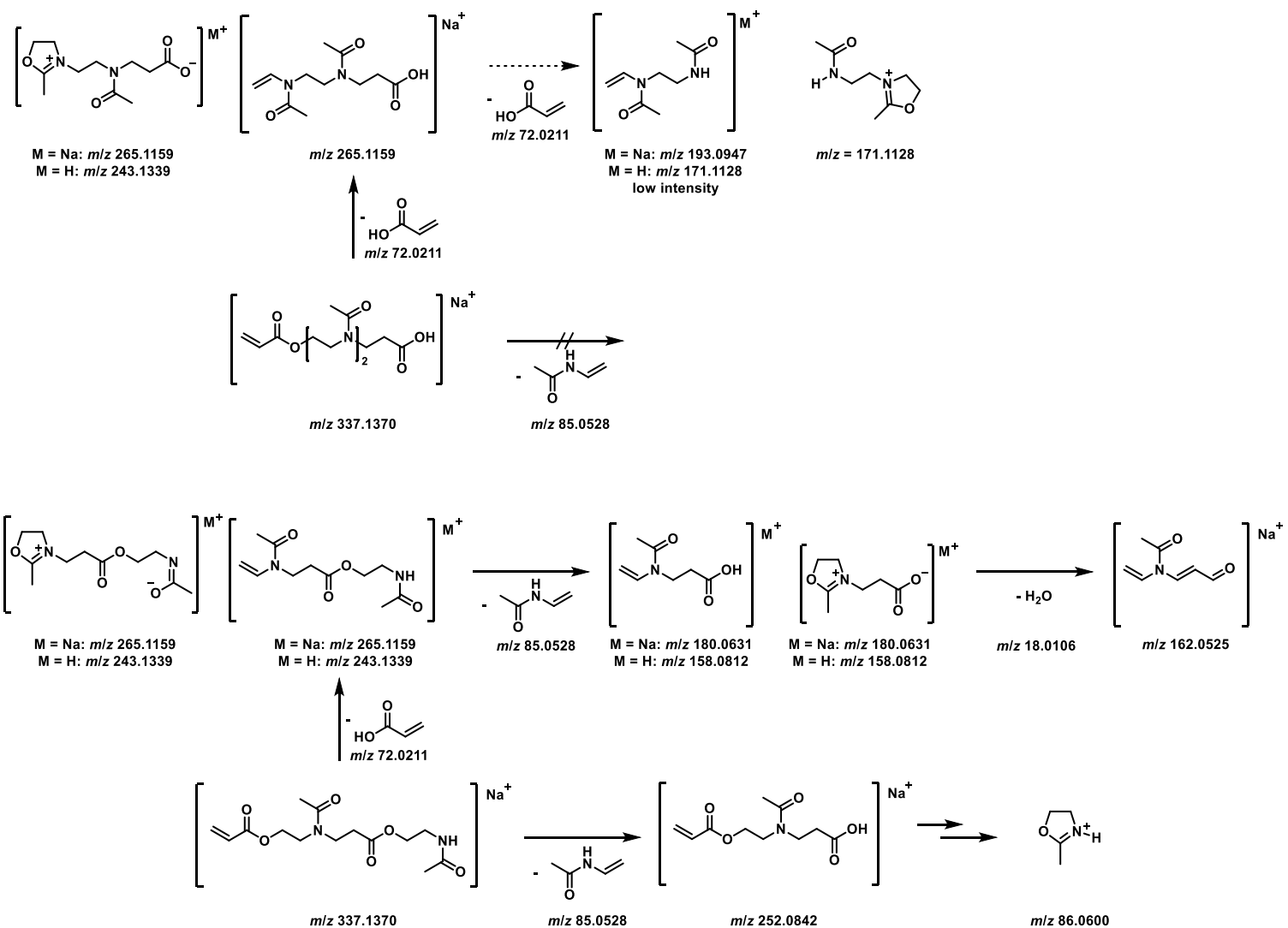
Scheme C 6 Fragmentation scheme for precursor ion at 337.1368 *m/z* with an HCD energy of 20 eV. Approx. 5% homocoupling have been identified comparing the product ion at 193 *m/z* with the product ion at 180 *m/z*.
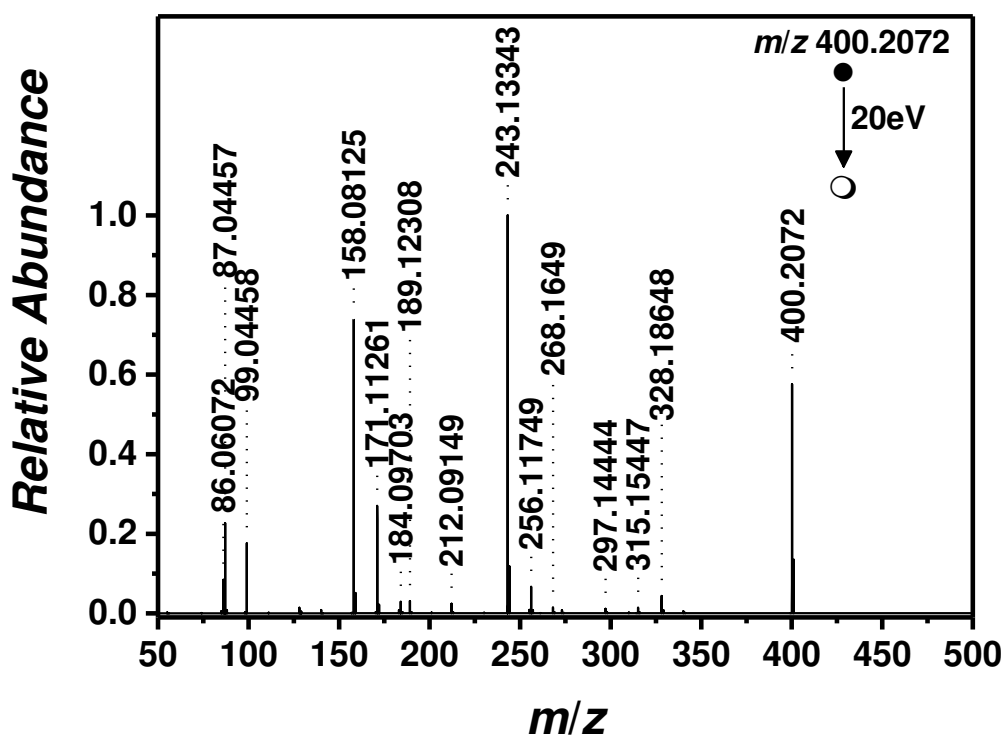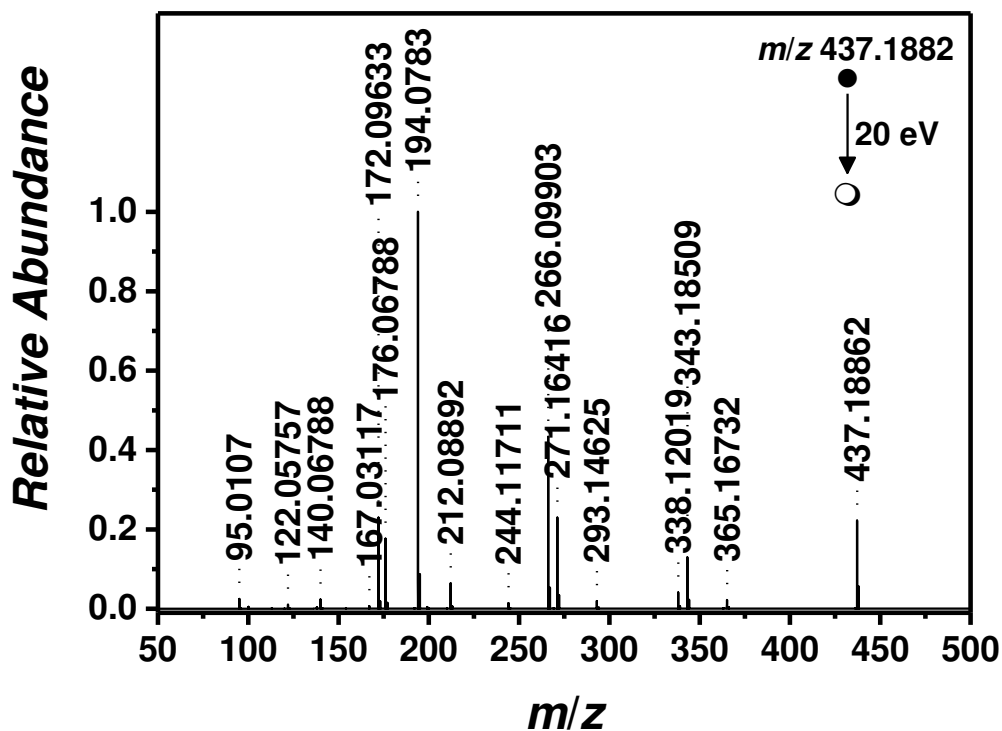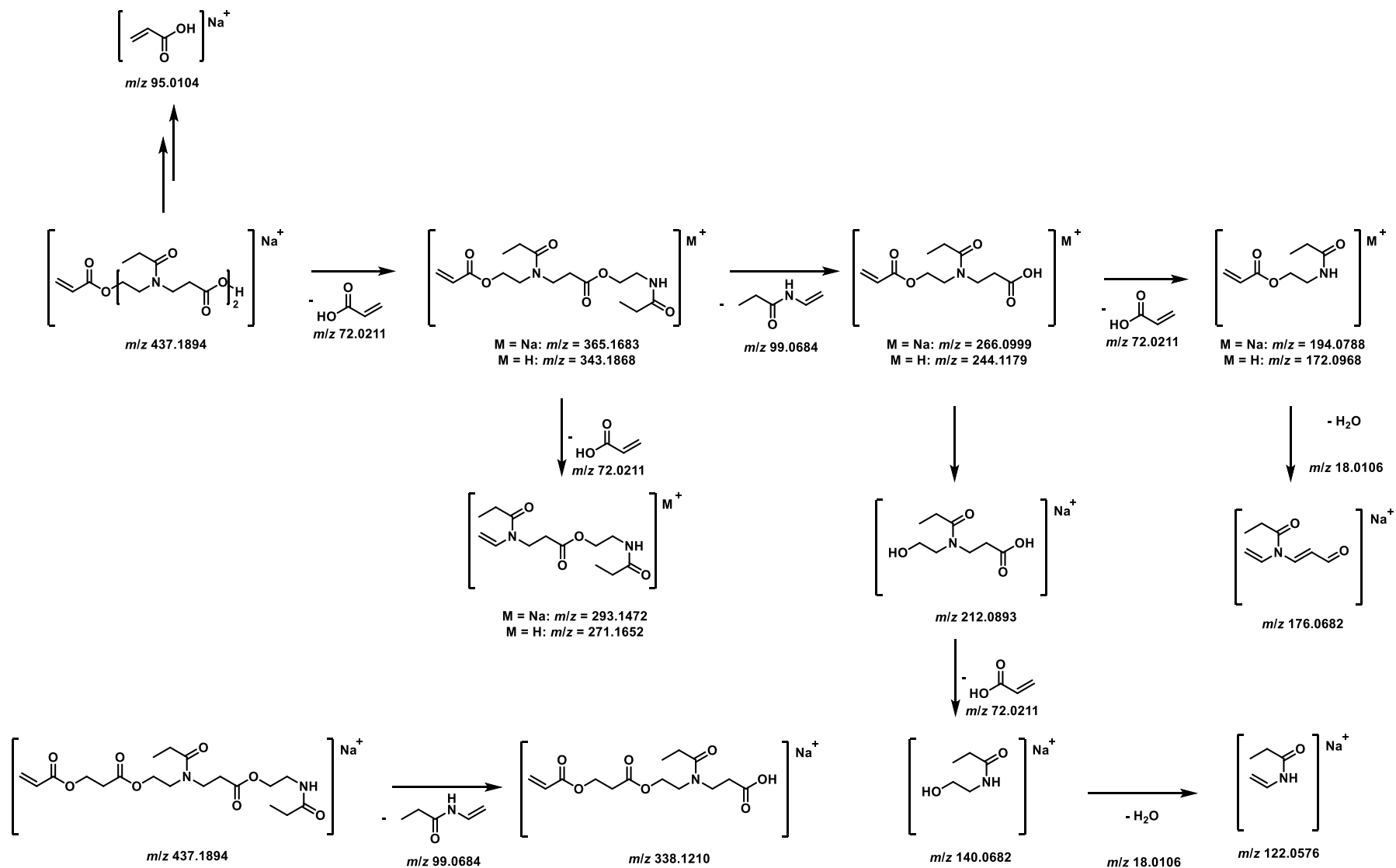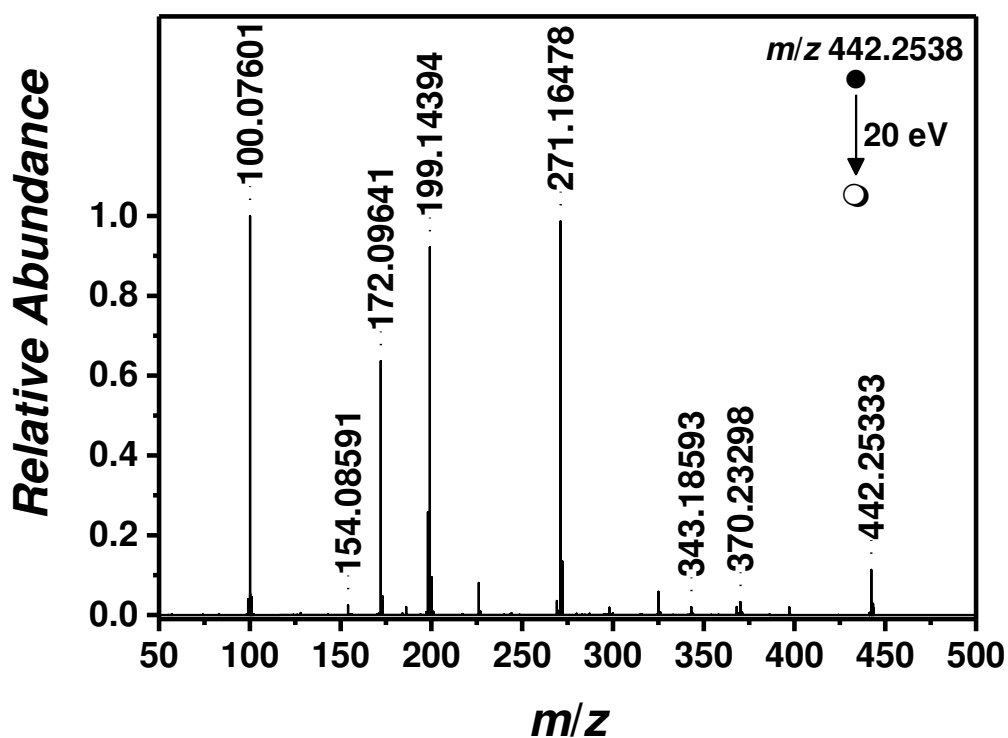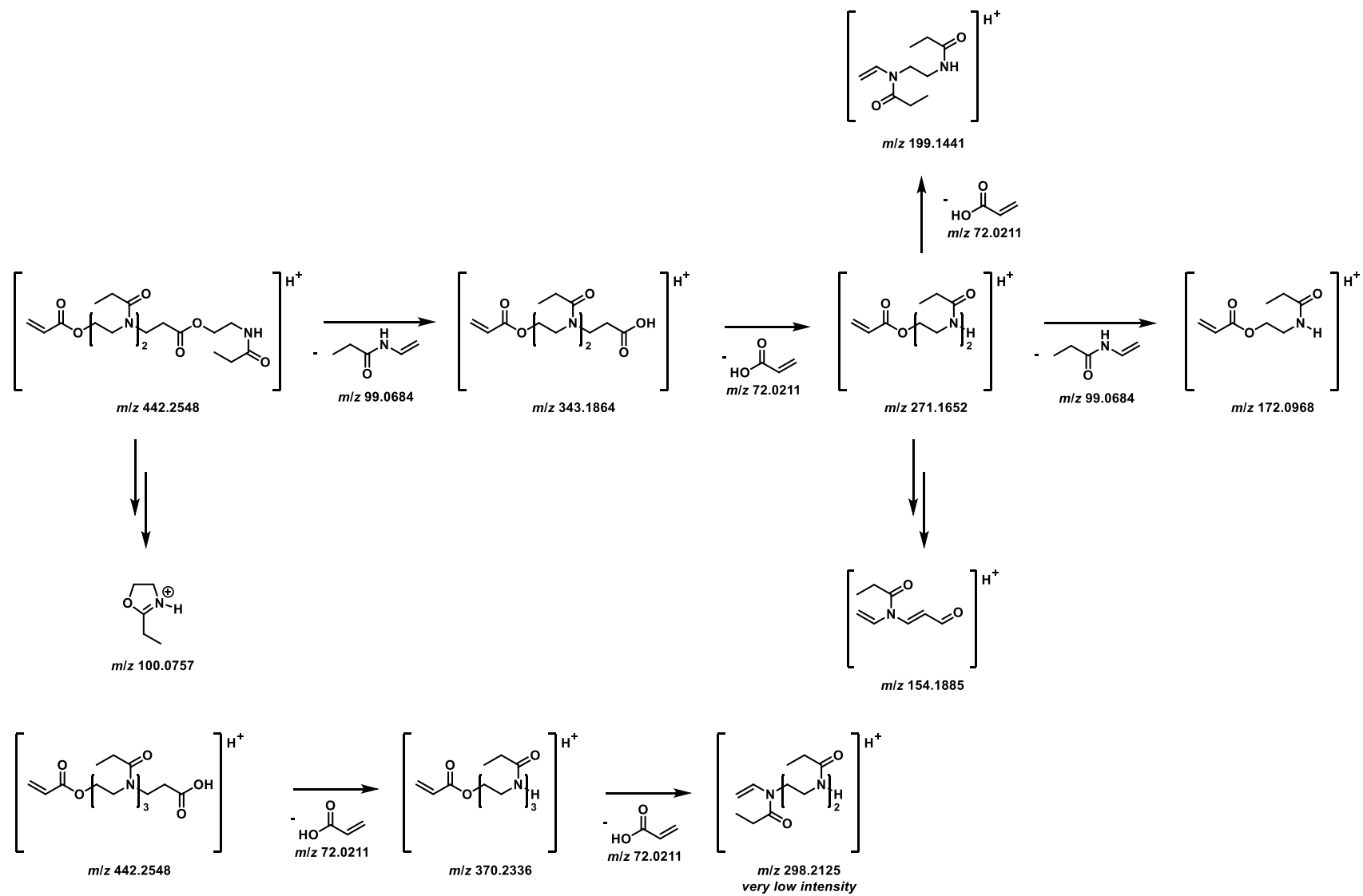
Fig. C 25 ESI MS/MS (tandem MS in positive ion mode) of MeOx/AA (1/1) isolating a species at 400 *m/z* with a HCD energy of 20 eV in the relevant range from 50 *m/z* and 500 *m/z*.

Tab. C 10 Peak assignment of ESI MS/MS experiment Fig. C 25) at 400.2072 *m/z* with a HCD energy of 20 eV showing the experimental *m/z*, the theoretical *m/z* values, and Δ*m/z*. The proposed structures can be found in Scheme C 7-9.

m/z(exp)	*m/z*(theo)	Δ*m/z*	Error / ppm
400.2072	400.2078	0.0006	1.50
328.1865	328.1867	0.0002	0.61
315.1545	315.1551	0.0006	1.90
297.1444	297.1445	0.0001	0.34
268.1649	268.1656	0.0007	2.61
256.1653	256.1656	0.0003	1.17
256.1175	256.1179	0.0004	1.56
243.1334	243.1339	0.0005	2.06
212.0915	212.0917	0.0002	0.94
189.1231	189.1234	0.0003	1.59
184.0970	184.0968	0.0002	1.09
171.1126	171.1128	0.0002	1.17
158.0813	158.0812	0.0001	0.63
99.0446	99.0441	0.0005	5.05
87.0446	87.0441	0.0005	5.74
86.0607	86.0600	0.0007	8.13
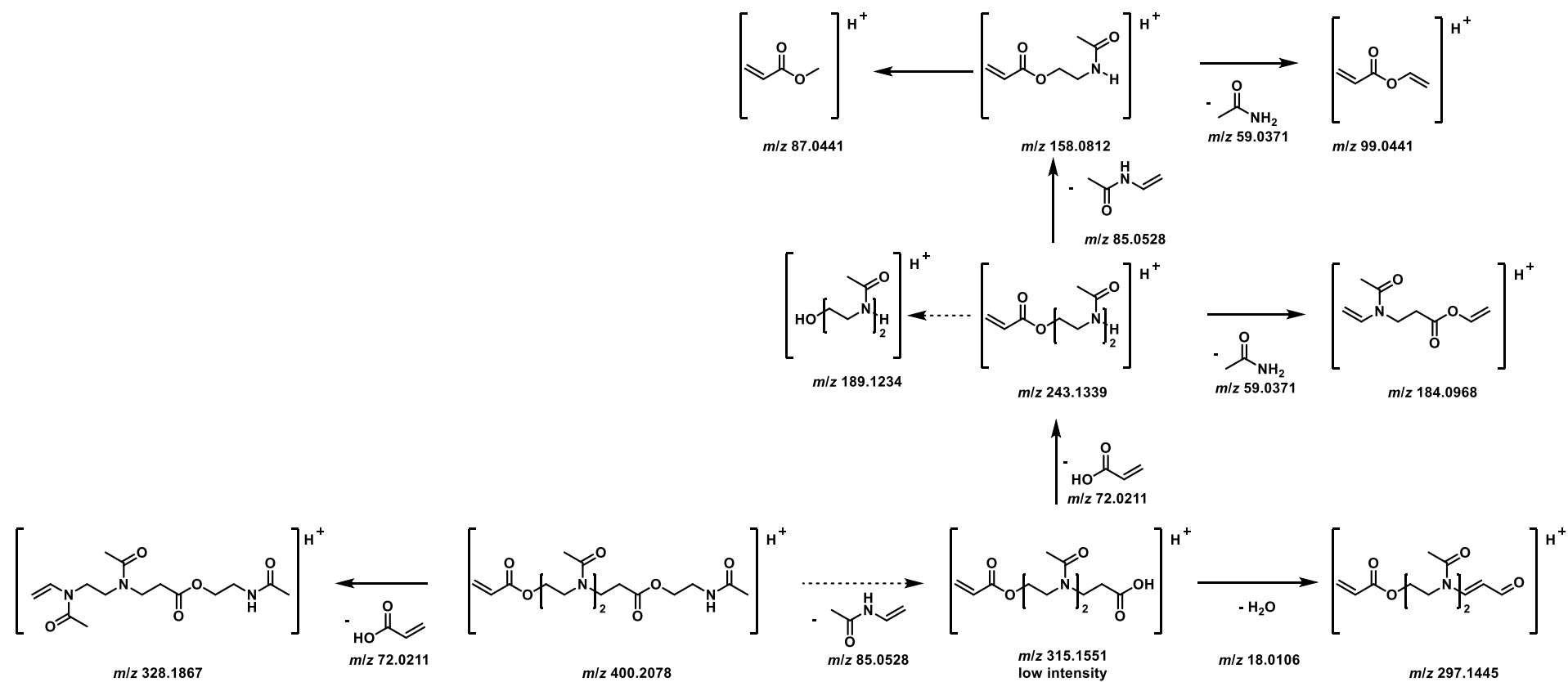
Scheme C 7 Fragmentation scheme for precursor ion at 400.2072 *m/z* with an HCD energy of 20 eV. Fragmentation scheme is based on an AABA oligomer (A = MeOx; B = AA).
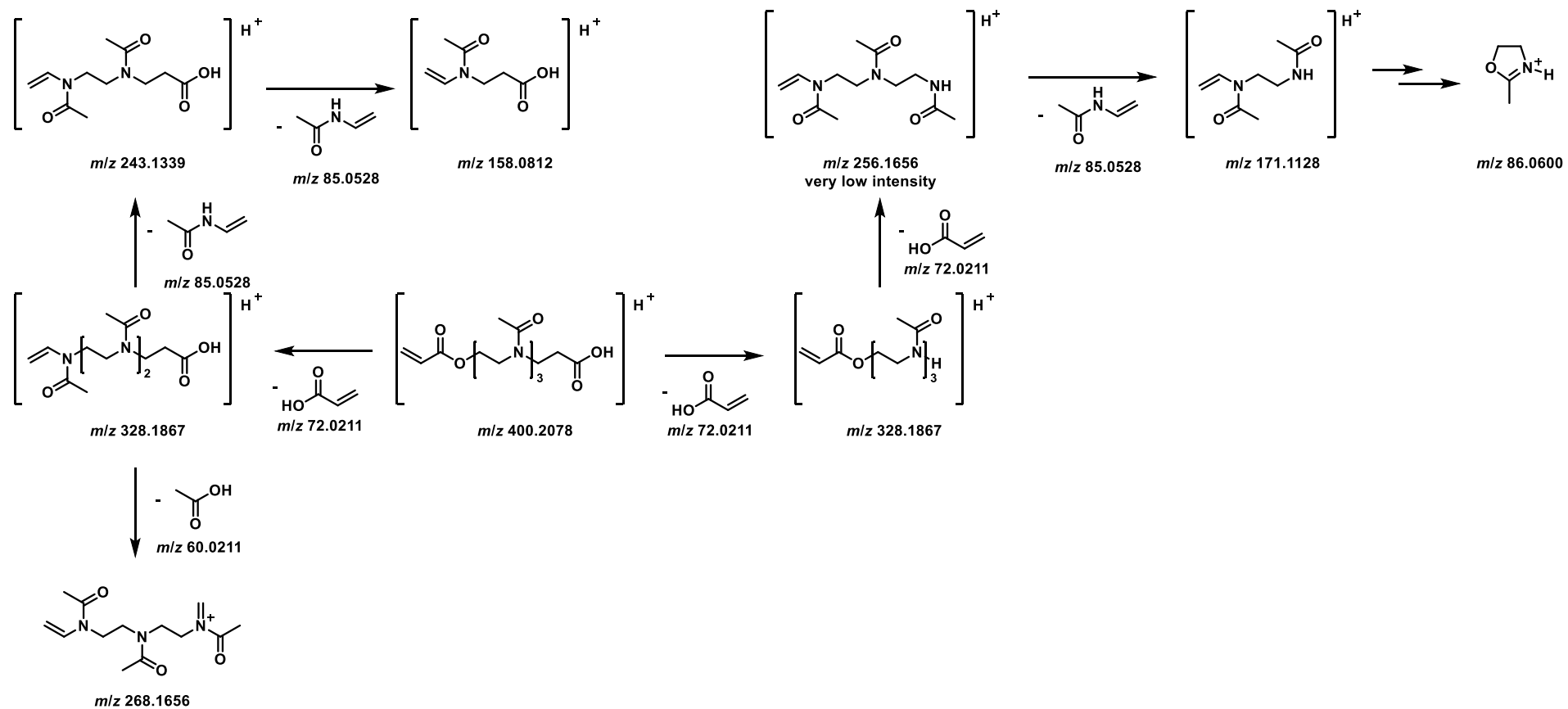
Scheme C 8 Fragmentation scheme for precursor ion at 400.2072 *m/z* with an HCD energy of 20 eV. Fragmentation scheme is based on an AAAB oligomer (A = MeOx; B = AA).

XC
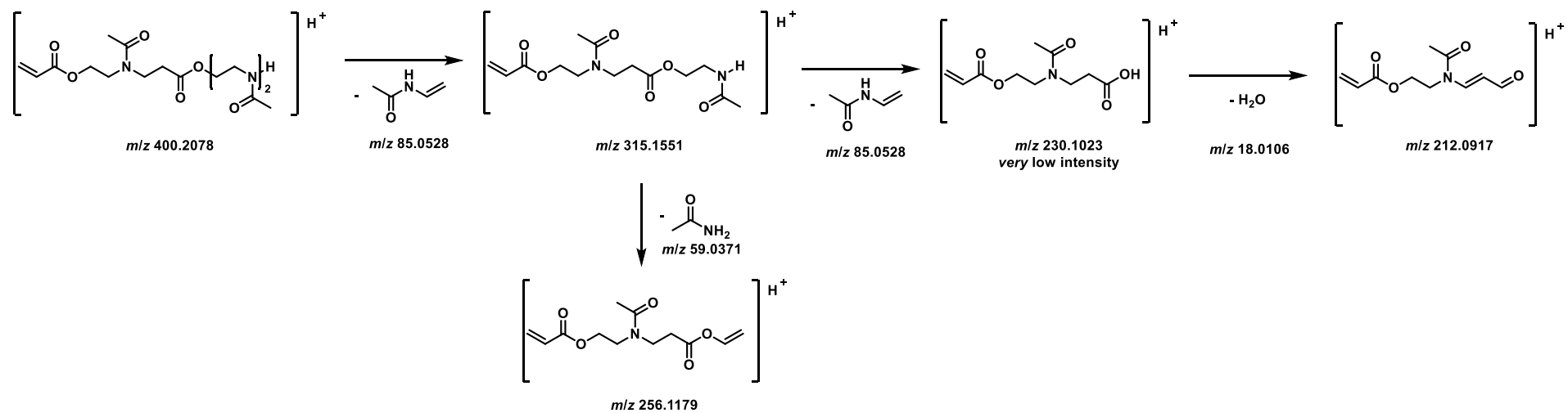
Scheme C 9 Fragmentation scheme for precursor ion at 400.2072 *m/z* with an HCD energy of 20 eV. Fragmentation scheme is based on an ABAA oligomer (A = MeOx; B = AA).
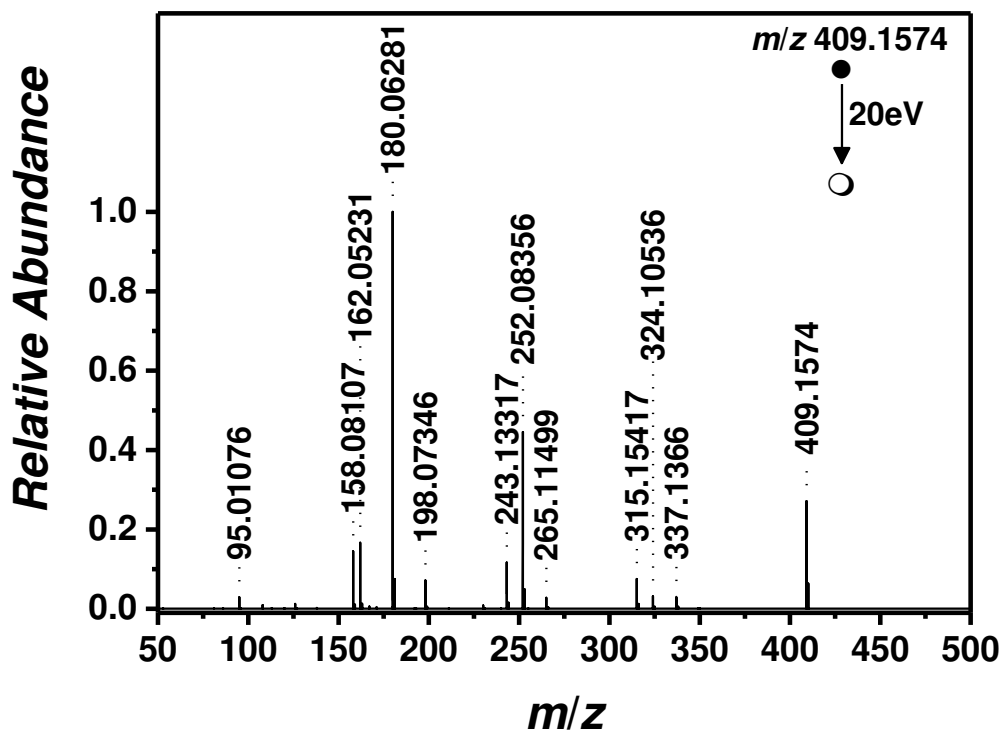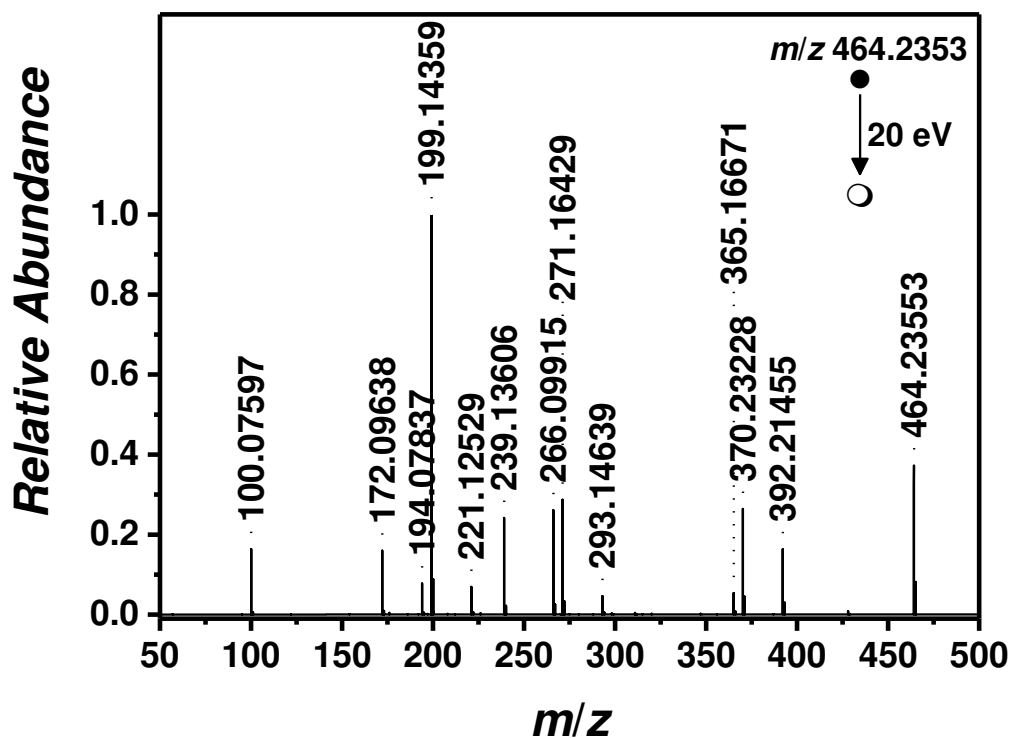
Fig. C 26 ESI MS/MS (tandem MS in positive ion mode) of MeOx/AA (1/1) isolating a species at 409 *m/z* with a HCD of 20 eV in the relevant range from 50 *m/z* and 500 *m/z*.

Tab. C 11 Peak assignment of ESI MS/MS experiment (Fig. C 26) at 409.1574 *m/z* with a HCD energy of 20 eV showing the experimental *m/z*, the theoretical *m/z* values, and Δ*m/z* and the proposed structure. The proposed structures can be found in Scheme C 10.

m/z(exp)	*m/z*(theo)	Δ*m/z*	Error / ppm
409.1574	409.1581	0.0007	1.71
337.1366	337.1370	0.0004	1.19
324.1054	324.1053	0.0001	0.31
315.1542	315.1551	0.0009	2.86
265.1150	265.1159	0.0009	3.39
252.0836	252.0842	0.0006	2.38
243.1332	243.1339	0.0007	2.88
198.0735	198.0737	0.0002	1.01
180.0628	180.0631	0.0003	1.67
162.0523	162.0525	0.0002	1.23
158.0811	158.0812	0.0001	0.63
95.0108	95.0104	0.0004	4.21
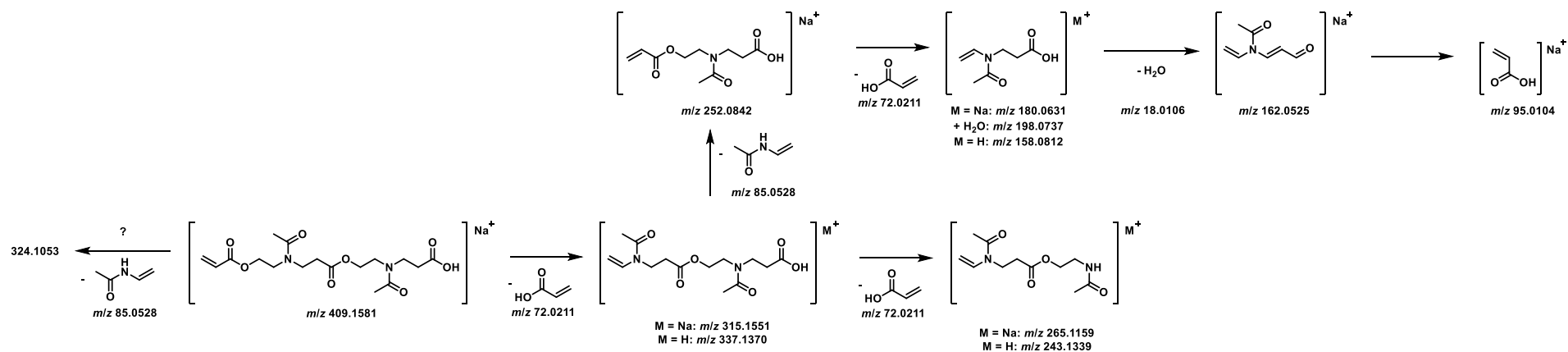
Scheme C 11 Fragmentation scheme for precursor ion at 409.1574 *m/z* with an HCD energy of 20 eV.
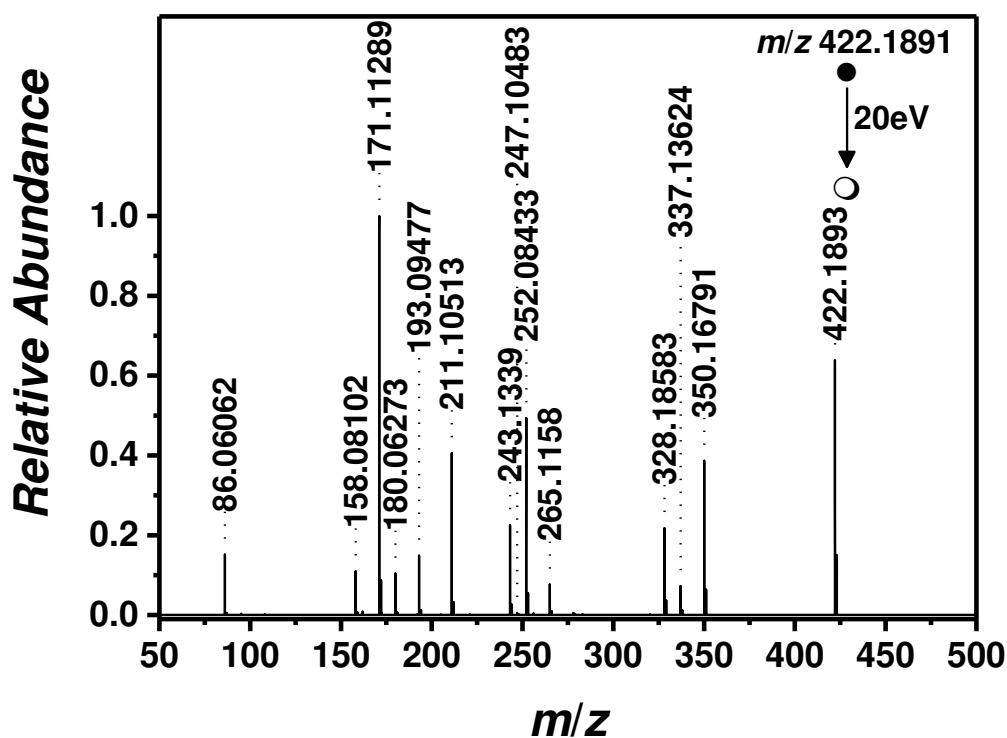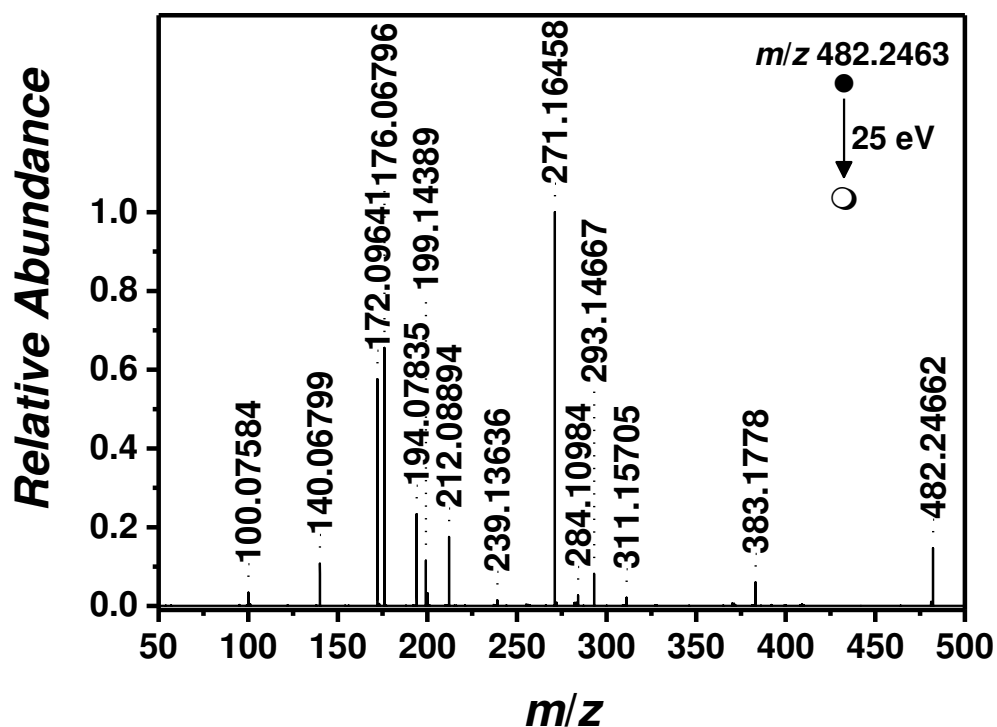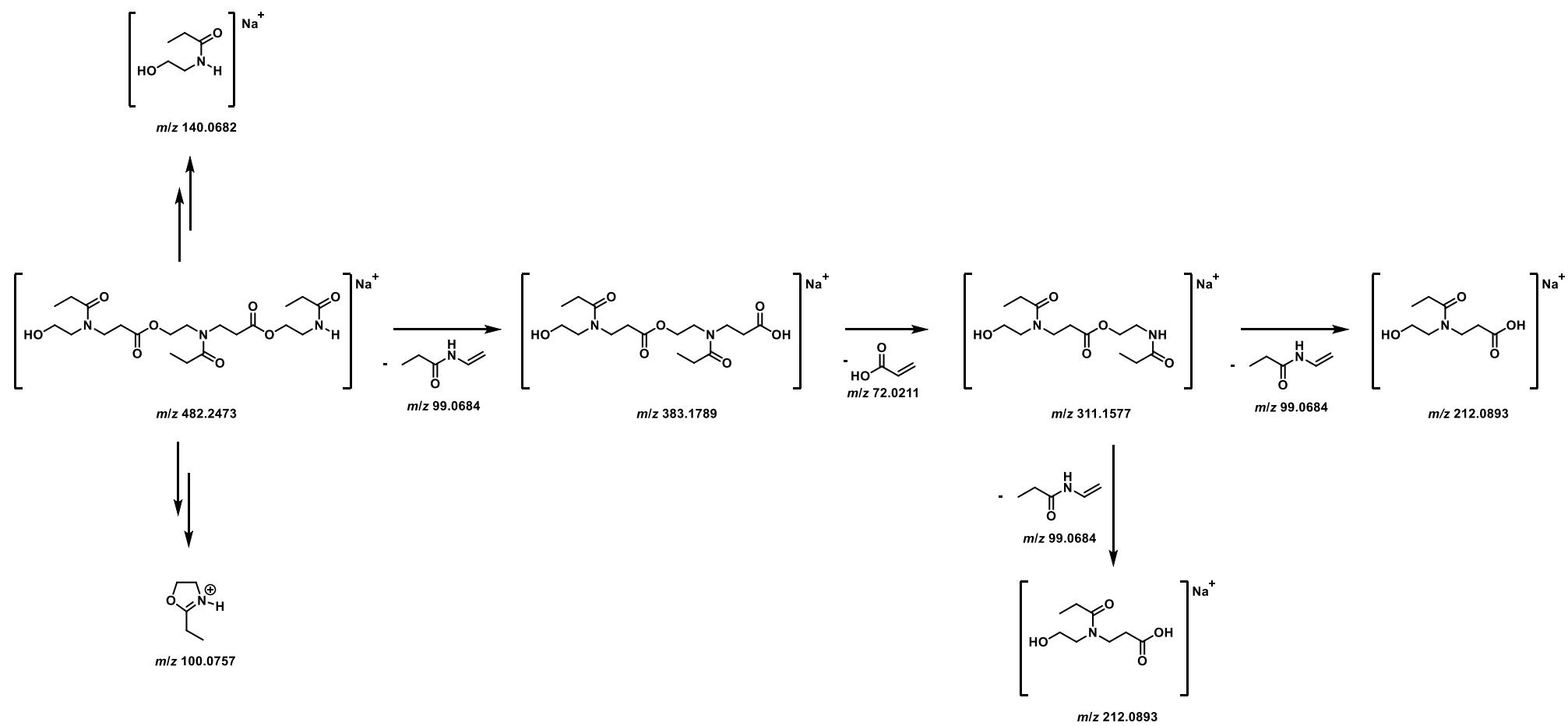
Fig. C 27 ESI MS/MS (tandem MS in positive ion mode) of MeOx/AA (1/1) isolating a species at 422 *m/z* with a HCD energy of 20 eV in the relevant range from 50 *m/z* and 500 *m/z*.

Tab. C 12 Peak assignment of ESI MS/MS experiment (Fig. C 27) at 422.1891 m/z with a HCD energy of 20 eV showing the experimental *m/z*, the theoretical *m/z* values, and Δ*m/z* and the proposed structure. The proposed structures can be found in Scheme C 12

m/z(exp)	*m/z*(theo)	Δ*m/z*	Error / ppm
422.1891	422.1898	0.0007	1.66
350.1679	350.1686	0.0007	2.00
337.1362	337.1370	0.0008	2.37
315.1542	315.1551	0.0009	2.86
265.1150	265.1159	0.0009	3.39
252.0836	252.0842	0.0006	2.38
243.1332	243.1339	0.0007	2.88
198.0735	198.0737	0.0002	1.01
180.0628	180.0631	0.0003	1.67
162.0523	162.0525	0.0002	1.23
158.0811	158.0812	0.0001	0.63
95.0108	95.0104	0.0004	4.21
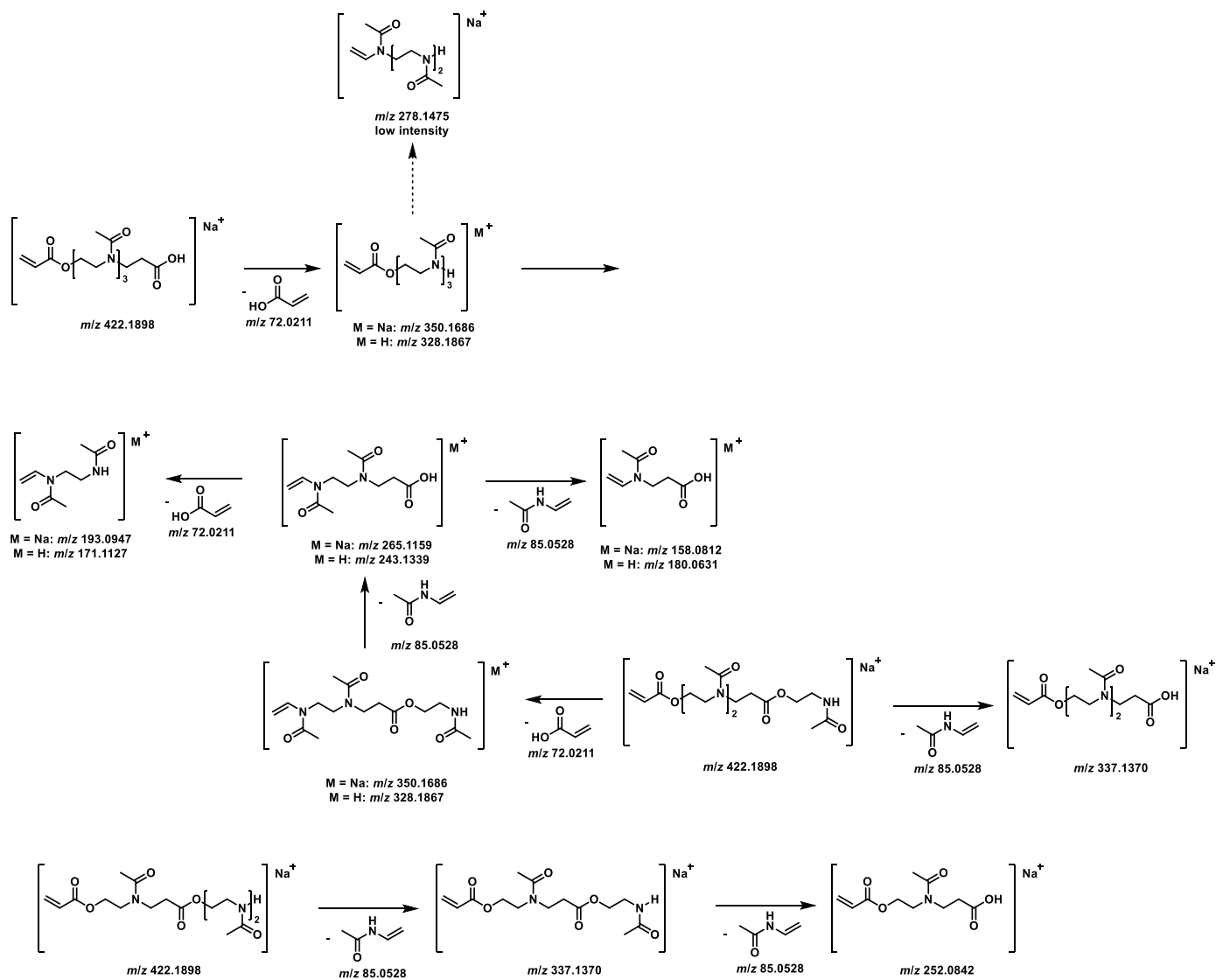
Scheme C 13 Fragmentation scheme for precursor ion at 422.1891 *m/z* with an HCD energy of 20 eV.
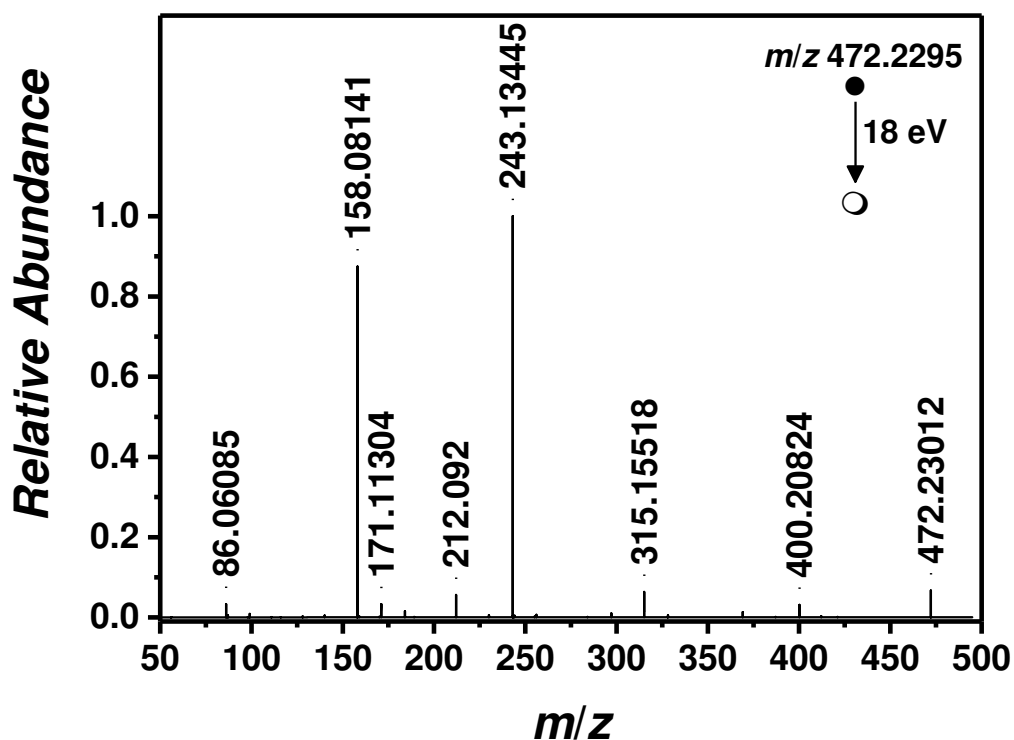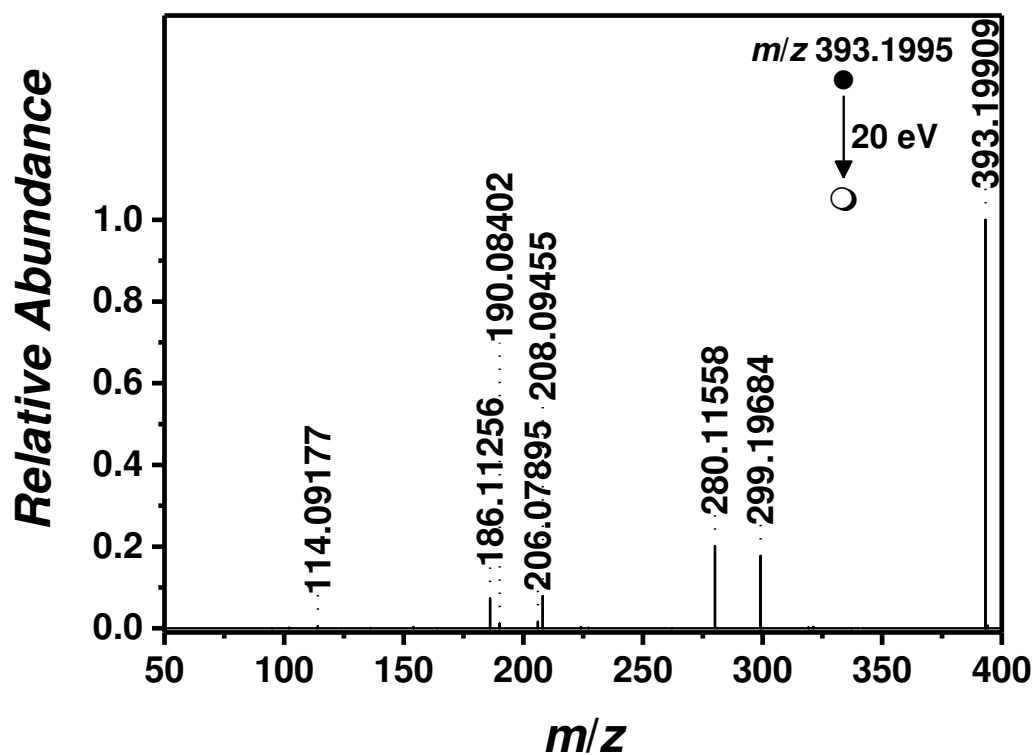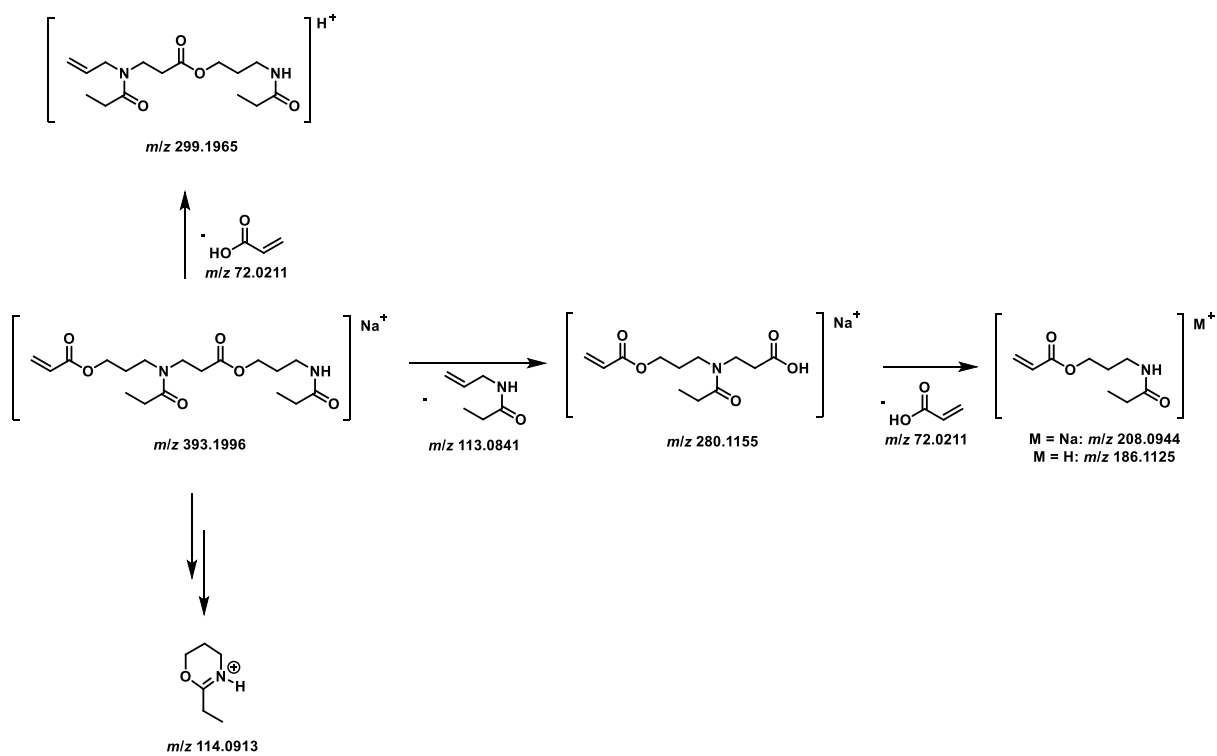
Fig. C 28 ESI MS/MS (tandem MS in positive ion mode) of MeOx/AA (1/1) isolating a species at 472 *m/z* with a HCD energy of 18 eV in the relevant range from 50 *m/z* and 500 *m/z*.

Tab. C 13 Peak assignment of ESI MS/MS experiment (Fig. C 28) at 472.2295 m/z with a HCD of 18 eV showing the experimental *m/z*, the theoretical *m/z* values, and Δ*m/z* and the proposed structure.

| *m/z*(exp)	*m/z*(theo)	Δ*m/z*	Error / ppm
472.2295	472.2290	0.0005	1.06
400.2082	400.2078	0.0004	1.00
315.1552	315.1551	0.0001	0.32
243.1345	243.1339	0.0006	2.47
212.0920	212.0917	0.0003	1.41
171.1130	171.1128	0.0002	1.17
158.0814	158.0812	0.0002	1.27
86.0609	86.0600	0.0009	10.46

Fig. C 29 ESI MS/MS (tandem MS in positive ion mode) of MeOx/AA (1/2) isolating a species at 481 *m/z* with a HCD energy of 18 eV in the relevant range from 50 *m/z* and 500 *m/z*.

Tab. C 14 Peak assignment of ESI MS/MS experiment (Fig. C 29) at 481.1797 m/z with a HCD energy of 18 eV showing the experimental *m/z*, the theoretical *m/z* values, and Δ*m/z* and the proposed structure.

| *m/z*(exp)	*m/z*(theo)	Δ*m/z*	Error / ppm
481.1797	481.1793	0.0004	0.83
409.1582	409.1581	0.0001	0.24
337.1374	337.1370	0.0004	1.19
324.1055	324.1053	0.0002	0.62
315.1550	315.1551	0.0001	0.32
252.0847	252.0842	0.0005	1.98
230.1025	230.1023	0.0002	0.87
198.0740	198.0737	0.0003	1.51
180.0633	180.0631	0.0002	1.11
167.0317	167.0315	0.0002	1.20
162.0528	162.0525	0.0003	1.85
158.0816	158.0812	0.0004	2.53
95.0111	95.0104	0.0007	7.37
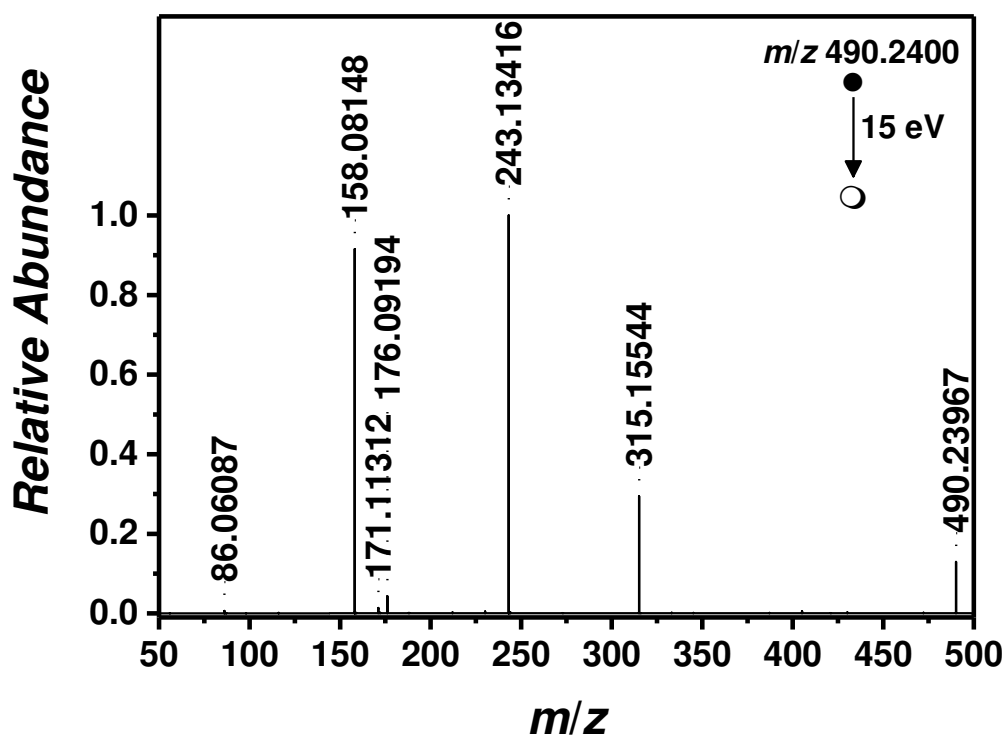
Fig. C 30 ESI MS/MS (tandem MS in positive ion mode) of MeOx/AA (1/1) isolating a species at 490 *m/z* with a HCD energy of 15 eV in the relevant range from 50 *m/z* and 500 *m/z*.

Tab. C 15 Peak assignment of ESI MS/MS experiment (Fig. C 30) at 490.2400 m/z with a HCD energy of 15 eV showing the experimental *m/z*, the theoretical *m/z* values, and Δ*m/z* and the proposed structure.

m/z(exp)	*m/z*(theo)	Δ*m/z*	Error /ppm
490.2400	490.2395	0.0005	1.02
315.1554	315.1551	0.0003	0.95
243.1342	243.1339	0.0003	1.23
176.0919	176.0917	0.0002	1.14
171.1131	171.1128	0.0003	1.75
158.0815	158.0812	0.0003	1.90
86.0609	86.0600	0.0009	10.46
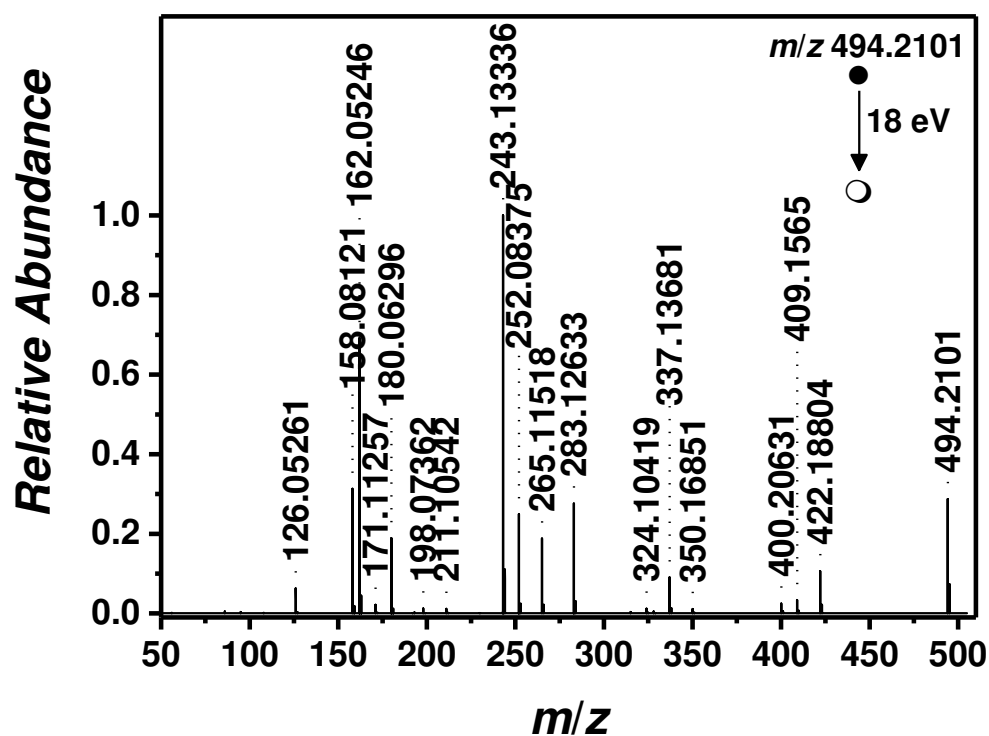
Fig. C 31 ESI MS/MS (tandem MS in positive ion mode) of MeOx/AA (1/1) isolating a species at 494 *m/z* with a HCD energy of 18 eV in the relevant range from 50 *m/z* and 500 *m/z*.

Tab. C 16 Peak assignment of ESI MS/MS experiment (Fig. C 31) at 494.2101 m/z with a HCD energy of 18 eV showing the experimental *m/z*, the theoretical *m/z* values, and Δ*m/z* and the proposed structure.

m/z(exp)	*m/z*(theo)	Δ*m/z*	Error /ppm
494.2101	494.2109	0.0008	1.62
422.1880	422.1898	0.0018	4.26
409.1565	409.1581	0.0016	3.91
400.2063	400.2078	0.0015	3.75
350.1685	350.1686	0.0001	0.29
337.1368	337.1370	0.0002	0.59
324.1042	324.1053	0.0011	3.39
283.1263	283.1264	0.0001	0.35
265.1152	265.1159	0.0007	2.64
252.0838	252.0842	0.0004	1.59
243.1334	243.1339	0.0005	2.06
211.1054	211.1053	0.0001	0.47
198.0736	198.0737	0.0001	0.50
180.0630	180.0631	0.0001	0.56
171.1126	171.1128	0.0002	1.17
162.0525	162.0525	0.0000	0.00
158.0812	158.0812	0.0000	0.00
126.0526	126.0525	0.0001	0.79

Fig. C 32 ESI MS/MS (tandem MS in positive ion mode) of MeOx/AA (1/1) isolating a species at 507 *m/z* with a HCD energy of 20 eV in the relevant range from 50 *m/z* and 550 *m/z*.

Tab. C 17 Peak assignment of ESI MS/MS experiment (Fig. C 32) at 507.2419 m/z with a HCD energy of 20 eV showing the experimental *m/z*, the theoretical *m/z* values, and Δ*m/z* and the proposed structure.

m/z(exp)	*m/z*(theo)	Δ*m/z*	Error /ppm
507.2419	507.2425	0.0006	1.18
435.2216	435.2214	0.0002	0.46
422.1888	422.1898	0.0010	2.37
413.2380	413.2395	0.0015	3.63
350.1676	350.1686	0.0010	2.86
337.1359	337.1370	0.0011	3.26
328.1870	328.1867	0.0003	0.91
296.1575	296.1581	0.0006	2.03
278.1475	278.1475	0.0000	0.00
265.1156	265.1159	0.0003	1.13
256.1654	256.1656	0.0002	0.78
252.0841	252.0842	0.0001	0.40
243.1337	243.1339	0.0002	0.82
193.0946	193.0947	0.0001	0.52
180.0632	180.0631	0.0001	0.56
171.1128	171.1128	0.0000	0.00
167.0792	?		
158.0809	158.0812	0.0003	1.90
86.0606	86.0600	0.0006	6.97

C

Fig. C 33 ESI MS/MS (tandem MS in positive ion mode) of EtOx/AA (1/1) isolating a species at 365 *m/z* with a HCD energy of 20 eV in the relevant range from 50 *m/z* and 400 *m/z*.

Tab. C 18 Peak assignment of ESI MS/MS experiment (Fig. C 33) at 365.1670 *m/z* with a HCD energy of 20 eV showing the experimental *m/z*, the theoretical *m/z* values, and Δ*m/z* and the proposed structure.

m/z(exp)	*m/z*(theo)	Δ*m/z*	Error / ppm
365.1670	365.1683	0.0013	3.56
293.1464	293.1472	0.0012	2.73
271.1643	271.1652	0.0009	3.32
266.0992	266.0999	0.0007	2.63
199.1436	199.1441	0.0005	2.51
194.0784	194.0788	0.0004	2.06
176.0677	176.0682	0.0005	2.84
172.0964	172.0968	0.0004	2.32
140.0679	140.0682	0.0003	2.14
100.0759	100.0757	0.0002	2.00
95.0106	95.0104	0.0002	2.11

Scheme C 14 Fragmentation scheme for precursor ion at 365.1670 *m/z* with an HCD energy of 20 eV.

CII

Fig. C 34 ESI MS/MS (tandem MS in positive ion mode) of EtOx/AA (1/1) isolating a species at 437 *m/z* with a HCD energy of 20 eV in the relevant range from 50 *m/z* and 500 *m/z*.

Tab. C 19 Peak assignment of ESI MS/MS experiment (Fig. C 34) at 437.1882 *m/z* with a HCD energy of 20 eV showing the experimental *m/z*, the theoretical *m/z* values, and Δ*m/z* and the proposed structure.

m/z(exp)	*m/z*(theo)	Δ*m/z*	Error / ppm
437.1882	437.1894	0.0012	2.74
365.1673	365.1683	0.0010	2.74
343.1851	343.1868	0.0017	4.95
338.1202	338.1210	0.0002	2.37
293.1463	293.1472	0.0009	3.07
271.1642	271.1652	0.0010	3.69
266.0990	266.0999	0.0009	3.38
244.1171	244.1179	0.0008	3.28
212.0889	212.0893	0.0004	1.89
194.0783	194.0788	0.0005	2.58
176.0678	176.0682	0.0004	2.27
172.0963	172.0968	0.0005	2.91
167.0312	?		
140.0678	140.0682	0.0004	2.86
122.0576	122.0576	0.0000	0.00
95.0107	95.0104	0.0003	3.16

Scheme C 15 Fragmentation scheme for precursor ion at 437.1894 *m/z* with an HCD energy of 20 eV.

CIV

Fig. C 35 ESI MS/MS (tandem MS in positive ion mode) of EtOx/AA (1/1) isolating a species at 442 *m/z* with a HCD energy of 20 eV in the relevant range from 50 *m/z* and 500 *m/z*.

Tab. C 20 Peak assignment of ESI MS/MS experiment (Fig. C 35) at 442.2538 *m/z* with a HCD energy of 20 eV showing the experimental *m/z*, the theoretical *m/z* values, and Δ*m/z* and the proposed structure.

m/z(exp)	*m/z*(theo)	Δ*m/z*	Error / ppm
442.2538	442.2548	0.0010	2.26
370.2330	370.2336	0.0006	1.62
343.1859	343.1864	0.0005	1.46
271.1648	271.1652	0.0004	1.48
199.1439	199.1441	0.0002	1.00
194.0784	194.0788	0.0004	2.06
172.0964	172.0968	0.0004	2.32
154.0859	154.0885	0.0006	16.87
100.0760	100.0757	0.0003	3.00

Scheme C 16 Fragmentation scheme for precursor ion at 442.2538 *m/z* with an HCD energy of 20 eV.

CVI

Fig. C 36 ESI MS/MS (tandem MS in positive ion mode) of EtOx/AA (1/1) isolating a species at 464 *m/z* with a HCD energy of 20 eV in the relevant range from 50 *m/z* and 500 *m/z*.

Tab. C 21 Peak assignment of ESI MS/MS experiment (Fig. C 36) at 464.2353 m/z with a HCD energy of 20 eV showing the experimental *m/z*, the theoretical *m/z* values, and Δ*m/z* and the proposed structure.

m/z(exp)	*m/z*(theo)	Δ*m/z*	Error / ppm
464.2353	464.2367	0.0014	3.02
392.2146	392.2156	0.0010	2.55
370.2323	370.2336	0.0013	3.51
365.1667	365.1683	0.0016	4.38
293.1464	293.1472	0.0008	2.73
271.1643	271.1652	0.0009	3.32
266.0992	266.0999	0.0007	2.63
239.1361	239.1366	0.0005	2.09
221.1253	221.1260	0.0007	3.17
199.1436	199.1441	0.0005	2.51
194.0784	194.0788	0.0004	2.06
172.0964	172.0968	0.0004	2.32
100.0760	100.0757	0.0003	3.00

Fig. C 37 ESI MS/MS (tandem MS in positive ion mode) of EtOx/AA (1/1) isolating a species at 482 *m/z* with a HCD energy of 25 eV in the relevant range from 50 *m/z* and 500 *m/z*.

Tab. C 22 Peak assignment of ESI MS/MS experiment (Fig. C 37) at 482.2463 *m/z* with a HCD energy of 25 eV showing the experimental *m/z*, the theoretical *m/z* values, and Δ*m/z* and the proposed structure.

m/z(exp)	*m/z*(theo)	Δ*m/z*	Error / ppm
482.2463	482.2473	0.0009	2.07
383.1778	383.1789	0.0011	2.87
311.1571	311.1577	0.0006	1.93
293.1467	293.1472	0.0005	1.71
284.1098	284.1105	0.0007	2.46
271.1646	271.1652	0.0006	2.21
239.1364	239.1366	0.0002	0.84
212.0889	212.0893	0.0004	1.89
199.1439	199.1441	0.0002	1.00
194.0784	194.0788	0.0004	2.06
176.0680	176.0682	0.0002	1.14
172.0964	172.0968	0.0004	2.32
140.0680	140.0682	0.0002	1.43
100.0760	100.0757	0.0003	3.00

Scheme C 17 Fragmentation scheme for precursor ion at 482.2463 *m/z* with an HCD energy of 25 eV.

Fig. C 38 ESI MS/MS (tandem MS in positive ion mode) of EtOz/AA (1/1) isolating a species at 393 *m/z* with a HCD energy of 20 eV in the relevant range from 50 *m/z* and 400 *m/z*.

Tab. C 23 Peak assignment of ESI MS/MS experiment (Fig. C 38) at 393.1995 m/z with a HCD energy of 20 eV showing the experimental *m/z*, the theoretical *m/z* values, and Δ*m/z* and the proposed structure.

m/z(exp)	*m/z*(theo)	Δ*m/z*	Error /ppm
393.1995	393.1996	0.0001	0.25
299.1968	299.1965	0.0003	1.00
280.1156	280.1155	0.0001	0.36
208.0946	208.0944	0.0002	0.96
186.1126	186.1125	0.0001	0.54
114.0918	114.0913	0.0005	4.38

Scheme C 18 Fragmentation scheme for precursor ion at 393.1995 *m/z* with an HCD energy of 20 eV.
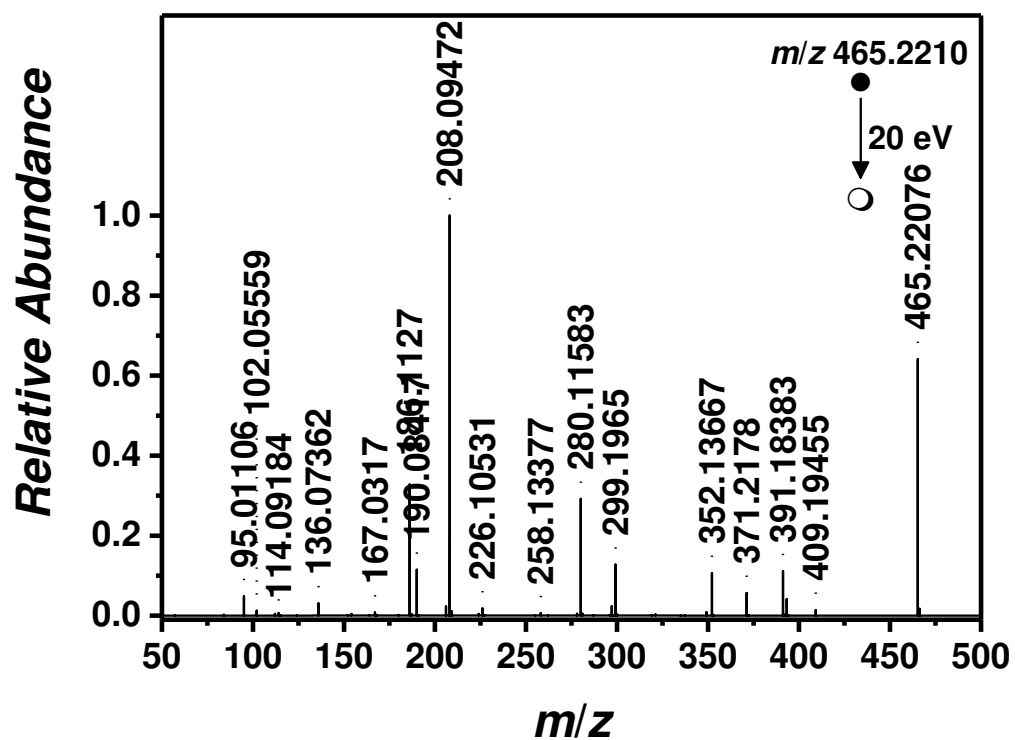
Fig. C 39 ESI MS/MS (tandem MS in positive ion mode) of EtOz/AA (1/1) isolating a species at 465 *m/z* with a HCD energy of 20 eV in the relevant range from 50 *m/z* and 500 *m/z*.

Tab. C 24 Peak assignment of ESI MS/MS experiment (Fig. C 39) at 393.1995 *m/z* with a HCD energy of 20 eV showing the experimental *m/z*, the theoretical *m/z* values, and Δ*m/z* and the proposed structure.

m/z(exp)	*m/z*(theo)	Δ*m/z*	Error /ppm
465.2210	465.2207	0.0003	0.25
409.1946	299.1965	0.0003	1.00
280.1156	280.1155	0.0001	0.36
208.0946	208.0944	0.0002	0.96
186.1126	186.1125	0.0001	0.54
114.0918	114.0913	0.0005	4.38
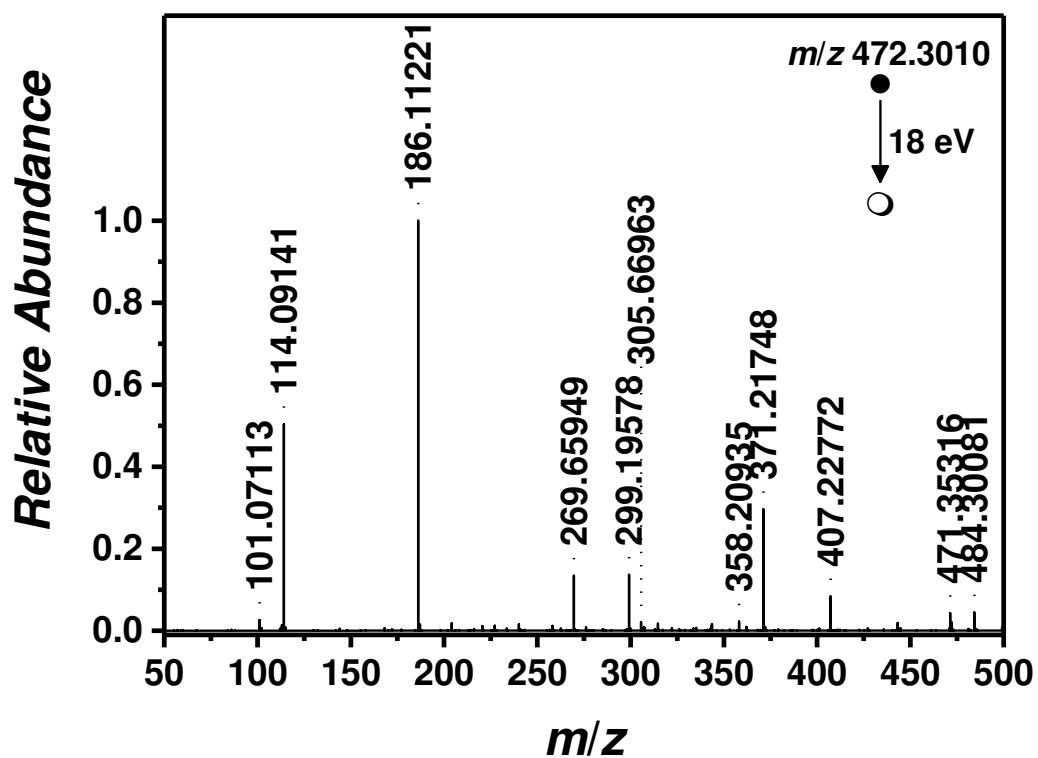
Fig. C 40 ESI MS/MS (tandem MS in positive ion mode) of EtOz/AA (1/1) isolating a species at 472 *m/z* with a HCD energy of 18 eV in the relevant range from 50 *m/z* and 500 *m/z*.
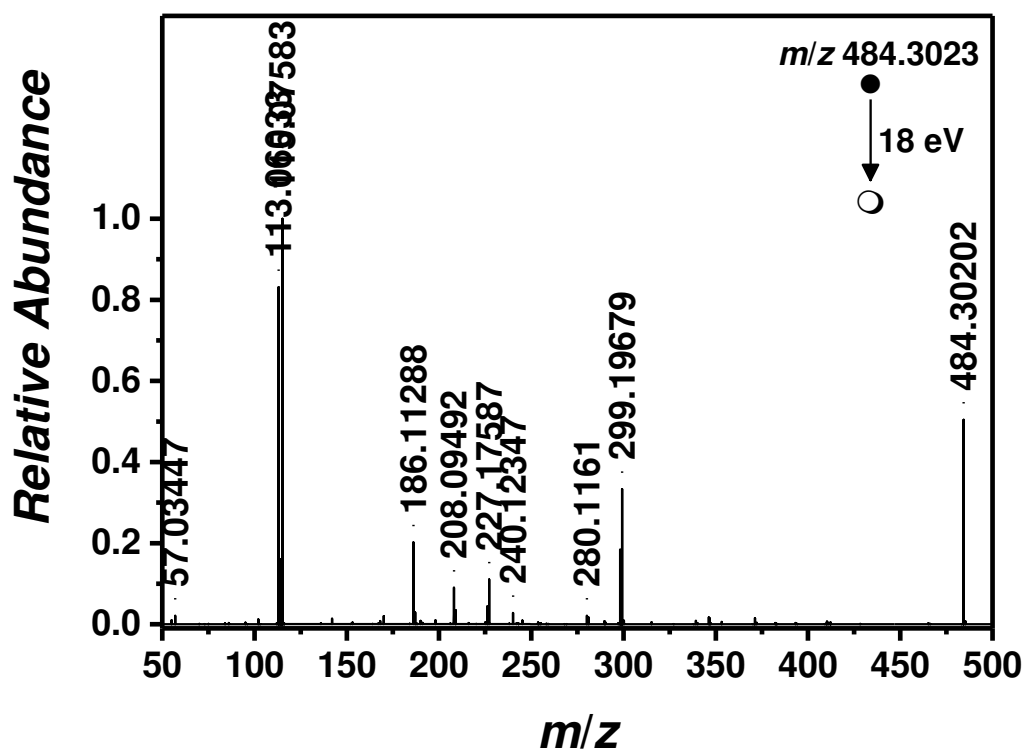
Fig. C 41 ESI MS/MS (tandem MS in positive ion mode) of EtOz/AA (1/1) isolating a species at 484 *m/z* with a higher-energy collision dissociation (HCD) of 18 eV in the relevant range from 50 *m/z* and 500 *m/z*.

D

APPENDIX

NMR and SEC Data
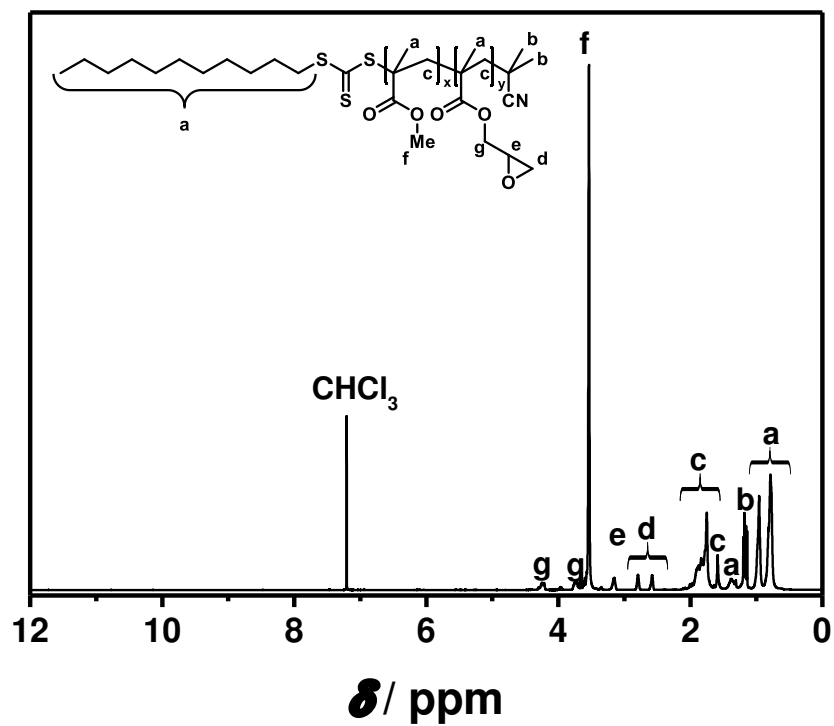
Fig. D 1 ^{1}H NMR (400 MHz, 298 K) of p(MMA-*stat*-GMA) (**17**) in CDCl₃.
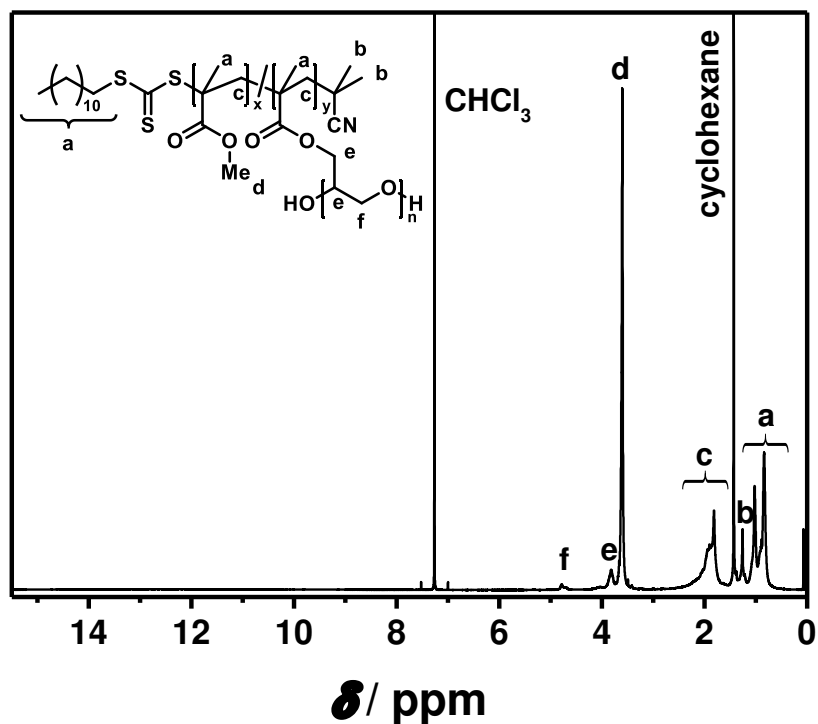
Fig. D 2 1H NMR (400 MHz, 298 K) of the SCNP (**18**) in CDCl3.
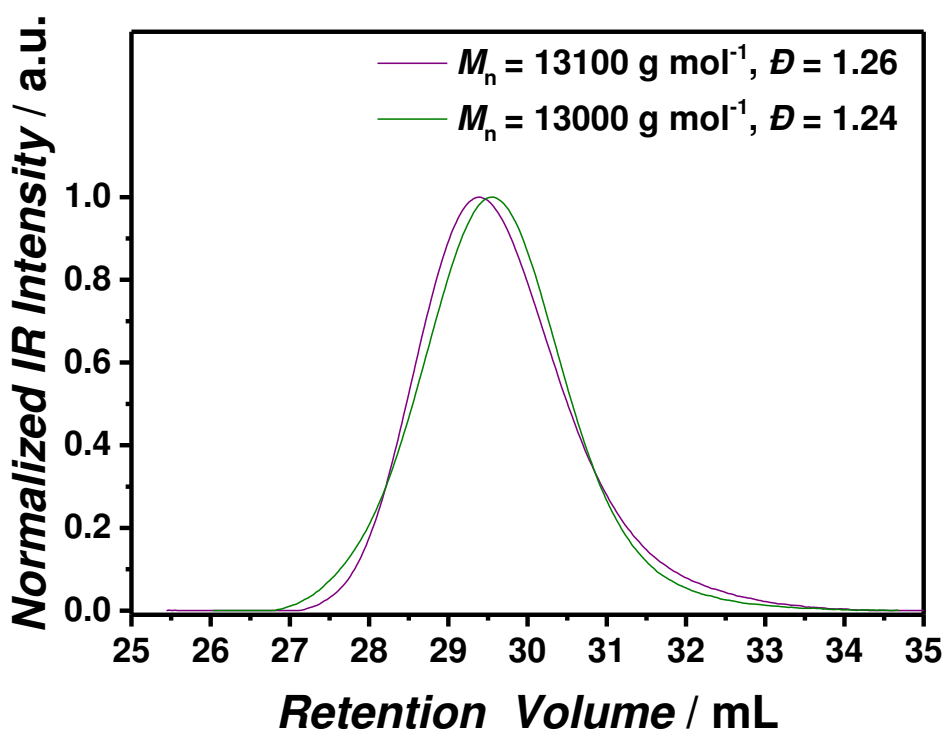
Fig. D 3 SEC traces for p(MMA-*stat*-GMA) (**17**) (purple line) and SCNP (**18**) obtained by using a syringe pump to inject $B(C_6F_5)_3$ with a flow rate of 1 mL·h^{-1} into a solution containing p(MMA-*stat*-GMA) (**17**) in 100 mL dry dichloromethane.

MS Data
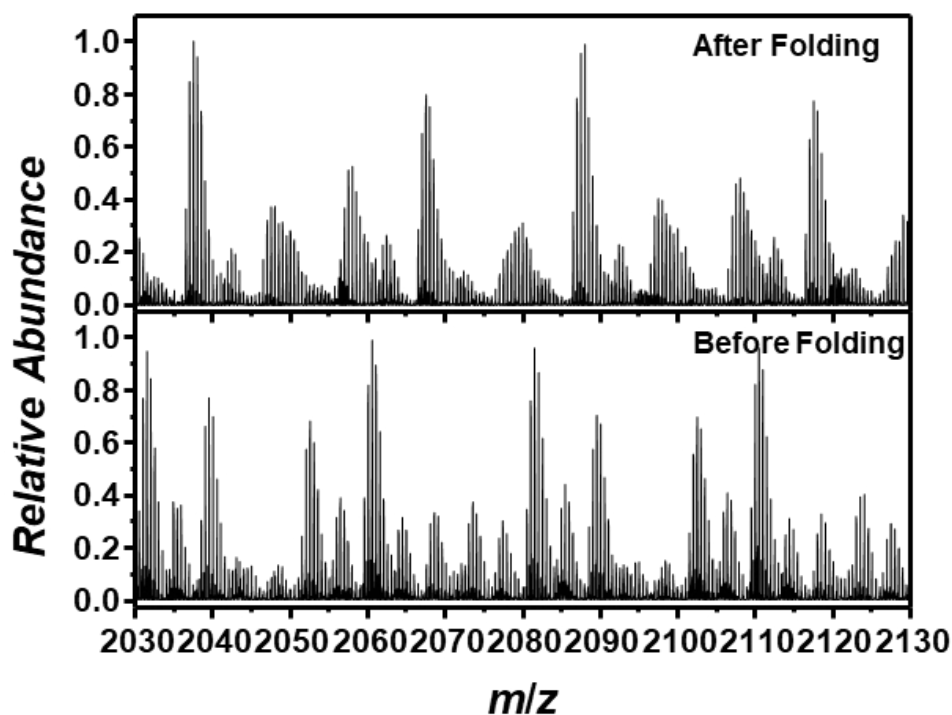
Fig. D 4 (Top) SEC-ESI Orbitrap mass spectrum after successful folding resulting in SCNP (**18**) formation; (bottom) SEC-ESI Orbitrap mass spectrum prior to the folding of p(MMA-*stat*-GMA) (**17**). The spectrum ranges from 2030 *m/z* to 2130 *m/z* illustrating doubly charged species of the precursor polymer and the SCNP.
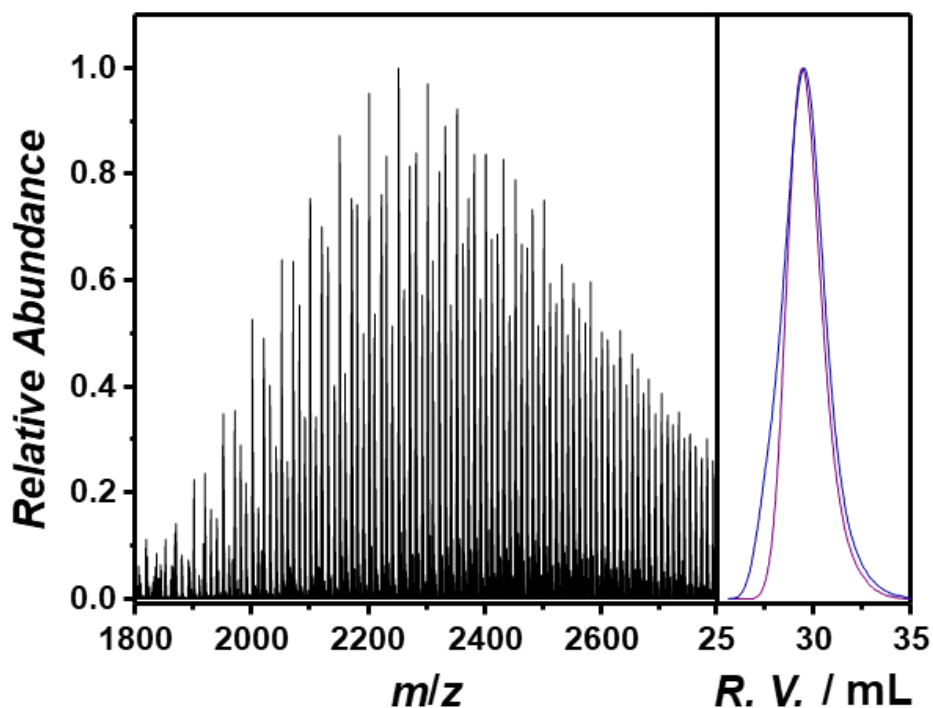
Fig. D 5 SEC-ESI Orbitrap mass spectrum (negative ion mode) obtained of p(MMA-*stat*-GMA) (**17**), in which all glycidyl moieties were ring-opened by water. The SEC trace depicts no shift from the parent polymer (purple trace) to the ring-opened polymer (blue trace). The ionization is by virtue of complexation to iodide.
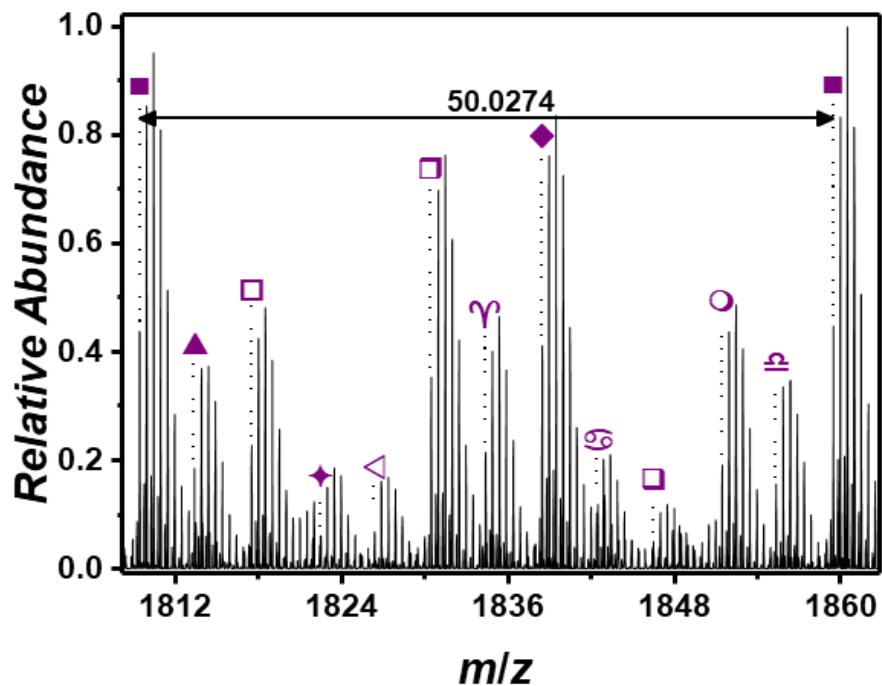
Fig. D 6 Zoomed SEC-ESI Orbitrap mass spectrum (positive ion mode) of p(MMA-*stat*-GMA) (**17**) between 1808 *m/z* and 1862 *m/z* obtained by summing all species between 14.71 mL and 15.13 mL retention volume. Labeled are the most abundant species and the repeating unit of pMMA (*m/z*(exp) 50.0274; *m/z*(theo) 50.0257). The minor distributions (slightly shifted isotopic pattern) stems from complexation by virtue of a second NaI and was not labeled in order to keep a good readability of the spectrum.
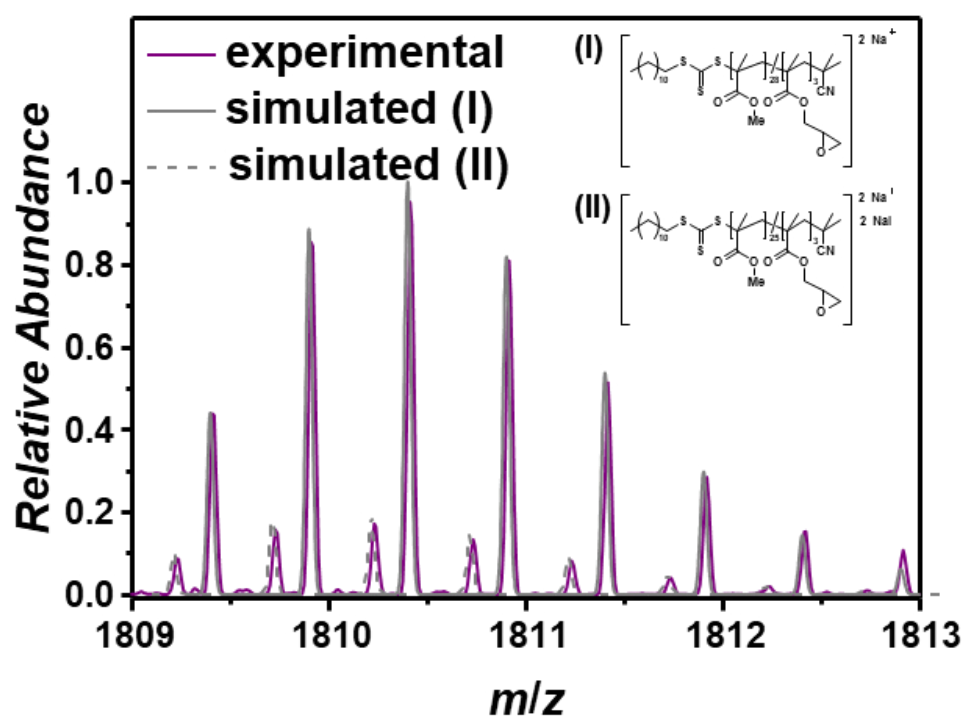
Fig. D 7 Isotopic simulation of a selected peak at 1813 m/z comparing the experiment (purple line) and the simulation (grey line) of (**I**) p(MMA$_{28}$-<u>stat</u>-GMA$_3$) ionized by virtue of complexation to sodium and (**II**) p(MMA$_{26}$-<u>stat</u>-GMA$_3$) ionized by virtue of complexation to sodium and formation of adducts to sodium iodide with a resolution of 48000.

Tab. D 1 Peak assignment of the SEC-ESI Orbitrap mass spectrum of p(MMA-*stat*-GMA) (**17**) showing the labels (corresponding to the species in Fig. D 8), the resolution (obtained by the Xcalibur software), the experimental *m/z* and theoretical *m/z* values, Δ*m/z* and the proposed chemical structures. The SEC-ESI Orbitrap mass spectrum was integrated from 14.71 mL to 15.13 mL to obtain a sufficient signal to noise ratio. The minor distributions (slightly shifted isotopic pattern) stems from a second complexation by virtue of NaI and was not labeled in order to keep a good readability of the spectrum.

Label	Resolution	*m/z*(exp)	*m/z*(theo)	Δ*m/z*	Structure
■	48000	1809.4139	1809.3987	0.0152	
▲	48000	1813.3304	1813.3143	0.0162	
□	40000	1817.4307	1817.4143	0.0164	
✦	46000	1822.4063	1822.3883	0.0180	
◁	43000	1826.3174	1826.3039	0.0135	

□	46000	1830.4180	1830.4039	0.0141

♈	49000	1834.3356	1834.3196	0.0160

♦	49000	1838.4356	1838.4196	0.0160

♋	49000	1842.3539	1842.3352	0.0187

▼	45000	1846.4538	1846.4352	0.0185

○	44000	1851.4204	1851.4092	0.0112

CXXI

♎ 47000 1855.3399 1855.3248 0.0150

CXXII
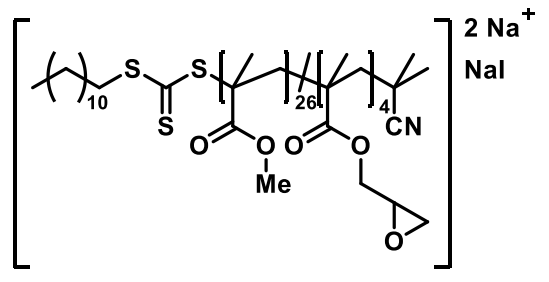
SEC-ESI MS data of SCNP (2) obtained by direct addition of B(C₆F₅)₃
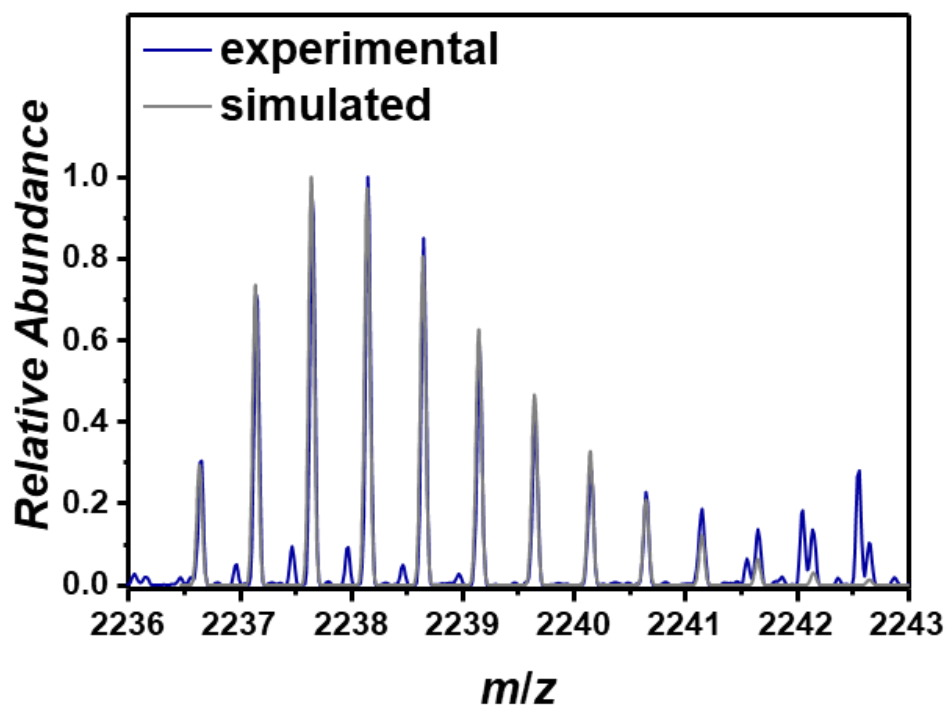
Fig. D 9 Isotopic simulation of a selected peak at 2238 *m/z* comparing the experiment (blue line) and the simulation (grey line) of SCNPs (**18**) with a resolution of 40000. Species ■ and species ⊗ have an approximated ratio of ■:⊗ = 5:1.
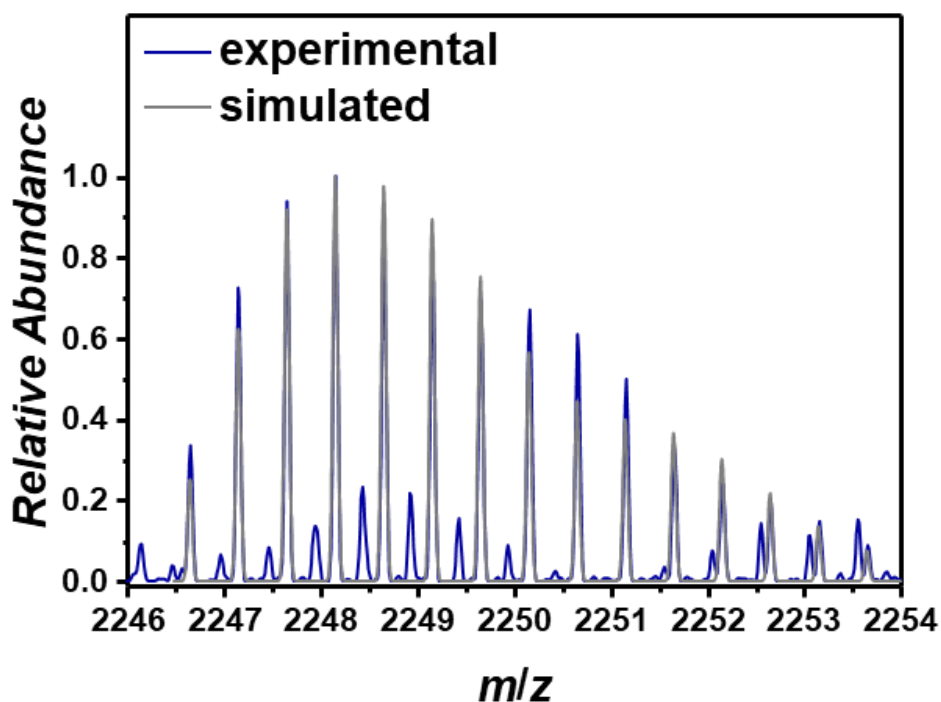
Fig. D 10 Isotopic simulation of a selected peak at 2248 *m/z* comparing the experiment (blue line) and the simulation (grey line) of SCNP (**18**) with a resolution of 40000. Species ●, ◀, ⊡ and species ❖ have an approximated ratio of ●:◀:⊡:❖ = 10:3:4:3.
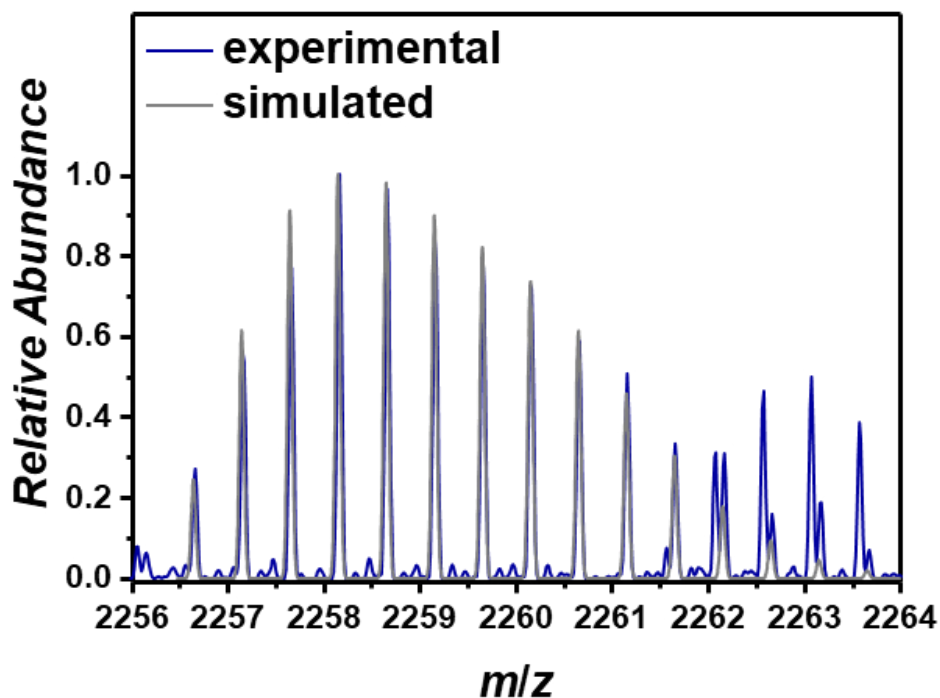
Fig. D 11 Isotopic simulation of a selected peak at 2258 *m/z* comparing the experiment (blue line) and the simulation (grey line) of SCNP (**18**) with a resolution of 40000. Species ϓ, ≋, ▶ and species ▽ have an approximated ratio of ϓ:≋:▶:▽ = 10:3:4:3.
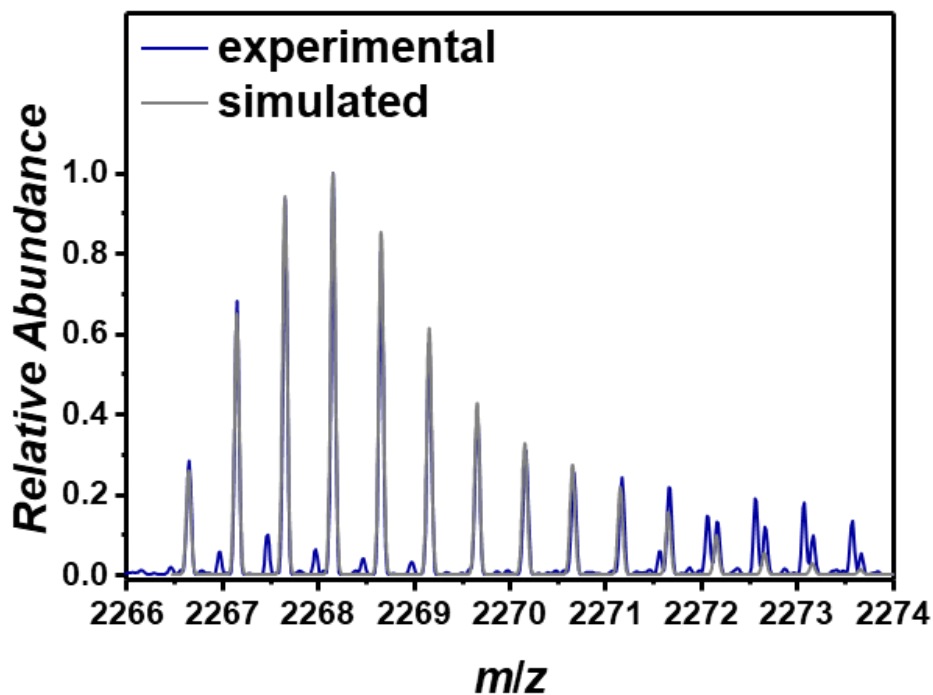
Fig. D 13 Isotopic simulation of a selected peak at 2268 *m/z* comparing the experiment (blue line) and the simulation (grey line) of SCNP (**18**) with a resolution of 40000. Species ◆, ✳ and species ⊠ have an approximated ratio of ◆:✳:⊠ = 5:1:1.
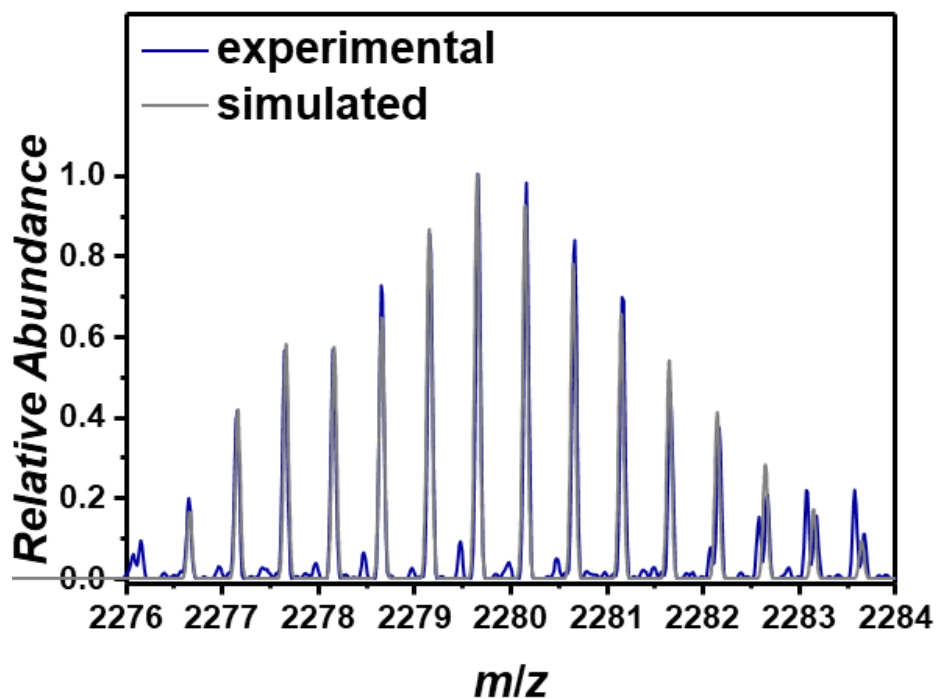
Fig. D 12 Isotopic simulation of a selected peak at 2258 *m/z* comparing the experiment (blue line) and the simulation (grey line) of SCNP (**18**) with a resolution of 40000. Species ◯, ▢, △ and species ⚡ have an approximated ratio of ◯:▢:△:⚡ = 2:2:3:1.

Tab. D 2 Peak assignment of the SEC-ESI Orbitrap mass spectrum of SCNP (**18**) showing the label, the resolution (obtained by the Xcalibur software), the experimental m/z and theoretical m/z values, $\Delta m/z$ and the proposed structures. SEC-ESI Orbitrap mass spectrum was integrated from 14.42 mL to 14.92 mL to obtain sufficient signal to noise ratio.

Label	Resolution	m/z(exp)	m/z(theo)	$\Delta m/z$	Structure
■	40000	2236.6506	2236.6436	0.0070	
⊗	44000	2239.6546	2239.6454	0.0093	
✖	44000	2241.5566	2241.5489	0.0077	
●	42000	2246.6452	2246.6385	0.0067	

CXXVI

◀	42000	2248.1500	2248.1492	0.0008
▣	40000	2249.6551	2249.6467	0.0084
❖	40000	2250.6579	2250.6423	0.0152
♎	40000	2251.5541	2251.5632	0.0090

CXXVII
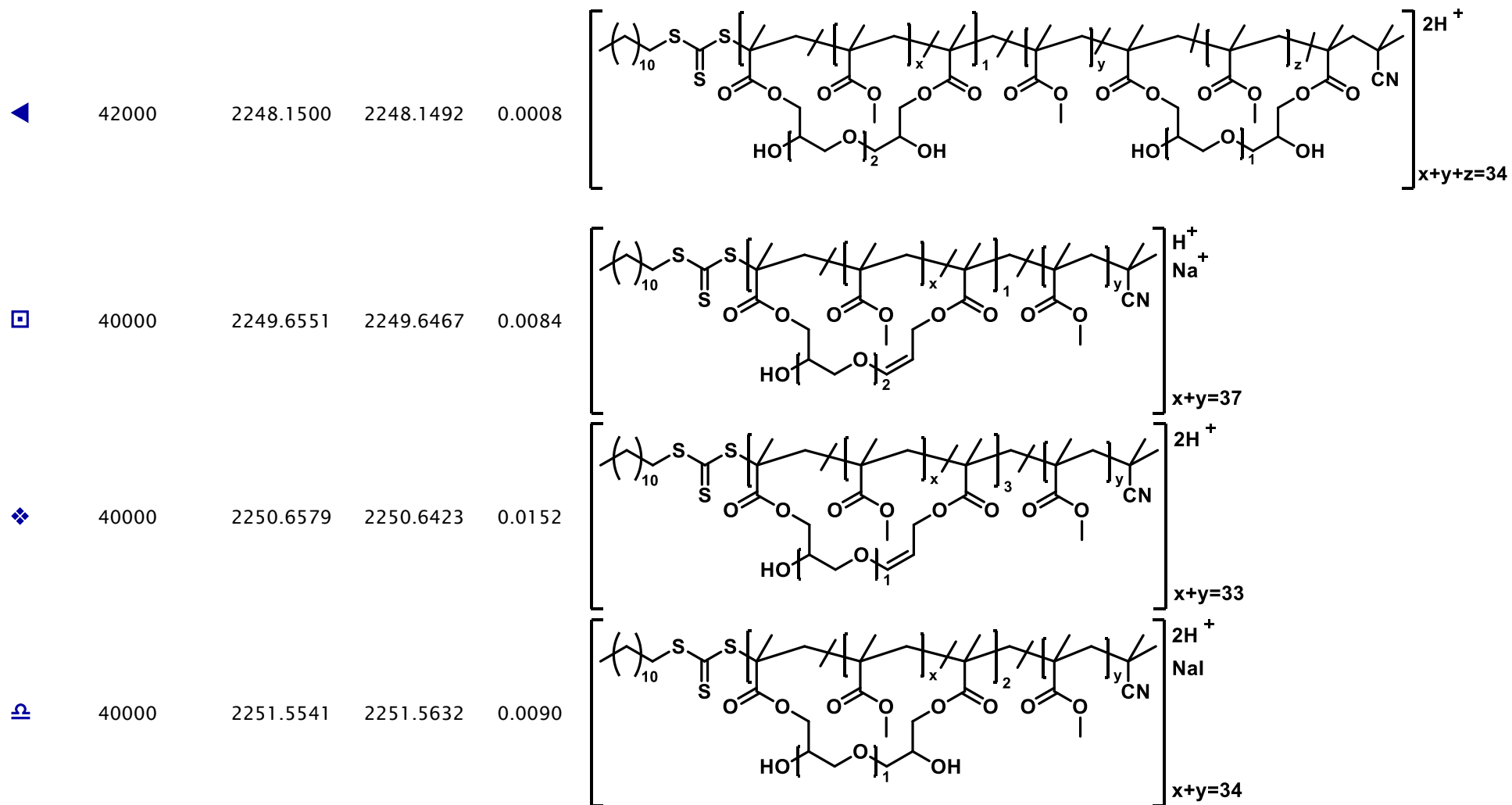
❅	42000	2252.5548	2252.5592	0.0045
♈	40000	2256.6660	2256.6528	0.0131
♋	43000	2258.6646	2258.6520	0.0126
▶	41000	2259.6600	226604	0.0004
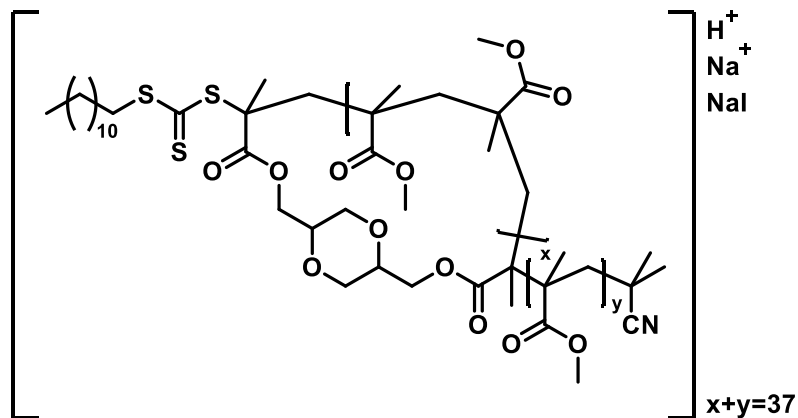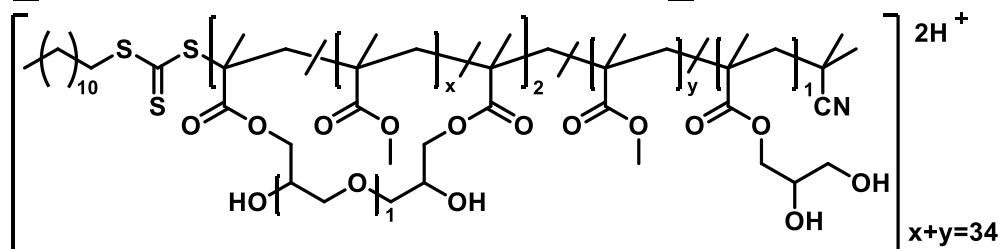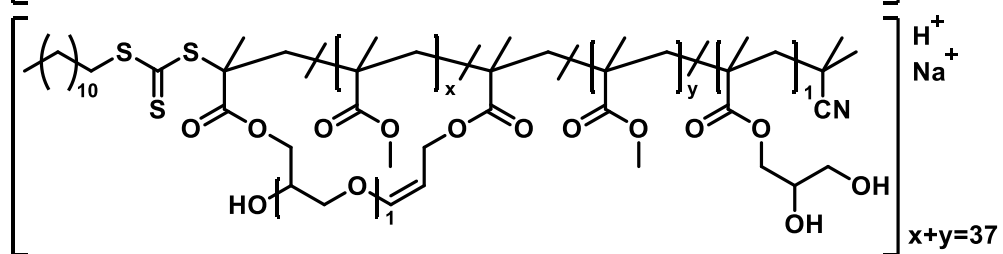
CXXVIII

▽	40000	2260.6594	2260.6506	0.0088
♋	48000	2261.5678	2261.5678	0.0032
◆	42000	2266.6604	2266.6542	0.0062
✳	44000	2268.6648	2268.6663	0.0015

CXXIX
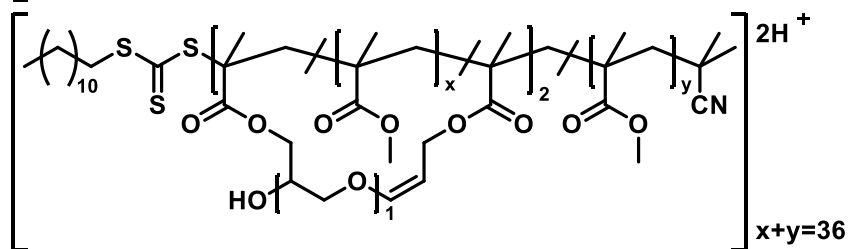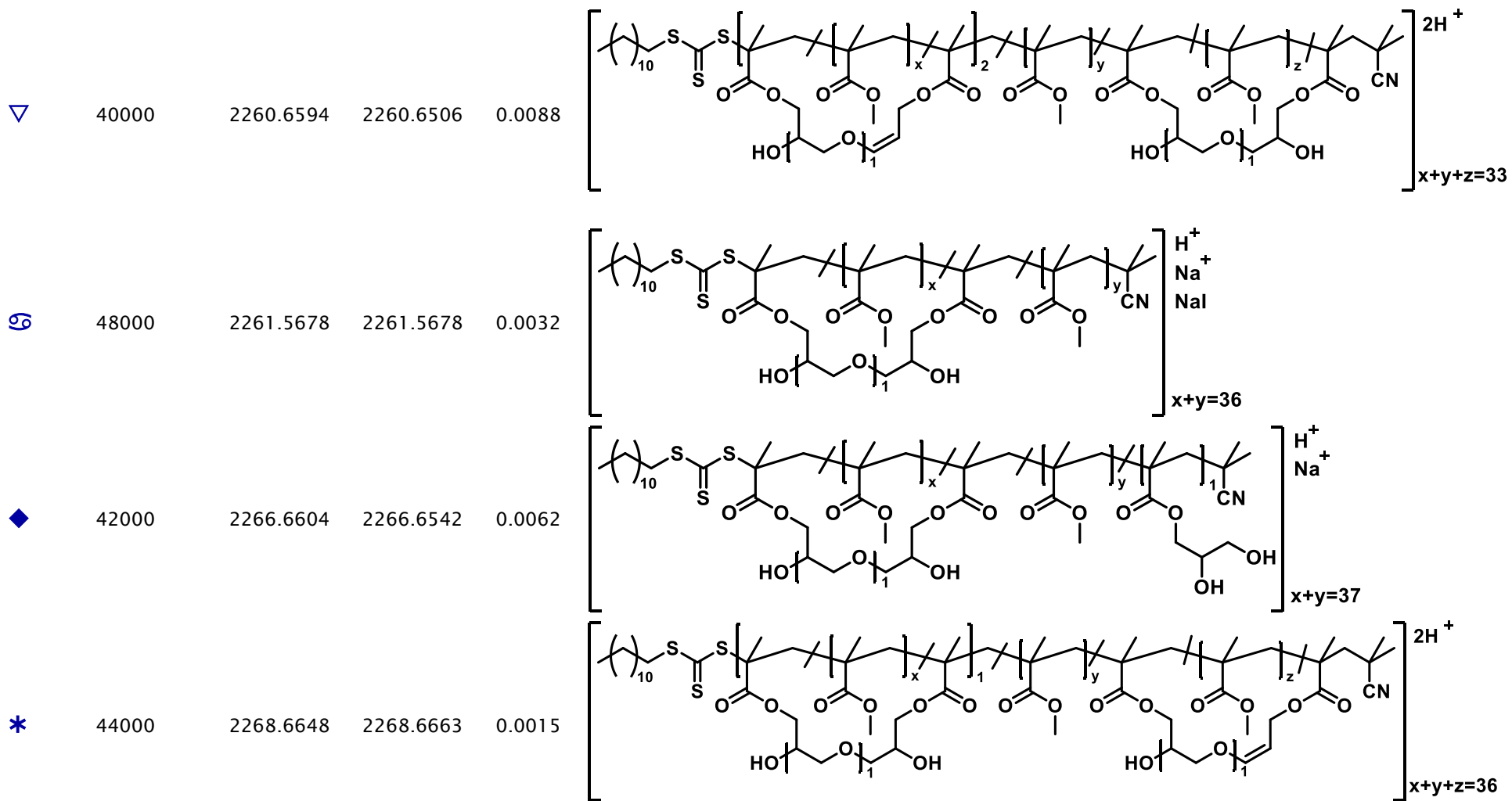
⊠ 40000 2270.6725 2270.6520 0.0205
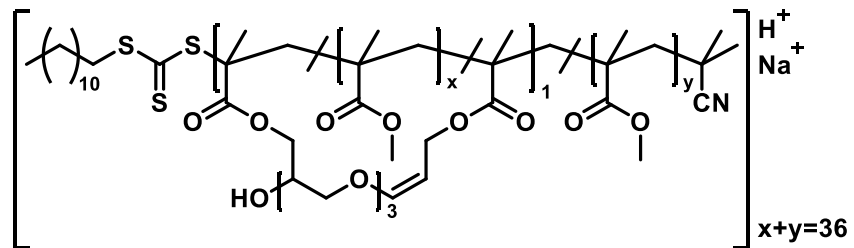
⌘ 39000 2271.5674 2271.5594 0.0080
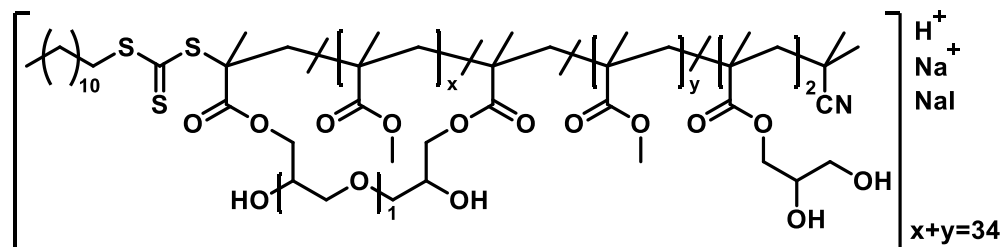
≋ 44000 2272.5667 2272.5685 0.0018
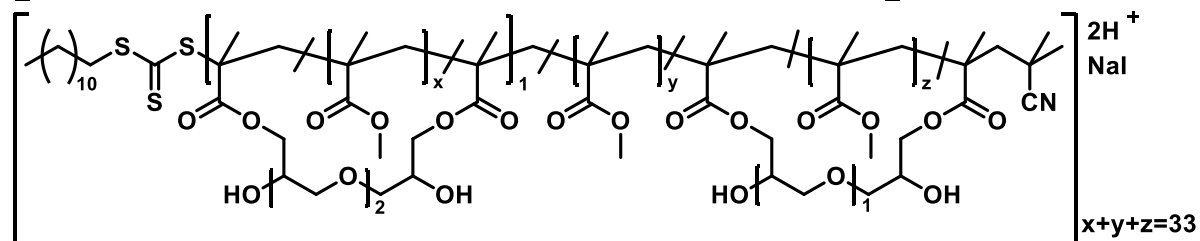
○ 40000 2276.6685 2276.6611 0.0074
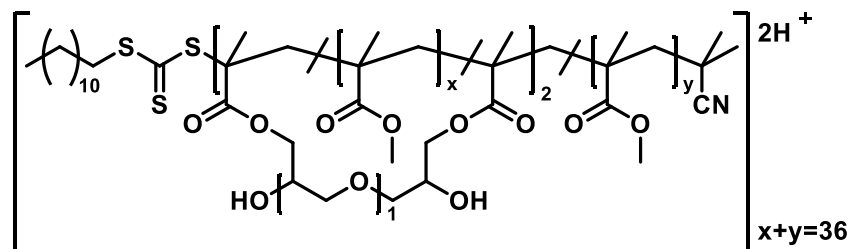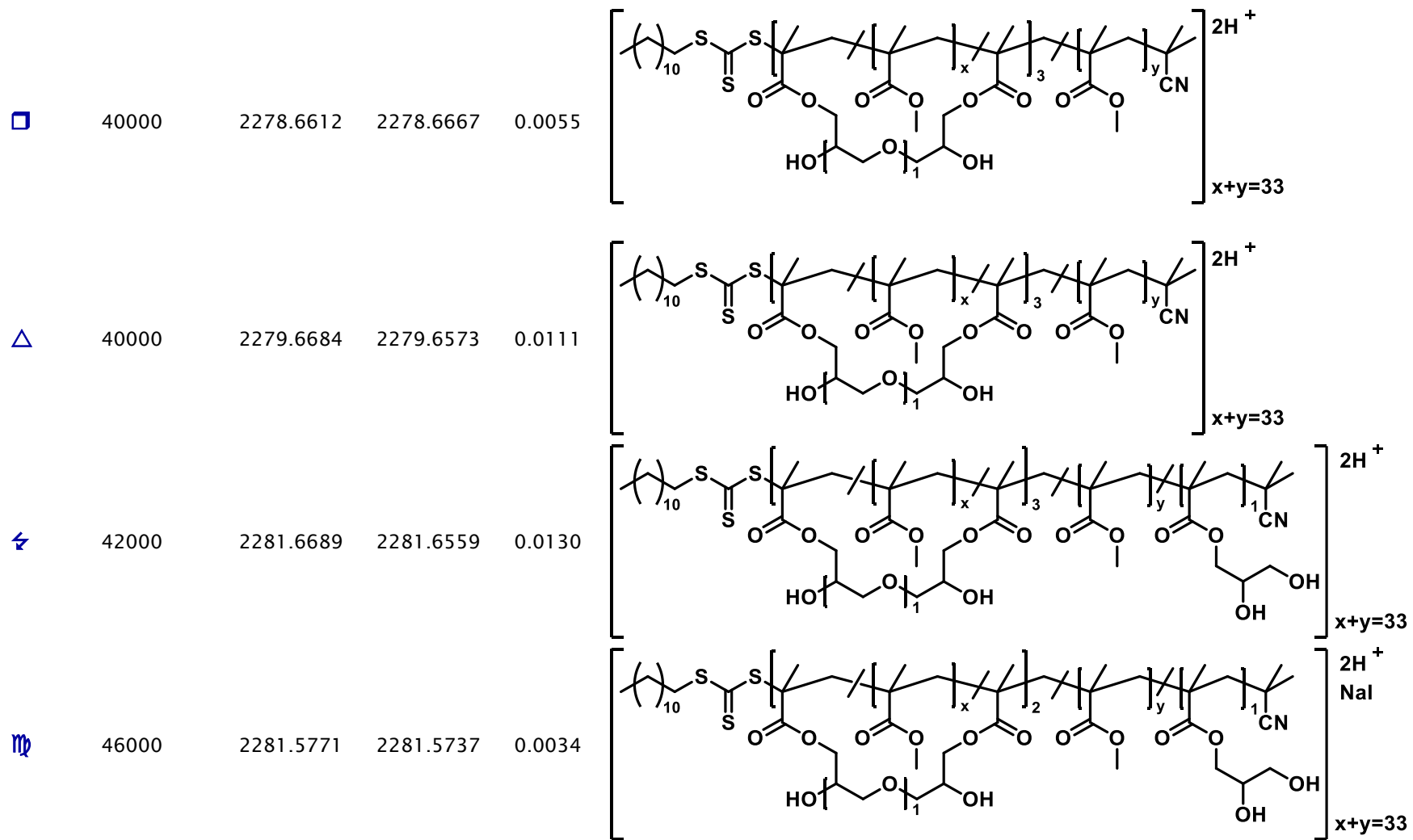
CXXX

□ 40000 2278.6612 2278.6667 0.0055

△ 40000 2279.6684 2279.6573 0.0111

⚡ 42000 2281.6689 2281.6559 0.0130

♍ 46000 2281.5771 2281.5737 0.0034

CXXXI

43000   2283.5826   2283.5729   0.0097

CXXXII

Radical-Induced Single-Chain Folding of Passerini Sequence-Regulated Polymers Visualized by High-Resolution Mass Spectrometry

NMR Data
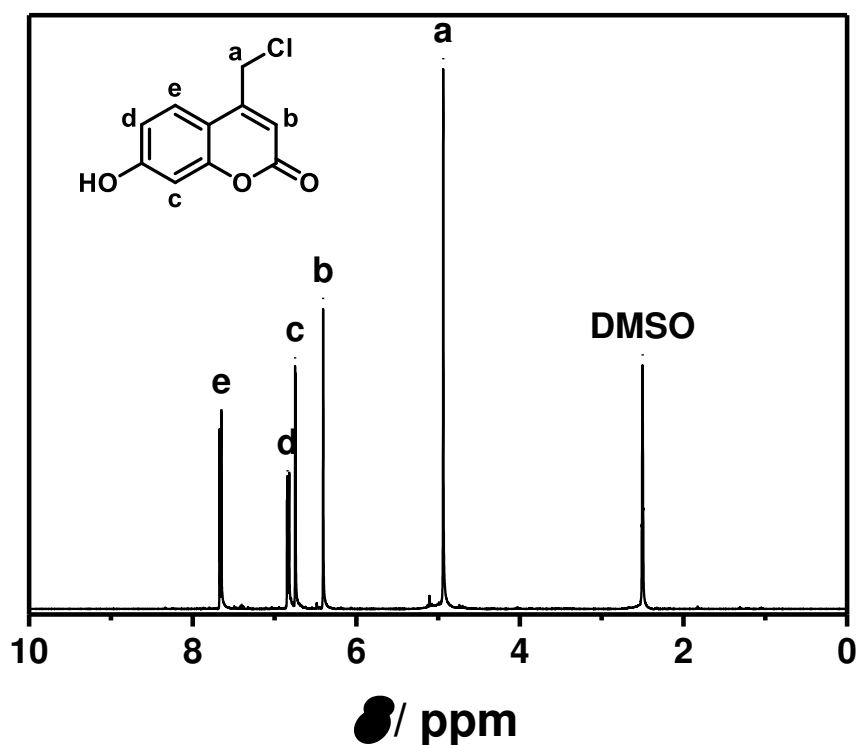
Fig. D 14 ^{1}H NMR (298 K, 400 MHz) of 4-(chloromethyl)-7-hydroxy-coumarin in DMSO-d$_6$.
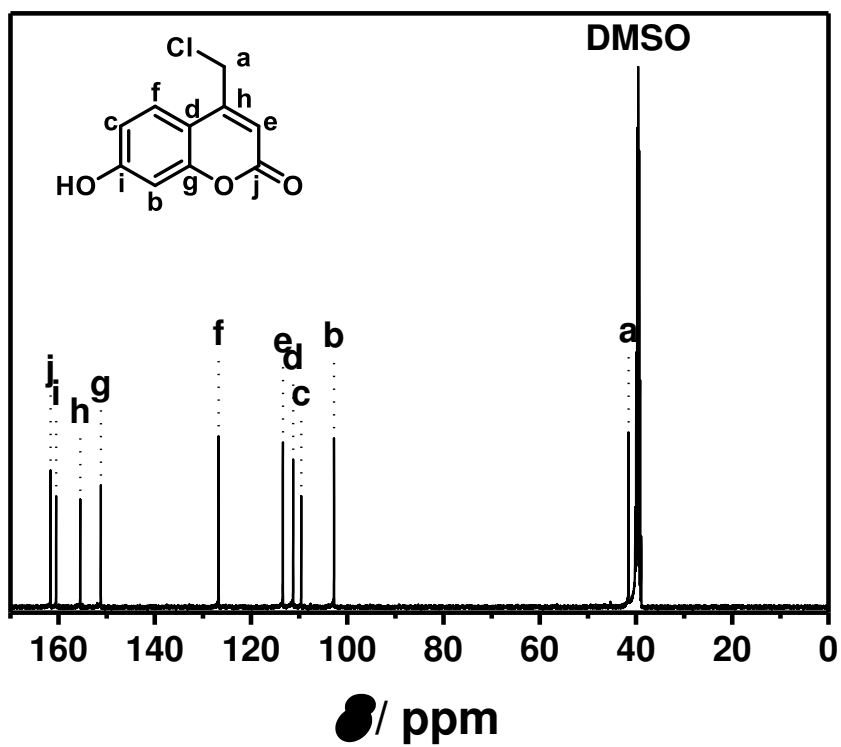
Fig. D 15 ^{13}C{^{1}H} NMR (298 K, 101 MHz) of 4-(chloromethyl)-7-hydroxy-coumarin in DMSO-d$_6$
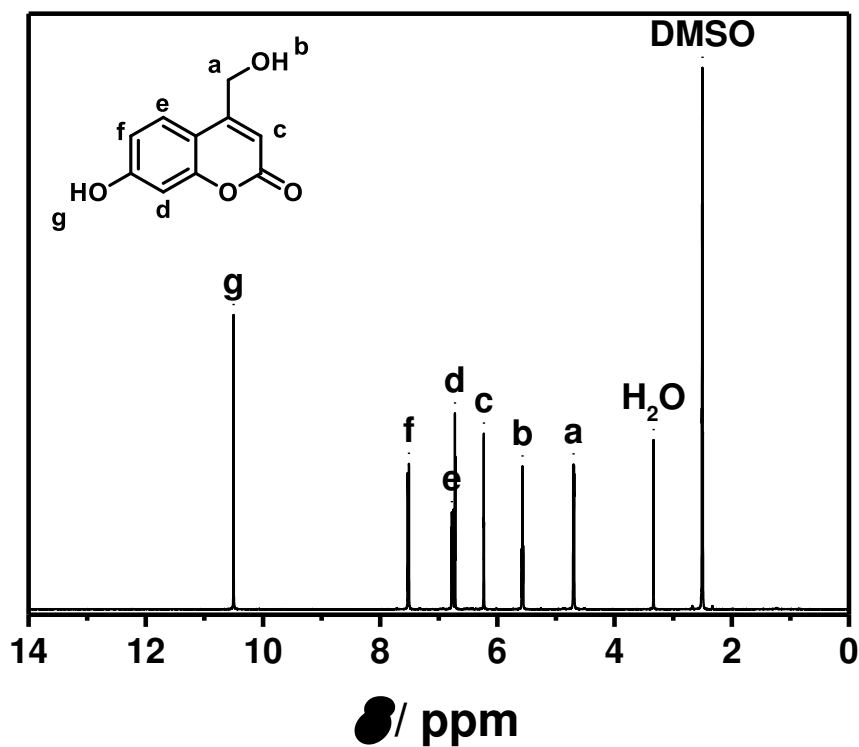
Fig. D 16 ^{1}H NMR (298 K, 400 MHz) of 4-(hydroxymethyl)-7-hydroxy-coumarin in DMSO-d$_6$.
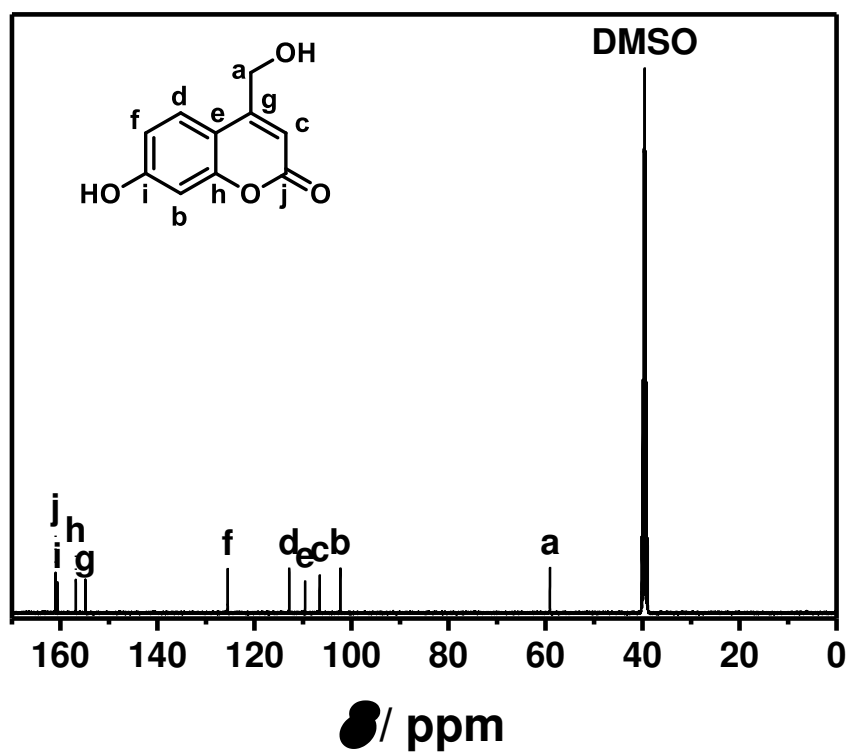
Fig. D 17 ^{13}C{^{1}H} NMR (298 K, 101 MHz) of 4-(hydroxymethyl)-7-hydroxy-coumarin in DMSO-d$_6$.
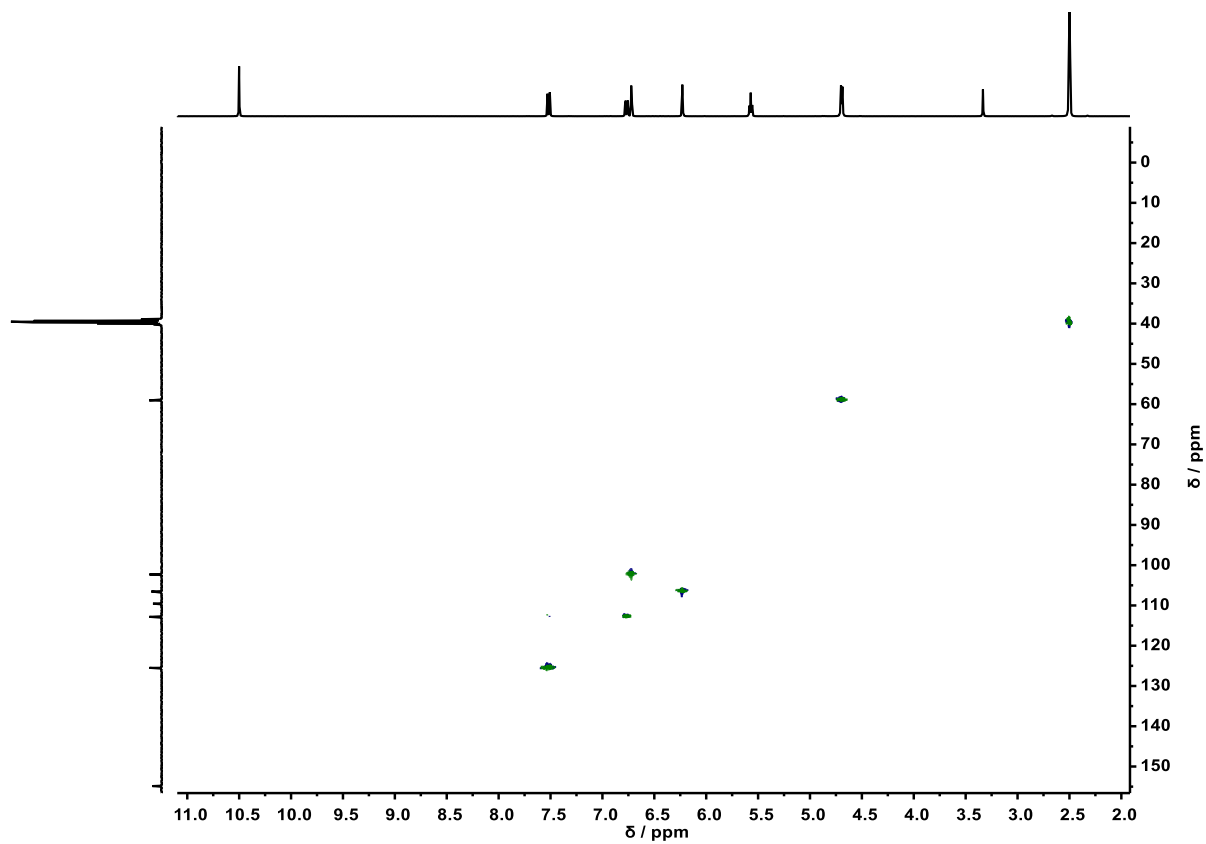
Fig. D 18 HSQC NMR (^{1}H-^{13}C{^{1}H}, 298 K) of 4-(hydroxymethyl)-7-hydroxy-coumarin in DMSO-d$_6$.
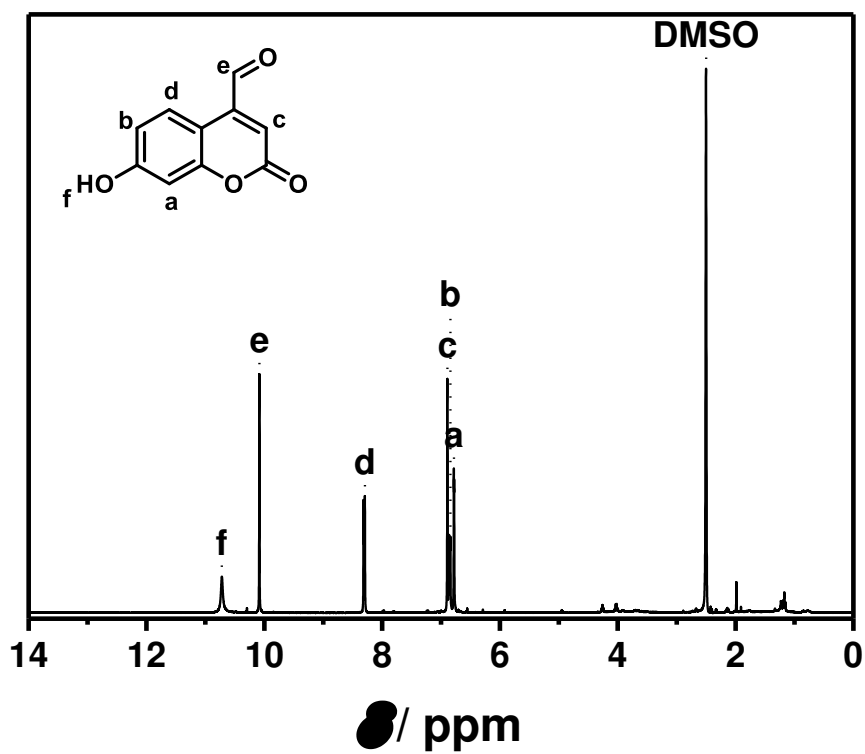
Fig. D 19 ^{1}H NMR (298 K, 400 MHz) of 4-formyl -7-hydroxy-coumarin in DMSO-d$_6$.
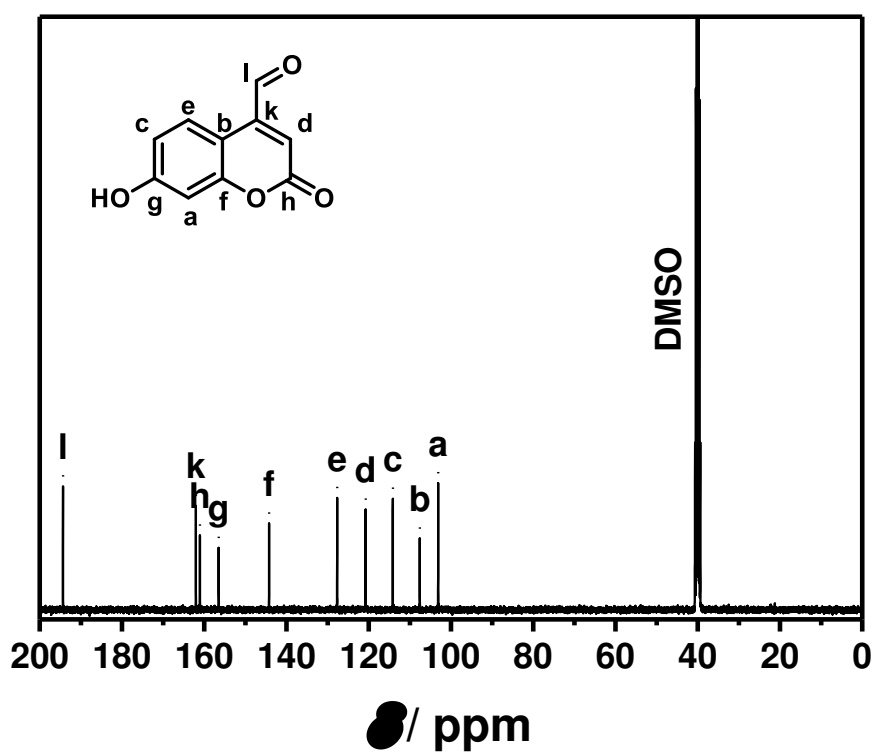
Fig. D 20 ^{13}C{^{1}H} NMR (298 K, 400 MHz) of 4-formyl -7-hydroxy-coumarin in DMSO-d$_6$.
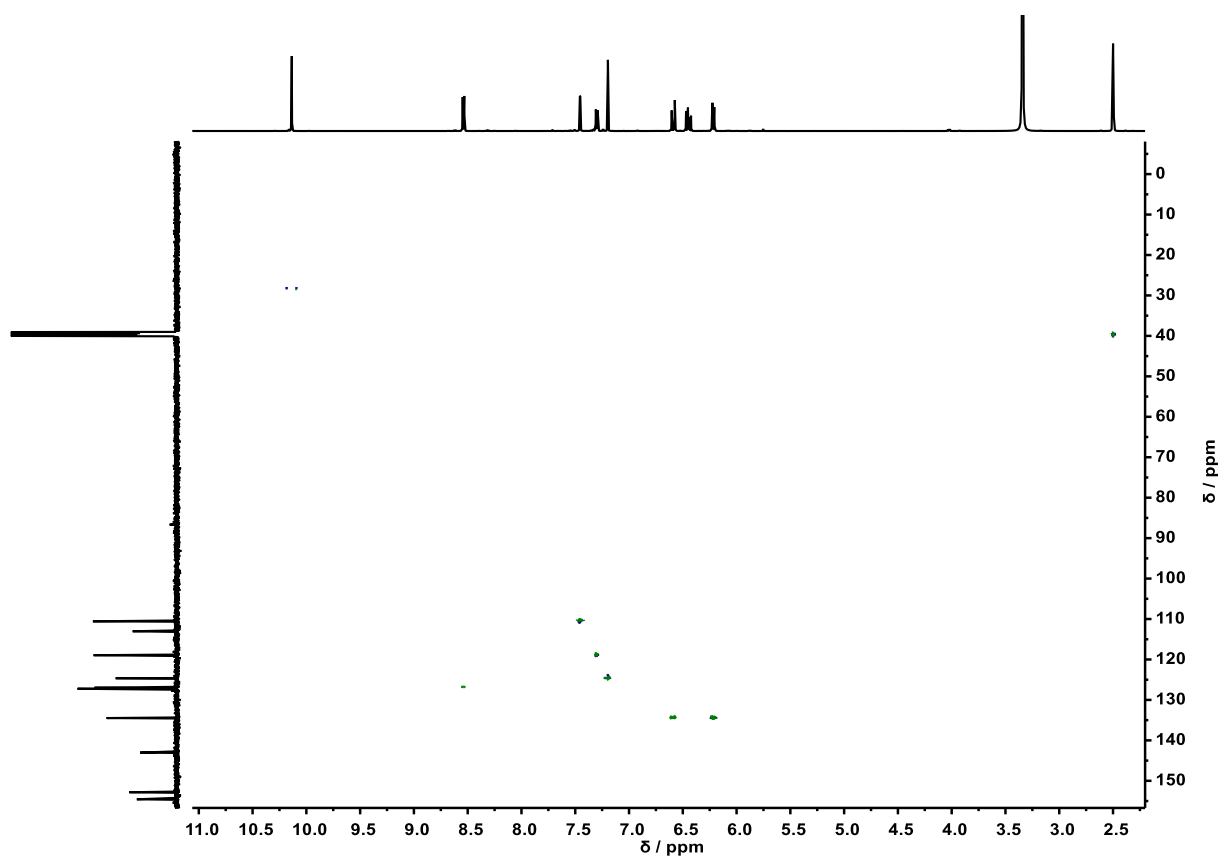
Fig. D 21 HSQC NMR (^{1}H-^{13}C, 298 K) of 4-formyl-7-hydroxy-coumarin in DMSO-d$_6$.
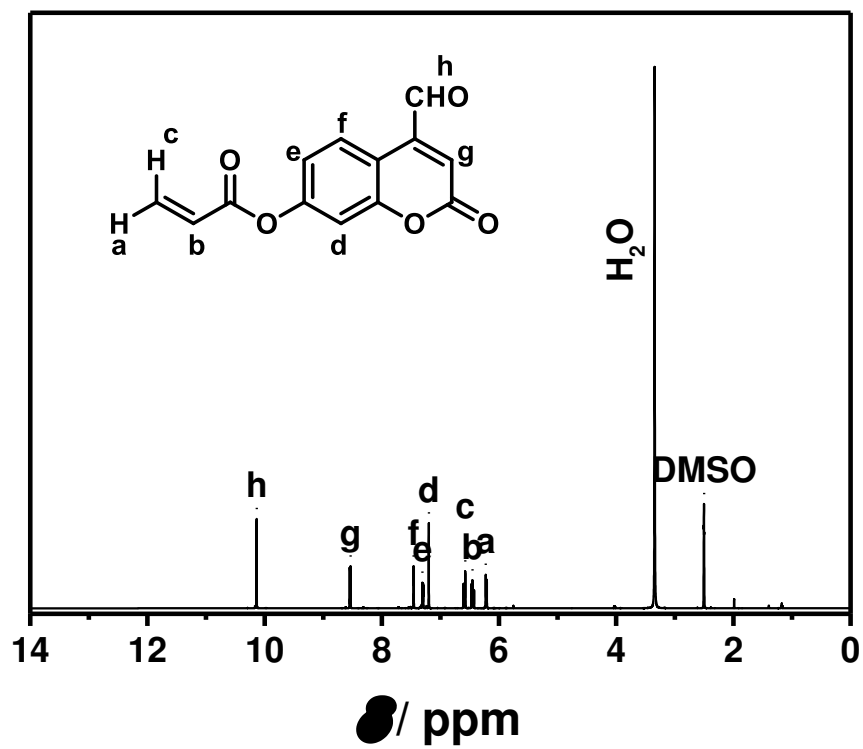
Fig. D 22 ^{1}H NMR (298 K, 600 MHz) of 4-formyl -coumarin-7-yl acrylate in DMSO-d$_6$.
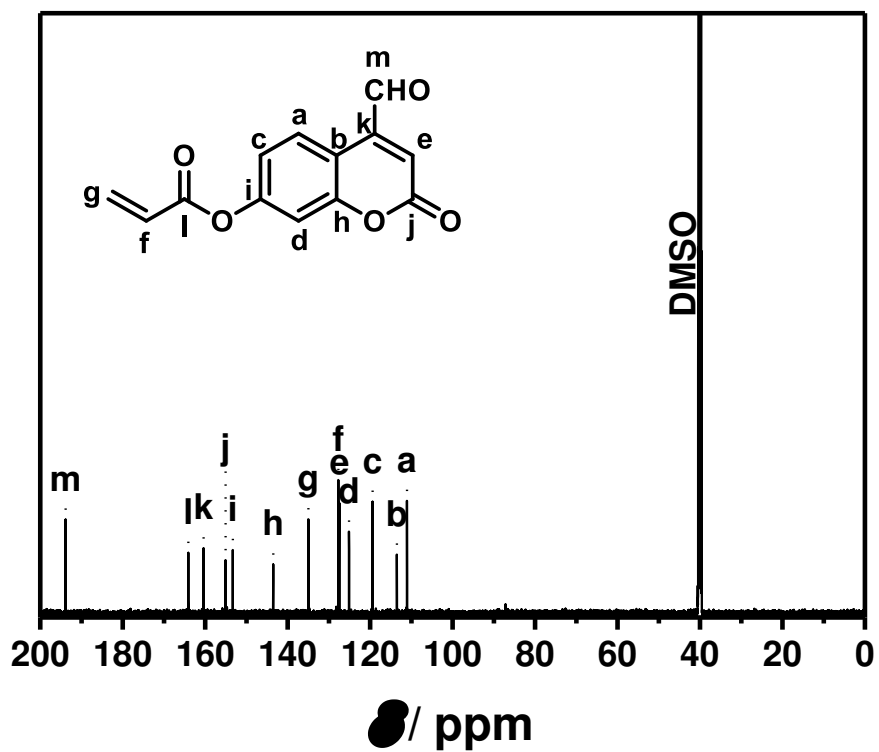
Fig. D 23 ¹H NMR (298 K, 151 MHz) of 4-formyl -coumarin-7-yl acrylate in DMSO-d₆.
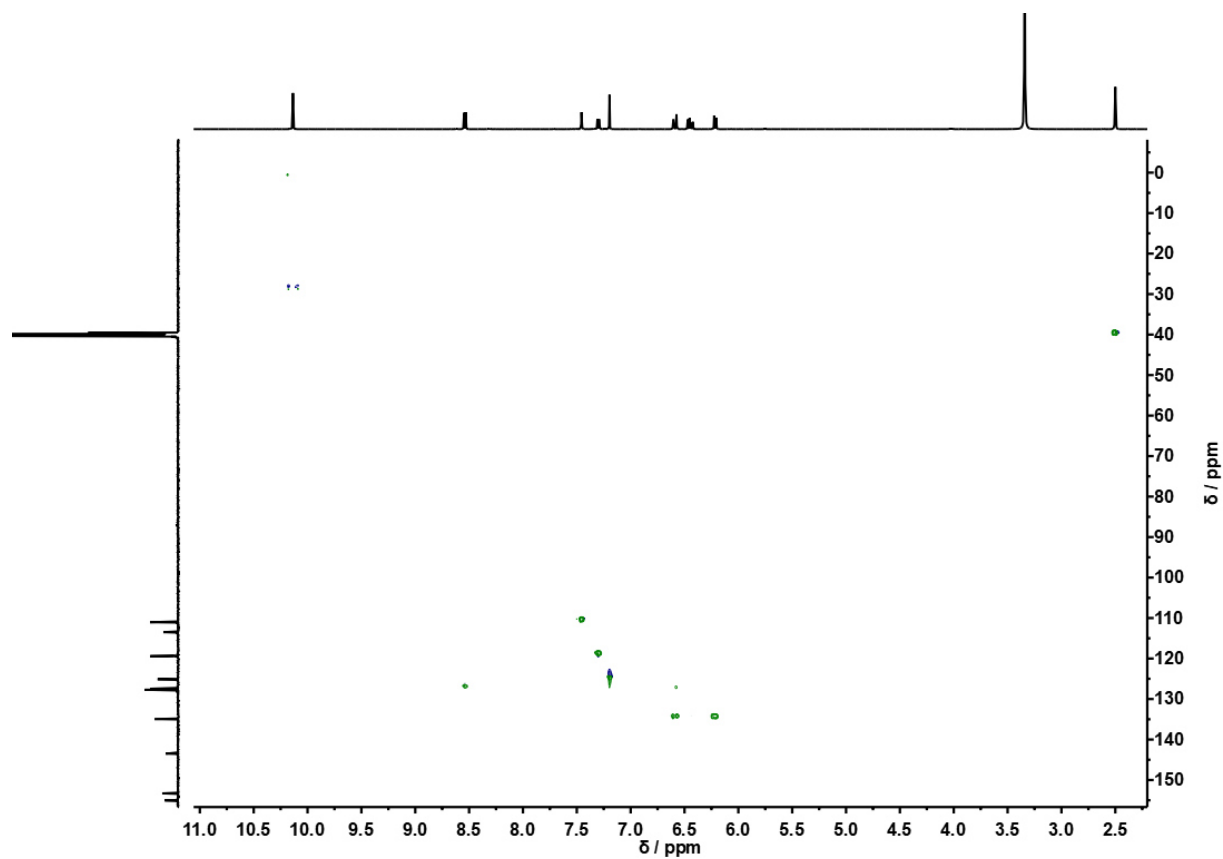
Fig. D 24 HSQC NMR (¹H-¹³C, 298 K) of 4-formyl-coumarin-7-yl acrylate in DMSO-d₆.
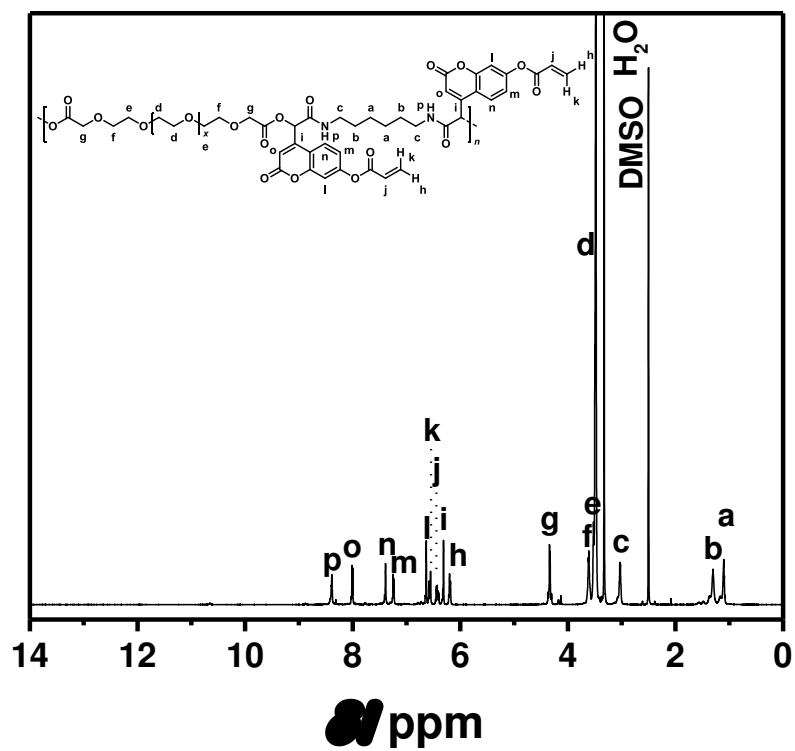
Fig. D 25 ^{1}H NMR (298 K, 600 MHz) of **19a** in DMSO-d_6.
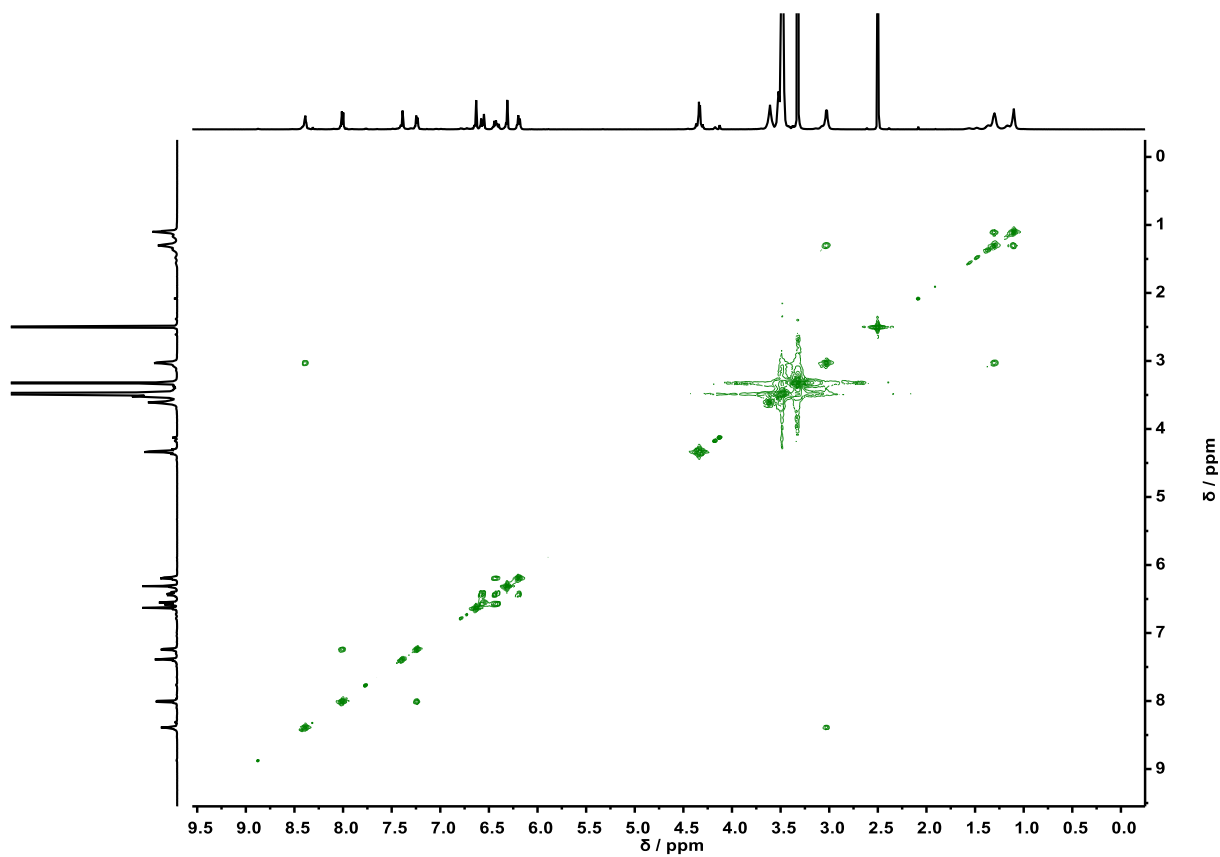
Fig. D 26 COSY NMR (^{1}H-^{1}H, 298 K, 600 MHz) of **19a** in DMSO-d_6.
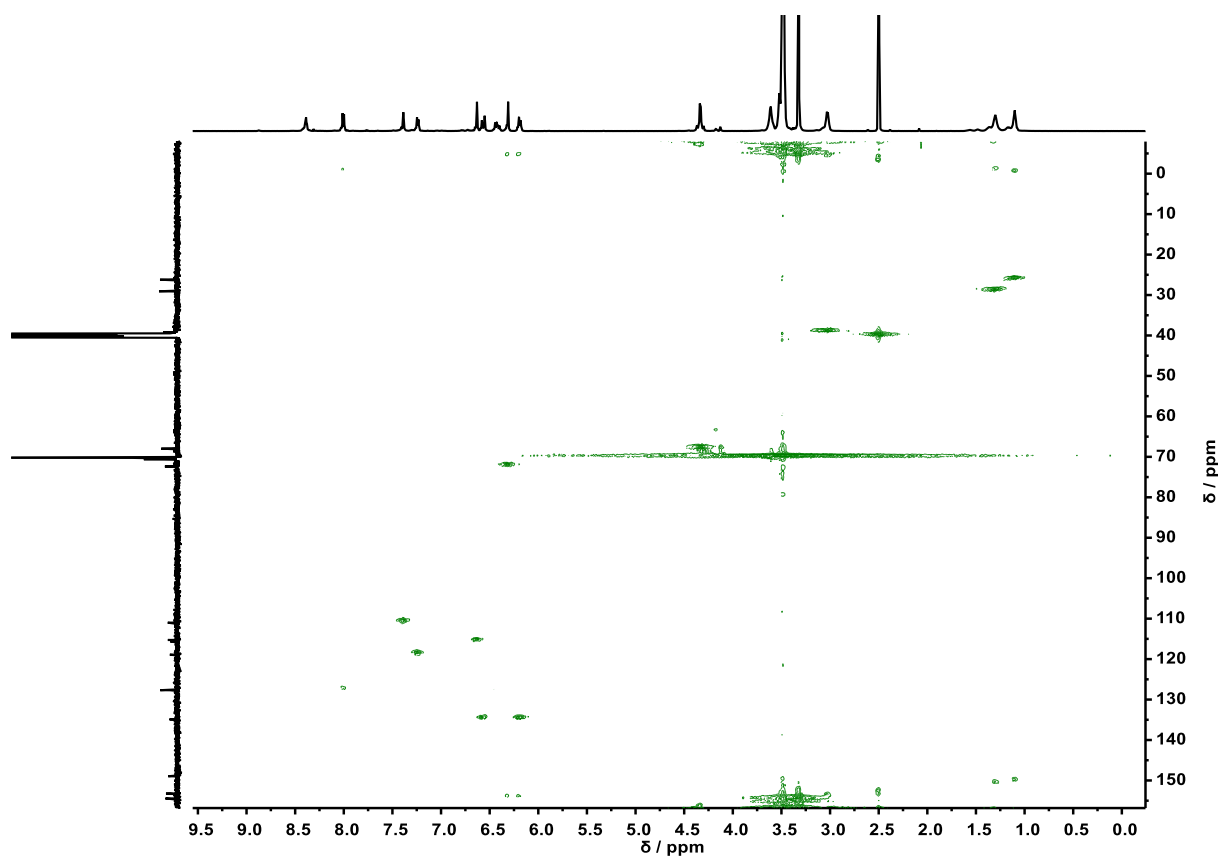
Fig. D 27 HSQC NMR (^{1}H-^{13}C, 298 K) of **19a** in DMSO-d$_6$.
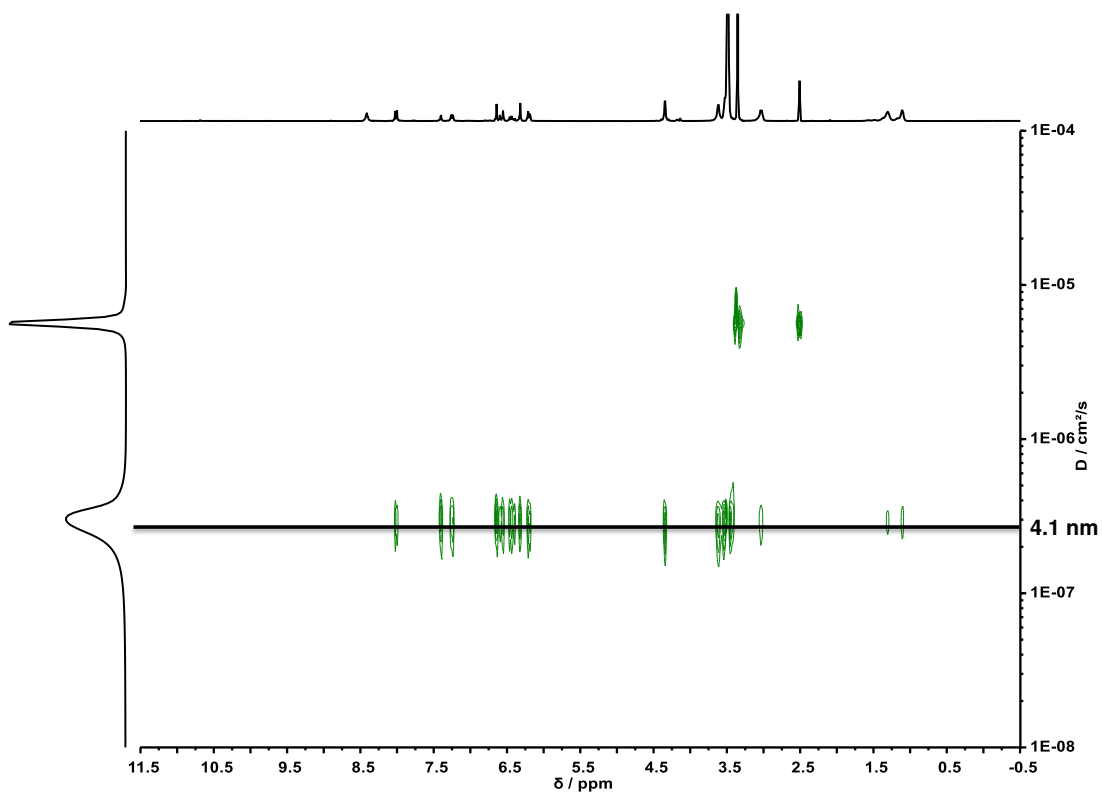
Fig. D 28 DOSY NMR of **19a** with a diffusion time (Δ) of 0.75 s and a gradient duration (δ) of 1500 μs.

CXL
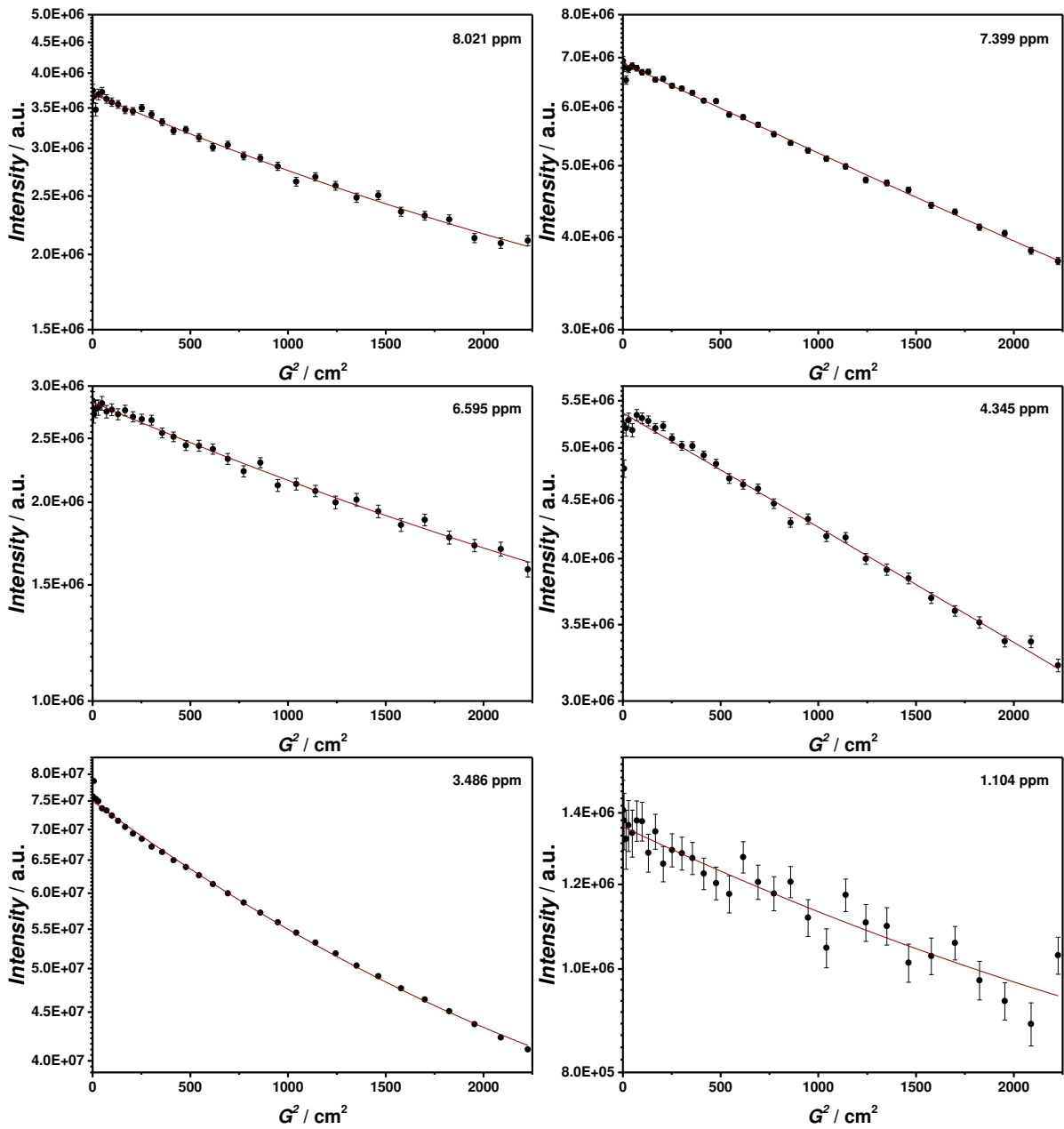
Fig. D 29 Echo intensity plotted against the gradient strength (G^2) to evaluate diffusion coefficients of **19a**. Parameter were as follows: diffusion time (Δ) of 0.75 s, gradient duration (δ) of 1500 µs, 400 MHz.
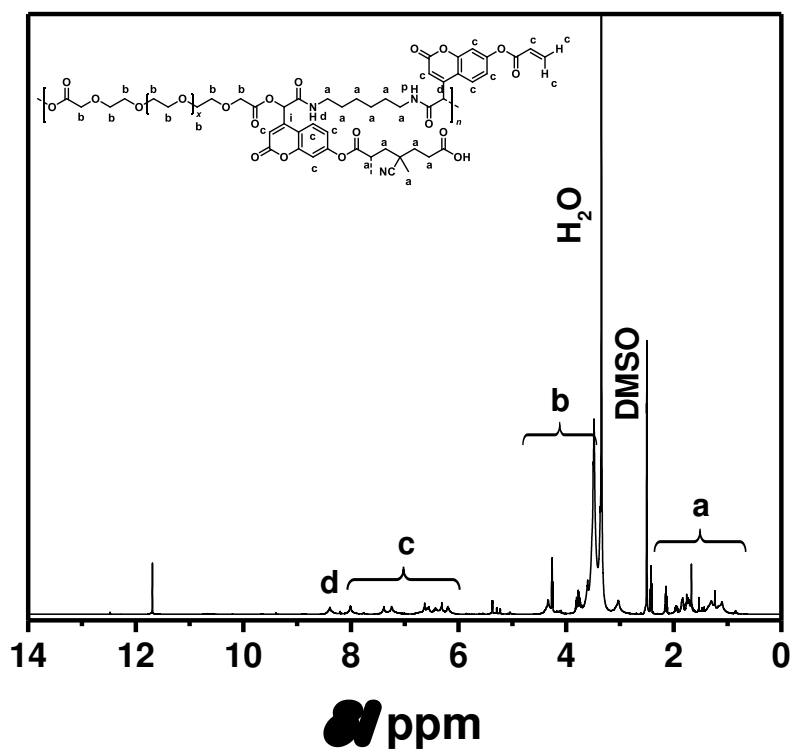
Fig. D 30 ^{1}H NMR (298 K, 600 MHz) of **20a** in DMSO-d$_6$.
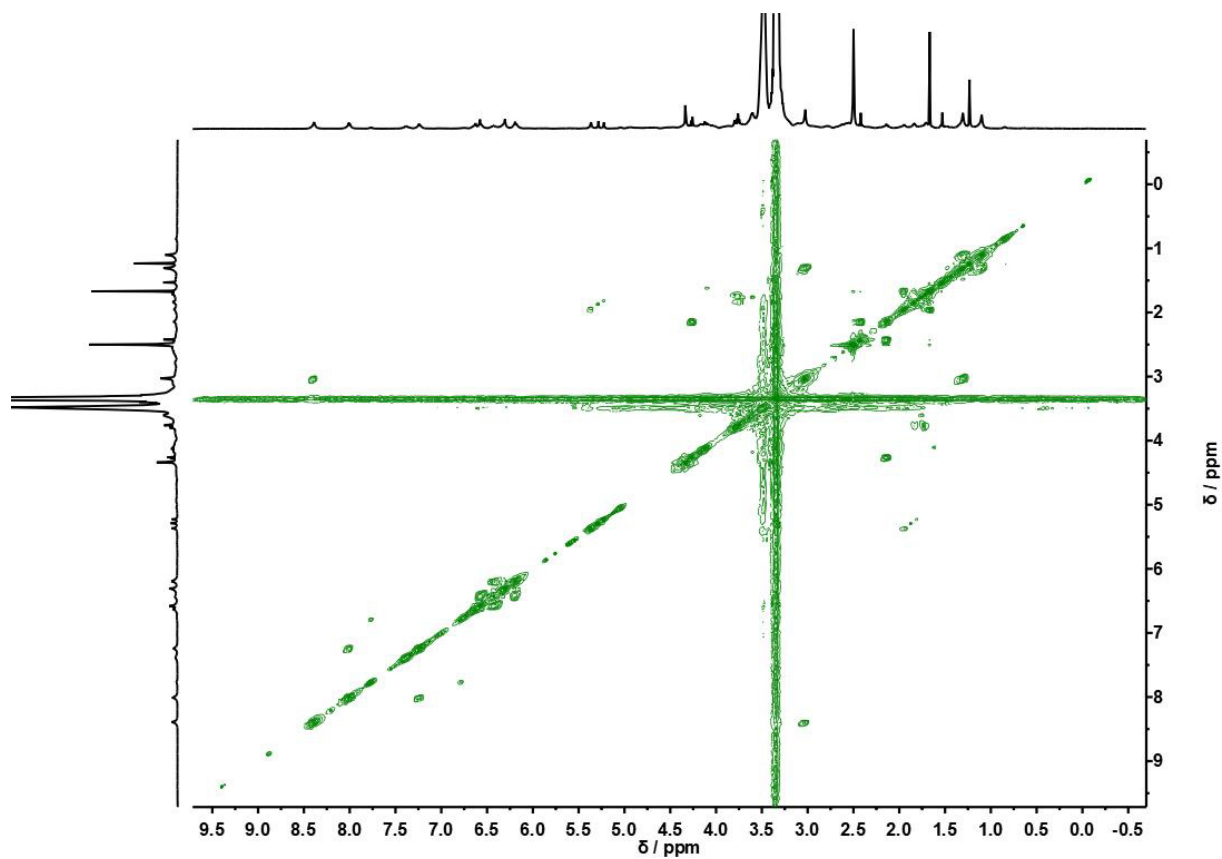
Fig. D 31 COSY NMR (^{1}H-^{1}H, 298 K, 600 MHz) of **20a** in DMSO-d$_6$.

CXLII
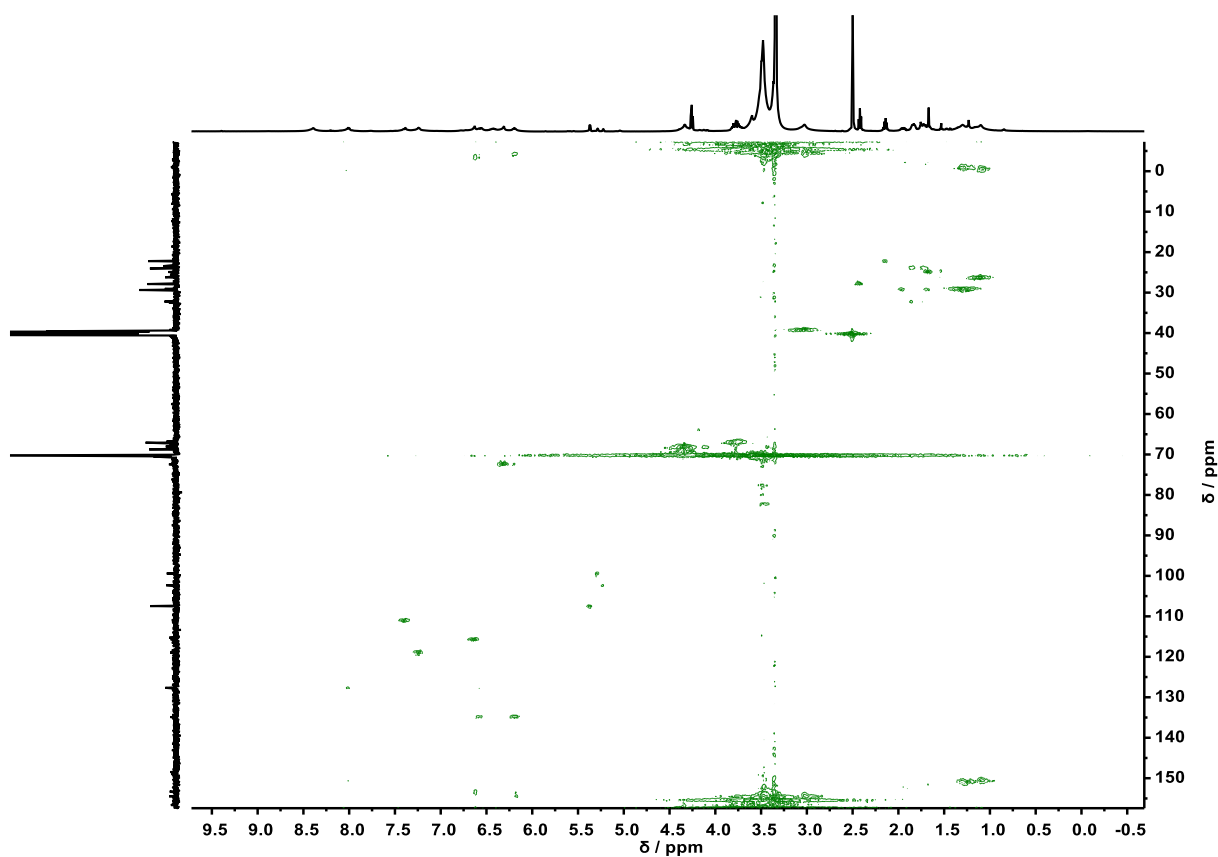
Fig. D 32 HSQC NMR (^{1}H-^{13}C, 298 K) of **20a** in DMSO-d$_6$.
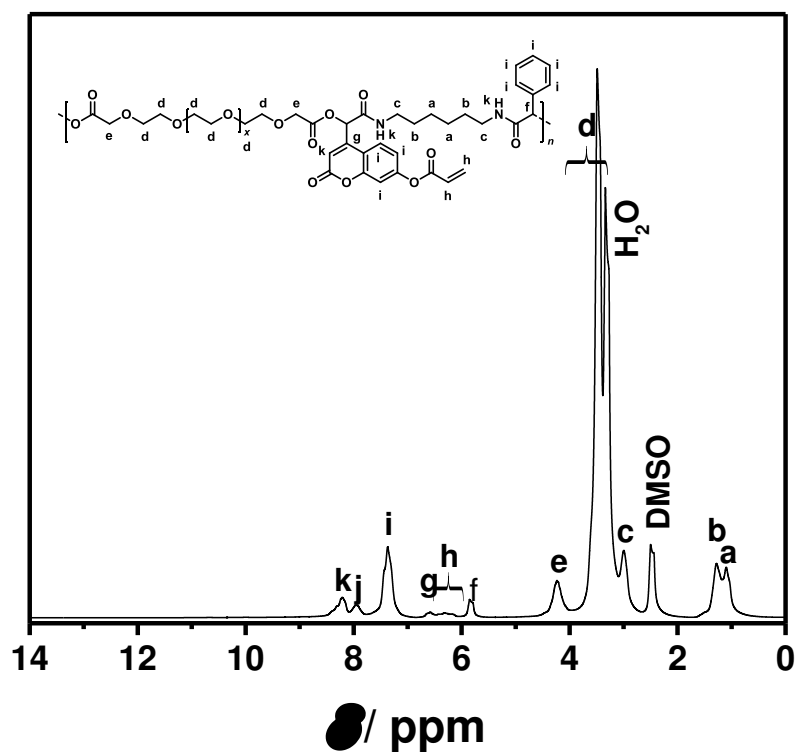
Fig. D 33 ^{1}H NMR (298 K, 600 MHz) of **19b** in DMSO-d$_6$.
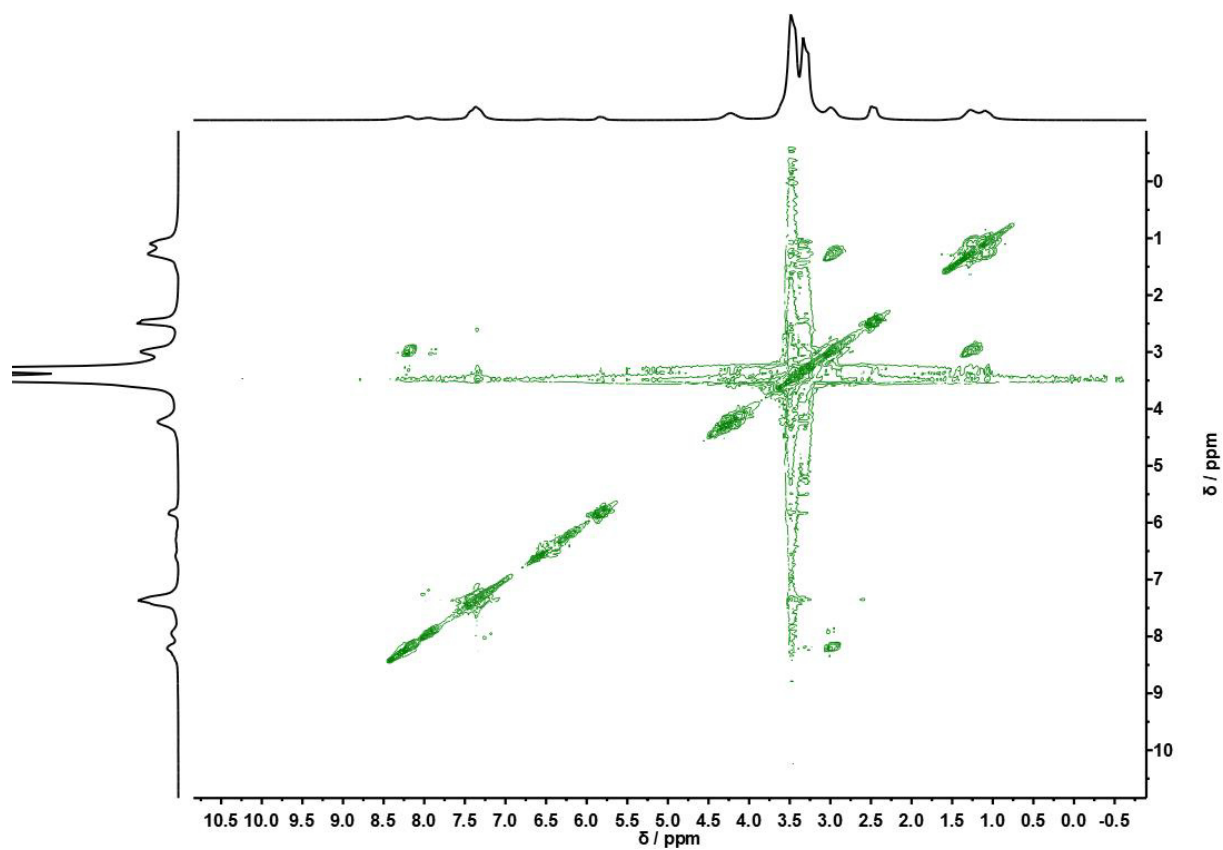
Fig. D 34 COSY NMR (^{1}H-^{1}H, 298 K, 600 MHz) of **19b** in DMSO-d$_6$.
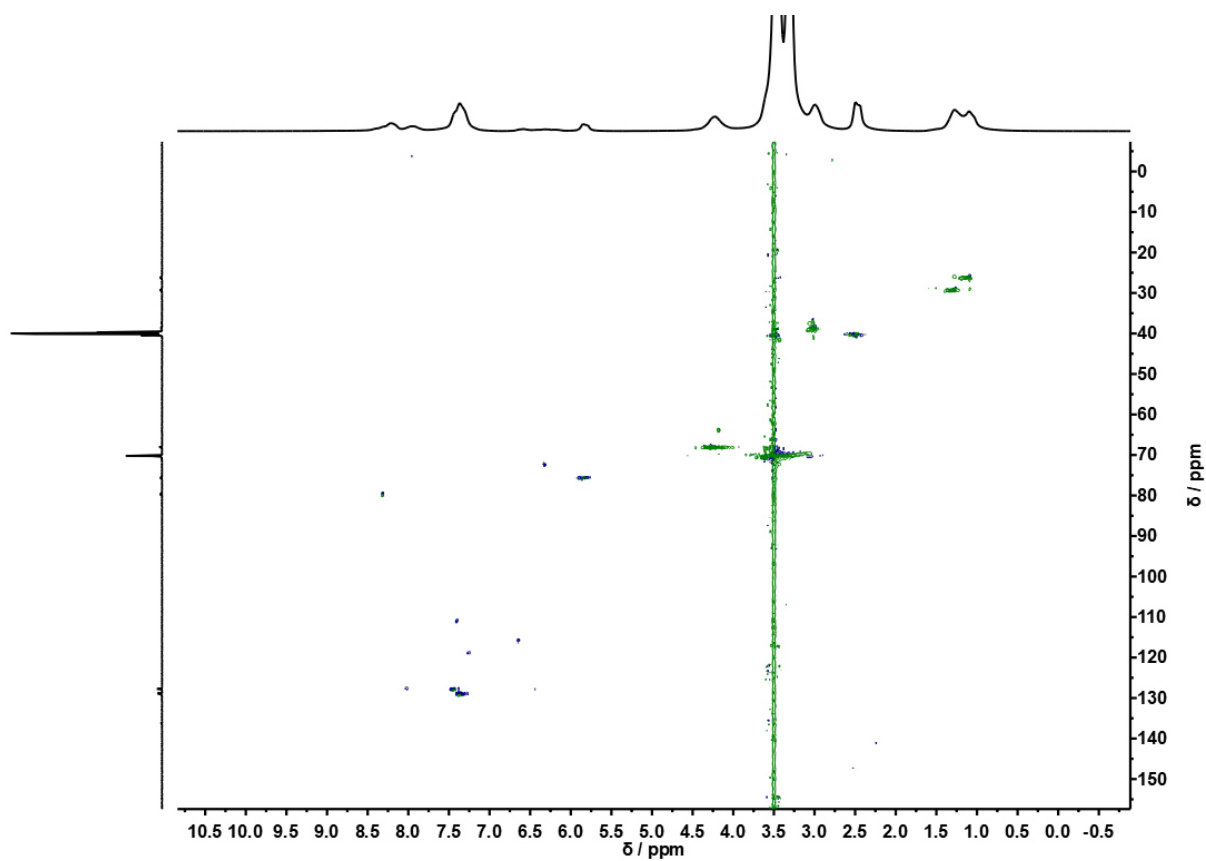
Fig. D 35 HSQC NMR (^{1}H-^{13}C, 298 K) of **19b** in DMSO-d$_6$.
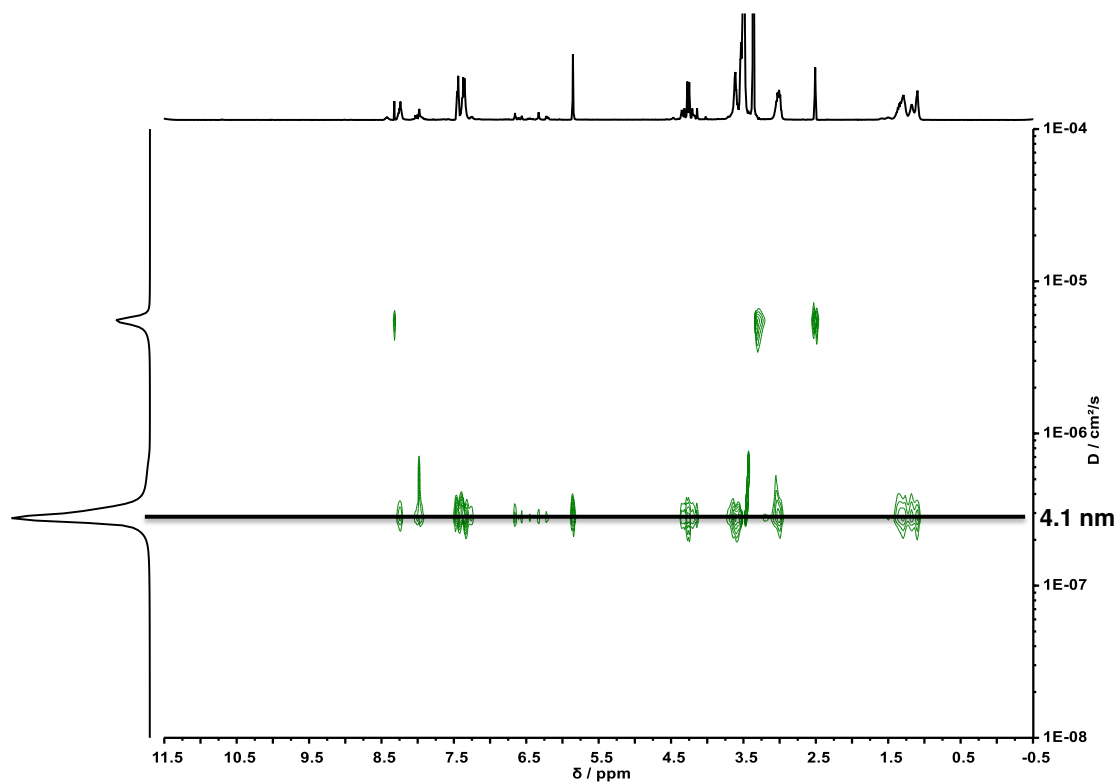
Fig. D 36 DOSY NMR of **19b** with a diffusion time (Δ) of 0.60 s and a gradient duration (δ) of 1500 µs.
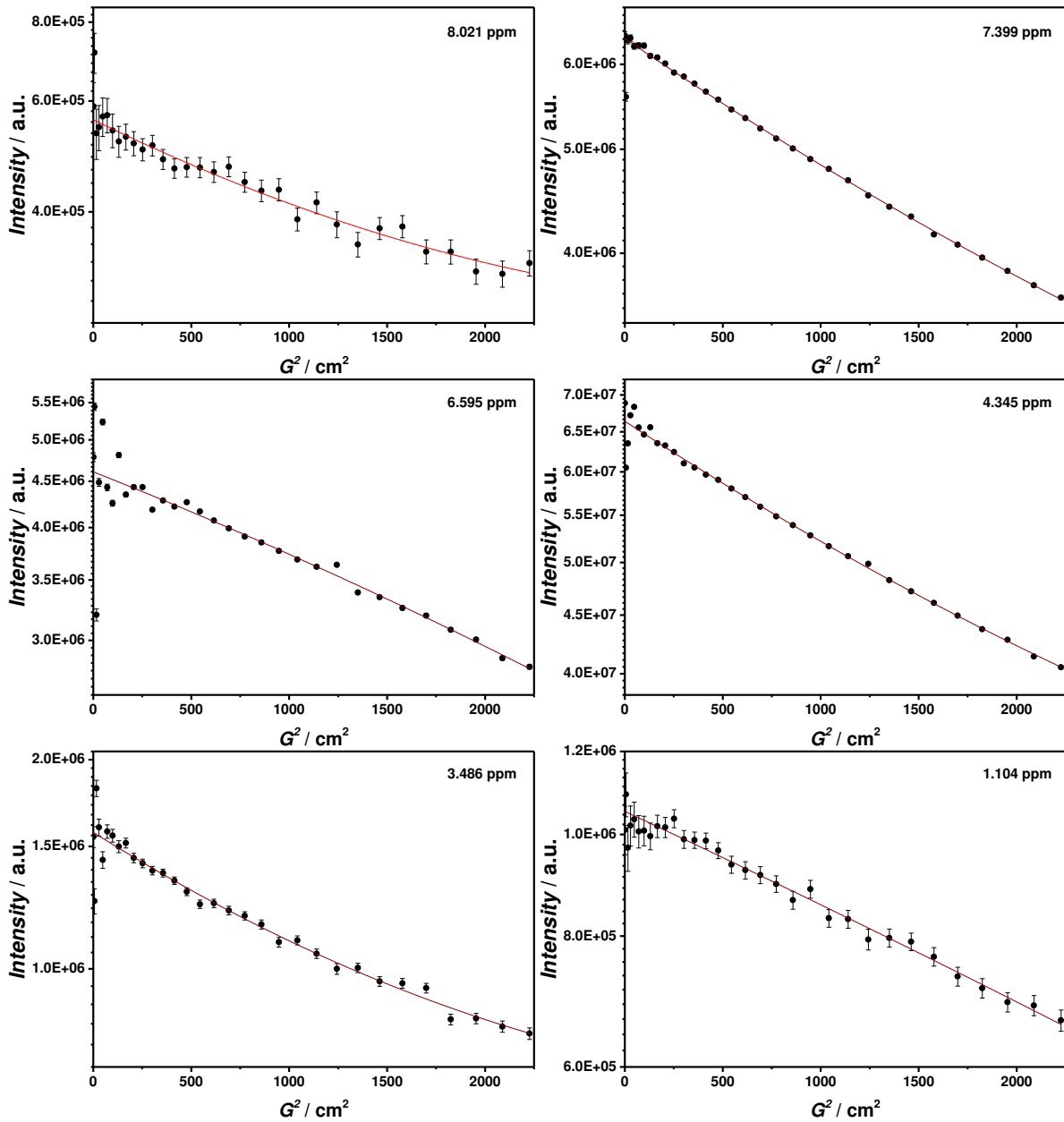
Fig. D 37 Echo intensity plotted against the gradient strength (G^2) to evaluate diffusion coefficients of P2. Parameter were as follows: diffusion time (Δ) of 0.60 s, gradient duration (δ) of 1500 µs, 400 MHz.
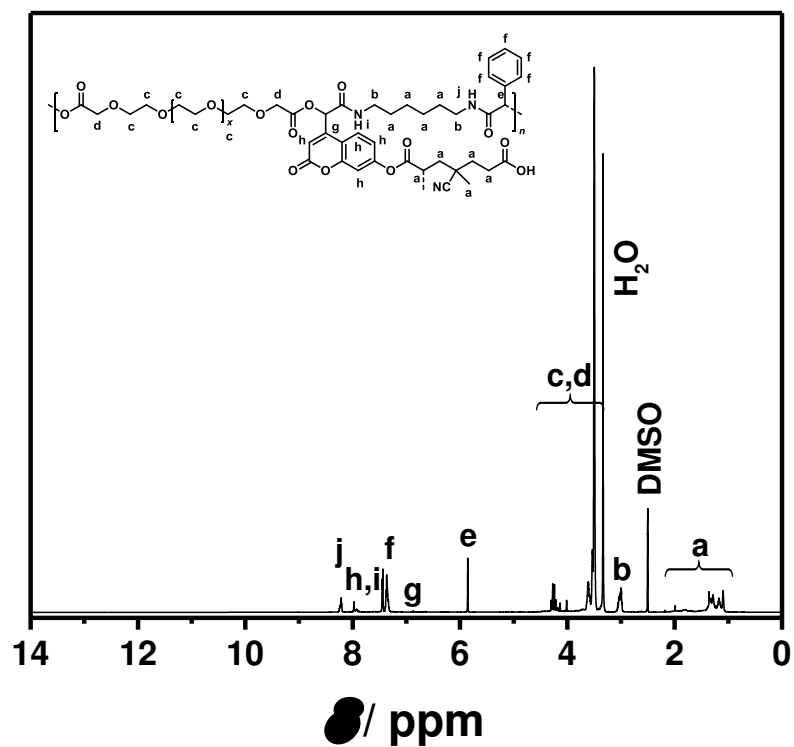
Fig. D 38 ^{1}H NMR (298 K, 600 MHz) of **20b** in DMSO-d$_6$.
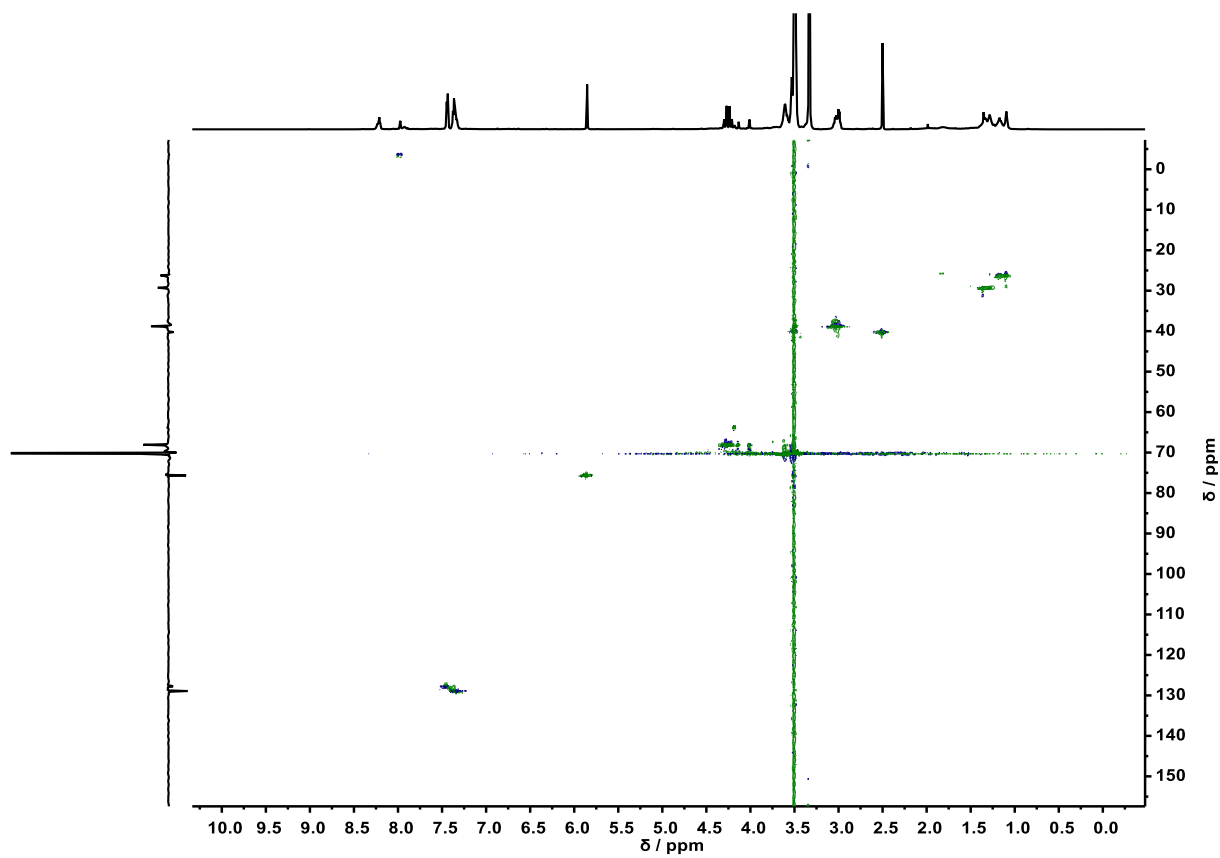
Fig. D 39 HSQC NMR (^{1}H-^{13}C, 298 K) of **20b** in DMSO-d$_6$.
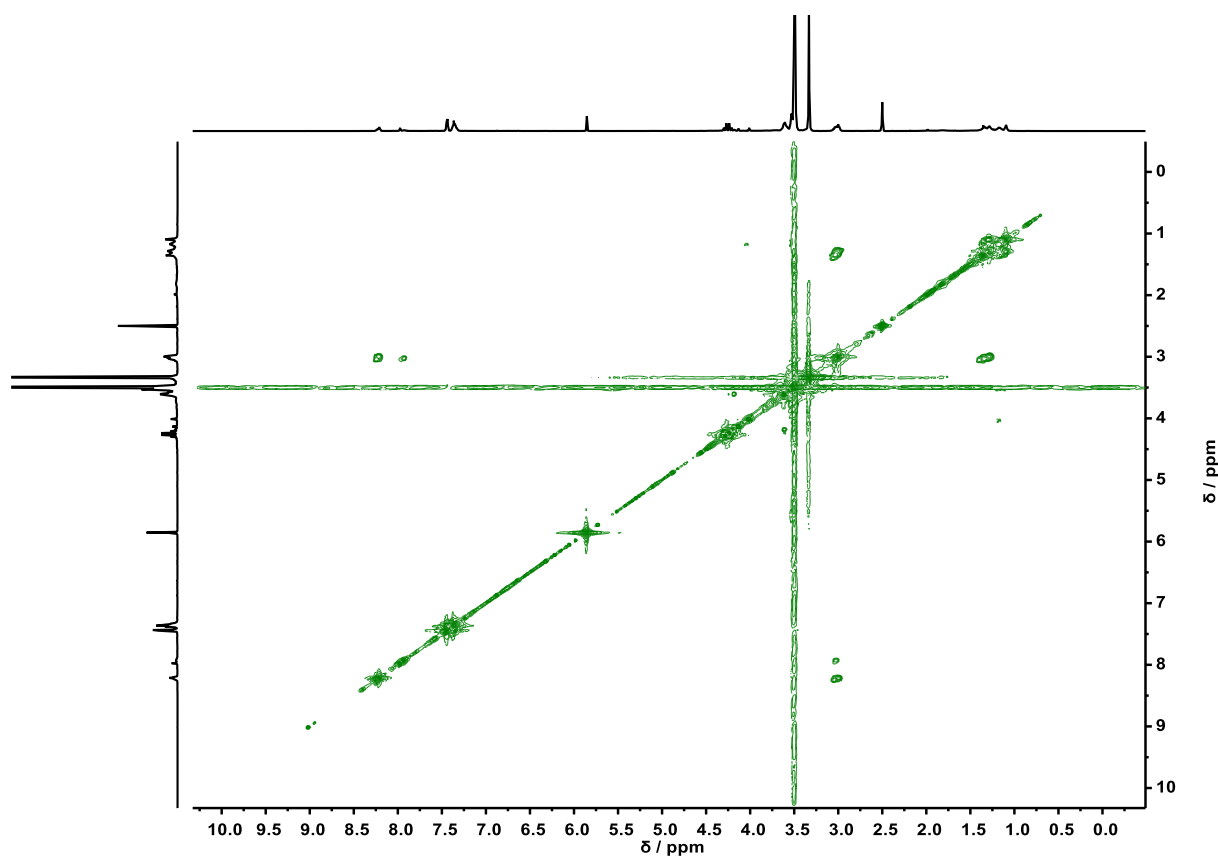
Fig. D 40 COSY NMR (^{1}H-^{1}H, 298 K, 600 MHz) of **20b** in DMSO-d$_6$.
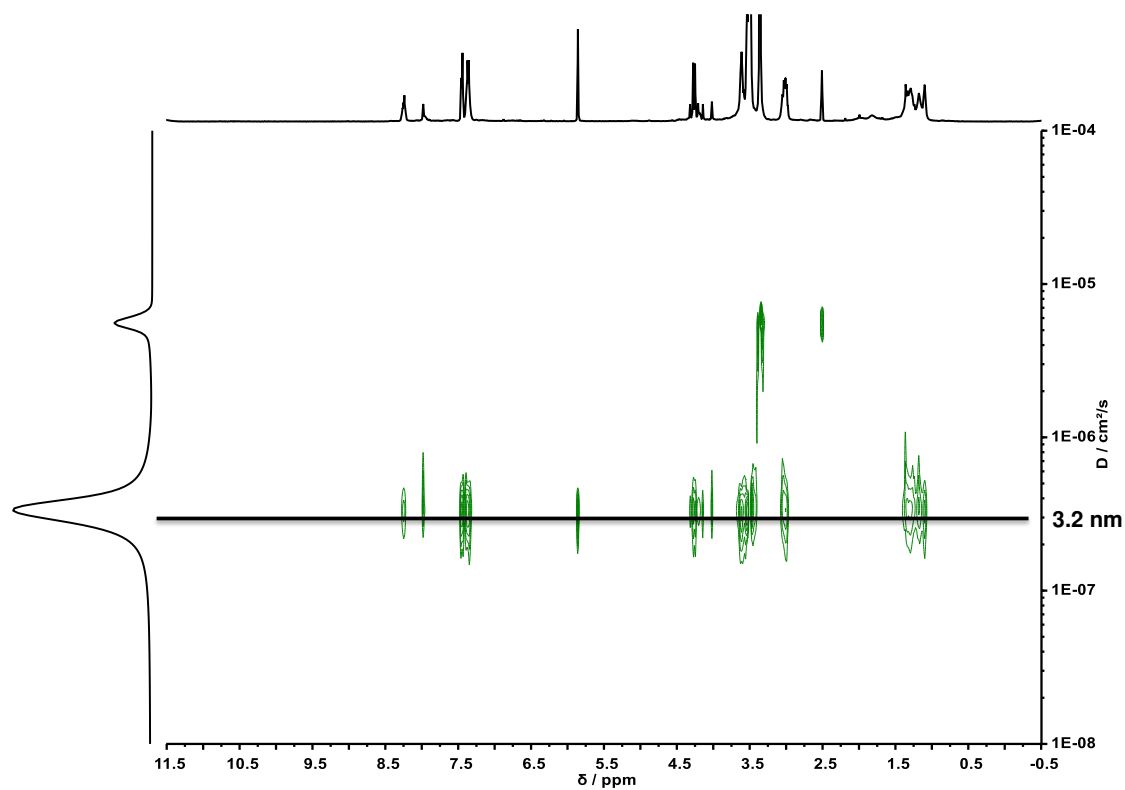
Fig. D 41 DOSY NMR of **20b** with a diffusion time (Δ) of 0.24 s and a gradient duration (δ) of 1500 μs.
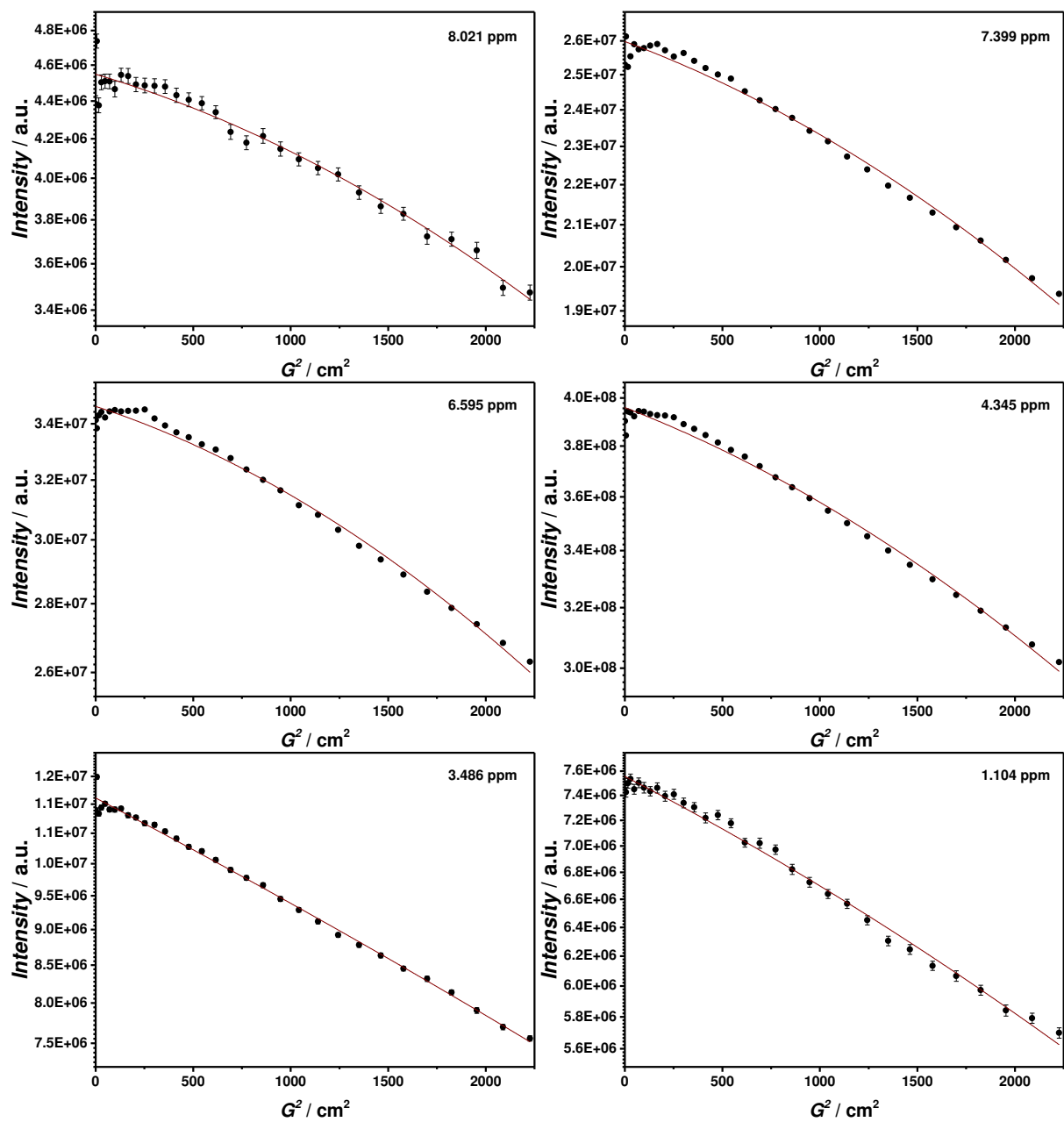
Fig. D 42 DOSY NMR of **20b** with a diffusion time (Δ) of 0.24 s and a gradient duration (δ) of 1500 µs.

Mass Spectrometric Results

Precursor 19a
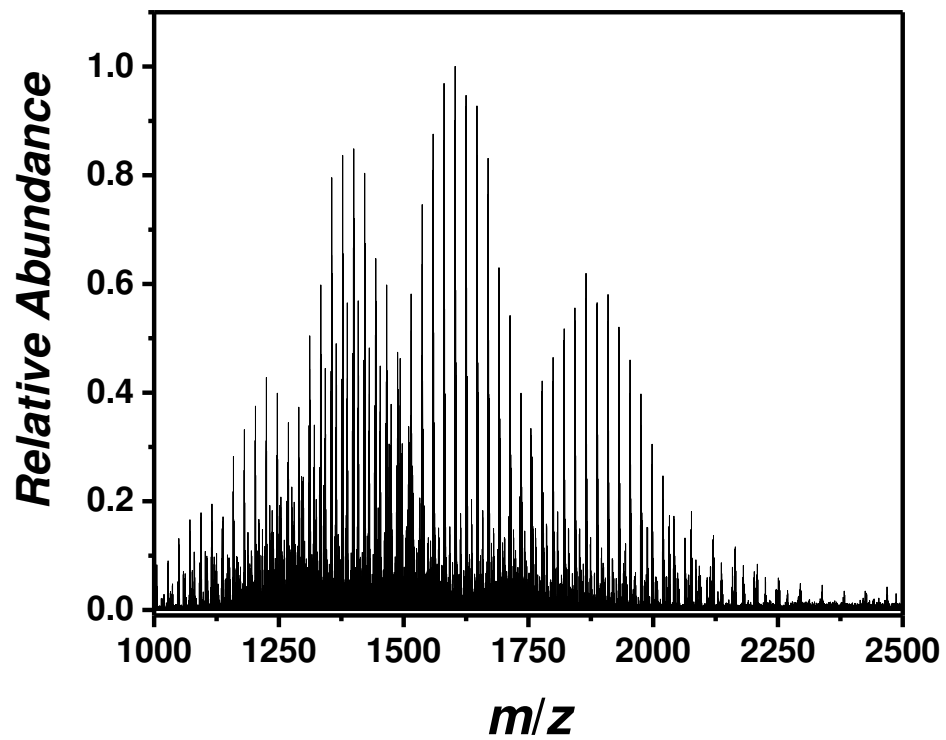
Fig. D 43 Overview SEC-ESI Orbitrap of **19a** between *m/z* 1000 and *m/z* 2500 obtained by summing all species between 16.98 mL and 17.92 mL retention volume.
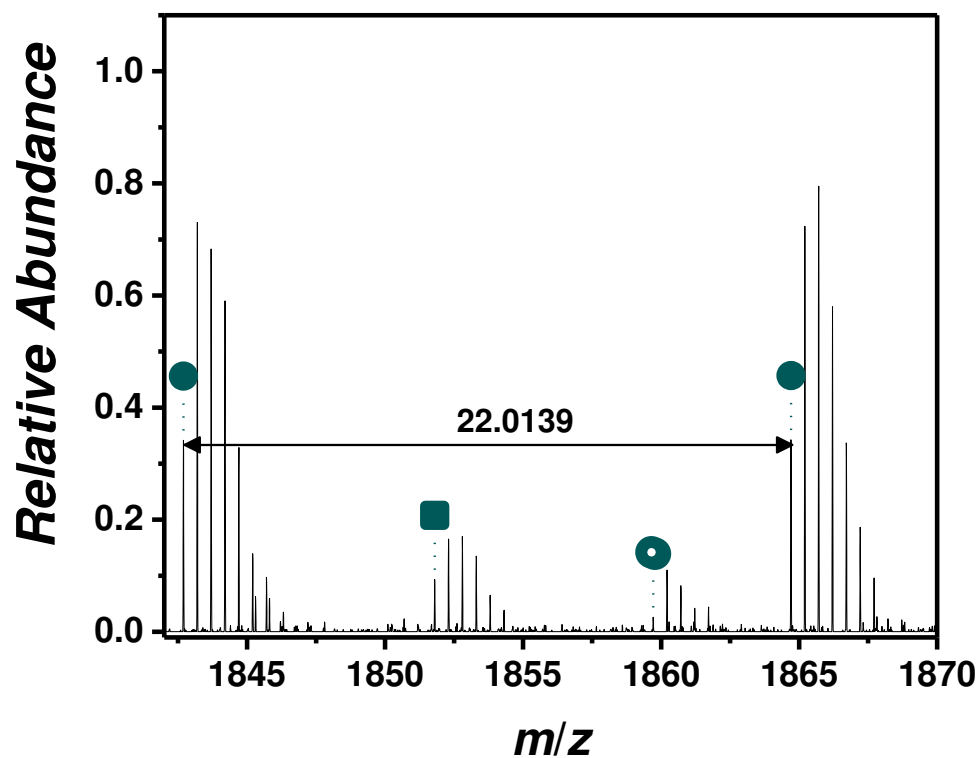
Fig. D 44 Expanded SEC-ESI Orbitrap mass spectrum (positive mode) of **19a** between 1842 *m/z* and 1870 *m/z* obtained by summing all species between 17.47 mL and 17.74 mL retention volume. Labeled are the most abundant species and the repeating unit of PEG (*m/z*(exp) 22.0139; *m/z*(theo) 22.0126).

Tab. D 3 Peak assignment of the SEC-ESI Orbitrap mass spectrum of **19a** showing the labels (corresponding to the species in Fig. D 44 Expanded SEC-ESI Orbitrap mass spectrum (positive mode) of **19a** between 1842 m/z and 1870 m/z obtained by summing all species between 17.47 mL and 17.74 mL retention volume. Labeled are the most abundant species and the repeating unit of PEG (m/z(exp) 22.0139; m/z(theo) 22.0126).), the resolution (obtained by the Xcalibur software), the experimental m/z and theoretical m/z values, $\Delta m/z$ and the proposed chemical structures. The SEC-ESI Orbitrap mass spectrum was integrated from 17.47 mL and 17.74 mL to obtain a sufficient signal to noise ratio.

Label	Resolution	m/z(exp)	m/z(theo)	$\Delta m/z$	Structure
●	90000	1842.6967	1842.6894	0.0073	
■	90000	1851.8015	1851.8092	0.0077	
○	86000	1859.7157	1859.7106	0.0051	

CLII
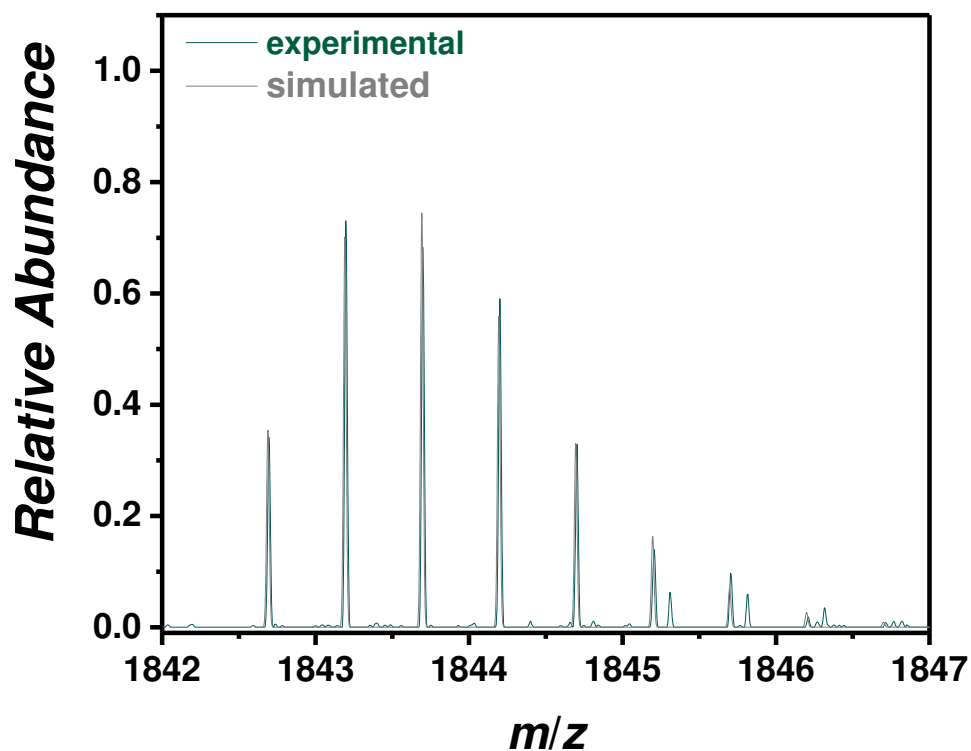
Fig. D 45 Isotopic simulation of a selected peak at 1842 *m/z* comparing the experiment (blue line) and the simulation (grey line) of **19a** with a resolution of 90000.
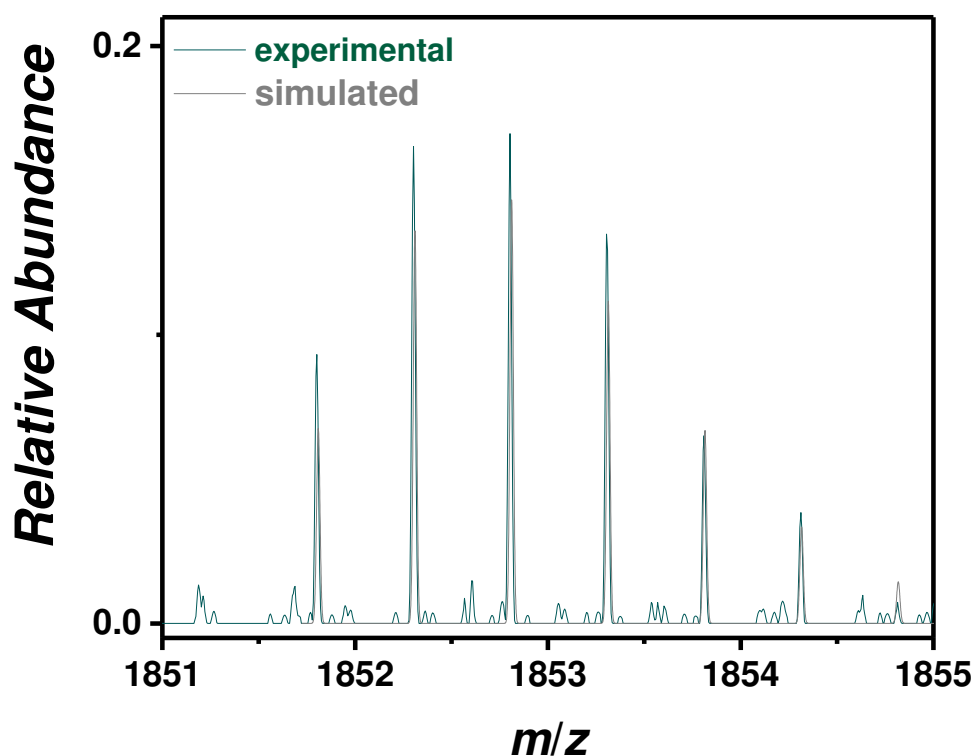
Fig. D 46 Isotopic simulation of a selected peak at 1851 *m/z* comparing the experiment (blue line) and the simulation (grey line) of **19a** with a resolution of 90000.
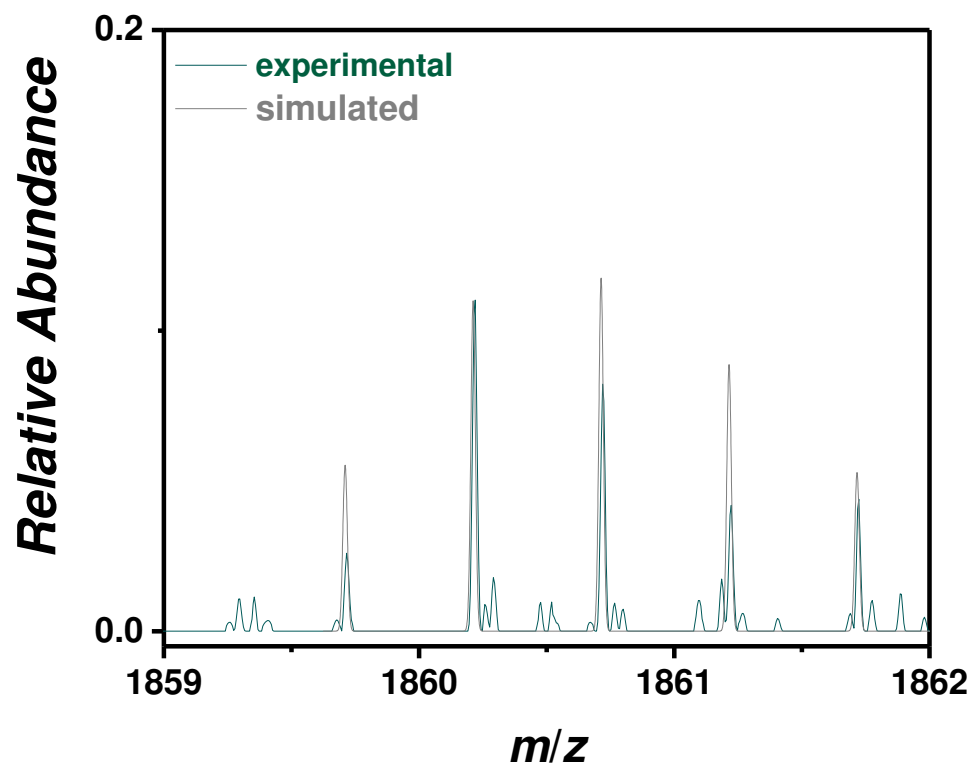
Fig. D 47 Isotopic simulation of a selected peak at 1859 *m/z* comparing the experiment (blue line) and the simulation (grey line) of **19a** with a resolution of 86000.

SCNP 20a
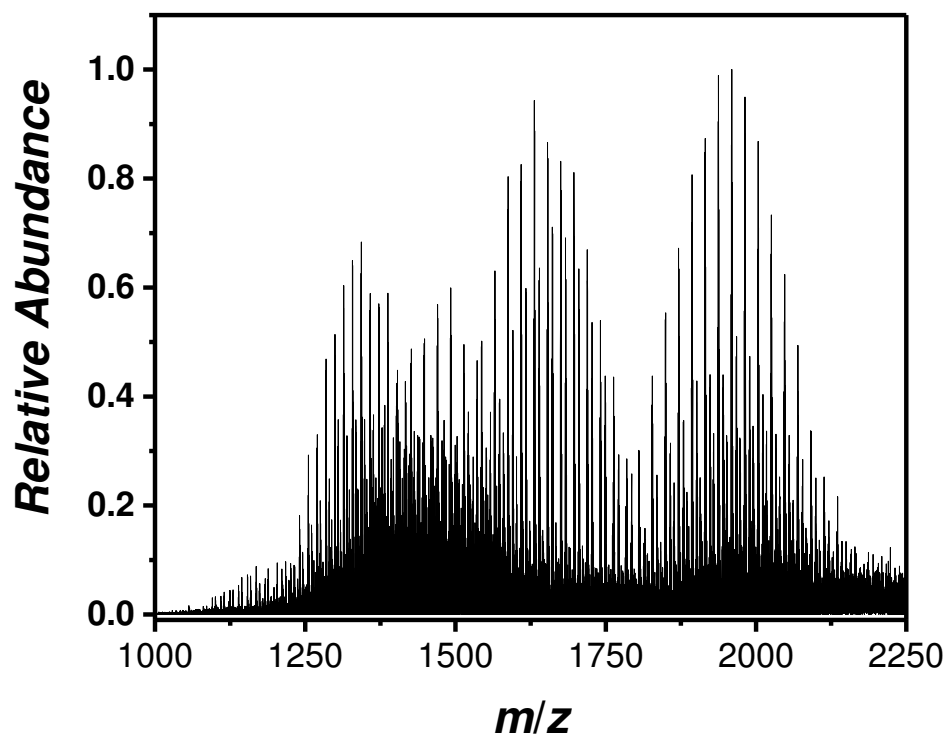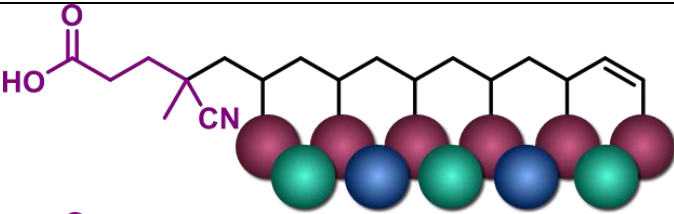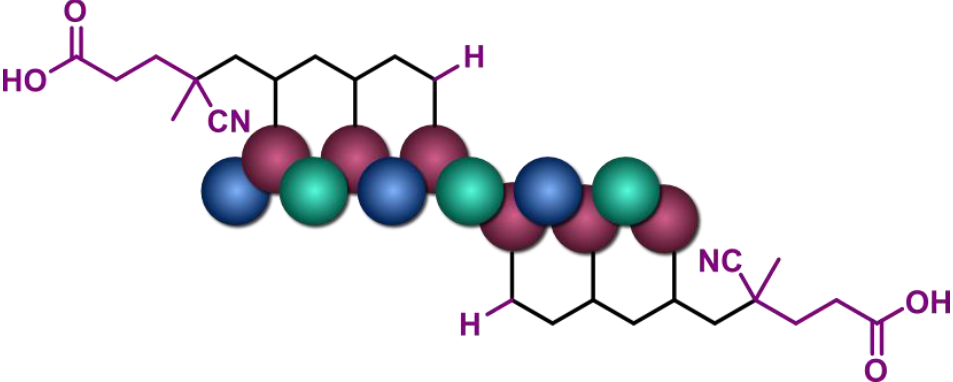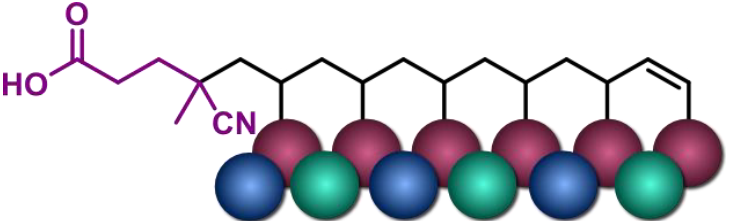
Fig. D 48 Overview SEC-ESI Orbitrap of SCNP **20a** between 1000 *m/z* and 2250 *m/z* obtained by summing all species between 17.80 mL and 18.10 mL retention volume.

Tab. D 4 Peak assignment of the SEC-ESI Orbitrap mass spectrum of SCNP **20a** showing the label, the resolution (obtained by the Xcalibur software), the experimental m/z and theoretical m/z values, $\Delta m/z$ and the proposed structures. The SEC-ESI Orbitrap mass spectrum was integrated from 17.91 mL to 18.08 mL to obtain sufficient signal to noise ratio. All species are triply charged by adduct formation with H⁺.

Label	Resolution	m/z(exp)	m/z(theo)	$\Delta m/z$	Structure
●	120000	1313.1832	1313.1845	0.0013	
○	100000	1313.5250	1313.5198	0.0053	
⊗	100000	1314.5249	1314.5248	0.0001	

CLVI

■	111000	1318.1782	1318.1753	0.0029
□	99000	1318.8509	1318.8501	0.0008
◆	116000	1322.5358	1322.5408	0.0050

CLVII
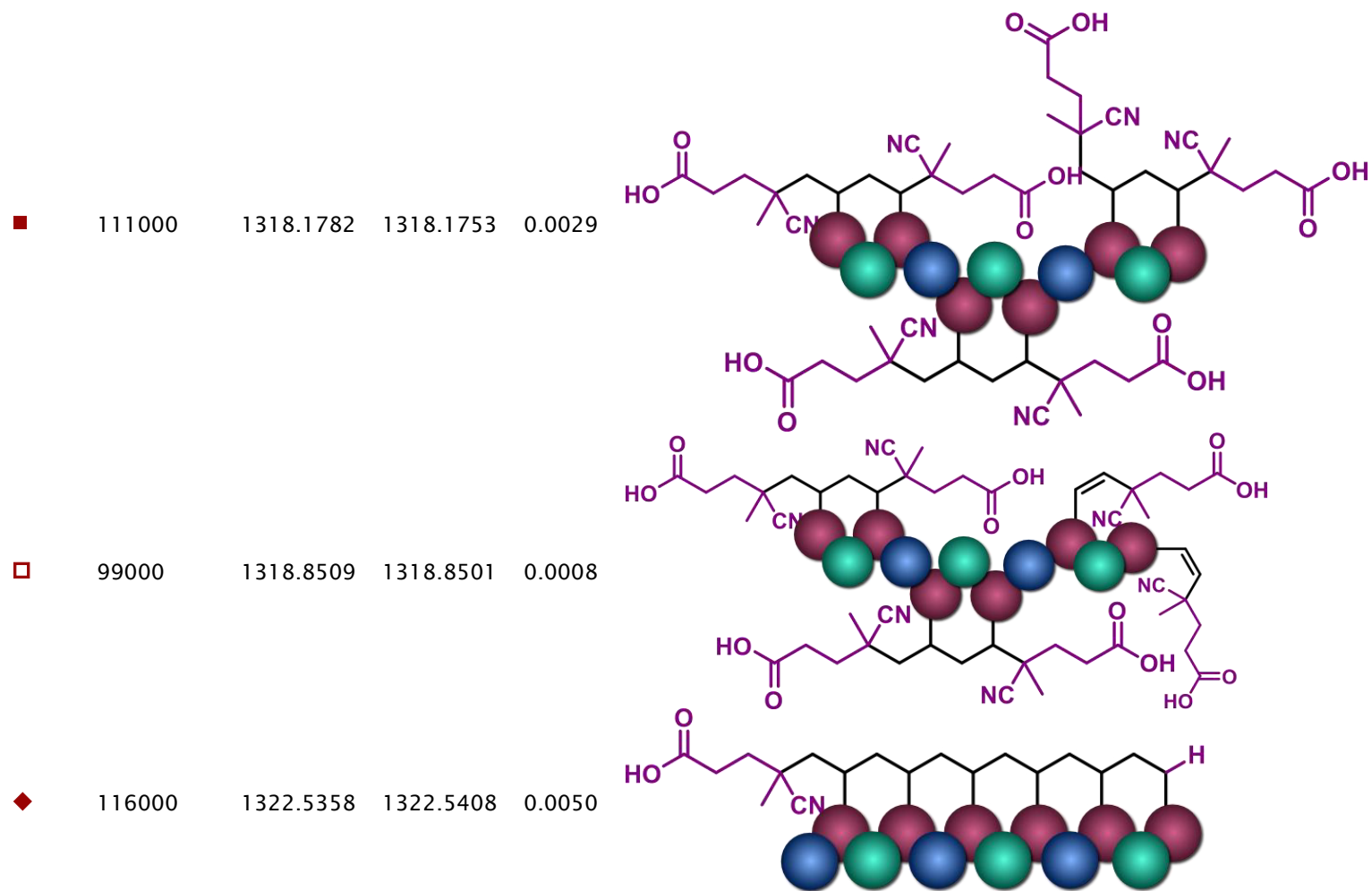
Tab. D 5 Peak assignment of the SEC-ESI Orbitrap mass spectrum of SCNP1 showing the label, the resolution (obtained by the Xcalibur software), the experimental m/z and theoretical m/z values, $\Delta m/z$ and the proposed structures. The SEC-ESI Orbitrap mass spectrum was integrated from 17.79 mL to 18.28 mL to obtain sufficient signal to noise ratio. All species are doubly charged by adduct formation with H^{+}.

Label	Resolution	m/z(exp)	m/z(theo)	$\Delta m/z$	Structure
①	40000	1935.2852	1935.2914	0.0062	
②	45000	1936.7732	1936.7737	0.0005	
③	43000	1938.7818	1938.7774	0.0044	

CLVIII

④   42000   1944.7704   1944.7662   0.0042

⑤   44000   1947.2844   1947.2857   0.0013

⑥   44000   1950.7933   1950.7999   0.0066

CLIX
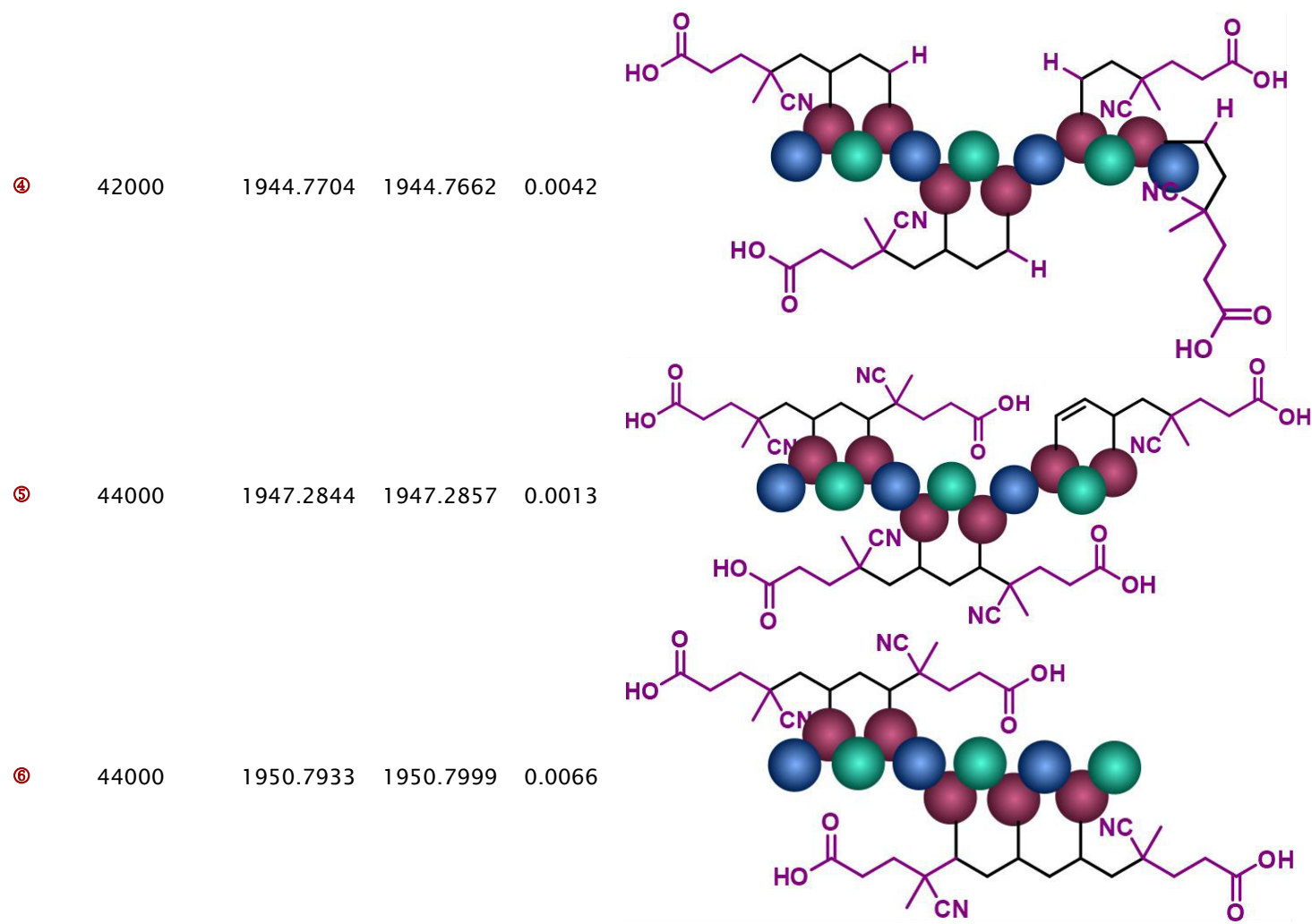
⑦ 41000 1952.2940 1952.2997 0.0057
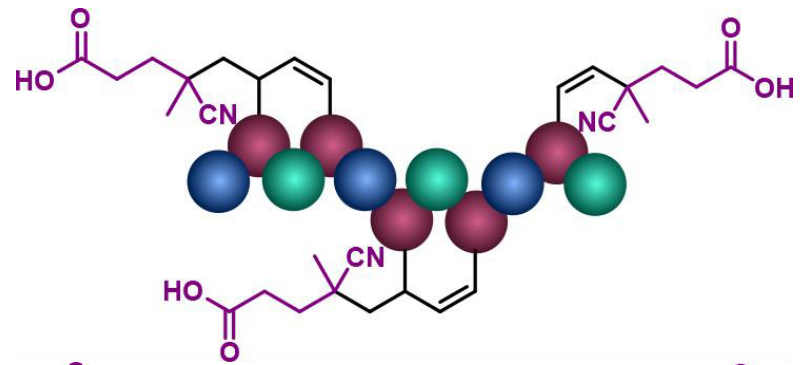
⑧ 36000 1953.2923 1953.2970 0.0047
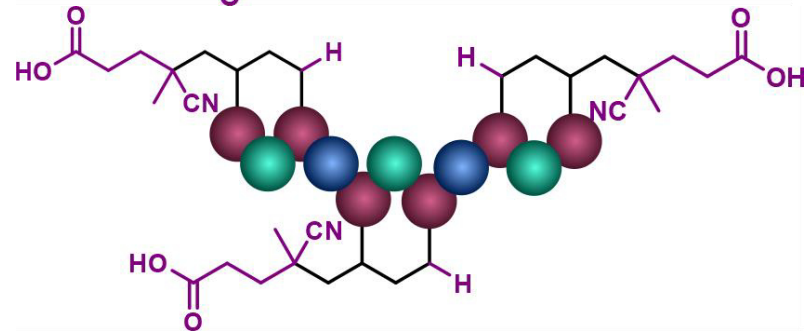
⑨ 37600 1956.2948 1956.2897 0.0051
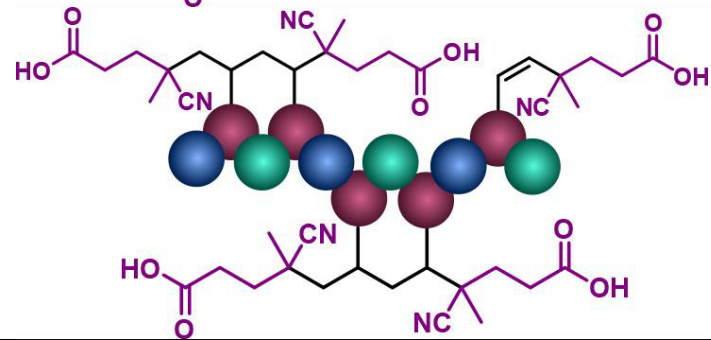
CLX
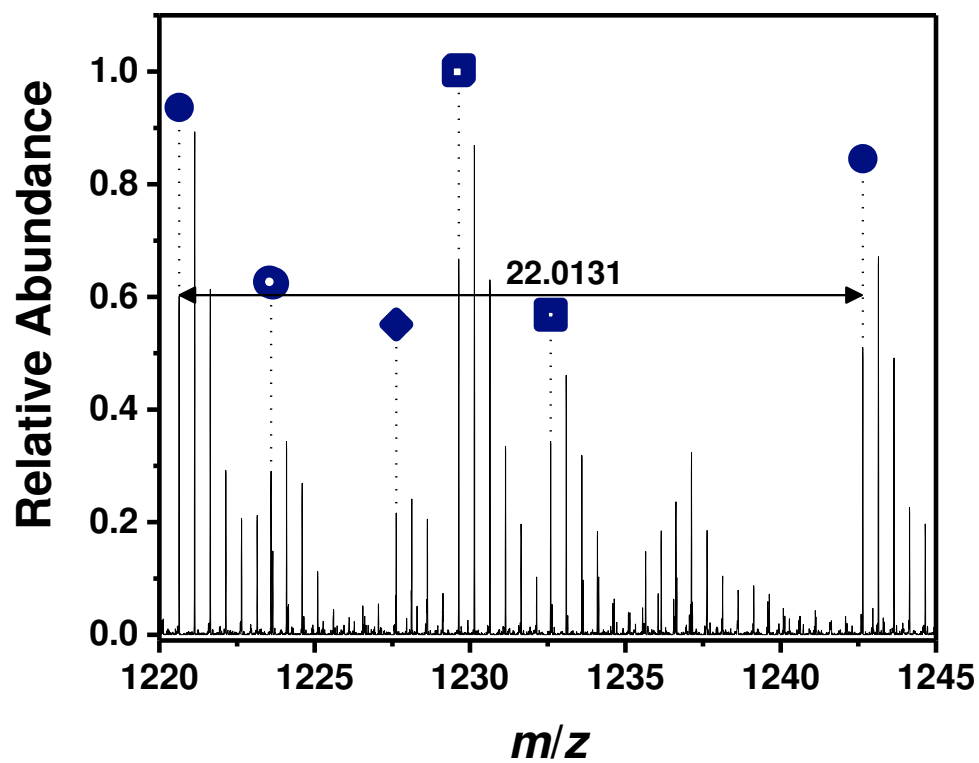
Fig. D 49 Expanded SEC-ESI Orbitrap mass spectrum (positive ion mode) of **P1** between 1842 *m/z* and 1870 *m/z* obtained by summing all species between 17.47 mL and 17.74 mL retention volume. Labeled are the most abundant species and the repeating unit of PEG (*m/z*(exp) 22.0139; *m/z*(theo) 22.0126).

Tab. D 6 Peak assignment of the SEC-ESI Orbitrap mass spectrum of **19b** showing the labels (corresponding to the species in Fig. D 49), the resolution (obtained by the Xcalibur software), the experimental *m/z* and theoretical *m/z* values, Δ*m/z* and the proposed chemical structures. The SEC-ESI Orbitrap mass spectrum was integrated from 17.47 mL and 17.74 mL to obtain a sufficient signal to noise ratio.

Label	Resolution	*m/z*(exp)	*m/z*(theo)	Δ*m/z*	Structure
●	110000	1220.6363	1220.6299	0.0064	
◐	110000	1223.5951	1223.5883	0.0069	
❖	110000	1227.6274	1227.6245	0.0029	

CLXII

□ 110000   1229.6419   1229.6352   0.0067

□ 110000   1232.6005   1232.5985   0.0020

CLXIII
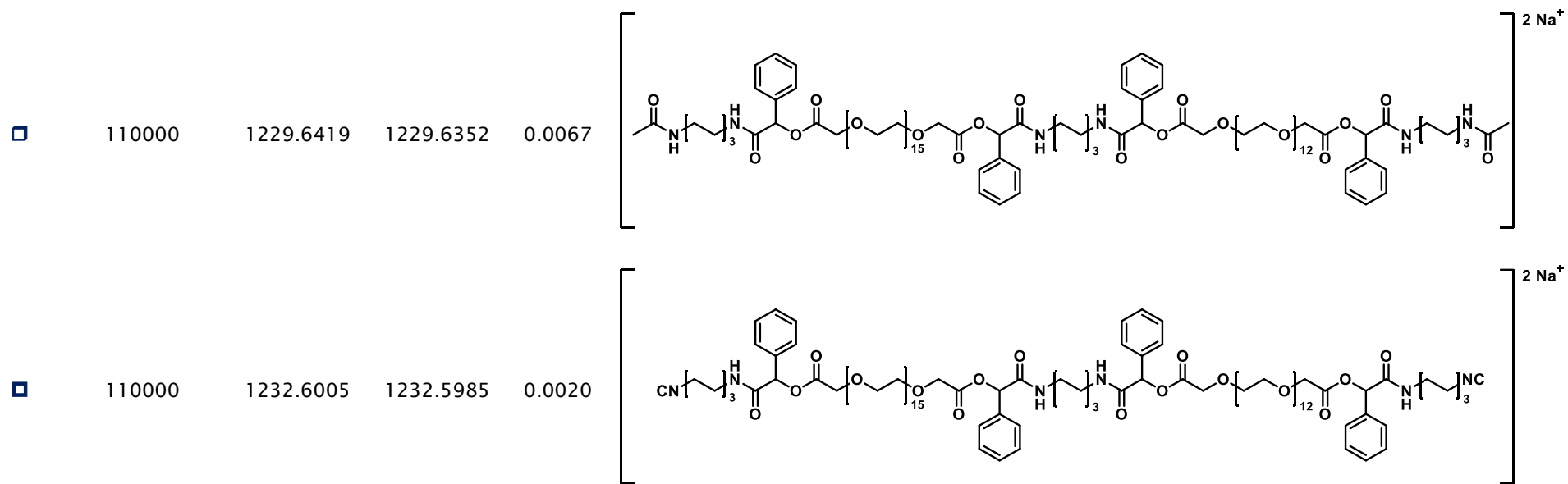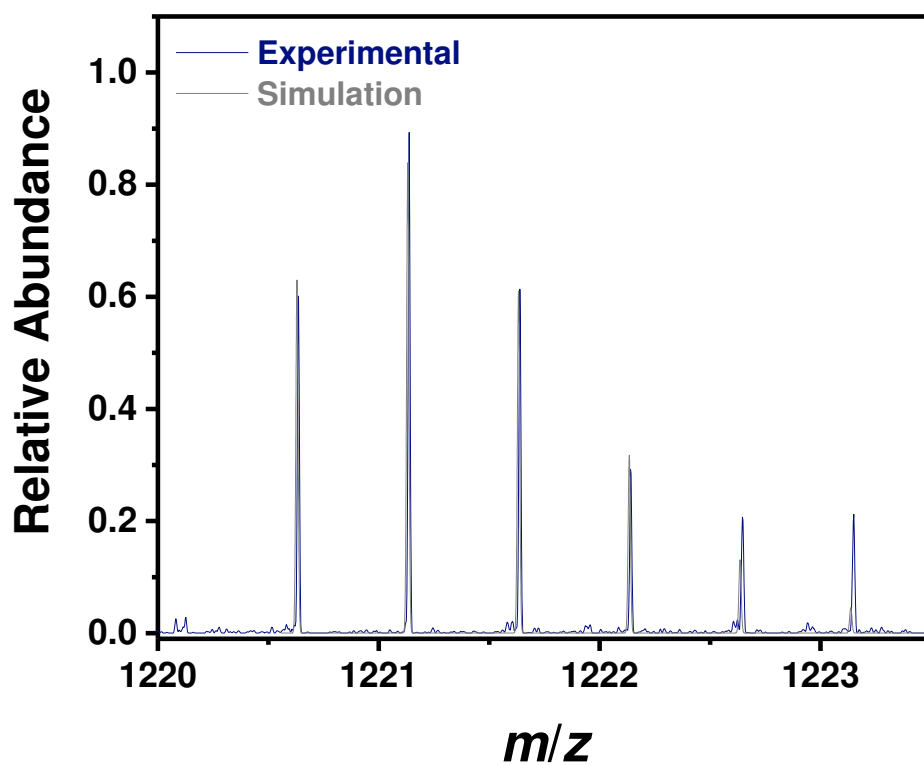
Fig. D 50 Isotopic simulation of a selected peak at 1220 *m/z* comparing the experiment (blue line) and the simulation (grey line) of **19b** with a resolution of 110000.
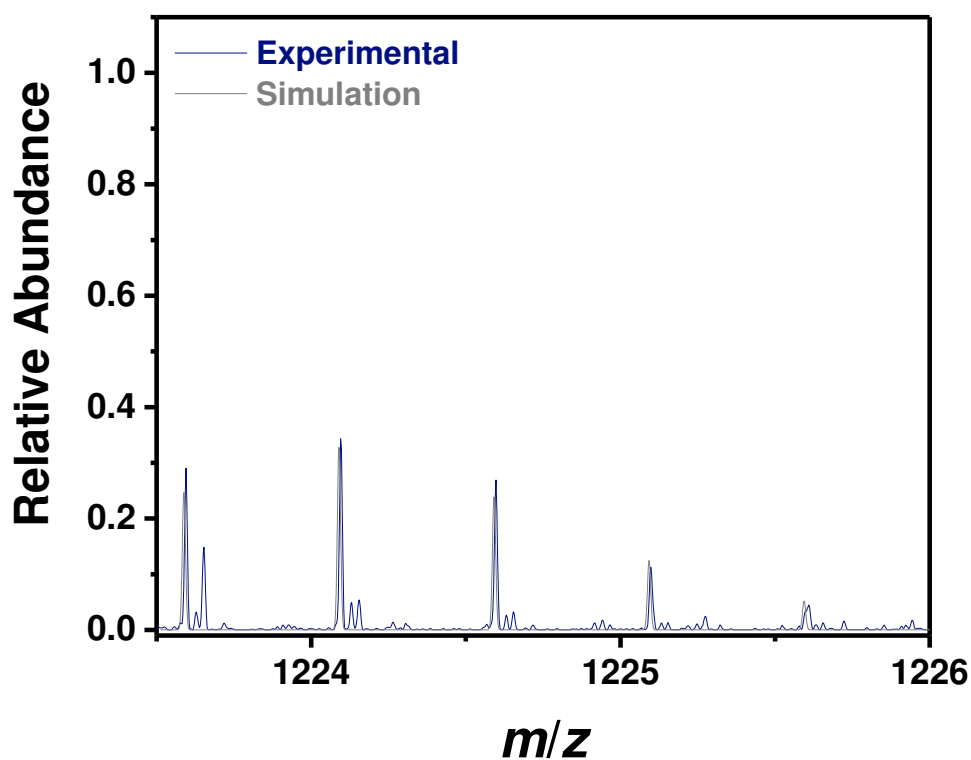

Fig. D 51 Isotopic simulation of a selected peak at 1223 *m/z* comparing the experiment (blue line) and the simulation (grey line) of **19b** with a resolution of 110000.
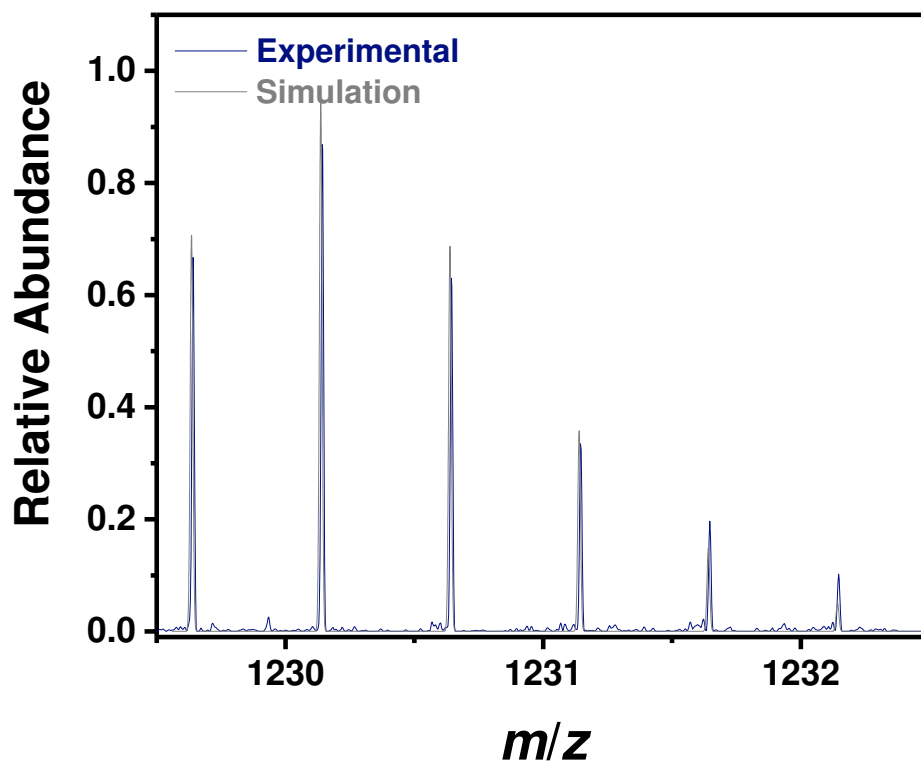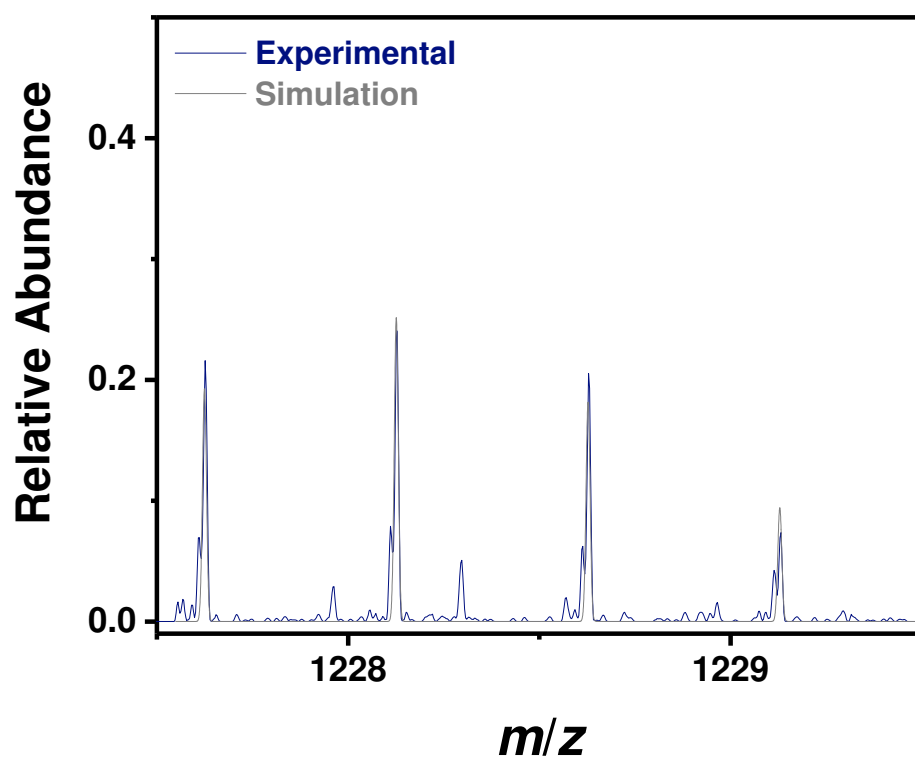
Fig. D 53 Isotopic simulation of a selected peak at 1229 *m/z* comparing the experiment (blue line) and the simulation (grey line) of **19b** with a resolution of 110000.

Fig. D 52 Isotopic simulation of a selected peak at 1227 *m/z* comparing the experiment (blue line) and the simulation (grey line) of **19b** with a resolution of 110000.
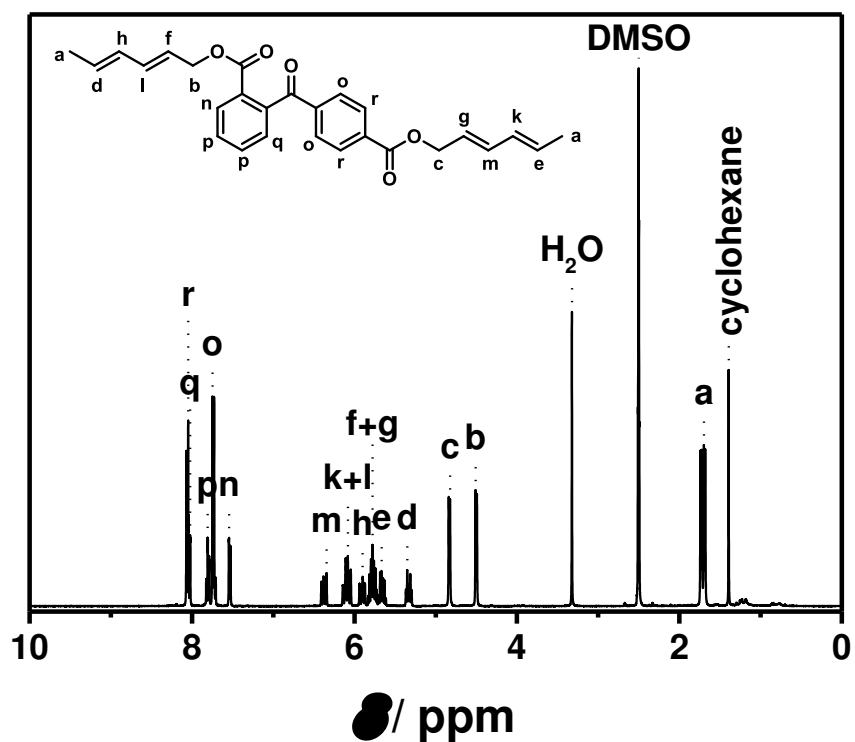
E

APPENDIX

NMR ANALYSIS

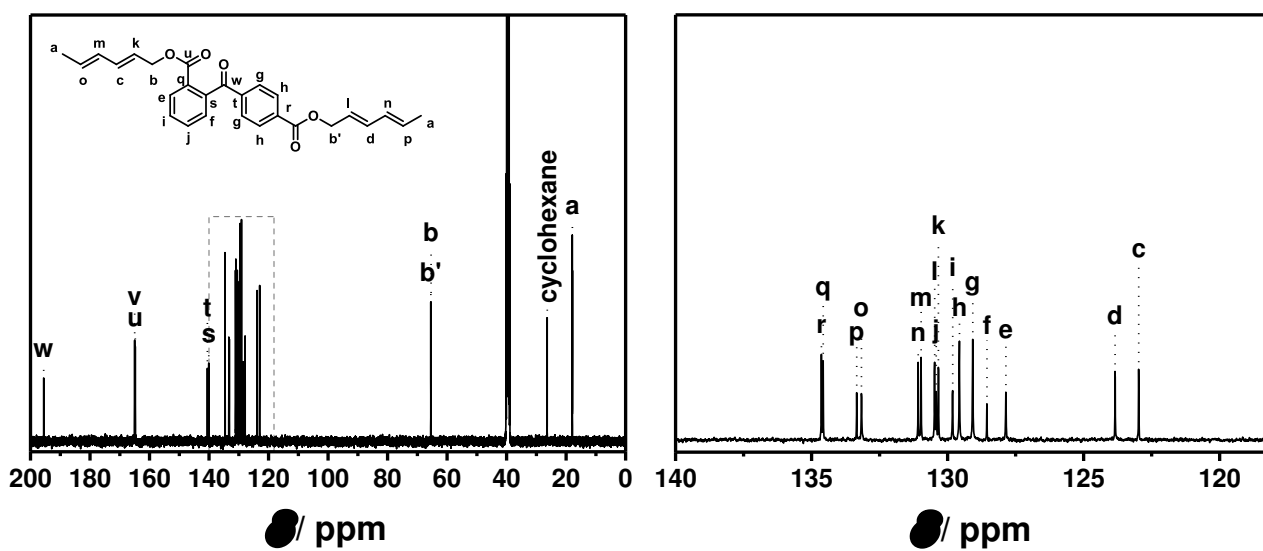Fig. E 1 ¹H NMR (400 MHz, 298 K) spectrum of monomer (**21a**) in DMSO-d$_6$.

Fig. E 2 ¹³C{¹H} NMR (101 MHz, 298 K) spectrum of monomer (**21a**) in DMSO-d$_6$.
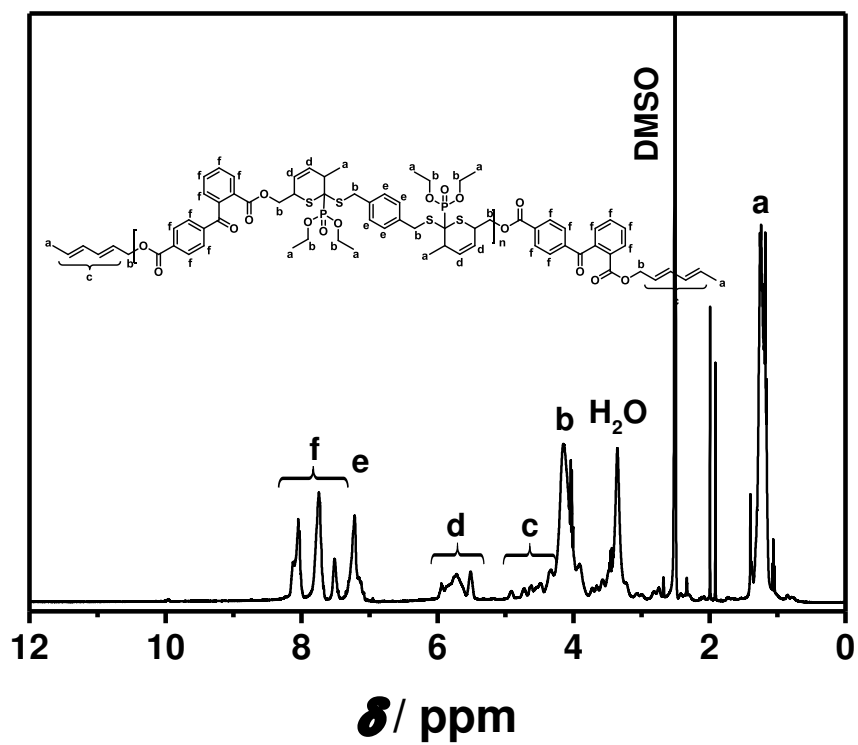
Fig. E 3 ^{1}H NMR (400 MHz, 298 K) spectrum of polymer (**22**) in DMSO-d$_6$. Not all potential isomers are depicted and assigned.
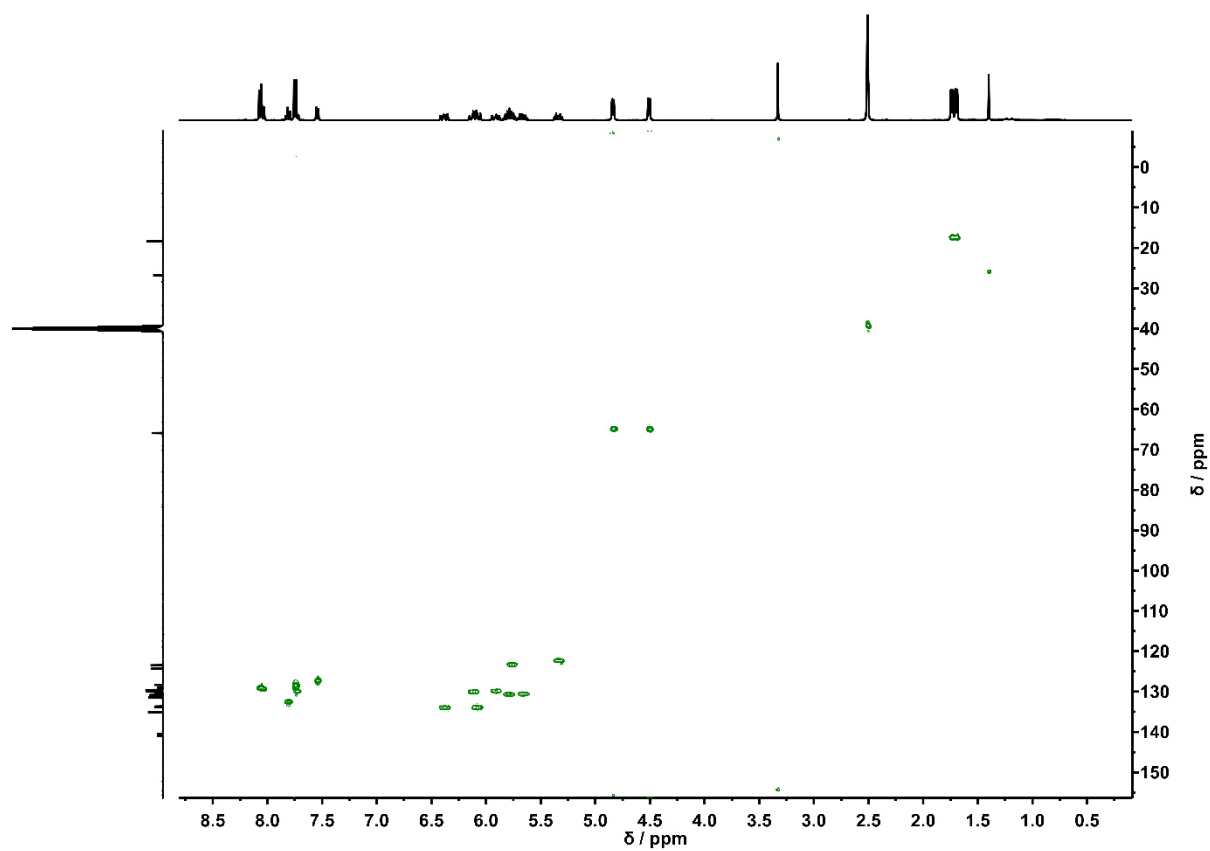

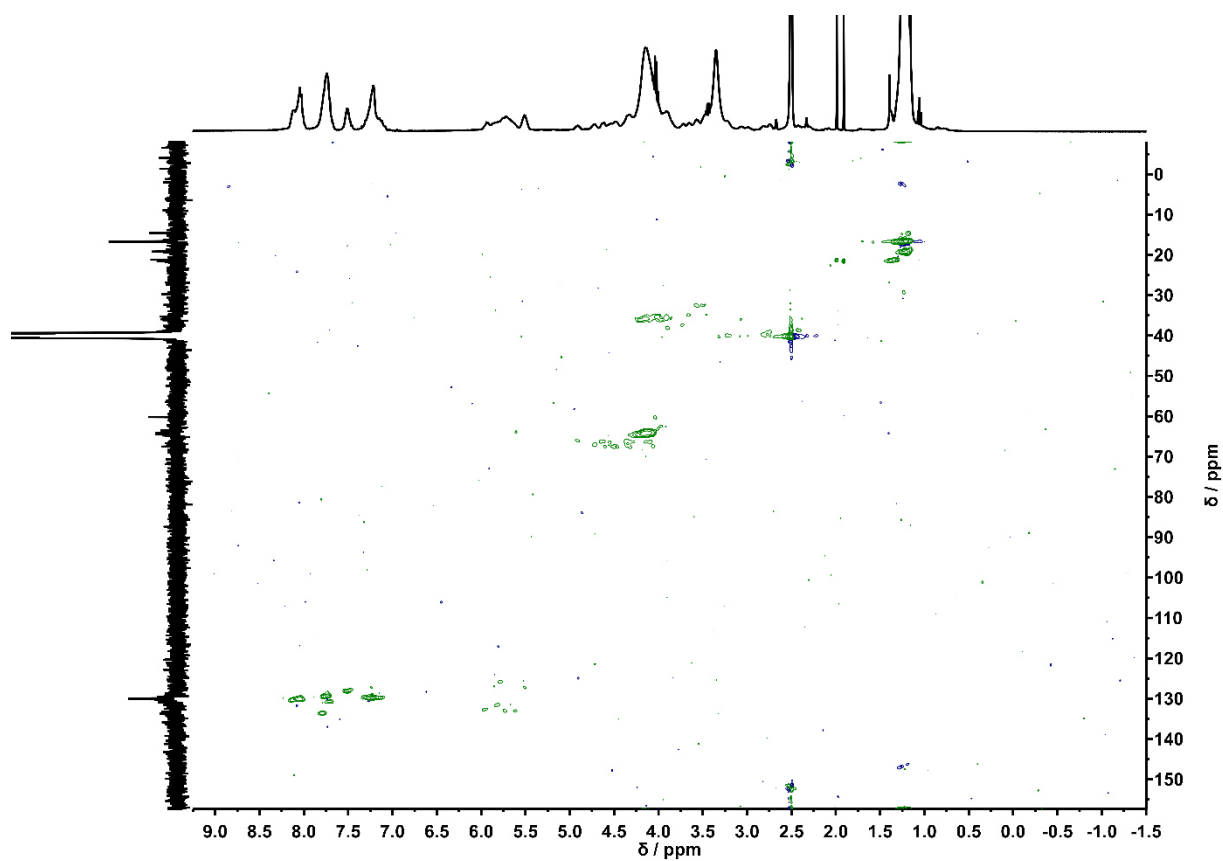Fig. E 4 ^{1}H-^{13}C HSQC (298 K) spectrum of **19a** in DMSO-d$_6$.

Fig. E 5 ^{1}H-^{13}C HSQC (298 K) spectrum of polymer **22** in DMSO-d$_6$.
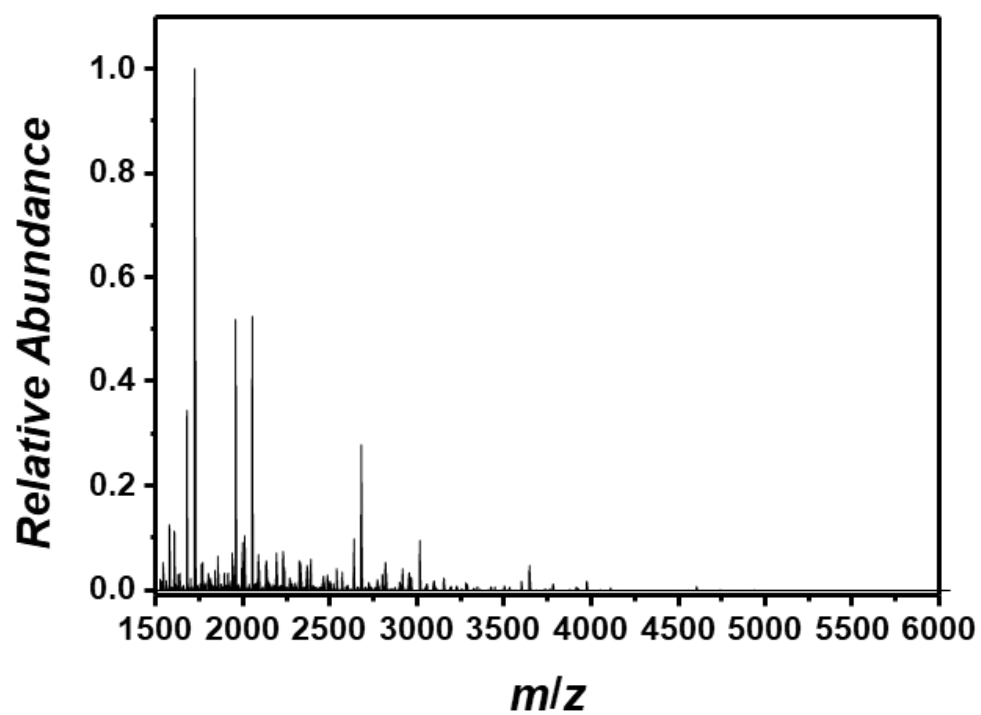
MS Data

Fig. E 6 ESI-Orbitrap mass spectrum of polymer **22** (M_n = 2200 g·mol^{-1}, M_w = 5600 g·mol^{-1}, $Đ$ = 2.19) recorded in negative ion mode in DCM:MeOH = 3:1 (v/v) from 1500 m/z to 6000 m/z.
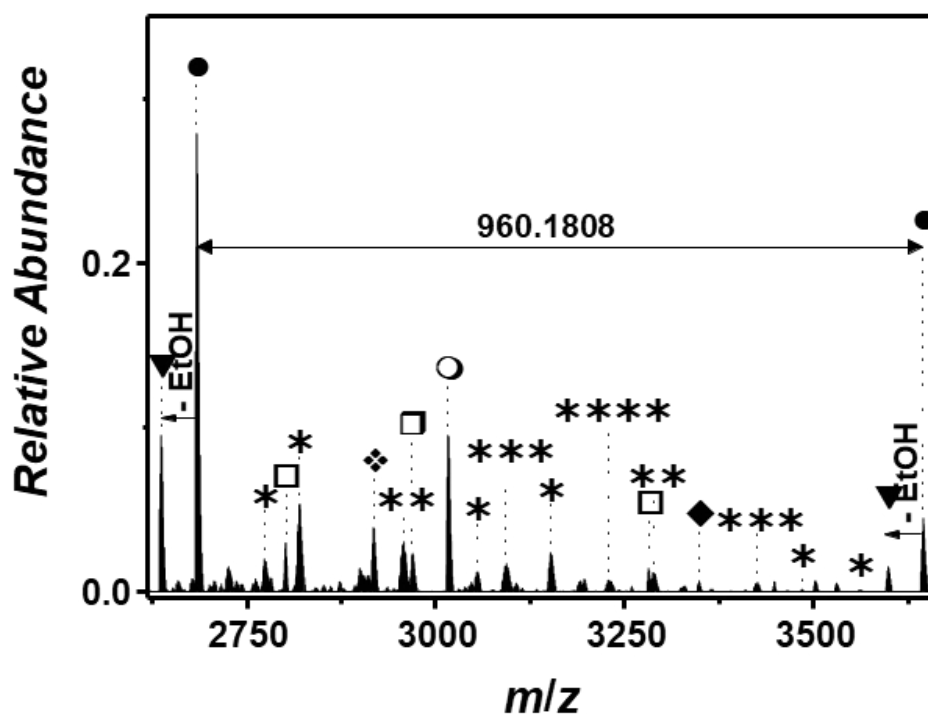
Fig. E 7 Expanded mass spectrum of polymer **22** (M_n = 2200 g·mol^{-1}, M_w = 5600 g·mol^{-1}, Đ = 2.19) displayed in a range between 2620 *m/z* to 3660 *m/z* depicting the repeating unit (m/z(exp) 960.1808; m/z(theo) 960.2024). Labeled are the most abundant species. Species labeled with ∗ stem from (multiple) attachment of ZnCl$_2$.

Tab. E 1 Peak assignment of the SEC-ESI Orbitrap mass spectrum of polymer **22** showing the labels (corresponding to the species in Fig. E 7), the resolution (obtained by the Xcalibur software), the experimental m/z and theoretical m/z values, $\Delta m/z$ and the proposed chemical structures. Minor species stemming from (multiple) attachment of $ZnCl_2$ or by elimination of EtOH are not depicted.

Label	Resolution	m/z(exp)	m/z(theo)	$\Delta m/z$	Structure
●	40000	2681.5327	2681.5450	0.0122	
□	37000	2798.5490	2798.5608	0.0118	
❖	40000	2915.5644	2915.5767	0.0123	
□	38000	2964.6035	2964.6132	0.0097	

CLXXII

| | 38000 | 3013.6313 | 3013.6498 | 0.0185 |
| | 35000 | 3345.7293 | 3345.7574 | 0.0254 |

CLXXIII
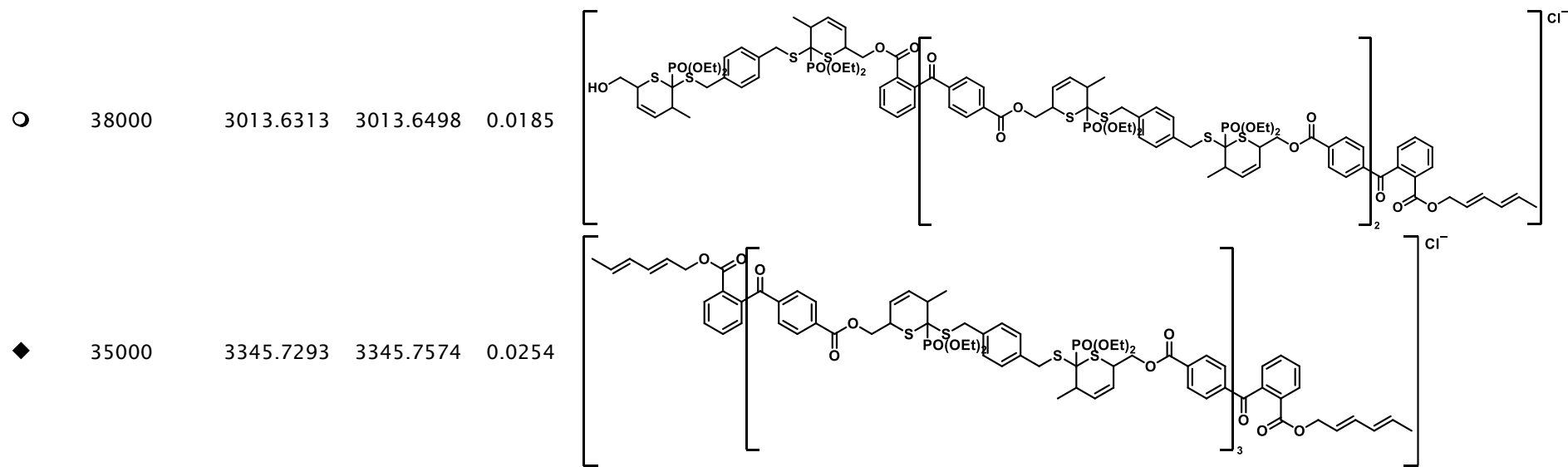
Fig. E 8 Isotopic simulation of a selected degradation species at 2015 *m/z* comparing the experiment (purple line) and the simulation (grey line) of degraded **22**. Since ZnCl$_2$ coordinates strongly to **22**, the slightly shifted low abundant peaks stem from polymer/ZnCl$_2$ complexes and are not assigned.
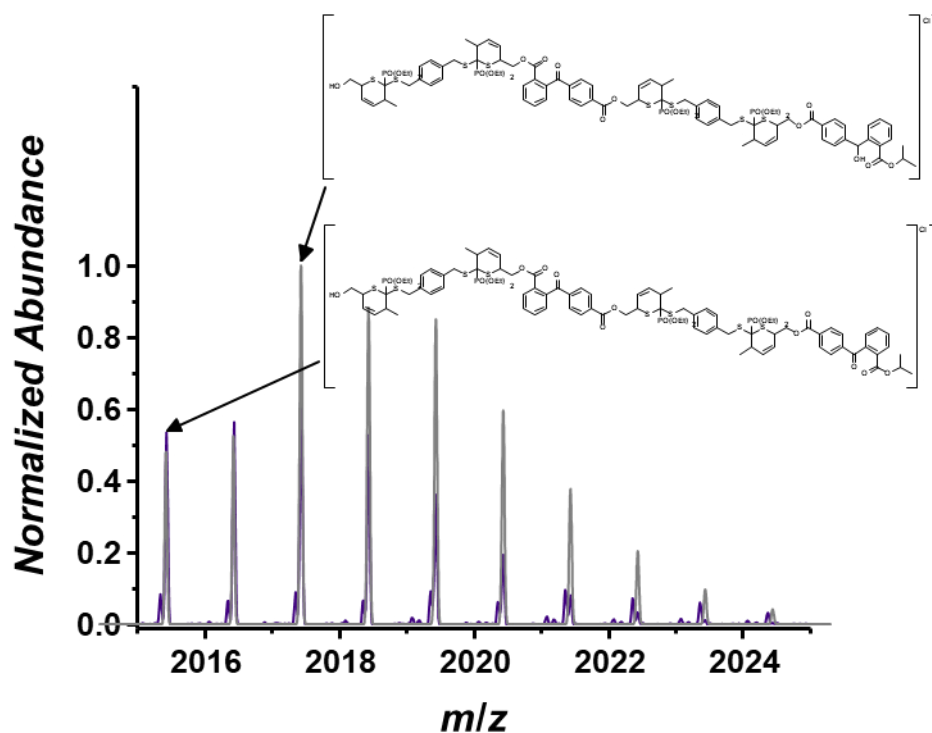

Fig. E 9 Isotopic simulation of a selected degradation species at 2091 m/z comparing the experiment (purple line) and the simulation (grey line) of degraded **22**. Since ZnCl$_2$ coordinates strongly to **22**, the slightly shifted low abundant peaks stem from polymer/ZnCl$_2$ complexes and are not assigned.

SEC-ESI MS data
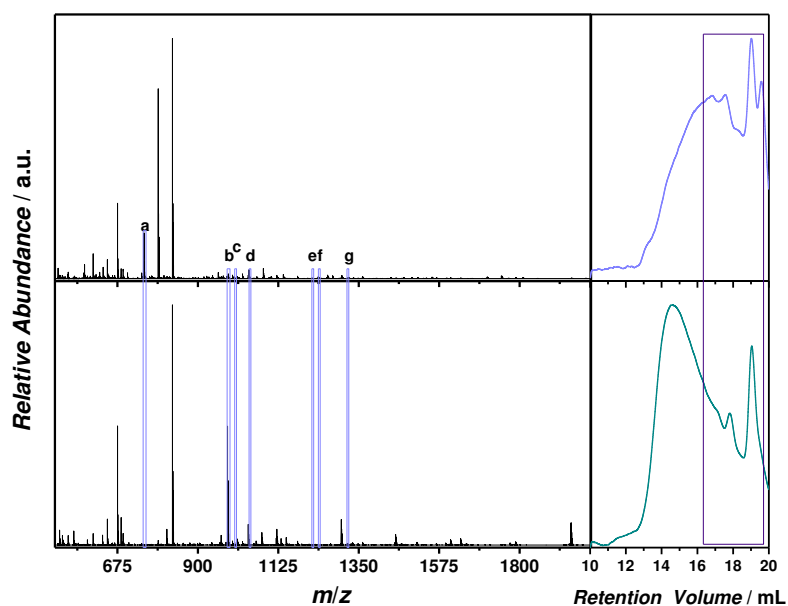
Fig. E 10 SEC-ESI Orbitrap mass spectrum (positive ion mode) of polymer **22** (bottom) and the degraded **22** (top) between 500 *m/z* and 2000 *m/z* obtained by summing all species between 16.33 mL and 19.70 mL retention volume. Labeled are the important degradation species (left). SEC traces obtained from the RI detector implemented in the SEC-ESI MS system of P1 (bottom) and the degraded P1 (top).
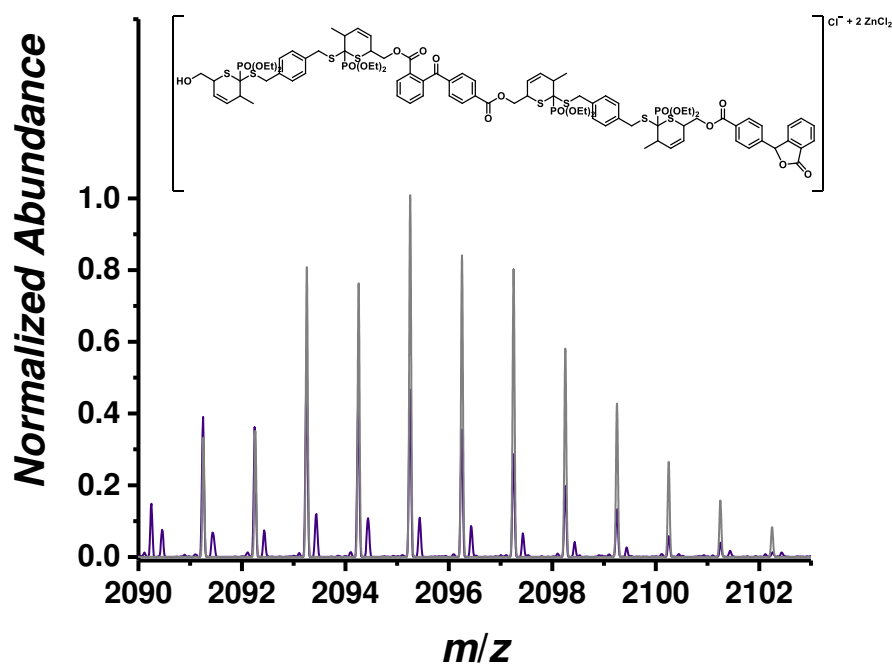

Fig. E 11 Isotopic simulation of a selected degradation species at 749 *m/z* comparing the experiment (purple line) and the simulation (grey line) of degraded **22** (bottom) with the intact polymer **22** (top).

Fig. E 12 Isotopic simulation of a selected degradation species at 985 *m/z* comparing the experiment (purple line) and the simulation (grey line) of degraded **22** (bottom) with the intact polymer **22** (top).

Fig. E 13 Isotopic simulation of a selected degradation species at 1003 *m/z* comparing the experiment (purple line) and the simulation (grey line) of degraded **22** (bottom) with the intact polymer **22** (top).

Fig. E 14 Isotopic simulation of a selected degradation species at 1043 *m/z* comparing the experiment (purple line) and the simulation (grey line) of degraded **22** (bottom) with the intact polymer **22** (top).
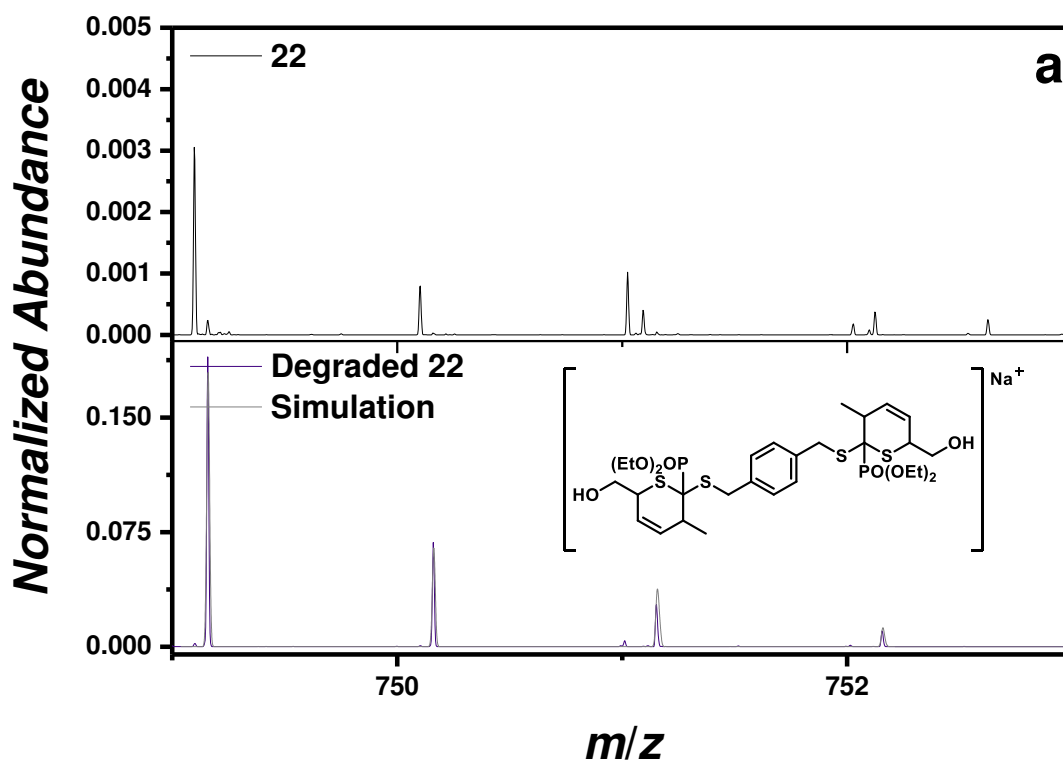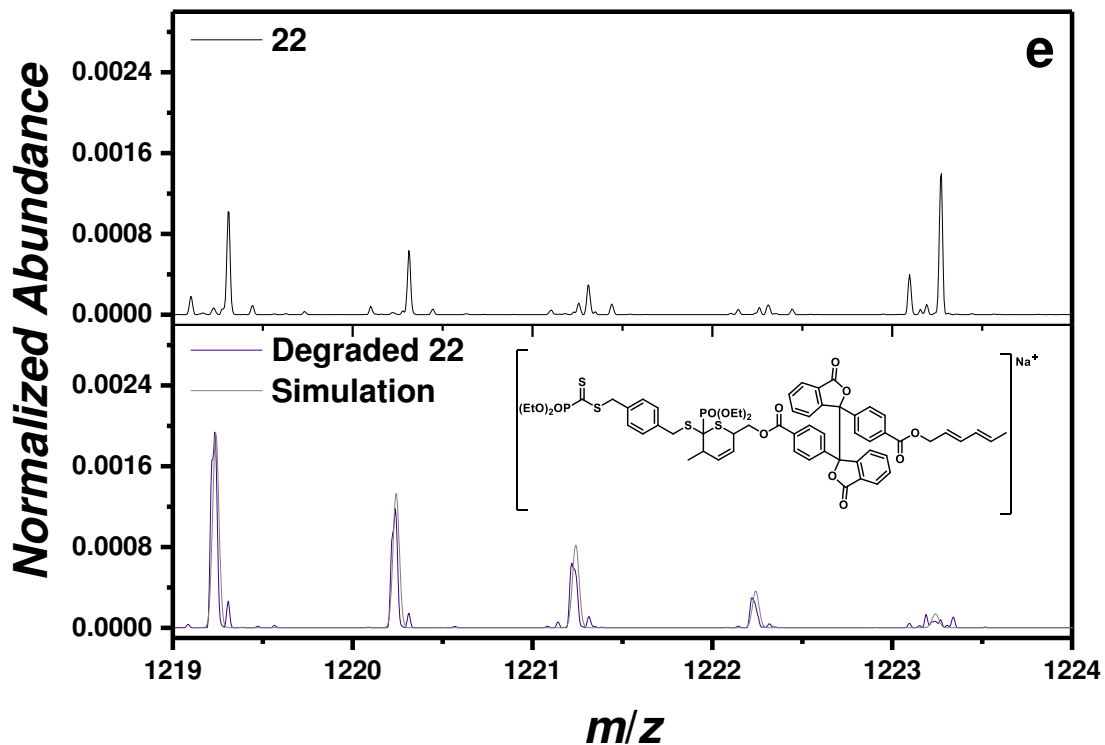

Fig. E 15 Isotopic simulation of a selected degradation species at 1219 *m/z* comparing the experiment (purple line) and the simulation (grey line) of degraded **22** (bottom) with the intact polymer **22** (top).
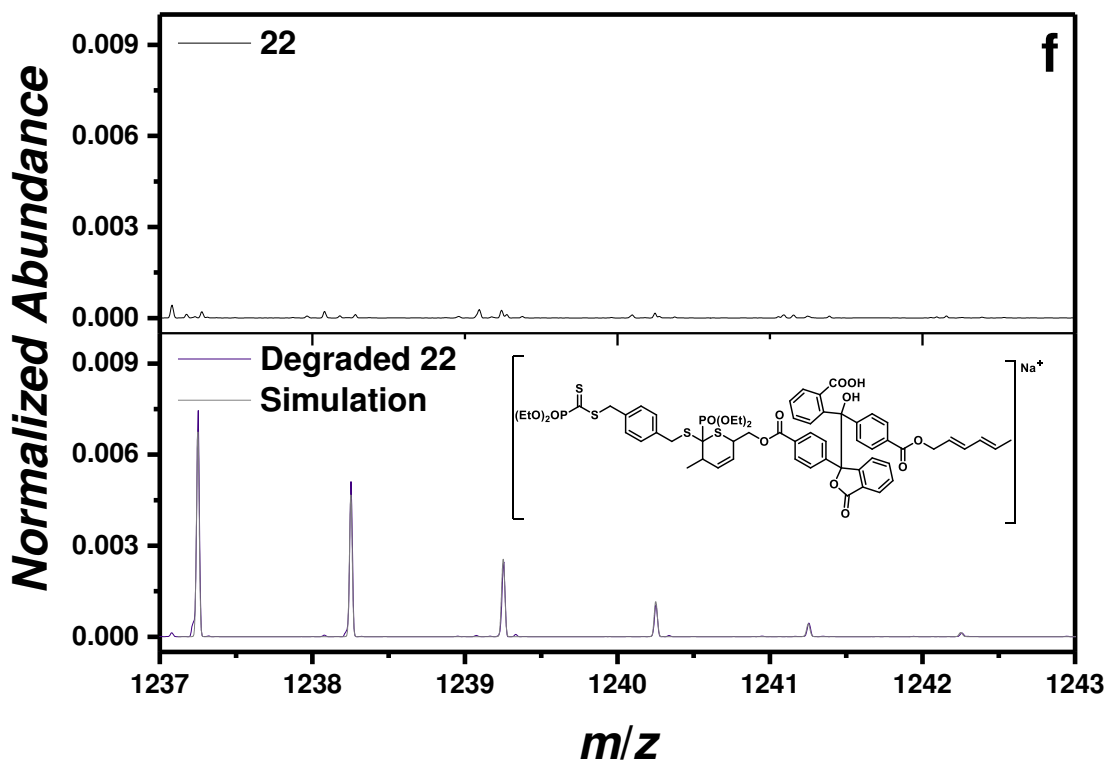
Fig. E 16 Isotopic simulation of a selected degradation species at 1237 *m/z* comparing the experiment (purple line) and the simulation (grey line) of degraded **22** (bottom) with the intact polymer **22** (top).
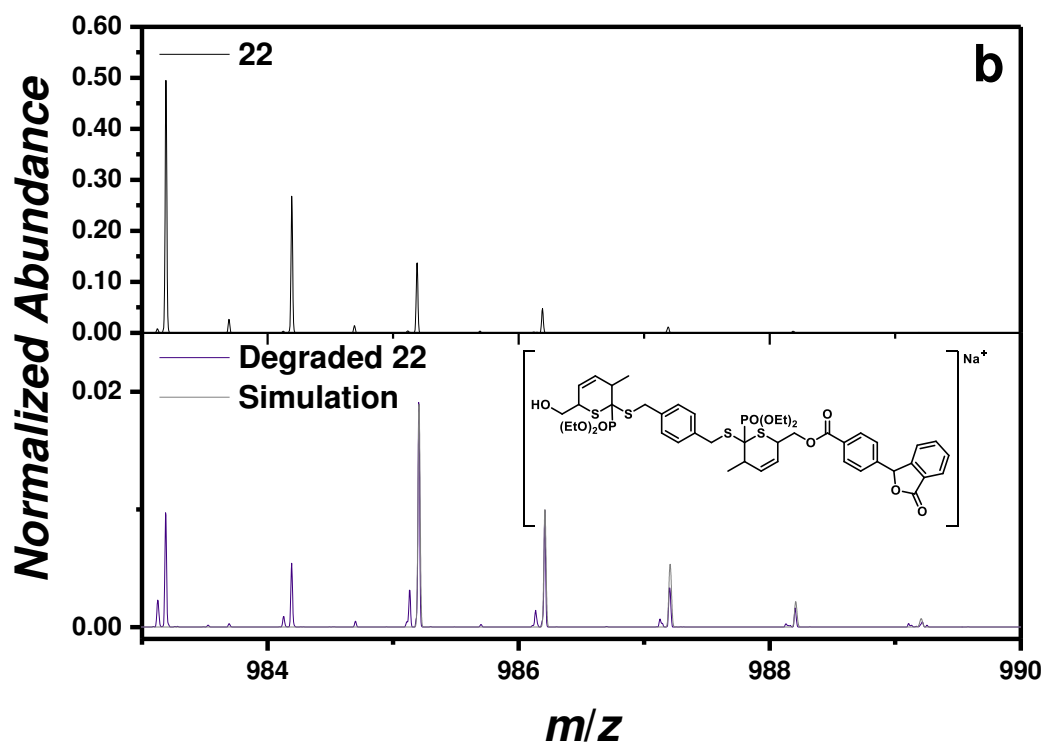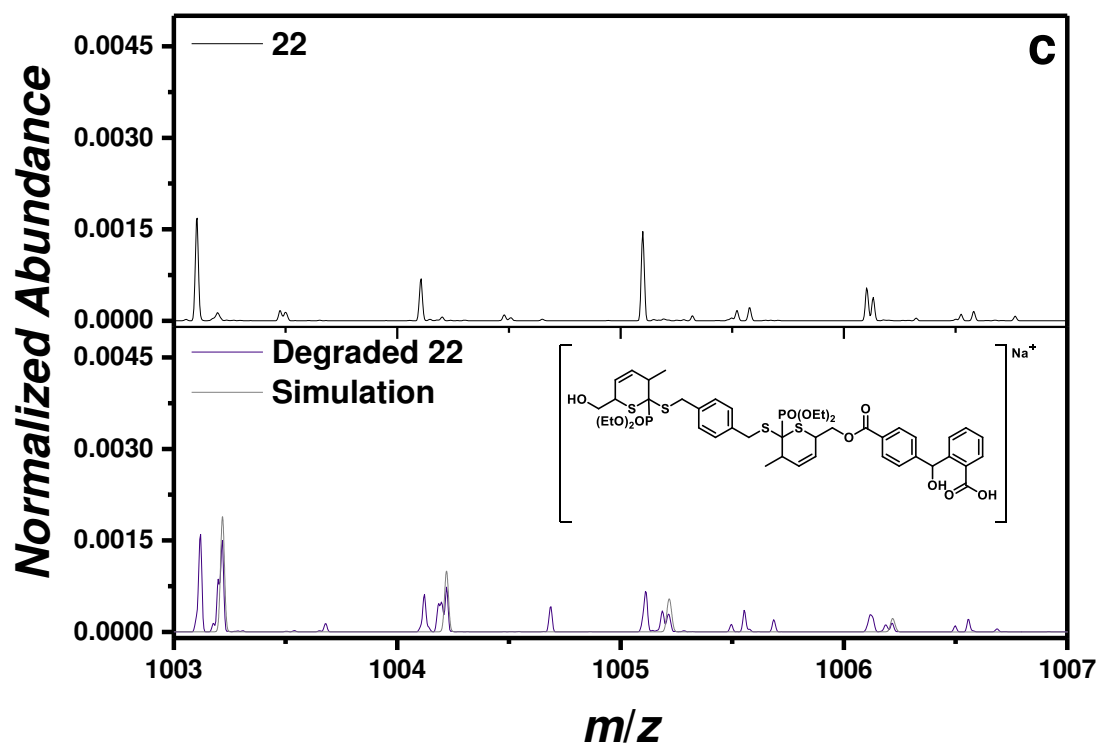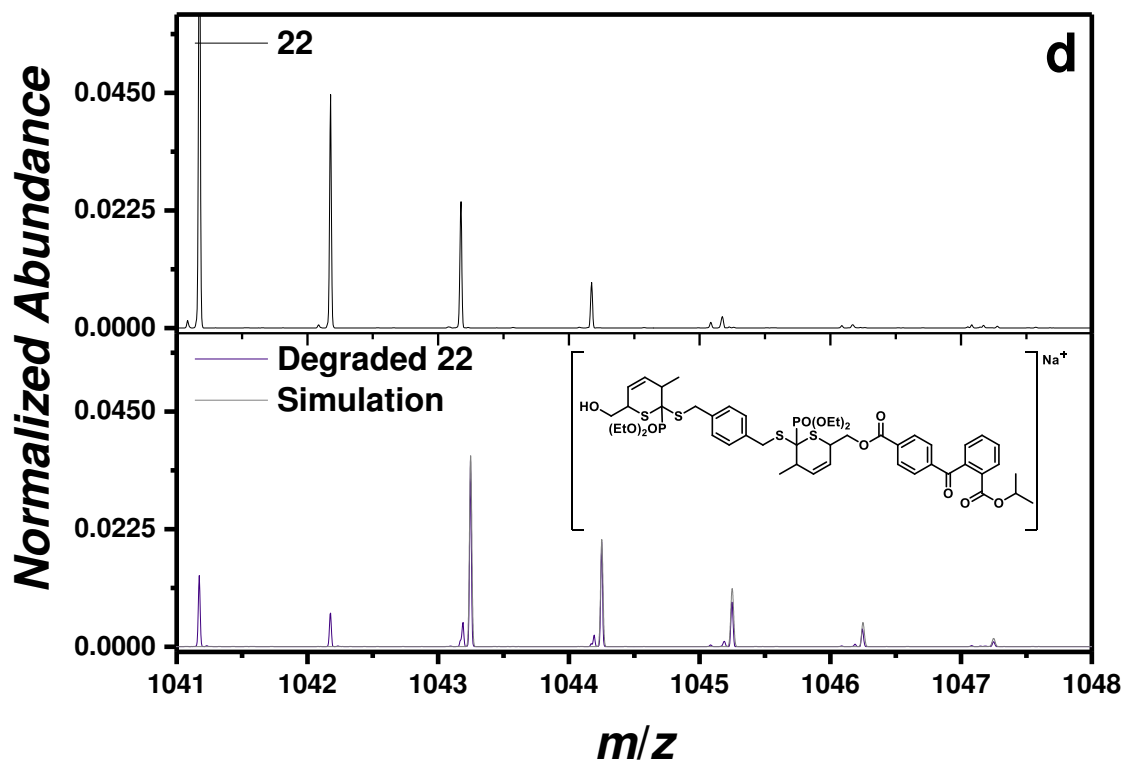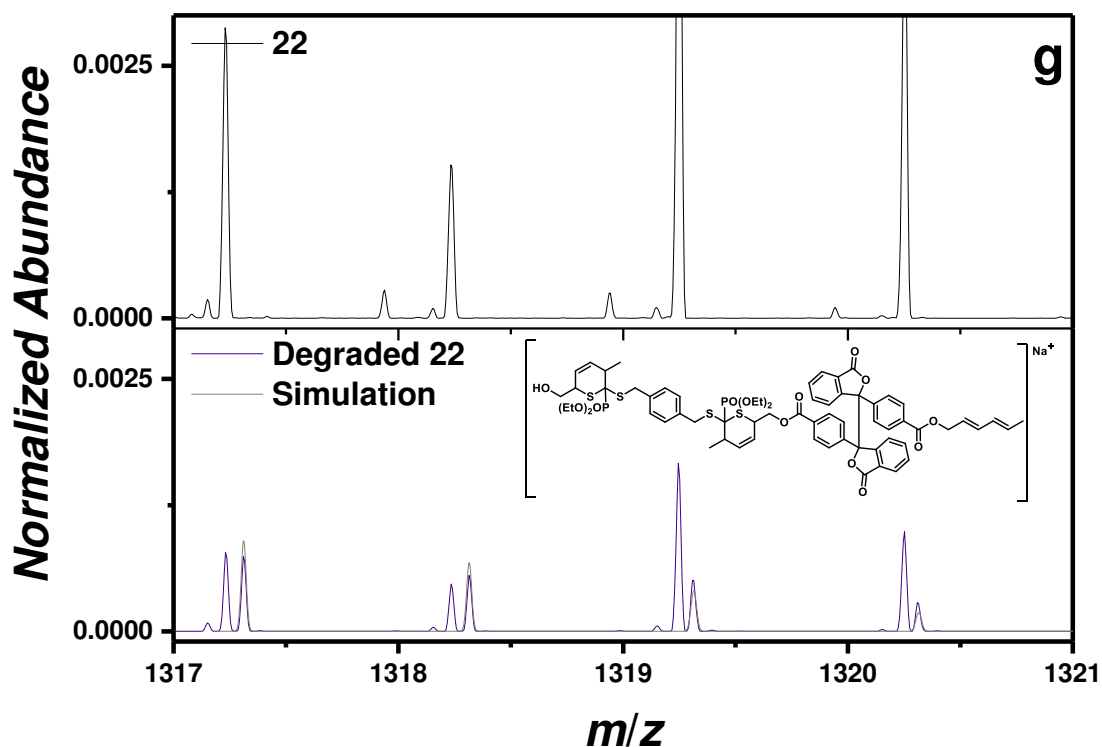

Fig. E 17 Isotopic simulation of a selected degradation species at 1317 *m/z* comparing the experiment (purple line) and the simulation (grey line) of degraded **22** (bottom) with the intact polymer **22** (top).

Set-up for irradiation experiments

The samples to be irradiated were placed on a metallic disc revolving around a compact low-pressure fluorescent lamp (Cleo PL-L, Philips Deutschland GmBH) emitting at 365 nm (±50 nm, 36 W) at a distance of 40-50 mm in a custom built photoreactor.

Fig. E 18 Emission spectrum of the employed compact low-pressure fluorescent lamp PL-L (36 W, λ_{max} = 365 nm). The emission spectrum was recorded with a UV sensor (Opsytec Dr. Gröbel GmbH; Ettlingen, Germany).

F

LIST OF ABBREVIATIONS

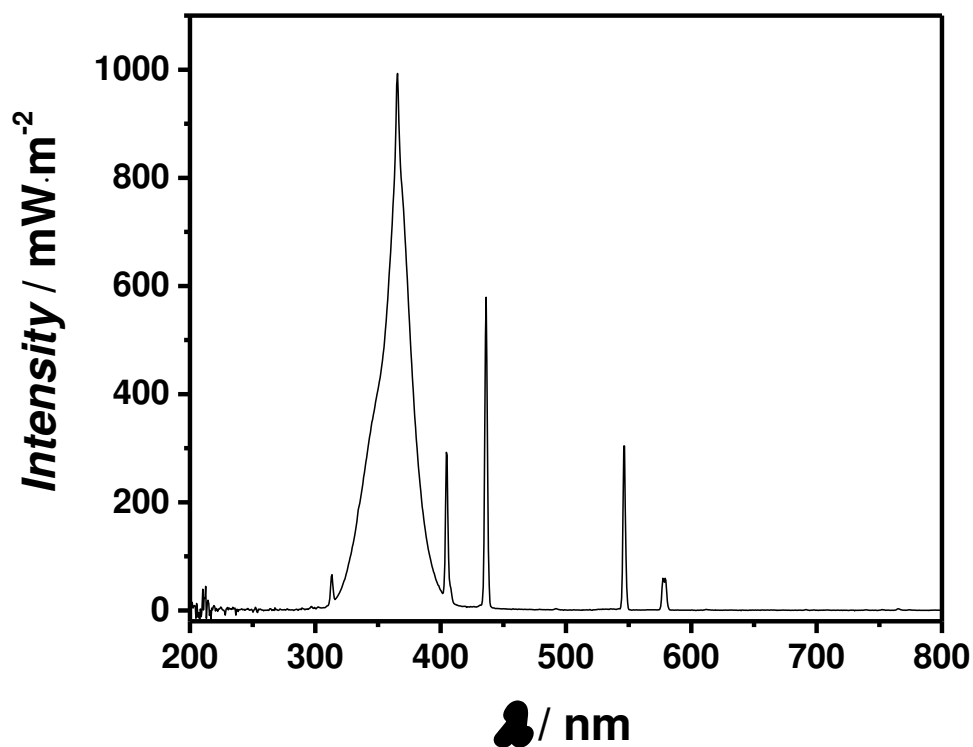|	
APTES	(3-aminopropyl)triethoxysilane
DoPAT	2-(dodecylthiocarbonothioylthio)propionic acid
AIBN	2,2′-azobis(2-methylpropionitril)
CPDT	2-cyano-2-propyl dodecyl trithiocarbonate
EtOz	2-ethyl-2-oxazine
EtOx	2-ethyl-2-oxazoline
MeOX	2-methyl-2-oxazoline
Upy	2-Ureido-4[1H]-pyrimidinone
DMAP	4-(dimethylamino)-pyridin
AVCA	4,4′-azobis(4-cyanovaleric acid)
4-carboxy-TEMPO	4-carboxy-2,2,6,6-tetramethylpiperidine 1-oxyl
MEHQ	4-methoxyphenol
MeCN	acetonitrile
AA	acrylic acid
Å	Angström
E	anti configuration
API	atmospheric pressure ionization
ATRP	atom transfer radical polymerization
AFM	atomic force microscopy
M_n	average number-weighted molecular weight
M_w	average wight-weighted molecular weight
BP	benzophenone
BuCN	butyronitrile
CEM	chain ejection model
CTA	chain transfer agents
CRM	charge residual model
CCD	charge-coupled device
δ	chemical shift in a magnetic field
CIEEL	chemically initiated electron-exchange luminescence
CID	collision induced dissociation
CSIRO	Commonwealth Scientific and Industrial Research Organisation
COSY	correlated spectroscopy
J	coupling constant
CIE	Cyclic imino ethers
Da	Dalton
°C	degree Celcius
DP_n	degree of polymerization
DANN	deoxyribonucleic acid
DCM	dichloromethane
DOSY	diffusion-ordered spectroscopy
DMSO	dimethyl sulfoxide
DMAc	dimethylacetamide
DMF	dimethylformamide

DMSO	dimethylsulfoxide
Đ	dispersity
dd	doublet of doublet
d	doublet; day
DLS	dynamic light scattering
eV	electron volt
ECD	electron-capture cross sections
ESI	electrospray ionization
eq	equivalents
et al.	et alii (
EtOH	ethanol
EtAc	ethyl acetate
EC	ethylene carbonate
e.g.	exempli gratia
FAB	fast atom bombardment
FT	Fourier transformation
GMA	glycidyl methacrylate
g	gramm
Hz	Hertz
HDA	hetero Diels-Alder
HSQC	heteronuclear single quantum coherence
HR	high resolution
HCD	higher-energy C-trap dissociation / higher-energy collision dissociation
HOMO	highest occupied molecular orbital
HPLC	high-pressure liquid chromatography
HT	high-termperature
h	hour
i.e.	id est
ICR	ion cyclotron resonance
IEM	ion ejection model
IL	ionic liquid
K	Kelvin
LACCC	liquid adsorption chromatography at critical conditions
LC	liquid chromatography
L	Liter
LUMO	lowest unoccupied molecular orbital
MADIX	macromolecular design by interchange of xanthates
MS	mass spectrometry
m/z	mass-to-charge ratio
MALDI	matrix assisted laser desoprtion ionization
MeOH	Methanol
MMA	methyl methacrylate
μ	micro
m	milli

m	milli; multiplet; meta
min	minutes
*m*NBA	*m*-nitrobenzyl alcohol
M	molar
MWCO	molecular weight cut off
MALLS	multi-angle laser light scattering
EDC·HCl	*N*-(3-Dimethylaminopropyl)-*N*′-ethylcarbodiimide hydrochloride
nm	nanometer
NIR	near infrared
NMP	Nitroxide-mediated polymerization
NMR	nuclear magnetic resonance spectroscopy
1D	one dimensional
o	ortho
p	para
ppm	part per million
PE	Photo-Enol
p([BVBIM]Tf$_2$N)	poly(1-butyl-3-(*p*-vinylbenzyl)-1*H*-imidazol-3-ium bis(trifluoromethanesulfonyl)imide)
p([BVBIM]Cl	poly(1-butyl-3-(p-vinylbenzyl)-1H-imidazolium chloride)
P(2VP)	poly(2-vinylpyridine)
P(AAm)	poly(acrylamide)
PBD	poly(butadiene)
PEA	poly(ester amide)
PEG	poly(ethylene glycol)
PEO	poly(ethylene oxide)
PIL	poly(ionic liquid)
PLA	poly(lactide)
PMA	poly(methyacrylate)
PPE	poly(phosphoester)s
PS	poly(styrene)
p(S-*stat*-VBC	poly(styrene-*stat*-vinylbenzyl chloride)
PVBC	poly(vinylbenzyl chloride)
PSS	Polymer Standard Service
PC	propylene carbonate
Q	quadrupole
RF	radiofrequency
RI	refractive index
RAFT	reversible addition-fragmentation chain transfer
RDRP	reversible-deactivation radical polymerization
ROP	ring-opening polymerization
RTIL	room temperature ionic liquid
SIMS	secondary ion mass spectrometer
s	seconds; singulet
S/N	signal-to-noise
SCNP	single-chain polymeric nanoparticle

SEC	size-exclusion chromatography
SAXS	small angle X-ray scattering
SLD	soft laser desorption
SZWIP	spontaneous zwitterionic copolymerization
stat	statistically copolymerized
STED	stimulated emission depletion
Z	syn configuration
MS/MS	tandem mass spectrometry
THF	tetrahydrofuran
3D	three dimensional
ToF	time-of-flight
TEM	transmission electron spectroscopy
TEA	triethylamine
TFA	trifluoroacetic acid
t	triplett
2D	two dimensional
UV	ultraviolet
v/v	volume percent
W	watt
WCA	weakly coordinating anion
w/w	weight percent
XPS	X-ray photoelectron spectroscopy

G

ACKNOWLEDGEMENTS

Although the thesis represents the work of a single PhD candidate, there are many people to acknowledge for their passionate contributions.

Firstly – and most importantly – I want to thank my PhD supervisor Christopher Barner-Kowollik, who gave me the chance to work in his team. The time I started my first project as an undergraduate, I did not know what to expect. Christopher's character embodies the passion to his profession, which makes it a pleasure to work with him. His encouraging handling of challenging situations in both, academic and personal life, is crucial to endure the burden that a PhD thesis sometimes can be. I will never forget the hours you spent to improve the manuscripts. I am forever grateful for what I learned during these periods. I will never forget how you sacrificed public holidays for paper submissions and how we spent hours of hours replying to reviewers' comments. I am grateful for all your support in my research interests. Starting my PhD, I would have never imagined the results of the current PhD

thesis. I will never forget when you announced that you would move to Australia, but I knew it would be the greatest adventure in my life – so far. I want to thank you for giving me the chance of being part of the QUT node for almost an entire year and to taste the life at the other side of the world. Christopher's devotion to his work and his entire group is admirable.

Secondly, my profound gratitude goes to Anja Goldmann. Thanks for adopting me as an undergraduate and to introduce me into a fascinating world of research. I will never forget our private conversations and your fantastic work in every aspect of Macroarc. You keep the show running!

Thirdly, I want to thank all my cooperation partners for the great collaborations we had. Most importantly, Martina M. Cecchini, who came to Karlsruhe for a short research stay and who became a close friend during that time. I will always keep our conversations in good memory. It was interesting how we empowered one another and pushed three publications from the very beginnings to entire projects. Thanks that you returned for a second – though shorter – stay. The Helium catastrophe will always be an anecdote I will love to tell. We deserved the Caipirinha at the end of this stressful day! As I believe that our paths will cross again, I am looking forward to what the future will provide.

Furthermore, I would like to thank all further research partners all over the world including Jiayin Yuan, Peter Roesky, Francesco de Angelis, Samantha Reale, Kristian Kempe, Patrick De Jongh and David Haddleton for amazing collaborations and fruitful discussions. Thank you, Kristian, for taking care of Anja and me as we were stranded in Melbourne.

Special thanks to Hatice Mutlu. The time you told me about your research I knew that it was special and unique. I will never forget how you spent all the time designing projects and supervising them. Profoundly gratefully I acknowledge that you thought me how to design my own research projects. Thank you for everything, for all the wonderful discussions, and intercontinental Skype meetings!

Thanks Charlotte for being part of the team. You accompanied me in my darkest hours. I will always keep our conversations in good memory and hope to visit you wherever you are.

Andrea, I miss our joined apartment already. Right now – typing these lines – I am taking a close look on every detail of our Australian home: the view from the 13th floor, the pool, the small kitchen and the ugly mustard-colored chair. God knows why

Bek bought this one. I will never forget your farewell party (although I forgot a lot already). Thanks for all the coffee hours and conversations. I am looking forward to our PhD party!

Special thanks to Doris and Kilian for our balcony summer events – and to Peggy for the balcony winter events. Thank you Peggy, for the many voice mails we exchanged, for the phone calls until your battery died and that you thought me many tricks for organic synthesis. I am sure we will collaborate at some point in the future! (An Inge is regarded as a collaboration!)

Special thanks to all Macroarcians on both continents and the Alumni. You are awesome! Hope to see some of you again in the future!

Thank you, Fabian, for your Bachelor thesis under my supervision and the time in our apartment. I had a wonderful time with you. Keep up the good work.

Katharina, Vincent and Miss Schneider: Thank you all for you passionate work!

Special thanks to Pavleta. I am profoundly grateful for the endless hours we spent at the NMR to fix the mismatched shims and to clean the probe head.

Thank you all for proof reading: Bryan, Christiane, Hannah, Anja, Eva, Charlotte, Hatice and Tobi.

Thanks to all of you who accompanied me during work and to those who become close friends with me. In particular, I want to thank Tobi. Although we know each other since the beginning of our studies, it was wonderful to experience a new side of you after my arrival in Australia. I am a person who believes in second changes in life. Keep the head up.

Meiner Familie gilt natürlich mein größter Dank. Ohne die emotionale und finanzielle Unterstützung meiner Eltern, Elke und Ralph, wäre das alles nicht möglich gewesen. Ich danke euch für euer Vertrauen!